Nanoscience & Nanotechnology Series

Carbon Nitride Nanostructures for Sustainable Energy Production and Environmental Remediation

Edited by Kamel Abdelmoniem Mohamed Eid
and Aboubakr M. Abdullah

ROYAL SOCIETY OF CHEMISTRY

Carbon Nitride Nanostructures for Sustainable Energy Production and Environmental Remediation

Nanoscience & Nanotechnology Series

Editor-in-chief:
Nguyễn T. K. Thanh, *University College London, UK*

Series editors:
Gabriel Caruntu, *Central Michigan University, USA*
Shinya Maenosono, *Japan Advanced Institute of Science and Technology, Japan*
Neerish Revaprasadu, *University of Zululand, South Africa*

Titles in the series:
1: Nanotubes and Nanowires
2: Fullerenes: Principles and Applications
3: Nanocharacterisation
4: Atom Resolved Surface Reactions: Nanocatalysis
5: Biomimetic Nanoceramics in Clinical Use: From Materials to Applications
6: Nanofluidics: Nanoscience and Nanotechnology
7: Bionanodesign: Following Nature's Touch
8: Nano-society: Pushing the Boundaries of Technology
9: Polymer-based Nanostructures: Medical Applications
10: Metallic and Molecular Interactions in Nanometer Layers, Pores and Particles: New Findings at the Yoctolitre Level
11: Nanocasting: A Versatile Strategy for Creating Nanostructured Porous Materials
12: Titanate and Titania Nanotubes: Synthesis, Properties and Applications
13: Raman Spectroscopy, Fullerenes and Nanotechnology
14: Nanotechnologies in Food
15: Unravelling Single Cell Genomics: Micro and Nanotools
16: Polymer Nanocomposites by Emulsion and Suspension
17: Phage Nanobiotechnology
18: Nanotubes and Nanowires, 2nd Edition
19: Nanostructured Catalysts: Transition Metal Oxides
20: Fullerenes: Principles and Applications, 2nd Edition
21: Biological Interactions with Surface Charge Biomaterials
22: Nanoporous Gold: From an Ancient Technology to a High-tech Material
23: Nanoparticles in Anti-microbial Materials: Use and Characterisation
24: Manipulation of Nanoscale Materials: An Introduction to Nanoarchitectonics
25: Towards Efficient Designing of Safe Nanomaterials: Innovative Merge of Computational Approaches and Experimental Techniques
26: Polymer–Graphene Nanocomposites
27: Carbon Nanotube-polymer Composites
28: Nanoscience for the Conservation of Works of Art
29: Polymer Nanofibers: Building Blocks for Nanotechnology
30: Artificial Cilia

31: Nanodiamond
32: Nanofabrication and its Application in Renewable Energy
33: Semiconductor Quantum Dots: Organometallic and Inorganic Synthesis
34: Soft Nanoparticles for Biomedical Applications
35: Hierarchical Nanostructures for Energy Devices
36: Microfluidics for Medical Applications
37: Nanocharacterisation, 2nd Edition
38: Thermometry at the Nanoscale: Techniques and Selected Applications
39: Nanoceramics in Clinical Use: From Materials to Applications, 2nd Edition
40: Near-infrared Nanomaterials: Preparation, Bioimaging and Therapy Applications
41: Nanofluidics, 2nd Edition
42: Nanotechnologies in Food, 2nd Edition
43: ZnO Nanostructures: Fabrication and Applications
44: Diatom Nanotechnology: Progress and Emerging Applications
45: Nanostructured Materials for Type III Photovoltaics
46: Chemically Derived Graphene: Functionalization, Properties and Applications
47: Graphene-based Membranes for Mass Transport Applications
48: Carbon Nanostructures for Biomedical Applications
49: Surface Chemistry of Colloidal Nanocrystals
50: Reducing Agents in Colloidal Nanoparticle Synthesis
51: Carbon Nitride Nanostructures for Sustainable Energy Production and Environmental Remediation

How to obtain future titles on publication:
A standing order plan is available for this series. A standing order will bring delivery of each new volume immediately on publication.

For further information please contact:
Book Sales Department, Royal Society of Chemistry, Thomas Graham House, Science Park, Milton Road, Cambridge, CB4 0WF, UK
Telephone: +44 (0)1223 420066, Fax: +44 (0)1223 420247
Email: booksales@rsc.org
Visit our website at www.rsc.org/books

Carbon Nitride Nanostructures for Sustainable Energy Production and Environmental Remediation

Edited by

Kamel Abdelmoniem Mohamed Eid
Qatar University, Qatar
Email: kamel.eid@qu.edu.qa

and

Aboubakr M. Abdullah
Qatar University, Qatar
Email: bakr@qu.edu.qa

ROYAL SOCIETY OF CHEMISTRY

Nanoscience & Nanotechnology Series No. 51

Print ISBN: 978-1-83916-213-8
PDF ISBN: 978-1-83916-460-6
EPUB ISBN: 978-1-83916-461-3
Print ISSN: 1757-7136
Electonic ISSN: 1757-7144

A catalogue record for this book is available from the British Library

The Royal Society of Chemistry is a charity, registered in England and Wales, Number 207890, and a company incorporated in England by Royal Charter (Registered No. RC000524), registered office: Burlington House, Piccadilly, London W1J 0BA, UK, Telephone: +44 (0) 20 7437 8656.

For further information see our web site at www.rsc.org

Printed in the United Kingdom by CPI Group (UK) Ltd, Croydon, CR0 4YY, UK

Biographies

Dr Kamel Eid was awarded a BSc from Al-Azhar University, Egypt, in 2005, MSc from Helwan University, Egypt in 2011, and PhD from the Chinese Academy of Sciences, China in 2016. Kamel has 12 years of experience in academia as well as two years in industry with nearly 65 published peer-reviewed articles in prestigious international journals including 14 articles in journals of the Royal Society of Chemistry such as Chemical Science, Nanoscale, Material Chemistry A, and Catalysis Science and Technology, as well as American Chemical Society publications such as Journal of the American Chemical Society, Langmuir, and Physical Chemistry C. In addition to participating in more than 30 international conferences in China, USA, UK, and Turkey such as MRS and ACS Meetings, Kamel has filed 10 US patents including 3 published and 1 granted. All patents are in the field of nanomaterials for water treatment, water desalination, CO/CO_2 conversion to fuels, and biomedical sensors. Kamel was the first PhD graduate student from the TWAS-UCAS Chinese Academy of Sciences in 2016. He was given the opportunity to work in prominent universities such as the American University in Cairo, Egypt; Chinese Academy of Sciences, China; and Zhejiang University of Technology, China. These opportunities allowed Kamel to develop an extensive experience and solid background in the field of nanotechnology and nanoscience including the development of novel methods for the fabrication of nanomaterials and their utilization in various applications to energy production and energy conversion technologies, including fuel cell and gas conversion reactions, and environmental remediation applications such as water desalination, and water treatment.

Nanoscience & Nanotechnology Series No. 51
Carbon Nitride Nanostructures for Sustainable Energy Production and Environmental Remediation
Edited by Kamel Abdelmoniem Mohamed Eid and Aboubakr M. Abdullah

Published by the Royal Society of Chemistry, www.rsc.org

Dr Aboubakr has 28 years of experience in academia and industry. He has published more than 150 peer-reviewed and conference proceedings articles in addition to four patents. He was awarded his BSc and MSc from The Chemistry Department, Faculty of Science, Cairo University, Egypt in 1993 and 1997, respectively, and PhD in Materials Science and Engineering from Pennsylvania State University, USA in 2003. Later, he worked as a postdoc in Kuwait University (2004–2006), Kuwait; Tokyo Institute of Technology (2006–2009), Japan; and University of Calgary (2009), AB, Canada. Since he joined The Center for Advanced Materials, Qatar University, Doha, Qatar, in 2012, he has managed more than ten research mega-projects funded from different agencies inside and outside Qatar, *e.g.*, Qatar National Research Fund (QNRF), Qatar University, Hydro/Qatalum, Qatar Petroleum (QP) and Qatar Shell (QS). He has undertaken several consultancy assignments for many different companies, *e.g.*, Ras Gas (now merged with Qatar Gas), Qatar Gas, Qatalum, Qatar Electricity and Water Company (QEWC), and Egyptian Liquefied Natural Gas (ELNG). He has also participated and worked in many projects under his ex supervisors at the beginning of his career, funded by International companies, *e.g.*, Aluminum Company of America (ALCOA, USA), Ballard (BC, Canada), and SANYO (Osaka, Japan). Furthermore, he has supervised 11 young professionals at Masters and PhD levels.

Dedication

This book is dedicated to my father, Abdelmoniem Mohamed Eid, who died on 29 December 2020 after long suffering from liver cancer. My dear father, without a shadow of a doubt, I know that I was your favorite son, although you did not reveal that, and I also consider you the most important person in my life. You taught me patience, self-confidence, and ambition. My father, I will always remember you and hope that anyone who reads this book wishes you all the best and asks mercy, blessing, and forgiveness.

Dr Kamel Eid

Nanoscience & Nanotechnology Series No. 51
Carbon Nitride Nanostructures for Sustainable Energy Production and Environmental Remediation
Edited by Kamel Abdelmoniem Mohamed Eid and Aboubakr M. Abdullah

Published by the Royal Society of Chemistry, www.rsc.org

Preface

The rational fabrication of graphitic carbon nitrides (gCNs) and their utilization in a wide range of energy and environmental remediation applications is a growing research area, especially in the last two decades. However, hitherto a book related to this area of research has not been published. Thereby, this book is dedicated to emphasizing the state-of-the-art of gCNs nanostructures and their related fundamentals, mechanisms, and utilization in multidisciplinary energy production, energy conversion, and environmental remediation applications. We strive to cover the achievements in the fabrication approaches of gCN nanostructures using various chemical and physical approaches besides modulating their properties. The book includes 9 chapters. The template-based and template-free fabrication methods of one-dimensional (1D) gCN nanostructures (*i.e.*, nanotubes, nanorods, nanofibers, and needles), and their mechanisms for thermal CO oxidation reaction are included in Chapter 1. Chapter 2 unveils gCNs, mainly g-C_3N_4-based chemiluminescence (CL) and electrochemiluminescence (ECL) sensors for using the top-down route and bottom-up route for the detection of organic or inorganic molecules and biomolecules (*i.e.*, nucleic acids, biomarkers, proteins, and cell-related determination, enzyme activity, and pharmaceutical ingredients). Chapter 3 discusses the utilization of gCNs in electrochemical energy conversion technologies, comprising fuel cell reactions (*i.e.*, oxygen reduction, alcohol oxidation, and water splitting) and energy production/storage (*i.e.*, supercapacitor and Li-ion batteries). Chapter 4 discloses the synthesis of self-standing and modified gCNs for water-splitting reactions from a theoretical view and related fundamentals. The win–win combination of a hybrid g-C_3N_4/polymer and g-C_3N_4-derived hydrogel materials for advanced applications are discussed in Chapter 5. This includes the photoinitiator,

Nanoscience & Nanotechnology Series No. 51
Carbon Nitride Nanostructures for Sustainable Energy Production and Environmental Remediation
Edited by Kamel Abdelmoniem Mohamed Eid and Aboubakr M. Abdullah

Published by the Royal Society of Chemistry, www.rsc.org

dispersibility, photocatalytic and mechanical properties of the hybrid g-C_3N_4/polymer and its modification for novel applications such as biosensors, electrochemical energy storage, photocatalysis, batteries, H_2 evolution, and thin films. Chapter 6 underlines the atomic and molecular functionalization of gCNs (*i.e.*, coating, assembling, solid/liquid mediated growth, and gas-phase noncontact growth) for solar cell devices (*i.e.*, dye-sensitized, organic, perovskite, and quantum dot solar cells).

Chapter 7 reports the recent achievements in the design of hybrid gCN-based devices for energy production and storage applications involving Li-ion batteries (LIBs), Li–S batteries (LSBs), and supercapacitors. Chapter 8 comprises the fabrication of hybrid gCN heterojunctions (*i.e.*, type II Z-scheme) and gCN composites (*i.e.*, metal/metal oxide, non-metal, and carbon) for the adsorption and photocatalytic reduction of CO_2. Chapter 9 summarizes the preparation of gCNs (*i.e.*, exfoliation, supramolecular assembly, molten and ionic liquid salt, hydrothermal technique, sol–gel technique, microwave, and sonication methods) and modulating the properties of gCNs for photocatalytic hydrogen generation and environmental remediation (*i.e.*, degradation of organic pollutants, dyes, and hydrogen production). All chapters discuss the practical applications of gCNs for energy production and environmental applications and their future outlook and new research directions that should be highlighted in the future.

This book could pave the way for new research entries of physicists, engineers, chemists, material scientists, students, and people working in industry to fabricate the next generation of gCN nanostructures with ameliorated performances for the development of novel renewable energy conversion devices and sustainable environments.

In pursuit of this aim, we have invited various well-known scientific pioneers who have made extensive achievements in the field of gCNs and their utilization in various applications to contribute with us in editing the book.

We greatly appreciate the time and effort of the authors and co-authors dedicated to editing the book. Lastly, we are grateful to Lewis Pearce and Katie Morrey, from the Royal Society of Chemistry, for their continuous support with the book's preparation and editing up to its final stages and publication. Lewis and Katie replied to our e-mails promptly and provided us with any help or assistance that we needed.

Kamel Eid,
Gas Processing Center, College of Engineering,
Qatar University, Qatar.

Aboubakr M. Abdullah,
Center for advanced materials,
Qatar University, Qatar.

Contents

Nanoscience & Nanotechnology Series No. 51
Carbon Nitride Nanostructures for Sustainable Energy Production and Environmental Remediation
Edited by Kamel Abdelmoniem Mohamed Eid and Aboubakr M. Abdullah

Published by the Royal Society of Chemistry, www.rsc.org

CHAPTER 1

Recent Advances in the Controlled Design of One-dimensional Carbon Nitrides for Thermal CO Oxidation Reaction

KAMEL EID*[a], SARAH MOHAMMED HAILAN[b], YASSEEN S. IBRAHIM[b], BELAL SALAH[b] AND ABOUBAKR M. ABDULLAH*[a]

[a]Gas Processing Center, College of Engineering, Qatar University, Doha 2713, Qatar; [b]Center for Advanced Materials, Qatar University, Doha 2713, Qatar
*E-mail: kamel.eid@qu.edu.qa, bakr@qu.edu.qa

1.1 Introduction

The excessive utilization of nonrenewable fossils has caused the emission of huge amounts of hazardous gasses (*i.e.*, CO, CO_2, and CH_4) that have harmful effects on humans (*i.e.*, headache, nausea, coma, fainting, oxidative stress/endothelial dysfunction, and kidney calcification) and the environment (*i.e.*, climate change, global warming, smog/acid rain, and melting ice), so it is critical to reduce these gas emissions. The new generations of green, renewable, and zero-emission energy conversion technologies (*i.e.*, solar

Nanoscience & Nanotechnology Series No. 51
Carbon Nitride Nanostructures for Sustainable Energy Production and Environmental Remediation
Edited by Kamel Abdelmoniem Mohamed Eid and Aboubakr M. Abdullah

Published by the Royal Society of Chemistry, www.rsc.org

cells, water splitting, oxygen reduction, alcohol oxidation fuel cells) driven by metal-based catalysts are among the most promising ways to reduce CO_2/CO emission.[1–15] Another effective way is gas conversion reactions, including CO_2 reduction reaction (CO_2RR) and CO oxidation reaction (CO OR) on graphitic carbon nitrides (gCNs) that are of great importance in industrial, environmental, and fundamental applications.[16,17] The materials used are polymeric materials comprising C, N, and H, heterocycles of heptazine or triazine rings linked *via* carbon sp^2-bonded nitrogen atoms ($N(C)_3$ units), or –NH– groups. In 1834, J. Liebig[18] prepared a melon for the first time, which is a polymer that contains tri-*s*-triazines *via* secondary nitrogen; however, the breakthrough in the fabrication and utilization of gCNs was just attained in the last two decades.[16,17,19–26] gCNs have electron-rich properties, basic surface functionalities, and H-bonding motifs in addition to great thermal stability, chemical stability in different solvents, and mechanical properties, active and sites of gCNs that are significant merits in multidisciplinary catalytic, energy, and environmental applications.[16,17,19–24] Also, gCNs are semiconductors with a band gap energy of 2.7 eV and great visible light absorption < 450 nm that enhances the photocatalytic performance towards water splitting, dye degradation, and solar cells.[17,27,28] Gas capture or conversion reactions, including CO_2RR and CO ORs on gCNs are of great importance in industrial, environmental, and fundamental applications due to the hazardous effects of the use of fossil fuels on humans and the environment.[29–34]

The unique composition of gCNs contains an electronegative nitrogen atom bonded to positive carbon, resulting in electron-deficiency on the carbon atom in the form of carbon$^+$–nitrogen$^-$ that is favored for the electrophilic and nucleophilic attack alongside promoting the charge transfer and adsorption of CO molecules.[21–24,35–38] One-dimensional gCN nanostructures (*i.e.*, nanotubes, nanorods, nanofibers, nanowires, and needles) possess various advantages over other shapes (*i.e.*, zero-dimensional and two-dimensional). One-dimensional nanostructures have a greater surface area, multiple adsorption sites, quicker charge migration, short electron-diffusion, and less-tendency for aggregation.[24,39–43] There are various methods for the controlled fabrication of 1D gCN nanostructures such as template-based, solvothermal, self-assembly, and thermal condensation. Notably, CO oxidation on 1D gCN nanostructures is not emphasized enough relative to other applications.[34,44,45] There are some recently published reviews about the fabrication of 1D gCN nanostructures for various catalytic applications, but not for CO oxidation.[34,46–50]

This chapter emphasizes the controlled synthesis of 1D gCN nanostructures for CO oxidation. This includes the fabrication of nanotubes, nanorods, nanofibers, and needles and their related mechanisms. This is in addition to the challenges and outlooks of gCNs for gas conversion reactions.

1.2 Template-based Preparation of 1D gCNs

Template-based methods (*i.e.*, hard, soft, and hybrid templates) are the most effective for the rational synthesis of uniform 1D gCN nanostructures in high yield, with tunable shape composition driven by proper selection of

a template (*i.e.*, foam, tubes, and rods).[51–53] The reaction parameters (*i.e.*, template type, reactant concentrations, pH, solvent, and temperature) are not only the most critical factor determining the uniformity and morphology, but also tuning the physicochemical (*i.e.*, stability, surface area, and mechanical properties), catalytic, photocatalytic properties of the final 1D gCN product.[28,51–53]

1.2.1 Hard Templating

The hard templating method is widely used for 1D gCNs, due to its simplicity and low level of precautionary measures compared with the soft-template method. The process is based on the initial filling of a rigid template (*i.e.*, ZnO, SiO_2, anodic aluminum oxide membranes (Al_2O_3), calcium carbonate, or any other inorganic material) with a carbon–nitrogen precursor, followed by pyrolysis to allow condensation and polymerization of the precursor inside the pore or channel of the template and finally erosion of the template by acidic/alkaline etchants (Figure 1.1A).[7,54–56] However, AAO and SiO_2 are the most common templates. They are widely used in the fabrication of 1D gCNs due to their high thermal stability, ease of handling, availability, low cost, uniformity, and stability against side reactions with the gCN monomers during the condensation process. Meanwhile, the fabrication of 1D gCN nanostructures using hard templating is not emphasized enough compared to other 3D or 2D structures.[54–57]

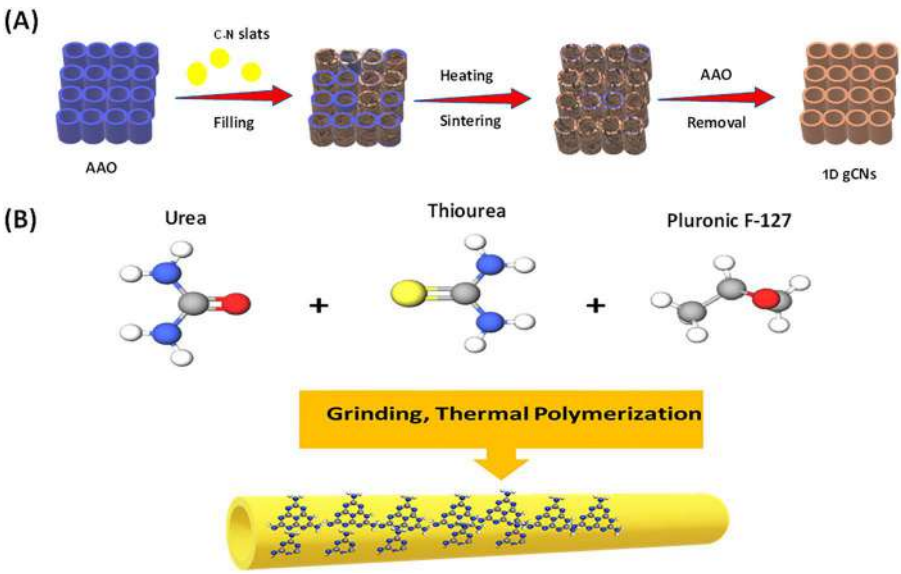

Figure 1.1 (A) The hard-templating method steps. (B) The soft-templating method steps.[68] Reproduced from ref. 68 with permission from Elsevier, Copyright 2018.

Nickel-modified AAO enabled the preparation of uniform small gCN nanorods (10–20 nm) with unique catalytic performance and includes the initial deposition of nickel on AAO using an impregnation approach to form NiO/Al_2O_3 filled with ethylenediamine and tetrachloride. This was followed by annealing at 600 °C in Ar to allow the conversion process as well as reducing NiO to Ni nanoparticles that nearly distributed over three to four layers of the gCN nanorods.[58] This unique composition has great electronic effect, with the electron-donating merits of Ni nanoparticles, the rich electron density of the gCN nanorods enhanced the catalytic hydrogenation of *p*-nitrobenzoic acid at various pH with an impressive durability.[58] Silica 'SBA-15' was used as a template for the preparation of mesoporous gCN rod-like shaped gCN nanostructures (but not 1D shapes) with a high surface area up to 517 $m^2\ g^{-1}$, based on the acidification of SBA-15 by hydrochloric acid at 80 °C. It was then dried and mixed with cyanamide under sonication, vacuumed, mixed with water, then dried and annealed at 550°, finally eroding SBA-15 by NH_4HF_2.[59] Likewise, a mesoporous rod-like shaped g-C_3N_4 nanocomposite decorated with Ag nanoparticles with a high surface area of 563.4 $m^2\ g^{-1}$ was prepared using SBA-15 as a template, based on the dissolving of dicyandiamide in water solution containing $AgNO_3$. It was mixed with g SBA-15 while stirring at 80 °C until the evaporation of water, and the resultant powder was annealed at 550 °C under nitrogen.[60] Notably, the SiO_2-based template is usually used to prepare 2D or 3D gCNs, with hardly any reports on gCNs with 1D shapes.[55,57,61] However, SiO_2-based templates are feasible for different modifications (*i.e.*, cross-linking, doping, and co-polymerization) and easily combined with other methods for tailoring shapes of gCN nanostructures.[55,61–64] Porous 1D gCN nanotubes were prepared *via* the polymerization of ethylenediamine and carbon tetrachloride in the presence of an AAO template at 600 °C under nitrogen, then etching of AAO by NaOH solution.[65] The as-obtained gCN nanotubes were used as a substrate for supporting the deposition of Pt nanoparticles for the catalytic hydrogenation of cyclohexene.[65] Confined 1D gCN nanorods, free from defects or free NH_2 group, were prepared by the polymerization of cyanamide using an AAO template 600 °C under nitrogen and then by etching AAO by hydrochloric acid.[66] Using AAO as a template enhanced the crystallinity, reduced the highest occupied molecular orbital (HOMO) position, and enhanced the photocatalytic properties of the thus obtained gCN nanorods for a full water-splitting reaction (*i.e.*, hydrogen evolution and oxygen evolution).[66] This indicates the possibility of modulating the optical and photo properties of gCN materials using an AAO membrane with various dimensions in the presence of different carbon–nitrogen monomers. Despite great progress in the hard template for the synthesis of 1D gCNs, using hazardous etchants, multiple steps, and unavoidable defects remain great challenges. Additionally, filling the template with carbon–nitrogen monomers is still difficult and requires high precautionary measures.

1.2.2 Soft Templating

Unlike the hard template, the soft template is based on the self-assembly of a nitrogen-carbon monomer with surfactants or ionic liquids or block polymers including ionic co-polymers (*i.e.*, cetyltrimethylammonium bromide (CTAB) and benzylhexadecyldimethylammonium chloride (BDAC)), non-ionic co-polymers (*i.e.*, polyvinylpyrrolidone (PVP), Pluronic F127, Plurong P123, Brig-58), or their hybrids to build block shapes (*i.e.*, rods, tubes, or 3D micelles) enabling the formation of gCN nanoarchitectonics in different shapes.[51] The built blocks are then decomposed during the condensation process due to their lower thermal stability and subsequently remove the need for an additional etching step as in the hard templating method.[51]

The soft template's concentration should be above the crucial micelle's concentration to allow the self-assembly process; meanwhile, the solvent type and pH are critical factors determining the final shape and properties of the gCNs.[51] Wang *et al.* used various soft templates (*i.e.*, Pluronic P123 and Triton X-100, Pluronic F12Brij-x) for the rational synthesis of a mesoporous gCN nanostructure using dicyandiamide as a monomer while carrying out the condensation at 550 °C, but not for 1D gCNs.[67] Both Triton and Pluronic F127 were preferred for the production of gCNs with a high surface area. This study opens the way for the soft-templating approach in the preparation of 1D gCN nanostructures.

For instance, Pluronic F127 was used as a template for the synthesis of g-C_3N_4 nanotubes *via* the co-polymerization of urea and thiourea at two annealing steps at 350 °C and then at 600 °C (Figure 1.1B).[68] Following that, g-C_3N_4 nanotubes were used as a substrate to support PtNi nanoparticles' growth by the chemical reduction method using $NaBH_4$. Although there was a low Brunauer–Emmett–Teller (BET) surface area of those formed g-C_3N_4 nanotubes (20 m^2 g^{-1}), the photocatalytic performance for hydrogen evolution reaction was outstanding. Likewise, g-C_3N_4 nanotubes co-doped with Na and S were prepared by the co-polymerization of urea and thiourea in the presence of Pluronic F127 as a template and $NaHCO_3$ as Na source and then annealed.[69] The surface area of the doped g-C_3N_4 nanotubes was significantly higher than the bulk g-C_3N_4; also, the surface area depended on the Na content.[69] This method is flexible and can allow mono doping with either Na or S *via* selecting the initial type or concentration of the used reactants. Although there has been great progress in the soft template, it is not emphasized enough to synthesize 1D gCNs. The template's self-assembly mechanism with the carbon-monomer is still ambiguous, and it is not easy to decipher.[51] Meanwhile, the precautions, including concentrations of the template and reaction conditions, remain unreproducible and not feasible for large-scale applications.[51]

1.3 Preparation of 1D gCN Nanotubes

One-dimensional gCN nanotubes are of great importance in various catalytic applications due to their high surface area, accessible sites, low density, quick charge mobility, and abundant adsorption sites for the reactant molecules, so massive effort has been dedicated to their fabrication.[55] An early attempt at the rational design of g-C_3N_4 nanotubes was made by Guo *et al.* They prepared g-C_3N_4 nanotubes with an average size of 50–100 nm and wall thickness of 20–50 nm, synthesized using the facile benzene-thermal process (Figure 1.2A and B).[25] This included mixing 1,3,5-trichlorotriazine

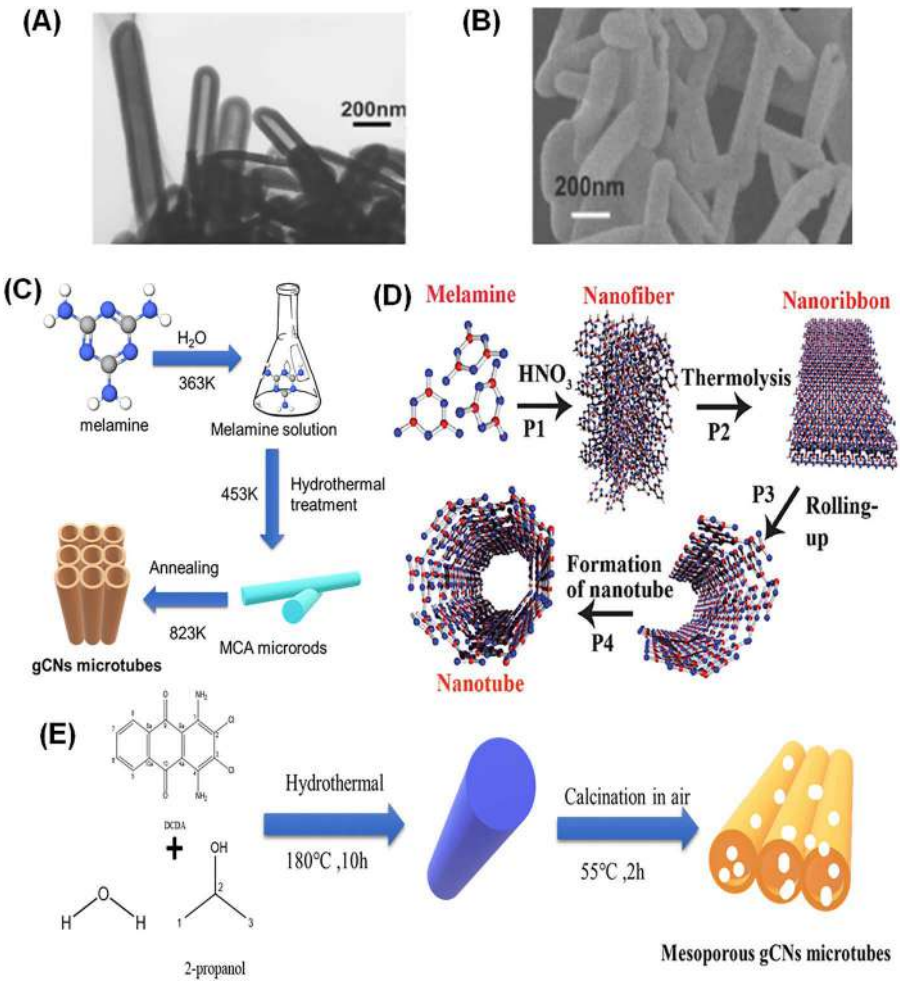

Figure 1.2 (A) TEM images of the gCN nanotubes prepared. (B) SEM of the gCNs. Reproduced from ref. 25 with permission from the Royal Society of Chemistry. (C) The preparation *via* a MCA microrods intermediate. (D) The mechanism of formatting gCNs through a fibrous intermediate. Reproduced from ref. 24 with permission from the Royal Society of Chemistry. (E) The self-assembly preparation method of P-CNM.[70]

and sodium azide in benzene, then autoclaving at 220 °C for 15 h; after cooling, the obtained powder was washed with benzene and water and then dried under vacuum.[25] g-C_3N_4 nanotubes were prepared by the direct annealing of a melamine-cyanuric acid complex at 400 °C under nitrogen to form nanorods, then calcination was performed at 550 °C under nitrogen to form nanotubes.[71] The same mechanism was found in the preparation of g-C_3N_4 microtubes by the polymerization of melamine–cyanuric acid under autoclaving at 180 °C to form complex melamine–cyanuric acid (MCA) microrods with an average length of 20–50 μm and width of 1–2 μm average diameter, which converted to nanotubes with a wall thickness of 50 nm after annealing under nitrogen at 550 °C (Figure 1.2C).[72] The mechanism was attributed to the initial formation of a MCA hexagonal plate shape that consequently converted to hexagonal microrods upon hydrothermal treatment based on the longitudinal growth direction with the assistance of water, meanwhile during annealing under nitrogen, this allowed the quick sublimation for the triazine molecules in the internal part or microrod to grow outward to form g-C_3N_4 tube morphology.[72] The surface area of the g-C_3N_4 microtubes was 2.2 times higher than that of bulk g-C_3N_4 along with a superior photocatalytic activity by 3.1-fold.[72] Porous gCN nanotubes decorated with Rh nanoparticles were prepared by the initial preparation of gCN nanosheets by the direct pyrolysis of melamine at 550 °C in air, and then gCN nanotubes were mixed with ethanol/water and RhCl3 followed by the addition of $NaBH_4$ as a reducing agent to facilitate the reduction of $RhCl_3$ with the assistance of sonication.[73] The use of sonication and ethanol/water solvents and the high reduction power of $NaBH_4$ under sonication may be the main reason for the formation of porous nanotubes.[73]

Millimeter-long g-C_3N_4 nanotubes with an exterior size of 300–500 nm were prepared in a simple one-pot method, including protonation of melamine in ethylene glycol solution by nitric acid, then thermal sintering at 350 °C (Figure 1.2D).[24] The formation mechanism includes the protonation of the abundant active amino groups of melamine by nitric acid.[24] The protonated melamine was polymerized into an *s*-triazine ring-based nanofiber, and then the ribbons rolled up to the nanotubes upon heating to reduce the surface free energy of the intermediate fiber ribbons.[24] The presence of nitric acid is necessary to direct nanotube formation while using $NaNO_3$ and HCl drove the formation of the g-C_3N_4 nanofiber. Additionally, using other acids like sulfuric or phosphoric acid did not form 1D nanostructures.[24] The as-obtained g-C_3N_4 nanotubes and nanofibers revealed a great luminescent emission, quick photoresponse, and high photoconductivity.[24] Notably, most of the reported 1D gCN nanotubes were undoped, and it is known that doping can enhance the catalytic properties and improve the physicochemical properties of gCN materials. In this context, *hierarchical* porous g-C_3N_4 nanotubes doped with oxygen (Og-C_3N_4NTs) composed of multi-walled nanotubes with a size of 20–30 nm were synthesized using thermal oxidation exfoliation and curling-condensation of bulk g-C_3N_4.[74] In particular, bulk g-C_3N_4 was obtained by direct condensation of melamine at 550 °C that consequently annealed at 600 °C for 4 h under both nitrogen and air.[74] The formation

mechanism is based on the exfoliation of g-C_3N_4 nanosheets to individual sheets driven by breaking the hydrogen bonds that turn into nanotubes under the driving force of airflow.[74] With airflow assistance, g-C_3N_4 nanotubes condense and self-assemble into a hierarchical porous nanotube on the tubular furnace.[74] The BET surface area of Og-C_3N_4NTs (36 m^2 g^{-1}) was superior to bulk g-C_3N_4NTs (9 m^2 g^{-1}) by four times in addition to the higher photocatalytic activity for CO_2 reduction, due to the excellent CO_2 adsorption, light absorption, delay electron–hole recombination, and quick charge mobility. Likewise, phosphorus-doped g-C_3N_4 nanotubes with mesoporous < 25 nm were produced by the direct one-step annealing of melamine and sodium hypophosphite monohydrate at 550 °C after cooling. The obtained powder was ground, washed with water, and dried at 70 °C.[75] The phosphine gas generated from the thermal decomposition of $NaH_2PO_2{\cdot}H_2O$ induces the formation of P-g-C_3N_4 nanotubes from g-C_3N_4 nanosheets.[75] The BET surface area of phosphorus-doped g-C_3N_4 nanotubes (13.38 m^2 g^{-1}) was 4.4 times higher than undoped g-C_3N_4 (3.02 m^2 g^{-1}) in addition to higher optical and photo properties along with higher CO_2 absorption, lower zeta potential, and charge separation.[75]

Porous C_3N_4 nanotubes with controllable nitrogen (N-g-C_3N_4) and tunable nitrogen vacancies were prepared by the thermal etching method, including the initial preparation of C_3N_4 *via* autoclaving of cyanuric chloride and melamine in acetonitrile at 180 °C, that were subsequently pyrolyzed at 550 °C under nitrogen to form C_3N_4 nanotubes.[76] This was followed by annealing under air at 550 °C for 15, 30, 45, and 60 min to integrate nitrogen-deficiency into the C_3N_4 nanotubes.[76] Increasing the annealing time from 15 to 60 min not only increases the nitrogen vacancies but also increases the BET surface area from 23 m^2 g^{-1} to 207 m^2 g^{-1}, in addition to maximizing the utilization of visible light, providing more active sites for capturing photoexcited electrons that preclude the electron–hole recombination, and increasing the CO_2 adsorption.[76]

Likewise, nitrogen doped (g-C_3N_4) with adjustable nitrogen content was prepared by the supramolecular self-assembly strategy, including mixing hydroxylammonium chloride and melamine in water, then autoclaving at 120 °C to form a supramolecular intermediate that dried at 60 °C after washing, and then annealing at 520 °C under ammonia gas with different flow rates of 50, 100, 200, and 400 mL min^{-1}.[77] The nitrogen content of the N-g-C_3N_4 nanotubes increased with increasing flow rate but almost collapsed the nanotube shape at the highest rate, 400 mL min^{-1}, due to the etching properties of ammonia.[77] Interestingly, the g-N-g-C_3N_4 nanotubes' surface area reached 135.8 m^2 g^{-1}, which was 15.7 times higher than that of bulk g-C_3N_4.[77] Meanwhile, annealing under air, argon, and nitrogen atmospheres instead of ammonia also results in g-C_3N_4 nanotubes but with less porosity.[77] Owing to the porous nanotube shape, Lewis basicity, high surface area, and rich nitrogen content of N-g-C_3N_4 nanotubes, its photocatalytic properties, and CO_2 adsorption/desorption increased significantly.[77] Long aligned g-C_3N_4 nanotubes with lengths over 4 μm with the open end of 60 nm, were prepared by

dispersion of melamine in water at 80 °C, followed by addition of salicylic acid with different amounts (0.92, 0.69, 0.55, 0.46, and 0.39 g). After drying, the obtained powder was subjected to a low annealing step at 550 °C under nitrogen and then under air to allow the thermal-oxidative etching process. Increasing the amount of salicylic acid leads to increasing pore volume due to its ability to act as a pore modulator; however, it decreases the surface area. The thermal etching process and the decomposition of salicylic acid during annealing possibly allow the rolling mechanism to form nanotubes.[78] The photocatalytic properties, charge carrier mobility, and light absorption were enhanced using a higher amount of salicylic acid. This study opens new avenues for utilizing organic acids as a pore generator for C_3N_4 1D shapes.

Similarly, porous g-C_3N_4 microtubes were prepared by a liquid–liquid interfacial self-assembly method, including mixing dicyandiamide in a mixture of solvents of water and isopropanol under stirring, then autoclaving at 180 °C to form the initial supramolecular precursors that were annealed a 550 °C in air after being purified and dried[70] (Figure 1.2E). The surface area of 82.84 $m^2\ g^{-1}$ was 13.3 times higher than that of bulk g-C_3N_4 prepared by direct annealing of dicyandiamide along with superior photocatalytic activities and higher redox-active sites.[70] Intriguingly, using double solvent water with isopropanol is a prerequisite to allow nanotube formation driven by the formation of 1D hexagonal supramolecular pillars afterwards. Comparatively, using individual water or isopropanol forms an irregular flake-like or sheet-like shape.[70] Water with isopropanol creates 1D hexagonal supramolecular pillars after autoclaving, as water probably creates the inner part of the 1D pillar. In contrast, isopropanol generates the hexagonal framework of the 1D pillar as an outer layer.[70] g-C_3N_4 nanotubes were prepared using a melamine sponge as a template that is soaked in urea solution and then frozen at −20 °C, and then freeze-dried before being finally annealed at 550 °C under a N_2 atmosphere (Figure 1.3A).[79] The BET surface area of the g-C_3N_4 nanotubes was 1.6 times higher than that of bulk g-C_3N_4 prepared without a melamine sponge.[79] This study may allow the utilization of melamine-based foam or sponge for the tailored fabrication of 1D gCN nanostructures with tunable shapes and compositions.

3D g-C_3N_4 nanotubes composed of 1D thick tubes decorated with multiple thin tubes were prepared by the thermal polymerization of cyanuric acid and melamine in water with the assistance of phosphorous acid under an autoclave and heated at 180 °C to form nanorods and then a second annealing process at 550 °C was performed under nitrogen to form 3D nanotubes (Figure 1.3B).[80] The BET surface area 3D g-C_3N_4 nanotubes (71 $m^2\ g^{-1}$) was superior to bulk g-C_3N_4 by 11-fold alongside enhancement of the photocatalytic properties.

Although the formation of tabular gCNs is the most reported, other morphologies were also reported using different chemical methods. Table 1.1 summarizes the fabrication process of various 1D gCN nanostructures for different applications that clearly showed rare reports on CO_2RR and CO oxidation relative to other applications. As shown in Table 1.1, the template-based

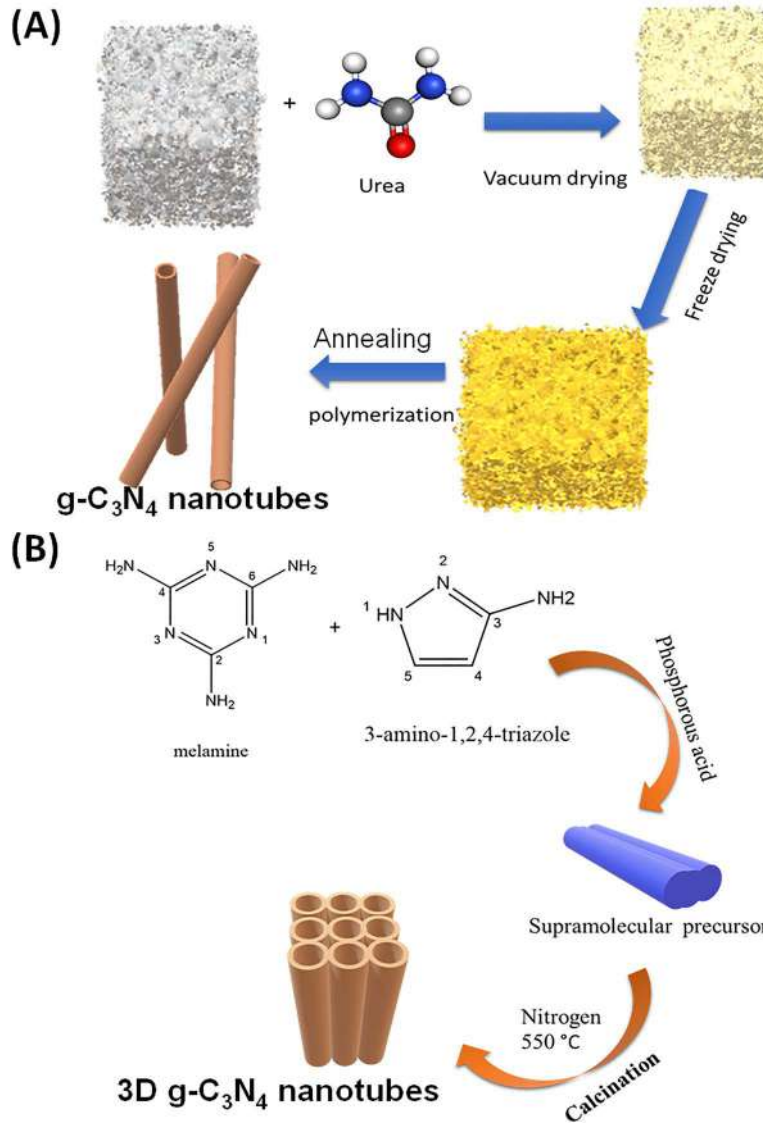

Figure 1.3 (A) The formation mechanism of gCN nanotubes through a melamine sponge.[79] (B) The mechanism of the as-synthesized 3D gCN cage consisting of nanotubes.[80]

method is the most common in the rational synthesis of 1D gCN nanostructures or microstructures. Also, melamine is usually used as an initial precursor for 1D gCNs, due to its ease of handling and polymerization under mild conditions, as well as its stability against side reactions with the template. Additionally, melamine is feasible for coupling with other precursors like urea and cyanuric acid to tailor uniform, high-yield, and well-defined 1D gCN nanostructures.

Table 1.1 The fabrication methods of 1D gCN nanostructures using different carbon–nitrogen (C–N) precursors for various applications.

C–N precursors	1D shapes	Composition	Fabrication methods	Application	Reference
Urea	Nanotubes	gCNs implanted by carbon quantum dots	Thermal polymerization of urea	H_2 evolution	81
Cyanamide	Condensed nanorods	gCNs	Thermal condensation and anodic alumni oxide (AAO) template	Water splitting	66
Melamine	Tapered C-PAN/gCN nanotubes	Polyacrylonitrile-derived carbon (C-PAN)/gC_3N_4 composite nanotubes	Self-assembly	H_2 evolution	66
Cyanamide procurer by silica (SBA-15) template	Twisted hexagonal rod structure	Helical graphitic carbon nitride	Nanocasting and chiral silicon dioxides as templates	H_2 evolution, water splitting, and CO_2 reduction	82
Melamine and urea	Nanotubes	g-C_3N_4	Thermal polymerization	H_2 evolution	71
Melamine	Helical porous tubes	O-doped gCNs	Thermal oxidative exfoliation	CO_2 reduction	74
Melamine	Nanotubes	Na-doped-gCNs	Hydrothermal and thermopolymerization	Water splitting	83
Melamine	Nanotubes	g-C_3N_4/TiO_2 composite	Hydrothermal	Isoniazid degradation	84
Melamine	Fibers in nanotubes	Pt SAC on gCNs/SnO_2	Electrospinning	Gas sensing	85
Cyanuric chloride and melamine	Composite films	TiO_2/gCNs	Hydrothermal	Water splitting	86
Urea	Nanorods	B-doped gCNs/TiO_2	Thermal polymerization method	Water oxidation	87
Dicyandiamide and 2-aminobenzonitrile	Nanotubes	P-doped gCN modified vertically-aligned TiO_2 nanotubes	Electrochemical anodization, wet-dipping, and thermal polymerization	Water splitting and dye degradation	88
Dicyanamide	Nanotubes	A composite of 2D/1D MoS_2 nanoflake/g-C_3N_4 nanotube	Thermal condensation and freezing	H_2 evolution	89

(*continued*)

Table 1.1 (*continued*)

C–N precursors	1D shapes	Composition	Fabrication methods	Application	Reference
Urea, thiourea and F127	Nanotubes	Bimetallic PtNi-decorated gCN nanotubes	Thermal condensation and Pluronic F127 soft template	H_2 evolution	68
Melamine	Nanotubes	TiO_2/gCNss	Molten salts method	Dye degradation	90
Melamine	Nanotubes	gCN/CdS composite	Hydrothermal co-deposition	Dye degradation and H_2 evolution	91
Melamine and hydroxylammonium chloride	Nanotubes	gCNs	Hydrothermal and annealing under NH_3	CO_2 reduction	77
1.3.5-trichlorotriazine, melamine, urea, acetonitrile, $AgNO_3$	Nanotubes	AgCl/gCNs	Solvothermal and ultrasonic precipitation	Dye degradation	92
Melamine and cyanuric acid	Nanotubes	boron-doped gCNs	Calcining self-assembly supramolecular precursors	NOx removal	93
Melamine, cyanuric acid and urea	Tubes	g-C_3N_4 isotype heterojunction	Hydrothermal	H_2 evolution	94
Melamine	Nanofiber	gCN/carbon fiber composite	Electrospinning and calcination, and gas–solid method	Dye degradation	95
Dicyanamide	Nanorods	Ni_2P-$Cd_{0.9}Zn_{0.1}$ S/g-C_3N_4	Hydrothermal	H_2 evolution	96
Melamine	Nanorods	ZnO/gCNs	Vapor condensation process	Dye degradation	97
Tetracyanoethylene	1D, 2D, and 3D gCNs (theoretical prediction)		Polymerization under high pressure using a diamond anvil cell.		98
Graphitic carbon nitride	Microfibers	g-C_3N_4	Thermal evaporation and vapor transfer		99
Formamide	Nanowires	RuO_2/gCNs	Thermal heating process	Hydrogen and oxygen evolution	100

Graphene oxide and g-C_3N_4	Nanoribbons	Hierarchically structured g-C_3N_4 nanoribbons–graphene hybrids	Hydrothermal process	H_2 evolution	101
Melamine	Nanotubes	gCNs	Vapor deposition polymerization (VDP) and AAO template	Ionic photodetector	102
Melamine	Nanotubes	gCNs	Vapor deposition polymerization (VDP) and AAO template	Ion pump and energy conversion	103
C_2H_2 and N_2	Directed AAO template		AAO template		104 and 105
Melamine	Nanotubes	gCNs	CVD method including sublimation and condensation of melamine into gCNs under argon gas flow at 520 °C	Controlling water flow	106
Cyanamide and zinc oxalate	Nanotubes	gCNs	AAO template	Deoxynivalenol degradation	107
Melamine precursor	Nanotubes	gCNs	AAO template	Ion diode	108
Melamine, $NaHCO_3$, and thiourea	Nanotubes	Na and S co-doped gCNss	Thermal condensation	H_2 evolution and dye/phenol degradation	69
Melamine	Nanotubes	Cyano and potassium-rich gCNss hollow tubes	Molten salts method	H_2 evolution	109
Melamine	Nano seaweed	gCNs	Molten salts method	Luminescent detection of tetracycline	110
Melamine	Tetragonal nanotubes	gCNs	Molten salt	Dye and phenol degradation	111
Melamine formaldehyde with urea	Nanotubes	gCNs	Co-polymerization	H_2 evolution	112

(*continued*)

Table 1.1 (*continued*)

C–N precursors	1D shapes	Composition	Fabrication methods	Application	Reference
Urea	Nanotubes	gCNs	Calcination	Hydrogen evolution	113
Melamine	Nanotubes	Nitrogen defective gCNs	Self-assembly, and calcination	H_2 evolution	114
Melamine and cyanuric acid	Bunchy tubes	N_2 deficient gCNs	Thermal treatment then freeze-drying	H_2 evolution	115
Melamine and cyanuric acid	Tubes	Graphene quantum dots modified on hexagonal tubular gCNs	Thermal treatment	H_2 evolution	116
Melamine	Tubes	O-doped, and carbon defective gCNs	Self-assembly	H_2 evolution	117
Melamine and cyanuric acid	Tubes	P-doped hexagonal carbon nitride tubes	Melamine and cyanuric acid self-assembly formed *in situ* hydrolyses of melamine under H_3PO_4 assisted hydrothermal conditions; then, pyrolysis of precursors was carried out	H_2 evolution	118
Melamine	Nanotubes	Defective gCNs	Autoclaving then annealing	H_2 evolution	119
Melamine	Nanotubes	gCNs	Supermolecule self-assembly	Contamination degradation	120
Oxamide and urea	Nanotubes	gCNs	Self-assembly	H_2 evolution	121
Dicyanamide	Hollow porous prismatic	Nitrogen vacancies oxygen-doped gCNs	Hydrothermal	Nitrogen fixation	122
Dicyandiamide and melamine	Nanotubes and nanobelts	gCNs	Polycondensation		123
Melamine	Nanotubes	Bimetallic Cu-Ag/ gCNs	H_2O phase-transfer process	H_2 evolution	124

Melamine	Nanotubes	gCNs	Anti-solvent induced scrolling	H_2 evolution	125
Melamine	Nanotubes	gCNs	Two consequent thermal condensation	Dye degradation	126
Melamine and silver nitrate	Nanotubes	Ag/CNs composite	Hydrothermal	Dye degradation	127
Melamine	Nanotubes	Pt/CNs	Solvothermal	Dye degradation	128
Melamine	Nanotubes	Ag and La co-doped gCNs	Thermal decomposition then protonation by nitric acid	Methane bireforming	129
Melamine	Nanotubes	CNs	Ultrasonic exfoliation and H_2O phase-transfer process	Dye degradation H_2 evolution	130
Melamine and sodium hypophosphite	Nanotubes	P-doped gCNs	Thermal decomposition	CO_2 capture	75
Melamine	Microtubes	Ba and P co-doped gCNs	Hydrothermal	H_2 evolution	131
Melamine	Nanotubes	gCNs	Calcination followed by condensation NH_3	Examining fluorescent properties of formed gCNs	132
Melamine and salicylic acid	Nanotubes	gCNs	Thermal polycondensation	CO_2 reduction, and oxidation of 2-propanol vapors	78
Melamine	Hollow tetragonal prism	gCNs	Polycondensation of melamine in CCl_4	H_2 evolution	133
Melamine	Nanotubes	P-doped gCNs with carbon defects	Thermal polymerization of supramolecular assemblies	H_2 evolution	134
Melamine	Tetragonal microtubes	NaCl-doped gCNs	Self-template supramolecular hydrogel approach	H_2 evolution	135
Melamine and cyanuric acid	Tubes	gCNs with carbon and nitrogen vacancies	Polycondensation	H_2 evolution	136
Melamine, cyanuric acid, and caffeine	Tubes	gCNs	Supramolecular polycondensation	Dye degradation	43

(*continued*)

Table 1.1 (*continued*)

C–N precursors	1D shapes	Composition	Fabrication methods	Application	Reference
Melamine and cyanuric acid	Tubes	Phosphorous red quantum dots decorated on gCNs	Supramolecular vapor deposition	NADH generation	137
Ethylenediamine, and carbon tetrachloride	Nanotubes	gCNs	AAO hard templating and thermal decomposition	Methanol electrooxidation	138
Melamine	Nanotubes	gCNs	Halloysite template *via* a facial vapor deposition	H_2 evolution	139
Melamine and cyanuric acid	Nanotubes	gCN/multi-walled carbon nanotubes nanocomposites	Supramolecular self -assembly	Dye degradation	140
Urea	Nanofibers	gCN nanofibers decorated with MoS_2, and S, N-doped graphene	Hydrothermal	H_2 evolution	141
Melamine	Rod	1D/0D gCN/Mo_2C hybrids	Polymerization by nitric acid, then calcination at 550 °C	H_2 evolution	142
Dicyanamide	Nanowires	g-C_3N_4/TiO_2	Templating by $Na_2Ti_2O_7$	Dye degradation	143
Urea	Nanofibers	PAN/gCNs/BiOI	Electrospinning	Floating Photocatalysis	144
Melamine	Nanorods	Oxygen-doped gCNs	Heating of hydrous melamine	H_2 evolution	145
Melamine	Nanorods	gCNs/$Sr_2KNb_5O_{15}$ composite	Thermal condensation, then growth of $Sr_2KNb_5O_{15}$	H_2 evolution and dye degradation	146
Urea	Nanofibers	gCNs/SiO_2-Au composite	Heat treatment with a mixture of urea powder, and fibrous SiO_2–Au	Dye degradation	147

1.4 Preparation of 1D gCN Rods

Compared to bulk gCNs, 1D gCN nanorods possess various inimitable inherent catalytic/photocatalytic properties due to their superior surface area, light absorption, quick charge-carrier migration with a higher magnitude, and proper aspect ratio. Also, 1D gCN nanorods enhance the interaction between electrolyte and electrode, owing to the short diffusion length for the electrolyte's electrons and ions. However, the fabrication of 1D gCN nanorods has not been studied enough relative to bulk gCNs or 2D gCN, or 1D gCN nanotubes. To this end, Atonietti's group synthesized 1D gCN nanorods with a length up to 5 μm and width of 260 nm *via* the thermal condensation of cyanamide in the presence of AAO membrane as a template. The photocatalytic water-splitting performance of nanorods was superior to bulk gCNs.[66] Likewise, Wang's group obtained conjugated C_3N_4 nanorods *via* the supercritical fluid technique, including autoclaving of cyanuric chloride and melamine in acetonitrile solvent at 180 °C.[148] This developed solution-processing approach allows the facile bottom-up design of 1D gCN nanorods at low temperature driven by the one-pot solution assembly, crystallization, and cross-linking chemistry. The as-obtained 1D gCN nanorods showed a lower decreased band gap energy and greater light-harvesting compared with bulk gCNs. Following that, various efforts were dedicated to rational fabrication of gCN nanorods. For instance, g-C_3N_4 nanorods were prepared by the simple reflux of g-C_3N_4 nanoplates in an aqueous methanol–water solution based on the exfoliation and regrowth followed by a subsequent rolling mechanism.[149] This includes the initial preparation of g-C_3N_4 nanoplates by the polycondensation of dicyandiamide at 550 °C, followed by dispersion in methanol/H_2O solution and refluxing at 68 °C at different times 1–6 h (Figure 1.4A).[149] The BET surface area, uniformity/size, crystallinity, and catalytic properties of the thus obtained g-C_3N_4 nanorods increased with increasing the refluxing time and methanol concentration.[149] Similarly, nanoporous g-C_3N_4 microrods were synthesized *via* exfoliation and etching of bulk gC_3N_4 using concentrated H_2SO_4 (Figure 1.4B).[150] Initially, bulk g-C_3N_4 nanosheets were obtained by the direct annealing of melamine at 520 °C and then dispersed in concentrated H_2SO_4 in an ice bath container for 12 h to allow the exfoliation and delamination process. Water was added under stirring before centrifugation and then annealing at 550 °C in air.[150] The synthetic mechanism is attributed to the strong oxidative properties of sulfuric acid that delaminate the g-C_3N_4 structure into separated nanosheets resulting from the internal stresses due to the intercalation of sulfate ions with g-C_3N_4 sheets that can be rolled up into microrods.[150] The intercalation of sulfate ions also results in the formation of interconnected nanopores throughout the microrods.[150] Sulfuric acid is necessary for the fabrication of nanoporous microrods. In contrast, using concentrated hydrochloric and nitric acids instead of sulfuric acid did not exfoliate or form g-C_3N_4 microrods due to their inferior oxidation properties relative to the sulfuric acid.[150] Although sulfuric acid can have hazardous effects and is difficult to handle, this study opens new ways to

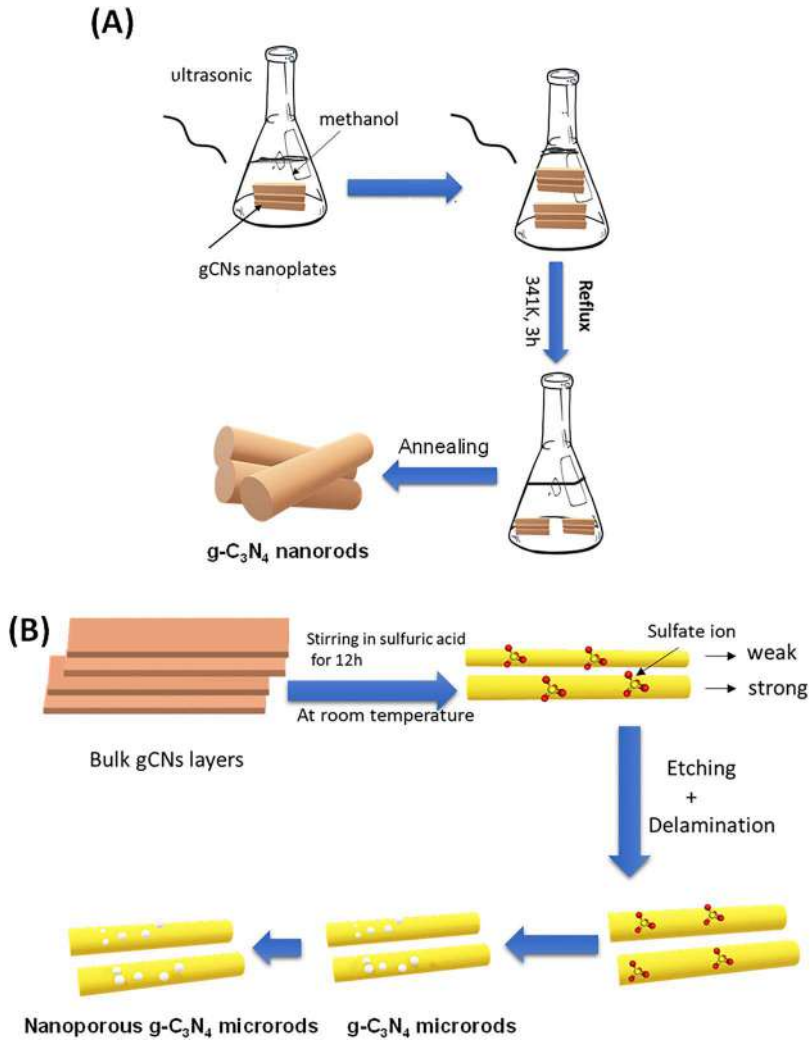

Figure 1.4 (A) The preparation method of g-C_3N_4 nanorods by the refluxing method.[149] (B) The mechanism of formatting gCN nanorods *via* exfoliation and etching.[150]

utilize strong acids for the controlled preparation of porous 1D gCNs without templates. However, the template-based method is still the most favored for the tailored design of 1D gCN nanorods with uniform size, shape, and controllable pore size/volume. To this end, mesoporous g-C_3N_4 nanorods with hexagonal mesostructured pores were prepared using chiral mesostructured SiO_2 nanorods, obtained initially using F127 and CTAB as templates.[151] The final nanorod product should be condensed at 550 °C in air, followed by the removal of SiO_2 by ammonium hydrogen NH_4HF_2. Another attempt for the green synthesis of 1D gCN nanostructures includes the fabrication of

hierarchical g-C_3N_4 porous nanorods by the simple sonication of melem in water solution to allow for molecular rearrangement, followed by annealing to reduce the defects.[152]

This includes the initial preparation of melem by direct annealing of melamine at 430 °C under air, then grinding before being mixed with water under ultrasonic irradiation to form melem hydrate followed by purification, drying, and finally annealing at 550 °C under air (Figure 1.5A).[152] The obtained hierarchical g-C_3N_4 porous nanorods possess a high surface area of 88.6 m^2 g^{-1}, porosity, greater electric conductivity, better crystallinity with fewer defects, higher photocatalytic properties when compared with g-C_3N_4 nanorods prepared using melamine instead of melem hydrate.[152] This method eliminates the need for using hazardous chemicals or multiple complicated reaction steps. However, the effect of sonication is not yet understood in the preparation process and needs further study. Likewise, 1D gCN rod-like nanostructures were prepared by a simple one-pot and template-free approach, including the polymerization of melamine in ethylene glycol solution using nitric acid and then drying and annealing at 450 °C (Figure 1.5B and C).[153] This is based on protonation of melamine and then deamination to form heptazine and then melon that

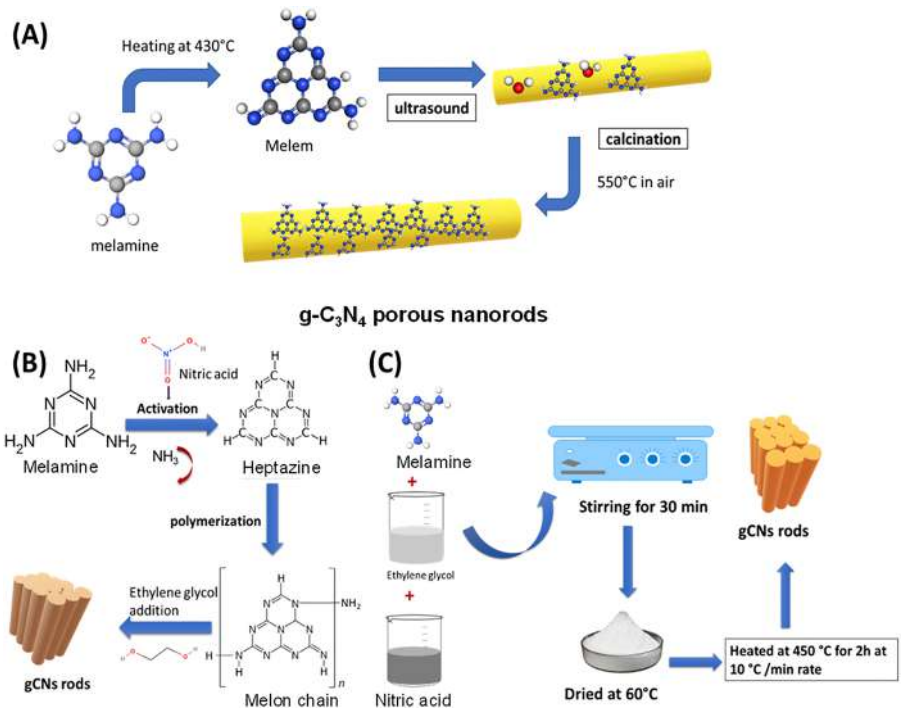

Figure 1.5 (A) The ultrasound-based mechanism of gCN nanorods.[152] (B) The formation mechanism of gCN nanorods. (C) The mechanism of growth of gCN rods.[153]

self-assembled into a rod-like shape morphology with the assistance of possible migration of carbonated species from inside to outwards during annealing.[153] This method was developed based on the initial attempts made by Tahir *et al.*[154] High crystalline and ordered g-C_3N_4 nanorods were prepared *via* molten salts and reflux methods of protonated melamine obtained after mixing with HCl solution melamine followed by leaching concentrated H_2SO_4.[155] The same method is feasible for the preparation of Cu single atoms impeded g-C_3N_4 nanorods (Figure 1.6A and B).[155]

Particularly, in the presence of HCl, $CuCl_2$ complexed to form $[CuCl_5]_n^{3n-}$, that directly complexed with the protonated melamine that directly polymerized hepatize-based g-C_3N_4 followed by molten salt at 550 °C and then refluxed in H_2SO_4 for leaching to form Cu–CCN nanorods.[155] The photocatalytic properties of g-C_3N_4 nanorods enhanced significantly after integration of a Cu single atom.[155] This may pave the way for the preparation of g-C_3N_4 nanorods with various metal-based single atoms for various catalytic and photocatalytic reactions.

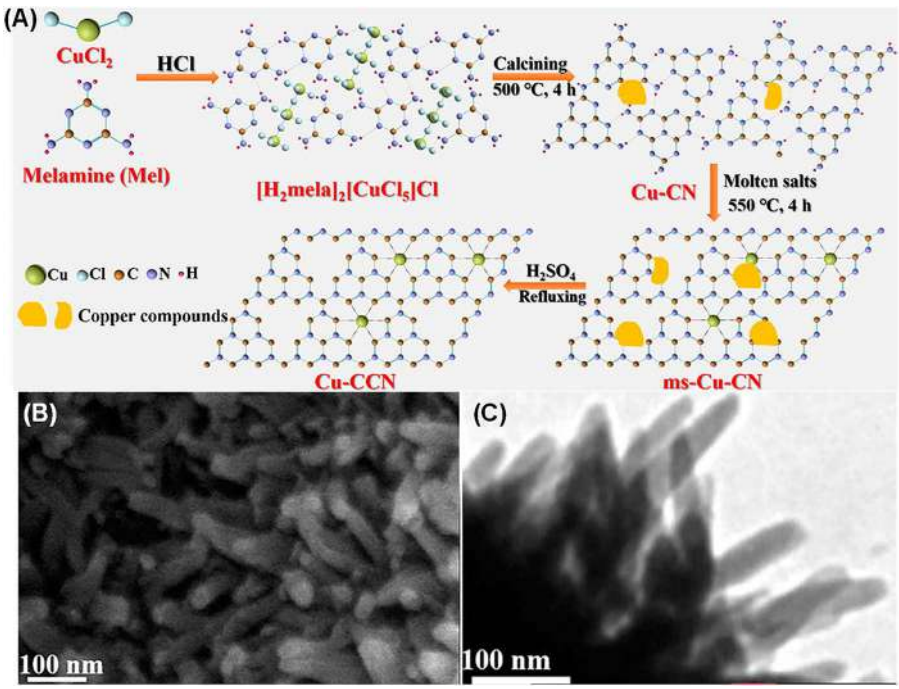

Figure 1.6 (a) The preparation method of C-CN/Cu *via* molten salts. (b) SEM image of the as-prepared C-CN/Cu, and (c) TEM image of C-CN/Cu. Reproduced from ref. 155 with permission from American Chemical Society, Copyright 2020.

1.5 Template-free Preparation of 1D gCNs for CO Oxidation

The fabrication of porous 1D gCNs not only involves multiple reaction steps and using templates besides hazardous etchants to remove the template, but also the obtained structures possess lower electrical conductivity and electrochemical surface area.[156]

To this end, 3D branched g-C_3N_4 nanorods were prepared by a modified ionothermal method, including the dispersion of grinding of bulk g-C_3N_4 (obtained by the direct condensation of melamine) with eutectic salts (KCl and LiCl), then degassing using argon, pyrolysis at 550 °C, while purging argon (Figure 1.7A).[157] Following cooling to room temperature, the powder was directly washed with ice water to allow the quenching process to remove any impurities and dried at 60 °C.[157] The eutectic salts promote the conversion of melon, the formation of nanorods, and induce crystallinity;

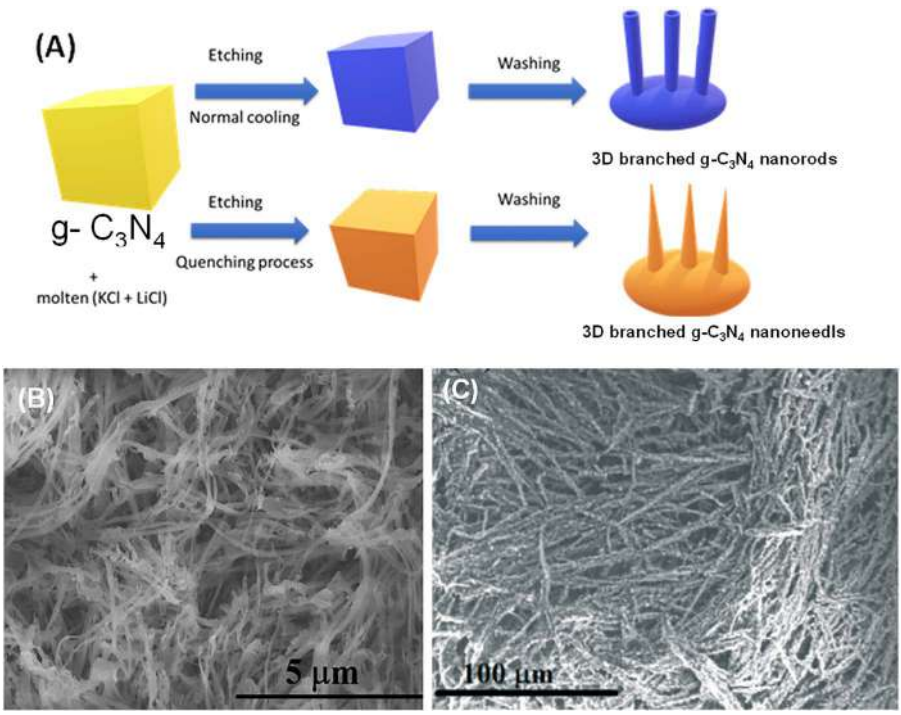

Figure 1.7 (A) The formation method of the 3D gCN nanorods and nanoneedles.[157] (B) SEM image of high magnification of gCN microfibers. Reproduced from ref. 158 with permission from American Chemical Society, Copyright 2014. (C) SEM image for the formed gCN micro-strings. Reproduced from ref. 159 with permission from the Royal Society of Chemistry.

meanwhile, LiCl acts as an etchant and erodes unstable parts.[157] The quenching provides dissimilar thermal stress at a different site, resulting from the inferior thermal conductance of water.[157] The same method was used to prepare 3D g-C_3N_4-N nanoneedles but with quenching of the annealed powder in the freezing deionized water.[157] The BET surface areas of 3D g-C_3N_4-N nanorods and nanorods were higher than that of bulk g-C_3N_4. Also, the surface area, photocatalytic properties, and charge mobility of nanoneedles and nanorods were superior to bulk g-C_3N_4.[157]

Tahir *et al.* developed a facile one-pot and template-free method for the preparation of g-C_3N_4 dense microfibers with an average length of 20 μm and width of 100 nm. This is based on the polymerization of melamine ethanol solution then dried at 450 °C in a chemical vapor deposition (CVD) furnace (Figure 1.7B).[158]

The same approach was used for the preparation of g-C_3N_4 nanotubes[160] as well as g-C_3N_4 micro-strings,[159] but using ethylene glycol instead of ethanol along with increasing the annealing time. Mainly melamine was polymerized in ethylene glycol solution using nitric acid, followed by drying and annealing at 400 °C, to result in ultra-long micro-strings of 2–4 μm length (Figure 1.7C).[159]

Screening the growth mechanism at different reaction times showed the formation of nanorods after 60 min annealing, that destructed to produce small beads, which subsequently formed a small string-like shape after fusion and annealing for 120 min and finally grew to a long micro-string after 150 min.[159] The BET surface area of the thus obtained micro-string (290 m^2 g^{-1}) was 29 times higher than that of bulk g-C_3N_4 (10 m^2 g^{-1}) and had better photocatalytic properties.[159] Another interesting example is the fabrication of a g-C_3N_4 ultra-long fiber with a diameter width of 0.8 mm and length up to 1 mm prepared by two annealing steps of melamine at 680 °C and then at 720 °C under nitrogen driven by the vapor–liquid–solid mechanism.[99] Mainly melamine is initially evaporated in the form of CN_x ($x > 1$) small nucleus vapor phase to the downstream region of a quartz tube with the assistance of a nitrogen carrier deposited on the inner wall of the quartz tube that acts as a substrate for supporting the growth of the CN_x nucleus to the short fiber. Upon increasing the annealing temperature and time, the micrometer-scale nuclei are produced and grew longer due to the greater condensation of vapor around the nuclei.[99] This study opens new avenues for the scalable fabrication of g-C_3N_4 fibers at the millimeter scale.

Recently, Eid *et al.* developed a facile, one-pot, and template-free approach for the rational design of various 1D gCN nanostructures *in situ* doped with mono or binary metals under ambient conditions inspired by the template-free approach mentioned above.[161] To this end, porous 1D gCN nanowires co-doped with Pd and Cu (Pd/Cu/gCN NWs) were prepared by the activation of melamine in an ethanol solution containing K_2PdC_{l4} and $CuCl_2$ with the assistance of nitric acid followed by drying and then annealing at 673 K under nitrogen.[161] Nitric acid allowed melamine activation to initiate the polymerization process to melon, which provides abundant adsorption sites

for the Pd/Cu precursor, and finally, the carbonization process occurred at high temperature under nitrogen. The as-synthesized Pd/Cu/gCN NWs had uniform nanowire structures with an average width of 80 nm and length up to 2000 nm; meanwhile, the nanowires are assembled in network-like porous structures. Elemental mapping showed the homogenous distribution of C, N, Pd, and Cu in the thus obtained Pd/Cu/gCN NWs. The ratio of C/N was about 41/57.8, which is close to the C_3N_4 phase, while the loading of Pd/CU was about 1.2 wt%. Interestingly, co-doping with Pd and Cu slightly increased the BET surface area of Pd/Cu/gCN NWs (120 $m^2\ g^{-1}$) compared to that of the metal-free gCN NWs (110 $m^2\ g^{-1}$).[161] The thermal CO oxidation activity of Pd/Cu/gCN NWs was tested relative to Cu/gCN NWs, Pd/gCN NWs, and metal-free gCN NWs under (4% CO and 20% O_2) while heating from room temperature to 723 K. The pretreatment for activation of all catalysts at 250 °C under air, and then under H_2, is needed prior to the CO oxidation tests.

The complete CO oxidation to CO_2 (100% conversion) was achieved on Pd/Cu/gCN NWs at (149 °C) compared to Pd/gCNs (283 °C), and Cu/gCN NWs (329 °C), whereas metal-free gCN NWs only showed inferior activity, 7% conversion at 450 °C. Co-doping with binary Pd/Cu plausibly enhances the CO-adsorption and O_2-adsorption/dissociation, accelerating the CO oxidation kinetics. Moreover, Pd/Cu/gCN NWs reserved their activity for 20 h while Pd/gCN NWs and Cu/gCN NWs revealed a slight loss in the activity. These results indicate the substantial effect of doping with either Pd/Cu or Pd or Cu on the CO oxidation activity of gCNs. Inspired by these results, this approach is extended to fabricate gC_3N_4 nanofibers co-doped atomically with Au and Pd (Au/Pd/gC_3N_4NFs), using isopropanol instead of ethanol.[162] The preparation process includes the polymerization of melamine in isopropanol solution involving $HAuCl_4$ and Na_2PdCl_4 by nitric acid and then drying before thermal pyrolysis at 480 °C under nitrogen (Figure 1.8).[19,162] Using isopropanol as a solvent and/or source for carbon allowed the fabrication of uniform Au/Pd/gC_3N_4 long nanofibers with a length up to 10 ± 1 μm and width of 80 ± 2 nm as confirmed by TEM and SEM images

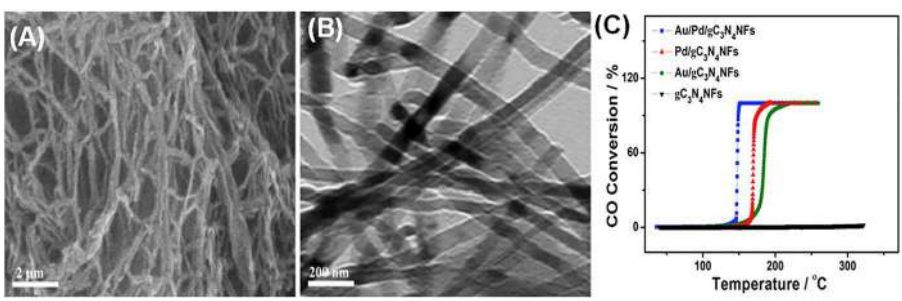

Figure 1.8 (A) SEM images of the Au/Pd/gCN NF. (B) TEM images of Au/Pd/gCN NF. (C) CO oxidation from 25 to 350 °C. Reproduced from ref. 162 with permission from Elsevier, Copyright 2019.[162]

(Figure 1.8A and B). The long aliphatic carbon chain of isopropanol plausibly increased the length of the gC_3N_4 nanofiber relative to the nanowires obtained using ethanol. The EDX and element mapping analysis revealed the presence of C/N with an atomic ratio of 40, 59, 0.55, and 0.45, respectively, and thus formed Au/Pd/gC_3N_4NFs. The BET surface area of doped Au/Pd/gC_3N_4NFs (85 $m^2\ g^{-1}$) was slightly larger than the undoped gC_3N_4NFs (72 $m^2\ g^{-1}$).[19,162] The CO oxidation to CO_2 on Au/Pd/gC_3N_4NFs was significantly higher than that of Pd/gC_3N_4NFs, Au/gC_3N_4NFs, and gC_3N_4NFs, due to the electronic effect of co-doping. Mainly, the complete CO conversion on Au/Pd/gC_3N_4NFs was achieved at 144 °C, which is lower than that of Pd/gC_3N_4NFs (191 °C) by 47 °C and Au/gC_3N_4NFs (205 °C) by 61 °C (Figure 1.8C). Meanwhile, undoped gC_3N_4NFs did not exhibit any significant conversion rate.[19,162] Intriguingly, the CO oxidation performance on Au/Pd/gC_3N_4NFs was superior to the previously reported metal and metal oxide-based catalysts (Table 1.2).[70,155,163–174] After a durability test for 20 h, the as-formed Au/Pd/gC_3N_4NFs did not exhibit any loss in activity, while Pd/gC_3N_4NFs lost 10% and Au/gC_3N_4NFs lost 15%. Thereby, co-doping with both Au and Pd enhances activity due to the electronic effect and catalytic merits of binary dopants and also boosts the durability.[19,162]

Table 1.2 The CO oxidation performance of our developed Au/Pd/gC_3N_4NFs, Pd/Cu/gC_3N_4NFs, and Au/Pd/gC_3N_4NFs, and Pd/Cu/gCN NWs relative to other reports. T_{100} is the temperature required for complete CO oxidation to CO_2.

Catalyst	Performance T_{100} (°C)	Reference
Au/Pd/gC_3N_4NFs	144	162
Pd/Cu/gCN NWs	149	161
Au/Pd/gC_3N_4NTs	165	175
Pd/Cu/gC_3N_4NTs	154	20 and 176
Pd-impeded nanohole structured 3D porous graphene	190	179
$AuPd/TiO_2$	190	180
Co/CN/SBA-16	175	181
$AuPd/SiO_2$	182	182
Pt/CN_x/SBA-15	250	44
Cu_2O/C_3N_4	200	38
Au/C_3N_4/SBA-15	270	183
$AuPd@Al_2O_3$	200	184
$Au_{0.75}Cu_{0.25}/SiO_2$	300	185
Pd/La-doped γ-alumina	175	186
Nanoarray-based $CuMn_2O_4$	320	187
Washed-coated $CuMn_2O_4$	350	
Cu_1/Mn_1	180	188
MnO_x	310	189
Co_3O_4/mesoporous g-C_3N_4	160	190
Pd-γ alumina	155	191
CuO/SiO_2	280	192

Later, gC_3N_4 nanotubes *in situ* co-doped with Au and Pd at the atomic level (Au/Pd/gC_3N_4NTs) were formed by the polymerization of melamine in ethylene glycol solution containing $HAuCL_4$ and K_2PdCl_4 using nitric acid before drying and then carbonization under nitrogen at 450 °C (Figure 1.9).[175] That drove the preparation of uniform gC_3N_4 nanotubes *in situ* co-doped with Au and Pd at the atomic level with a length of 1.3 μm and inner pore of 70 nm

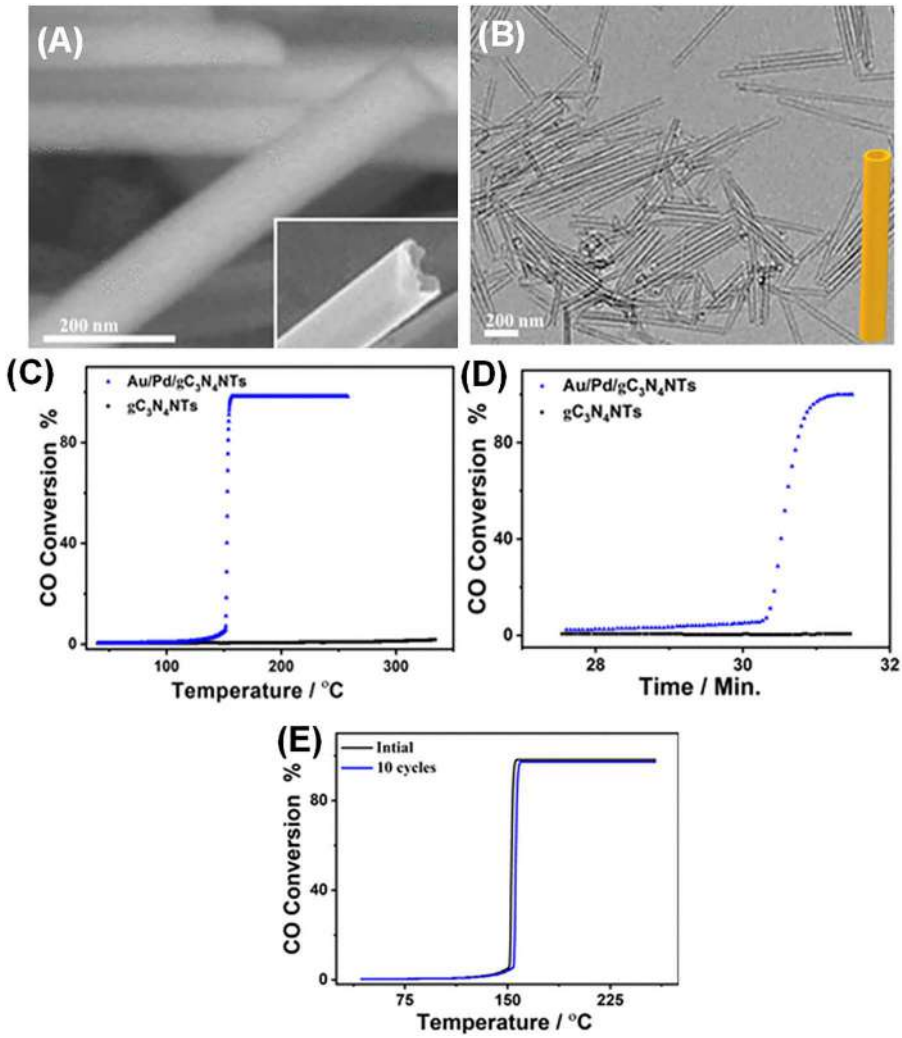

Figure 1.9 (A) SEM and (B) TEM images of Au/Pd/gC_3N_4NTs. CO oxidation as a function of temperature (C) and time (D) of Au/Pd/gC_3N_4NTs relative to gC_3N_4NTs, and (E) CO oxidation durability of Au/Pd/gC_3N_4NTs.[175] Reproduced from ref. 175 with permission from American Chemical Society, Copyright 2019.

with a wall thickness of 8 nm (Figure 1.9A and B).[175] The as-obtained Au/Pd/gC_3N_4NTs nanotubes had an exterior layer of polycrystalline graphitic layer, and the inner core of amorphous carbon comprises various defects and lattice distortion due to the co-doping effect.[175] The surface area of Au/Pd/gC_3N_4NTs (320.6 $m^2\ g^{-1}$) was higher than that of undoped gC_3N_4NTs (275.7 $m^2\ g^{-1}$). Au/Pd/gC_3N_4NTs with a high surface can afford abundant active catalytic sites for the adsorption/activation/dissociation of reactant, while pores promote the mass transfer and electron mobility during the catalytic applications.[175] Therefore, the CO conversion on Au/Pd/gC_3N_4NTs was completed at 165 °C compared to 1% only on metal-free gC_3N_4NTs, due to the electronic and synergetic effect of Au/Pd (Figure 1.9C).[175] The CO oxidation kinetics on Au/PdgC_3N_4NTs was quicker than metal-free as inferred in its complete conversion at 30 min under 165 °C relative to only 2% for gC_3N_4NTs (Figure 1.9D).[175] Furthermore, Au/PdgC_3N_4NTs maintained activity after 10 durability cycles without any significant loss (Figure 1.9E). Likewise, Pd/Cu/gC_3N_4NTs were formed using nitric acid to polymerize melamine in an ethylene glycol solution involving K_2PdCl_4 and $CuCl_2$, then dry annealing at 550 °C under nitrogen.[20,176]

Raising the annealing temperature and using Pd/Cu salts instead of Au/Pd salts drove the formation of shorter (1.5 μm) Pd/Cu/gC_3N_4NTs nanotubes with a smaller hollow interior of 60 nm. Interestingly, Pd/Cu/gC_3N_4NTs showed a great catalytic activity towards CO oxidation and CO_2 reduction compared to undoped gC_3N_4NTs.[20,176] Particularly, the complete CO oxidation to CO_2 was achieved at 154 °C, which was superior to Pd/gC_3N_4NTs (210 °C) by 56 °C and Cu/gC_3N_4NTs (250 °C) by 96 °C.[20,176]

Pd/Cu/gC_3N_4NTs allowed the electrochemical and photoelectrochemical CO_2RR to form formic acid as the main product with an inferior amount of ethanol at room temperature in an aqueous sol $NaHCO_3$. The electrochemical CO_2RR current of Pd/Cu/gC_3N_4NTs was higher than that of the metal-free gC_3N_4NTs by four-fold; meanwhile, the visible light enhanced the current density of Pd/Cu/gC_3N_4NTs by 2.92 times compared to dark conditions.[20,176] It should be noted that the CO oxidation performances of our newly developed Au/Pd/gC_3N_4NFs, Pd/Cu/gC_3N_4NTs, and Au/Pd/gC_3N_4NTs, and Pd/Cu/gCN NWs were superior to metal nanoparticles (*i.e.*, Au/Pd, Pd, and Pt) and metal oxides (*i.e.*, Co_3O_4, MnOx, and Cu_2O) over various supports (Table 1.2).[21–23,35–37,162,177] These results open new ways to utilize 1D gCNs in thermal CO oxidation. In pursuit of this aim, 1D gCN nanorods were co-doped with Pd and Pt (PtPd/gCNs) for electrochemical and photoelectrochemical CO ORs.[178] The synthesis process including using HCl and $NaNO_3$ for the polymerization of melamine in ethylene glycol solution contains K_2PdCl_4 and Na_2PtCl_4, under sonication, then drying and annealing at 550 °C under nitrogen (Figure 1.10A).[178] The mechanism is proposed according to the *in situ* formation of HNO_3 (H^+ from HCl and NO_3 from $NaNO_3$) to allow the amino group's protonation (–NH_2) of melamine, to form melem and melon sheets similar to other reports.[24,158–160] So, HCl and $NaNO_3$ should be used together; also, the reaction parameters like addition and solvent should be considered to avoid the formation of undesired shapes like sheets, flakes, or wires.[178]

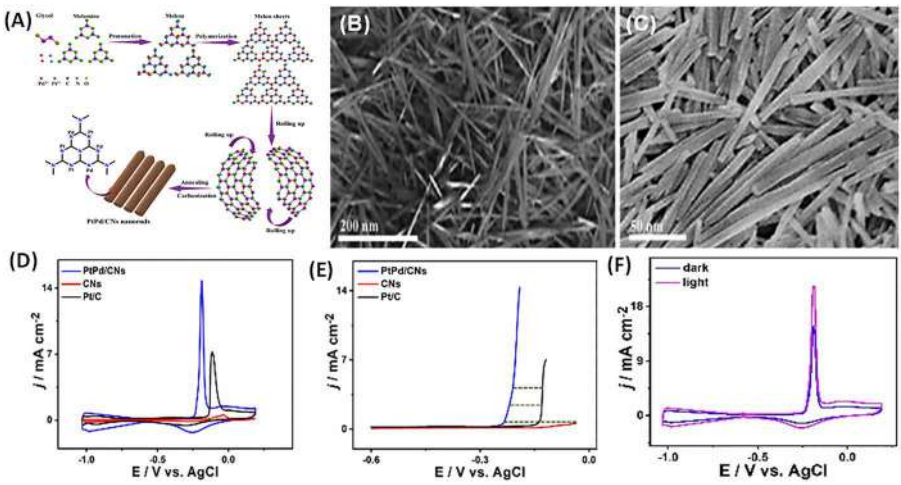

Figure 1.10 (A) The formation mechanism of Pt/Pd/gCNs. (B) SEM image of Pt/Pd/gCN NRs. (C) TEM image of Pt/Pd/gCNs. (D) CVs and (E) LSV tested in CO-saturated 0.1 M KOH at 50 mV s^{-1}. (F) CVs of PtPd/CNs under light in CO-saturated 0.1 M KOH at 50 mV s^{-1}. (B and C) Reproduced from ref. 178 with permission from the Royal Society of Chemistry.

Melon sheets with various interlayers provide massive adsorption sites for Pt/Pd atoms. Finally, melon sheets are rolled up to form nanorod shapes after the carbonization process. The nanorods had a rough surface with a twined end surface and an average length and width of 94 ± 2 nm and 11 ± 1 nm, respectively (Figure 1.10B and C).[178] The BET surface area of PtPd/CNs (155.2 m^2 g^{-1}) was superior to metal-free nanorods gCN nanorods (149. 2 m^2 g^{-1}).

The electrochemical CO oxidation activity and stability of PtPd/CNs nanorods (containing PtPd 1.5 wt%) measured in KOH solution were significantly superior to the commercial Pt/C catalyst (containing 20 wt% Pt) and undoped gCNs.[178] This is obvious in the higher CO oxidation current density of PtPd/CNs (14.75 mA cm^{-2}) than Pt/C by 2.01 times and gCN nanorods by 23.41 times under the same potential (Figure 1.10D).[178] Additionally, the CO oxidation current of PtPd/CNs under any applied potential was higher than that of either the Pt/C or gCN nanorods (Figure 1.10E). This is due to the great electrochemical active surface area of the PtPd/CNs nanorods (75 m^2 g^{-1}) compared to the gCN nanorods (68 m^2 g^{-1}) and Pt/C (64 m^2 g^{-1}), as well as the electronic and synergetic effect of PtPd.[178] Furthermore, the photoelectrochemical CO oxidation current of PtPd/CNs increased 1.48-fold than under dark conditions (Figure 1.10F), originating from the unique photocatalytic properties of gCN nanorods, and catalytic properties of PtPd.[178]

1.6 Conclusion

This chapter summarized the recent advances in the fabrication process of 1D gCN nanostructures, including self-assembly and template-based methods (*i.e.*, soft template and hard template). The template-based method is based on the simple filling of the carbon–nitrogen precursors (*i.e.*, melamine, urea, cyanuric acid) into the hard template (*i.e.*, AAO and SBA-15) or the soft template (non-ionic copolymers P123 and F127) followed by solidification or sintering and then template removal by acid (hydrogen fluoride or ammonium difluoride). These methods allowed the fabrication of uniform and well-aligned 1D nanorods, nanowires, nanofibers, nanotubes, and nanoneedles. The diameter, shape, compositions, surface area, conductivity, catalytic, photocatalytic, physiochemical merits, and crystallinity of the thus obtained 1D nanostructures are shaped by the type of precursors, template, and reaction conditions (*i.e.*, solvents, annealing temperature, and reactant concatenations). However, the multiple reaction steps, using hazardous chemicals or solvents, and high-cost templates are the main drawbacks of template-based methods. Also, the unavoidable reaction between templates and carbon–nitrogen precursors may lead to undesired shapes or phases. There are also newly developed methods for preparing one-dimensional nanostructures like hydrothermal, sol–gel, sonication, and molten salts. Although these methods are eco-friendlier and low-cost, they could not produce uniform or aligned 1D nanostructures as in the template methods. These methods also still comprise multi-step reactions. Recent advances include the combination of different methods to reduce the cost and improve the quality and yield of the products, like thermal condensation with templates or sonication, or acid etching/exfoliation, or molten salts. Our group developed a novel one-pot, green, and template-free approach for the rational fabrication of 1D gCN nanostructures doped with mono and binary metal dopants (*i.e.*, PdPt, Pd, Cu, Au, AuPd) including nanowires, nanofibers, nanorods, and nanotubes, *via* the simple polymerization of melamine in organic solvents (*i.e.*, ethanol, methanol, isopropanol, and ethylene glycol) with the assistance of mild nitric acid followed by annealing. The catalytic performance of 1D gCNs towards CO oxidation and CO_2RR was discussed in detail, supported by various examples. The CO_2RR allowed the production of various hydrocarbons (*i.e.*, formic acid, methanol, methane, and CO), but most reported articles were photoelectrochemical without enough emphasis on the electrocatalytic activities. The thermal CO oxidation on 1D gCNs formed CO_2 at mild temperatures 140–190 °C due to their unique adsorption/dissociation of O_2 along with retarding the intermediates. However, the CO oxidation and CO_2RR on 1D gCNs remain impractical and need further improvements (*i.e.*, ease of preparation methods, reduction of cost, enhancement of the production yield, reduction of the thermal oxidation temperature).

The electrocatalytic CO oxidation and CO_2RR on 1D gCNs have not been studied enough compared to other applications. There is a critical need for future theoretical and experimental studies to tailor the catalytic properties

of 1D gCN (*i.e.*, activate the surface area, electrical conductivity, and charge dynamic) and photocatalytic properties (*i.e.*, reduce band gap energy, delay the electron–hole recombination, and enhance the visible light absorption > 450 nm) to allow scalable CO oxidation and CO_2RR on 1D gCNs. These targets could be achieved by combining 1D gCNs with various catalysts such as porous metal catalysts, especially those that are multimetallic, due to their unique redox properties at room temperature;[193,194] likewise, carbon materials (*i.e.*, fullerenes, carbon dots, graphene oxide, carbon nanotubes), metal carbide or nitride, transition metal oxides (*i.e.*, Cu_2O, TiO_2, Ce_2O), due to their great catalytic performance for gas conversion reactions under ambient conditions.[116–121,124–126,195–198] There is also a need to obtain more insight into the structural-related fundamentals of 1D gCNs for various gas conversion reactions rather than CO and CO_2, such as methane and ammonia.

References

1. K. Eid, V. Malgras, P. He, K. Wang, A. Aldalbahi, S. M. Alshehri, Y. Yamauchi and L. Wang, *RSC Adv.*, 2015, **5**, 31147–31152.
2. K. Eid, H. Wang, P. He, K. Wang, T. Ahamad, S. M. Alshehri, Y. Yamauchi and L. Wang, *Nanoscale*, 2015, **7**, 16860–16866.
3. H. Wang, S. Yin, K. Eid, Y. Li, Y. Xu, X. Li, H. Xue and L. Wang, *ACS Sustainable Chem. Eng.*, 2018, **6**, 11768–11774.
4. K. Eid, K. A. Soliman, D. Abdulmalik, D. Mitoraj, M. H. Sleim, M. O. Liedke, H. A. El-Sayed, A. S. AlJaber, I. Y. Al-Qaradawi, O. Mendoza Reyes and A. M. Abdullah, *Catal. Sci. Technol.*, 2020, **10**, 801–809.
5. S. Kundu, K. Bramhaiah and S. Bhattacharyya, *Nanoscale Adv.*, 2020, **2**, 5130–5151.
6. F. Wu, K. Eid, A. M. Abdullah, W. Niu, C. Wang, Y. Lan, A. A. Elzatahry and G. Xu, *ACS Appl. Mater. Interfaces*, 2020, **12**, 31309–31318.
7. W.-J. Ong, L.-L. Tan, Y. H. Ng, S.-T. Yong and S.-P. Chai, *Chem. Rev.*, 2016, **116**, 7159–7329.
8. K. Eid, H. Wang, V. Malgras, Z. A. Alothman, Y. Yamauchi and L. Wang, *J. Phys. Chem. C*, 2015, **119**, 19947–19953.
9. S. Lu, K. Eid, M. Lin, L. Wang, H. Wang and H. Gu, *J. Mater. Chem. A*, 2016, **4**, 10508–10513.
10. L. Sun, H. Wang, K. Eid, S. M. Alshehri, V. Malgras, Y. Yamauchi and L. Wang, *Electrochim. Acta*, 2016, **188**, 845–851.
11. Q. Lu, H. Wang, K. Eid, Z. A. Alothman, V. Malgras, Y. Yamauchi and L. Wang, *Chem. - Asian J.*, 2016, **11**, 1939–1944.
12. S. Lu, K. Eid, D. Ge, J. Guo, L. Wang, H. Wang and H. Gu, *Nanoscale*, 2017, **9**, 1033–1039.
13. S. Lu, K. Eid, Y. Deng, J. Guo, L. Wang, H. Wang and H. Gu, *J. Mater. Chem. A*, 2017, **5**, 9107–9112.
14. K. Eid, Y. H. Ahmad, S. Y. AlQaradawi and N. K. Allam, *Catal. Sci. Technol.*, 2017, **7**, 2819–2827.

15. K. Eid, Y. H. Ahmad, H. Yu, Y. Li, X. Li, S. Y. AlQaradawi, H. Wang and L. Wang, *Nanoscale*, 2017, **9**, 18881–18889.
16. J. Liu, H. Wang and M. Antonietti, *Chem. Soc. Rev.*, 2016, **45**, 2308–2326.
17. I. F. Teixeira, E. C. M. Barbosa, S. C. E. Tsang and P. H. C. Camargo, *Chem. Soc. Rev.*, 2018, **47**, 7783–7817.
18. J. Liebig, *Ann. Pharm.*, 1834, **10**, 1–47.
19. K. Eid, M. H. Sliem, A. S. Eldesoky and A. M. Abdullah, *Data Brief.*, 2019, **27**, 104734.
20. K. Eid and A. M. Abdullah, *Data Brief.*, 2019, **26**, 104495.
21. J. Zhu, P. Xiao, H. Li and S. A. C. Carabineiro, *ACS Appl. Mater. Interfaces*, 2014, **6**, 16449–16465.
22. F. Ding, D. Yang, Z. Tong, Y. Nan, Y. Wang, X. Zou and Z. Jiang, *Environ. Sci.: Nano*, 2017, **4**, 1455–1469.
23. J. Lai, S. Li, F. Wu, M. Saqib, R. Luque and G. Xu, *Energy Environ. Sci.*, 2016, **9**, 1210–1214.
24. J. Gao, Y. Zhou, Z. Li, S. Yan, N. Wang and Z. Zou, *Nanoscale*, 2012, **4**, 3687–3692.
25. Q. Guo, Y. Xie, X. Wang, S. Zhang, T. Hou and S. Lv, *Chem. Commun.*, 2004, **4**, 26–27.
26. D. Wang, Z. Wang, W. Liu, Arramel, J. Zhou, Y. P. Feng, K. P. Loh, J. Wu and A. T. S. Wee, *ACS Nano*, 2020, **14**, 14008–14016.
27. F. Pitterl, J.-P. Chervet and H. Oberacher, *Anal. Bioanal. Chem.*, 2010, **397**, 1203–1215.
28. Y. Zheng, J. Liu, J. Liang, M. Jaroniec and S. Z. Qiao, *Energy Environ. Sci.*, 2012, **5**, 6717–6731.
29. W. Huang, G. Sun and T. Cao, *Chem. Soc. Rev.*, 2017, **46**, 1977–2000.
30. G. Singh, J. Lee, A. Karakoti, R. Bahadur, J. Yi, D. Zhao, K. AlBahily and A. Vinu, *Chem. Soc. Rev.*, 2020, **49**, 4360–4404.
31. G. Zhang, G. Li, T. Heil, S. Zafeiratos, F. Lai, A. Savateev, M. Antonietti and X. Wang, *Angew. Chem., Int. Ed.*, 2019, **58**, 3433–3437.
32. P. Xia, M. Antonietti, B. Zhu, T. Heil, J. Yu and S. Cao, *Adv. Funct. Mater.*, 2019, **29**, 1900093.
33. Y. Xia, K. Xiao, B. Cheng, J. Yu, L. Jiang, M. Antonietti and S. Cao, *ChemSusChem*, 2020, **13**, 1730–1734.
34. S. Samanta and R. Srivastava, *Mater. Adv.*, 2020, **1**, 1506–1545.
35. J. Zhao, M. R. H. S. Gilani, Z. Liu, R. Luque and G. Xu, *Polym. Chem.*, 2018, **9**, 4324–4331.
36. X. Hu, Y. Wu, H. Li and Z. Zhang, *J. Phys. Chem. C*, 2010, **114**, 9603–9607.
37. Y. Wang, X. Wang and M. Antonietti, *Angew. Chem., Int. Ed.*, 2012, **51**, 68–89.
38. Y. Shi, X. Hu, J. Zhao, X. Zhou, B. Zhu, S. Zhang and W. Huang, *New J. Chem.*, 2015, **39**, 6642–6648.
39. J. Barrio, L. Lin, P. Amo-Ochoa, J. Tzadikov, G. Peng, J. Sun, F. Zamora, X. Wang and M. Shalom, *Small*, 2018, **14**, 1800633.
40. A. Jin, Y. Jia, C. Chen, X. Liu, J. Jiang, X. Chen and F. Zhang, *J. Phys. Chem. C*, 2017, **121**, 21497–21509.

41. S. Tragl, K. Gibson, J. Glaser, V. Duppel, A. Simon and H.-J. Meyer, *Solid State Commun.*, 2007, **141**, 529–534.
42. Q. Han, B. Wang, J. Gao and L. Qu, *Angew. Chem., Int. Ed.*, 2016, **55**, 10849–10853.
43. T. Jordan, N. Fechler, J. Xu, T. J. K. Brenner, M. Antonietti and M. Shalom, *ChemCatChem*, 2015, **7**, 2826–2830.
44. P. Xiao, Y. Zhao, T. Wang, Y. Zhan, H. Wang, J. Li, A. Thomas and J. Zhu, *Chem. - Eur. J.*, 2014, **20**, 2872–2878.
45. S. Wang, Y. Feng, M. Yu, Q. Wan and S. Lin, *ACS Appl. Mater. Interfaces*, 2017, **9**, 33267–33273.
46. Z. Sun, H. Wang, Z. Wu and L. Wang, *Catal. Today*, 2018, **300**, 160–172.
47. W.-J. Ong, L. K. Putri and A. R. Mohamed, *Chem. - Eur. J.*, 2020, **26**, 9710–9748.
48. Y. Li, T. Kong and S. Shen, *Small*, 2019, **15**, 1900772.
49. H. Starukh and P. Praus, *Catalysts*, 2020, **10**(10), 1119.
50. U. Ghosh, A. Majumdar and A. Pal, *J. Environ. Chem. Eng.*, 2021, **9**, 104631.
51. Z. Yang, Y. Zhang and Z. Schnepp, *Soft and Hard Templating of Graphitic Carbon Nitride*, Royal Society of Chemistry, 2015, vol. 3.
52. H. Liu, X. Wang, H. Wang and R. Nie, *J. Mater. Chem. B*, 2019, **7**, 5432–5448.
53. Y. Zheng, L. Lin, B. Wang and X. Wang, *Angew. Chem., Int. Ed.*, 2015, **54**, 12868–12884.
54. X. Jin, V. V Balasubramanian, S. T. Selvan, D. P. Sawant, M. A. Chari, G. Q. Lu and A. Vinu, *Angew. Chem., Int. Ed.*, 2009, **48**, 7884–7887.
55. J. Barrio, M. Volokh and M. Shalom, *J. Mater. Chem. A*, 2020, **8**, 11075–11116.
56. F. Goettmann, A. Fischer, M. Antonietti and A. Thomas, *Angew. Chem., Int. Ed.*, 2006, **45**, 4467–4471.
57. J. Sun, J. Zhang, M. Zhang, M. Antonietti, X. Fu and X. Wang, *Nat. Commun.*, 2012, **3**, 1139.
58. T. Fu, M. Wang, W. Cai, Y. Cui, F. Gao, L. Peng, W. Chen and W. Ding, *ACS Catal.*, 2014, **4**, 2536–2543.
59. J. Zhang, F. Guo and X. Wang, *Adv. Funct. Mater.*, 2013, **23**, 3008–3014.
60. Y. Ling, G. Liao, W. Feng, Y. Liu and L. Li, *J. Photochem. Photobiol., A*, 2017, **349**, 108–114.
61. J. Liu, J. Yan, H. Ji, Y. Xu, L. Huang, Y. Li, Y. Song, Q. Zhang, H. Xu and H. Li, *Mater. Sci. Semicond. Process.*, 2016, **46**, 59–68.
62. S. Le, T. Jiang, Q. Zhao, X. Liu, Y. Li, B. Fang and M. Gong, *RSC Adv.*, 2016, **6**, 38811–38819.
63. Y. Guo, Q. Liu, Z. Li, Z. Zhang and X. Fang, *Appl. Catal., B*, 2018, **221**, 362–370.
64. H.-M. Zhao, C.-M. Di, L. Wang, Y. Chun and Q.-H. Xu, *Microporous Mesoporous Mater.*, 2015, **208**, 98–104.
65. S. W. Bian, Z. Ma and W. G. Song, *J. Phys. Chem. C*, 2009, **113**, 8668–8672.

66. X. H. Li, J. Zhang, X. Chen, A. Fischer, A. Thomas, M. Antonietti and X. Wang, *Chem. Mater.*, 2011, **23**, 4344–4348.
67. Y. Wang, X. Wang, M. Antonietti and Y. Zhang, *ChemSusChem*, 2010, **3**, 435–439.
68. W. Peng, S. S. Zhang, Y. B. Shao and J. H. Huang, *Int. J. Hydrogen Energy*, 2018, **43**, 22215–22225.
69. K. L. Chen, S. S. Zhang, J. Q. Yan, W. Peng, D. P. Lei and J. H. Huang, *Int. J. Hydrogen Energy*, 2019, **44**, 31916–31929.
70. Q. Liu, C. Chen, K. Yuan, C. D. Sewell, Z. Zhang, X. Fang and Z. Lin, *Nano Energy*, 2020, **77**, 105104.
71. X. Wang, C. Zhou, R. Shi, Q. Liu, G. I. N. Waterhouse, L. Wu, C. H. Tung and T. Zhang, *Nano Res.*, 2019, **12**, 2385–2389.
72. Z. Chao, S. Run, S. Lu, W. Li-Zhu, T. Chen-Ho and Z. Tierui, *Nano Res.*, 2018, **11**, 3462–3468.
73. J. Xu, S. Zhang, X. Liu, F. Bian and H. Jiang, *Catal. Sci. Technol.*, 2019, **9**, 6938–6945.
74. J. Fu, B. Zhu, C. Jiang, B. Cheng, W. You and J. Yu, *Small*, 2017, **13**, 1603938.
75. B. Liu, L. Ye, R. Wang, J. Yang, Y. Zhang, R. Guan, L. Tian and X. Chen, *ACS Appl. Mater. Interfaces*, 2018, **10**, 4001–4009.
76. S. Guo, H. Zhang, P. Yang, Y. Chen, X. Yu, B. Yu, Y. Zhao, Z. Yang and Z. Liu, *Catal. Sci. Technol.*, 2019, **9**, 2485–2492.
77. Z. Mo, X. Zhu, Z. Jiang, Y. Song, D. Liu, H. Li, X. Yang, Y. She, Y. Lei, S. Yuan, H. Li, L. Song, Q. Yan and H. Xu, *Appl. Catal., B*, 2019, **256**, 117854.
78. L. Jia, X. Cheng, X. Wang, H. Cai, P. He, J. Ma, L. Li, Y. Ding and X. Fan, *Ind. Eng. Chem. Res.*, 2020, **59**, 1065–1072.
79. X. Li, K. Pan, Y. Qu and G. Wang, *Nano Res.*, 2018, **11**, 1322–1330.
80. C. Zhao, Q. Li, Y. Xie, L. Zhang, X. Xiao, D. Wang, Y. Jiao, C. A. Hurd Price, B. Jiang and J. Liu, *J. Mater. Chem. A*, 2020, **8**, 305–312.
81. Y. Wang, X. Liu, J. Liu, B. Han, X. Hu, F. Yang, Z. Xu, Y. Li, S. Jia, Z. Li and Y. Zhao, *Angew. Chem., Int. Ed.*, 2018, **57**, 5765–5771.
82. Y. Zheng, L. Lin, X. Ye, F. Guo and X. Wang, *Angew. Chem., Int. Ed.*, 2014, **53**, 11926–11930.
83. L. Zhang, N. Ding, M. Hashimoto, K. Iwasaki, N. Chikamori, K. Nakata, Y. Xu, J. Shi, H. Wu, Y. Luo, D. Li, A. Fujishima and Q. Meng, *Nano Res.*, 2018, **11**, 2295–2309.
84. W. K. Jo and T. S. Natarajan, *Chem. Eng. J.*, 2015, **281**, 549–565.
85. H. Shin, W. G. Jung, D. H. Kim, J. S. Jang, Y. H. Kim, W. T. Koo, J. Bae, C. Park, S. H. Cho, B. J. Kim and I. D. Kim, *ACS Nano*, 2020, **14**, 11394–11405.
86. X. Fan, T. Wang, B. Gao, H. Gong, H. Xue, H. Guo, L. Song, W. Xia, X. Huang and J. He, *Langmuir*, 2016, **32**, 13322–13332.
87. Z. Yu, Y. Li, J. Qu, R. Zheng, J. M. Cairney, J. Zhang, M. Zhu, A. Khan and W. Li, *Chem. Eng. J.*, 2021, **404**, 126458.
88. J. Su, P. Geng, X. Li, Q. Zhao, X. Quan and G. Chen, *Nanoscale*, 2015, **7**, 16282–16289.

89. J. Sun, S. Yang, Z. Liang, X. Liu, P. Qiu, H. Cui and J. Tian, *J. Colloid Interface Sci.*, 2020, **567**, 300–307.
90. X. Yan, Q. Gao, J. Qin, X. Hui, Z. Ye, J. Li and Z. Ma, *Mater. Lett.*, 2018, **217**, 1–4.
91. B. Chong, L. Chen, D. Han, L. Wang, L. Feng, Q. Li, C. Li and W. Wang, *Chin. J. Catal.*, 2019, **40**, 959–968.
92. J. Xie, C. Wu, Z. Xu, C. Tian, M. Li and J. Huang, *Mater. Lett.*, 2019, **234**, 179–182.
93. Z. Wang, M. Chen, Y. Huang, X. Shi, Y. Zhang, T. Huang, J. Cao, W. Ho and S. C. Lee, *Appl. Catal., B*, 2018, **239**, 352–361.
94. Z. Tong, D. Yang, Y. Sun, Y. Nan and Z. Jiang, *Small*, 2016, **12**, 4093–4101.
95. T. Ma, J. Bai and C. Li, *Vacuum*, 2017, **145**, 47–54.
96. Z. Qin, F. Xue, Y. Chen, S. Shen and L. Guo, *Appl. Catal., B*, 2017, **217**, 551–559.
97. T. J. Park, R. C. Pawar, S. Kang and C. S. Lee, *RSC Adv.*, 2016, **6**, 89944–89952.
98. M. Khazaei, M. Arai, T. Sasaki and Y. Kawazoe, *J. Phys. Chem. C*, 2013, **117**, 712–720.
99. Y. Zhao, Z. Liu, W. Chu, L. Song, Z. Zhang, D. Yu, Y. Tian, S. Xie and L. Sun, *Adv. Mater.*, 2008, **20**, 1777–1781.
100. T. Bhowmik, M. K. Kundu and S. Barman, *ACS Appl. Mater. Interfaces*, 2016, **8**, 28678–28688.
101. Y. Zhao, F. Zhao, X. Wang, C. Xu, Z. Zhang, G. Shi and L. Qu, *Angew. Chem., Int. Ed.*, 2014, **53**, 13934–13939.
102. K. Xiao, B. Tu, L. Chen, T. Heil, L. Wen, L. Jiang and M. Antonietti, *Angew. Chem., Int. Ed.*, 2019, **58**, 12574–12579.
103. K. Xiao, L. Chen, R. Chen, T. Heil, S. D. C. Lemus, F. Fan, L. Wen, L. Jiang and M. Antonietti, *Nat. Commun.*, 2019, **10**, 74.
104. S. L. Sung, S. H. Tsai, C. H. Tseng, F. K. Chiang, X. W. Liu and H. C. Shih, *Appl. Phys. Lett.*, 1999, **74**, 197–199.
105. S. L. Sung, S. H. Tsai, X. W. Liu and H. C. Shih, *J. Mater. Res.*, 2000, **15**, 502–510.
106. S. Casanova, M. K. Borg, Y. M. J. Chew and D. Mattia, *ACS Appl. Mater. Interfaces*, 2019, **11**, 1689–1698.
107. X. Bai, H. Li, Z. Zhang, X. Zhang, C. Wang, J. Xu and Y. Zhu, *Catal. Sci. Technol.*, 2019, **9**, 1680–1690.
108. K. Xiao, B. Kumru, L. Chen, L. Jiang, B. V. K. J. Schmidt and M. Antonietti, *Beilstein J. Nanotechnol.*, 2019, **10**, 1316–1323.
109. J. Yang, Y. Liang, K. Li, G. Yang, K. Wang, R. Xu and X. Xie, *Catal. Sci. Technol.*, 2019, **9**, 3342–3346.
110. Y. Wang, Y. Li, W. Ju, J. Wang, H. Yao, L. Zhang, J. Wang and Z. Li, *Carbon*, 2016, **102**, 477–486.
111. L. Tian, J. Li, F. Liang, J. Wang, S. Li, H. Zhang and S. Zhang, *Appl. Catal., B*, 2018, **225**, 307–313.

112. X. Zhao, Y. Zhang, X. Zhao, X. Wang, Y. Zhao, H. Tan, H. Zhu, W. Ho, H. Sun and Y. Li, *ACS Appl. Mater. Interfaces*, 2019, **11**, 27934–27943.
113. J. Bai, Q. Han, Z. Cheng and L. Qu, *Chem. - Asian J.*, 2018, **13**, 3160–3164.
114. Y. Wang, S. Zhao, Y. Zhang, J. Fang, W. Chen, S. Yuan and Y. Zhou, *ACS Sustainable Chem. Eng.*, 2018, **6**, 10200–10210.
115. G. Ge, X. Guo, C. Song and Z. Zhao, *ACS Appl. Mater. Interfaces*, 2018, **10**, 18746–18753.
116. Y. Gao, F. Hou, S. Hu, B. Wu, Y. Wang, H. Zhang, B. Jiang and H. Fu, *ChemCatChem*, 2018, **10**, 1330–1335.
117. Z. Sun, W. Wang, Q. Chen, Y. Pu, H. He, W. Zhuang, J. He and L. Huang, *J. Mater. Chem. A*, 2020, **8**, 3160–3167.
118. S. Guo, Z. Deng, M. Li, B. Jiang, C. Tian, Q. Pan and H. Fu, *Angew. Chem., Int. Ed.*, 2016, **55**, 1830–1834.
119. Z. Mo, H. Xu, Z. Chen, X. She, Y. Song, P. Yan, L. Xu, Y. Lei, S. Yuan and H. Li, *Appl. Catal., B*, 2018, **225**, 154–161.
120. F. Xu, Z. Mo, J. Yan, J. Fu, Y. Song, W. El-Alami, X. Wu, H. Li and H. Xu, *J. Colloid Interface Sci.*, 2020, **560**, 555–564.
121. G. Zhang, A. Savateev, Y. Zhao, L. Li and M. Antonietti, *J. Mater. Chem. A*, 2017, **5**, 12723–12728.
122. T. Huang, S. Pan, L. Shi, A. Yu, X. Wang and Y. Fu, *Nanoscale*, 2020, **12**, 1833–1841.
123. J. Li, C. Cao and H. Zhu, *Nanotechnology*, 2007, **18**, 115605.
124. Y. Zhu, A. Marianov, H. Xu, C. Lang and Y. Jiang, *ACS Appl. Mater. Interfaces*, 2018, **10**, 9468–9477.
125. Z. Huang, F. Li, B. Chen and G. Yuan, *RSC Adv.*, 2015, **5**, 102700–102706.
126. Z. Jin, Q. Zhang, S. Yuan and T. Ohno, *RSC Adv.*, 2015, **5**, 4026–4029.
127. T. Shu, W. Yang, K. Li, L. Yan, Y. Dai and H. Guo, *Energy Environ. Focus*, 2018, **4**, 107–115.
128. K. Li, Z. Zeng, L. Yan, S. Luo, X. Luo, M. Huo and Y. Guo, *Appl. Catal., B*, 2015, **165**, 428–437.
129. B. Tahir, M. Tahir and N. A. S. Amin, *Appl. Catal., B*, 2019, **248**, 167–183.
130. Z. Zeng, K. Li, L. Yan, Y. Dai, H. Guo, M. Huo and Y. Guo, *RSC Adv.*, 2014, **4**, 59513–59518.
131. D. Long, W. Chen, S. Zheng, X. Rao and Y. Zhang, *Ind. Eng. Chem. Res.*, 2020, **59**, 4549–4556.
132. S. Wang, C. Li, T. Wang, P. Zhang, A. Li and J. Gong, *J. Mater. Chem. A*, 2014, **2**, 2885–2890.
133. H. Li, X. Bao, Z. Wang, Z. Zheng, P. Wang, Y. Liu, X. Zhang, X. Qin, Y. Dai, Y. Li, H. Zou and B. Huang, *Int. J. Hydrogen Energy*, 2019, **44**, 28780–28788.
134. S. Guo, Y. Tang, Y. Xie, C. Tian, Q. Feng, W. Zhou and B. Jiang, *Appl. Catal., B*, 2017, **218**, 664–671.
135. X. Liu, X. Wu, D. Long, X. Rao and Y. Zhang, *J. Photochem. Photobiol., A*, 2020, **391**, 112337.
136. G. Ge and Z. Zhao, *Catal. Sci. Technol.*, 2019, **9**, 266–270.
137. D. Yang, Y. Zhang, H. Zou, S. Zhang, Y. Wu, Z. Cai, J. Shi and Z. Jiang, *ACS Sustainable Chem. Eng.*, 2019, **7**, 285–295.

138. X. Lu, H. Wang, S. Zhang, D. Cui and Q. Wang, Synthesis, characterization and electrocatalytic properties of carbon nitride nanotubes for methanol electrooxidation, *Solid State Sci.*, 2009, **11**(2), 428–432.
139. W. Wang, Z. Shu, J. Zhou, T. Li, P. Duan, Z. Zhao, Y. Tan, C. Xie and S. Cui, *Appl. Clay Sci.*, 2018, **158**, 143–149.
140. F. Ding, Z. Zhao, D. Yang, X. Zhao, Y. Chen and Z. Jiang, *Ind. Eng. Chem. Res.*, 2019, **58**, 3679–3687.
141. S. Kang, J. Jang, S. H. Ahn and C. S. Lee, *Dalton Trans.*, 2019, **48**, 2170–2178.
142. J. Zhang, M. Wu, B. He, R. Wang, H. Wang and Y. Gong, *Appl. Surf. Sci.*, 2019, **470**, 565–572.
143. M. Sun, S. Shen, Z. Wu, Z. Tang, J. Shen and J. Yang, *Ceram. Int.*, 2018, **44**, 8125–8132.
144. X. Zhou, C. Shao, S. Yang, X. Li, X. Guo, X. Wang, X. Li and Y. Liu, *ACS Sustainable Chem. Eng.*, 2018, **6**(2), 2316–2323.
145. Y. Zeng, X. Liu, C. Liu, L. Wang, Y. Xia, S. Zhang, S. Luo and Y. Pei, *Appl. Catal., B*, 2018, **224**, 1–9.
146. P. Wang, I. Sinev, F. Sun, H. Li, D. Wang, Q. Li, X. Wang, R. Marschall and M. Wark, *RSC Adv.*, 2017, **7**, 42774–42782.
147. X. Zhou, G. Zhang, C. Shao, X. Li, X. Jiang and Y. Liu, *Ceram. Int.*, 2017, **43**, 15699–15707.
148. Y. Cui, Z. Ding, X. Fu and X. Wang, *Angew. Chem., Int. Ed.*, 2012, **51**, 11814–11818.
149. X. Bai, L. Wang, R. Zong and Y. Zhu, *J. Phys. Chem. C*, 2013, **117**, 9952–9961.
150. R. C. Pawar, S. Kang, J. H. Park, J. H. Kim, S. Ahn and C. S. Lee, *Sci. Rep.*, 2016, **6**, 1–14.
151. J. Liu, J. Huang, H. Zhou and M. Antonietti, *ACS Appl. Mater. Interfaces*, 2014, **6**, 8434–8440.
152. Z. Huang, F. W. Yan and G. Q. Yuan, *ACS Sustainable Chem. Eng.*, 2018, **6**, 3187–3195.
153. D. Das, D. Banerjee, N. S. Das, B. Das, U. K. Ghorai and K. K. Chattopadhyay, *Solid State Sci.*, 2018, **82**, 99–105.
154. M. Tahir, N. Mahmood, J. Zhu, A. Mahmood, F. K. Butt, S. Rizwan, I. Aslam, M. Tanveer, F. Idrees, I. Shakir, C. Cao and Y. Hou, *Sci. Rep.*, 2015, **5**, 1–10.
155. Y. Li, B. Li, D. Zhang, L. Cheng and Q. Xiang, *ACS Nano*, 2020, **14**, 10552–10561.
156. F.-X. Xiao, J. Miao, H. B. Tao, S.-F. Hung, H.-Y. Wang, H. Bin Yang, J. Chen, R. Chen and B. Liu, *Small*, 2015, **11**, 2115–2131.
157. Z. Zeng, X. Quan, H. Yu, S. Chen and S. Zhang, *J. Catal.*, 2019, **375**, 361–370.
158. M. Tahir, C. Cao, N. Mahmood, F. K. Butt, A. Mahmood, F. Idrees, S. Hussain, M. Tanveer and I. Aslam, *ACS Appl. Mater. Interfaces*, 2014, **6**, 1258–1265.
159. M. Tahir, C. Cao, F. K. Butt, S. Butt, F. Idrees, Z. Ali, I. Aslam, M. Tanveer, A. Mahmood and N. Mahmood, *CrystEngComm*, 2014, **16**, 1825–1830.

160. Z. Muhammad Tahir, C. Cao, F. K. Butt, F. Idrees, N. Mahmood, T. M. Ali, I. Aslam, M. Tanvir and M. Rizwan, *J. Mater. Chem. A*, 2013, **1**, 13949–13955.
161. K. A. M. Eid and A. M. Abdullah, *US Pat.*, US20200239311A1, 2020.
162. K. Eid, M. H. Sliem, A. S. Eldesoky, H. Al-Kandari and A. M. Abdullah, *Int. J. Hydrogen Energy*, 2019, **44**, 17943–17953.
163. L. E. Gómez, I. S. Tiscornia, A. V. Boix and E. E. Miró, *Int. J. Hydrogen Energy*, 2012, **37**, 14812–14819.
164. R. Liu, H. M. Chen, L. P. Fang, C. Xu, Z. He, Y. Lai, H. Zhao, D. Bekana and J. F. Liu, *Environ. Sci. Technol.*, 2018, **52**, 4244–4255.
165. D. Varade, H. Abe, Y. Yamauchi and K. Haraguchi, *ACS Appl. Mater. Interfaces*, 2013, **5**, 11613–11617.
166. T. Ward, L. Delannoy, R. Hahn, S. Kendell, C. J. Pursell, C. Louis and B. D. Chandler, *ACS Catal.*, 2013, **3**, 2644–2653.
167. P. Kast, G. Kučerová and R. J. Behm, *Catal. Today*, 2015, **244**, 146–160.
168. W. Zhan, J. Wang, H. Wang, J. Zhang, X. Liu, P. Zhang, M. Chi, Y. Guo, Y. Guo, G. Lu, S. Sun, S. Dai and H. Zhu, *J. Am. Chem. Soc.*, 2017, **139**, 8846–8854.
169. A. Piednoir, M. A. Languille, L. Piccolo, A. Valcarcel, F. J. C. S. Aires and J. C. Bertolini, *Catal. Lett.*, 2007, **114**, 110–114.
170. A. Luengnaruemitchai, K. Srihamat, C. Pojanavaraphan and R. Wanchanthuek, *Int. J. Hydrogen Energy*, 2015, **40**, 13443–13455.
171. S. Tanaka, J. Lin, Y. V. Kaneti, S. I. Yusa, Y. Jikihara, T. Nakayama, M. B. Zakaria, A. A. Alshehri, J. You, M. S. A. Hossain and Y. Yamauchi, *Nanoscale*, 2018, **10**, 4779–4785.
172. X. Wei, B. Shao, Y. Zhou, Y. Li, C. Jin, J. Liu and W. Shen, *Angew. Chem., Int. Ed.*, 2018, **57**, 11289–11293.
173. R. W. J. Scott, C. Sivadinarayana, O. M. Wilson, Z. Yan, D. W. Goodman and R. M. Crooks, *J. Am. Chem. Soc.*, 2005, **127**, 1380–1381.
174. J. Xu, T. White, P. Li, C. He, J. Yu, W. Yuan and Y. F. Han, *J. Am. Chem. Soc.*, 2010, **132**, 10398–10406.
175. K. Eid, M. H. Sliem, H. Al-Kandari, M. A. Sharaf and A. M. Abdullah, *Langmuir*, 2019, **35**, 3421–3431.
176. K. Eid, M. H. Sliem, K. Jlassi, A. S. Eldesoky, G. G. Abdo, S. Y. Al-Qaradawi, M. A. Sharaf, A. M. Abdullah and A. A. Elzatahry, *Inorg. Chem. Commun.*, 2019, **107**, 107460.
177. Y. Shi, X. Hu, J. Zhao, X. Zhou, B. Zhu, S. Zhang and W. Huang, *New J. Chem.*, 2015, **39**, 6642.
178. K. Eid, M. H. Sliem and A. M. Abdullah, *Nanoscale*, 2019, **11**, 11755–11764.
179. R. Kumar, J. H. Oh, H. J. Kim, J. H. Jung, C. H. Jung, W. G. Hong, H. J. Kim, J. Y. Park and I. K. Oh, *ACS Nano*, 2015, **9**, 7343–7351.
180. A. A. Teixeira-Neto, R. V. Gonçalves, C. B. Rodella, L. M. Rossi and E. Teixeira-Neto, *Catal. Sci. Technol.*, 2017, **7**, 1679–1689.
181. H. Yang, W. Yang, K. Lv, J. Zhu, Y. Xia, D. Tang and L. Wen, *Microporous Mesoporous Mater.*, 2018, **255**, 36–43.

182. A. M. Venezia, L. F. Liotta, G. Pantaleo, V. La Parola, G. Deganello, A. Beck, Z. Koppány, K. Frey, D. Horváth and L. Guczi, *Appl. Catal., A*, 2003, **251**, 359–368.
183. A. J. Binder, Z. A. Qiao, G. M. Veith and S. Dai, *Catal. Lett.*, 2013, **143**, 1339–1345.
184. Z. Suo, C. Ma, M. Jin, T. He and L. An, *Catal. Commun.*, 2008, **9**, 2187–2190.
185. P. Destro, S. Marras, L. Manna, M. Colombo and D. Zanchet, *Catal. Today*, 2017, **282**, 105–110.
186. E. J. Peterson, A. T. DeLaRiva, S. Lin, R. S. Johnson, H. Guo, J. T. Miller, J. H. Kwak, C. H. F. Peden, B. Kiefer, L. F. Allard, F. H. Ribeiro and A. K. Datye, *Nat. Commun.*, 2014, **5**, 1–11.
187. S.-Y. Chen, W. Tang, J. He, R. Miao, H.-J. Lin, W. Song, S. Wang, P.-X. Gao and S. L. Suib, *J. Name*, 2013, **00**, 1–3.
188. Y. Guo, J. Lin, C. Li, S. Lu and C. Zhao, *Catal. Lett.*, 2016, **146**, 2364–2375.
189. Y. Xie, Y. Guo, Y. Guo, L. Wang, W. Zhan, Y. Wang, X. Q. Gong and G. Lu, *Catal. Sci. Technol.*, 2016, **6**, 8222–8233.
190. H. Yang, K. Lv, J. Zhu, Q. Li, D. Tang, W. Ho, M. Li and S. A. C. Carabineiro, *Appl. Surf. Sci.*, 2017, **401**, 333–340.
191. A. S. Ivanova, E. M. Slavinskaya, R. V. Gulyaev, V. I. Zaikovskii, O. A. Stonkus, I. G. Danilova, L. M. Plyasova, I. A. Polukhina and A. I. Boronin, *Appl. Catal., B*, 2010, **97**, 57–71.
192. X. Xi, S. Ma, J. F. Chen and Y. Zhang, *J. Environ. Chem. Eng.*, 2014, **2**, 1011–1017.
193. M. M. A. Abualrejal, K. Eid, R. Tian, L. Liu, H. Chen, A. M. Abdullah and Z. Wang, *Chem. Sci.*, 2019, **10**, 7591–7599.
194. M. M. A. Abualrejal, K. Eid, A. M. Abdullah, A. A. Numan, H. Chen, H. Zhang and Z. Wang, *Microchim. Acta*, 2020, **187**, 527.
195. K. Noh, K. S. Brammer, T. Y. Seong and S. Jin, *Nano*, 2011, **6**, 541–555.
196. H. Zhao, L. Liu and Y. Lei, *Front. Chem. Sci. Eng.*, 2018, **12**, 481–493.
197. H. I. Abdu, K. Eid, A. M. Abdullah and X. Lu, *Data Brief.*, 2020, **30**, 105520.
198. S. A. Rawool, A. Samanta, T. G. Ajithkumar, Y. Kar and V. Polshettiwar, *ACS Appl. Energy Mater*, 2020, **3**, 8150–8158.

CHAPTER 2

Graphitic Carbon Nitride-based Chemiluminescent and Electrochemiluminescent Sensors

ISLAM M. MOSTAFA[a,b,c], FANGXIN DU[a,b] AND GUOBAO XU*[a,b]

[a]State Key Laboratory of Electroanalytical Chemistry, Changchun Institute of Applied Chemistry, Chinese Academy of Sciences, Changchun, Jilin 130022, PR China; [b]University of Science and Technology of China, Hefei, 230000, PR China; [c]Department of Analytical Chemistry, Faculty of Pharmacy, Minia University, 61519, Minia, Egypt
*E-mail: guobaoxu@ciac.ac.cn

2.1 Introduction

The need to detect valuable important analytes has increased, so enormous efforts have been made to establish novel nanomaterials-based biosensors and their application as sensitive and specific biosensors for sensing various samples (for example, metal ions, DNA, biomarkers, and metabolites). Many different biosensors (chemiluminescent, electrochemiluminescent, optical, and electrochemical sensors) have been developed based on nanomaterials.[1–4] These biosensors offer superior advantages over the traditional diagnostic biosensors in terms of rapidity, simplicity, sensitivity, and selectivity. Many patents, papers, books, and reviews have been focused on

Nanoscience & Nanotechnology Series No. 51
Carbon Nitride Nanostructures for Sustainable Energy Production and Environmental Remediation
Edited by Kamel Abdelmoniem Mohamed Eid and Aboubakr M. Abdullah

Published by the Royal Society of Chemistry, www.rsc.org

nanomaterials.[1–4] Recently, one of the most important and applicable nanostructures in the field of biosensors is graphitic carbon nitride ($g\text{-}C_3N_4$), because it has many important properties such as optical, mechanical, and thermal properties as well as excellent physicochemical stability.[5–8] In addition, it has special electroluminescent and photoelectrochemical properties.[9–12] Many articles and reviews have focused on the application of $g\text{-}C_3N_4$ nanomaterials in many different fields such as biosensors, catalysis, nanomedicine, and bioimaging.[13–22]

$g\text{-}C_3N_4$ is a new type of nanomaterial that consists of a polymeric structure from covalently connected sp^2-hybridized carbon and many nitrogen atoms in two-dimensional (2D) form.[23] In 1996, Teter and Hemley discovered five structural types of $g\text{-}C_3N_4$ (α-phase, β-phase, cubic phase, quasi-cubic phase, and graphitic-like phase).[24] It was observed that the hardness of the graphitic phase is lower than the other phases. From that time, $g\text{-}C_3N_4$ nanomaterials have received great attention because of their distinct properties (resistance, suitable band gap (2.7 eV), chemical inertness, low toxicity, and favorable biocompatibility).[25,26] Regarding its chemical structure, there are two structural polymorphs of $g\text{-}C_3N_4$ depending on the precursors and fabrication method. Figure 2.1A represents the condensed s-triazine unit structure, while Figure 2.1B shows the tri-*s*-triazine (tri-ring of C_6N_7) structure. Utilizing density functional theory (DFT), the authors noticed that the tri-*s*-triazine structure unit is energetically and thermodynamically more stable and constant than *s*-triazine $g\text{-}C_3N_4$.[27,28]

In this chapter we aim to show the recent research status of $g\text{-}C_3N_4$-based CL and ECL biosensors. Also, it is characterized over the previously reported reviews by addressing the preparation pathways and characterization

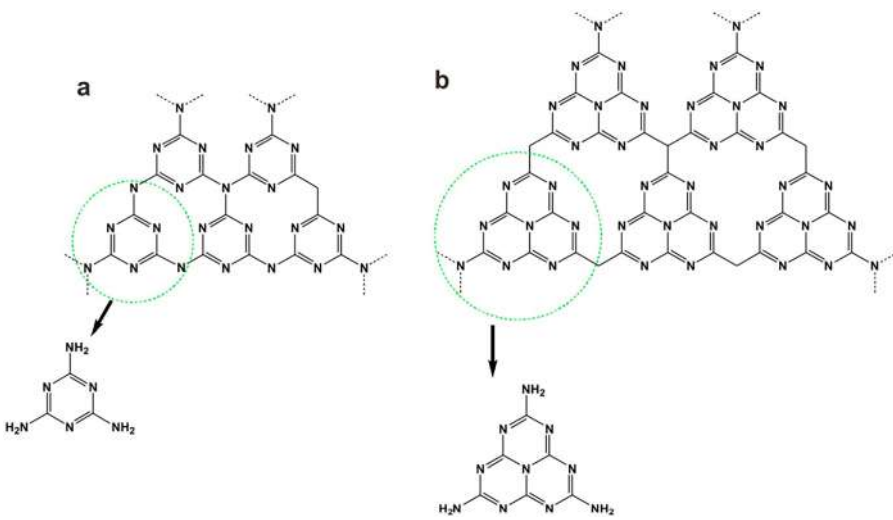

Figure 2.1 $g\text{-}C_3N_4$ compositional units, (A) *s*-triazine, and (B) tri-*s*-triazine. Reproduced from ref. 29 with permission from Elsevier, Copyright 2020.

methods of g-C_3N_4. In addition, we address the advances and progress of g-C_3N_4-based CL and ECL biosensors in various applications such as the detection of metal ions and inorganic anions, biomolecules, nucleic acids, biomarkers, proteins, *etc.* to the year 2020. Furthermore, insights and prospects for future work have been discussed to design more advanced g-C_3N_4-based CL and ECL biosensors. We think that this chapter will be important for interested readers to realize the updated progress and directions of g-C_3N_4-based CL and ECL biosensors.

2.2 Fabrication of g-C_3N_4

2.2.1 Synthesis of Bulk g-C_3N_4

Traditionally, compounds rich with nitrogen such as melamine, ammonium thiocyanate, thiourea, dicyandiamide, cyanamide, urea or mixtures have been employed for the production of g-C_3N_4 through a simple polymerization process.[30–33] However, bulky g-C_3N_4 obtained from this simple procedure is difficult to employ in important analytical applications in biological as well as catalysis applications, since bulky g-C_3N_4 has poor dispersibility, limited surface area as well as a less active site.[34–37] Therefore, researchers have tried to make various controllable nanoarchitectures such as nanodots, nanosheets, nanorods, and nanocomposites of g-C_3N_4. By applying different fabrication methods, they have fabricated diverse nanostructures of g-C_3N_4 with an enhancement in the catalytic and physicochemical properties (Scheme 2.1).[15]

2.2.2 Preparation Pathways of g-C_3N_4 Nanostructures

g-C_3N_4 nanostructures were fabricated by two different synthetic approaches (top–down and bottom–up pathways[16,20]). Two pathways can be achieved by different processes like chemical exfoliation, thermal decomposition, ultrasonic exfoliation, chemical vapor deposition, solvothermal synthesis, solid-state reactions, microwave heating, and electrodeposition.[16,20,38,39] Kweku and Ao[40] and Mishra[41] have published reviews focusing on the construction methods and pathways of g-C_3N_4, and different properties of g-C_3N_4. Applying different synthetic strategies and using various types of precursors during the fabrication method can modify the physicochemical properties of g-C_3N_4 nanostructures.[42]

2.2.2.1 Top-down Route

In this route, small molecule g-C_3N_4 can be obtained from the broken bulk of g-C_3N_4. As represented in Figure 2.2A, this approach leads to uniform g-C_3N_4 and various g-C_3N_4 morphologies such as nanosheets, nanodots, bulks, and nanolines.[15] This strategy has many advantages; for instance, a simple

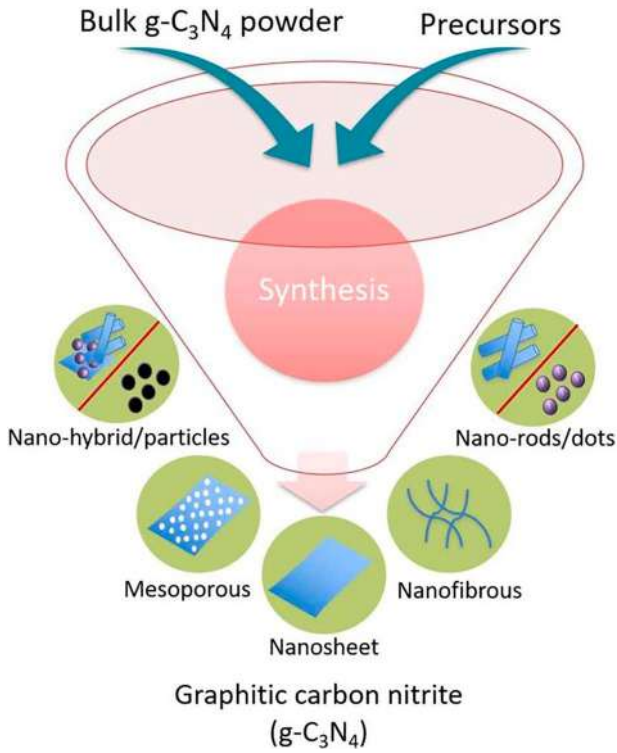

Scheme 2.1 Fabrications of various g-C_3N_4 nanostructures as sensing platforms by utilizing bulk g-C_3N_4 or precursors. Reproduced from ref. 15 with permission from IOP Publishing, Copyright 2019 The Electrochemical Society.

process, low temperature requirement, and cost effectiveness. The aforementioned merits are significant in the large-scale fabrication and extensive implementations of g-C_3N_4.[43]

2.2.2.2 Bottom-up Route

This strategy allows g-C_3N_4 to have carboxyl groups on the surface, which consequently allows further modifications of g-C_3N_4. In 2013, a novel and facile synthetic route for g-C_3N_4 was published by Zhang and his group.[44] As illustrated in Figure 2.2B, sodium citric acid as the carbon source and urea as nitrogen source were reacted together at a higher temperature to create g-C_3N_4.

In conclusion, different approaches were employed for achieving top-down and bottom-up strategies.[29,43,44] The observed advantages of the top-down strategy include simplicity, time-effectiveness, high efficiency and the production of g-C_3N_4 with relatively high crystallinity as well as

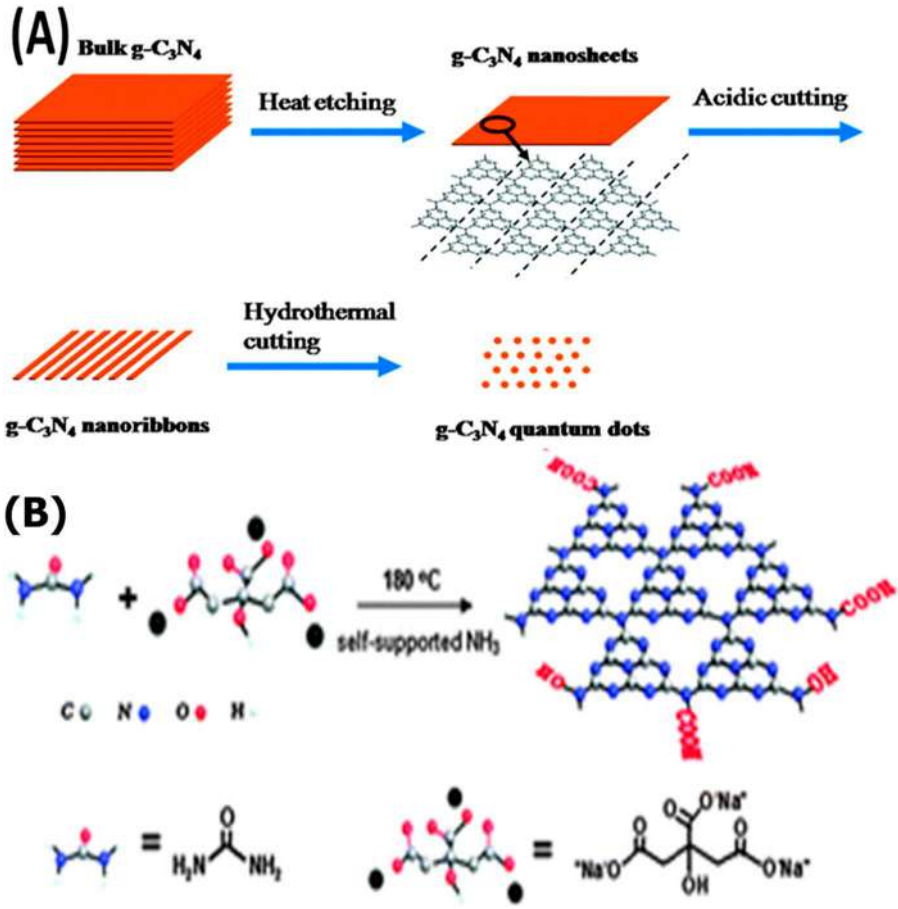

Figure 2.2 (A) A recent top-down approach for the fabrication of g-CNs. Different nanostructures as g-CN nanosheets, nanoribbons, and quantum dots could be obtained by applying the thermal etching split method. (B) Bottom-up approach for the formation of g-CNs using small molecular composition of C and N-containing compounds as the elements' sources. Reproduced from ref. 44 and ref. 45 with permission from the Royal Society of Chemistry.

thinner layers. However, this approach suffers from drawbacks such as being expensive, requiring the use of hazardous strong acid, is environmentally unfriendly, and produces g-C_3N_4 lacking an ordered texture, well-regulated morphology and porous construction.[29,44] On the other hand, the bottom-down approach has many advantages such as being facile, eco-friendly, highly efficient, and produces g-C_3N_4 with relatively high crystallinity as well as thinner layers. The disadvantages of this approach are that it is time-consuming, costly, with low efficiency and a complicated preparation process.[29]

2.3 Characterization of g-C_3N_4

2.3.1 UV-visible and Fluorescence Analysis

UV–vis absorption and fluorescence techniques were used for characterization of g-C_3N_4 with different morphologies such as g-CNQDs and g-CNTs.[46] g-CNQDs showed only a wide absorption band at 200 to 400 nm and no obvious sharp absorption peak was detected. This is attributed to the n–π* transition of C=O.[46,47] Also, a bright blue color was observed by its exposure to UV light at 365 nm. Meanwhile, g-CNTs exhibited a sharp intense absorption peak centered in the UV region at 285 nm, in addition to a weak peak (shoulder type) at 365 nm.[48–50]

The photoluminescence (PL) feature of g-CNQDs was sensitive to the excitation wavelength, indicating excitation-dependent fluorescence behavior. Aqueous solution of g-CNQDs showed a narrow emission peak at 440 nm (λ_{ex} 360 nm).[51,52]

2.3.2 Scanning Electron Microscopy and Transmission Electron Microscopy Analysis

Analysis of the sample for scanning electron microscopy (SEM) imaging requires a special sample preparation, which involves the construction of thin films of carbon coating on copper grids. Dropping a very small amount of the sample onto the grip enables the development of these thin films. The residual amount of the solution was cleaned with blotting paper, after that a mercury lamp (5 min only) was used for the drying process.[53]

Transmission electron microscopy (TEM) sample characterization includes putting a droplet of the sample solution on a carbon-covered copper grip. Then the drop is dried at chamber room temperature. The remaining solution is taken away with the blotting paper. SEM and TEM give an indication about the morphological structure and different shapes of g-C_3N_4. SEM as well as TEM images of different reports of g-CNQDs showed that g-CNQDs are spherical in shape with a diameter of 5 nm (Figure 2.3A),[53] while g-CNTs appeared as a structure with layers of stacked sheets (Figure 2.3B).[54]

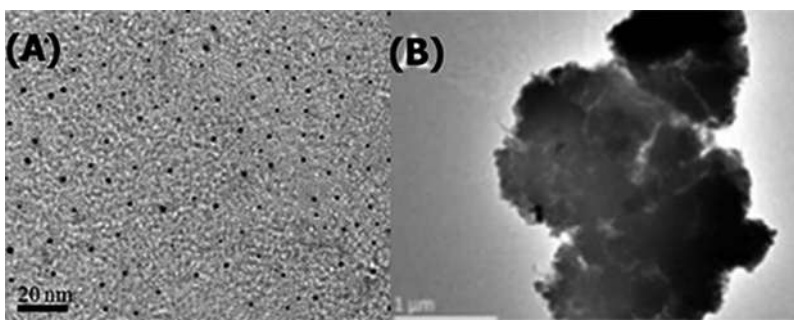

Figure 2.3 TEM photos of the fabricated (A) g-CNQDs as well as (B) g-CNTs. Reproduced from ref. 53 with permission from American Chemical Society, Copyright 2018 and from ref. 54 with permission from the Royal Society of Chemistry.

2.3.3 Fourier-transform Infrared Spectroscopy Analysis

Fourier-transform infrared spectroscopy (FT-IR) was employed to estimate the surface composition of g-C_3N_4.[53] For example, the g-CNQDs FTIR spectrum was characterized by a very distinguished band positioned at 800.92 cm^{-1}. This band was assigned to the heptazine units. The stretching vibration peaks of C–N and H–C appear at 1167 and 1097 cm^{-1}, respectively. Also, the stretching mode of C=C can be observed at about 1402 and 1448 cm^{-1}. The bands at 1619 and 1665 are given to the stretching vibrations of C=N as well as O–C=O, respectively. Moreover, the broad bands appearing in 3201 and 3343 cm^{-1} are related to the stretching vibrations of N–H and O–H, respectively.[52,55]

2.3.4 X-ray Photoelectron Spectroscopy Analysis

X-ray photoelectron spectroscopy (XPS) gives information on the chemical composition as well as the structure of the as-prepared nanomaterials. The g-C_3N_4 XPS spectrum was characterized by the existence of three binding energy peaks positioned at 284.58, 399.74, 530.98 eV, which were assigned to C1s, N1s, O1s, respectively.[52] The C1s spectra have four main Gaussian peaks, positioned at 284.6, 286.1, 288.0, and 289.02 eV. sp^2 C–C bonds showed a binding energy peak at 284.6 eV, while sp^2 N–C=N bonds showed 288.0 eV. The presence of the C–O bond exhibited a binding energy peak at 286.07 eV, while O–C=O bonds showed the peak at 289.02 eV.[54] The N1s spectrum exhibited three characteristic peaks at 398.8, 399.8, and 400.4 eV, which were referred to as C=N–C, C–N–C, and N–$(C)_3$ moieties, respectively. Also, the O1s spectrum showed two peaks at 531.0 eV for the C=O group and 532.5 eV for the C–OH/C–O–C group.[52,56]

2.4 Chemiluminescence of g-C_3N_4 and its Sensing Application

Chemiluminescence (CL) is a redox chemical reaction between the luminophore and its co-reactant resulting in emission of light at a specific wavelength.[57] Recently, research efforts have incorporated different synthesized nanomaterials such as quantum dots and nanoclusters into CL systems to improve and promote CL applications.[58–60] One type of g-C_3N_4 is quantum dots (g-CNQDs), which can act as a CL luminophore to produce CL emission at a specific wavelength. Lv's group was the first group to investigate the g-CNQDs CL properties.[61] They used a microwave treatment method for the fabrication of g-CNQDs through a simple single synthetic step reaction between guanidine hydrochloride and EDTA (capping and stabilizing agent). Guanidine hydrochloride and EDTA were added and mixed well into H_2O and homogenized well by stirring, heated *via* a microwave oven for 2 min, and then centrifuged to remove the large particles. Finally, a supernatant of a light brown color containing g-CNQDs was obtained with

an average particle size of 5 nm (Figure 2.4A). g-CNQDs were found to be water soluble and uniform in shape with strong fluorescence emission at 555 nm. The authors studied the CL emission from the reaction between NaClO and g-CNQDs. As shown in Figure 2.4B, there is a high CL emission peak at 555 nm due to the recombination of electrons in the g-CNQD and oxidant-injected holes. Also, O_2 was produced from the reactive oxygen species (ROS) on the g-CNQDs surface, thus accelerating the energy transfer to g-CNQDs. Based on the developed g-CNQD-NaClO CL system, a flow injection platform was utilized for the assay of free chlorine (Figure 2.4C) in boiling and tap water samples with a low detection limit and high specificity.

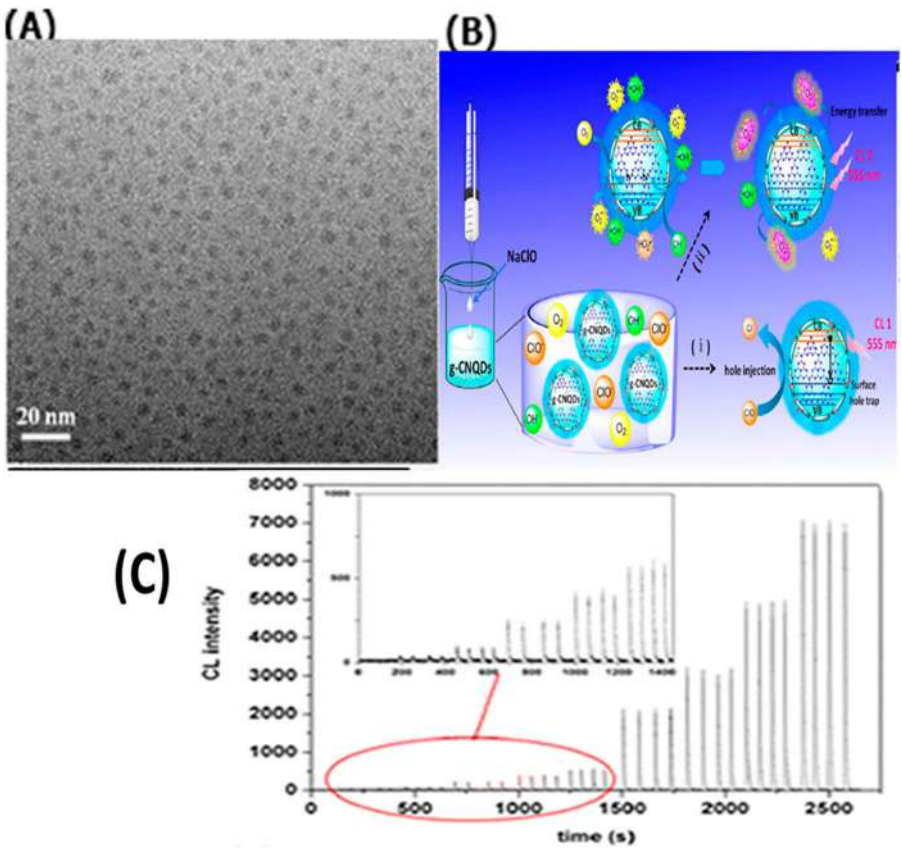

Figure 2.4 (A) g-CNQDs TEM photo. (B) Diagram representation of the fabricated g-CNQDs by a microwave-assisted method and the g-CNQD–NaClO system CL mechanism. (C) Calibration graph for the assay of free chlorine from 20–10 000 nM. Reproduced from ref. 61 with permission from American Chemical Society, Copyright 2014.

In the same way, another report has been published by Fan and co-workers about the fabrication of highly luminescent g-CNQDs using a simple synthetic pathway.[52] They synthesized g-CNQDs using the reaction of melamine and EDTA precursors by applying a thermal condensation process through mixing two substances in a mortar and converting them to fine powder. After that, the powder mixture was transferred into an alumina crucible containing a cover and heated for 1 h at 350 °C (Figure 2.5A-a). The final obtained solution of brownish-black was purified by using a centrifuge. The prepared g-CNQDs can act as a CL emitter and produce high CL intensity in alkaline media containing $K_3[Fe(CN)_6]$ co-reactant (Figure 2.5A-b). A dopamine (DA) neurotransmitter could efficiently compete with g-CNQDs to react with $K_3[Fe(CN)_6]$, producing a dramatic decrease in the CL intensity of the proposed CL system. As a result, DA was detected linearly from 1×10^{-8}–2×10^{-6} M (Figure 2.5B) and was also detected in serum samples by applying the proposed g-CNQD–K_3 $[Fe(CN)_6]$ CL platform.

Taking the CL properties of the previously reported g-CNQD–$K_3[Fe(CN)_6]$ CL system,[62] Abdolmohammad-Zadeh *et al.* used this system for the determination of mercury ion (Hg^{2+}).[63] Hg^{2+} ion could selectively decrease the CL intensity of this CL system. The selective quenching behavior of Hg^{2+} results from the selective interaction between g-CNQDs and Hg^{2+} that leads to the generation of a stable non-emitting complex. Thus, the selective and ultra-sensitive detection of Hg^{2+} ion was achieved by applying the mentioned CL system with wide linearity (0.25–10 ng mL^{-1}). Fan and co-authors[64] observed that Ce^{4+} and SO_3^{2-} could enhance the g-CNQDs CL emission. They used a g-CNQD–Ce^{4+}–SO_3^{2-} CL system for the detection of iodine, as iodine could clearly decrease the CL intensity of this platform.

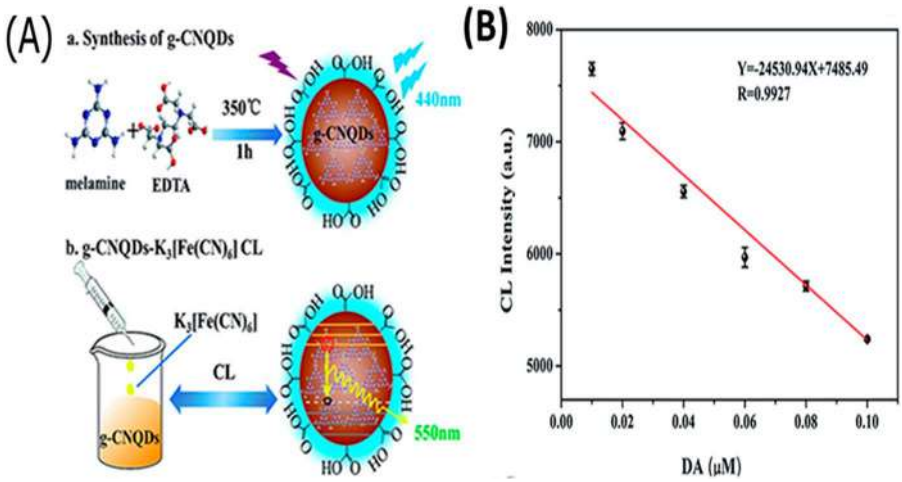

Figure 2.5 (A) Diagram representation of (a) fabrication of g-CNQDs using a thermal condensation method; (b) CL of the developed g-CNQDs–$K_3[Fe(CN)_6]$ platform; and (B) calibration graph for the detection of DA. Reproduced from ref. 52 with permission from the Royal Society of Chemistry.

The quenching related to the competitive interaction between I^- with Ce^{4+}. The developed CL system was utilized for the assay of I^- in urine samples. Bagheri *et al.* prepared new spherical g-CNQDs with an average diameter size of 9 nm using a hydrothermal method for the assay of H_2O_2 as well as glucose.[65] They noticed that g-CNQDs can act as strong enhancers for the CL signal of the H_2O_2–Cu^{2+} CL platform. This is referred to as the catalytic action of g-CNQDs on the H_2O_2–Cu^{2+} CL system, which leads to a remarkable increase in the generation of oxyradicals. As a result of the produced radicals (hydroxyl and superoxide radicals), g-CNQDs$^+$ and g-CNQDs$^-$ were produced from the interaction of these radicals with g-CNQDs. Finally, the excited g-CNQDs* were created and went back to the ground state accompanied by strong CL emission. The proposed H_2O_2–Cu^{2+}–g-CNQDs CL system has achieved excellent detection for the sensitive assay of H_2O_2 (LOD = 10 nM) and glucose (LOD = 100 nM). Lin *et al.* reported g-CNQDs prepared from urea and sodium citrate by the solvothermal method.[56] The CL intensity of the H_2O_2–$NaHSO_3$ platform was greatly enhanced in the existence of the as-prepared g-CNQDs through the generation of singlet oxygen ($^1O_2$), superoxide anion radical and SO_3 radical anion. Interestingly, the presence of ascorbic acid (AA) in the linear range from 285 nM to 285 μM could quench the CL intensity of the established H_2O_2–$NaHSO_3$–g-CNQDs system. The AA LOD was estimated to be 80 nM.

Regarding the use of g-C_3N_4 nanosheets (g-CNTs) as CL biosensors, Yi Lv and co-workers designed g-CNTs using the solid-phase method.[66] The developed nanosheets have a special long persistent luminescence property. The synthetic route of g-CNTs was achieved through the pyrolysis of guanidine hydrochloride using a heating temperature that reaches 650 °C for 3 h with a heating rate of 2.5 °C min^{-1} in an electric furnace to gain yellow g-C_3N_4 powders. Figure 2.6 demonstrates the SEM and TEM images of a typical layered platelet-like morphology of g-CNTs. It was observed that silver ion (Ag^+) could be adsorbed onto g-CNTs resulting in loss of the luminescence of g-CNTs. By the addition of biothiols as cysteine (Cys), glutathione (GSH) and homocysteine (Hcy) in the sample solution, they could interrupt the quenching effect by their interaction with the Ag^+ ion and recover the luminescence emission

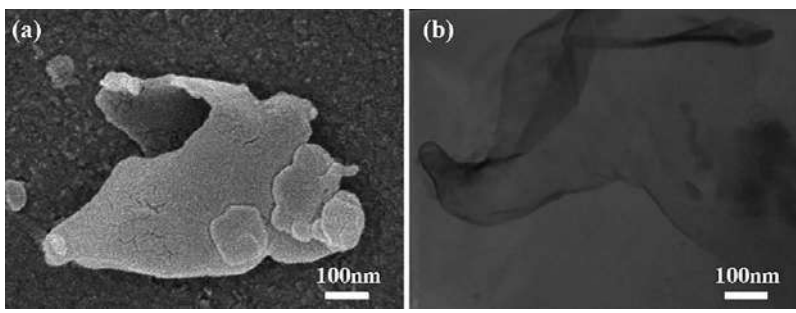

Figure 2.6 (a) g-CNTs SEM photo, and (b) g-C_3N_4 TEM photo fabricated from guanidine hydrochloride using the pyrolysis method. Reproduced from ref. 66 with permission from American Chemical Society, Copyright 2013.

intensity. The proposed platform could be applied selectively for the assay of the three mentioned biothiols with a very low limit of detection (9.6, 8.1, and 6.4, nM for GSH, Hcy and Cys, respectively).

Another paper has been published by Duan and co-authors for the fabrication of g-CNTs by calcining thiourea precursor.[67] They noticed that g-CNTs could act as a CL enhancer for the traditional luminol–H_2O_2 CL system and the reason for that is the catalytic behavior of g-CNTs on H_2O_2 to generate hydroxyl radicals. Hydroxyl radicals could interact with luminol and H_2O_2 anions, producing a high light emission compared with the luminol-H_2O_2 CL system alone. The strong oxidation ability of the hydroxyl radical could efficiently decompose TNT through a redox reaction, causing a significant inhibition in the CL intensity. Dependent on this, the detection of TNT was successfully achieved by applying the new CL approach with a LOD of 0.75 pM and a wide calibration range from 0.001 to 1 nM. In contrast, Huang and colleagues fabricated g-CNTs by using chemical oxidation and a liquid exfoliation method.[68] They fabricated nanosheets by heating melamine powder at 550 °C (the heating rate = 3 °C min^{-1}) for 2 h using a muffle furnace. The bulk g-C_3N_4 was collected as a yellow solid product. Then, 80 mL of HNO_3 (5 M) was added on the yellow obtained g-C_3N_4 powder. The solution was sonicated for 1 h, refluxed for 24 h, cooled at room temperature, and finally centrifuged. The precipitates were collected, and then the precipitate was dispersed in distilled water, sonicated for 16 h and lastly centrifuged to obtain g-CNTs solution with a good dispersion. Figure 2.7A–C shows TEM, atomic force microscopy (AFM) images and the thickness of the as-prepared g-CNTs. It showed a good planar structure with an average diameter size ranging from 40 to 80 nm, while the thickness was about 6–8 nm. Surprisingly, the CL signal intensity of the classical luminol-H_2O_2 system was greatly quenched by the existence of g-CNTs. This new discovery was employed for the assay of carcinoembryonic antigen (CEA) utilizing modified hemin/G-quadruplex DNAzyme–g-CNTs. The electron transfer route of the modified g-CNTs caused a significant quenching in the CL of luminol. In the presence of the CEA target, a DNA–DNA duplex was produced as a result of the DNA hybridization reaction and target recognition impact. Therefore, luminol CL

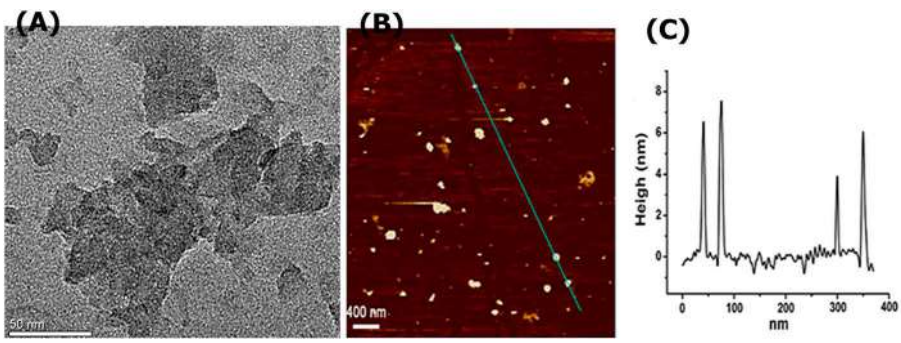

Figure 2.7 (A) g-CNTs TEM image. (B) g-CNTs AFM image. (C) g-CNTs thickness as well as its average size. Reproduced from ref. 68 with permission from Elsevier, Copyright 2019.

emission intensity at 440 nm could be increased owing to the blocking of the electron transfer. The CL probe has been used for the sensitive monitoring of the CEA antigen (LOD = 63.0 pg mL^{-1}).

An effective CL platform was proposed for the determination of H_2S, dependent on the fabrication of copper ion modified g-CNTs (Cu^{2+}/g-CNTs).[55] Firstly, g-CNTs were fabricated by annealing melamine powder at 550 °C for 4 h. After that Cu^{2+}/g-CNTs were fabricated by the sonication of the as-prepared g-CNTs with $CuCl_2$ in water at 80 °C. As shown in Figure 2.8A–D, the authors used different techniques such as TEM, STEM-EDS spectrum, and elemental mappings for the characterizations of Cu^{2+}/g-CNTs. Interestingly, S^{2-} anion could form a stable complex with copper ion to form CuS precipitate on the g-CNTs surface, leading to a quenching impact on the CL intensity of the g-CNTs. Based on this, S^{2-} anion was detected as pure form and in human plasma by a selective, facile and highly sensitive CL sensor (LOD = 2.0 pM).

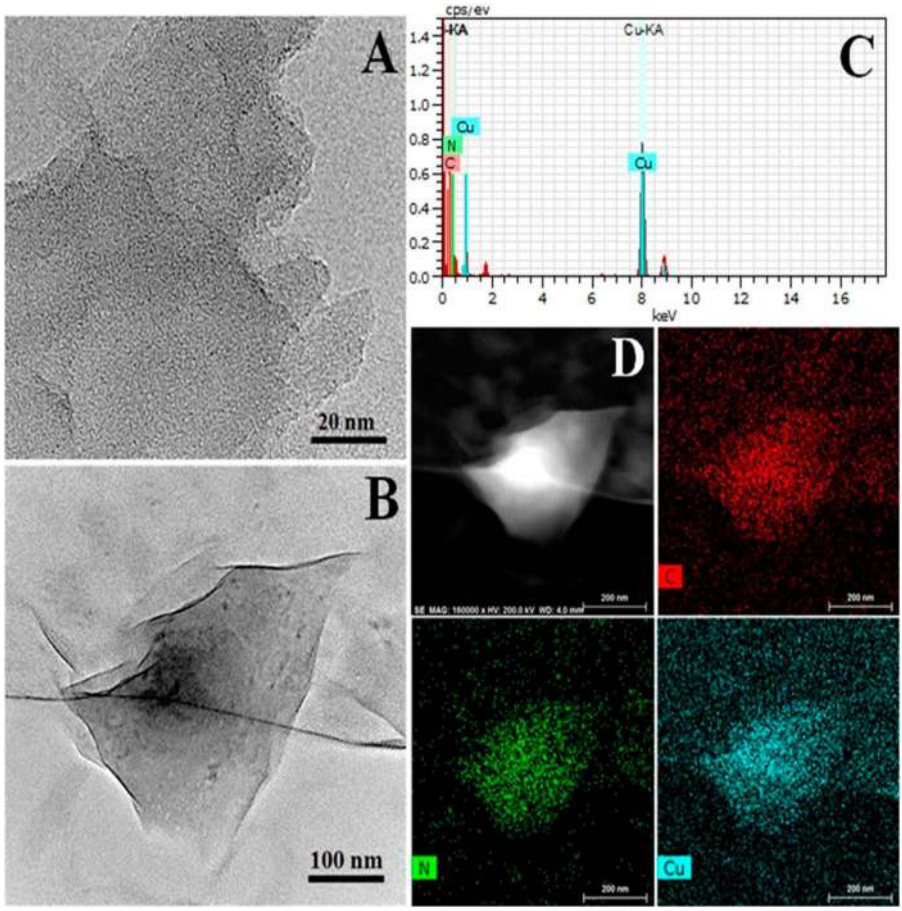

Figure 2.8 (A) g-CNTs TEM images, (B) Cu^{2+}/g-CNTs TEM photo, and (C) Cu^{2+}/g-CNTs STEM-EDS photo, and (D) Cu^{2+}–g-CNTs EDS elemental mappings of C, N, and Cu elements. Reproduced from ref. 55 with permission from Elsevier, Copyright 2020.

2.5 Applications of g-C_3N_4 as ECL Sensors

Electrochemiluminescence (ECL), also known as electrogenerated chemiluminescence, combines both features of electrochemistry and chemiluminescence.[69–71] It is a light-emitting phenomenon producing an electron–transfer reaction between electrogenerated species at or near the surface of the electrode.[69–71] It has many advantages over other analytical techniques because it is fast, selective, simple, sensitive and reproducible.[71] Therefore, ECL-based biosensors have been extensively used for the estimation of various analytes, such as biomolecules, biomarkers, metal ions, immunoassays, explosives substances, food adulterants, and so on. Fabrication of smaller size nanomaterials with unique properties, low toxicity, diversity in shapes, and specific structures has significantly contributed to the recent development and progress of ECL-based biosensors.[69–72]

In former years, g-C_3N_4 has been broadly utilized in ECL-detecting frameworks due to its several properties including the wide specific surface area, which serves as a matrix for the anchoring of various kinds of molecules, high electroconductivity in addition to its catalytic properties.[75–77] Here, g-C_3N_4-based ECL sensor achievements will be discussed in detail.

2.5.1 Detection of Metal Ions and Inorganic Anions

We all are aware that heavy metal pollution can lead to harmful toxicity for humans even at low concentrations and has thus become one of our living environment's serious problems.[73,74] Several ECL sensors have been fabricated and designed for the estimation of several metal ions dependent on the strong adsorption capacity between g-C_3N_4 and metal ions.[75,76]

The first report about ECL behavior of g-C_3N_4 was published by Xiao's group in 2012.[77] They fabricated a yellow g-C_3N_4 by thermal condensation of melamine powder at 550 °C for 4 h under open air conditions. They studied the ECL performance of a g-C_3N_4 emitter with $K_2S_2O_8$ as a co-reactant. In this study, the electro-reduced forms of g-C_3N_4 and persulphate could react together at the interface of a modified g-C_3N_4 carbon paste electrode to produce an excited state of g-C_3N_4, which returned to the ground state emitting stable and high ECL intensity (Figure 2.9). The ECL intensity of this system could be efficiently quenched by a Cu^{2+} ion. It is known that the standard redox potential (E^0) of Cu^{2+}/Cu is 0.159 V (*versus* NHE), which is found between the conduction (−0.83 V) and the valence bands (1.83 V) of g-C_3N_4. This permits the negatively charged g-C_3N_4 to transfer the electron to Cu^{2+}, leading to a notable quenching in the ECL intensity. This system has been utilized for detection of Cu^{2+} ions with ultra-sensitivity (LOD 900 pM).

Later, Sun *et al.* established a selective ECL platform for the detection of Cu^{2+}.[76] The authors fabricated g-CNTs by using simple one-step and high-yield synthesis procedures. The nanosheets were fabricated by pyrolyzing a melamine–KBH_4 mixture under Ar. They used XRD, SEM, Tyndall effect, AFM, and HRTEM for characterization as shown in Figure 2.10A–F. They used g-C_3N_4 as an efficient luminophore and $Na_2S_2O_8$ as a co-reactant for the development of the ECL platform. They have observed high and stable ECL

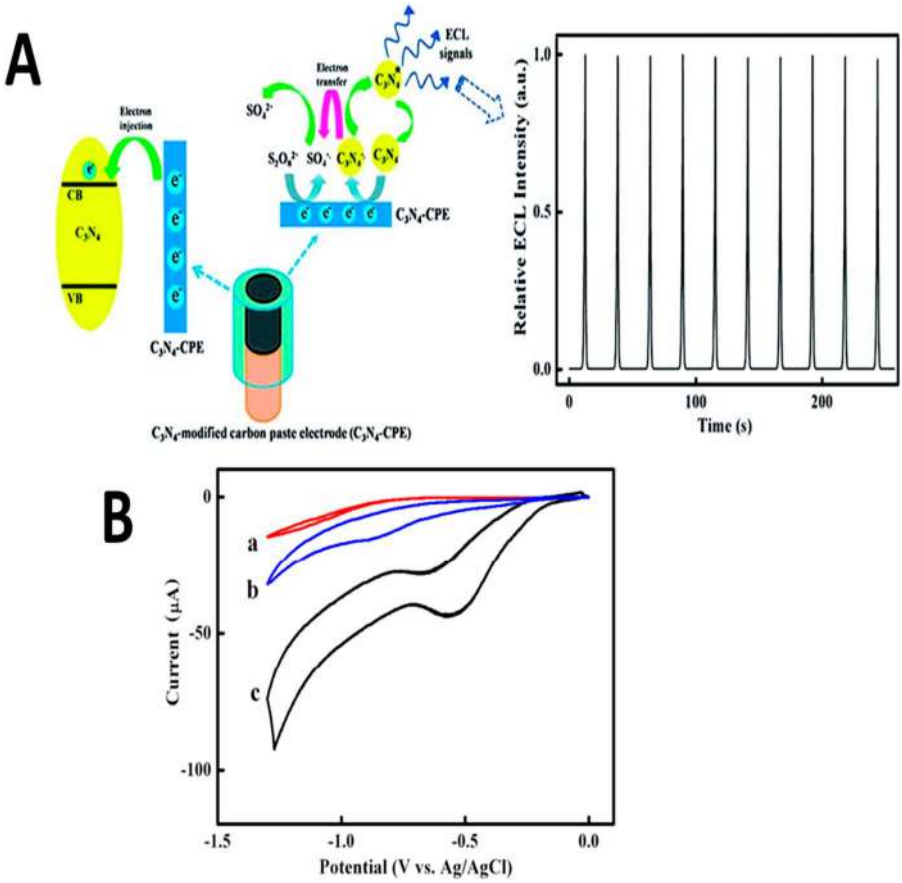

Figure 2.9 (A) Diagram representation of the g-C_3N_4–$K_2S_2O_8$ ECL platform. (B) CV curves of the pure carbon paste electrode (a, b) and g-CNTs-modified carbon paste electrode (c) in 0.10 M $K_2S_2O_8$ in the absence (a) and presence of (b, c) $K_2S_2O_8$ (3.0 mM). Reproduced from ref. 77 with permission from American Chemical Society, Copyright 2012.

signals by scanning a fluorine-doped tin oxide (FTO) glass electrode altered with g-CNTs in Na_2SO_4 (0.1 M) and $Na_2S_2O_8$ (3.0 mM) at 100 mV s^{-1}. Among different metal ions, Cu^{2+} could quench the strong ECL intensity of this system. The good selectivity of the Cu^{2+} ion compared to other metal ions is due to its redox potential that lies between the valence and conduction bands of g-CNTs. Furthermore, the transfer of the electron between Cu^{2+} and g-CNTs is more convenient and preferable than the electron transfer of other metal cations owing to the higher value of the Cu^{2+} redox potential than that of other metal ions. The calibration curve for Cu^{2+} detection was constructed between ECL intensity and Cu^{2+} concentration from 0 to 45 nM.

Yang's group hybridized g-C_3N_4 with graphene oxide (GO) using the ultrasonication of g-C_3N_4 and GO for 2 h to design a "signal-off" ECL sensor for monitoring Cu^{2+}.[78] Figure 2.11A–C shows SEM images for g-C_3N_4, GO, and a g-C_3N_4/GO hybrid. The g-C_3N_4/graphene oxide (GO) hybrid/O_2 system

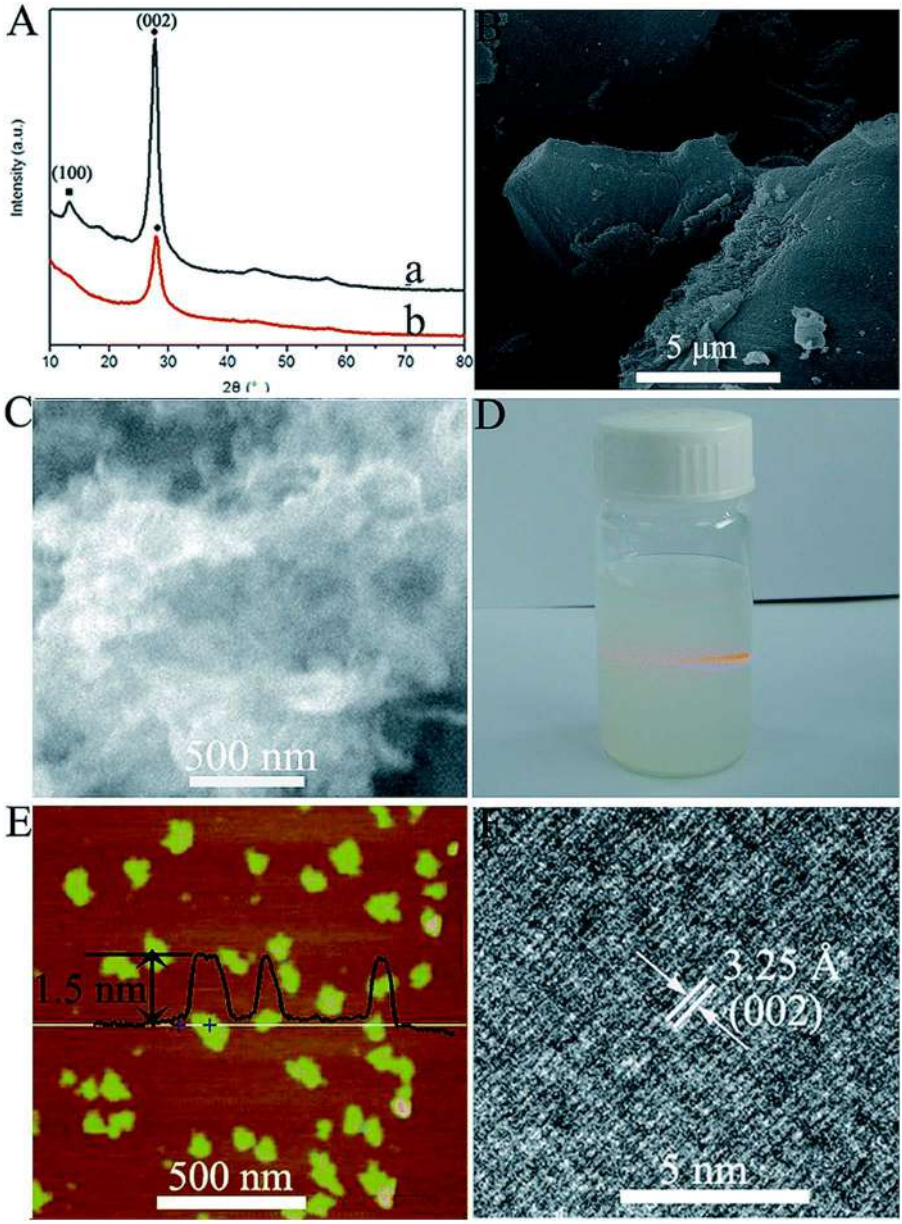

Figure 2.10 (A) XRD profiles of b-g-C_3N_4 (a), and g-CNTs nanosheets (b). SEM photo of (B) b-g-C_3N_4, and (C) g-CNTs nanosheets. (D) Tyndall effect obtained by aqueous distribution of g-CNTs nanosheets passed through with red laser light. (E) AFM photo and height profile, and (F) HRTEM photo of g-CNTs nanosheets. Reproduced from ref. 76 with permission from the Royal Society of Chemistry.

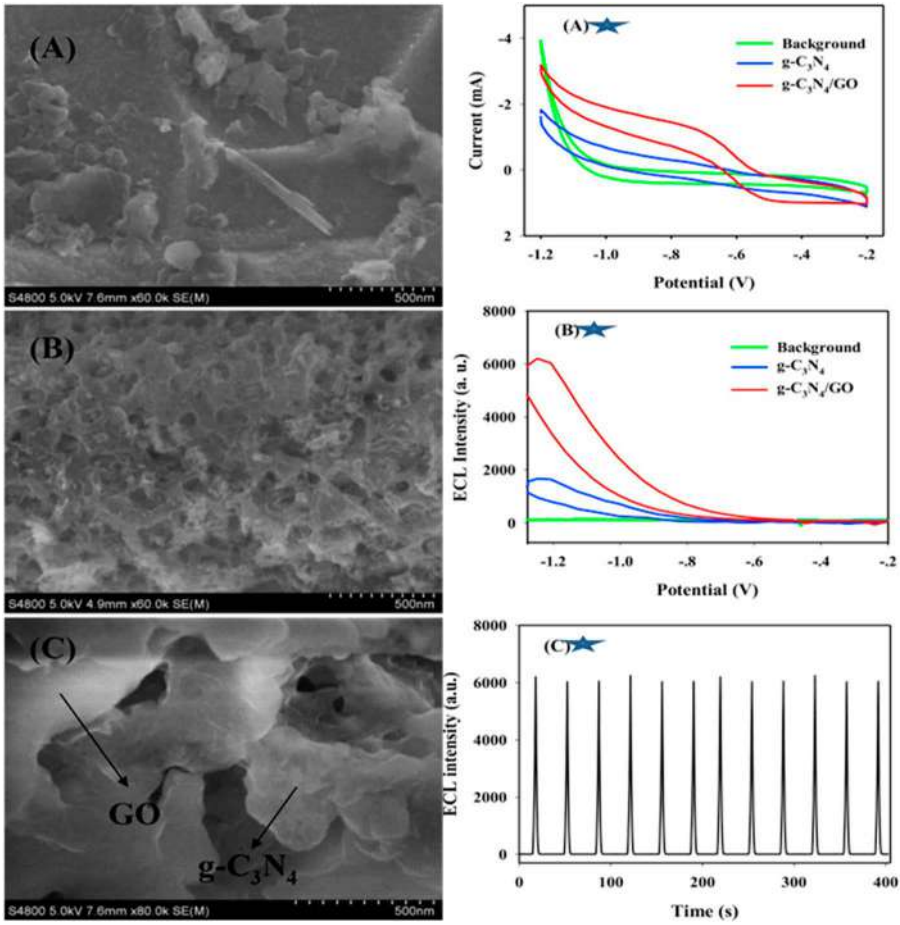

Figure 2.11 SEM photos of (A) GO, (B) g-C_3N_4, as well as (C) g-C_3N_4/GO. (A*) CVs and (B*) ECL potential graphs of background (green line), g-C_3N_4 (blue line), and g-C_3N_4/GO (red line) on titanium ribbon in 0.067 M pH 7 PBS. (C*) g-C_3N_4/GO ECL emission intensities by using continuous 12 cycles of CV. Reproduced from ref. 78 with permission from Elsevier, Copyright 2015.

exhibited a stronger current and higher ECL intensity than pure g-C_3N_4 (Figure 2.11A*–C*). GO acts as a cathodic ECL signal amplifier and a matrix for the immobilization of g-C_3N_4. The amplified cathodic ECL was used for sensing Cu^{2+} ions with high sensitivity (LOD = 10 pM). The proposed sensor has a superior sensitivity than the formerly published ECL reports. The feasibility of the ECL platform is also tested in a real wastewater sample.

Moreover, Zhang *et al.* employed a liquid-exfoliation pathway to produce structure-controllable g-CNTs.[79] Interestingly, the fabricated g-CNTs showed a different ECL behavior toward several metal ions. So, the prepared g-CNTs were used for multiple metal ions' detection (Ni^{2+}, Cd^{2+}, and Cu^{2+}) without any tagging and masking chemical reagents. As represented in Figure 2.12A,

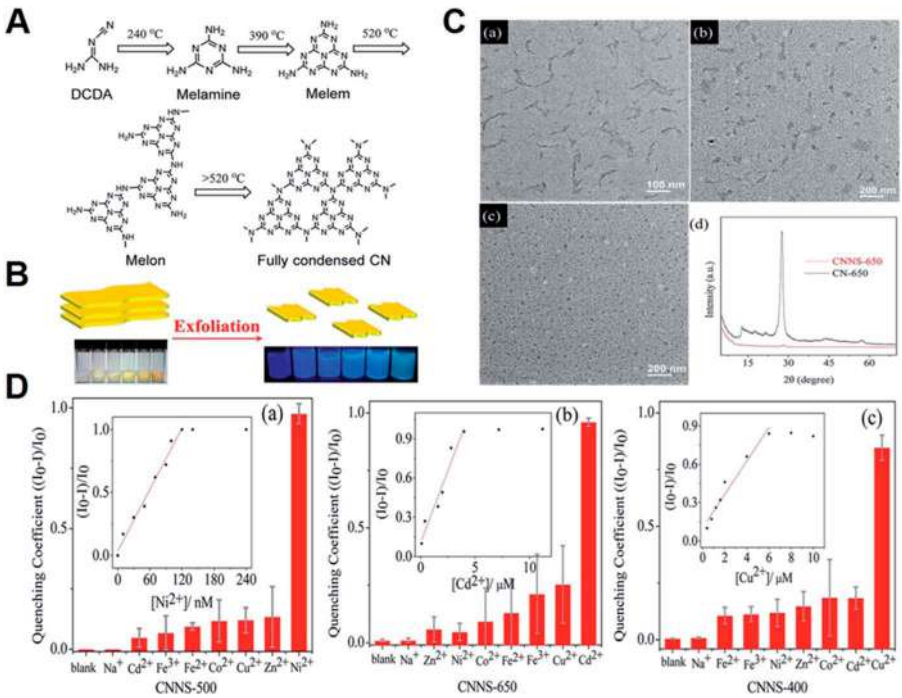

Figure 2.12 (A) The reaction route for the synthesis of condensed CN; (B) the exfoliation method of g-CNTs; (C) TEM of (a) CNNS-400, (b) CNNS-500, and (c) CNNS-650, (d) CNNS-650 and CN-650 XRD spectra; and (D) ECL intensities of (a) CNNS-500, (b) CNNS-650, and (c) CNNS-400 with various metal ions at the cathodic potential range. Inset: Standard calibration graphs for estimation of (a) Ni^{2+}, (b) Cd^{2+}, and (c) Cu^{2+}. Reproduced from ref. 79 with permission from American Chemical Society, Copyright 2016.

they fabricated the bulk carbon nitride with a different degree of polymerization at reaction temperatures between 400 and 650 °C. Figure 2.12C and D show the liquid exfoliation process and ECL responses to different metal ions, respectively. Based on the inner filter effect (or electron transfer) and the increase caused by the catalytic reaction of g-$CNs^{\bullet+}$/$TEA^{\bullet}$ species, accurate and reproducible sensors were designed for the detection of Cu^{2+}, Cd^{2+}, and Ni^{2+} with a LOD of 250, 20, and 1 nM, respectively.

g-CNTs were also used for the determination of inorganic anions; for example, Xu *et al.* prepared a new nanocomposite from a different g-C_3N_4 nanostructure (g-CNQD@g-CNTs).[80] The developed g-CNQD@g-CNTs nanocomposite was utilized as an ECL platform for the determination of nitrites (NO_2^-). It was found that the ECL response of the g-CNQD@g-CNTs/$S_2O_8^{2-}$ ECL system was significantly quenched by the addition of NO_2^- into the solution. $SO_4^{-\bullet}$ radical, produced from the electroreduction of $S_2O_8^{2-}$, is a strong oxidant and could oxidize NO_2^- to NO_3^-, causing a decrease in the concentration

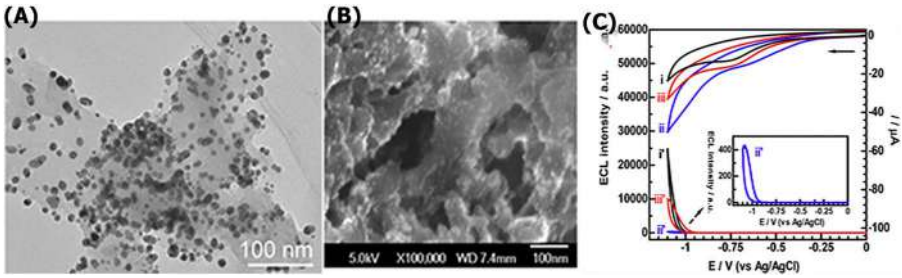

Figure 2.13 (A) TEM photo of Au–g-CNTs nanohybrids. (B) SEM photo of the Au–g-CNT nanohybrid film on GCE. (C) CV and ECL intensities of (i, i′) CNTs' film, (ii, ii′) Au–CNTs' film, and (iii, iii′) Au–CNTs' film dipped in 1 mM CN^- solution for 30 min, in PBS (0.1 M) of pH 7.4 having $K_2S_2O_8$ (10 mM). Reproduced from ref. 81 with permission from Elsevier, Copyright 2018.

of $SO_4^{-\bullet}$. Therefore, generated g-CNQD@CNNS*$^-$ was decreased and ECL was quenched. Using the optimized conditions of the developed sensor, a calibration curve was constructed for a NO_2^- anion from 0.28 to 40 μM and the LOD was assessed to be 0.12 μM. Another example for the application of g-CNTs for the detection of inorganic anions was reported by Chi's group.[81] The developed method was based on the fabrication of nanohybrids from gold nanoparticles (AuNPs) and g-CNTs (Au-g-CNTs nanohybrids, Figure 2.13A) for the detection of cyanide anion (CN^-). As shown in Figure 2.13B and C, GCE was modified by Au–g-CNTs nanohybrids, and cyclic voltammetry and ECL responses were recorded in buffered solution containing CN^-. Initially, Förster resonance energy transfer (FRET) from g-CNTs to AuNPs occurred, producing a strong decline in the ECL emission intensity. On the other hand, the CN^- anion etched the AuNPs and recovered this quenching effect. On this basis, a "signal-on" type of ECL sensor has been employed for CN^- anion assay from 50 nM to 1 mM with high specificity owing to the high binding affinity between CN^- and Au to form a stable complex.

2.5.2 Biomolecule Detection

Many ECL biosensors dependent on g-C_3N_4 have been used for the determination of biomolecules. For example, the monitoring of glucose in human biological fluid was achieved by Du and co-authors through the fabrication of a simple ratiometric ECL sensor.[82] The developed sensor was based on the *in situ* production of H_2O_2 from glucose and dissolved oxygen. H_2O_2 production was initiated by the catalytic reaction of glucose oxidase (GOx), which was fixed on g-C_3N_4-supported Au nanocomposites (GOx/Au–g-C_3N_4). Au–g-C_3N_4 exhibited a high cathodic ECL intensity in the presence of dissolved O_2 (DO) as a co-reactant. In the presence of glucose, GOx catalyzes the glucose oxidation and thus H_2O_2 was produced. Then, the reactive oxygen species

(ROS) generated from the conversion of H_2O_2 by AuNPs could significantly quench the cathodic ECL intensity and enhance the luminol anodic ECL peak intensity. The constructed glucose ratiometric ECL biosensor has shown an excellent linearity for glucose monitoring in the linear range of 0.1–8000 μM. Also, it has been extended for real samples' application with excellent selectivity and high recoveries. Another example for the detection of glucose without utilizing the enzymatic action of GOx was reported by Li *et al.*[83] They developed a non-enzymatic ECL sensor with extremely high sensitivity for glucose detection. They synthesized PdNW-functionalized Ag–g-CNTs as a luminophore. GCE was modified by PdNW-functionalized Ag–g-CNTs, which had a wide surface area and excellent electrocatalytic activity. The first "signal-on" was obtained through the π–π interaction binding of phenoxy dextran (DexP) on the interface of the electrode to give high ECL intensity; while a "signal-off" state was achieved by the binding between ConA and DexP. By immersing the modified electrode into a glucose sample solution, the glucose competes with DexP for the binding sites of ConA. Therefore, ConA was released from the surface of the electrode and the second "signal-on" state was achieved by increasing ECL intensity. The constructed "on-off-on" biosensor platform exhibited ultra-high sensitivity for the assay of glucose and the LOD was assessed to be 3.0 pM.

Chen and colleagues established a "signal-on" ECL biosensor for a DA assay.[84] The proposed sensor consists of gold nanoflower@graphitic carbon nitride polymer nanosheet–polyaniline hybrids (AuNF@g-C_3N_4–PANI). The ECL behavior of AuNF@g-C_3N_4–PANI/GCE was tested in PBS buffer (0.10 M) solution containing $K_2S_2O_8$. It was observed that the ECL peak intensity was highly improved with the existence of different concentrations of DA. This enhancement was related to the generation of g-$C_3N_4^{\bullet-}$ from the charge transfer complex between DA and AuNF@g-C_3N_4–PANI. Based on this ECL enhancement, a calibration plot for DA was constructed from 5 nM to 1.6 μM. Another ECL sensor for DA was developed by Chen *et al.*[85] A dual recognition sandwich ECL platform was achieved using two different recognition molecules (dithiobis-succinimidyl propionate and 3-aminophenylboronic acid) for capturing DA. DA was captured by dithiobis-(succinimidyl propionate), which was immobilized on Au–gCNTs nanocomposites. Then, 3-aminophenylboronic acid functionalized polyaniline APBA/PANI was fixed into the electrode *via* a chemical identification reaction between the diol of DA and the boronic acid of APBA. Based on the quenching effect of PANI on the ECL intensity of g-CNTs, a dual recognition ECL biosensor platform was developed for DA determination from 0.10 to 5000 pM. Later Jia's group constructed a DA ECL biosensor with excellent sensitivity of detection.[86] They synthesized a silver–carbon nitride (Ag–g-C_3N_4) nanocomposite and used it for GCE modification. The modified GCE showed a low ECL signal, while a stable and strong ECL intensity was obtained in a solution containing different concentrations of DA and $S_2O_8^{2-}$ co-reactant. This enhancement was related to the role of the amino moiety of DA in the generation of $SO_4^{\bullet-}$ from $S_2O_8^{2-}$, which produced an enhancement in the ECL peak intensity. Using the

optimized experimental conditions, the developed biosensor displayed a linear relationship between DA concentrations (0.015 to 150 μM) and enhanced ECL intensities.

Lu and co-authors developed a new bimodal ECL system for AA determination.[53] The new system was composed of g-CNQDs as a single luminophore and two co-reactants ($K_2S_2O_8$) and tetrabutylammonium bromide. Adjusting the potential window between −3 and 3 V, two peaks (ECL-1 at 2.82 V and ECL-2 at 1.73 V) were detected. In the presence of AA, the intensity of ECL-1 was quenched linearly with increasing AA concentrations, while ECL-2 remained unchanged. The LOD was calculated to be 110 pM, which indicates the high sensitivity of the developed bimodal sensors. Yang *et al.* successfully fabricated g-CNTs using a facile and green liquid exfoliation process.[87] The fabricated nanosheets and multi-walled carbon nanotubes (MWCNTs) were used as luminophore and signal intensity enhancer, respectively. They found that epinephrine (EP) could quench the ECL signal by electron transfer from g-CNTs to EP. The ECL sensor has been designed for EP determination from 1 to 1500 nM based on the EP quenching effect. Chi *et al.* fabricated a g-CNTs/reduced graphene oxide (RGO) nanohybrid for the development of a folic acid (FA) ECL biosensor.[88] g-CNTs/rGO nanohybrids give a stable and high ECL emission compared to bare g-CNTs because rGO prevents over electrochemical reduction of g-C3N4. The stable and strong ECL emission of this nanohybrid was significantly inhibited by the addition of FA in the testing solution. This platform was employed for FA detection in human serum and the detection limit was calculated to be 62 pM. In another paper, Li and his group proposed a new ECL platform for determination of FA.[89] They fabricated sulfur-doped g-CNTs (S-g-CNTs) and used them as anodic luminophores with nitrogen-doped carbon dots (N-CDs) as co-reactants. The ECL signal intensity of the developed ECL system could be quenched by FA with a concentration range from 50 nM to 200 μM. Furthermore, the ECL sensor was conducted for the assay of FA in human serum samples. Lu *et al.* fabricated g-CNQDs for an ECL emitter.[90] High ECL intensity was gained from the g-CNQDs–$K_2S_2O_8$ ECL system. Interestingly, the ECL signal was selectively diminished by adding riboflavin (RF). A decrease in the ECL signal intensity was due to the resonance energy transfer (RET) between g-CNQDs as donors and RF as receptor. The detection limit of RF was 0.63 nM. Also, high recoveries for RF were achieved through human serum assay. Hosseini's group established an ECL sensor for the detection of pyridoxine.[91] They fabricated g-CNTs from heating melamine powder at 550 °C in an alumina crucible for 5 h to obtain bulk g-CNTs. After that, bulk g-CNTs powder was exfoliated by refluxing with nitric acid for 12 h at 125 °C to attain final g-CNTs (Figure 2.14). Finally, Sm_2O_3 nanoparticle-decorated g-CNTs were prepared by sonication of the g-CNTs and the prepared Sm_2O_3 nanoparticles in distilled water. As illustrated in Figure 2.14, they modified bare GCE with Sm_2O_3 nanoparticle-decorated g-CNTs to boost the ECL signals of a pyridoxine-$Ru(bpy)_3^{2+}$ ECL platform. It was noticed that the established ECL system was even more sensitive (LOD = 44 pM) than the previously reported methods for the same analyte.

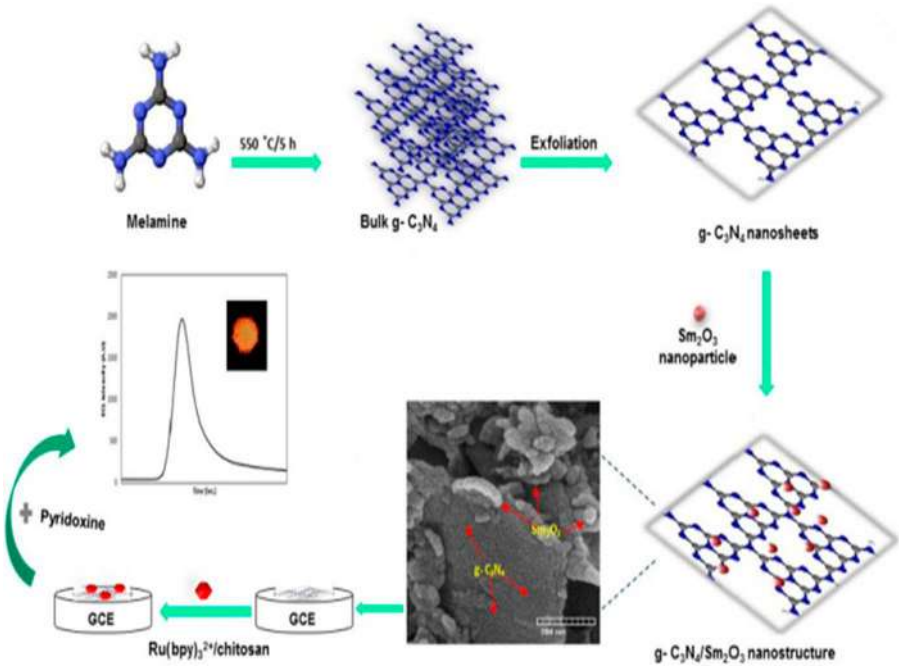

Figure 2.14 Diagram illustrating the construction of a pyridoxine ECL biosensor. Reproduced from ref. 91 with permission from Elsevier, Copyright 2019.

Based on the previously reported paper about the quenching impact of Cu^{2+} ions on g-C_3N_4 ECL emission, Chi and his colleagues developed an ECL biosensor system for the determination of pyrophosphate ion (PPi).[92] The chelation of PPi with Cu^{2+} enabled them to construct an ECL system and it was applied for the selective assay of PPi found in synovial fluid. The linear concentration range of the developed PPi biosensor was 2.0–800 nM (LOD 75 pM).

For analyzing total cholesterol at a single cell, Chen and co-workers developed a g-CNTs-modified microwell array for the estimation of total cholesterol in a cell.[93] The developed imaging approach has been applied for the determination of the membrane and intracellular cholesterol at a single cell with better visible sensitivity. The mechanism of the detection relies on the generation of H_2O_2 from the reaction of cholesterol oxidase with membrane cholesterol and cholesterol oxidase and cholesterol esterase with the intracellular cholesterol found inside the cell. The produced H_2O_2 gives a high ECL signal that enables total cholesterol analysis in a single cell. Chen's group proposed a selective ECL sensor for the assay of lactate. The sensor was dependent on the construction of a nanocomposite from g-C_3N_4–hemin nanocomposite and hollow gold nanoparticles (HGNPs).[94] HGNPs were used as an adsorbing matrix for lactate oxidase to serve as a lactate sensor. Interestingly, ECL intensity of luminol–H_2O_2 could be enhanced by the g-C_3N_4–hemin nanocomposite and HGNPs. In the presence of a lactate sample, lactate was oxidized by lactate oxidase in the presence of oxygen to give H_2O_2, which gives a high ECL intensity. The intensity of the ECL biosensor

was directly related to the amount of lactate, and the LOD was 5.5 nM. Wang *et al.* constructed a Eu_2O_3/g-C_3N_4 nanocomposite as an efficient luminophore.[95] The as-prepared nanocomposite was utilized as an augmented ECL biosensor for the detection of 17B-estradiol (E2). Eu_2O_3 clusters with oxygen vacancies could dramatically increase the g-C_3N_4 ECL signal intensity. It was found that E2 was collected on the surface of a sensing detection platform and the ECL emission intensity was significantly reduced. On that basis, the constructed ECL aptasensor has shown excellent sensitivity and acceptable detection selectivity for an E2 assay. Hu and co-authors established a sandwich ECL biosensor for the detection of sepsis biomarkers called procalcitonin (PCT).[96] The developed biosensor consists of carbon nanotubes (CNT) and AuNPs-functionalized g-C_3N_4 (g-C_3N_4–CNT@Au) and CuO nanospheres coated with a polydopamine (PDA) layer (CuO@PDA). AuNPs were used as an ECL signal amplifier and for carrying an amount of primary antibody (Ab1). The quenching-type ECL immunosensor was applied for PCT with extremely high sensitivity (LOD = 25.7 fg mL^{-1}).

g-C_3N_4 biosensors were used for the assay of biothiols' levels in biological fluids. Li's group proposed a "signal-on" type biosensor for the selective assay of L-cysteine (L-Cys).[97] The developed sensor was based on the fabrication of sulfur-doped g-CNTs (S-g-CNTs) from trithiocyanuric acid for the first attempt. S-g-CNTs ECL signal intensity is higher than pure g-CNTs. They found that ECL intensity was decreased by the presence of Cu^{2+}. The competitive coordination chemistry between Cu^{2+} and L-Cys resulted in restoring the ECL intensity of the S-g-CNTs. The ECL intensity was increased by increasing L-Cys concentration from 30 nM to 0.2 mM and the LOD of this sensor was 5 nM. A 2D/2D heterostructured ECL–RET-based ECL biosensor was constructed for glutathione (GSH) determination.[98] The developed sensor was composed of g-CNTs/MnO_2 using g-CNTs as energy donors and MnO_2 nanosheets as energy acceptors. The ECL response of g-CNTs was dramatically reduced by MnO_2 due to ECL–RET (ECL signal "off"). MnO_2 was reduced to Mn^{2+} by the addition of different concentrations of GSH; therefore, the g-CNTs signal intensity was recovered gradually by increasing GSH concentration (ECL signal "on"). The "signal-on" ECL sensor has shown a low limit of detection (0.05 μM).

2.5.3 Nucleic Acid Bioanalysis

Nucleic acids are very important for cell functioning, and therefore for life. They are considered the basic foundation of gene expression. Nanomaterials have participated significantly in the progress and innovation of nucleic acid biosensors. For instance, Shan's group designed an ultra-sensitive and selective ECL platform for DNA assay.[99] The developed sensor used connecting the conformational conversion of biotinylated capture DNA and the convenient electrocatalytic properties of g-CNTs@cobalt(II) protoporphyrin IX (CoPPIX@C_3N_4) biotag. The hairpin structure of the captured DNA was unfolded through a recognition reaction in the presence of the target sequence, and the biotinylated 5 extremity was exposed. Then, a binding reaction between the exposed biotin and streptavidin-functionalized CoPPIX@g-C_3N_4

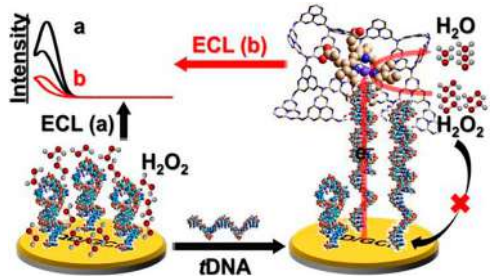

Scheme 2.2 Diagram representing the formation of CoPPIX@C_3N_4 for highly sensitive determination of DNA *via* the depletion of co-reactants. Reproduced from ref. 99 with permission from American Chemical Society, Copyright 2015.

(biotin–streptavidin linkage) took place, resulting in the immobilization of streptavidin-functionalized CoPPIX@g-C_3N_4 on the electrode surface. Subsequently, H_2O_2 was electrochemically reduced and the ECL response was quenched (Scheme 2.2.). The target DNA could be monitored down to 0.37 fM by the designed biosensor.

Ju and co-workers fabricated g-CNTs as a cathodic-type ECL luminophore with the existence of DO for the biological sensing of DNA.[100] Chitosan/GCE was modified by g-CNTs, then hemin tagged ssDNA was adsorbed on the modified electrode. This adsorption resulted in a hemin-mediated electrocatalytic reduction of the DO, therefore the generation of the H_2O_2 co-reactant was diminished and ECL emission of the g-CNTs was quenched. Using the optimized variables, the proposed biosensor exhibited good selectivity, high reproducibility and sensitivity for sensing DNA (LOD = 2.0 fM). Later, Yan's group designed a new ECL platform on the basis of the hybridization abilities of Au-g-CNTs with the target DNA for the selective detection of specific sequences DNA.[101] The developed sensor used Au/Pt-CNTs as a substrate as well as the favorable ECL properties of Au–g-CNTs. In the presence of $S_2O_8^{2-}$, the hybridization of Au–g-CNTs with the target DNA produces an impressive enhancement in the cathodic ECL signal. With the linear range of 40 to 50 pm, the proposed ECL sensor could be employed selectively for the sensing of target DNA. Another report for DNA sensing was published by Zhang and co-workers.[102] The developed sensor was based on the fabrication of g-CNTs, which attached to a DNA probe. g-CNTs–DNA binding led to a diminishing impact on the g-CNTs ECL emission intensity. Cu^{2+} ions were able to attach to the N7 position of DNA bases producing a DNA–Cu^{2+} complex, so the ECL intensity was decreased. There is a direct relationship between the amount of Cu^{2+} attached to DNA and the total amount of DNA. This shows that the decline in ECL intensity was directly proportionate to the increase in DNA on the interface of the electrode. The developed sensor is considered a highly sensitive sensor for DNA (LOD = 3.6×10^{-14} M). In 2019, Hu *et al.* used a solid-state method for the synthesis of g-CNQD for the determination of DNA.[103] They have constructed an ECL sensor dependent on the ECL–RET procedure between g-CNQDs (emitter) and AuNPs (acceptor). In the presence of $S_2O_8^{2-}$ co-reactant in PBS buffer, g-CNQD exhibits high ECL signals. When

the hairpin DNA was fixed on g-CNQDs, the ECL intensity decreased due to ECL–RET that occurred by AuNPs. ECL–RET was hindered by the existence of target DNA, because the hairpin-DNA looped structure was decomposed, and AuNPs were removed from g-CNQDs. Finally, the ECL intensity was produced again according to the amount of DNA. The ECL biosensor was linear from 0.02 fM to 0.1 pM for target DNA detection. Another example for the application of g-CNTs in a nucleic acid biosensor was represented by Xu and coworkers.[104] They developed a new ECL sensor on the basis of the RET between g-CNTs and $Ru(bpy)_3^{2+}$ luminophore and estimated the $ECL_{460\ nm}/ECL_{620\ nm}$ ratio for the detection of microRNA. A stable and high ECL peak at 460 nm of AuNPs-functionalized g-CNTs matched with the $Ru(bpy)_3^{2+}$ absorption peak, in addition to the emission peak of $Ru(bpy)_3^{2+}$ at 620 nm (Figure 2.15A). Once

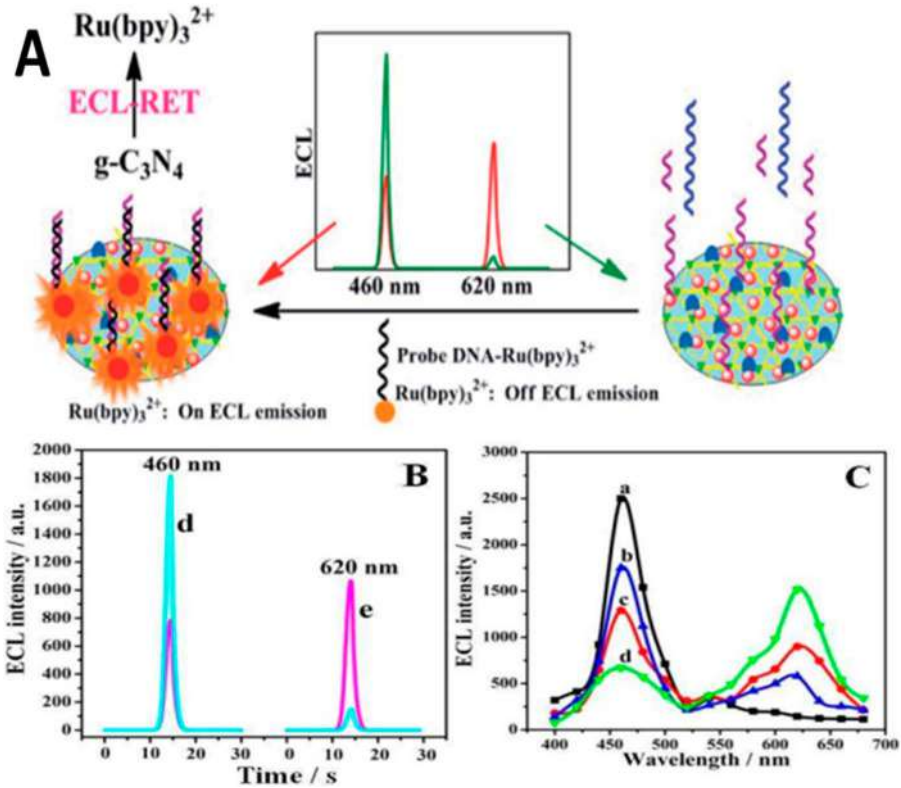

Figure 2.15 (A) Diagram of a new dual-wavelength ratiometric ECL–RET platform for the assay of microRNA. (B) The obtained ECL intensities of (d) MCH/molecular beacon/Au–g-C_3N_4 NH/GCE after hybridization with 10 pM miRNA-21 and 0.1 U μL^{-1} DSN, and (e) additional incubation with probe DNA–$Ru(bpy)_3^{2+}$ were separately estimated *via* an optical filter (at 460 nm as well as 620 nm) and PMT was adjusted at −500 V. (C) The ECL spectrum of molecular beacons/MCH/Au-g-C_3N_4 NH modified electrode measured in the incubation of probe DNA–$Ru(bpy)_3^{2+}$ with diverse miRNA-21 concentrations (from a: 0, b: 10 fM, c: 1 pM to d: 100 pM). Reproduced from ref. 104 with permission from American Chemical Society, Copyright 2016.

the target microRNA was present, a specific duplex nuclease destroyed the formed DNA–RNA duplex and microRNA was generated to begin the next phase for signal enhancement. Then, the remaining single-strand DNA on the modified electrode could be captured as a DNA– $Ru(bpy)_3^{2+}$ probe, leading to a quenching effect on the ECL signal intensity positioned at 460 nm and an enhancement of ECL intensity at 620 nm (Figure 2.15B and C). The established ECL platform opened another way for the bioassay of different nucleic acids using the dual-wavelength ECL method.

2.5.4 Cancer Biomarker Detection

The fascinating properties of g-C_3N_4 nanomaterials have enabled researchers to develop many ECL immunosensors for the detection of different cancer biomarkers. For instance, Chen's group constructed an ECL immunosensor dependent on the hybridization between AuNPs and g-C_3N_4 for monitoring carcinoembryonic antigen (CEA) concentrations in human serum.[105] AuNPs could capture and save the electrons from the conduction band (CB) of g-C_3N_4, in addition to its catalytic action for the reduction of $S_2O_8^{2-}$ to give $SO_4^{\bullet-}$, thus achieving a strong and high cathodic ECL response (Scheme 2.3). The surface of GCE was modified by AuNPs-functionalized g-C_3N_4 and CEA antibody (anti-CEA). As shown in Scheme 2.3, the target CEA in the sample solution was captured and the steric hindrance of the generated protein layers could

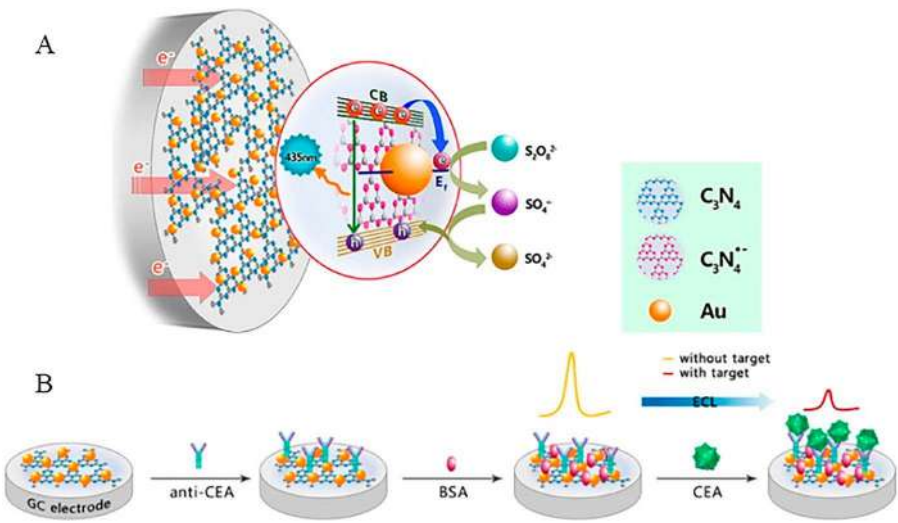

Scheme 2.3 (A) Diagram illustrating the mechanism of the Au–g-C_3N_4 nanohybrid-co-reactant platform ECL emission. (B) Au–g-C_3N_4 nanohybrid ECL immunosensor principles. Reproduced from ref. 105 with permission from American Chemical Society, Copyright 2014.

limit the electrons' transfer and diffusion of the $S_2O_8^{2-}$ co-reactants. Therefore, the ECL intensity was quenched linearly by increasing the target CEA concentrations from 0.02 to 80 ng mL^{-1}.

In another report, Wei *et al.* established a selective sandwich ECL immunosensor for the assay of CEA using ferrocene for amplifying the CEA quenching impact on the emission intensity of AgNPs-functionalized g-C_3N_4 (Ag@g-g-C_3N_4).[106] The primary antibody (Ab1) was anchored on the Ag@g-g-C_3N_4 by the adsorption effect of AgNPs to exhibit strong and stable ECL signals. A ferrocene carboxylic acid (Fc-COOH) labeled secondary antibody was fixed on Au-doped mesoporous Al_2O_3 nanorods (Au@Al_2O_3–FcCOOH@Ab2). A sandwich-type immunoreaction occurred and resulted in a remarkable decreasing effect in the ECL peak intensity due to the diminishing impact of Au@Al_2O_3–Fc-COOH@Ab2 on the emission of Ag@g-C_3N_4. ECL intensity *versus* concentrations of CEA are directly related in the concentration range of 1 pg mL^{-1} to 100 ng mL^{-1} (LOD = 0.35 pg mL^{-1}). Another immunosensor for the estimation of a CEA biomarker was described by Zou *et al.*[107] They synthesized carboxylated g-CNT and it was used as tags. They used CEA as a model sample analyte. The modified polymerized 2-aminoterephthalic acid (ATA) film/GCE (GCE/ATA) was secondly modified by g-CNTs and signal CEA antibody (Ab2) bio-conjugates to form GCE/ATA-Ab1-Ag-Ab2-NSs. GCE/ATA plays a significant role in the electron transfer resistance (R_{et}) of GCE/ATA-Ab1-Ag-Ab2-NSs for ECL. Then, they used scanning GCE/ATA-Ab1-Ag-Ab2-NSs in $K_2S_2O_8$ + H_2O_2 solution from 0 to −1.6 V to reduce the R_{et}. They observed that ECL of the tenth scan cycle was higher than the first one by about 3.3 times, and it was about 10.2 times higher than the ECL of GCE/ATA-Ab1-Ag-Ab2-NSs in a medium without $S_2O_8^{2-}$. Based on this, an amplified immunosensor was developed and used for the assay of CEA with good linearity (0.1–1000 pg mL^{-1}).

Guo *et al.* used an ECL biosensor for simultaneous determination of carbohydrate antigen 125 (CA125) and squamous cell carcinoma antigen (SCCA) using two different luminophores, Au NP-functionalized g-CNTs and Ru–NH_2 as cathodic and anodic luminophores, respectively.[108] In this immunoassay, the bare gold electrode surface was modified by the adhesion of both anti-$CA125_1$ as well as anti-$SCCA_1$ as capture probes. When the antibodies catch the two targets (CA125 and SCCA), two different stable and high ECL emission peaks were recorded at 1.25 V and 1.3 V, respectively. The detection limits of the developed potential-resolved "in-electrode" type biosensor were 400 μU mL^{-1} for CA125 and 0.33 pg mL^{-1} for SCCA. Li and co-workers used the same principles and synthesized a carboxylated g-C_3N_4/graphene nanohybrid for the assay of SCCA.[109] Graphene has a high ability to transfer electrons and form graphene/carboxylated g-C_3N_4 nanohybrids. After polishing the GCE, the surface was modified by the deposition of g-C_3N_4/graphene and covalent binding of anti-SCCA. A selective immunoreaction between SCCA and its antibody occurred and the distribution of the co-reactant to the surface of the electrode was hindered. Therefore, the relationship between the ECL quenching against the logarithm concentration (Log C) of SCCA was directly linear from 0.025 to 10 ng mL^{-1}. Also, Guo

and co-workers developed a consumable and label-free ECL immunosensor for the assay of CA125.[110] They used multi-functionalized g-C_3N_4 modified one-off screen-printed carbon electrodes (SPCEs). Then, the surface of the carboxylated g-C_3N_4 was consequentially functionalized by the Fe_3O_4 and CA125 antibody (anti-CA125). Fe_3O_4 nanoparticles were introduced in the outer Helmholtz plane of the biosensor to boost the ECL intensity of g-C_3N_4 by increasing the rate of electron transfer between SPCEs and g-C_3N_4. The CA125 was selectively and specifically bound with anti-CA125, causing a remarkable reduction in the ECL signal intensity. The linear detection range of this biosensor was 0.001–5 U mL^{-1}.

For investigation of the nuclear matrix protein 22 (NMP 22), Wei *et al.* fabricated a novel ECL immunosensor.[111] The designed sensor relied on the fabrication of AuNPs and g-C_3N_4 nanohybrids. The combination of AuNPs with g-C_3N_4 results in an enhancement in the electron transfer and consequently an enhancement in the g-C_3N_4 ECL intensity. Interestingly, ECL intensity was decreased when the electrode surface was modified by the nanohybrids and anti-NMP 22. After scanning the modified electrode in the sample solution containing NMP 22, ECL intensity was highly decreased. The quenching effect is because NMP 22 specifically reacted with anti-NMP 22, and the emitter reagent and electrons diffusion to the electrode surface were impeded by the protein on the electrode. The developed sensor achieved a linear relationship for the estimation of NMP 22 from 50.0–2.000 pg mL^{-1} (R^2 = 0.988).

Kim and colleagues developed an amazing label-free ECL sensor for protease and nuclease detection.[112] It was the first time that a material other than DNA was used in the fabrication of a logic-based ECL detection model. They fabricated a suitable layer-by-layer assembly of various substrates to enable the sensor for simultaneous detection of two enzymes at the same solution with excellent selectivity and sensitivity. In the presence of the target enzymes, the hybrid polyelectrolyte multilayered (PEM) assembly film is hydrolyzed and decomposed. The ECL intensity of the Au–g-C_3N_4 film was recovered due to the efflux of co-reactants toward the electrode surface. The real applicability of this sensor was checked by applying the proposed sensor in high-throughput drug monitoring and for medical diagnostics.

Chen's group designed a ratiometric ECL sensor for the assay of calcitonin (CT) as a calcium(II) regulator.[113] They used two different luminophores g-C_3N_4 and *N*-(aminobutyl)-*N*-(ethylisoluminol) (ABEI). Two different and well distinguished potential peaks were obtained from the ECL reaction of the luminophores, $S_2O_8^{2-}$ and dissolved oxygen. The electrode surface was modified by AuNPs/g-C_3N_4 for the fixing of primary antibody (Ab1). Then, CT will bind to the electrode, followed by the incubation of the secondary antibody (Ab2) modified with polyaniline (PANI) and ABEI into the electrode. The ECL intensity of g-C_3N_4 was quenched by PANI as the amount of CT increased, concurrently the ECL intensity of ABEI was increased. The ratiometric sensor has been employed for a CT assay from 0.1 to 40 pg mL^{-1} (LOD = 23 fg mL^{-1}).

Xu's group developed a ratiometric spatial-resolved ECL device that relied on using Au@g-C_3N_4 nanocomposites for the sensitive and selective assay of prostate specific antigen (PSA).[114] They modified a bipolar electrode (BPE)

surface using cathodic luminophore (Au@g-C_3N_4) and anodic luminophore ($Ru(bpy)_3^{2+}$). Pt-polyamidoamine (PAMAM)–DNAzyme on the cathodic surface could decrease the ECL intensity of g-C_3N_4 through RET. At the same time, PAMAM–DNAzyme promotes the catalytic reduction of O_2, resulting in increased flow of faradaic current and increase in the ECL $Ru(bpy)_3^{2+}$ reaction at the anode. Relying on the release of Pt–PAMAM–DNAzyme, they designed an "off–on" ECL at the cathode and "on–off" ECL at the anode. The constructed biosensor has been utilized for the reproducible and selective determination of PSA in the linear range from 100 pg mL^{-1} to 200 ng mL^{-1}. Later, Wei *et al.* manufactured an AuNPs-functionalized mesoporous graphite-like carbon nitride (mpg-C_3N_4) nanohybrid as an ECL biosensor for the screening of PSA.[115] They fabricated mpg-C_3N_4 with a very wide surface area and high porosity by the pyrolysis of urea and dicyandiamide precursors. They found that the nanohybrid could amplify luminol–H_2O_2 ECL intensity because of the catalytic improvement impact of Au on the ECL peak intensity of luminol. After loading AuNPs and luminol on mpg-C_3N_4, a primary antibody (Ab1) was attached to mpg-C_3N_4/Au *via* the Au–NH_2 bond. The enhanced ECL intensity of mpg-C_3N_4/Au was reduced linearly with increasing PSA concentration due to the proteins' insulating impact. Applying the experimental conditions, the ECL sensor has shown a sensitive and highly selective response to PSA in a wide linear concentration range from 0.001–15 ng mL^{-1} (LOD = 0.927 pg mL^{-1}). Recently, Jin and co-workers fabricated a new ECL biosensor for the determination of PSA on the basis of modifying GCE with CdS/Chito/g-C_3N_4 nanocomposites and DNA1 was labeled at the 5′ end with thiol.[116] They used ferrocene (Fc) labeled DNA2 at the 3′ end to bind with DNA1 based on the base pairing theory. The result of this pairing was that the ECL intensity was effectively quenched through the energy transfer and photoexcitation electron transfer between the CdS/Chito/g-C_3N_4 emitter and the Fc quencher. In the presence of PSA, DNA2 reacted with PSA and then shifted away together from the surface of the modified electrode, causing an enhancement in the ECL intensity. Using the experimental conditions, the designed sensor displayed a linear relationship for PSA detection from 1 pg mL^{-1} to 100 ng mL^{-1}.

Zhou and co-authors fabricated Au–g-CNTs-modified GCE for the determination of alpha fetoprotein (AFP).[117] AuNPs can enhance the ECL intensity of the g-C_3N_4 cathodic emitter due to the promotion of the electron transfer and electrocatalytic reduction of $S_2O_8^{2-}$ co-reactants to generate high quantities of $SO_4^{\bullet-}$ hole donors. Based on the antigen and the immobilized alpha fetoprotein antibody recognition reaction, ECL intensity was quenched linearly by increasing the AFP concentrations. The LOD was estimated to be 500 ng mL^{-1}. Recently, Shen and colleagues synthesized porous g-CNTs and carbon nanotubes (CNTs) for the development of a ratiometric ECL platform for evaluation of AFP.[118] They modified GCE with a mixture of porous g-CNTs and CNTs. CuS nanoparticles were used as labels for the secondary antibodies. After the immune recognition reaction took place, the ECL of g-CNTs was decreased due to dissolving of CuS nanoparticles as Cu^{2+}, which were spread mostly within the Helmholtz layer of GCE/CNTs–g-C_3N_4. The concentration of the target antigen was evaluated by an indirect method through the determination of the amount of Cu^{2+}. The ECL intensity ratio of

GCE/CNTs–g-C_3N_4 (Cu^{2+}) to GCE/CNTs–g-C_3N_4 (Cu) achieved an ultra-sensitive biosensor for the determination of AFP (LOD = 0.1 fg mL^{-1}). The ultra-high sensitivity was attributed to the enriched Cu^{2+} ions, which reduced to Cu on the surface of GCE/CNTs–g-C_3N_4.

2.5.5 Analysis of Proteins

Proteins are very important substances for humans. They are the key substances for the construction of cells as well as tissues in the human body. Proteins can be evaluated by ECL biosensors that rely on g-C_3N_4. For instance, concanavalin A (Con A) was detected by utilizing phenoxy dextran (DexP)-g-C_3N_4 as a signal probe for the fabrication of a "signal-on" ECL biosensor.[119] Graphene–AuNPs were synthesized as a 3D structure (3D-GR–AuNPs). The as-prepared GR–AuNPs were used as a matrix for the assembly of GOx, which could specifically identify the target Con A. After the specific interaction between DexP–g-C_3N_4 carbohydrate-Con A, an enhancement in the ECL signal intensity was developed. This ECL intensity enhancement was directly proportional with Con A concentration and the linear range of the developed biosensor was found to be 0.05–100 ng mL^{-1}. Thereafter, Wei and co-authors developed a new "turn-off" ECL biosensor for an ultra-sensitive assay of Con A that relied on using a polyaniline-3,4,9,10-perylenetetracarboxylic acid–DexP conjugate (PANI-PTCA-DexP) as an Ag–g-C_3N_4 ECL signal quencher.[120] The bare electrode was modified with DexP/Ag–g-C_3N_4. Then, a selective carbohydrate-ConA reaction allowed the anchoring of Con A onto the modified DexP/Ag–g-C_3N_4 film. Based on the sandwich structure of DexP, Con A and PANI–PTCA–DexP, a favorable "signal-off" ECL biosensor was obtained. The quenching effect is linearly correlated with Con A concentrations from 1 pg mL^{-1} to 50 ng mL^{-1} (LOD 0.3 pg mL^{-1}). In 2019, another report for detection of Con A was published by Jia *et al.* that relied on the ECL–RET mechanism.[121] In this work, they fabricated glucose-functionalized carboxylic g-CNTs (g-C_3N_4–COOH@Glu) and carboxylic multi-walled carbon nanotubes covered by MnO_2 nanoparticles (BSA@MnO_2–MWCNTs–COOH@Glu). The MWCNTs acted as a carrier for loading MnO_2, while glucose was used as the identification substance for binding with Con A. Incubation of BSA@MnO_2–MWCNTs–COOH@Glu onto the modified electrode resulted in a selective carbohydrate-Con A reaction and therefore a drastic decline in the g-C_3N_4–COOH@Glu/$S_2O_8^{2-}$ ECL intensity. The designed sensor platform exhibited a very wide linearity from 0.0 pg mL^{-1} to 10 μg mL^{-1} (LOD = 2.2 fg mL^{-1}) for the detection of Con A. Moreover, it has been effectively employed in the evaluation of Con A in actual serum biological samples.

Chi's group designed an aptasensor ("signal-on" type) for the assay of platelet-derived growth factor BB (PDGF–BB).[122] The fabricated sensor was based on the fabrication of g-CNTs enriched with QDs nanocomposites (QD@g-CNTs) by an H_2O_2 oxidation method to improve the ECL intensity of the bulk g-CNTs. Figure 2.16A illustrates the SEM of the QD@g-CNTs nanocomposite. It is clear that QD@g-CNTs nanocomposites show an irregular tissue-like 2D nanosheet structure. As shown in Figure 2.16B, the

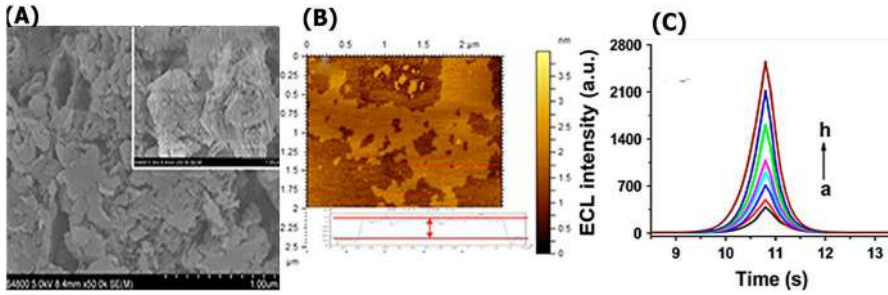

Figure 2.16 (A) SEM photo of a QD@CNNS nanocomposite. Inset: SEM photo of the bulk g-C_3N_4. (B) AFM photo of a QD@CNNS nanocomposite and its cross–sectional profile. (C) ECL responses of the standard solution of PDGF–BB with different concentrations. Reproduced from ref. 122 with permission from Elsevier, Copyright 2017.

cross-sectional AFM photo shows that the thickness is uniform and about 0.89 nm. Notably, the ECL intensity decreased when the Fc label was coupled with QD@g-CNTs through π–π conjugation as well as electrostatic interaction. The ECL signal was efficiently improved again by the addition of PDGF due to the creation of a PDGF–BB/aptamer complex (Figure 2.16C). The recovery in the ECL response was linear with PDGF–BB concentrations from 0.02–80 nM.

Wang *et al.* reported another "turn-on" ECL biosensor for the monitoring of PDGF–BB.[123] The developed sensor was based on the fabrication of a β-cyclodextrin functionalized g-C_3N_4 (β-CD/g-C_3N_4) composite for the first attempt. β-CD was used for enhancing the anchoring of the adamantine-labeled DNA on the interface of the electrode and also to enhance the ECL quenching effect of the Fc quencher by both energy transfer and photo-excited electron transfer routes. The ECL emission intensity of Ad-DNA/β-CD/g-C_3N_4 was decreased dramatically in the existence of Fc. The ECL intensity was largely improved again by the addition of the PDGF–BB and this was due to the interaction between the target and Fc-DNA, which resulted in the liberation of Fc from the electrode surface. The developed aptamer was used for the detection of PDFF–BB with an ultra-high sensitivity (LOD 2.6 × 10^{-13} g mL^{-1}).

2.5.6 Cell-related Bioanalysis

A cell is the fundamental unit of the structure, and work of the organism and humans. Cell-related bioanalysis based on ECL of g-C_3N_4 has earned more attention from researchers due to the significance of human health and life. Liu *et al.* for example, constructed a reusable ECL biosensor for cancer cell determination as well as their surface *N*-glycan estimation.[124] They detected a cancer cell and its surface by applying dual-potential conditions utilizing $Ru(phen)_3^{2+}$ as anodic and AuNPs–g-C_3N_4 as cathodic signal probes.

They modified the bare GCE electrode by reduced MoS_2 nanosheets, and then the hybridized capture DNA/aptamer was anchored on the nanosheets. Double-strand DNA trapped $Ru(phen)_3^{2+}$ in its groove. At the target cells, a selective recognition interaction between the DNA aptamer and target cells occurred, resulting in a break of the duplex DNA and release of $Ru(phen)_3^{2+}$. At the same time, Con A@AuNPs-modified g-C_3N_4 (Con A@Au–C_3N_4) was employed as a cathodic ECL nanoprobe through the formation of a sandwich-type modified electrode between mannose and a Con A@Au–C_3N_4 nanoprobe. Dependent on the ECL signal of the negative (cathodic) and positive (anodic) potential ($\Delta ECL_n/\Delta ECL_p$) ratio, the developed sensor exhibited a favorable and desirable sensitivity and specificity for the determination of cancer cells. In addition, it bypassed the routine procedures for cell counting. Similarly, Ju and co-workers fabricated an ECL platform for the simultaneous determination of circulating tumor cells (CTCs) and the relevant glycan expression.[125] A g-CNTs aptamer was used along with luminol-reduced AuNPs (LuAuNPs) as the cathodic and anodic luminophore, respectively. g-CNTs were decorated by AuNPs (AuNPs@CNNS) for the specific capture of CTCs through g-CNTs coupling of the aptamer, while lectin-functionalized LuAuNPs were used for the specific identification and recognition of surface glycans. After the addition of the model target (MCF-7 CTCs), two different responses were achieved regarding the cathodic and anodic ECL signal. Cathodic ECL signal intensity was decreased due to the CTCs-based steric impact and the ECL anodic signal intensity was increased due to the decorated luminol substances. The developed ECL platform has been demonstrated for the ultra-sensitive determination of cells (LOD = 2 cells), furthermore, it has been efficiently employed for determination of the difference of glycans present on the cell surface.

For HL-60 cancer cell detection, Xu's group developed an ECL platform by applying g-CNTs and Ag–PAMAM–luminol nanocomposites as two different ECL emitters.[126] The aptamer was conjugated with DNA-functionalized Ag-PAMAM-luminol nanocomposites on magnetic bead surfaces. In the presence of HL-60 cells, Ag-PAMAM-luminol was released from the magnetic bead and the capture DNA could be hybridized on the g-CNTs' modified electrode. So, the ECL of g-CNTs was quenched due to the RET of AgNPs, while the anodic luminol ECL was enhanced. The LOD of this biosensor was 150 cells.

Liu *et al.* synthesized an ECL platform for the determination of exosomes and their surface proteins.[127] The fabricated sensor was based on using g-C_3N_4 conjugated polydopamine-coated Galinstan liquid–metal shell–core nanohybrids (g-C_3N_4@Galinstan-PDA) nanoprobes and multivalent PAMAM–AuNPs electrode interface to design an ultra-sensitive ECL platform for determination of exosomes as well as their surface proteins. PAMAM–AuNPs were modified by the GPC1 antibody (anti-GPC1) and finally coated on the surface of the electrode. This antibody modified electrode can enhance the exosomes' capture efficacy and Galinstan NPs were used as the nanoprobe. In the presence of exosomes, the antibody modified g-C_3N_4@Galinstan-PDA can identify the exosomes specifically and exhibits a high ECL signal intensity. The ECL enhancement mechanism was reasoned to be due to the favorable properties

of the Galinstan NPs in smoothing the movement of electrons and decreasing g-C_3N_4 passivation during electrochemical reductions. On this basis, an effective ECL biosensor was proposed for HeLa cell-derived exosomes with a very low detection limit (31 particles μL^{-1}).

2.5.7 Detection of Enzyme Activity

Zhu and co-workers reported a simple and sensitive label-free ECL biosensor to determine acetylcholinesterase (AChE).[128] The developed sensor used AuNPs-decorated g-C_3N_4 as luminophore and TEA as co-reactant. By the addition of AChE enzyme to the electrochemical cell, acetylthiocholine (ATCl) substrate was hydrolyzed to generate an acetate anion. The acetate anion could interact with the triethylamine (Et_3N) co-reactant, resulting in a remarkable quenching in the anodic ECL intensity. ECL quenching occurred linearly to the AChE concentrations from 0.0001–10 ng mL^{-1}. Liu and co-authors designed an ECL biosensor to assay galactosyltransferase (Gal T) activity.[129] The analysis used g-CNTs as the emitter. Also, they used a polystyrene microsphere to increase sensitivity through inhibiting the rate of the electron transfer on the modified electrode surface. Firstly, they modified the GC electrode surface by carboxylated g-CNTs. Subsequently, they anchored *N*-acetylglucosamine conjugated BSA (GlcNAc–BSA) on the g-C_3N_4 surface modified electrode. By the addition of Gal T and uridine 50-diphosphogalactose (UDP-Gal) as a co-reactant, galactose was combined with GlcNAc–BSA, and the ECL was decreased. The LOD of the constructed biosensor was 7×10^{-5} U mL^{-1}.

Qiu *et al.* investigated the impact of Au NCs on the ECL intensity of g-C_3N_4 for the detection of protein kinase activity (PKA).[130] Interestingly, they noticed that BSA–AuNCs could effectively increase the ECL intensity of g-C_3N_4. In the existence of ATP-s and PKA, BSA–Au NCs were fixed to the phosphorylated peptides modified g-C_3N_4/GCE by the Au–S bond. BSA-AuNCs could significantly enhance the ECL intensity of g-C_3N_4 by about 4.5 times due to its catalytic effect. The developed biosensor has been used for the assay of PKA in biological fluids. Furthermore, it has been utilized for kinase inhibition monitoring, reflecting the importance of the developed sensor in clinical biodiagnosis.

2.5.8 Detection of Pharmaceutical Active Ingredients

Graphitic carbon nitrides were also used for the detection of pharmaceutical active ingredients. For example, gatifloxacin antibiotic (GAT) was determined by using a reduced graphene oxide-copper sulfide (rGO–CuS) composite coupled with a g-CNTs' modified glassy carbon electrode.[131] The rGO–CuS nanocomposite was fabricated by a simple hydrothermal method. The fabricated rGO–CuS nanocomposite was used for enhancing the sensitivity of GAT detection through facilitating the diffusion of the electrons between the electrode and electroactive center of the g-CNTs. The decrease in the ECL

response and GAT concentrations was linear from 0.1–100 μM. Moreover, the developed sensor has been utilized for the analysis of mouse plasma samples with acceptable obtained recoveries from 98.36% to 104.7%. Also, Li and co-workers developed an ECL sensor for detecting diclofenac (DCF) by using graphene oxide coupled g-C_3N_4 (GO–g-C_3N_4) as a signal probe.[132] GO was used for amplifying the ECL signal intensity of carboxylated g-C_3N_4 owing to its excellent charge transport properties. They fabricated MWCNTs–AuNPs as a sensing platform. MWCNTs–AuNPs act as a suitable carrier for anchoring a high quantity of coating antigen and accelerating the electronic transmission rate to increase the signal intensity. Dependent on the combined impact between GO–g-C_3N_4 and the MWCNTs–AuNP composite, the fabricated sensor exhibited high detection sensitivity for determination of DCF (LOD = 1.7 pg mL^{-1}). Recently, Fu and co-workers synthesized cadmium carbonate ($CdCO_3$) and g-C_3N_4 (g-C_3N_4–$CdCO_3$) nanocomposites as a chiral ECL sensor ("signal-off" type) for the differentiation and determination of propranolol (Pro) enantiomers.[133] The sensor has the ability to differentiate between two forms of Pro enantiomers and give a different ECL signal response for S-Pro and R-Pro. The mechanism of recognition was explained by the theoretical estimation of binding constant and the water contact angle experiments. The spatial configuration of R-Pro might match better with g-C_3N_4–$CdCO_3$ than S-Pro, so their behavior on the ECL of the g-C_3N_4–$CdCO_3$/$S_2O_8^{2-}$ ECL system were different. Therefore, various decreasing effects on the ECL intensities were obtained. Based on this, the developed chiral sensor has been applied for recognition of Pro enantiomers at a large concentration range from 1–1000 μM.

2.5.9 Detection of Pesticides

Yuan's group fabricated a "signal-on" type ECL platform for the determination of organophosphate pesticides (OPs).[54] They modified GCE by β-CD functionalized g-C_3N_4. Acetylcholinesterase (AChE) was bound into the inclusion complex of the modified electrode. In the absence of OPs, acetylthiocholine was hydrolyzed by AChE and generates acetic acid (HAc), which interacted with the Et_3N co-reactant to produce a diminishing impact on the ECL intensity. However, the addition of OPs could successfully decrease activity of AChE, so consuming of the Et_3N was decreased, resulting in an increase in the ECL response. Yang and co-authors developed an ECL sensor ("signal-off" type) for the sensitive determination of pentachlorophenol (PCP).[134] The fabricated sensor is very simple and based on a g-C_3N_4/GR modified Ti foil working electrode. They used graphene (GR) as a matrix for immobilization of g-C_3N_4 and a cathodic signal amplifier of g-C_3N_4 (~4.7 times) since it accelerates the electron transfer among the g-C_3N_4 emitter and the electrode. The g-C_3N_4/GR Ti modified electrode showed a higher ECL intensity than g-C_3N_4 itself. PCP could be adsorbed onto the g-C_3N_4 interface and be reduced by the negatively charged g-C_3N_4*, causing a diminishing effect on the ECL signal intensity. Inspired by this, the proposed ECL sensor was utilized for the simple and selective determination of PCP with a LOD of 10 pM.

2.5.10 Other Experiments

In 2013, Xiao's group used g-C_3N_4 as an emitter and triethanolamine (TEA) as a co-reactant for the detection of rutin.[135] They observed the effective transfer of energy from g-C_3N_4 towards the oxidating product of rutin, which could selectively quench the ECL intensity. Reliant on this, a selective and reproducible anodic ECL sensor for the determination of rutin is proposed. The linear response of the demonstrated ECL sensor is 0.20–45.0 μM. What's more, the developed sensor platform has been utilized for the detection of the analyte in its tablet dosage form and the obtained recoveries were very high. Similarly, Liu *et al.* established a new and selective ECL platform for the determination of catechol relying on the same quenching mechanism.[136] They developed a $Ru(bpy)_3^{2+}$/g-CNQDs ECL system and they found that catechol has a quenching impact on the ECL signal intensity. In PBS with pH 7.5, the $Ru(bpy)_3^{2+}$/g-CNQDs system exhibited a strong ECL signal intensity. The addition of catechol in the sample solution permits its electro-oxidization to 1,2-benzoquinone. Thus, the electron of $Ru(bpy)_3^{2+}$* was moved to 1,2-benzoquinone, causing a quenching in the ECL signal intensity. The developed sensor has been applied for the assay of catechol in pure form (10 nM–2 mM) and TEA samples with excellent selectivity. Bisphenol A (BPA) was detected by using an ECL aptasensor based on a smart permeability gate platform.[137] A GCE electrode was modified by the negatively charged Au-g-C_3N_4 and target mediated polyelectrolyte-aptamer multilayer film. The detection was based on adjustment of the diffusion rate of the co-reactant. As represented in Figure 2.17A, the modified Au–g-C_3N_4/GCE was further modified by several layers of polyethyleneimine (PEI)/polystyrene sulfonate (PSS) using a layer-by-layer technique. Upon the addition of different concentrations of BPA, specific binding of target molecules occurred and the formed PEI/aptamer gate was destroyed, resulting in an increase in the ECL response (Figure 2.17B and C). The developed sensor displayed favorable selectivity and sensitivity for BPA detection (LOD of 50 pg mL^{-1}).

Yuan's group designed a sandwich ECL biosensor for the estimation of one important glycoprotein called soybean agglutinin (SBA).[138] They fabricated carboxylated carbon nitride (C-g-C3N4) and used it as a luminophore, while D-galactosamine (galM) was used as an identification substance. The surface of the GCE was modified by C-g-C3N4 and AuNPs for catching the galM through the Au–N bond. In the existence of SBA, a selective identification reaction between galM and SBA occurred and SBA was captured, thus the anodic ECL signal intensity was increased. The developed "signal-on" ECL sensor achieved good linearity for SBA detection from 0.001–10 μg mL^{-1}. Zhang and co-workers developed a fascinating biomimetic ECL biosensor for 8-hydroxy-2′-deoxyguanosine (8-OHdG) detection on the basis of two competitive catalytic/steric hindrance mechanisms.[139] They conjugated the hemin/G-quadruplex assembly to the g-CNTs–AuNPs' modified GCE to produce two competitive mechanisms in the single ECL biosensor. In the presence of 8-OHdG analyte, the capture process occurred and the aptamer probe was protected. To destroy the unbound aptamer probes and produce

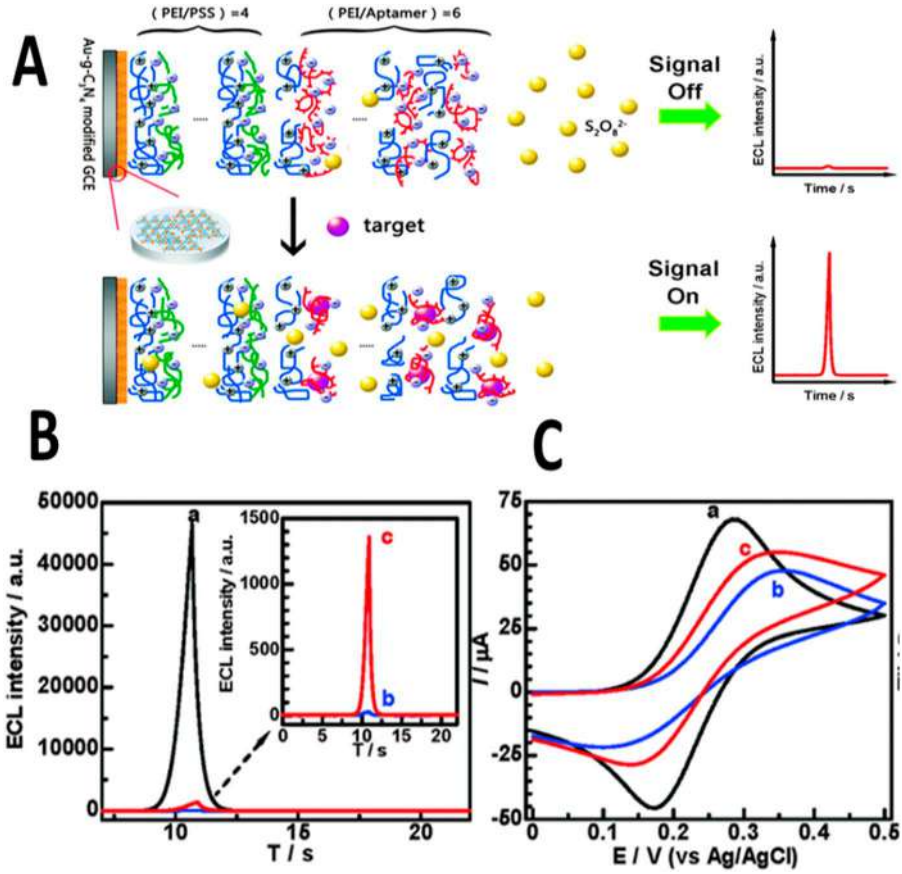

Figure 2.17 Diagram representation of (A) the developed permeability gate-based ECL aptasensors based on the target-responsive polyelectrolyte–aptamer films. (B) ECL and CV (C) intensities of (a) Au–g-C_3N_4 film/GCE, (b) [$(PEI/PSS)_4(PEI/aptamer)_6$]/Au–g-$C_3N_4$ film/GCE, (c) (b) using of BPA (5 ng mL^{-1}) for 40 min. Reproduced from ref. 137 with permission from the Royal Society of Chemistry.

the protected aptamer probes (8-OHdG–Apt), two kinds of exonuclease (Exo I and III) were introduced. Then a continuous opening of the hairpin probe and the production of active G-quadruplex structures occurred by recycling of 8-OHdG–Apt. Finally, by adding hemin, the liberated G quadruplexes were folded into a supramolecular hemin/G-quadruplex, which has a dual function depending on the 8-OHdG concentration. At low concentration of 8-OHdG, the hemin/G-quadruplex works by catalytic action on H_2O_2 and converts it into OH^-. Hence, the inhibition for ECL of g-CNTs–AuNPs by H_2O_2 would be recovered, while using high concentration of 8-OHdG leads to the assembly of hemin/G-quadruplex on g-CNTs–AuNPs. This resulted in a decrease in the electron transfer and the distribution rate of $S_2O_8^{2-}$ to the vicinity of g-CNTs.

When these steric hindrances were predominant, the ECL of g-CNTs would be diminished. Based on the two competitive mechanisms, a new biosensor has developed for the detection of 8-OHdG.

2.6 Summary and Future Outlook

In this chapter, we have discussed the different applications of the g-C_3N_4–CL and ECL-based biosensors with representative examples. In comparison to spectroscopic and chromatographic analytical devices, g-C_3N_4-based biosensors can be simply applied to analyze various targets selectively and sensitively including metal ions, inorganic anions, small biomolecules, cancer biomarkers, nucleic acids, drugs, amino acid and proteins, and cells. g-C_3N_4-based biosensors have many properties such as simple experimental instrumentation, weak background, and the use of non-toxic solvents, which have encouraged researchers for further developments. A comprehensive understanding of the fundamental basics of the construction of g-C_3N_4 and the mechanism of generating a CL and ECL signal response is the key to designing new biosensors for the future. We expect that g-C_3N_4-based biosensor work will focus on improving detection performance in the future. We believe that researchers will develop new g-C_3N_4 luminophores such as chemically modified g-CNTs and new g-CNQDs. Also, researchers will apply these nanomaterials with higher CL and ECL response for the sensitive detection of various analytes. In addition, we think much more attention will be considered for the establishment of more selective CL platforms for the selective determination of biomolecules, metal ions, and biomarkers. Moreover, researchers will try to improve and boost the sensing properties and features of the g-C_3N_4 sensors and their selectivity by combining g-C_3N_4 with other nanostructures and biomaterials, for example, hybridization with different nanoparticles, nanoclusters and multi-walled carbon nanotubes. What's more, since most of the ECL sensors can only quantify one analyte, we believe that future work regarding g-C_3N_4-based ECL biosensors can be used for the simultaneous or multiplex detection for more than one analyte. Finally, researchers may try to apply g-C_3N_4 in microfluidic paper-based devices and improve the selectivity of g-C_3N_4-based ECL for application in a complicated matrix such as human urine, serum, saliva, and spinal fluids. Successful achievement of these goals will result in the construction of a g-C_3N_4-based biosensor for multiple detections of different analytes in complicated matrices with high sensitivity and selectivity. Also, the developed sensor will be used for different applications in biological and environmental analysis as well as disease diagnosis.

Acknowledgements

We appreciate the kind support from the Ministry of Science and Technology of the People's Republic of China (No. 2016YFA0201300), the National Natural Science Foundation of China (Nos. 21675148 and 21874126), and the

Chinese Academy of Sciences (CAS) - the Academy of Sciences for the Developing world (TWAS) president's Fellowship program, and Minia University of Egypt. We are thankful to all our family members for their continuous encouragement.

References

1. E. Hutter and D. Maysinger, *Trends Pharmacol. Sci.*, 2013, **34**, 497.
2. Y. Su, Y. Xie, X. Hou and Y. Lv, *Appl. Spectrosc. Rev.*, 2014, **49**, 201.
3. M. I. Halawa, W. Gao, M. Saqib, S. A. Kitte, F. Wu and G. Xu, *Biosens. Bioelectron.*, 2017, **95**, 8.
4. M. Valcárcel and Á. I. López-Lorente, *Gold Nanoparticles in Analytical Chemistry*, Elsevier, 2014.
5. K. Eid, M. H. Sliem, A. S. Eldesoky, H. Al-Kandari and A. M. Abdullah, *Int. J. Hydrogen Energy*, 2019, **44**, 17943–17953.
6. K. Eid, M. H. Sliem, H. Al-Kandari, M. A. Sharaf and A. M. Abdullah, *Langmuir*, 2019, **35**, 3421–3431.
7. K. Eid, M. H. Sliem and A. M. Abdullah, *Nanoscale*, 2019, **11**, 11755–11764.
8. M. A. Ahsan, T. He, K. Eid, A. M. Abdullah, M. L. Curry, A. Du, A. R. Puente Santiago, L. Echegoyen and J. C. Noveron, *J. Am. Chem. Soc.*, 2021, **143**, 1203–1215.
9. M. M. Xavier, P. R. Nair and S. Mathew, *Analyst*, 2019, **144**, 1475–1491.
10. H. Jin, C. Guo, X. Liu, J. Liu, A. Vasileff, Y. Jiao, Y. Zheng and S.-Z. Qiao, *Chem. Rev.*, 2018, **118**, 6337.
11. Y. Chen, Z. Fan, Z. Zhang, W. Niu, C. Li, N. Yang, B. Chen and H. Zhang, *Chem. Rev.*, 2018, **118**, 6409.
12. P. Mu, G. Zhou and C.-L. Chen, *Nano-Struct. Nano-Objects*, 2018, **15**, 153.
13. H. Wang, X. Zhang and Y. Xie, *Mater. Today*, 2019, **23**, 72.
14. W. Wen, Y. Song, X. Yan, C. Zhu, D. Du, S. Wang, A. M. Asiri and Y. Lin, *Mater. Today*, 2018, **21**, 164.
15. R. Ahmad, N. Tripathy, A. Khosla, M. Khan, P. Mishra, W. A. Ansari, M. A. Syed and Y.-B. Hahn, *J. Electrochem. Soc.*, 2019, **167**, 037519.
16. M. B. E. Chan-Park, N. Murugan and A. K. Sundramoorthy, *J. Electrochem. Soc.*, 2019, **166**, B3163.
17. Z. Zhou, Y. Zhang, Y. Shen, S. Liu and Y. Zhang, *Chem. Soc. Rev.*, 2018, **47**, 2298.
18. G. Yang, C. Zhu, D. Du, J. Zhu and Y. Lin, *Nanoscale*, 2015, **7**, 14217.
19. Q. Han, N. Chen, J. Zhang and L. Qu, *Mater. Horiz.*, 2017, **4**, 832.
20. L. Chen and J. Song, *Adv. Funct. Mater.*, 2017, **27**, 1702695.
21. Y. Dong, Q. Wang, H. Wu, Y. Chen, C. H. Lu, Y. Chi and H. H. Yang, *Small*, 2016, **12**, 5376.
22. H. Song, L. Zhang, Y. Su and Y. Lv, *J. Anal. Test.*, 2017, **1**, 274.
23. H. Song, Y. Su, L. Zhang and Y. Lv, *Luminescence*, 2019, **34**, 530.
24. D. M. Teter and R. J. Hemley, *Science*, 1996, **271**, 53.
25. F. Cui and D. Li, *Surf. Coat. Technol.*, 2000, **131**, 481.

26. X. Wang, K. Maeda, A. Thomas, K. Takanabe, G. Xin, J. M. Carlsson, K. Domen and M. Antonietti, *Nat. Mater.*, 2009, **8**, 76.
27. E. Kroke, M. Schwarz, E. Horath-Bordon, P. Kroll, B. Noll and A. D. Norman, *New J. Chem.*, 2002, **26**, 508.
28. W. Zheng, N.-B. Wong, X. Liang, X. Long and A. Tian, *J. Phys. Chem.*, 2004, **108**, 840.
29. G. Liao, F. He, Q. Li, L. Zhong, R. Zhao, H. Che, H. Gao and B. Fang, *Prog. Mater. Sci.*, 2020, 100666.
30. Y. Wang, S. Zhao, Y. Zhang, J. Fang, W. Chen, S. Yuan and Y. Zhou, *ACS Sustainable Chem. Eng.*, 2018, **6**, 10200.
31. A. Speltini, A. Pisanu, A. Profumo, C. Milanese, L. Sangaletti, G. Drera, M. Patrini, M. Pentimalli and L. Malavasi, *RSC Adv.*, 2018, **8**, 39421.
32. J. Zhu, P. Xiao, H. Li and S. A. Carabineiro, *ACS Appl. Mater. Interfaces*, 2014, **6**, 16449.
33. M. Wu, Y. Gong, T. Nie, J. Zhang, R. Wang, H. Wang and B. He, *J. Mater. Chem.*, 2019, **7**, 5324.
34. S. Cao and J. Yu, *Phys. Chem. Lett.*, 2014, **5**, 2101.
35. A. Nikokavoura and C. Trapalis, *Appl. Surf. Sci.*, 2018, **430**, 18.
36. Y. Qi, Q. Liang, R. Lv, W. Shen, F. Kang and Z.-H. Huang, *R. Soc. Open Sci.*, 2018, **5**, 180187.
37. S. Kumar, S. Karthikeyan and A. F. Lee, *Catalysts*, 2018, **8**, 74.
38. J. Zhang, Y. Chen and X. Wang, *Energy Environ. Sci.*, 2015, **8**, 3092.
39. L. Wang, C. Wang, X. Hu, H. Xue and H. Pang, *Chem.–Asian J.*, 2016, **11**, 3305.
40. W. K. Darkwah and Y. Ao, *Nanoscale Res. Lett.*, 2018, **13**, 388.
41. A. Mishra, A. Mehta, S. Basu, N. P. Shetti, K. R. Reddy and T. M. Aminabhavi, *Carbon*, 2019, **149**, 693.
42. A. Wang, C. Wang, L. Fu, W. Wong-Ng and Y. Lan, *Nano-Micro Lett.*, 2017, **9**, 47.
43. L. Li, G. Wu, G. Yang, J. Peng, J. Zhao and J.-J. Zhu, *Nanoscale*, 2013, **5**, 4015–4039.
44. J. Zhou, Y. Yang and C.-Y. Zhang, *Chem. Commun.*, 2013, **49**, 8605.
45. W. Wang, C. Y. Jimmy, Z. Shen, D. K. Chan and T. Gu, *Chem. Commun.*, 2014, **50**, 10148.
46. X. Guo, L. Xu, L. Zhang, H. Wang, X. Wang, X. Liu, J. Yao and A. Hao, *J. Lumin.*, 2018, **196**, 100.
47. H. Zhang, Y. Chen, M. Liang, L. Xu, S. Qi, H. Chen and X. Chen, *Anal. Chem.*, 2014, **86**, 9846.
48. J. Han, H. Y. Zou, M. X. Gao and C. Z. Huang, *Talanta*, 2016, **148**, 279.
49. X. Zhang, X. Xie, H. Wang, J. Zhang, B. Pan and Y. Xie, *J. Am. Chem. Soc.*, 2013, **135**, 18.
50. X.-L. Zhang, C. Zheng, S.-S. Guo, J. Li, H.-H. Yang and G. Chen, *Anal. Chem.*, 2014, **86**, 3426.
51. Y. Li and S. Han, *Microchem. J.*, 2020, **154**, 104638.
52. X. Fan, Y. Feng, Y. Su, L. Zhang and Y. Lv, *RSC Adv.*, 2015, **5**, 55158.

53. H. Wang, G. Pu, S. Devaramani, Y. Wang, Z. Yang, L. Li, X. Ma and X. Lu, *Anal. Chem.*, 2018, **90**, 4871.
54. B. Wang, H. Wang, X. Zhong, Y. Chai, S. Chen and R. Yuan, *Chem. Commun.*, 2016, **52**, 5049.
55. J.-T. Cao, W.-S. Zhang, X.-L. Fu, H. Wang, S.-H. Ma and Y.-M. Liu, *Spectrochim. Acta, Part A*, 2020, **230**, 118040.
56. B. Chen, F. Wang, W. Yao, Z. Lin, X. Zhang, S. Luo, L. Zheng and X. Lin, *Anal. Methods*, 2018, **10**, 474.
57. X.-M. Chen, B.-Y. Su, X.-H. Song, Q.-A. Chen, X. Chen and X.-R. Wang, *TrAC, Trends Anal. Chem.*, 2011, **30**, 665.
58. H. Chen, L. Lin, H. Li, J. Li and J.-M. Lin, *ACS Nano*, 2015, **9**, 2173.
59. C. Wang, Y. Lan, F. Yuan, T. H. Fereja, B. Lou, S. Han, J. Li and G. Xu, *Microchim. Acta*, 2020, **187**, 50.
60. Z.-F. Zhang, H. Cui, C.-Z. Lai and L.-J. Liu, *Anal. Chem.*, 2005, **77**, 3324.
61. Y. Tang, Y. Su, N. Yang, L. Zhang and Y. Lv, *Anal. Chem.*, 2014, **86**, 4528.
62. H. Abdolmohammad-Zadeh and E. Rahimpour, *Sens. Actuators, B*, 2016, **225**, 258.
63. M. Xu, G. He, Z. Li, F. He, F. Gao, Y. Su, L. Zhang, Z. Yang and Y. Zhang, *Nanoscale*, 2014, **6**, 10307.
64. X. Fan, Y. Su, D. Deng and Y. Lv, *RSC Adv.*, 2016, **6**, 76890.
65. T. Hallaj, M. Amjadi, Z. Song and R. Bagheri, *Microchim. Acta*, 2018, **185**, 67.
66. Y. Tang, H. Song, Y. Su and Y. Lv, *Anal. Chem.*, 2013, **85**, 11876.
67. H. Yu, Y. He, W. Li and T. Duan, *Sens. Actuators, B*, 2015, **220**, 516.
68. K. L. Lin, T. Yang, H. Y. Zou, Y. F. Li and C. Z. Huang, *Talanta*, 2019, **192**, 400.
69. C. Chu, M. Li, S. Ge, L. Ge, J. Yu, M. Yan, X. Song, L. Li, B. Han and J. Li, *Biosens. Bioelectron.*, 2013, **47**, 68.
70. L. Hu and G. Xu, *Chem. Soc. Rev.*, 2010, **39**, 3275.
71. J. Li, S. Guo and E. Wang, *RSC Adv.*, 2012, **2**, 3579.
72. Y. Zhang, F. Lu, Z. Yan, D. Wu, H. Ma, B. Du and Q. Wei, *Microchim. Acta*, 2015, **182**, 1421.
73. B. Bansod, T. Kumar, R. Thakur, S. Rana and I. Singh, *Biosens. Bioelectron.*, 2017, **94**, 443.
74. P. Wu, T. Zhao, S. Wang and X. Hou, *Nanoscale*, 2014, **6**, 43.
75. X. Chen, J. Zhang, X. Fu, M. Antonietti and X. Wang, *J. Am. Chem. Soc.*, 2009, **131**, 11658.
76. N. Cheng, P. Jiang, Q. Liu, J. Tian, A. M. Asiri and X. Sun, *Analyst*, 2014, **139**, 5065.
77. C. Cheng, Y. Huang, X. Tian, B. Zheng, Y. Li, H. Yuan, D. Xiao, S. Xie and M. M. Choi, *Anal. Chem.*, 2012, **84**, 4754.
78. B. Xia, M. Chu, S. Wang, W. Wang, S. Yang, C. Liu and S. Luo, *Anal. Chim. Acta*, 2015, **891**, 113.
79. Z. Zhou, Q. Shang, Y. Shen, L. Zhang, Y. Zhang, Y. Lv, Y. Li, S. Liu and Y. Zhang, *Anal. Chem.*, 2016, **88**, 6004.
80. X. Zhu, F. Kou, H. Xu and G. Yang, *RSC Adv.*, 2016, **6**, 105331.

81. Y. Feng, L. Shi, H. Wu, L. Chen and Y. Chi, *Electrochim. Acta*, 2018, **261**, 29.
82. J. Jiang, D. Chen and X. Du, *Sens. Actuators, B*, 2017, **251**, 256.
83. Y. Fan, S. Chen, S. Wei, J. Guo and Y. Li, *Anal. Methods*, 2020, **12**, 8.
84. Q. Lu, J. Zhang, X. Liu, Y. Wu, R. Yuan and S. Chen, *Analyst*, 2014, **139**, 6556.
85. F. Zuo, L. Jin, X. Fu, H. Zhang, R. Yuan and S. Chen, *Sens. Actuators, B*, 2017, **244**, 282.
86. Y. Wang, W. Guo and N. Jia, *ChemElectroChem*, 2018, **5**, 3786.
87. Y. Sun, Y. Wang, Y. Yang and M. Yang, *Chem. Lett.*, 2019, **48**, 215.
88. C. Zhou, Y. Chen, P. Shang and Y. Chi, *Analyst*, 2016, **141**, 3379.
89. R. Zhu, Y. Zhang, J. Wang, C. Yue, W. Fang, J. Dang, H. Zhao and Z. Li, *Anal. Bioanal. Chem.*, 2019, **411**, 7137.
90. H. Wang, Q. Ma, Y. Wang, C. Wang, D. Qin, D. Shan, J. Chen and X. Lu, *Anal. Chim. Acta*, 2017, **973**, 34.
91. F. Mesgari, S. M. Beigi, F. Salehnia, M. Hosseini and M. R. Ganjali, *Inorg. Chem. Commun.*, 2019, **106**, 240.
92. H. Xu, X. Zhu, Y. Dong, H. Wu, Y. Chen and Y. Chi, *Sens. Actuators, B*, 2016, **236**, 8.
93. J. Xu, D. Jiang, Y. Qin, J. Xia, D. Jiang and H.-Y. Chen, *Anal. Chem.*, 2017, **89**, 2216.
94. H. Chen, X. Tan, J. Zhang, Q. Lu, X. Ou, Y. Ruo and S. Chen, *RSC Adv.*, 2014, **4**, 61759.
95. X. Du, D. Jiang, L. Dai, W. Zhu, X. Yang, N. Hao and K. Wang, *Anal. Chem.*, 2018, **90**, 3615.
96. C. Song, X. Li, L. Hu, T. Shi, D. Wu, H. Ma, Y. Zhang, D. Fan, Q. Wei and H. Ju, *ACS Appl. Mater. Interfaces*, 2020, **12**, 8006.
97. R. Zhu, Y. Zhang, X. Fang, X. Cui, J. Wang, C. Yue, W. Fang, H. Zhao and Z. Li, *J. Mater. Chem.*, 2019, **7**, 2320.
98. X.-L. Fu, F. Hou, F.-R. Liu, S.-W. Ren, J.-T. Cao and Y.-M. Liu, *Biosens. Bioelectron.*, 2019, **129**, 72.
99. S. Deng, P. Yuan, X. Ji, D. Shan and X. Zhang, *ACS Appl. Mater. Interfaces*, 2015, **7**, 543.
100. Y. Feng, Q. Wang, J. Lei and H. Ju, *Biosens. Bioelectron.*, 2015, **73**, 7.
101. Y. Wang, L. Zhang, L. Shen, S. Ge, J. Yu and M. Yan, *Microchim. Acta*, 2017, **184**, 2587.
102. J. Ji, J. Wen, Y. Shen, Y. Lv, Y. Chen, S. Liu, H. Ma and Y. Zhang, *J. Am. Chem. Soc.*, 2017, **139**, 11698.
103. Z. Liu, X. Zhang, X. Ge, L. Hu and Y. Hu, *Sens. Actuators, B*, 2019, **297**, 126790.
104. Q.-M. Feng, Y.-Z. Shen, M.-X. Li, Z.-L. Zhang, W. Zhao, J.-J. Xu and H.-Y. Chen, *Anal. Chem.*, 2016, **88**, 937.
105. L. Chen, X. Zeng, P. Si, Y. Chen, Y. Chi, D.-H. Kim and G. Chen, *Anal. Chem.*, 2014, **86**, 4188.
106. X. Li, Z. Guo, J. Li, Y. Zhang, H. Ma, X. Pang, B. Du and Q. Wei, *Anal. Chim. Acta*, 2015, **854**, 40.

107. Y. Jin, Q. Kang, X. Guo, B. Zhang, D. Shen and G. Zou, *Anal. Chem.*, 2018, **90**, 12930.
108. Z. Guo, L. Wu, Y. Hu, S. Wang and X. Li, *Biosens. Bioelectron.*, 2017, **95**, 27.
109. X. Li, X. Zhang, H. Ma, D. Wu, Y. Zhang, B. Du and Q. Wei, *Biosens. Bioelectron.*, 2014, **55**, 330.
110. L. Wu, Y. Sha, W. Li, S. Wang, Z. Guo, J. Zhou, X. Su and X. Jiang, *Sens. Actuators, B*, 2016, **226**, 62.
111. T. Han, X. Li, Y. Li, W. Cao, D. Wu, B. Du and Q. Wei, *Sens. Actuators, B*, 2014, **205**, 176.
112. L. Chen, X. Zeng, A. Dandapat, Y. Chi and D. Kim, *Anal. Chem.*, 2015, **87**, 8851.
113. C. Zhang, D. Liu, H. Zhang, X. Tan and S. Chen, *Microchim. Acta*, 2019, **186**, 771.
114. Y.-Z. Wang, W. Zhao, P.-P. Dai, H.-J. Lu, J.-J. Xu, J. Pan and H.-Y. Chen, *Biosens. Bioelectron.*, 2016, **86**, 683.
115. H. Ma, Y. Zhao, L. Li, H. Wang and Q. Wei, *Talanta*, 2018, **188**, 729.
116. B. Huang, X.-P. Liu, J.-S. Chen, C.-J. Mao, H.-L. Niu and B.-K. Jin, *Microchim. Acta*, 2020, **187**, 155.
117. X. Zheng, X. Hua, X. Qiao, F. Xia, D. Tian and C. Zhou, *RSC Adv.*, 2016, **6**, 21308.
118. L. Chen, X. Wang, Q. Zhang, Z. Li, Q. Kang and D. Shen, *Analyst*, 2020, **145**, 2389.
119. X. Ou, X. Tan, X. Liu, Q. Lu, S. Chen and S. Wei, *Biosens. Bioelectron.*, 2015, **70**, 89.
120. Y. Fan, X. Tan, X. Ou, Q. Lu, S. Chen and S. Wei, *Electrochim. Acta*, 2016, **202**, 90.
121. H. Sha, Y. Zhang, Y. Wang, H. Ke, X. Xiong and N. Jia, *Biosens. Bioelectron.*, 2019, **124**, 59.
122. H. Xu, S. Liang, X. Zhu, X. Wu, Y. Dong, H. Wu, W. Zhang and Y. Chi, *Biosens. Bioelectron.*, 2017, **92**, 695.
123. J. Gao, H. Xiong, W. Zhang, Y. Wang, H. Wang, W. Wen, X. Zhang and S. Wang, *Carbon*, 2018, **130**, 416.
124. Y. He, J. Li and Y. Liu, *Anal. Chem.*, 2015, **87**, 9777.
125. Y. Feng, F. Sun, L. Chen, J. Lei and H. Ju, *Electroanal. Chem.*, 2016, **781**, 48.
126. Y.-Z. Wang, N. Hao, Q.-M. Feng, H.-W. Shi, J.-J. Xu and H.-Y. Chen, *Biosens. Bioelectron.*, 2016, **77**, 76.
127. Y. Zhang, F. Wang, H. Zhang, H. Wang and Y. Liu, *Anal. Chem.*, 2019, **91**, 12100.
128. Q. Liu, Y. J. Peng, J. C. Xu, C. Ma, L. Li, C. J. Mao and J. J. Zhu, *ChemElectroChem*, 2017, **4**, 1768.
129. S. Xie, F. Wang, Z. Wu, L. Joshi and Y. Liu, *RSC Adv.*, 2016, **6**, 32804.
130. Q.-X. Luo, Y. Li, R.-P. Liang, S.-P. Cao, H.-J. Jin and J.-D. Qiu, *J. Electroanal. Chem.*, 2020, **856**, 113706.

131. L. Jiang, G. Mo, C. Yu, D. Ya, X. He, W. Mo and B. Deng, *Colloids Surf., B*, 2019, **173**, 378.
132. L. Hu, J. Zheng, K. Zhao, A. Deng and J. Li, *Biosens. Bioelectron.*, 2018, **101**, 260.
133. S. Zhu, P. Ran, J. Wu, M. Chen and Y. Fu, *Electroanal*, 2020, **32**, 185.
134. B. Xia, Q. Yuan, M. Chu, S. Wang, R. Gao, S. Yang, C. Liu and S. Luo, *Sens. Actuators, B*, 2016, **228**, 565.
135. C. Cheng, Y. Huang, J. Wang, B. Zheng, H. Yuan and D. Xiao, *Anal. Chem.*, 2013, **85**, 2601.
136. Z. Liu, H. Wu, X. Ge, H. Zhan and L. Hu, *J. Electroanal. Chem.*, 2020, **860**, 113910.
137. L. Chen, X. Zeng, A. R. Ferhan, Y. Chi, D.-H. Kim and G. Chen, *Chem. Commun.*, 2015, **51**, 1035.
138. C. Zhang, F. Hu, H. Zhang, S. Chen and R. Yuan, *Anal. Bioanal. Chem.*, 2019, **411**, 6049.
139. Y. Lv, S. Chen, Y. Shen, J. Ji, Q. Zhou, S. Liu and Y. Zhang, *J. Am. Chem. Soc.*, 2018, **140**, 2801.

CHAPTER 3

Template-based Fabrication of Porous Carbon Nitride Nanostructures for Electrochemical Energy Conversion

QINGQING LU*[a,b], WENPENG LI[a,b], LIGANG GAI*[a] AND KAMEL EID*[c]

[a]Engineering & Technology Center of Electrochemistry, School of Chemistry and Chemical Engineering, Qilu University of Technology (Shandong Academy of Sciences), Jinan 250353, China; [b]Shandong Key Laboratory of Biochemical Analysis, College of Chemistry and Molecular Engineering, Qingdao University of Science and Technology, Qingdao 266042, China; [c]Gas Processing Center, College of Engineering, Qatar University, Doha 2713, Qatar
*E-mail: qqlu@qlu.edu.cn, liganggai@qlu.edu.cn, kamel.eid@qu.edu.qa

3.1 Introduction

In the past few decades, the ever-increasing demand for energy and the need to address serious environmental pollution have greatly motivated the development of sustainable energy storage, energy production, renewable fuels, and conversion systems.[1–12] As a non-metallic polymer semiconductor,

Nanoscience & Nanotechnology Series No. 51
Carbon Nitride Nanostructures for Sustainable Energy Production and Environmental Remediation
Edited by Kamel Abdelmoniem Mohamed Eid and Aboubakr M. Abdullah

Published by the Royal Society of Chemistry, www.rsc.org

graphitic carbon nitride (gCN), due to the intriguing structural and chemical properties such as good thermal and chemical stability, adjustable porous surface as well as low cost, has shown huge potential as an electrode material for various applications.[13–22] In addition, two-dimensional gCN can be considered as a nitrogen heteroatom-substituted graphite framework formed through sp^2 hybridization of carbon and nitrogen atoms. Depending on the nitrogen-containing precursor and synthesis condition, various gCN materials have been developed up to now, including C_3N_3, C_3N_4, C_6N_7, $C_6N_9H_3$, *etc.*[23] Among them, g-C_3N_4 is the most stable allotrope of gCN and has received intense research interest in recent years.[13,24] It is speculated that there are two types of building blocks for gCN. One is *s*-triazine units (C_3N_3; Figure 3.1A) with a periodic array of single carbon vacancies; the other is tri-*s*-triazine units (C_6N_7; Figure 3.1B) cross-linked by trigonal N atoms.[25] By contrast, the latter is more energetically favored and confirmed to be the most stable local connection pattern.[26] Although gCN materials possess unique physicochemical properties, the low surface area and non-porous nature greatly limit their wide application. In particular, an electrochemical reaction is closely related to the surface structure of used materials. In this regard, fine control over the pore structure of gCN materials is expected to expose more surface areas and facilitate the adsorption/transfer of reaction species, thereby improving the electrochemical performance.[27]

Generally, there are two types of synthesis methods for porous gCNs: bottom–up strategies, including template-directed synthesis and supramolecular assembly, and top-down methods like chemical delamination and thermal oxidation. Among them, template-based methods were confirmed to be the most reliable way to control the pore size, structure, and morphology of porous gCNs.[27] There are a few reviews in the literature regarding synthesis of gCN nanostructures for various catalytic and photocatalytic applicants, but not enough underlining the electrochemical energy conversion technologies.[27]

To this end, this chapter highlights the recent progress in the controlled template-based synthesis of gCN nanostructures and their characterizations. This is alongside the electrochemical energy conversion technologies of

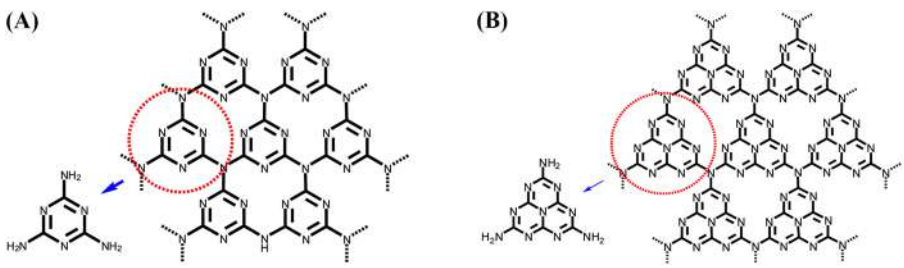

Figure 3.1 (A) *s*-Triazine and (B) tri-*s*-triazine as tectons of gCNs. Reproduced from ref. 25 with permission from American Chemical Society, Copyright 2012.

gCNs that comprises fuel cell reactions (*i.e.*, oxygen reduction, alcohol oxidation, and water splitting) and energy production/storage (*i.e.*, supercapacitor and Li-ion batteries).

3.2 Template-based Synthesis of Porous gCNs

Templating strategy usually involves the following three main steps: (1) selecting or synthesizing suitable templates with the desired pore structure, (2) filling the channel of ordered matrices with a target precursor and then converting them into a solid phase through appropriate methods, (3) removing the template if necessary and obtaining the porous structure. Two key points should be taken into account when choosing the original template. One is that the template structure must be well maintained and not cause any side reaction during the conversion process. The other is that the template should be removed easily and not bring in any residue. According to the nature of the template, they can be categorized into hard templates such as silica, metal oxides, as well as soft templates such as surfactant micelles.

3.2.1 Hard Template Method

To date, various natural and artificial materials have been reported to be hard templates for synthesizing porous gCNs.[28,29] Among them, silica materials are commercially available and easy to synthesize, which hold great advantages over other templates. Porous gCNs with different structures have been fabricated using diverse silica templates such as SBA-15, SBA-16, FDU-12, and KIT-6.[30] For example, Vinu *et al.* synthesized highly ordered one-dimensional mesoporous gCNs *via* polymerization between ethylenediamine (EDA) and carbon tetrachloride (CTC) using two-dimensional (2D) SBA-15 as a template.[31] The pore diameter, textural parameter, and nitrogen content can be adjusted by changing the pore size of SBA-15 and the weight ratio of EDA/CTC.[32] To increase the surface area and pore volume, cage-type SBA-16, and FDU-12 were chosen as templates to obtain highly ordered three-dimensional (3D) mesoporous gCNs, respectively.[33,34] Nevertheless, the product still possesses a low C/N ratio of 3.3–4.5 in the above synthesis. As is well-known, the high nitrogen content of gCNs can enhance the conductivity, mechanical strength, and energy-storage capacity. The same group found that the nitrogen content could increase two-fold when replaced with a mesoporous ultra-small silica template. It is due to the fact that the nanostructures contribute greatly to keep high nitrogen content in the carbon framework at high temperature.[35] Apart from the aforementioned template, spherical mesoporous cellular silica foams (MCFs) were developed to fabricate hierarchical mesoporous gCN spheres.[36] Generally speaking, the higher carbonization temperature could prevent mesoporous CNs' formation with a C/N ratio of 3/4. Goettmann *et al.* proposed a successful synthesis strategy of mesoporous g-C_3N_4 based on the self-condensation of cyanamide (CY) precursor using colloidal silica spheres as a hard template.[37,38] Similarly, 2D hexagonal and 3D cubic mesoporous g-C_3N_4 were fabricated by

choosing SBA-15 and KIT-6 as a template, respectively.[39–41] In this way, chiral mesoporous silica (CMS) was developed to be the template of helical rod-like g-C_3N_4 (HR-CN).[42] As displayed in Figure 3.2A, CMS is pre-acidified to facilitate the infiltration of CY precursor into the channels of the CMS template. After the thermal polymerization under N_2 atmosphere and the etching treatment with NH_4HF_2, the rod-like morphologies of CMS are faithfully replicated in HR-CN. Furthermore, employing mesoporous core–shell SiO_2 as a template, precursor CY could fill the voids of the mesoporous SiO_2 shell and in the meantime avoid the loss of active constituents in the calcination process, and thus 3D ordered macroporous g-C_3N_4 were constructed.[43] Zhang and his colleagues fabricated nanospherical g-C_3N_4 composed of nanosheets using KCC-1 silica spheres as templates.[44] The combined structures of hollow nanospheres and nanosheets are advantageous for mass transfer and charge transfer. Featured with the hierarchical porous skeleton, the diatom frustule has been widely applied as the sacrificial template for biomimetic synthesis.[45] A typical example is that Liu *et al.* constructed a CN nanorod array by replicating the regular nanochannel of diatom frustules.[46] Considering the toxicity and cost of CY, the oxygen-containing precursor urea was first developed to prepare porous gCNs by a thermal polymerization process using silica spheres as a template.[47,48] The specific surface area, pore diameter, and morphology can be varied by the initial mass ratio of urea and silica. In addition, another aminoguanidine hydrochloride precursor with a high nitrogen content was proposed by Vinu's group, and the resultant gCNs possessed a significantly higher N/C ratio than theoretically predicted C_3N_4 using SBA-15 as a template.[49] The employment of hexamethylenetetramine as precursor in the synthesis of porous gCNs has also been reported *via* a nano-casting approach.[50,51] Another successful finding is that the polymerization of aromatic 3-amino-1,2,4-triazine into the porous channels of a KIT-6 template could lead to a high N content of porous gCNs, and its surface area is much higher than that reported elsewhere.[52] It is well-known that melamine can polymerize into bulk g-C_3N_4. In virtue of the sublimation

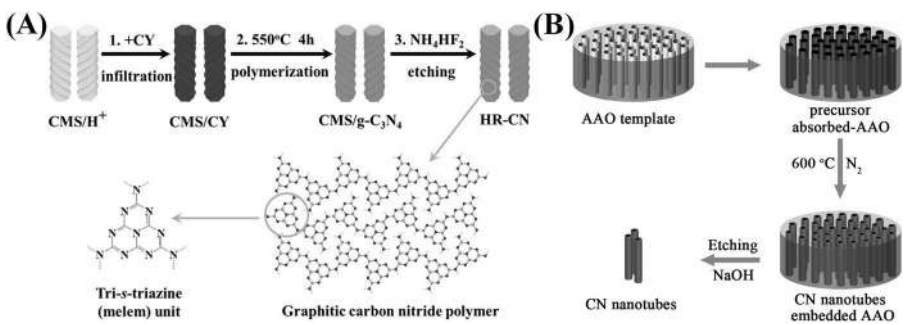

Figure 3.2 (A) The synthetic process for helical rod-like g-C_3N_4 (HR-CN). Reproduced from ref. 42 with permission from John Wiley & Sons, Copyright 2014 WILEY-VCH Verlag GmbH & Co. KGaA, Weinheim. (B) The synthetic process for carbon nitride nanotubes. Adapted from ref. 55 with permission from American Chemical Society, Copyright 2009.

feature of melamine, porous g-C_3N_4 with various morphologies could be expected by selecting different templates.[53,54]

Except for silica, another common metal oxide template is porous anodic alumina oxide (AAO). Porous AAO membranes possess a well-defined close-packed array of columnar hexagonal cells. The resultant product size can be regulated by changing the pore diameter and thickness of the AAO templates. Figure 3.2B shows the detailed synthesis procedure of CN nanotubes by Song's group.[55] First, the commercial AAO membranes were immersed into the precursor solution to fill the AAO pores. After the polymerization and carbonization at high temperature, CN nanotubes were obtained by etching AAO membranes with NaOH solution. The outer diameter of the nanotubes replicates the size of the pores of the AAO template. Furthermore, it was discovered that the thermal polymerization of CY inside the nanochannel of the AAO template benefits the formation of rod-like g-C_3N_4.[56] The confinement effect can direct the growth direction and crystallinity degree of g-C_3N_4, and thus a more ideal stoichiometric ratio for C/N.

In addition, by the melamine-involved vapor deposition on the natural kaolin clay and the followed etching treatment, the obtained g-C_3N_4 could replicate the 2D structure of natural kaolin; meanwhile, interconnected nanopores could be clearly observed (Figure 3.3A).[57] Recently, it has been

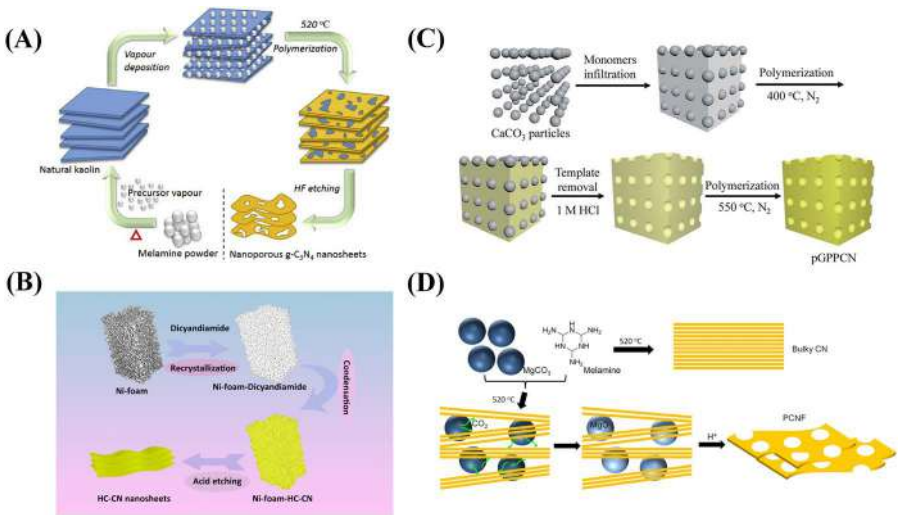

Figure 3.3 The preparation procedure of (A) nanoporous g-C_3N_4 nanosheets, (B) high-crystallinity g-C_3N_4 nanosheets, (C) porous gCNs, and (D) PCNF. (A) Reproduced from ref. 57 with permission from Elsevier, Copyright 2018. (B) Reproduced from ref. 58 with permission from American Chemical Society, Copyright 2018. (C) Reproduced from ref. 60 with permission from the Royal Society of Chemistry. (D) Reproduced from ref. 61 with permission from Elsevier, Copyright 2017.

demonstrated that Ni-foam can not only be used for depositing 2D g-C_3N_4 nanosheets, but also catalyze the polymerization and crystallization of g-C_3N_4.[58] As a result, the high-crystalline g-C_3N_4 nanosheets with fewer structural defects were constructed after acid etching of Ni-foam (Figure 3.3B).[58]

Being more environmentally-friendly and economical, commercial calcium carbonate ($CaCO_3$) particles show great promise for preparing porous gCNs. For example, Chen *et al.* demonstrated a facile thermal polycondensation strategy for mesoporous g-C_3N_4 by using dicyandiamide (DCDA) as the precursor and $CaCO_3$ as the template.[59] They found that the simple condensation of DCDA on $CaCO_3$ could bring in some undesirable side reactions, accompanied by a certain amount of carbon dopants. Figure 3.3C [60] shows the slightly modified synthesis strategy for porous gCNs.[60] Briefly, the homogeneous mixture of DCDA and $CaCO_3$ was first heated at 400 °C to establish the basic framework. Then, the obtained solid powder was dissolved in diluted hydrochloric acid solution to remove the $CaCO_3$ template. Finally, porous gCNs were formed by calcining at 500 °C for 2 h. Similarly, porous g-C_3N_4 flakes (PCNFs) were obtained by thermal polycondensation of melamine in the presence of the $MgCO_3$ template (Figure 3.3D).[61] Additionally, metal salts such as $ZnCl_2$ can act as a pore-directing template for porous g-C_3N_4.[62] It turned out that the addition of $ZnCl_2$ helps to increase the specific surface areas; meanwhile, the pore distribution depends on the concentration of acidic etching solution. More importantly, these $ZnCl_2$ templates can be recycled after leaching.

Considering that the template removal is usually tedious and complicated, a self-sacrificial template is highly desirable to obtain porous gCN. Melamine sponge (MS) and polyurethane (PU) shrink and decompose completely into gasses under heating conditions, which can be regarded as ideal templates for synthesizing porous gCNs.[63] For example, Liang *et al.* successfully fabricated a macroscopic 3D porous gCN monolith (PCNM) *via* one-step thermal condensation of urea inside the skeleton of the MS.[63] The resultant PCNM consists of 2D porous gCN nanosheets. In a typical synthesis (Figure 3.4A),[63] the commercial MS was first soaked in a saturated urea solution. After freeze-drying, the obtained sample was heated at 550 °C for 4 h under flowing N_2 to obtain 3D PCNM. Note that both urea and melamine act as precursors during the synthesis process. In another work, porous g-C_3N_4 foam with interconnected micron-pores and nano-pores was reported by sintering the mixture of PU and DCDA (Figure 3.4B).[64] Nowadays, metal–organic frameworks (MOFs) have been widely applied in gas separation, catalysis, and drug delivery owing to their tunable pore diameters and high adsorption capacities.[65] Recently, various efforts have been concentrated on porous gCNs utilizing MOF as templates.[66] For instance, porous amorphous CNs were derived from zeolitic imidazolate frameworks 8 (ZIF-8) by a facile pyrolysis process, and its nitrogen content was found to be as high as 20.4%.[67]

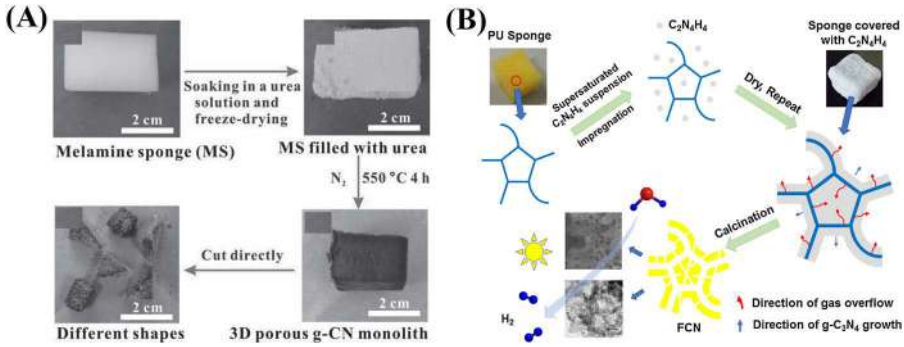

Figure 3.4 The synthetic process of (A) macroscopic 3D PCNM and (B) porous g-C_3N_4 foam. (A) Reproduced from ref. 63 with permission from John Wiley & Sons, Copyright 2015 WILEY-VCH Verla GmbH & Co. KGaA, Weinheim. (B) Reproduced from ref. 64 with permission from Elsevier, Copyright 2018.

3.2.2 Soft Template Method

Compared with the hard-template method, soft-templating synthesis can simplify the synthesis procedure and avoid the usage of hazardous etching reagents, thereby attracting much research interest over the past few years. However, traditional approaches to obtaining bulk CNs were not suitable for porous g-CNs by soft templates. This is because the condensation temperature exceeds the decomposition temperature of the soft template. The commonly used soft templates contain various ionic liquids, surfactants, and block copolymers as well as gas bubbles.[68]

Wang *et al.* confirmed that a variety of nonionic surfactants could be combined with the precursor DCDA to obtain high yields of g-CNs with accessible pores, including Triton X-100, P123, and F127.[69] The side reaction between surfactant fragments and CNs intermediate was suppressed by the fine control of holding sequences near template decomposition temperature, followed by final high-temperature condensation. But the strong hydrogen bonds between DCDA and PEO blocks might result in high carbon content, which is not beneficial for their potential application. In this regard, Yan *et al.* replaced DCDA with the low activity of melamine and adopted P123 as a soft template to prepare porous g-C_3N_4.[70] The carbon-doping amount was greatly reduced due to the absence of a direct chemical reaction between precursor and surfactant during thermal treatment. Fan *et al.* proposed the fabrication of porous g-CNs by heating a Triton X-100-modified-melamine sulfate mixture, and the effect of the added amount of Triton X-100 and heating temperature on g-CNs was discussed in detail.[71] In this case, melamine sulfate can suppress the sublimation of melamine and separate easily from the surfactant. Subsequently, bimodal mesoporous CN was synthesized by using melamine and glutaraldehyde as precursors, and the mesopore sizes concentrate on 3.8 nm and 10–40 nm.[72] As shown

in Figure 3.5A,[73] Wang's group synthesized porous g-C_3N_4 nanosheets using urea and sodium oleate as precursor and surfactant, which achieved the simultaneous oxygen-doping and morphology modification.[73] Recently, 3D assembled carbon nitride sheets were obtained by using various nonionic surfactants (*e.g.*, F127, P123, and Triton X-100) as templates and melamine cyanurate hydrogen-bonded complex as precursor.[74] The resultant morphologies (*e.g.*, sheet, hollow spheres, tubes, or highly porous networks) highly depend on the synthesis approach and the surfactant/precursor ratio. With an increased amount of surfactant, both the carbon residue and surface areas increase accordingly. Besides, Devaraj's group confirmed that the interactions between surfactants and precursors could affect the polycondensation degree of the precursors, and thus the textural properties of mesoporous gCN.[75] The C/N ratio and surface functionalities for the resultant samples were apparently distinct from each other by examining various surfactants such as Triton X-100, CTAB, and SDS.

Featured with a lower melting point, non-volatility, trivial vapor pressure, and high-temperature stability, ionic liquids (ILs) have been widely applied in multiple fields such as solvents, electrolytes, and catalysts.[76] In recent

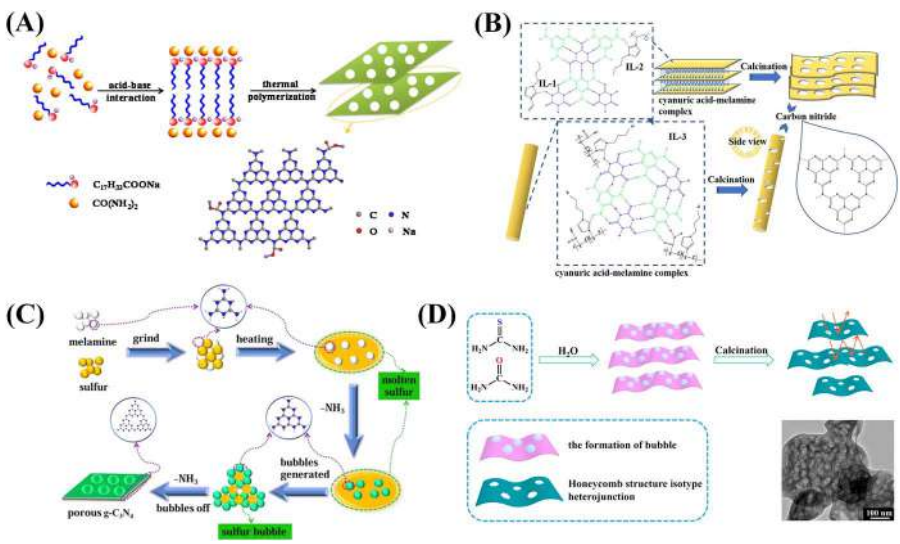

Figure 3.5 A schematic illustration for preparing (A) porous g-C_3N_4 nanosheets using urea as the precursor and sodium oleate as the surfactant. (B) Carbon nitride using cyanuric acid–melamine complex as the precursor and ionic liquid as the surfactant. (C) Porous g-C_3N_4 using the sulfur-bubble template. (D) Honeycomb-like carbon nitride isotype heterojunction. (A) Reproduced from ref. 73 with permission from Elsevier, Copyright 2017. (B) Reproduced from ref. 81 with permission from American Chemical Society, Copyright 2018. (C) Reproduced from ref. 86 with permission from the Royal Society of Chemistry. (D) Reproduced from ref. 87 with permission from American Chemical Society, Copyright 2018.

years, they have turned out to be attractive soft templates for fabricating porous materials.[77] Wang *et al.* first explored a series of imidazolium- and pyridine-based ILs in the synthesis of mesoporous gCNs.[69] It was found that both ionic liquids containing hexafluorophosphate and dicyanamide counterion (*e.g.*, $BmimPF_6$, BmimDCN) gave perfect graphitic structure with accessible porosity. In addition, 1-butyl-3-methylimidazolium tetrafluoroborate ($BmimBF_4$) was adopted as a soft template to synthesize boron- and fluorine-containing mesoporous CNs, and the surface areas were highly dependent on the ratio of $BmimBF_4$ to DCDA.[78] Surprisingly, the resulting materials show a high content of nitrogen, boron, and fluorine, as well as a high surface area along with local graphitic order. Similarly, inexpensive precursor urea was polymerized with $BmimBF_4$ to achieve the simultaneous textural engineering and doping of porous gCN nanosheets, in which urea creates a delamination effect and ionic liquid acts as a texture modifier as well as B/F dopant source.[79] Zhao and co-workers used 1-butyl-3-vinyl imidazolium bromide and cyanuric acid–melamine complex to obtain hollow mesoporous g-C_3N_4 spheres with ultra-thin nanosheets in DMSO.[80] To further discuss the effect of solvent and ionic liquid on the assembly behavior, the same group extended the application of cyanuric acid–melamine complex and ionic liquid in water.[81] The texture and morphology were adjusted by the concentration and type of ionic liquid. As shown in Figure 3.5B,[81] a disordered hollow carbon nitride box with pores distributed around the wall could be obtained under lower IL1 concentration. With the increased ionic liquid content, the layered structure appeared. The disordered nanosheets and hollow tubes with large pores in the shell could be observed by using IL-2 and IL-3 as templates, respectively.[81] The results demonstrated that the final structure of CNs highly depends on the supramolecular assembly of cyanuric acid and melamine, the template effect as well as the interaction between precursor and template. To study the effect of ionic liquid on the morphology and structure of CNs, they further fabricated 3D porous CNs by the thermal condensation of freeze-dried cyanuric acid–melamine supramolecular aggregates modified by ionic liquid.[82] The high-temperature decomposition of ionic liquid and precursor could generate a 3D interconnected framework structure, which is beneficial for the direct contact of reactants with active sites and meanwhile improve the charge transfer rate.

In comparison with other soft-template syntheses, the gas bubbles generated during the formation process of carbon nitride can not only avoid the introduction of any impurities but also help the carbon nitride condensation, which is the perfect template for the synthesis of porous materials.[83] Zhang *et al.* examined the contribution of different single precursors (DCDA, thiourea, and urea) on the resulting structure of g-C_3N_4.[84] Although all of g-C_3N_4 showed a characteristic graphitic-like layer structure and repeating units, the use of urea is more advantageous for increased surface areas, narrow pore size distribution, and enlarged pore volume. It is likely that DCDA passes through a more direct polyaddition path to form melamine, and little NH_3 causes the formation of a well-structured polymer. Taking the chemical structure of thiourea and urea into consideration, the urea pyrolysis prefers a less condensed and more porous product due to the much stronger

electronegativity of O atom and C–O bond energy in the urea molecule. Moreover, porous g-C_3N_4 was synthesized by the *in situ* pyrolysis of a mixture of $(NH_4)_2S_2O_8$ and melamine in air.[85] During the polymerization process of melamine, the decomposition product of $(NH_4)_2S_2O_8$ (*e.g.*, NH_3, SO_2, and O_2) would act as bubble templates for the porous structure. The surface area of the resultant porous g-C_3N_4 was regulated by the mass ratio of $(NH_4)_2S_2O_8$/melamine. He *et al.* proposed a sulfur-bubble directed strategy for porous g-C_3N_4 by thermal polymerization of sublimed sulfur and melamine.[86] As shown in Figure 3.5C,[86] a certain mass of sublimed sulfur was first mixed with melamine homogenously. Upon heating at a higher temperature, the molten flux of sublimed sulfur could accelerate reactive species diffusion. Meanwhile, melamine would condense and rearrange to form tris-*s*-triazine. Along with the rise of temperature, sublimed sulfur would volatilize into bubbles.[87] Porous g-C_3N_4 sheets are finally obtained by condensing the tris-*s*-triazine unit around the bubble template, and the sulfur species were removed simultaneously. Lu's group synthesized a honeycomb-like CN isotype heterojunction by thermal treatment of thiourea and urea mixing with ultra-pure water.[87] The addition of water is crucial to the unique structure (Figure 3.5D).[87] First, water can induce a low degree of polymerization. Second, the generated NH_3 and CO_2 gasses burst in the water, thus generating a large number of pores. Liu and co-workers used melamine and NH_4HCO_3 as precursors to synthesize porous g-C_3N_4.[88] Once the mixed precursors were calcined at a higher temperature, NH_4HCO_3 would decompose into CO_2, NH_3 and H_2O, creating lots of holes on the g-C_3N_4 sheet. Likewise, Fei *et al.* used NH_4Cl as a bubble-generated porogen for the fabrication of porous g-C_3N_4 due to the fact that NH_4Cl can decompose into NH_3 and HCl during the condensation of melamine.[89] Interestingly, the resultant g-C_3N_4 seemed like a yolk–shell cake, in which the shell region contains numerous thin sheets with a rich porous structure, while the yolk region contains lots of cross-linked large hollow particles. Recently, Mao's group employed ammonium lauryl sulfate as a gaseous bubbles templating agent to synthesize spherical worm-like g-C_3N_4, and the decomposition (NH_3, CO_2, SO_2) of ammonium lauryl sulfate is near to the thermal polymerization temperature of g-C_3N_4 precursor.[90] Wu *et al.* reported the preparation of g-C_3N_4 with nitrogen vacancies by a $N_2H_4{\cdot}H_2O$-assisted thermal polymerization method.[91] $N_2H_4{\cdot}H_2O$ would decompose into reductive species *i.e.*, H_2 and NH_3 in the calcining process, facilitating the introduction of nitrogen vacancies. As a kind of renewable feedstock, biopolymer is promising for synthesizing porous g-C_3N_4. A typical example is the synthesis of porous g-C_3N_4 by using starch as a dynamic gas template to release the carbonaceous gasses and ammonia.[92]

3.3 Characterization of Porous gCNs

The characterization for porous gCNs is indispensable to evaluate its synthesis quality. Generally, they can be assessed in four aspects, including morphology and size characterization, element or composition analysis, crystal structure characterization, and optical measurement.

3.3.1 Morphology and Size Characterization

The morphology and size of gCNs are usually evaluated by scanning electron microscopy (SEM) and transmission electron microscopy (TEM). SEM works by scanning a focused beam of electrons across an object, and the secondary electrons or elastic scattering electrons are detected as image signals according to electronic intensity. The signal strength greatly depends on specimen topography, and the resolution can reach up to 1 nm. Different from SEM, the electron beam of TEM can penetrate into the sample, and the resultant transmission signals construct different TEM images. Owing to the smaller de Broglie wavelength of electrons, TEM gives images with ultra-high resolution, which can even reach the atomic size. Normally, the successful preparation of a porous structure is first checked by SEM and TEM images. For example, we can clearly observe the 3D interconnected network structure of PCNM, and the diameter of the hierarchical pores is between 200 and 400 nm (Figure 3.6A).[63] The magnified SEM image in Figure 3.6B displays the irregular 2D porous nanosheets with a thickness of 30 nm. The TEM images in Figure 3.6C and D [63] verified that g-CN nanosheets could join together to constitute the interconnected structure and the abundant pores range from

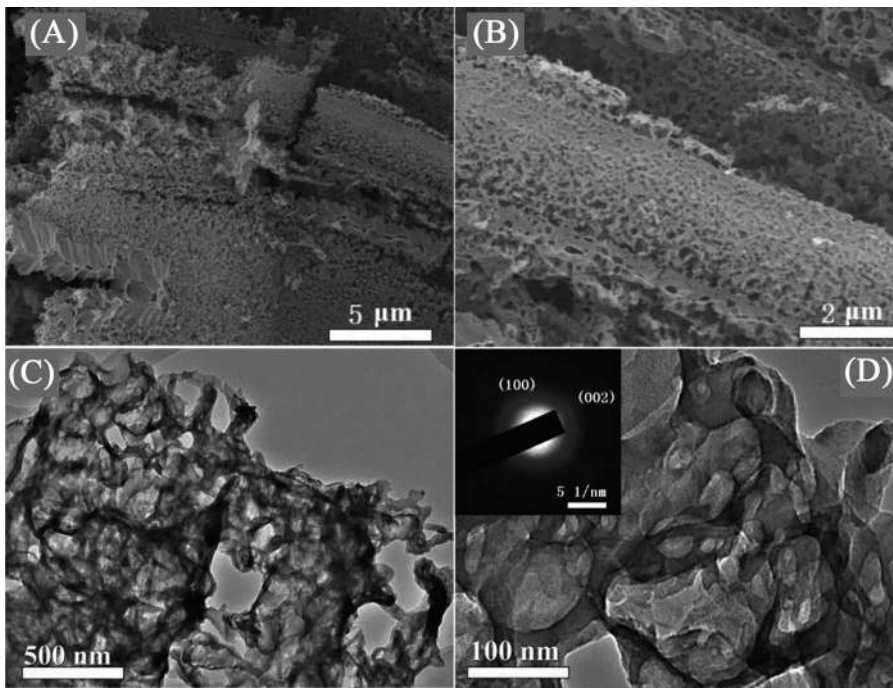

Figure 3.6 (A, B) SEM and (C, D) TEM images of macroscopic 3D PCNM. The inset in (D) is its corresponding SAED pattern. Reproduced with the permission of ref. 63 with permission from John Wiley & Sons, Copyright 2015 WILEY-VCH Verlag GmbH & Co. KGaA, Weinheim.

30 to 150 nm. Moreover, the two diffuse diffraction rings for the selected area electron diffraction (SAED) pattern reveal the disordered structure for the resultant PCNM (inset of Figure 3.6D).[63]

Notably, the major advantage of porous gCNs over their bulk counterparts lies in their high specific surface areas. In this aspect, the Brunauer–Emmett–Teller (BET) method is usually selected to determine the specific surface areas from the nitrogen adsorption/desorption isotherm, and the pore size distribution is analyzed by the Barrett–Joyner–Halenda (BJH) theory. As seen from Figure 3.7A,[59] all samples possess type IV isotherms with a clean hysteresis loop located at P/P_0 between 0.6 and 1.0, suggesting the existence of rich mesopores. Moreover, the mpg-CN exhibits a larger BET surface area than g-C_3N_4 owing to its porous structure and smaller particle size. The determined average pore diameter for mpg-CN locates between 22 and 26 nm, as shown in Figure 3.7B.[59]

3.3.2 Element and Composition Analysis

X-ray photoelectron spectroscopy (XPS) and energy dispersive spectroscopy (EDS) are effective tools for determining elemental composition. The XPS technique mainly relies on the unique spectroscopy of each atom, and thus XPS is called electron spectroscopy for chemical analysis. When the single atom is irradiated by X-ray with a specific wavelength, the atom's electrons can absorb the energy of X-ray photons and escape from the atom to form photoelectrons. The kinetic energies of the photoelectrons are measured, and thus the electron binding energies of the photoelectrons can be calculated.[59] Therefore, the electron binding energy can be obtained by measuring the photoelectron's kinetic energy. The plotted electron counts *versus* binding energy are called the X-ray photoelectron spectra, which could be employed to analyze elements quantitatively and qualitatively. In virtue of the electron binding energies, the element can be identified qualitatively. In virtue of the number of photoelectrons, the amount of elements can be determined quantitatively. Limited by the penetration ability of X-ray photons and photoelectrons, the XPS technique can only provide element information in depth within 5 nm on the surface. Furthermore, the XPS technique also enables the analysis of chemical bonds in the materials, as the chemical bond can affect the binding energy of electrons. For example, the XPS spectra of bulk g-C_3N_4 and mpg-CN-1.0 are shown in Figure 3.7C–E.[59] The survey spectra display binding energies assigned to C1s, N1s, and O2s, confirming the presence of three elements (C, N, O) for both bulk g-C_3N_4 and mpg-CN-1.0 (Figure 3.7C).[59] The C1s peak can be fitted into three kinds of carbon atoms with a binding energy of 284.7, 288.2, and 293.7 eV (Figure 3.7D).[59] The higher peak intensity at 284.7 eV observed for mpg-CN-1.0 than for g-C_3N_4, demonstrated that extra carbon species were formed in mpg-CN-1.0. The main peak at 288.2 eV belongs to sp^2 carbon bound to three adjacent nitrogen atoms. In comparison, the peak at 293.7 eV is related to sp^2-hybridized C atoms in the aromatic ring connected to terminal uncondensed amino groups. Similarly,

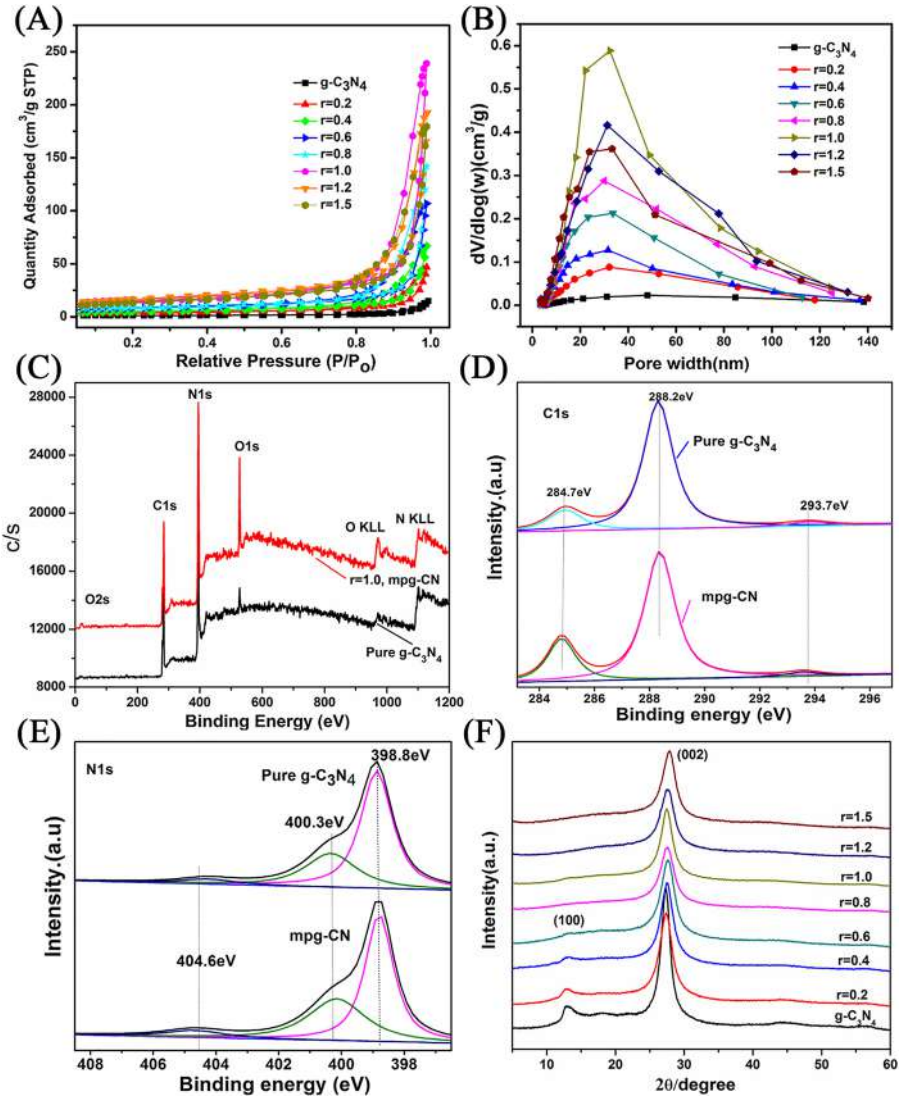

Figure 3.7 (A) Nitrogen adsorption–desorption isotherms and (B) pore size distribution of bulk g-C_3N_4 and mpg-CN-*r* (*r* = 0.2, 0.4, 0.6, 0.8, 1.0, 1.2, and 1.5). (C) XPS survey spectra, (D) C1s, and (E) N1s spectra of bulk g-C_3N_4 and mpg-CN-1.0. (F) XRD patterns of bulk g-C_3N_4 and mpg-CN-*r* (*r* = 0.2, 0.4, 0.6, 0.8, 1.0, 1.2, and 1.5). Reproduced from ref. 59 with permission from Elsevier, Copyright 2017.

the high-resolution N1s spectrum can be fitted into three kinds of nitrogen atoms with a binding energy of 398.8, 400.3, and 404.6 eV (Figure 3.7E).[59] Among them all, the main peak at 398.8 eV belongs to sp^2-hybridized aromatic nitrogen bound to carbon atoms, while the peak at 400.3 eV can be attributed to bridging nitrogen atoms. Likewise, the peak at 404.6 eV is

assigned to the charging effect or positive localization in heterocycles. Furthermore, EDS analysis can couple with the SEM or TEM techniques to map the *in situ* elements' distribution.[59]

3.3.3 Crystal Structure Characterization

Powder XRD measurements can reflect the crystal structure information of gCN materials. Once a monochromatic beam of X-ray irradiates the powder, the scattered X-ray light is detected as output signals. The XRD pattern is plotted by the scattered X-ray intensity *versus* incident angle, and the peak position is characterized by the phase composition. Moreover, the crystalline grain size is able to be estimated utilizing the Scherrer equation, in light of the internal relationship between the peak broadening and the grain size. Figure 3.7F[59] shows the XRD patterns of the bulk g-C_3N_4 and mpg-CN-*r* (*r* = 0.2, 0.4, 0.6, 0.8, 1.0, 1.2, and 1.5, respectively), and *r* represents the mass ratio of calcium carbonate template to dicyandiamide precursor.[59] It is apparent that all samples exhibit similar diffraction patterns to the graphite-like g-C_3N_4 phase, and no other phase is formed. The peak at 27.5° can be assigned to the interlayer-stacking (002) plane, while the peak at 13° corresponds to an in-plane stacking. The gradually decreased peak intensity of mpg-CN with the increased value implies an incomplete condensed skeleton and smaller particle size.

3.3.4 Optical Properties

The optical measurements, including Fourier transform infrared (FTIR) spectroscopy, Raman spectroscopy, ultraviolet-visible (UV-vis) absorption spectroscopy, and photoluminescence (PL) spectroscopy, are commonly used for characterizing gCN materials. The FTIR spectroscopy applies the Fourier transform to convert the raw data to a spectrum, which enables the measurement of light absorption in the wavelength range of 10 000–400 cm^{-1}. The FTIR technique primarily provides the information of functional groups in the materials, which could be used to characterize the residue groups, adsorption species, and the chemical impurities of the as-synthesized gCNs. The FI-IR spectra of MCN-6 obtained by using KIT-6 with various pore diameters are displayed in Figure 3.8A.[93] The bands located at 1257 cm^{-1} are relevant to the stretching modes of aromatic C–N heterocycles in g-C_3N_4, whereas the peak at 1570 cm^{-1} corresponds to the aromatic ring. The peak at 3412 cm^{-1} in MCN-6 derives from the stretching mode of N–H groups bound to the aromatic ring. The UV-vis absorption spectroscopy can collect the absorption information of gCN in the wavelength ranging from 200 to 800 nm, in which the wavelength in 200–400 and 400–800 nm belongs to the ultraviolet region and visible light, respectively.[93] The UV-vis spectra can be obtained by measuring the particle dispersing agent under the UV-vis absorption spectrophotometer. Alternatively, the UV-vis spectra can also be obtained by measuring the reflectance spectra compared to a blank control such as $BaSO_4$ powder.

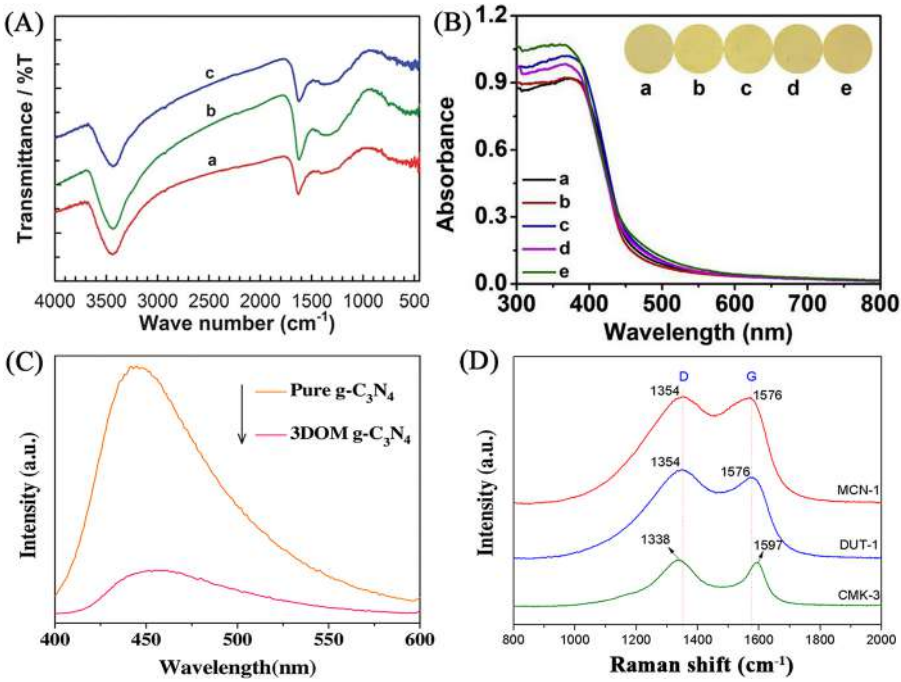

Figure 3.8 (A) FTIR spectra of MCN-6 obtained by using KIT-6 with different pore diameters as hard templates: (a) MCN-6-100; (b) MCN-6-130; (c) MCN-6-150. Reproduced from ref. 93 with permission from the Royal Society of Chemistry. (B) UV-vis diffused reflectance spectra and the corresponding photographs of (a) bulk g-C_3N_4, (b) PC-CN0, (c) PC-CN0.05, (d) PC-CN0.1, and (e) PC-CN0.2. Reproduced from ref. 94 with permission from Elsevier, Copyright 2020. (C) PL spectra of g-C_3N_4 and 3DOM g-C_3N_4 under 340 nm excitation wavelength. Reproduced from ref. 43 with permission from Elsevier, Copyright 2016. (D) Raman spectra of DUT-1, MCN-1, and CMK-3. Reproduced from ref. 51 with permission from American Chemical Society, Copyright 2014.

PL spectra are measured by the emission signal with the excitation of monochromatic light. Both UV-vis and PL spectra depend on the electronic structure of the materials, which can characterize the bandgap and defects. Figure 3.8B[94] displays the UV-vis diffuse reflectance spectra of bulk g-C_3N_4 and porous g-C_3N_4 samples synthesized by adding different mass of $NaHCO_3$ template.[94] The PC-CN0 exhibits a similar absorption edge at around 460 nm to bulk g-C_3N_4, which is related to the 2.70 eV band gap.[94] Clearly, the formation of a porous structure by using the $NaHCO_3$ template can increase UV light harvesting, as observed by the upshift of absorption intensity. The PL test of pure g-C_3N_4 and three-dimensionally ordered macroporous (3DOM) g-C_3N_4 is shown in Figure 3.8C.[43] The much lower PL emission intensity of 3DOM g-C_3N_4 indicates that its porous structure greatly limits the recombination of photogenerated electron–hole pairs and prolongs the life of the

charge carrier, which is beneficial to the photocatalytic application. Raman spectroscopy can identify the chemical composition and detect the doping effect based on molecular vibration. Figure 3.8D depicts the Raman spectroscopy of DUT-1, mesoporous carbon CMK-3, and mesoporous carbon nitride MCN-1.[51] The two bands at around 1350 and 1580 cm^{-1} can be assigned to D (A1g mode) and G (E2g mode) bands, respectively. In comparison with CMK-3, the enhanced intensity for DUT-1 and MCN-1 reveals the enhanced graphitic nature for N-doped carbon materials.[51] Moreover, the shift of G-band and D-band confirms the successful incorporation of nitrogen atoms into the carbon matrix.

3.4 Electrochemical Energy Storage and Conversion Application

In this section, the related application of gCN materials in electrochemical energy conversion (*e.g.*, fuel cells, water splitting) and storage (*e.g.*, supercapacitor, a lithium-ion battery) together with the enhanced mechanism and representative parameters will be described.

3.4.1 Fuel Cells

As a new type of electrochemical energy conversion device which can directly convert chemical energy into electricity, fuel cells have shown tremendous potential in virtue of the high energy conversion efficiency, low emission, near room temperature operation, and convenient transportation as well as storage.[95] Fuel cells are operated by the oxidation of fuel (*e.g.*, H_2, methanol, HCOOH) at the anode and the oxygen reduction reaction (ORR) at the cathode. However, platinum-based electrocatalysts are subject to sluggish kinetics, high cost, and low reserves, which severely hinder the wide application of fuel cells. Therefore, it is necessary to search for high-performance and cost-effective materials for catalyzing alcohol oxidation reaction at the anode and ORR at the cathode.

3.4.1.1 Small Molecule Anodic Oxidation Reaction

Currently, Pt-based noble metals supported by carbon black are widely applied as commercial electrocatalysts for alcohol oxidation reaction at the anode. However, Pt nanoparticles suffer from aggregation, Ostwald ripening, and detachment from support during the fuel cell operation. The search for alternative catalyst support is one of the feasible strategies to enhance both activity and stability of Pt-based electrocatalysts. Interestingly, a series of gCN materials have been confirmed to be effective support materials for Pt-based nanoparticles in virtue of their excellent mechanical strength and anticorrosion ability as well as abundant anchoring sites.[96] For example, Yu and coworkers successfully fabricated highly ordered g-C_3N_4 nanostructures with

uniform pore arrays through condensation of CY with colloidal silica, and the resultant g-C_3N_4 was employed for the first time to evaluate the support effect on the electrocatalytic performance in direct methanol fuel cells.[97] The Pt–Ru alloy nanoparticles with an average particle size of 3.0 nm are homogeneously supported on the C_3N_4 surface. For comparison, supported Pt_{50}–Ru_{50} catalysts were also prepared by using ordered macroporous carbon (OMC) and Vulcan XC-72 as supports, respectively. In a single-cell measurement of direct methanol fuel cell (DMFC), the Pt–Ru/C_3N_4 catalyst showed superior activity and stability compared to Pt–Ru/Vulcan XC-72 and Pt–Ru/OMC. The higher methanol oxidation current of Pt–Ru/C_3N_4 is attributed to the unique graphitic structure and framework N atoms for the nanoporous C_3N_4 network, which can promote the diffusion of fuels and electron transfer through the conduction layer. Lu *et al.* prepared carbon nitride nanotubes (CNNTs) with the assistance of the AAO template and sol–gel polymerization. The resultant CNNTs were used for the first time as catalysts for methanol electrooxidation.[98] There are two weak peaks observed in both the forward and backward scans in the cyclic voltammograms, which are related to the oxidation of methanol and intermediates on the CNNT catalysts, respectively. Chronoamperometry measurements demonstrated that as-synthesized CNNTs possess good durability toward methanol electrooxidation in acid media. It is likely that both the defect and lone pairs of electrons are beneficial to better catalytic activity. Brett's group examined the effect of three different graphitic carbon nitride materials with different crystallinity, porosity, and composition on the electrocatalytic performance.[99] All gCNs displayed remarkably improved durability relative to commercial carbon black (Vulcan XC-72R) in the accelerated corrosion testing, which is confirmed to be suitable support material in polymer electrolyte fuel cells (PEFCs). It was observed that the stability of gCN supported Pt catalysts highly relates to the initial electrochemical surface area (ECSA), and the good metal–support interaction could improve particle dispersion and reduce the detachment and aggregation. More importantly, all gCN supported Pt electrocatalysts showed superior methanol oxidation performance per ECSA compared to the Pt/Vulcan catalyst. To overcome the low electron conductivity of gCNs, Li *et al.* chose g-C_3N_4 nanosheet coated Vulcan XC-72R carbon (C@g-C_3N_4 NS) as support to deposit PtRu nanoparticles (NPs).[100] The resultant PtRu NPs showed more uniform distribution and small particle size on the C@g-C_3N_4 NS surface than the PtRu/C catalyst. As illustrated in Figure 3.9A,[100] PtRu/C@g-C_3N_4 NS exhibits a 2.1 times higher mass activity than PtRu/C. Moreover, the ratio of the forward peak current density (I_f) to the backward peak current density (I_b) represents the anti-poisoning ability of catalysts. The much higher I_f/I_b ratio of PtRu/C@g-C_3N_4 NS indicates that the oxidation of methanol molecules to CO_2 is more completely on the PtRu/C@g-C_3N_4 NS catalyst than that on PtRu/C.[100] The long-term stability of PtRu/C@g-C_3N_4 NS and PtRu/C toward methanol electrooxidation was measured by continued CV cycles (Figure 3.9B).[100] PtRu/C@g-C_3N_4 NS reveals a rapid decrease at 200 cycles and reduced 39.5% of activity, whereas PtRu/C maintains only 46.5% of activity at 1000 cycles. The significantly improved performance for PtRu/C@g-C_3N_4 NS mainly originates from the increased electron conductivity as well as the strong metal–support interaction between PtRu NPs and composite support.[100] Li and co-workers

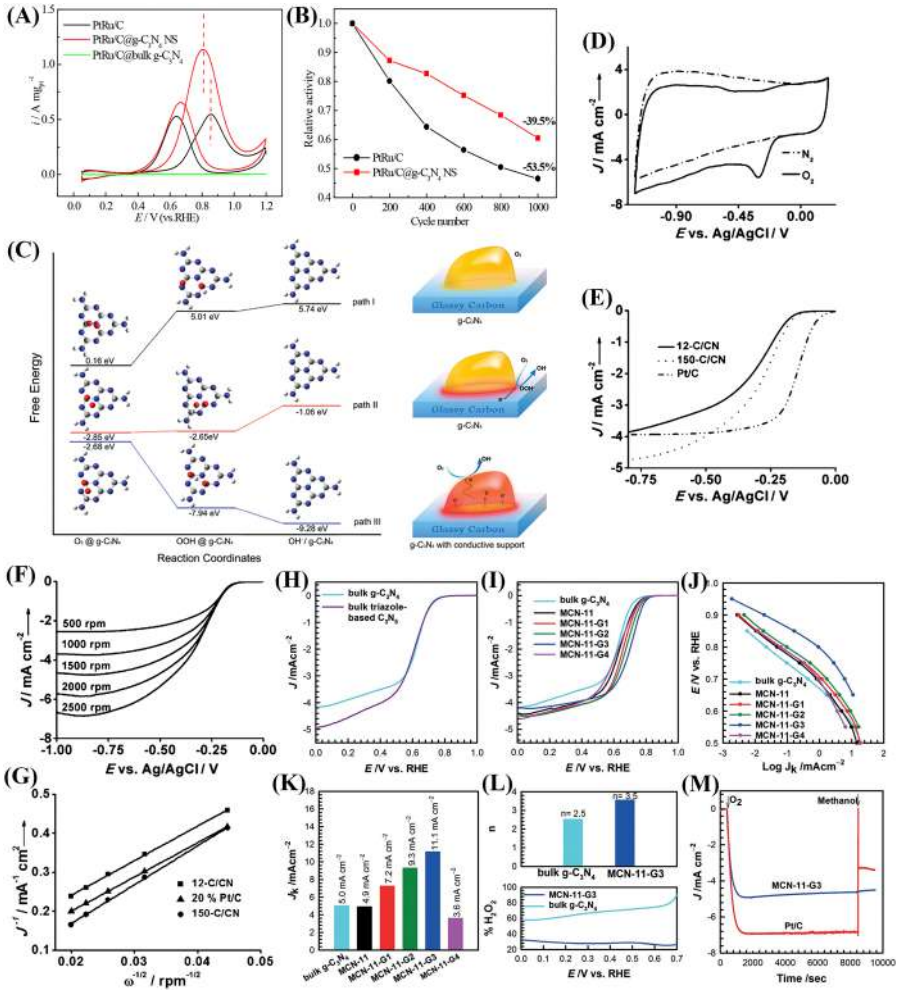

Figure 3.9 (A) The CVs of methanol electro-oxidation for PtRu/C, PtRu/C@g-C_3N_4 NS, and PtRu/C@bulk g-C_3N_4 in Ar-saturated 0.5 M H_2SO_4 and 0.5 M CH_3OH solution at a scan rate of 50 mV s^{-1}. (B) The relationship between normalized peak current plots with cycle number for PtRu/C@g-C_3N_4 NS and PtRu/C catalysts. (A, B) Reproduced from ref. 100 with permission from the Royal Society of Chemistry. (C) The free energy plots of ORR and optimized structures of adsorbed species on g-C_3N_4 when zero, two, and four electrons participated as path I, II, and III. Reproduced from ref. 116 with permission from American Chemical Society, Copyright 2011. (D) The CVs of 150-C/CN in O_2 and N_2-saturated 0.1 M KOH solution, respectively. (E) The LSVs of 12-C/CN, 150-C/CN, and Pt/C at 1500 rpm and scan rate of 5 mV s^{-1}. (F) The LSVs for 150-C/CN at various rotating rates of 500, 1000, 1500, 2000, and 2500 rpm. (G) K-L plots for 12-C/CN, 150-C/CN, and Pt/C. (D–G) Reproduced from ref. 121 with permission from John Wiley & Sons, Copyright 2012 WILEY-VCH Verlag GmbH & Co. KGaA, Weinheim. (H) The LSVs of g-C_3N_4 and C_3N_5. (I) The LSV, (J) Tafel plots, (K) kinetic current densities, (L) electron transfer number, and %H_2O_2 of bulk g-C_3N_4, MCN-11, MCN-11-G1, MCN-11-G2, MCN-11-G3, and MCN-11-G4. (M) Chronoamperometric curves of MCN-11-G3 and Pt/C in N_2-saturated 0.1 M KOH solution followed by the introduction of O_2 and methanol. Figures H–M were reproduced from ref. 122 with permission from John Wiley & Sons, Copyright 2018 WILEY-VCH Verlag GmbH & Co. KGaA, Weinheim.

reported the g-C_3N_4-based Pd electrocatalysts for ethanol oxidation reactions.[101] Compared with Pd@g-C_3N_4, Pd@GC, and Pd@amorphous carbon, the Pd@g-C_3N_4/graphite carbon (GC) catalyst displayed the highest activity and stability, such as high oxidation current density and low onset potential. Wang *et al.* further studied the effect of metal–nitrogen interactions by loading Pd NPs on the hybrid support composed of carbon nitride and graphene (CN_x/G).[102] Owing to the introduction of graphene support with a high surface area and the strong interaction between Pd NPs and nitrogen atoms, the as-synthesized Pd–CN_x/G catalyst exhibits better activity and selectivity toward C3 products for glycerol electrooxidation than Pd NPs supported on carbon black. The same group successfully utilized 3D hierarchically porous carbon nanocomposites consisting of g-C_3N_4 and reduced graphene oxide (rGO) as support to load Pt NPs, and the Pt–g-C_3N_4–rGO catalyst displayed an unusual electrocatalytic performance for methanol electrooxidation.[103] The electron transfer kinetics and improved anti-poisoning ability for the Pt–g-C_3N_4–rGO catalyst are based on the following points. First, g-C_3N_4 could facilitate the formation of hydroxyl species and the subsequent removal of absorbed CO species. Further, g-C_3N_4 can weaken the binding energy between CO and Pt according to density functional theory (DFT) analysis, thus exposing more active sites for methanol electrooxidation. Recently, highly dispersed Pd NPs were deposited on the 3D hybrid of boron-doped graphene with carbon nitride (BG–CN) for formic acid oxidation.[104] The mass and specific activity of Pd/BG–CN are higher than those of commercial Pd/C because the BG–CN support could effectively prevent Pd atoms from detachment and oxidation. An alternative way to reduce the catalyst cost and meanwhile enhance the electrocatalytic activity is to use Ni or Cu-based catalysts.[105] Pieta and co-workers successfully embedded Ni, Cu, and Cu–Ni nanostructures on ultra-thin 2D g-C_3N_4 for methanol electrooxidation under alkaline medium.[106] It was observed that the Ni/CN catalyst showed higher current density and lower onset potential than the Cu–Ni/CN and Cu/CN catalysts, suggesting that the Ni catalyst has superior electrocatalytic activity. The mass activity of reported gCN-based electrocatalysts for anodic oxidation reaction is listed in Table 3.1.

Table 3.1 Electrocatalytic performance comparison of gCN-based catalysts for small molecule oxidation reaction.

Catalysts	Electrolyte	Mass activity (mA mg^{-1})	References
Pt–Pd–gCN–CB	1.0 M NaOH + 1.0 M CH_3OH	4420	96
PtRu/C@g-C_3N_4	0.5 M H_2SO_4 + 0.5 M CH_3OH	1140	100
Pd@g-C_3N_4/GC	1.0 M EtOH + 1.0 M KOH	2156	101
Pd–CN_x/G	0.5 M glycerol + 0.5 M NaOH	1136	102
Pt–g-C_3N_4–rGO	0.5 M H_2SO_4 + 1.0 M CH_3OH	705	103
Pd/BG–CN	0.5 M H_2SO_4 + 0.5 M HCOOH	2215	104
Ni/gCN	3.0 M EtOH + 1.0 M KOH	122.5	107
PtNi/NC	0.5 M H_2SO_4 + 0.5 M CH_3OH	1500	108
Pd NPs/CN_x	0.5 M H_2SO_4 + 0.5 M HCOOH	1640	109
Pt/CN_x	1.0 M H_2SO_4 + 1.0 M CH_3OH	310	110

3.4.1.2 Oxygen Reduction Reaction (ORR)

The oxygen reduction reaction (ORR) at the cathode is crucial to the overall performance of fuel cells, and it is highly desirable to develop highly efficient and highly stable ORR electrocatalysts for commercial applications. In particular, fuel methanol easily permeates through the perfluorosulfonic solid polymer film into the cathode chamber, resulting in excessive overpotential and fuel consumption. The ORR can proceed either through (i) an undesirable two-step, two-electron pathway with the formation of hydrogen peroxide intermediates or (ii) a four-electron complete oxidation process. Taking into account the prohibitive cost and limited supply of Pt, intensive research efforts have been devoted to non-noble-metal electrocatalysts as a potential alternative for the next generation of fuel cell technology.[95] It has been reported by Dai's group that the nitrogen-doped carbon nanotubes exhibited superior electrochemical activity, long-term durability, and better tolerance to methanol crossover than Pt/C catalyst for ORR in alkaline fuel cells.[111] It was reasonable to speculate that the introduction of electron-accepting nitrogen atoms could impart a relatively high positive charge density on neighboring carbon atoms and thus desirable adsorption of oxygen. From this viewpoint, nitrogen-rich carbon nitride electrodes are a potential Pt-free oxygen reduction catalyst. In 2009, Lyth *et al.* first explored the ORR activity of g-C_3N_4.[112] Although g-C_3N_4 possesses a higher onset potential than carbon black, their current density was low because of the insufficient surface areas. The onset potential and current density of g-C_3N_4 could be improved significantly by the mixture with carbon black support. Similarly, the ORR on high crystallinity of g-C_3N_4 synthesized by Xia's group was confirmed to pass through a two-step and two-electron pathway.[113] To address the aforementioned issues, Joo's group prepared ordered mesoporous carbon nitride (OMCN) by using SBA-15 mesoporous silica as a template and examined the ORR performance in an acidic medium.[114] Because of the high surface area and rich nitrogen groups, the OMCN displayed significantly improved current density and onset potential compared to bulk carbon nitride and ordered mesoporous carbon. To further improve the nitrogen content of carbon nitride, Pandiaraj *et al.* synthesized mesoporous carbon with a nitrogen content of 7.0% for ORR, and they showed comparable activity to commercial Pt/C.[115] As shown in Figure 3.9C, Qiao and co-workers elucidated the major barrier for ORR on g-C_3N_4 surface based on DFT analysis.[116] The results indicate that oxygen could not be reduced spontaneously on the pristine g-C_3N_4 surface if no electron participates. Once introducing two electrons, the first $2e^-$ the reaction can easily go on, but a huge barrier still exists in the second reaction, resulting in excess OOH^- species accumulated on g-C_3N_4.[116] It was found that the barrier can be removed effectively by the introduction of four electrons, and the adsorbed O_2 molecules finally form OH^- in alkaline solutions. From this insight, various electron-conductive carbon supports were introduced into g-C_3N_4 by different routes to improve their electron transfer ability.[116]

For example, g-C_3N_4@CMK-3 composites were developed by Zheng *et al.* through the incorporation of g-C_3N_4 into the CMK-3 porous skeleton, and they demonstrated competitive catalytic activity with a commercial Pt/C catalyst.[116] It is believed that the ordered mesopores and high surface area of CMK-3 provide sufficient active sites and accelerate the mass transfer of oxygen molecules. Given the excellent conductivity and the layered structure of graphene, Yang *et al.* developed a valid strategy for synthesizing graphene-based carbon nitride (G-CN) nanosheets by a nano casting technology.[117] The G-CN nanosheets possess superior electrocatalytic performance for ORR than pure CN sheets and commercial Pt/C in terms of high electrocatalytic activity, long-term stability, and high selectivity. It turns out that both the electrical conductivity and the content of pyridinic N are essential to the high-performance nitrogen-doped carbon electrodes. Shi's group immobilized graphitic carbon nitride (GCN) on the surface of chemically converted graphene (CCG) by the direct polymerization of melamine precursors on CCG.[118] The electrocatalytic performance of the G-GCN composite was compared with GCN and CCG electrodes. The higher reduction potential and wave current in CVs implied that G-GCN exhibits much better electrocatalytic activity than GCN or CCG. Sun's group constructed a porous g-C_3N_4/rGO hybrid through a solution self-assembly route.[119] The rGO sheets act as "highways" for electron transfer, and the direct contacts between adjacent rGO sheets are facilitated by g-C_3N_4. Consequently, an outstanding ORR catalytic performance is found on the 3D g-C_3N_4/rGO hybrid. The $Ni(OH)_2$/C_3N_4/rGO (NCG) nanocomposites were fabricated by coating the precursors onto a glassy carbon electrode (GCE), followed by *in situ* electrochemical reduction of GO and Ni precursors.[120] Importantly, the novel nanocomposite exhibited excellent electrocatalytic activity, selectivity, and better durability, which is promising as a non-precious metal cathode catalyst in fuel cells. Given that the porosity of a catalyst is crucial to mass transfer during the ORR, Liang *et al.* systematically studied the effect of pore structure for the carbon substrate on the electrocatalytic properties of g-C_3N_4/C hybrids.[121] Macroporous and mesoporous g-C_3N_4/C were obtained by using 150 and 12 nm silica spheres as hard templates, respectively. Figure 3.9D–G displays the electrochemical behaviors of all electrocatalysts in alkaline media.[121] Compared with the CVs recorded in N_2-saturated 0.1 M KOH solution, a characteristic reduction peak appeared when O_2 was introduced (Figure 3.9D).[121] In the linear sweep voltammograms (LSVs), macroporous g-C_3N_4/C exhibited much higher onset potential and current density than mesoporous material (Figure 3.9E). Because of the shorter diffusion distance at high speeds, the current density increases with the increase of rotation speeds (Figure 3.9F).[121] From the Koutecký–Levich plots, we can see that macroporous g-C_3N_4/C exhibits the largest current density among the three catalysts, revealing its remarkable catalytic activity (Figure 3.9G).[121] The calculated electron transfer number is 3, suggesting that the ORR follows an integrated reaction path of both two-electrons and four-electrons.[121] Furthermore, it is of great interest to

design triazole-based N-rich carbon nitride hybrids due to the fact that the abundant pyrrolic N sites are beneficial for ORR activities. Vinu's group synthesized mesoporous C_3N_5-graphene hybrids by using KIT-6 mesoporous silica as a template.[122] The resultant products were labeled as MCN-11, MCN-11-G1, MCN-11-G2, MCN-11-G3, and MCN-11-G4 when the added graphene oxide content is 0, 0.7, 1.4, 2.1, and 2.8 wt%, respectively. The effect of triazole moiety on ORR activity was assessed by LSVs shown in Figure 3.9H.[122] As expected, a higher diffusion-limiting current density was observed on triazole-based C_3N_5 compared with that on bulk g-C_3N_4. On one hand, O_2 prefers to adsorb on positive carbon caused by the adjacent N–N bond in the triazole moiety. On the other hand, sp^2-hybridized nitrogen offers more electrons to π–π conjugation, helping to complete 4e-transfer for ORR. As illustrated in Figure 3.9I,[122] both the 3D mesoporous structure and the coupling with graphene can obviously reduce the onset potential. Among them, MCN-11-G3 with an optimum graphene content possesses the highest onset potential of 0.81 V *vs.* RHE. The enhanced ORR kinetics is further reflected by the Tafel plots in Figure 3.9J, among which the minimum slope is achieved for MCN-11-G3. It can be seen from Figure 3.9K [122] that the kinetic current density (J_k) determined by Koutecký–Levich (K–L) equation increases as increased graphene content, and then decreases. The homogeneous hybridization between these components in MCN-11-G3 is beneficial to the improved ORR kinetics. Compared to bulk g-C_3N_4, MCN-11-G3 delivers a higher electron transfer number of 3.5 and lower HO_2^- yield of 23% (Figure 3.9L).[122] Except for the superior oxygen reduction activity, MCN-11-G3 also exhibits excellent stability and methanol tolerance than commercial Pt/C during the chronoamperometric measurements, implying its great potential for commercial applications (Figure 3.9M).[122] Due to the rich sp^2 hybrid carbon atoms in carbon nanotubes (CNTs), the hybridization of CNTs with g-C_3N_4 can endow good conductivity and promote charge transfer.[122] Wang's group reported various CNTs@g-C_3N_4 materials through polymerizing CY with moderate amounts of CNTs.[123] As expected, the onset and peak potential of these composites for ORR shifted positively compared with those of pure CNTs, whereas little catalytic activity was observed for bare g-C_3N_4. To expose more ORR active sites, Qiu and co-workers intercalated phosphorus-doped g-C_3N_4 (P-g-C_3N_4) nanosheets with NH_2-modified carbon black (NH_2-CB) to construct a 3D P-g-C_3N_4@NH_2-CB hybrid.[124] Benefiting from the combined effect between P and N in tri-*s*-triazine rings of CNs and the interaction between each other, the ORR activity of 3D P-g-C_3N_4@NH_2-CB exceeds that of Pt/C in terms of electron transfer number and Tafel slope.

Currently, amorphous carbon black (a-CB) is widely used as a support material for ORR, but it suffers from serious electrochemical corrosion. In this regard, gCNs have been confirmed to be ideal candidates in terms of stability and support–metal interaction. Noto *et al.* systematically studied the correlation between the CN support and electrochemical performance of ORR.[125,126] It was found that pyrolysis temperature influences greatly the

Table 3.2 Electrocatalytic performance comparison of gCN-based catalysts for ORR.

Catalysts	Onset potential (V)	Electron transfer number	Tafel slope (mV dec^{-1})	References
MOFCN900	0.035 (*vs.* Hg/HgO)	3.12		115
g-C_3N_4/rGO	−0.12 (*vs.* Ag/AgCl)	3.8		119
NCG	0.97	3.93	75	120
MCN-11-G3	0.81	3.5	51.4	122
g-C_3N_4/CNTs	−0.155 (*vs.* SCE)	4.0		123
P-g-C_3N_4/@ NH_2-CB	0.87	3.83	89	124
S-C_3N_4	0.77	3.64	115	132
BCNT/Co	1.12	3.89–3.98	83.6	133
Ag/g-C_3N_4	−0.05 (*vs.* Ag/AgCl)	4	117	134

structural disorder of CN support and then the catalyst tolerance towards oxidizing conditions. The CN support with N content above 13 wt% can effectively stabilize Pd(II) species and thus improve the catalyst's durability. Through the integration of polymeric gCN (pg-CN) and a-CB, the resultant core@shell a-CB@pg-CN possesses a unique polymeric graphitic structure with nitrogen-rich surface functionalities.[127] Significantly, both the ORR activity and stability of a-CB@pg-CN supported Pt catalyst outperformed those of well-developed Pt materials in a real proton exchange membrane fuel cell device. DFT calculations evidenced that the combination of pg-CN and a-CB could effectively reduce the electrochemical corrosion rate and promote catalyst–support interaction. Recently, Kim *et al.* successfully immobilized Pd and Pt single atoms on the composite support of C@C_3N_4 and examined their electrocatalytic performance with a nanoparticle counterpart.[128] The absence of ensemble sites in C@C_3N_4–Pd_1 is beneficial to the two-electron pathway for ORR, and the H_2O_2 yield reaches up to 94%.

In addition, a few studies have been carried out to engineer the electronic structure of gCN materials through metal or heteroatom doping.[129,130] Dey's group synthesized a series of non-precious metal-doped g-C_3N_4 (M-g-C_3N_4, where M = Fe, Cu, Co, Ni) without any conductive carbon support, and the Fe–g-C_3N_4 exhibited the most positive half-wave potential ($E_{1/2}$), superior stability, and excellent methanol tolerance toward ORR in an alkaline medium.[131] It is due largely to the presence of Fe-N_x active sites with three-coordinated Fe atoms with nitrogen atoms. Additionally, different heteroatoms (S, B, P) were doped into C_3N_4 for investigating their electrocatalytic performance toward ORR.[132] Interestingly, the S-C_3N_4 reveals excellent catalytic activity with a higher onset potential, smaller Tafel slope, and four-electron transfer process because of the synergistic interaction between N and S and the modified electronic structure caused by S doping. The electrocatalytic performance of gCN-based electrocatalysts toward ORR is compared in Table 3.2, including the onset potential, electron transfer number, and Tafel slope.

3.4.2 Water Splitting

With an increasing energy crisis and serious environmental pollution, hydrogen has been recognized as a suitable candidate for fossil fuel because of its zero-emission and high energy density. At present, hydrogen is mainly produced from natural gas reformation accompanied with CO_2 emission. In this case, developing an electrocatalytic water-splitting device is highly anticipated, in which hydrogen evolution reaction (HER) and oxygen evolution reaction (OER) take place at the cathode and anode, respectively.

3.4.2.1 Hydrogen Evolution Reaction (HER)

Platinum-based materials are well-known for their superior electrocatalytic properties toward HER, but the prohibitive cost and scarcity greatly hinder their commercial applications. Therefore, searching for highly efficient and low-cost non-precious metal electrocatalysts for HER is the key to developing a water-splitting device. Generally speaking, an ideal electrocatalyst toward HER should possess a low overpotential, high current density, small Tafel slope, and superior stability. Until now, various metal nitrides, carbides, and phosphides have been proved to effectively catalyze HER, but the intrinsic corrosion and oxidation issues still have not been resolved yet. Featured with graphite-like C–N structure, low cost, and high thermal stability against oxidation, gCN is pursued as a prospective catalyst material. Moreover, its low surface area and poor conductivity can be easily conquered by heteroatom doping and the insertion of conductive support. Shalom *et al.* presented a universal approach to deposit highly ordered C_3N_4 rods on various substrates such as a fluorine-doped tin oxide (FTO) and porous metal oxide (TiO_2, ZnO, *etc.*).[135] Figure 3.10A–D shows the CVs of C_3N_4 on FTO and TiO_2 in neutral and alkaline media. For the C_3N_4/FTO catalyst (Figure 3.10A and B), the obvious catalytic current occurred at 0.25 and 0.1 V (*vs.* RHE) in pH 6.9 and 13.1, respectively.[135] By contrast, FTO just exhibits the reduction peak of SnO_2 to SnO at 0.1 V, revealing an improved electron transfer and HER activity upon hybridizing with C_3N_4. A similar phenomenon was further observed on the C_3N_4/TiO_2 catalyst (Figure 3.10C and D).[135] The significant current density observed for bare TiO_2 in neutral media is not due to the HER but the accumulation of electrons within TiO_2, whereas there is only a negligible current density under basic conditions due to the almost completely occupied TiO_2 surface. At pH 6.9, the anodic peak of the C_3N_4/TiO_2 catalyst quenches, and the cathodic current decreases, implying that the cathodic current originates from electron transfer to the solution. The C_3N_4/TiO_2 catalyst demonstrates an improved hydrogen evolution activity in basic media with a low overpotential of 0.1 V and a larger current density. Qiao's group combined g-C_3N_4 with nitrogen-doped graphene (NG) to form a C_3N_4@NG hybrid, and its outstanding hydrogen evolution performance was compared with that of g-C_3N_4, NG, C_3N_4/NG mixture, and Pt/C (Figure 3.10E–H).[136] The HER polarization plots

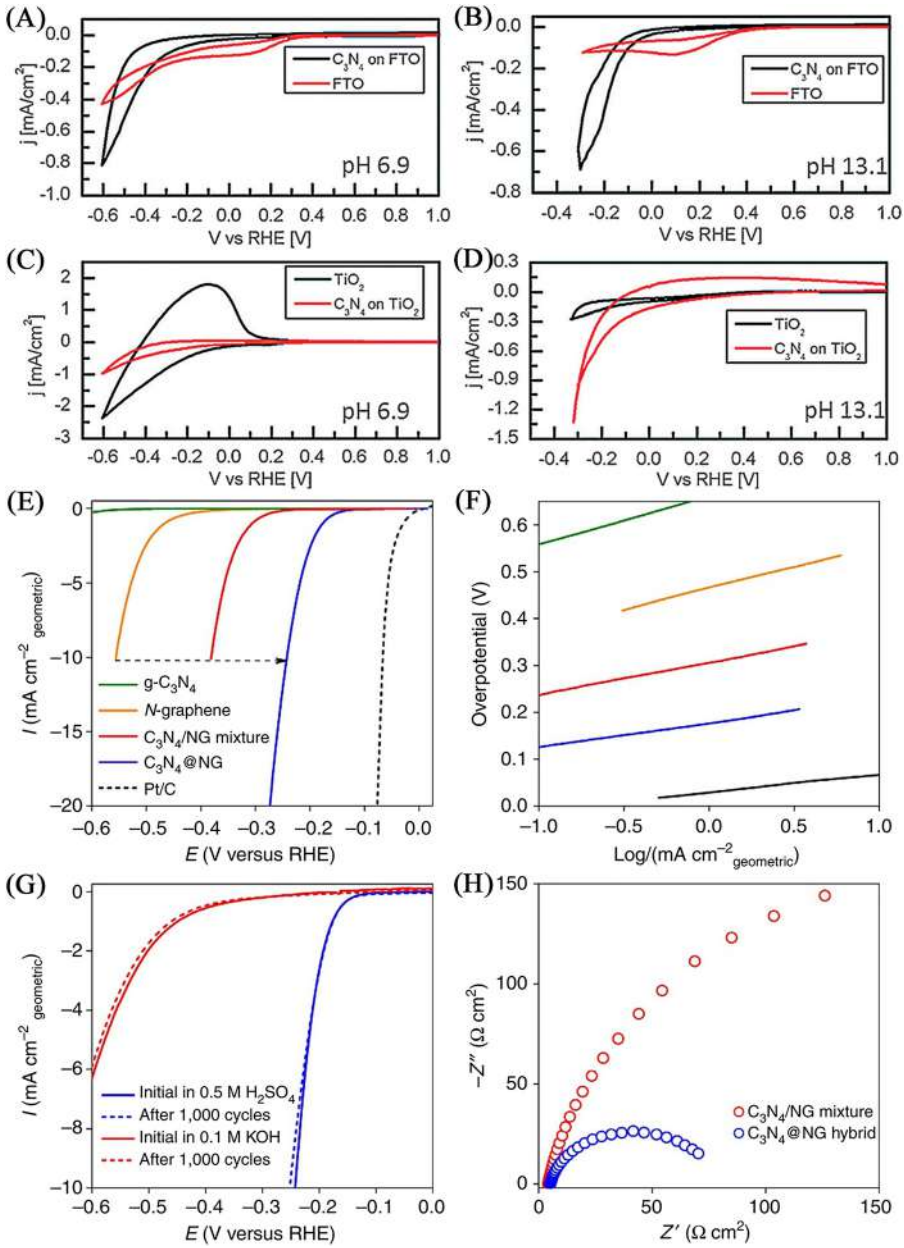

Figure 3.10 CVs of C_3N_4/FTO in (A) 0.1 M buffer solution and (B) 0.1 M KOH solution at a scan rate of 25 mV s^{-1}. CVs of C_3N_4/TiO_2 in (C) 0.1 M buffer and (D) 0.1 M KOH solution at a scan rate of 25 mV s^{-1}. Figures A–D were reproduced from ref. 135 with permission from John Wiley & Sons, Copyright 2014 WILEY-VCH Verlag GmbH & Co. KGaA, Weinheim. (E, F) The polarization curves and Tafel plots of g-C_3N_4,

shown in Figure 3.10E reveal that C_3N_4@NG needs an overpotential of 240 mV to deliver a current density of 10 mA cm^{-2}, which is much lower than g-C_3N_4, NG, and C_3N_4/NG mixture. The hydrogen evolution activity of bare g-C_3N_4 and NG is almost negligible owing to the limited conductivity and inert reaction kinetics. The Tafel slope of C_3N_4@NG is low to 51.5 mV dec^{-1}, revealing their improved electrode kinetics (Figure 3.10F).[136] Moreover, the HER activity of C_3N_4@NG can be highly maintained in both acidic and alkaline solutions after 1000 potential cycles (Figure 3.10G). Electrochemical impedance spectroscopy (EIS) measurements shown in Figure 3.10H reveal that the chemical and electronic couplings in C_3N_4@NG can obviously reduce faradaic resistance and accelerate the charge-transfer.[136] DFT calculations further confirmed the synergistic effect between g-C_3N_4 and NG, in which g-C_3N_4 offers highly active sites for hydrogen adsorption, while NG benefits the electron-transfer process during the proton reduction reaction. Subsequently, the same group constructed a flexible 3D film by assembling porous C_3N_4 nanolayers with N-doped graphene.[137] Benefiting from the highly exposed active sites and the synergistic effect of two components, it exhibits a lower overpotential close to the Pt/C catalyst, outperforming all of the previously reported non-metal electrocatalysts. Furthermore, the synthesis of a MoS_2-decorated g-C_3N_4 heterostructure could increase the exposed active sites and reduce the charge-carrier recombination for HER than for those pure counterparts.[138,139] Similarly, Cao *et al.* prepared Ni_2B-modified g-C_3N_4 as a highly efficient hydrogen evolution electrocatalyst.[140]

On the one hand, the Ni_2B nanoparticles act as a spacer and conductive material to improve both conductivity and active surface areas. On the other hand, the synergistic interaction helps to narrow the adsorption barrier and then reduce the overpotential of HER. By adjusting silver contents and subsequently modifying with hemoglobin (Hb), the optimum Hb/Ag@CN nanohybrids just need an overpotential of 79 mV to afford a current density of 10 mA cm^{-2}, which is competitive to most reported hydrogen evolution electrocatalysts.[140] It is deemed that the nitrogen structural defects introduced by Hb could accelerate the hydronium ions' adsorption and enhance the HER performance. Table 3.3 compares the HER parameters of gCN-based electrocatalysts from onset overpotential, the overpotential needed for a current density of 10 mA cm^{-2} and Tafel slope.

N-graphene, C_3N_4/NG mixture, C_3N_4@NG, and Pt/C catalyst toward HER in 0.5 M H_2SO_4 at a scanning rate of 5 mV s^{-1}. (G) The LSV curves of C_3N_4@NG before and after 1000 potential cycles in 0.5 M H_2SO_4 and 0.1 M KOH solution, respectively. (H) EIS of C_3N_4@NG and C_3N_4/NG mixture in 0.5 M H_2SO_4. (E–H) Reproduced from ref. 136 with permission from Springer Nature, Copyright 2014.

Table 3.3 Electrocatalytic performance comparison of gCN-based catalysts for HER.

Catalysts	Onset overpotential (mV)	η (mV)	Tafel slope (mV dec^{-1})	References
C_3N_4@NG		240	51.5	136
PCN nanolayers@ N-graphene	8	80	49.1	117
MoS_2/g-C_3N_4	240	260	63	138
0.5%MSNS-CN	90	200	96	139
Ni_2B-decorated g-C_3N_4	300	707	221	140
g-C_3N_4/Cu_3P	5	67	45	141
Ni/C_3N_4		222	128	142
Hb/20Ag@CN		79	155	143
g-C_3N_4@P-pGr	76	340	90	144
C_3N_4–rGO–Ru		80	55	145
Cu_2O/g-C_3N_4		148.7	55	146

3.4.2.2 *Oxygen Evolution Reaction (OER)*

The main reason for the high overpotential of water splitting (above 1.23 V) is primarily due to the sluggish kinetics of OER. The OER involves two water molecules and a four-electron transfer to form one molecular oxygen, which is more complex than HER. At present, the state-of-art electrocatalysts toward OER are Ir- and Ru-based noble metals, and the search for highly efficient alternatives is still urgent and difficult.[147] In virtue of rich pyridinic and quaternary nitrogen atoms, the overpotential for N-doped graphitic carbon to afford a current density of 10 mA cm^{-2} is 1.61 V *vs.* RHE, which is comparable to commercial IrO_2/C.[148] In this respect, gCN is an ideal precursor to introduce nitrogen atoms because of the high nitrogen content, low cost, and readily tunable structure. Sun's group first used g-C_3N_4 as a metal-free OER electrocatalyst and its further integration with graphene.[149] Based on XPS analysis, the active site for OER is the pyridinic-N in g-C_3N_4. Qiao's group self-assembled g-C_3N_4 nanosheets (NSs) with CNTs to construct a strongly coupled g-C_3N_4 NS–CNT composite by π–π stacking and electrostatic interactions.[150] Notably, they demonstrated the best activity among non-metal OER catalysts and long-term stability among noble-metal catalysts. We can see from the LSVs shown in Figure 3.11A[150] that there is negligible OER activity for both CNT and g-C_3N_4 NS, while the co-existence of two components can remarkably improve the OER response. Though g-C_3N_4 NS–CNT gives a slightly higher onset potential, its current density exceeds that of IrO_2–CNT at a higher potential of 1.62 V. The catalytic reaction kinetics toward OER was evaluated by Tafel plots (Figure 3.11B).[150] Obviously, g-C_3N_4 NS–CNT displays the smallest Tafel slope of 83 mV dec^{-1} relative to IrO_2-CNT (90 mV dec^{-1}) and bulk g-C_3N_4 NS–CNT (105 mV dec^{-1}). The stability of g-C_3N_4 NS–CNT was evaluated by a chronoamperometric curve (Figure 3.11C), and the current density can maintain 86.7% within 10 h.[150] During the chronoamperometric response, the potential for g-C_3N_4 NS–CNT to reach 3.0 mA cm^{-2} has almost no changes within 800 s, whereas IrO_2–CNT exhibits a more positive potential of 32 mV. The current density for g-C_3N_4 NS–CNT at 1.60 V drops only 8.8%, and the LSV

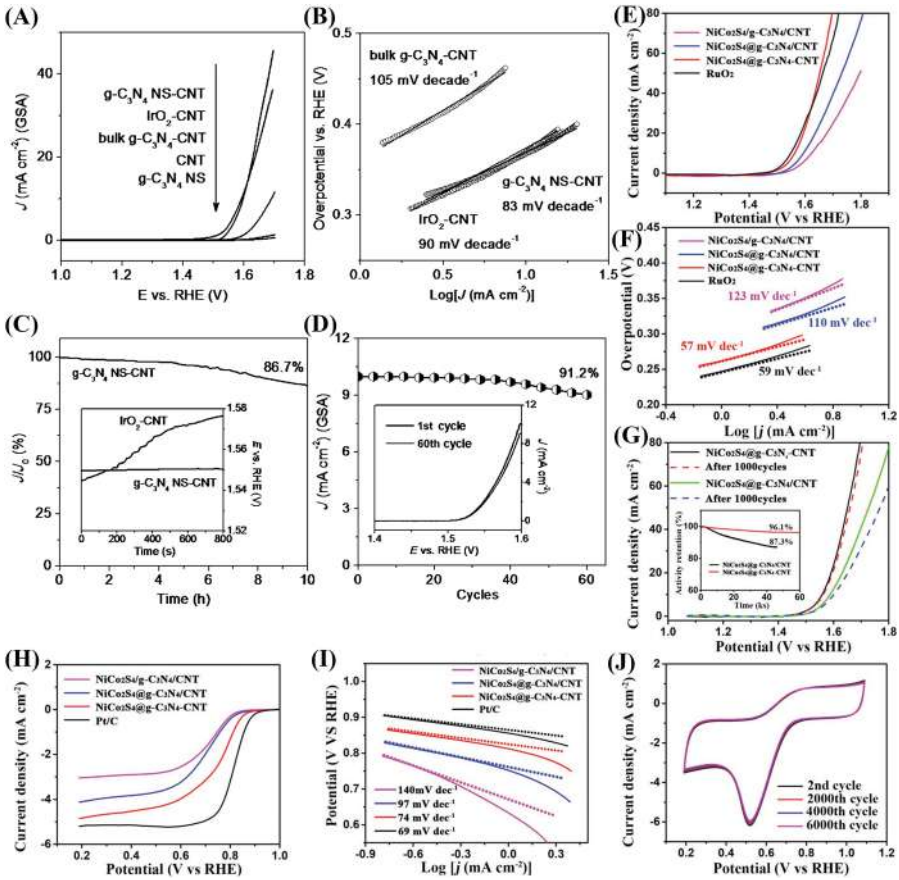

Figure 3.11 (A) The LSVs and (B) Tafel plots of g-C_3N_4 NS–CNT, IrO_2–CNT, bulk g-C_3N_4–CNT, CNT, and g-C_3N_4 NS for OER in O_2-saturated 0.1 M KOH solution at a scan rate of 5 mV s^{-1} and rotating speed of 1500 rpm. (C) The chronoamperometric curves of g-C_3N_4 NS–CNT at a fixed potential of 1.54 V. Inset: the chronopotentiometric curves of g-C_3N_4 NS–CNT and IrO_2–CNT at a constant current density of 3.0 mA cm^{-2}. (D) The current density plots of g-C_3N_4 NS–CNT with cycle number at 1.60 V. Inset: LSVs of g-C_3N_4 NS–CNT before and after 60 scan cycles at a scan rate of 5 mV s^{-1}. (A–D) Reproduced from ref. 150 with permission from John Wiley & Sons, Copyright 2014 WILEY-VCH Verlag GmbH & Co. KGaA, Weinheim. (E) LSVs and (F) Tafel plots of $NiCo_2S_4$/g-C_3N_4/CNT, $NiCo_2S_4$@g-C_3N_4/CNT, $NiCo_2S_4$@g-C_3N_4–CNT, and RuO_2 film in N_2-saturated 1 M KOH solution. (G) LSVs of $NiCo_2S_4$@g-C_3N_4/CNT and $NiCo_2S_4$@g-C_3N_4–CNT before and after 1000 cycles. Inset: the galvanostatic curves at 10 mA cm^{-2}. (H) LSVs and (I) Tafel plots for all samples toward ORR in O_2-saturated 0.1 M KOH at 5 mV s^{-1}. (J) CVs of $NiCo_2S_4$@g-C_3N_4–CNT with different cycles at a scan rate of 200 mV s^{-1}. (E–J) Reproduced from ref. 152 with permission from John Wiley & Sons, Copyright 2019 WILEY-VCH Verlag GmbH & Co. KGaA, Weinheim.

curve only shifts slightly after 60 potential cycles (Figure 3.11D).[150] The superior electrocatalytic performance for g-C_3N_4 NS–CNT is ascribed to the following points. First, the high pyridinic nitrogen for g-C_3N_4 NS–CNT can impart a more positive charge density to the neighboring carbon atoms, facilitating the adsorption of OH^- ions, electron transfer, and favorable recombination of two adsorbed oxygen atoms during the OER in basic media. Second, compared with nonporous bulk g-C_3N_4 NS–CNT, the highly porous 3D structure benefits the infiltration of electrolytes, the reaction species diffusion, and the product emission. Thirdly, the strong coupling between CNTs and g-C_3N_4 is beneficial to smooth electron transport.[150] Given that the heteroatom (B, P, S, *etc.*) doping could change the electronic structure and improve the charge transfer ability, Zhu *et al.* anchored Co_3O_4 nanocrystals on phosphorus-doped C_3N_4 (P-CN) sheets for highly efficient OER.[151] Because of the Co–N bond induced high-conductivity and ample active sites for porous P-CN, the Co_3O_4/P-CN composites display lower overpotential relative to pure Co_3O_4 at a current density of 10 mA cm^{-2}. Among them, the 60% Co_3O_4/P-CN possesses the highest oxygen evolution performance in terms of the lowest overpotential, the lowest Tafel slope, and the best durability. Deng's group reported the fabrication of a $NiCo_2S_4$@g-C_3N_4–CNT hybrid and its potential use in the OER and ORR.[152] For comparison, $NiCo_2S_4$/g-C_3N_4/CNT, $NiCo_2S_4$@g-C_3N_4/CNT, and RuO_2 were also measured under the same conditions. As shown in the LSVs of Figure 3.11E,[152] the overpotential required for $NiCo_2S_4$@g-C_3N_4–CNT to afford a current density of 10 mV cm^{-2} is 330 mV, which is lower than that of the reference sample and competes with commercial RuO_2 (320 mV). Moreover, the smallest Tafel slope for $NiCo_2S_4$@g-C_3N_4–CNT indicates its favorable reaction kinetics (Figure 3.11F).[152] The LSV of $NiCo_2S_4$@g-C_3N_4–CNT has a slightly positive shift after 10 000 cycles, but the OER behavior of $NiCo_2S_4$@g-C_3N_4/CNT is lost severely (Figure 3.11G). This fact can be verified by the galvanostatic measurements, in which the current density of $NiCo_2S_4$@g-C_3N_4–CNT and $NiCo_2S_4$@g-C_3N_4/CNT decays 3.9% and 12.7% for 60 000 and 45 000 s, respectively (inset of Figure 3.11G). Similarly, the ORR activity and stability for $NiCo_2S_4$@g-C_3N_4-CNT are displayed in Figure 3.11H–J.[152] Theoretical calculations confirm that the unique electronic transfer from Ni/Co active sites to pyridinic-N could downshift the d-band center and benefit the intermediate's adsorption/desorption, and thus improve reaction kinetics. Wang *et al.* developed a novel composite of multi-layered g-C_3N_4 supported $NiSe_2$ ($NiSe_2$/g-C_3N_4) to be a highly efficient catalyst for OER.[153] It can deliver higher current density and lower onset potential than pure $NiSe_2$ and multi-layered g-C_3N_4, suggesting it as a potential candidate as a substitute for noble metal catalysts. Furthermore, the overpotentials of gCN-based electrocatalysts at a given current density are compared in Table 3.4.

3.4.3 Supercapacitors

In addition, in the search for a clean energy source, the increasing energy demand along with the rapid popularization of portable electronics has stimulated extensive efforts in the development of novel energy storage devices. Because of the higher power capability, rapid charge/discharge rate, and

Table 3.4 Electrocatalytic performance comparison of gCN-based catalysts for OER.

Catalysts	J (mA cm^{-2})	η (mV)	References
N/C-700	10	380	148
g-C_3N_4/graphene	10	539	149
g-C_3N_4 NS-CNT	10	370	150
PCN–CNP	10	400	154
Co_3O_4/P-CN	10	320	151
$NiCo_2S_4$@g-C_3N_4–CNT	10	330	152
$NiSe_2$/g-C_3N_4/NF	40	290	153
Co/Co,N,S-doped graphene-900	10	337	155
Ir/g-C_3N_4/NG	10	287	156
CoS_x@PCN/rGO	10	340	157
Ni–Co–CN	10	195	158
g-CN	10	316	159
α-Fe_2O_3@g-C_3N_4–NCs	10	425	160
$Fe_{0.2}Co_{0.8}Se_2$/g-C_3N_4	10, 50	230, 360	161

long cycling life, supercapacitors have gained much attention for meeting such high-level requirements compared to conventional batteries. Generally, supercapacitors can be categorized into pseudocapacitors and electrical double-layer capacitors (EDLCs) based on whether Faradaic redox reactions happen or not. Given that the performance of a supercapacitor largely relies on the electrode material, the search for new electrode materials is the main research interest. At present, a series of carbon materials such as carbon black, graphene, and carbon nanotubes have been studied for electrode materials of supercapacitors because of the low cost, large surface areas, and excellent stability, but the deficient capacitance still restricts their commercialization.[162] It is well known that the introduction of nitrogen atoms with lone electron pairs into the carbon matrix can improve the electrode wettability, increase the surface polarity and consequently, facilitate charge mobility. In this aspect, porous gCN materials possess distinct advantages over other carbon materials due to their inherent high nitrogen content and high surface areas.[163] However, the poor conductivity and easier restacking properties restrict its commercialization. Until now, various strategies have been employed to improve its efficiency through structural engineering, doping with other heteroatoms, and hybridizing with other components.[164] For example, Tahir *et al.* proposed a facile approach to fabricate tubular g-C_3N_4 and explored its electrochemical properties as an electrode for supercapacitors.[165] Figure 3.12A shows the first five galvanostatic charge/discharge curves of tubular g-C_3N_4 at a current density of 0.2 and 0.5 A g^{-1}, respectively. Though the charge/discharge potential exhibits a linear relation with time, the discharge time for the former is obviously larger. After the 1000th cycle, the discharge time is very close to that of the first discharge at both current densities, indicating its excellent capacitance retention properties (Figure 3.12B).[165] The cycling performance of tubular and bulk g-C_3N_4 is delineated in Figure 3.12C. The tubular g-C_3N_4 possesses a specific capacitance of 233 F g^{-1} at a current density of 0.2 A g^{-1} for the first cycle and 212 F g^{-1} for the 1000th cycle, revealing its long-term cycling stability.

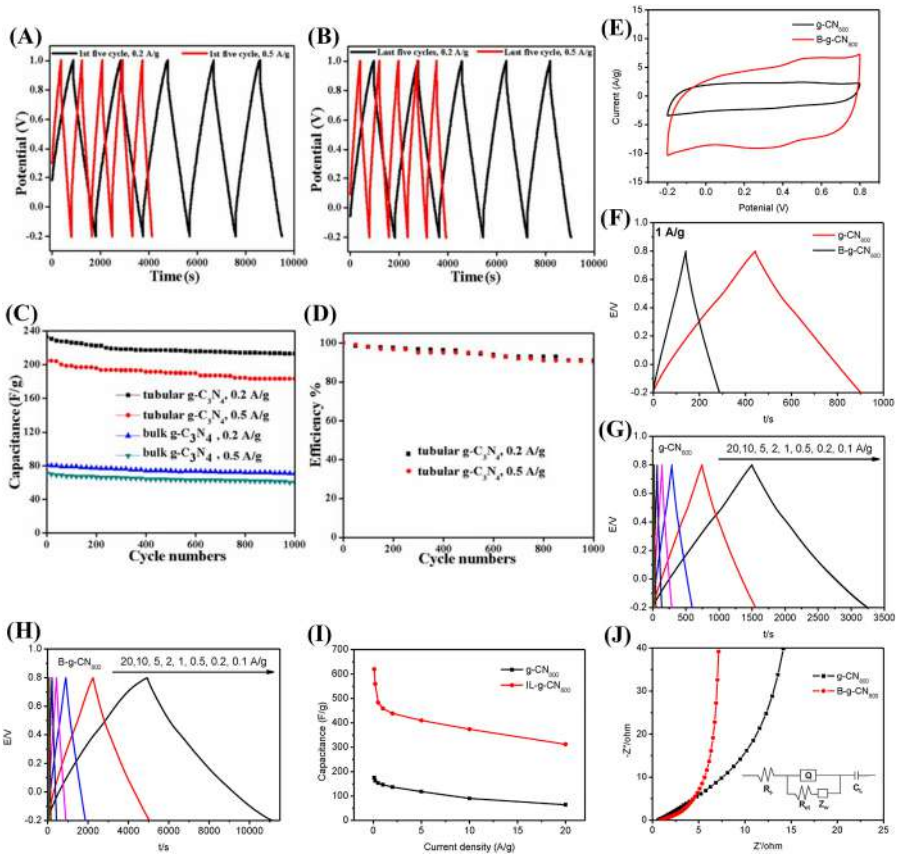

Figure 3.12 (A) First and (B) last five charging/discharging curves for tubular g-C_3N_4 in a potential ranging from −0.2 to 1.0 V at the current density of 0.2 and 0.5 A g^{-1}, respectively. (C) Specific capacitance of tubular and bulk g-C_3N_4 at the current density of 0.2 and 0.5 A g^{-1}. (D) The efficiency of tubular g-C_3N_4 at a current density of 0.2 and 0.5 A g^{-1}. (A–D) Reproduced from ref. 165 with permission from the Royal Society of Chemistry. (E) CV curves of g-CN_{800} and B-g-CN_{800} within the potential window of −0.2–0.8 V at a sweep rate of 100 mV s^{-1}. (F) The charge–discharge curves of g-CN_{800} and B-g-CN_{800} at a current density of 1 A g^{-1}. The charge–discharge curves of (G) g-CN_{800} and (H) B-g-CN_{800} at various current densities. (I) The specific capacitance of g-CN_{800} and B-g-CN_{800} at different current densities. (J) Nyquist plots of supercapacitors on the basis of g-CN_{800} and B-g-CN_{800} electrode materials. (E–J) Reproduced from ref. 166 with permission from Elsevier, Copyright 2017.

For comparison, the specific capacitance for bulk g-C_3N_4 is 81 F g^{-1} at a current density of 0.2 A g^{-1} for the first cycle, which is 2.88 times lower than that of tubular g-C_3N_4. It is well known that the cycling performance is essential to determine the practical application of an electrode material. The calculated specific capacitance of tubular g-C_3N_4 is 204 F g^{-1} for the first cycle at the current density of 0.5 A g^{-1}, and it can retain the capacitance of 182 F g^{-1} even after 1000 cycles. As expected, the tubular g-C_3N_4 has an excellent

retention capability of 91% at 0.2 A g^{-1} and 89% at 0.5 A g^{-1} after 1000 cycles (Figure 3.12D).[165] We believe that the high surface area and nitrogen content in tubular g-C_3N_4 synergistically promote the electrode–electrolyte contact and mass transfer.[165] Devaraj's group employed various surfactants (CTAB, Triton X-100, SDS) to obtain mesoporous gCNs and studied their capacitance performance comparatively.[75] Among them, the sample synthesized with Triton X-100 exhibits the highest specific capacitance of 279 F g^{-1} at the current density of 0.5 A g^{-1}. Moreover, its rate performance also exceeds the other two samples. When integrated into the electrode material of a symmetrical supercapacitor, it can produce an energy density of 20.97 W h kg^{-1}, 499.94 W kg^{-1} power density, and exhibit stable cycling over 10 000 cycles, outperforming previously reported various nitrogen-doped carbon materials.

Considering that heteroatom doping (*e.g.*, B, S, P) can provide additional pseudo-capacitance through surface Faradaic redox reaction, Kong *et al.* synthesized a boron-doped g-CN (B-g-CN) nanosheet by employing IL as both pore-directing agent and B source. Meanwhile, its electrochemical capacitive properties were compared with undoped g-CN.[166] As illustrated in Figure 3.12E, there exists a couple of redox peaks within the tested potential window, indicating the simultaneous electrochemical double-layer and Faradaic capacitive behavior. The larger redox peak and current response for B-g-CN_{800} reveal its superior pseudocapacitive and capacitive properties. Meanwhile, the larger enclosing area is related to high storage capacitance.[166] Figure 3.12F–H displays the chronopotentiometric curves of two samples recorded at various current densities. Obviously, the discharge time duration for B-g-CN_{800} at a given current density is significantly longer than that of g-CN_{800}. The specific capacitance of B-g-CN_{800} is calculated to be 459.0 F g^{-1} at a current density of 1 A g^{-1}, which is 3.1 times larger than that of 146.4 F g^{-1} for g-CN_{800}. As the current density for charge/discharge increases, the specific capacitance decreases correspondingly because the insufficient charge/discharge time cannot guarantee the diffusion of electrolyte ions into the electrode (Figure 3.12I).[166] The specific capacitance of B-g-CN_{800} reaches up to 620.0 F g^{-1} and is competitive with most reported nitrogen-doped graphitic carbon materials at a current density of 0.1 A g^{-1}. Electrochemical impedance spectroscopy (EIS) analysis can be used to assess the electrode reaction kinetics; meanwhile, the equivalent circuit was illustrated in the inset of Figure 3.12J.[166] There are three regions in the EIS, including the high-frequency *X*-intercept corresponding to solution resistance (R_s), the depressed semicircle related to charge transfer resistance (R_{ct}), a low-frequency vertical tail derived from pseudocapacitance, and Warburg resistance. According to the fitting results, the B-g-CN_{800} electrode exhibits a smaller R_{ct} of 7.01 Ω than g-CN_{800} (17.67 Ω), though its R_s value is slightly higher. It can be concluded that B-doping helps to reduce the ion's resistance to diffuse into the whole electrode, and thus creates a high specific capacitance.[166] The carbon self-repairing g-C_3N_4 (C-C_3N_4) was integrated with rGO to obtain nitrogen-rich porous carbon materials (C-C_3N_4@rGO).[167] Differing from the pristine g-C_3N_4, the specific capacity and energy density for the optimal C-C_3N_4@rGO reach 379.7 F g^{-1} and 52.7 W h Kg^{-1} at a current density of 0.25 A g^{-1}, respectively. Meanwhile, the electrode could maintain 85% of capacity even after 10 000 cycles at a high current

density of 10 A g^{-1}. It is probable that the 3D porous structure, the oxygen-containing groups as well as the carbon near nitrogen atoms jointly contribute to its exceptional performance.

Due to the large volume change during charge/discharge, hematite α-Fe_2O_3 suffers from poor cycling performance. Xu *et al.* further synthesized g-C_3N_4/α-Fe_2O_3 hollow microspheres utilizing iron ion-containing IL.[168,169] In the CV and chronopotentiometry measurements, they display larger specific capacitance, excellent cycling stability, and higher Coulombic efficiency as compared to g-C_3N_4/α-Fe_2O_3 nanoparticles and bare α-Fe_2O_3. Limited by the poor surface area and poor electrical conductivity, the capacitance performance of pure transitional metal molybdates still cannot fulfill the practical demands. Recently, a high specific capacitance of 1275 F g^{-1} was achieved on g-C_3N_4/$NiMoO_4$ hybrid at 0.25 A g^{-1} due to the interconnected structure and the incorporation of g-C_3N_4.[170] In particular, the assembled device composed of positive g-C_3N_4/$NiMoO_4$ and a negative rGO electrode displayed good electrochemical properties with a specific capacitance of 146 F g^{-1} and energy density of 90 W h kg^{-1}. Given that transition metal sulfides possess a higher electrical conductivity and ionic intercalation than their oxide counterparts, hybridizing transition metal sulfides with gCNs is promising to improve the electrochemical energy storage performance in comparison with their single analogs. Joseph *et al.* fabricated a novel electrode material by the deposition of MoS_2 on porous g-C_3N_4 sheets.[171] The synergistic coupling between these two components could provide a maximum specific capacity of 515 C g^{-1} at a current density of 1 A g^{-1} and capacitive retention of 66%, even at a current density of 20 A g^{-1}. The g-C_3N_4/MoS_2 is then used for both positive and negative electrode material to fabricate an asymmetric two-electrode cell. Surprisingly, its energy density could attain 46 W h kg^{-1} at a high power density of 26.74 kW kg^{-1}; meanwhile the capacitance can retain 89% after 8000 cycles. In addition, g-C_3N_4 nanosheets decorated CoAl-layered double hydroxide (CoAl-LDH) nanoflowers were evaluated as a novel electrode material for supercapacitors.[172] The optimum nanocomposite exhibits a specific capacitance of 343.3 F g^{-1} at a current density of 5 A g^{-1}. They further devised an asymmetric supercapacitor by using as-obtained nanocomposite and activated carbon as positive and negative electrode materials, respectively. To our delight, the supercapacitor could deliver an energy density of 61.15 W h kg^{-1} at a power density of 13 994.66 W kg^{-1} and retain 93% of initial capacitance after 6000 cycles. More importantly, a red light emitting diode could be lightened for 20 min by two series of supercapacitors, showing the high potential for practical application. Such excellent capacitance behavior is ascribed to the integration of the redox reactivity of LDH with highly conductive g-C_3N_4, which helps the high-rate electron transfer and mass diffusion. Conductive polymers (*e.g.*, polyaniline, polypyrrole, polythiophene) are suitable candidates for pseudocapacitors because of their controllable electrical conductivity and facile redox behavior, but the slow electrolyte infiltration rate and charge transfer often results in insufficient power energy and poor cycling stability.[173] The single-layer g-C_3N_4 nanosheet easily restacks due to the van der Waals force, and the integration between g-C_3N_4 and conductive polymer may

provide an effective strategy to overcome both limitations. For example, Zhou and co-workers constructed a flower-like nanocomposite electrode (PANI/g-C_3N_4) by covering g-C_3N_4 sheets with polyaniline (PANI).[174] The obtained specific capacitance for PANI/g-C_3N_4 is as high as 585.3 F g^{-1} at 1 A g^{-1} current density, and the capacitance can retain 81.91% after 1000 cycles.

In addition, a series of electrode materials have been exploited by using gCN as both sacrificial template and N source.[133,175] For example, Yang's group pioneered the synthesis of a mesoporous carbon nanofiber (NMCNF) film with a high specific surface area and high N-doping level.[176] As expected, the NMCNFs showed a significantly improved specific capacitance and better rate capability than microporous CNFs obtained under identical experimental conditions except for the use of g-C_3N_4 nanosheets. The initial capacitance exhibits only a 3% decrease after 10 000 successive charge/discharge cycles at the high current density of 10 A g^{-1}. When used in the two-electrode cell, the NMCNF film can give an energy density of 12.5 W h kg^{-1} at a power density of 72 W kg^{-1}.

Although much noteworthy research progress has been made in porous gCN-based materials, broad room for improvement still remains; for instance, there are no reports of the supercapacitor application for gCN and metal phosphide composites. Besides, the design of a well-established porous structure would further favor mass transfer and charge accumulation. Table 3.5 gives the specific capacitance and capacitance retention of reported gCN-based electrode materials for supercapacitors.

3.4.4 Li-ion Batteries

Among all the rechargeable batteries, lithium-ion batteries (LIBs) are a dominant battery technology owing to their high energy density, superior rate capability, light weight, and prolonged cycling life. ILBs are composed of three parts, including cathode, anode, and solid-state electrolyte. Their operations rely on the movement of Li^+ between the anode and cathode. Currently, graphite and $LiCoO_2$ are used as commercial anode and cathode material for LIBs, respectively. One of the main barriers to the development of LIBs is its relatively lower theoretical capacity of 372 mA h g^{-1} for the graphite anode owing to the formation of the LiC_6 structure. Therefore, the

Table 3.5 Comparison of gCN-based electrode materials for supercapacitors.

Materials	Specific capacitance, C (F g^{-1})/current density (A g^{-1})	Capacitance retention/cycle number	References
B-g-CN	620/0.1, 312/20	101.3%/2500	166
C-C_3N_4@rGO	379.7/0.25	85%/10 000	167
g-C_3N_4/α-Fe_2O_3	580/1	96%/1000	168
g-C_3N_4/MoS_2	515/1		171
g-C_3N_4@CoAl-LDH	343.3/5		172
PANI/g-C_3N_4	584.3/1	81.91%/1000	174
N-doped Ti_2CT_x	327/1	96.2%/5000	175
NMCNFs	220/0.2	97%/1000	176

exploitation of novel alternatives is urgently needed for next-generation LIBs. In addition, nitrogen doping was confirmed to be a powerful way to increase reversible capacity and improve the cycling performance of various carbon anodes.[177] Benefiting from the high N content and open structure, the theoretical specific capacity for the g-C_3N_4 anode is 520 mA h g^{-1}, and the corresponding electrochemical reaction is as follows: g-C_3N_4 + 2Li^+ + 2e^- = Li_2-g-C_3N_4. However, there are still several bottlenecks that need to be overcome for g-C_3N_4: (1) its poor electrical conductivity greatly influences the electron transport, resulting in a limited power capability; (2) the high Li adsorption energy on pyridinic-N sites can cause a low Coulombic efficiency, irreversible capacity loss, and slow Li diffusion rate; (3) the Li intercalation easily causes its structural distortion, and thus the worst cycling stability. Consequently, g-C_3N_4 should be further optimized or functionalized to overcome these drawbacks. For example, Wang's group coupled g-C_3N_4 covalently with rGO with different ratios and further explored their application in lithium storage.[178] The optimal g-C_3N_4-rGO possesses an exceptional and stable reversible capacity of 1525 mA h g^{-1} at a high current of 100 mA g^{-1} after 50 cycles. When at a larger current density of 1000 mA g^{-1}, a reversible capacity of 943 mA h g^{-1} is attained. The superior electrochemical performance is due to its unique structural design and the synergistic effect between g-C_3N_4 and rGO. First, porous g-C_3N_4 can act as an effective substrate for the dispersion of Li^+. Meanwhile, the topological defects of rGO could offer more Li^+ diffusion paths. Moreover, the deposition of g-C_3N_4 on two sides of rGO nanosheets could enlarge the surface areas for Li^+ adsorption/intercalation. All of the above synergistically contribute to the increase of reversible capacity. Second, the g-C_3N_4-rGO possesses high structural integrity due to the covalent interactions between these two components, which is beneficial to the excellent cycling stability. Third, the improved conductivity for g-C_3N_4–rGO offers an easier charge transfer, and thus a high-rate capability. It is reported that pyridine N is crucial for a large lithium uptake, and graphitic nitrogen is unfavorable for the stability of g-C_3N_4 materials.[179] Based on this point, nitrogen-deficient g-C_3N_4 (ND-g-C_3N_4) was fabricated as anode material for improved lithium storage properties.[180] As depicted in Figure 3.13A, the typical peak at 0.5 V is related to the irreversible formation of solid-electrolyte interphase (SEI) film in the Li-insertion process. The initial irreversible capacity in the first cycle is due to the easy trap in pores. The as-obtained ND-g-C_3N_4 possesses stable reversibility as confirmed by the almost overlapped CV curves from the second cycle onward. A peak at 0 V is observed during the Li^+ intercalation process.[180] The peaks close to 0.25 and 1.25 V are due to Li extraction from graphene layers and pores/defects, respectively, whereas the two peaks at 2.6 V are attributed to Li binding with heteroatoms on the anode surface. The efficient reaction kinetics of g-C_3N_4 and ND-g-C_3N_4 is reflected by EIS (Figure 3.13B).[180] The Nyquist plots of g-C_3N_4 and ND-g-C_3N_4 exhibit a semicircle from high to medium frequency region, associated with the interfacial charge transfer between electrode and electrolyte. It is noted that ND-g-C_3N_4 exhibits a favorable charge transfer process and smaller

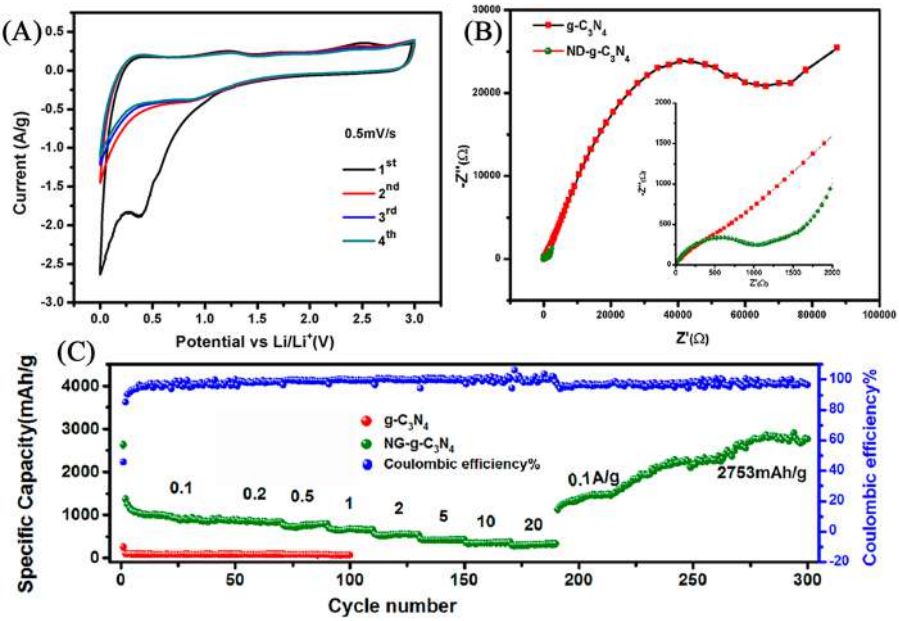

Figure 3.13 (A) The first four CV curves of ND-g-C_3N_4 electrode within a potential window of 0–3 V at a scan rate of 0.5 mV s^{-1}. (B) EIS of g-C_3N_4 and ND-g-C_3N_4 electrode. (C) The rate performance of ND-g-C_3N_4 electrode at a current density of 0.1, 0.2, 0.5, 1, 2, 5, 10, and 20 A g^{-1} and galvanostatic discharge curves for g-C_3N_4. (A–C) Reproduced from ref. 180 with permission from American Chemistry Society, Copyright 2017.

lithium-ion diffusion resistance than g-C_3N_4. The rate performance of ND-g-C_3N_4 was tested at various current densities of 0.1, 0.2, 0.5, 1, 2, 5, 10, and 20 A g^{-1} (Figure 3.13C). The first discharge and charge capacities are 2627 and 1362 mA h g^{-1}, respectively. The irreversible capacity loss originates from the incomplete Li extraction and the formation of SEI, which is consistent with the CV curve in Figure 3.12A. To our delight, the capacity for ND-g-C_3N_4 has no obvious decrease during subsequent cycling, demonstrating its excellent rate performance. The average capacity of ND-g-C_3N_4 ranges from 860 to 359 mA h g^{-1} when the current density increases from 0.1 to 10 A g^{-1}. Even at a larger current density of 20 A g^{-1}, the capacity of ND-g-C_3N_4 can reach 328 mA h g^{-1}. They could attain 1121 mA h g^{-1} instantly when the current density goes back to 0.1 A g^{-1}, showing their remarkable reversibility.[180] Surprisingly, ND-g-C_3N_4 can attain a maximum specific capacity of 2753 mA h g^{-1} after 300 cycles, whereas g-C_3N_4 only remain 61 mA h g^{-1} after 100 cycles. Importantly, Coulombic efficiency improved remarkably from 45.7% for the first cycle. The superior electrochemical performance for ND-g-C_3N_4 is related to its increased conductivity, high specific surface areas, and unique graphene backbone.[180] As for the heteroatom doping strategy, Kesavan *et al.* proposed the preparation of P-doped MCN (P-MCN-1) as LIB anode material.[181] Amazingly, the reversible

discharge capacity of P-MCN-1 could achieve 963 mA h g^{-1} at a current density of 1 A g^{-1} after 1000 cycles, which is much larger than that of g-C_3N_4, pristine MCN-1, and B-doped MCN-1. Additionally, Zhang's group fabricated interwoven N, P dual-doped hollow carbon fibers/g-C_3N_4 (*hu*CP/g-C_3N_4) as a self-supporting anode for LIB.[182] The *hu*CP/g-C_3N_4 could deliver high reversible capacities of 1030 mA h g^{-1} at 1 A g^{-1} after 1000 cycles and 360 mA h g^{-1} at 10 A g^{-1} even after 4000 cycles, as well as superior rate performance. It is probable that the highly doped N and P as well as g-C_3N_4 not only provide more defects and active sites for Li^+ intercalation/deintercalation but also endow conductive network planes. Transition metal oxides (TMOs) are widely studied as anode materials in LIBs owing to their relatively high specific capacity (600–1300 mA h g^{-1}) and superior rate capability. However, they suffer from severe volume change, particle pulverization, and aggregation during the lithiation/delithiation process. To address these issues, an effective strategy is to integrate TMOs with gCNs to limit agglomeration and buffer volume change, then higher specific capacity and better cycling performance could be realized. For example, Mohamed *et al.* demonstrated the synthesis of mesoporous CuO/O-doped g-C_3N_4 nanospheres with superior electrochemical properties.[183] The CuO/O-doped g-C_3N_4 nanospheres could deliver a higher reversible specific capacity of 738 mA h g^{-1} at a current density of 100 mA g^{-1} than pure CuO and O-doped g-C_3N_4. The capacity retention for CuO/O-doped g-C_3N_4 nanospheres is 75.3% after 100 cycles, whereas pure CuO and O-doped g-C_3N_4 nanospheres are 47% and 53%, respectively. The improved specific capacity and rate capability can be explained as follows: First, the immobilization of CuO nanospheres on O-doped g-C_3N_4 could limit its aggregation, benefiting lithium-ion transfer and electrolyte penetration. Second, the porous structure provides enough Li^+ transfer sites, thereby avoiding volume changes. Third, the narrow bandgap for O-doped g-C_3N_4 makes up the insufficient electrical conductivity. Moreover, the strong interaction between each other also ensures their enhanced structural stability during cycling. Except for the single gCNs, hybrid carbon supports were developed to anchor various TMOs.[184] For example, Wang's group successfully deposited cubic Co_3O_4 on g-C_3N_4-modified N-graphene support as a high-performance LIBs anode.[185] The use of hybrid carbon support was confirmed to synergistically promote the electrochemical property in terms of specific capacity, cycling stability, and rate capability. Apart from the single TMOs, mixed transition metal oxides such as $NiCo_2O_4$ and Zn_2GeO_4 possess higher energy storage ability due to the different working potential window of individual TMOs.[186,187] Given the high theoretical capacity of 1072 mA h g^{-1} for $ZnFe_2O_4$, Joshi *et al.* synthesized the composite (ZFCN) of $ZnFe_2O_4$ with g-CN nanosheets for the first time.[188] As a consequence, the optimal ZFCN exhibits a reversible specific capacity of 1550 mA h g^{-1} at 50 mA g^{-1} and attains 934 mA h g^{-1} at 1000 mA g^{-1} after 20 cycles. Furthermore, nano-sized spinel ferrites MFe_2O_4 (M = Mn, Ni, Cu, Co) were combined with gCN covalently functionalized nitrogen-doped graphene to improve lithium storage performance.[189]

Table 3.6 Comparison of gCN-based anode materials for LIBs.

Materials	Current density (mA g^{-1})	Capacity(mA h g^{-1})/ cycle number	References
g-C_3N_4-rGO	100	1525/50	178
ND-g-C_3N_4	100	2753/300	180
P-MCN-1	1000	963/1000	181
*hu*CP/g-C_3N_4	1000	1030/1000	182
CuO/O-doped gC_3N_4	100	738/100	183
Fe_2O_3/CN-G	50	980/50	184
Co_3O_4/CN-NG	100	1043/50	185
$NiCo_2O_4$/g-C_3N_4	100	1252/100	186
Zn_2GeO_4/g-C_3N_4	200	1370/140	187
ZFCN	1000	934/20	188
$MnFe_2O_4$/CN-NG(0.4)	100	1060/50	189
$Co_{1-x}S$@g-C_3N_4	100	789.59/210	190
SnS_2/CN	100	444.7/100	191

Similar to TMOs, transition metal sulfides have attracted tremendous interest as low-cost anode material for LIBs.[190] Bare transition metal sulfides possess higher theoretical capacity than commercial graphite, but suffer from large volume change during the charge/discharge process and structural instability, resulting in poor rate performance and fast capacity degradation. Based on this, g-C_3N_4 nanosheets were combined with a SnS_2 nanoflower by Yin *et al.* to enhance cycling stability and high-rate capacity.[191] It has been confirmed that triazole-based C_3N_5 (denoted as MCN-11) possesses a higher N content and extended gallery height than g-C_3N_4.[122] When modified with MoS_2 as an anode material in LIBs, the reversible adsorption of lithium ions on a C_3N_5/MoS_2 hybrid is prior to that on C_3N_5 and g-C_3N_4. The optimized C_3N_5/MoS_2 hybrid exhibits a 3.86 times increase in reversible capacities than mesoporous g-C_3N_4.[192] As a nitrogen-rich compound, g-C_3N_4 can also act as an ideal precursor to fabricate N-doped carbon material used in LIB anodes. For instance, Tang *et al.* prepared highly N-doped graphene-like carbon (NGC) anode material *via* the simultaneous carbonization of polypyrrole and g-C_3N_4 nanosheets.[193] In virtue of the high nitrogen content, larger specific surface areas and abundant mesopores, the resultant NGC could deliver an initial discharge capacity of 2749 mA h g^{-1} at 50 mA g^{-1} current density and stable cycling capacity of 1143 mA h g^{-1} even after 200 cycles as well as excellent rate performance of 440 mA h g^{-1} at 2 A g^{-1}. Finally, the current density and the capacity after cycling are shown in Table 3.6.

3.5 Conclusion

This chapter offers an updated overview of porous graphitic carbon nitride-based materials, including template-guided synthesis strategy, various characterization technologies, and electrochemical applications, including fuel

cell reactions (*i.e.*, oxygen reduction, alcohol oxidation, and water splitting) and energy production/storage (*i.e.*, supercapacitor and Li-ion batteries). The template-based methods, including hard/soft templates, enabled the fabrication of uniform gCNs in different porous nanostructures such as tubes, rods, spheres, and those that are three-dimensional with various compositions including metal nanoparticles, metal oxide or non-metals (*i.e.*, N, O, P, S). The crystallinity, physicochemical, and catalytic properties of gCNs highly depended on the template type and fabrication process. However, the template method requires multi-reaction steps and use of hazardous chemicals, as well as unavoidably affecting shape or merits during the template removal step. Additionally, the template method is still not emphasized deeply enough for the tailored design of one-dimensional gCN nanostructures, and it should be studied more in the future.

The electrochemical applications of gCNs were studied in-depth towards water splitting, especially HER relative to other fuel cell applications. Also, owing to the high nitrogen content, high specific surface areas, and unique structure analogous to graphite, porous gCNs have stimulated increasing attention as electrocatalysts or electrode materials in electrochemical energy storage and conversion devices. Notably, the structure of porous gCNs needs to be rationally optimized in some cases; also, its functionalization with suitable heteroatoms or metal oxides could offer desirable properties. Nevertheless, several challenges and bottlenecks for porous gCNs still need to overcome: (1) the reported gCN materials mostly focused on nanosheets or nanotubes, the synthesis of other unique structures is highly anticipated; (2) the synergistic mechanism between gCN and conductive materials are usually not clearly illustrated based on experimental results, which should be further combined with theoretical calculations; (3) the adjustment over nitrogen type and nitrogen content of gCN should be made to promote the electrochemical performance in future studies. We believe that porous gCN materials will have broader electrochemical applications in the near future. The future prospects of gCNs for electrochemical energy production and conversion technologies should be directed towards combining gCN with other materials such as porous Pt-based metal nanostructures, upconversion, MXenes, metal–organic frameworks for further developing the next generation of energy or fuel cell devices.[1–11,194–198] Additionally, efforts should be dedicated to a one-step design of novel gCNs without templates under ambient conditions.

Acknowledgements

This work was financially supported by the Natural Science Foundation of Shandong Province (ZR2020QB070), the Introduction and Cultivation Plan of Young Innovative Talents in Colleges and Universities of Shandong Province, and Key Technology Research and Development Program of Shandong Province (2019GSF111014).

References

1. H. Wang, Y. Li, C. Li, K. Deng, Z. Wang, Y. Xu, X. Li, H. Xue and L. Wang, *J. Mater. Chem. A*, 2019, **7**, 801–805.
2. S. Lu, K. Eid, D. Ge, J. Guo, L. Wang, H. Wang and H. Gu, *Nanoscale*, 2017, **9**, 1033–1039.
3. K. Eid, H. Wang, V. Malgras, S. M. Alshehri, T. Ahamad, Y. Yamauchi and L. Wang, *J. Electroanal. Chem.*, 2016, **779**, 250–255.
4. K. Eid, H. Wang, V. Malgras, Z. A. Alothman, Y. Yamauchi and L. Wang, *J. Phys. Chem. C*, 2015, **119**, 19947–19953.
5. K. Eid, H. Wang, P. He, K. Wang, T. Ahamad, S. M. Alshehri, Y. Yamauchi and L. Wang, *Nanoscale*, 2015, **7**, 16860–16866.
6. H. Wang, S. Yin, K. Eid, Y. Li, Y. Xu, X. Li, H. Xue and L. Wang, *ACS Sustainable Chem. Eng.*, 2018, **6**, 11768–11774.
7. H. Zhang, H. Wang, K. Eid and L. Wang, *Part. Part. Syst. Charact.*, 2015, **32**, 863–868.
8. C. Wei, H. Wang, K. Eid, J. Kim, J. H. Kim, Z. A. Alothman, Y. Yamauchi and L. Wang, *Chem. Eur. J.*, 2017, **23**, 637–643.
9. H. I. Abdu, K. Eid, A. M. Abdullah and X. Lu, *Data Brief*, 2020, **30**, 105520.
10. H. Idris Abdu, K. Eid, A. M. Abdullah, M. H. Sliem, A. Elzatahry and X. Lu, *Green Chem.*, 2020, **22**, 5437–5446.
11. H. I. Abdu, K. Eid, A. M. Abdullah, Z. Han, M. H. Ibrahim, D. Shan, J. Chen, A. A. Elzatahry and X. Lu, *Renew. Energy*, 2020, **153**, 998–1004.
12. K. Eid, K. A. Soliman, D. Abdulmalik, D. Mitoraj, M. H. Sleim, M. O. Liedke, H. A. El-Sayed, A. S. AlJaber, I. Y. Al-Qaradawi and O. M. Reyes, *Catal. Sci. Technol.*, 2020, **10**, 801–809.
13. K. S. Lakhi, D. H. Park, K. Al-Bahily, W. Cha, B. Viswanathan, J. H. Choy and A. Vinu, *Chem. Soc. Rev.*, 2017, **46**, 72–101.
14. Y. Zheng, J. Liu, J. Liang, M. Jaroniec and S. Z. Qiao, *Energy Environ. Sci.*, 2012, **5,** 6717–6731.
15. M. A. Ahsan, T. He, K. Eid, A. M. Abdullah, M. L. Curry, A. Du, A. R. Puente Santiago, L. Echegoyen and J. C. Noveron, *J. Am. Chem. Soc.*, 2021, **143**, 1203–1215.
16. K. Eid, M. H. Sliem, A. S. Eldesoky, H. Al-Kandari and A. M. Abdullah, *Int. J. Hydrog. Energy*, 2019, **44**, 17943–17953.
17. K. Eid, M. H. Sliem, K. Jlassi, A. S. Eldesoky, G. G. Abdo, S. Y. Al-Qaradawi, M. A. Sharaf, A. M. Abdullah and A. A. Elzatahry, *Inorg. Chem. Commun.*, 2019, **107**, 107460.
18. K. Eid and A. M. Abdullah, *Data Brief*, 2019, **26**, 104495.
19. K. Eid, M. H. Sliem, A. S. Eldesoky and A. M. Abdullah, *Data Brief*, 2019, **27**, 104734.
20. K. A. M. Eid and A. M. Abdullah, *US Pat.*, US20200239311A1, 2020.
21. K. Eid, M. H. Sliem, H. Al-Kandari, M. A. Sharaf and A. M. Abdullah, *Langmuir*, 2019, **35**, 3421–3431.
22. K. Eid, M. H. Sliem and A. M. Abdullah, *Nanoscale*, 2019, **11**, 11755–11764.

23. Y. Wang, X. Wang and M. Antonietti, *Angew. Chem. Int. Ed.*, 2012, **51**, 68–89.
24. Y. Li, X. Li, H. Zhang and Q. Xiang, *Nanoscale Horiz.*, 2020, **5**, 765–786.
25. X. Wang, S. Blechert and M. Antonietti, *ACS Catal.*, 2012, **2**, 1596–1606.
26. Y. Gong, M. Li and Y. Wang, *ChemSusChem*, 2015, **8**, 931–946.
27. J. Barrio, M. Volokh and M. Shalom, *J. Mater. Chem. A*, 2020, **8**, 11075–11116.
28. T. O. Ajiboye, A. T. Kuvarega and D. C. Onwudiwe, *Nano-Struct. Nano-Objects*, 2020, **24**, 100577.
29. X. Ma, X. Zhao, J. Sun, D. Li and X. Yang, *RSC Adv.*, 2016, **6**, 7728–7735.
30. Z. Zhao, Y. Sun and F. Dong, *Nanoscale*, 2015, **7**, 15–37.
31. A. Vinu, K. Ariga, T. Mori, T. Nakanishi, S. Hishita, D. Golberg and Y. Bando, *Adv. Mater.*, 2005, **17**, 1648–1652.
32. A. Vinu, *Adv. Funct. Mater.*, 2008, **18**, 816–827.
33. A. Vinu, P. Srinivasu, D. P. Sawant, T. Mori, K. Ariga, J.-S. Chang, S.-H. Jhung, V. V. Balasubramanian and Y. K. Hwang, *Chem. Mater.*, 2007, **19**, 4367–4372.
34. K. S. Lakhi, W. S. Cha, S. Joseph, B. J. Wood, S. S. Aldeyab, G. Lawrence, J.-H. Choy and A. Vinu, *Catal. Today*, 2015, **243**, 209–217.
35. X. Jin, V. V. Balasubramanian, S. T. Selvan, D. P. Sawant, M. A. Chari, G. Q. Lu and A. Vinu, *Angew. Chem. Int. Ed.*, 2009, **48**, 7884–7887.
36. Q. Li, J. Yang, D. Feng, Z. Wu, Q. Wu, S. S. Park, C.-S. Ha and D. Zhao, *Nano Res.*, 2010, **3**, 632–642.
37. F. Goettmann, A. Fischer, M. Antonietti and A. Thomas, *Angew. Chem. Int. Ed.*, 2006, **45**, 4467–4471.
38. S. Hwang, S. Lee and J.-S. Yu, *Appl. Surf. Sci.*, 2007, **253**, 5656–5659.
39. Y.-S. Jun, W. H. Hong, M. Antonietti and A. Thomas, *Adv. Mater.*, 2009, **21**, 4270–4274.
40. E. Z. Lee, Y. S. Jun, W. H. Hong, A. Thomas and M. M. Jin, *Angew. Chem. Int. Ed.*, 2010, **49**, 9706–9710.
41. S. Naidu Talapaneni, K. Ramadass, S. J. Ruban, M. Benzigar, K. S. Lakhi, J.-H. Yang, U. Ravon, K. Albahily and A. Vinu, *Catal. Today*, 2019, **324**, 33–38.
42. Y. Zheng, L. Lin, X. Ye, F. Guo and X. Wang, *Angew. Chem. Int. Ed.*, 2014, **53**, 11926–11930.
43. B. Lin, G. Yang, B. Yang and Y. Zhao, *Appl. Catal., B*, 2016, **198**, 276–285.
44. J. Zhang, M. Zhang, C. Yang and X. Wang, *Adv. Mater.*, 2014, **26**, 4121–4126.
45. J. Liu and M. Antonietti, *Energy Environ. Sci.*, 2013, **6**, 1486–1493.
46. J. Liu, R. Cazelles, Z. P. Chen, H. Zhou, A. Galarneau and M. Antonietti, *Phys. Chem. Chem. Phys.*, 2014, **16**, 14699–14705.
47. S. C. Lee, H. O. Lintang and L. Yuliati, *Chem. Asian J.*, 2012, **7**, 2139–2144.
48. S. Obregón, A. Vázquez, M. A. Ruíz-Gómez and V. Rodríguez-González, *Appl. Surf. Sci.*, 2019, **488**, 205–212.
49. S. N. Talapaneni, G. P. Mane, A. Mano, C. Anand, D. S. Dhawale, T. Mori and A. Vinu, *ChemSusChem*, 2012, **5**, 700–708.
50. J. Xu, T. Chen, X. Wang, B. Xue and Y.-X. Li, *Catal. Sci. Technol.*, 2014, **4**, 2126–2133.

51. Z. Zhao, Y. Dai, J. Lin and G. Wang, *Chem. Mater.*, 2014, **26**, 3151–3161.
52. G. P. Mane, D. S. Dhawale, C. Anand, K. Ariga, Q. Ji, M. A. Wahab, T. Mori and A. Vinu, *J. Mater. Chem. A*, 2013, **1,** 2913–2920.
53. L. Gu, J. Wang, Z. Zou and X. Han, *J. Hazard. Mater.*, 2014, **268**, 216–223.
54. M. Ovcharov, N. Shcherban, S. Filonenko, A. Mishura, M. Skoryk, V. Shvalagin and V. Granchak, *Mater. Sci. Eng., B*, 2015, **202**, 1–7.
55. S.-W. Bian, Z. Ma and W.-G. Song, *J. Phys. Chem. C*, 2009, **113**, 8668–8672.
56. X.-H. Li, J. Zhang, X. Chen, A. Fischer, A. Thomas, M. Antonietti and X. Wang, *Chem. Mater.*, 2011, **23**, 4344–4348.
57. Z. Shu, C. Xie, J. Zhou, T. Li, Y. Chen, W. Wang, Y. Tan and Z. Zhao, *J. Alloys Compd.*, 2018, **747**, 140–148.
58. W. Xing, W. Tu, Z. Han, Y. Hu, Q. Meng and G. Chen, *ACS Energy Lett.*, 2018, **3**, 514–519.
59. D. Chen, J. Yang and H. Ding, *Appl. Surf. Sci.*, 2017, **391**, 384–391.
60. J. Wang, C. Zhang, Y. Shen, Z. Zhou, J. Yu, Y. Li, W. Wei, S. Liu and Y. Zhang, *J. Mater. Chem. A*, 2015, **3**, 5126–5131.
61. J. Yan, X. Han, X. Zheng, J. Qian, J. Liu, X. Dong and F. Xi, *Mater. Res. Bull.*, 2017, **94**, 423–427.
62. X. D. Sun, Y. Y. Li, J. Zhou, C. Hai Ma, Y. Wang and J. H. Zhu, *J. Colloid Interface Sci.*, 2015, **451**, 108–116.
63. Q. Liang, Z. Li, X. Yu, Z. H. Huang, F. Kang and Q. H. Yang, *Adv. Mater.*, 2015, **27**, 4634–4639.
64. Y. Li, Z. Ruan, Y. He, J. Li, K. Li, Y. Jiang, X. Xu, Y. Yuan and K. Lin, *Appl. Catal., B*, 2018, **236**, 64–75.
65. H. Gao, J. Xu, J. Zhou, S. Zhang and R. Zhou, *J. Colloid Interface Sci.*, 2020, **570**, 125–134.
66. S. Joseph, D. M. Kempaiah, M. Benzigar, A. V. Baskar, S. N. Talapaneni, S. H. Jhung, D.-H. Park and A. Vinu, *J. Mater. Chem. A*, 2017, **5**, 21542–21549.
67. J. M. Fan, J. J. Chen, Q. Zhang, B. B. Chen, J. Zang, M. S. Zheng and Q. F. Dong, *ChemSusChem*, 2015, **8**, 1856–1861.
68. Z. Yang, Y. Zhang and Z. Schnepp, *J. Mater. Chem. A*, 2015, **3**, 14081–14092.
69. Y. Wang, X. Wang, M. Antonietti and Y. Zhang, *ChemSusChem*, 2010, **3**, 435–439.
70. H. Yan, *Chem. Commun.*, 2012, **48,** 3430–3432.
71. Q. Fan, J. Liu, Y. Yu and S. Zuo, *RSC Adv.*, 2014, **4**, 61877–61883.
72. W. Shen, L. Ren, H. Zhou, S. Zhang and W. Fan, *J. Mater. Chem.*, 2011, **21,** 3890–3894.
73. H. Chen, J. Yao, P. Qiu, C. Xu, F. Jiang and X. Wang, *Mater. Res. Bull.*, 2017, **91**, 42–48.
74. M. Peer, M. Lusardi and K. F. Jensen, *Chem. Mater.*, 2017, **29**, 1496–1506.
75. M. B. Idris and S. Devaraj, *Electrochim. Acta*, 2019, **303**, 219–230.
76. R. L. Vekariya, *J. Mol. Liq.*, 2017, **227**, 44–60.
77. Y. Wang, X. Wang, M. Antonietti and Y. Zhang, *ChemSusChem*, 2010, **3**, 435–439.

78. Y. Wang, J. Zhang, X. Wang, M. Antonietti and H. Li, *Angew. Chem. Int. Ed.*, 2010, **49**, 3356–3359.
79. Z. Lin and X. Wang, *ChemSusChem*, 2014, **7**, 1547–1550.
80. S. Zhao, Y. Zhang, Y. Zhou, Y. Wang, K. Qiu, C. Zhang, J. Fang and X. Sheng, *Carbon*, 2018, **126**, 247–256.
81. S. Zhao, Y. Zhang, J. Fang, H. Zhang, Y. Wang, Y. Zhou, W. Chen and C. Zhang, *ACS Sustainable Chem. Eng.*, 2018, **6**, 8291–8299.
82. S. Zhao, J. Fang, Y. Wang, Y. Zhang, Y. Zhou and S. Zhuo, *J. Colloid Interface Sci.*, 2020, **561**, 601–608.
83. B. Babu, J. Shim, A. N. Kadam and K. Yoo, *Catal. Commun.*, 2019, **124**, 123–127.
84. Y. Zhang, J. Liu, G. Wu and W. Chen, *Nanoscale*, 2012, **4**, 5300–5303.
85. L. Shi, L. Liang, F. Wang, M. Liu, T. Liang, K. Chen and J. Sun, *RSC Adv.*, 2015, **5**, 63264–63270.
86. F. He, G. Chen, Y. Yu, Y. Zhou, Y. Zheng and S. Hao, *Chem. Commun.*, 2015, **51**, 425–427.
87. X. Li, D. Chen, N. Li, Q. Xu, H. Li, J. He and J. Lu, *ACS Sustainable Chem. Eng.*, 2018, **6**, 11063–11070.
88. C. Liu, Y. Zhang, F. Dong, X. Du and H. Huang, *J. Phys. Chem. C*, 2016, **120**, 10381–10389.
89. B. Fei, Y. Tang, X. Wang, X. Dong, J. Liang, X. Fei, L. Xu, Y. Song and F. Zhang, *Mater. Res. Bull.*, 2018, **102**, 209–217.
90. W. Iqbal, B. Yang, X. Zhao, M. Waqas, M. Rauf, C. Guo, J. Zhang and Y. Mao, *Appl. Catal. A*, 2019, **573**, 13–21.
91. J. Wu, N. Li, H.-B. Fang, X. Li, Y.-Z. Zheng and X. Tao, *Chem. Eng. J.*, 2019, **358**, 20–29.
92. W. Iqbal, L. Wang, X. Tan and J. Zhang, *J. Environ. Chem. Eng.*, 2017, **5**, 3500–3507.
93. S. N. Talapaneni, S. Anandan, G. P. Mane, C. Anand, D. S. Dhawale, S. Varghese, A. Mano, T. Mori and A. Vinu, *J. Mater. Chem.*, 2012, **22**, 9831–9840.
94. X. Wu, H. Ma, W. Zhong, J. Fan and H. Yu, *Appl. Catal., B*, 2020, **271**, 118899.
95. Q. Lu, H. Wang, K. Eid, Z. A. Alothman, V. Malgras, Y. Yamauchi and L. Wang, *Chem. Asian J.*, 2016, **11**, 1939–1944.
96. H. Qian, S. Chen, Y. Fu and X. Wang, *J. Power Sources*, 2015, **300**, 41–48.
97. M. Kim, S. Hwang and J.-S. Yu, *J. Mater. Chem.*, 2007, **17**, 1656–1659.
98. X. Lu, H. Wang, S. Zhang, D. Cui and Q. Wang, *Solid State Sci.*, 2009, **11**, 428–432.
99. N. Mansor, A. B. Jorge, F. Cora, C. Gibbs, R. Jervis, P. F. McMillan, X. Wang and D. J. Brett, *J. Phys. Chem. C*, 2014, **118**, 6831–6838.
100. C.-Z. Li, Z.-B. Wang, X.-L. Sui, L.-M. Zhang, D.-M. Gu and S. Gu, *J. Mater. Chem. A*, 2014, **2**, 20139–20146.
101. Z. Li, R. Lin, Z. Liu, D. Li, H. Wang and Q. Li, *Electrochim. Acta*, 2016, **191**, 606–615.
102. H. Wang, L. Thia, N. Li, X. Ge, Z. Liu and X. Wang, *ACS Catal.*, 2015, **5**, 3174–3180.

103. W. Zhang, Y. Fu, J. Wang and X. Wang, *Adv. Mater. Interfaces*, 2017, **4**, 1601219.
104. L. Yang, X. Wang, D. Liu, G. Cui, B. Dou and J. Wang, *Appl. Catal. B*, 2020, **263**, 118304.
105. R. Nazir, A. Kumar, M. Ali Saleh Saad and S. Ali, *J. Colloid Interface Sci.*, 2020, **578**, 726–737.
106. I. S. Pieta, A. Rathi, P. Pieta, R. Nowakowski, M. Hołdynski, M. Pisarek, A. Kaminska, M. B. Gawande and R. Zboril, *Appl. Catal. B*, 2019, **244**, 272–283.
107. A. Lewalska-Graczyk, P. Pieta, G. Garbarino, G. Busca, M. Holdynski, G. Kalisz, A. Sroka-Bartnicka, R. Nowakowski, M. Naushad, M. B. Gawande, R. Zbořil and I. S. Pieta, *ACS Sustainable Chem. Eng.*, 2020, **8**, 7244–7255.
108. X. Teng, A. Shan, Y. Zhu, R. Wang and W.-M. Lau, *Electrochim. Acta*, 2020, **353**, 136542.
109. T. Bhowmik, M. K. Kundu and S. Barman, *Int. J. Hydrogen Energy*, 2017, **42**, 212–217.
110. M. Sadhukhan, M. K. Kundu, T. Bhowmik and S. Barman, *Int. J. Hydrogen Energy*, 2017, **42**, 9371–9383.
111. K. Gong, F. Du, Z. Xia, M. Durstock and L. Dai, *Science*, 2009, **323**, 760–764.
112. S. M. Lyth, Y. Nabae, S. Moriya, S. Kuroki, M.-a. Kakimoto, J.-i. Ozaki and S. Miyata, *J. Phys. Chem. C*, 2009, **113**, 20148–20151.
113. H.-S. Zhai, L. Cao and X.-H. Xia, *Chin. Chem. Lett.*, 2013, **24**, 103–106.
114. K. Kwon, Y. J. Sa, J. Y. Cheon and S. H. Joo, *Langmuir*, 2012, **28**, 991–996.
115. S. Pandiaraj, H. B. Aiyappa, R. Banerjee and S. Kurungot, *Chem. Commun.*, 2014, **50**, 3363–3366.
116. Y. Zheng, Y. Jiao, J. Chen, J. Liu, J. Liang, A. Du, W. Zhang, Z. Zhu, S. C. Smith, M. Jaroniec, G. Q. Lu and S. Z. Qiao, *J. Am. Chem. Soc.*, 2011, **133**, 20116–20119.
117. S. Yang, X. Feng, X. Wang and K. Mullen, *Angew. Chem. Int. Ed.*, 2011, **50**, 5339–5343.
118. Y. Sun, C. Li, Y. Xu, H. Bai, Z. Yao and G. Shi, *Chem. Commun.*, 2010, **46**, 4740–4742.
119. J. Tian, R. Ning, Q. Liu, A. M. Asiri, A. O. Al-Youbi and X. Sun, *ACS Appl. Mater. Interfaces*, 2014, **6**, 1011–1017.
120. M. Amiri, S. K. Konda and A. Chen, *ChemElectroChem*, 2017, **4**, 997–1001.
121. J. Liang, Y. Zheng, J. Chen, J. Liu, D. Hulicova-Jurcakova, M. Jaroniec and S. Z. Qiao, *Angew. Chem. Int. Ed.*, 2012, **51**, 3892–3896.
122. I. Y. Kim, S. Kim, X. Jin, S. Premkumar, G. Chandra, N. S. Lee, G. P. Mane, S. J. Hwang, S. Umapathy and A. Vinu, *Angew. Chem. Int. Ed.*, 2018, **57**, 17135–17140.
123. Y. Gong, J. Wang, Z. Wei, P. Zhang, H. Li and Y. Wang, *ChemSusChem*, 2014, **7**, 2303–2309.
124. Y. Qiu, L. Xin, F. Jia, J. Xie and W. Li, *Langmuir*, 2016, **32**, 12569–12578.
125. V. Di Noto, E. Negro, S. Polizzi, P. Riello and P. Atanassov, *Appl. Catal. B*, 2012, **111–112**, 185–199.

126. E. Negro, K. Vezzù, F. Bertasi, P. Schiavuta, L. Toniolo, S. Polizzi and V. Di Noto, *ChemElectroChem*, 2014, **1**, 1359–1369.
127. I. H. Lee, J. Cho, K. H. Chae, M. K. Cho, J. Jung, J. Cho, H. J. Lee, H. C. Ham and J. Y. Kim, *Appl. Catal. B*, 2018, **237**, 318–326.
128. H. E. Kim, I. H. Lee, J. Cho, S. Shin, H. C. Ham, J. Y. Kim and H. Lee, *ChemElectroChem*, 2019, **6**, 4757–4764.
129. Z. Pei, J. Zhao, Y. Huang, Y. Huang, M. Zhu, Z. Wang, Z. Chen and C. Zhi, *J. Mater. Chem. A*, 2016, **4**, 12205–12211.
130. F. He, K. Li, C. Yin, Y. Wang, H. Tang and Z. Wu, *Carbon*, 2017, **114**, 619–627.
131. S. Sarkar, N. Kamboj, M. Das, T. Purkait, A. Biswas and R. S. Dey, *Inorg. Chem.*, 2020, **59**, 1332–1339.
132. J. Jin, H. Wu, S. Wang, Y. Ding and S. Yin, *Int. J. Hydrogen Energy*, 2017, **42**, 20579–20588.
133. C. Yang, J. Liu, X. Song, L. Zhao, P. Zhang and L. Gao, *Mater. Lett.*, 2020, **266**, 127498.
134. N. Bhandary, P. P. Ingole and S. Basu, *ChemistrySelect*, 2017, **2**, 8151–8157.
135. M. Shalom, S. Gimenez, F. Schipper, I. Herraiz-Cardona, J. Bisquert and M. Antonietti, *Angew. Chem. Int. Ed.*, 2014, **53**, 3654–3658.
136. Y. Zheng, Y. Jiao, Y. Zhu, L. H. Li, Y. Han, Y. Chen, A. Du, M. Jaroniec and S. Z. Qiao, *Nat. Commun.*, 2014, **5**, 3783.
137. J. Duan, S. Chen, M. Jaroniec and S. Z. Qiao, *ACS Nano*, 2015, **9**, 931–940.
138. P. Fageria, K. Y. Sudharshan, R. Nazir, M. Basu and S. Pande, *Electrochim. Acta*, 2017, **258**, 1273–1283.
139. Y. Liu, X. Xu, J. Zhang, H. Zhang, W. Tian, X. Li, M. O. Tade, H. Sun and S. Wang, *Appl. Catal. B*, 2018, **239**, 334–344.
140. M. Cao, X. Zhang, J. Qin and R. Liu, *ACS Sustainable Chem. Eng.*, 2018, **6**, 16198–16204.
141. S. Riyajuddin, S. K. Tarik Aziz, S. Kumar, G. D. Nessim and K. Ghosh, *ChemCatChem*, 2020, **12**, 1394–1402.
142. J. Gao, Y. Wang, S. Zhou, W. Lin and Y. Kong, *ChemCatChem*, 2017, **9**, 1708–1715.
143. D. Rodriguez-Padron, A. R. Puente-Santiago, M. Cano, A. Caballero, M. J. Munoz-Batista and R. Luque, *ACS Appl. Mater. Interfaces*, 2020, **12**, 2207–2215.
144. S. S. Shinde, A. Sami and J.-H. Lee, *ChemCatChem*, 2015, **7**, 3873–3880.
145. Y. Peng, W. Pan, N. Wang, J. E. Lu and S. Chen, *ChemSusChem*, 2018, **11**, 130–136.
146. A. M. Paul, A. Sajeev, R. Nivetha, K. Gothandapani, P. Bhardwaj, K. Govardhan, V. Raghavan, G. Jacob, R. Sellapan, S. K. Jeong and A. N. Grace, *Diamond Relat. Mater.*, 2020, **107**, 107899.
147. Q. Shi, C. Zhu, D. Du and Y. Lin, *Chem. Soc. Rev.*, 2019, **48**, 3181–3192.
148. Y. Zhao, R. Nakamura, K. Kamiya, S. Nakanishi and K. Hashimoto, *Nat. Commun.*, 2013, **4**, 2390.
149. J. Tian, Q. Liu, A. M. Asiri, K. A. Alamry and X. Sun, *ChemSusChem*, 2014, **7**, 2125–2130.

150. T. Y. Ma, S. Dai, M. Jaroniec and S. Z. Qiao, *Angew. Chem., Int. Ed.*, 2014, **53**, 7281–7285.
151. M. Zhu, S. Yu, R. Ge, L. Feng, Y. Yu, Y. Li and W. Li, *ACS Appl. Energy Mater.*, 2019, **2**, 4718–4729.
152. X. Han, W. Zhang, X. Ma, C. Zhong, N. Zhao, W. Hu and Y. Deng, *Adv. Mater.*, 2019, **31**, 1808281.
153. S. Wang, P. He, L. Jia, M. He, T. Zhang, F. Dong, M. Liu, H. Liu, Y. Zhang, C. Li, J. Gao and L. Bian, *Appl. Catal. B*, 2019, **243**, 463–469.
154. T. Y. Ma, J. Ran, S. Dai, M. Jaroniec and S. Z. Qiao, *Angew. Chem. Int. Ed.*, 2015, **54**, 4646–4650.
155. G. Zhang, P. Wang, W. T. Lu, C. Y. Wang, Y. K. Li, C. Ding, J. Gu, X. S. Zheng and F. F. Cao, *ACS Appl. Mater. Interfaces*, 2017, **9**, 28566–28576.
156. B. Jiang, T. Wang, Y. Cheng, F. Liao, K. Wu and M. Shao, *ACS Appl. Mater. Interfaces*, 2018, **10**, 39161–39167.
157. W. Niu, Z. Li, K. Marcus, L. Zhou, Y. Li, R. Ye, K. Liang and Y. Yang, *Adv. Energy Mater.*, 2018, **8**, 1701642.
158. H. Yang, H. Guo, K. Pang, P. Fan, X. Li, W. Ren and R. Song, *Nanoscale*, 2020, **12**, 7024–7034.
159. B. Z. Desalegn, H. S. Jadhav and J. G. Seo, *ChemCatChem*, 2019, **11**, 2870–2878.
160. O. Alduhaish, M. Ubaidullah, A. M. Al-Enizi, N. Alhokbany, S. M. Alshehri and J. Ahmed, *Sci. Rep.*, 2019, **9**, 14139.
161. M. Zulqarnain, A. Shah, M. A. Khan, F. Jan Iftikhar and J. Nisar, *Sci. Rep.*, 2020, **10**, 6328.
162. A. Borenstein, O. Hanna, R. Attias, S. Luski, T. Brousse and D. Aurbach, *J. Mater. Chem. A*, 2017, **5**, 12653–12672.
163. M. Ashritha and K. Hareesh, *J. Energy Storage*, 2020, **32**, 101840.
164. M. Ghaemmaghami and R. Mohammadi, *Sustainable Energy Fuels*, 2019, **3**, 2176–2204.
165. M. Tahir, C. Cao, F. K. Butt, F. Idrees, N. Mahmood, Z. Ali, I. Aslam, M. Tanveer, M. Rizwan and T. Mahmood, *J. Mater. Chem. A*, 2013, **1**, 13949–13955.
166. L. Kong, Q. Chen, X. Shen, C. Xia, Z. Ji and J. Zhu, *Electrochim. Acta*, 2017, **245**, 249–258.
167. Y. Ding, Y. Tang, L. Yang, Y. Zeng, J. Yuan, T. Liu, S. Zhang, C. Liu and S. Luo, *J. Mater. Chem. A*, 2016, **4**, 14307–14315.
168. L. Liu, J. Wang, C. Wang and G. Wang, *Appl. Surf. Sci.*, 2016, **390**, 303–310.
169. L. Xu, J. Xia, H. Xu, S. Yin, K. Wang, L. Huang, L. Wang and H. Li, *J. Power Sources*, 2014, **245**, 866–874.
170. X. Xu, Q. Liu, T. Wei, Y. Zhao and X. Zhang, *J. Mater. Sci.: Mater. Electron.*, 2019, **30**, 5109–5119.
171. N. Joseph and A. C. Bose, *Electrochim. Acta*, 2019, **301**, 401–410.
172. S. Sanati and Z. Rezvani, *Chem. Eng. J.*, 2019, **362**, 743–757.
173. G. Dong, H. Fan, K. Fu, L. Ma, S. Zhang, M. Zhang, J. Ma and W. Wang, *Compos. B Eng.*, 2019, **162**, 369–377.
174. S.-X. Zhou, X.-Y. Tao, J. Ma, L.-T. Guo, Y.-B. Zhu, H.-L. Fan, Z.-S. Liu and X.-Y. Wei, *Vacuum*, 2018, **149**, 175–179.

175. Y. Yoon, M. Lee, S. K. Kim, G. Bae, W. Song, S. Myung, J. Lim, S. S. Lee, T. Zyung and K.-S. An, *Adv. Energy Mater.*, 2018, **8,** 1703173.
176. Q. Liang, L. Ye, Q. Xu, Z.-H. Huang, F. Kang and Q.-H. Yang, *Carbon*, 2015, **94**, 342–348.
177. W. Ren, D. Li, H. Liu, R. Mi, Y. Zhang, L. Dong and L. Dong, *Electrochim. Acta*, 2013, **105**, 75–82.
178. Y. Fu, J. Zhu, C. Hu, X. Wu and X. Wang, *Nanoscale*, 2014, **6**, 12555–12564.
179. M. Hankel, D. Ye, L. Wang and D. J. Searles, *J. Phys. Chem. C*, 2015, **119**, 21921–21927.
180. J. Chen, Z. Mao, L. Zhang, D. Wang, R. Xu, L. Bie and B. D. Fahlman, *ACS Nano*, 2017, **11**, 12650–12657.
181. T. Kesavan, T. Partheeban, M. Vivekanantha, N. Prabu, M. Kundu, P. Selvarajan, S. Umapathy, A. Vinu and M. Sasidharan, *ACS Appl. Mater. Interfaces*, 2020, **12**, 24007–24018.
182. H. Tao, L. Xiong, S. Du, Y. Zhang, X. Yang and L. Zhang, *Carbon*, 2017, **122**, 54–63.
183. H. S. H. Mohamed, L. Wu, C. F. Li, Z. Y. Hu, J. Liu, Z. Deng, L. H. Chen, Y. Li and B. L. Su, *ACS Appl. Mater. Interfaces*, 2019, **11**, 32957–32968.
184. M. Shi, T. Wu, X. Song, J. Liu, L. Zhao, P. Zhang and L. Gao, *J. Mater. Chem. A*, 2016, **4**, 10666–10672.
185. W. Zhang, Y. Fu and X. Wang, *Appl. Surf. Sci.*, 2018, **439**, 447–455.
186. Y. Liu, S. He, Y. Zhong, X. Xu and Z. Shao, *J. Alloys Compd.*, 2019, **805**, 522–530.
187. X. Li, Y. Feng, M. Li, W. Li, H. Wei and D. Song, *Adv. Funct. Mater.*, 2015, **25**, 6858–6866.
188. B. Joshi, E. Samuel, T.-G. Kim, C.-W. Park, Y.-I. Kim, M. T. Swihart, W. Y. Yoon and S. S. Yoon, *J. Alloys Compd.*, 2018, **768**, 525–534.
189. J. Tian, D. Wang, S. Li, Y. Pei, M. Qiao, Z.-H. Li, J. Zhang and B. Zong, *ACS Sustainable Chem. Eng.*, 2019, **8**, 594–603.
190. H. Zhang, J. Yin, Y. Liu, Z. Lang, Y. Liu, W. He, L. Ma, J. Cui and J. Sun, *J. Electroanal. Chem.*, 2020, 862.
191. X. Tian, Y.-J. Sun, J.-Y. He, X.-J. Wang, J. Zhao, S.-Z. Qiao and F.-T. Li, *J. Mater. Chem. A*, 2019, **7**, 7628–7635.
192. S. Kim, M. Hankel, W. Cha, G. Singh, J. M. Lee, I. Y. Kim and A. Vinu, *Nano Energy*, 2020, **72,** 104702.
193. Y. Tang, J. Chen, X. Wang, X. Wang, Y. Zhao, Z. Mao and D. Wang, *Electrochim. Acta*, 2019, **324,** 134880.
194. M. M. Abualrejal, K. Eid, R. Tian, L. Liu, H. Chen, A. M. Abdullah and Z. Wang, *Chem. Sci.*, 2019, **10**, 7591–7599.
195. M. M. Abualrejal, K. Eid, A. M. Abdullah, A. A. Numan, H. Chen, H. Zhang and Z. Wang, *Microchim. Acta*, 2020, **187**, 1–13.
196. X. Xu, T. Yang, Q. Zhang, W. Xia, Z. Ding, K. Eid, A. M. Abdullah, M. S. A. Hossain, S. Zhang and J. Tang, *Chem. Eng. J.*, 2020, **390**, 124493.
197. Y. Ibrahim, A. Mohamed, A. M. Abdelgawad, K. Eid, A. M. Abdullah and A. Elzatahry, *Nanomaterials*, 2020, **10**, 1916.
198. K. Jlassi, K. Eid, M. H. Sliem, A. M. Abdullah, M. M. Chehimi and I. Krupa, *Environ. Sci. Eur.*, 2020, **32**, 1–13.

CHAPTER 4

Graphitic Carbon Nitride Nanostructures as Potent Catalysts for Water Splitting: Theoretical Insights

AHMED S. MOHAMED[a], ALI ABDULLA[b], YASSMIN IBRAHIM[b,c], KAMEL EID*[d], ABOUBAKR M. ABDULLAH*[b] AND KENNETH I. OZOEMENA*[c]

[a]Department of Mechanical and Industrial Engineering, College of Engineering, Qatar University, Doha 2713, Qatar; [b]Center for Advanced Materials, Qatar University, Doha 2713, Qatar; [c]Molecular Sciences Institute, School of Chemistry, University of the Witwatersrand, Private Bag 3, P O Wits, Braamfontein, Johannesburg 2050, South Africa; [d]Gas Processing Center College Center for Advanced Materials, Qatar University, Doha 2713, Qatar
*E-mail: bakr@qu.edu.qa, kenneth.ozoemena@wits.ac.za, kamel.eid@qu.edu.qa

4.1 Introduction

Energy and global warming demands represent some of the key challenges of the human race, so it critical to find new and clean energy resources and systems (such as fuel cells, solar and biomass-derived electricity), and water resources (*i.e.*, desalination and wastewater treatment) along with decreasing global warming (*i.e.*, reducing emission or conversion or capture of

Nanoscience & Nanotechnology Series No. 51
Carbon Nitride Nanostructures for Sustainable Energy Production and Environmental Remediation
Edited by Kamel Abdelmoniem Mohamed Eid and Aboubakr M. Abdullah

Published by the Royal Society of Chemistry, www.rsc.org

greenhouse gasses).[1–7] Water splitting is of particular interest as a sustainable and clean energy source due to its high energy yield and zero emissions.[8–10] Finding an efficient, durable, low-cost catalyst is the main barrier precluding large-scale application of water-splitting-based fuel cells.[8–10] Various metal-oxides (such as TiO_2, Fe_2O_3, $BiVO_4$, and Cu_2O), noble metals (*i.e.*, Pt, Pd, Ru, and Ir), perovskite (*i.e.*, $Ni_{0.5}Co_{0.5}P$/carbon, CoPi-$LaTaON_2$, and $NdBaMn_2O_{5.5}$), and carbon materials (*i.e.*, carbon nanotubes, graphene oxide, and carbon dots) have been developed for efficient water splitting.[8,9,11–15]

Carbon nitride (gCN) materials are important in various energy and environmental applications in the last ten years.[16–19] gCNs were used for the first time for efficient photocatalytic water reduction in 2009.[20] Unlike other catalysts, gCNs possess exceptional thermal stability (up to 600 °C), chemical stability (*i.e.*, acidic/alkaline media and organic solvents), optical/semiconducting properties (*i.e.*, high electronic density, visible light absorption, great photocurrent density, the low band gap of 2.7 eV), and catalytic properties (*i.e.*, conductivity, active sites, high surface area, and inner vacancies).[21–25] Also, gCNs can be easily prepared from abundant, green, and inexpensive resources (*i.e.*, urea, melamine, dicyandiamide, and cyanuric acid) in a high yield (up to kilogram scale), making gCNs feasible for large-scale applications.[26] The dipole of nitrogen anion-carbon cation bond of gCN is preferred for electrophilic and nucleophilic attack, which can boost water splitting under low potential besides tolerating the adsorption of intermediates.[19] Moreover, gCNs could be easily integrated with other catalysts (*i.e.*, noble metals, transition metals, perovskites, and carbonaceous materials) for boosting the activity and durability of the water-splitting performance.[21–25]

Inspired by these merits, the number of research articles related to gCNs for water splitting has increased significantly in the last ten years, resulting in over 22 000 articles, including only 1547 about water splitting and 4237 related to photocatalytics in the ISI Web of Science (Figure 4.1). There are

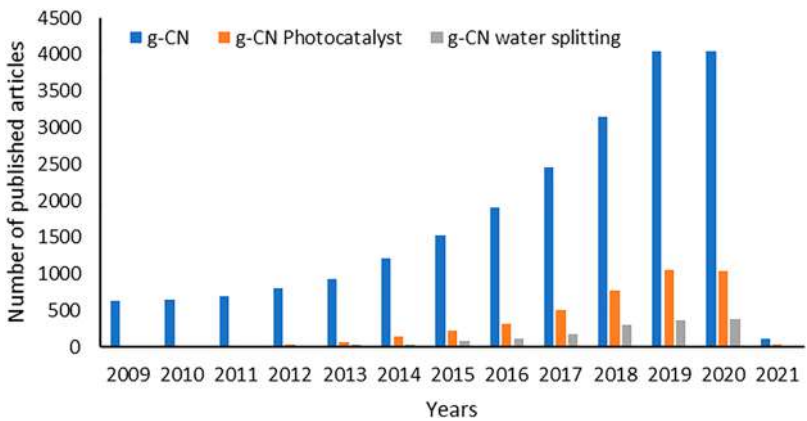

Figure 4.1 Number of articles related to gCNs obtained from the ISI Web of Science, 19th December 2020. The keywords are "carbon nitride", "carbon nitride photocatalyst", and "carbon nitride water splitting".

several article reviews about the utilization of gCNs for various energy and environmental applications, but without enough emphasis on the fundamental insights.[22,25,27–29]

Unlike previous reviews and chapters, this chapter emphasizes the recent advances in gCNs as electrodes for water-splitting reactions from a theoretical perspective rooting from self-standing gCNs to transition metals/gCNs, noble metals/gCNs, and doped gCNs for both water oxidation and water reduction. In addition, attempts have been made to emphasize the fundamentals and mechanisms of water-splitting reactions on gCN materials and their challenges.

4.2 Density Functional Theory

The current growth of research aspects of water splitting may partially be attributed to the development of density functional theory (DFT).[30] DFT calculations boosted the research on water splitting by enabling in-depth investigation up to the atomic scale of the known catalysts.[30] It also simulates the intrinsic reaction that may cost time and effort in empirical work. Several physical and chemical preparation methods demand special experience and high cost. Despite these challenges, a suitable catalyst appears after the whole fabrication process. Using DFT allows one to expand the investigation of new catalysts and to better understand and tune their physico–chemical properties for improved performance. By analyzing catalysts and calculating their performance and enhancement, DFT can enable the design of new catalysts.[30,31] Although a considerable number of functional models are available, DFT efficiency goes beyond them in many cases.[32] Hohenberg, Kohn, and Sharm introduced it and proved that ground-state properties could be determined with no *N*-electron wavefunction interaction. With time, DFT became enhanced to release robust results and efficient configuration, predicting new catalysts.[31] The excellent work on DFT led to the Nobel Prize in Chemistry in 1998, shared by Walter Kohn and John Pople. Prediction of material structures and photocatalytic properties is a crucial achievement of DFT. Simulated annealing, an evolutionary algorithm, and topological modeling methods are of great significance to structure prediction.[31] On the other hand, band gap, UV absorption, and charge carrier separation are determinants of catalytic properties that could be handled with DFT. Local density approximation (LDA) and its correction generalized gradient approximation (GGA) could be effective for systems with a diversity of electron density. Improving the accuracy of calculation and electronic structures is a crucial feature of hybrid functionals.[31] Becke exchange/Lee–Yang–Parr correlation (BLYP), and Perdew–Burke–Ernzerhof (PBE) are also examples of semi-empirical functionals. The expanded usage of DFT returns to its ability to mimic material structures, demonstrate material electronic properties, and calculate reaction interaction energies.[32] Density of state is favorable to calculate energy band gap and analyze electronic structure. *Ab initio* molecular dynamics (AIMD) is a simulation model used for observation. However, balancing the DFT model is a trade-off between high accuracy and cost.[32]

4.3 Water Splitting

Water splitting is an energy conversion reaction that is essential for mankind to achieve reliance on renewable energy. The ultimate objective of water splitting is to generate hydrogen and oxygen using an environmentally benign method.[33] Water splitting is an arduous reaction that requires 237 kJ mol^{-1} of energy in standard Gibb's free energy (ΔG).[33–35] This reaction produces oxygen and hydrogen in a molecular ratio of 1 : 2 (eqn (4.1)) and needs to be boosted by additional energy such as solar energy.[35]

$$2H_2O \rightarrow 2H_2 + O_2 \tag{4.1}$$

To create this photocatalytic reaction, the semiconductor should possess some standards to be theoretically capable of handling the reaction.[35] The valence band (VB) of the semiconductor should be greater than that of the H_2O oxidation potential (+1.23 V *vs.* normal hydrogen electrode (NHE)), while the conduction band (CB) should be lower than that of the reduction potential (0 V *vs.* NHE). However, the generation of H_2 and O_2 gases after water splitting results in water formation again.[34] Thus, a suitable semiconductor for water splitting should have a band gap energy of 1.23 eV,[33] while the band gap for practical reactions should exceed 1.8 eV. This challenging trade-off demands proper design of the semiconductor since the light absorption is enhanced by a narrow band gap. However, the driving force required for a water-splitting sub-reaction is relatively proportional to the band gap.[33] Also, the semiconductor should be stable against corrosion in the electrolyte solution under light irradiation[35] besides high visible light absorption.[31] Following the Nernst equation, the pH value affects the potential of the hydrogen evolution reaction (HER) and oxygen evolution reaction (OER).[33] It is a huge challenge and uphill reaction to apply the HER and OER reaction at the same conditions.[36]

The HER is identified to be at the core of understanding the mechanism behind electrochemical water splitting. Hence, HER always requires an effective and durable catalyst to meet the requirements of industrial applications.[37–39] Over the years, many investigations have proposed a wide variety of catalysts. However, Pt supported on carbon exhibited excellent HER properties, in which high current density and small Tafel slope were achieved.[40] However, the Pt catalyst's relatively high cost paved the way to develop alternatives to accomplish sustainable hydrogen production with comparable electrocatalytic properties, including stabilities.[41,42]

Although numerous investigations have presented efficient HER electrocatalysts, mostly transition metals (Co, Ni, Fe, MO),[43–55] they are prone to corrosion during acidic photovoltaic (PV)–electrolysis, in which water splits into H_2 and O_2. Transition metal-free photocatalysts have attracted much interest in recent years due to potential advantages such as nontoxicity, low-cost, and environmentally-friendly features.[20,56–60] The features mentioned above could be found in carbon-based materials, in addition to their abundance

and high resistance to acid/alkaline environments, attributed to their tunable molecular structures.[61] However, the HER mechanism on such materials is poorly understood, and most of the experimental studies were mainly focused on their surface properties, while investigations on their catalytic behavior are very limited.[61] Compared to other photocatalysts, including elemental sulfur,[57] phosphor,[58] and boron,[59] graphitic carbon nitride (g-C_3N_4) is considered to be the most well-known photocatalyst and the most promising when it comes to photocatalytic activity. However, the relatively large optical band gap of g-C_3N_4 (2.7 eV)[20] hinders the photo-absorption in the visible-light region, in addition to the fast electron–hole recombination.[62] Therefore, it is important to enhance the visible-light absorption and decrease the electron–hole recombination, which could be accomplished by coupling g-C_3N_4 with transition metal-free co-catalysts.

4.4 Hydrogen Evolution Reaction

Many tactics were used in the hydrogen evolution half-reaction of water splitting, which could be carried out *via* electrochemical, photochemical, and photo-electrochemical (PEC) methods.[34,63] Photo-excited electrons are generated by the driving force of the band bending at the surface interface between the photo-electrode and electrolyte.[34] The aim is to get rapid separation and migration of charge carriers to the photocatalysts avoiding the electron–hole recombination.[35] The ultimate gas evolution reaction hinders the migration of charge carriers towards active sites in which the HER occurs.[33] Since the reaction consumes enormous energy, solar energy is required as external energy that passes the energy barrier.[33] Visible light photons with energy larger than that of the semiconductor are mandatory for the generation of electrons.[31,33,34,63,64] The minimum conduction band (CB) of the photocatalyst must be more negative than the H^+/H_2 reduction potential.[33] Photo-generated electrons function as a reduction agent of H^+ into H_2.[34]

Reduction half-reaction:

$$4H^+ + 4e^- = 2H_2 \tag{4.2}$$

4.4.1 Mechanism of HER Under Acidic and Basic Conditions on Model Materials

In acidic media, the HER (*i.e.*, cathodic half-cell reaction) involves three reaction pathways (eqn (4.3)–(4.5)) occurring at the active site on the surface of the electrocatalyst (M*):[65,66]

- *Volmer reaction step*: an initial discharge step (*i.e.*, proton-reduction on the active site of the catalyst surface, M*, generating an adsorbed proton atom on the catalyst, M^*H_{ads})

$$M^* + H_3O^+ + e^- \rightarrow M^*H_{ads} + H_2O \tag{4.3}$$

- *Heyrovsky reaction step*: an electrochemical-desorption step (*i.e.*, HER through proton/electron transfer):

$$M^*H_{ads} + H_3O^+ + e^- \rightarrow M^* + H_2 + H_2O \quad (4.4)$$

- *Tafel reaction step*: recombination of two adsorbed protons:

$$M^*H_{ads} + M^*H_{ads} \rightarrow 2M^* + H_2 \quad (4.5)$$

The overall reaction mechanism usually involves two or three of these reaction steps.

Similar to the acidic media, the HER in alkaline media (eqn (4.6)–(4.8)) also involves the Volmer–Heyrovsky or Volmer–Tafel reaction steps, one of the differences being that (since the proton concentration is almost non-existent in the alkaline electrolyte) the Volmer and Heyrovsky reaction steps include an initial water-dissociation step

$$M^* + H_2O + e^- \rightarrow M^*H_{ads} + OH^- \text{ (Volmer reaction step)} \quad (4.6)$$

$$M^*H_{ads} + H_2O + e^- \rightarrow M^* + H_2 + OH \text{ (Heyrovsky reaction step)} \quad (4.7)$$

$$M^*H_{ads} + M^*H_{ads} \rightarrow 2M^* + H_2 \text{ (Tafel reaction step)} \quad (4.8)$$

The involvement of the initial water-dissociation process in the alkaline electrolyte introduces an additional energy barrier to HER and most likely impacts the overall reaction rate, thus making the overall HER in alkaline extremely sluggish compared to acidic media. Indeed, it is known that the switching of the proton donor (*i.e.*, from H_3O^+ in acid to H_2O in alkaline) can easily impede the Volmer reaction step. In both acid and alkaline media, the platinum electrocatalyst provides the fastest HER kinetics.[67]

4.4.2 The Importance of the Tafel Slope in Establishing the Underlying HER Mechanism

One of the HER mechanisms described by the Volmer, Heyrovsky, and Tafel reactions is the rate-determining step (rds) of the overall reaction. The rds is the slowest reaction step in the various reactions that leads to the final product (hydrogen in the HER case). For every experimental HER, it is important to determine the rds, and this can easily be obtained from the Tafel slope (which is indicative of the inherent property of the electrocatalyst) derivable from the polarization curve (linear sweep voltammetry) in accordance with the Tafel equation (eqn (4.9)) which is related to the Butler–Volmer equation for treating simple electrochemical redox reactions eqn (4.10):

$$\eta = a + b \log(j) \quad (4.9)$$

$$\eta = \frac{2.3RT}{\alpha nF}\log(j_o) - \frac{2.3RT}{\alpha nF}\log(j) \tag{4.10}$$

where η denotes the overpotential (*i.e.*, the difference between the electrode potential and that of the standard potentials ($\eta = E - E^0$)), a is the intercept of the linear curve (η *vs.* log(j)) which is the first term of eqn (4.10), j_o is the exchange current density (which is the descriptor of the electrocatalytic activity), j represents the current density, while b is the Tafel slope. Tafel analysis is used in different forms in many electrochemical redox reactions. In theoretical microkinetic analyses, the Tafel slopes for the three HER steps are given as follows:

- for the Volmer step,

$$b = \frac{2.3RT}{\alpha nF} = 118.2 \text{ mV dec}^{-1}$$

- for the Heyrovsky step,

$$b = \frac{2.3RT}{(1+\alpha)F} = 39.4 \text{ mV dec}^{-1}$$

- and for the Tafel step,

$$b = \frac{2.3RT}{nF} = 29.6 \text{ mV dec}^{-1}$$

where R is the ideal gas constant (8.3145 J K^{-1} mol^{-1}), T is the absolute temperature (298 K), α is the symmetry factor or the charge-transfer coefficient (assume 0.5), n is the number of the transferred electrons (1 for Volmer, 2 for Tafel), and F represents the Faraday constant (96 485 C mol^{-1}). The value of the Tafel slope can sometimes be observed to be higher than the theoretical value. For example, recent work with mesoporous graphitic carbon nitride-supported binary MPt (M: Co, Ni, Cu)[68] showed that the Tafel slope values exhibited $\gg$ 120 mV dec^{-1}. The reason for the high values was associated with the obstructed electron transfer process or high surface coverage of the adsorbed proton atoms on the catalyst's surface (M^*H_{ads}). The same argument of high surface coverage of the adsorbed proton atoms holds when the rds is the Heyrovsky step, instead of ~40 mV dec^{-1}, its Tafel slope is 120 mV dec^{-1}.[69]

4.5 Oxygen Evolution Reaction

The second half-reaction of water splitting is the oxygen evolution reaction (OER), which is a complex reaction that requires four electrons from two H_2O molecules to generate a double bond between two oxygen

atoms.[34] The transfer of the four electrons occurs one after another. This might increase the reaction overpotential and negatively affect the reaction speed. The side effects of transferring electrons one at a time lead to an accumulation of energy. Thus, the designed catalyst should consider these consequences to achieve more active sites and low overpotential.[70] The maximum VB of the photocatalyst must be more positive than H_2O/O_2 oxidation potential.[33] Photo-generated holes function as an oxidation agent of H^+ into H_2.[34]

Oxidation half-reaction:

$$2H_2O = O_2 + 4H^+ + 4e^- \quad (4.11)$$

4.6 Self-standing gCN Photocatalysts for Water Splitting

In this section, the potential of the self-standing gCN materials to act as water-splitting photocatalysts is discussed. Small band gap and appropriate band positions have been the main focus in pursuing the development of photocatalysts for effective water splitting and the stability of these catalysts in practical applications.[71] The prerequisites required to form a heterogeneous catalyst can be found in g-C_3N_4, a semiconductor with a band gap of 2.7 eV. Although this photocatalyst is effective in various reactions, the medium band gap of g-C_3N_4 makes it superior to overwhelm the endothermic character of the water-splitting reaction.[71]

Therefore, it is important to interpret the interaction between g-C_3N_4 and water molecules in the photocatalytic water-splitting process from a theoretical perspective. The photocatalytic water-splitting reaction mechanism was revealed using the spin-polarized DFT on *s*-triazine-based gCN.[72] The results showed that due to the hydrogen bonding between the water hydrogen atoms and nitrogen atoms of gCN, the water molecule calculated binding energy on the gCN surface reached approximately −0.56 eV. Besides, for the OER, the calculated overpotential was approximately 0.93 V, while that of the holes in the valence band was 2.64 eV.[72] As shown in Figure 4.2, for the 0 V potential, all the four OER steps are uphill with a free energy change of +4.92 eV. At an equilibrium potential of U = 1.23 V, steps (2) and (4) are found to be downhill, whereas steps (1) and (3) are uphill in nature. Thus, the holes located in the valence band, situated approximately at the OER potential, cannot oxidize water to oxygen. While at U = 2.2 V, the free energy profile shows that the reaction can occur, and none of the reactions are correlated with uphill energy.[72] Hence, holes located at a potential of 2.16 V and above can oxidize water to O_2 with an overpotential of 0.93 V. This indicates that gCN can enhance the OER without the need of any co-catalyst, and for designing an active photocatalyst, this is extremely attractive. However, that is not the case for HER since the study shows that gCN has just 0.26 eV over the HER level; thus, a co-catalyst is required.[72]

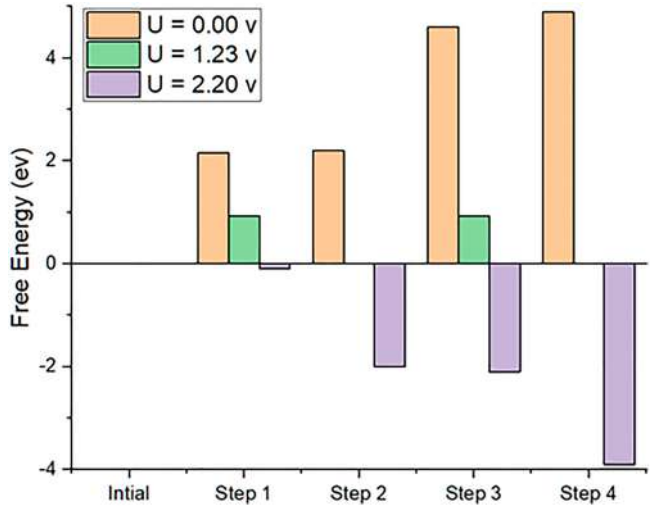

Figure 4.2 Calculated free energy changes at different potentials for the different intermediated reaction steps involved in the OER.[72] Adapted from ref. 72 with permission from the Royal Society of Chemistry.

Subsequently, a group examined the process systematically using DFT to elucidate the effect of water adsorption on the photocatalytic properties of single-sheet g-C_3N_4.[73] According to the results, the structure of g-C_3N_4 before interacting with water is a single planar sheet. However, once water molecules are adsorbed on one side of it, the initial flat structure becomes a buckle structure.[73] However, no structural changes were observed when water molecules were adsorbed on both sides of the single g-C_3N_4. More interestingly, during the structural transformation from flat to buckle after the water molecules' adsorption, the band structure changes from an indirect to a direct one, enhancing the optical adsorption.[73] However, the band gap of the buckle structure of 0.33 eV is larger than that of the planar one.[73] Moreover, by increasing the water coverage, the water adsorption process on g-C_3N_4 will be stabilized by the hydrogen bonds between the water molecules. Besides, valence and conduction bands of g-C_3N_4 could be decreased by water, promoting the water-splitting ability.[73]

The potential of *s*-triazine-based two-dimensional porous (g-CN) materials as photocatalysts for water splitting under visible light was investigated using first-principles DFT calculations.[74] In addition to studying the effect of doping with non-metal elements (boron and phosphorous) on the electronic band structure of gCN and g-C_3N_4, the results showed that the multilayer gCN materials enhanced visible light absorption more than the single-layer system due to the interlayer coupling. The charge carrier mobilities are enhanced since there were no localized states in the band dispersion plot.[74] The method implemented was found to be accurate since the band edge potentials and band gap of g-C_3N_4 calculated

are almost matched with the experimental results. The visible light absorption was found to be significantly improved, as indicated by the valence band maximum (VBM) and conduction band minimum (CBM), by substitutional doping with phosphorous in gCN, where the band gap was decreased to 2.31 eV without the presence of any mid-gap states, as shown in Figure 4.3.[74] Similarly, the optical absorption spectra were also enhanced significantly with phosphorous doping in visible light absorption efficiency.[74] The thermodynamic criteria for overall water splitting were satisfied with respect to water redox levels for the position of band edges in pure g-CN and phosphorous doped counterparts.

In another study, the feasibility of gCN materials to act as water-splitting photocatalysts was investigated numerically. This approach involved both time-dependent density functional theory (TD-DFT) and density functional theory (DFT) to predict the absorption spectra and the reduction potentials. Two cluster models were studied, the heptazine- and triazine-based structures.[75] Different configurations were considered for each structure; for the heptazine-based structures, six linear melem (Flat (F) and helical (H) classes) and ten graphitic structures, while for the triazine-based, 15 triazine units of graphitic structures (a sample is shown in Figure 4.4).[75] The absorption spectra show that the short linear helical heptazine-based structures (H3L and H4L) possess similar spectra to their respective flat conformers. The long linear helical chains (H5L, H6L) possessed the lowest energy, and the flat conformers showed increased intensity at long wavelengths but overall had very similar spectra. It was observed that, for both classes, increasing the number of heptazine units causes an overall absorption spectra redshift.[75] Also, for the linear structures, the wavelength of the first absorption feature, the absorption onset, is always less red-shifted than those of the graphitic structures. For instance, the absorption onset of H6G is about 450 nm, whereas that of H6L is 380 nm.[75]

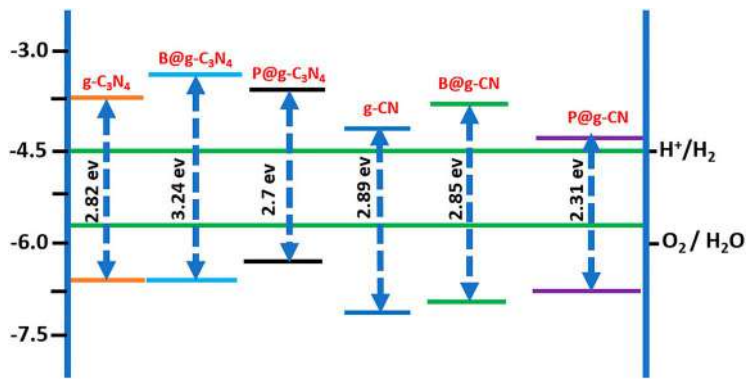

Figure 4.3 Predicted VBM and CBM positions of g-C_3N_4 and gCN along with their boron and phosphorous doped counterparts.[74] Adapted from ref. 74 with permission from American Chemical Society, Copyright 2014.

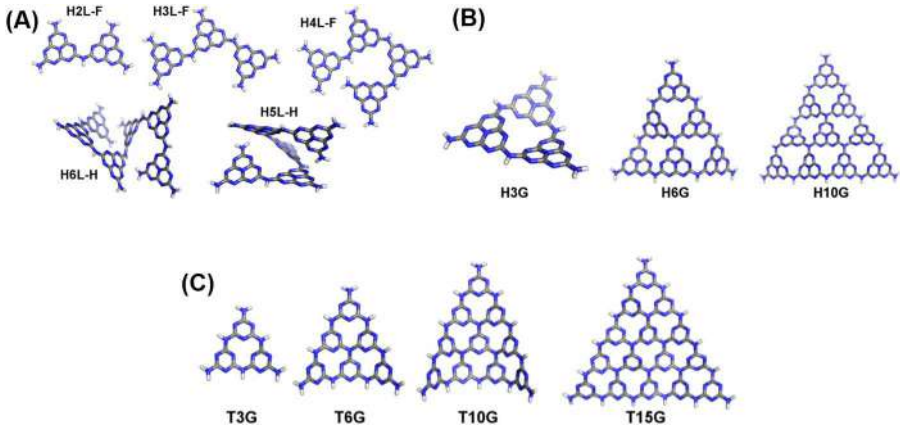

Figure 4.4 (A) Linear heptazine-based structure cluster models, where 'F' indicates a flat conformer, while 'H' is for helical conformers. (B) Graphitic heptazine-based structure cluster models. (C) Cluster models of graphitic triazine-based structures.[75] Reproduced from ref. 75 with permission from American Chemical Society, Copyright 2014.

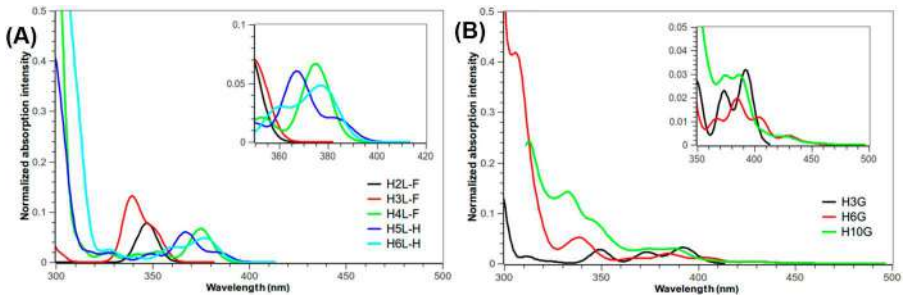

Figure 4.5 (A) Linear heptazine-based structures spectra using TD-B3LYP. (B) Graphitic heptazine-based structures spectra using TD-B3LYP.[75] Reproduced from ref. 75, https://pubs.acs.org/doi/10.1021/jp507372n, with permission from American Chemical Society, Copyright 2014. Further permissions requests related to the excerpted material should be directed to the ACS.

Figure 4.5 shows the spectra of the linear and graphitic heptazine-based structures, where they appear to be essentially converged, to a value of approximately 420 nm with cluster size, and within the same wavelength range as that of the experimental carbon nitride materials, which are based on heptazine cores.[76,77] It was found experimentally that low temperature (400–550 °C) synthesized materials have an absorption onset between 350 and 400 nm, whereas for those synthesized at high temperatures (600–650 °C), it is above 400 nm, with the possibility of some variations depending on the preparation conditions.[76]

Regarding the triazine-based materials, the absorption onset redshifts and converges to a value of approximately 330 nm, as the number of triazine units in the cluster increases.[75] For single layers, these results predict that the absorption spectrum for triazine-based materials should be more blue-shifted compared to heptazine-based materials.[75] The influence of adding polypyrrole nanoparticles to carbon nitride was also studied. This mixture was able to catalyze the overall splitting of water into hydrogen peroxide and hydrogen. The ionization potential (IP), Fermi energy (E_f) and electron affinity (EA) potentials of both the polypyrrole with 12 units (12-Py) long and the H10G graphitic heptazine-based cluster model are depicted in Figure 4.6. As shown, using graphitic heptazine-based materials alone, the oxidation of water to hydrogen peroxide is thermodynamically possible at pH 7, with an overpotential of ~0.3 V. On the other hand, both the EA and IP potentials of polypyrrole are significantly shifted positively relative to the graphitic heptazine-based carbon nitrides by more than 2 V. Thus, in polypyrrole, the reduction of protons to hydrogen by free electrons is expected to be strongly exothermic. However, the oxidation of water to hydrogen peroxide and molecular oxygen by free holes appears to be strongly endothermic. Another finding was that the polypyrrole nanoparticles' chain size, between 4 and 16 units, does not significantly affect the potentials.[75]

These findings suggest that the two heptazine-based classes have a substantial thermodynamic driving force for water splitting. However, the triazine-based structures have a stronger force for proton reduction than

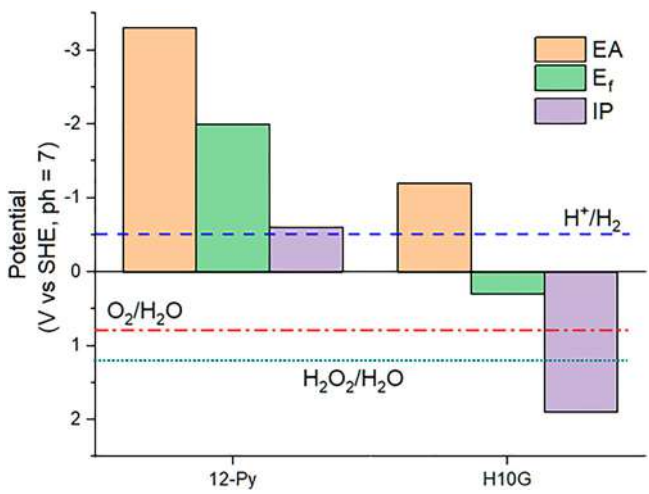

Figure 4.6 Calculated EA, Ef, and IP potentials using (TD-)B3LYP for 12-Py and H10G in water at pH 7.[75] Reproduced from ref. 75, https://doi.org/10.1021/jp507372n, under the terms of the ACS AuthorChoice/Editors' Choice *via* Creative Commons CC-BY agreement, https://pubs.acs.org/page/policy/authorchoice_ccby_termsofuse.html.

the heptazine-based counterparts, but water oxidation is predicted to be less exothermic.[75] Moreover, the effect of stacking is more dominant for triazine-based frameworks. Thus, carbon nitride materials of different structures should, under illumination, be able to thermodynamically drive the photocatalytic reduction of protons to hydrogen since water oxidation is strongly exothermic.[75] Besides, the built-in potential of carbon nitride–polypyrrole mixtures helps in isolation of electrons and holes.

In a different study, a comparison between different precursors (urea, dicyandiamide, and thiourea) for graphitic carbon nitride was made experimentally in terms of the hydrogen-evolution rate (HER) and turnover number (TON).[78] The results show that the urea-derived g-C_3N_4, under full arc and $\lambda \geq 395$ nm, exhibited a superb hydrogen-evolution rate which leads to a high turnover number. Compared with what was reported previously, the internal quantum yield in the visible region is nearly an order of magnitude higher, reaching 26.5%.[78] Moreover, the optimized g-C_3N_4 can produce approximately 20 000 μmol g^{-1} of hydrogen per hour from water under full-arc irradiation. While under irradiation with a 300 W Xe lamp, the optimized g-C_3N_4 could sustain an almost linear profile of H_2 production for 30 h, resulting in a TON of more than 640 in 6 h, which shows how stable it is.[78] The experimental results have shown that the HER rate could be boosted by increasing the degree of polymerization and decreasing the protonation status. Using DFT and TDDFT, this enhancement turned out to be because of a shift in the conduction band edge position, which increased the overpotential for reduction reactions at the surface.[78]

Another group explained the photocatalytic water splitting on g-C_3N_4 utilizing the DFT and density-functional tight-binding method.[79] The optimized adsorption geometries of intermediates during the H_2O oxidation half-reaction are illustrated in (Figure 4.7A). (For eqn (4.13)–(4.16), * represents the bare surface.)

$$2H_2O \rightarrow O_2 + 4H^+ + 4e^- \tag{4.12}$$

$$* + HO \rightarrow *OH + H^+ + e^- \tag{4.13}$$

$$*OH \rightarrow *O + H^+ + e^- \tag{4.14}$$

$$*O + HO \rightarrow *OOH + H^+ + e^- \tag{4.15}$$

$$*OOH \rightarrow * + O + H^+ + e^- \tag{4.16}$$

All the resulting geometries exhibited relatively high adsorption energies, which could restrain the potential diffusion processes and suggest stable configurations on the electron transfer timescale.[79] The OH and OOH radical intermediates are stabilized by the interaction of electrostatic and hydrogen

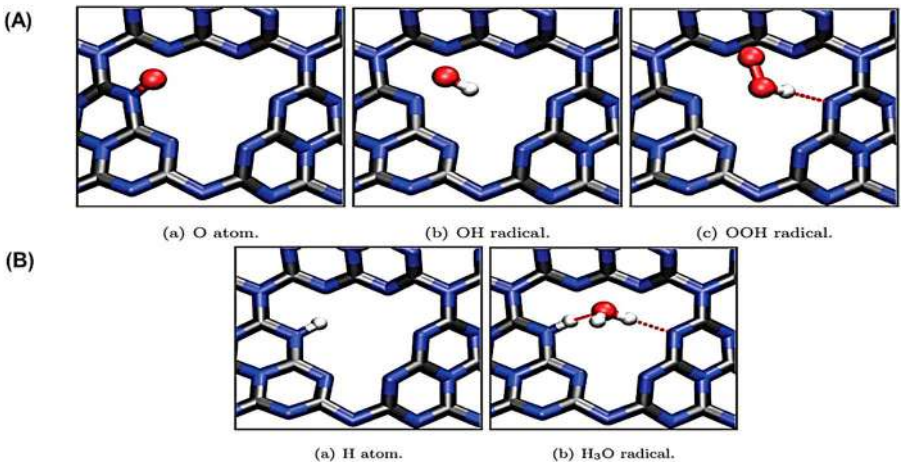

Figure 4.7 (A) Optimized adsorption geometries of intermediates during the H_2O oxidation half-reaction, explained in (eqn (4.13)–(4.16)). Bond lengths in (a) N–O = 1.28 Å, (b) N–O = 2.28 Å, and (c) N–O = 2.89 Å, O–O = 1.34 Å. (B) Optimized adsorption geometries of intermediates during the H^+ reduction half-reaction, explained in (eqn (4.17) and (4.18)). Reproduced from ref. 79 with permission from the Royal Society of Chemistry.

bonding (E_{ads} = 0.61 and 0.66 eV, respectively).[79] However, the single oxygen intermediate and the substrate nitrogen interacted through a covalent bond, establishing the *N*-oxide group, illustrated by its high adsorption energy of −2.73 eV. Using the same approach and substrate, the H^+ reduction half-reaction (eqn (4.18) and (4.19)) was also studied.[79]

$$4H^+ + 4e^- \rightarrow 2H_2 \tag{4.17}$$

$$* + H^+ + e^- \rightarrow *H \tag{4.18}$$

$$*H_2O + H^+ + e^- \rightarrow *H_3O \tag{4.19}$$

Likewise, the intermediate species, H atom and H_3O radical, were optimized on the hollow site (Figure 4.7B) and exhibited considerable adsorption energies of −2.43 and −3.39 eV, respectively.[79] These adsorption energies could be attributed to the covalently bonded adsorbate H and substrate N atom. While in the case of subtracting one H atom from H_3O radical, the H_2O molecule maintained a hydrogen-bonded arrangement as demonstrated in Figure 4.7B (b).[79]

After that, another study evaluated, using DFT, the atomic and electronic nature of the crystal structures of completely polymerized g-C_3N_4 and incompletely polymerized g-$C_6N_9H_3$ crystals based on the triazine and heptazine monomers.[80] Four models of bulk g-$C_xN_yH_z$ (gt = graphitic triazine; gh = graphitic heptazine) were studied, and their structures are shown in Figure 4.8.

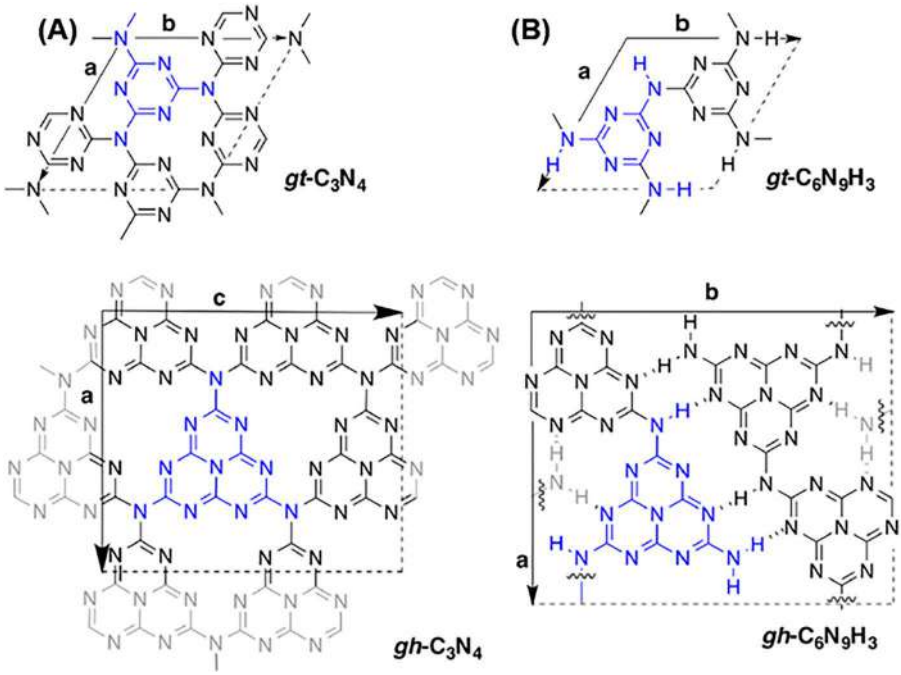

Figure 4.8 2D chemical structures of (A) completely and (B) incompletely polymerized gt- and gh-C_xN_y studied in this chapter. Individual tectons are highlighted in blue.[80] Reproduced from ref. 80 with permission from American Chemical Society, Copyright 2015.

The structure optimization results revealed that despite all starting geometries being corrugated, the incompletely polymerized structures formed stable planar structures with shorter interlayer distances, unlike the completely polymerized ones, which were highly corrugated. The incompletely polymerized system is not corrugated as it has a smaller number of interacting nitrogen lone pairs, which cause corrugation by repelling each other. Another finding was that the increased C–N–C angle of the bridge functionality was attributed to the flexibility in the molecular plane caused by the absence of the triazine unit. Moreover, hydrogen bonds do slightly stabilize the lone pairs present in the incompletely polymerized structure. Furthermore, an increase in the corrugated structures' stability was noticed when planarity was enforced, reaching values of 47 and 49 kJ mol^{-1} C_3N_4 for gt- and gh-C_3N_4 structures, respectively.

As for the photoactivity study, the band gap values were obtained using the Wannier–Mott model and were compared with those found in the literature, as depicted in Figure 4.9. This comparison shows that the adapted model gave very close results to the experimental results, especially for determining E_g^{opt}.

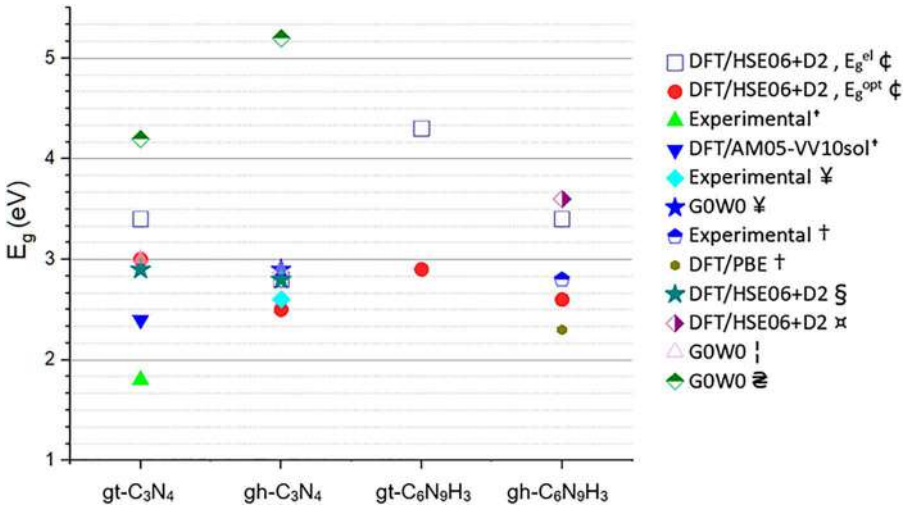

Figure 4.9 Comparison between the band gap values obtained here and in the literature, notes: ¢ ref. 80, * ref. 81, ¥ ref. 82, † ref. 83, § ref. 84, ¤ ref. 85, ¦ ref. 86, ₴ ref. 87.

It was noticed that the band gap decreases significantly upon going from triazine- to heptazine-based and from an incompletely to a completely polymerized system, by approximately 0.6 eV, which is a notable difference in their electronic properties. When planarity was enforced, the calculations performed on the g-C_3N_4 shapes revealed that for both the gt- and gh-structures, the corrugation of the g-C_3N_4 structures leads to an increase in E_g^{el} by 0.4 eV. Five layers of thick slabs were also studied, and the VB and CB edges were positioned for the redox potential of water. As shown in Figure 4.10, the delimited yellow zones highlight the pH dependence of the two half-reactions through the pH = 0 and pH = 14. All structures, except gh-C_3N_4, straddle the redox potentials of H_2O at all pH values.

It was found that the orbitals of the incompletely polymerized structures are more localized, and strong band curvature is only obtained in the polymerization directions, with some interlayer mobility in the case of gt-C_3N_4. In the polymerization directions, the monomer's nature does not significantly affect the charge carrier effective masses, but better mobility of both the electrons and the holes can be obtained from a complete polymerization. The lowest E_b for gh-C_3N_4 was attributed to the overall increases in charge carrier mobility and dielectric constant upon going from partially to completely polymerized and upon going from triazine (gt)- to heptazine (gh)-based systems. Due to the NHx termini's ability to bond to noble metal nanoparticles that perform the proton reduction reaction, the use of incompletely polymerized g-$C_6N_9H_3$ is very attractive.

The adsorption of H_2O on the g-C_3N_4 sheet was investigated using DFT and MD.[88] The results show that a stable adsorption structure, being coplanar

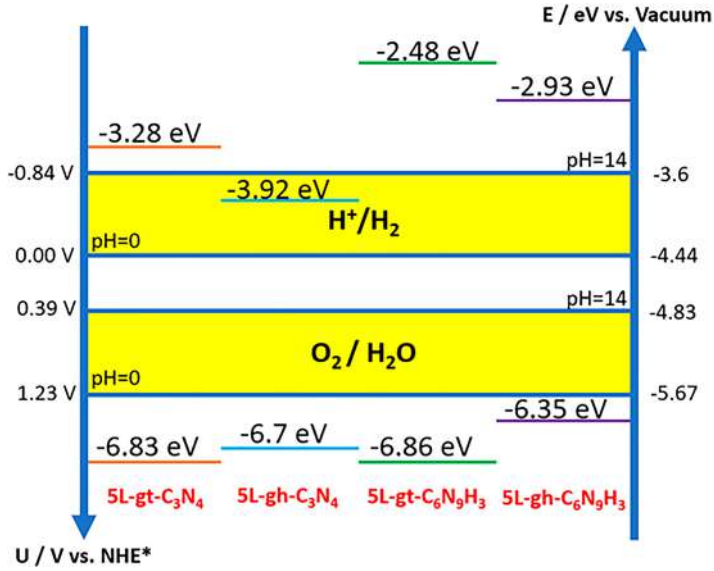

Figure 4.10 g-$C_xN_yH_z$ VB and CB edge positions with respect to the water-splitting half-reactions for the optimized five-layer (5L) slabs. The left and right axes represent the electrochemical potential and absolute energy scale, respectively.[80] Adapted from ref. 80 with permission from American Chemical Society, Copyright 2015.

with the g-C_3N_4 sheet, can be formed with H_2O monomer, dimer, and cluster with 3 and 4 molecules. MD simulations show the absence of H_2O splitting on the perfect g-C_3N_4 sheet but not on the one with a defect. Moreover, the thin interfacial liquid layer includes two different water orientations; one is water located at the intrinsic vacancy within g-C_3N_4, and the other is one of the H–O bond in water perpendicular to the g-C_3N_4 sheet. Water dissociates and forms a composite adsorption structure of hydrogen, hydroxyl, and water molecules at the defect site. The defects within the g-C_3N_4 sheet play an important role in the adsorption and splitting of H_2O.

In recent years, the photochemistry of the heptazine ($C_6N_7H_3$) chromophore in hydrogen-bonded $C_6N_7H_3$-water complexes was explored by *ab initio* computational approaches.[89] The results indicated that the active sites for the photochemical reaction over $C_6N_7H_3$-water complexes are indeed the peripheral *N*-heteroatoms of heptazine. What makes heptazine special is not only its high bond strength in the near-UV but its "pyridinic" nitrogen atoms embedded within the aromatic frame, known as electron-deficient atoms. The surrounding water molecules form hydrogen bonds with these N atoms, in which a proton transfers from the H_2O molecule to the N atom of $C_6N_7H_3$ through these bonds. More importantly, heptazinyl and OH radicals were formed as a sequence of the photo-induced transfer

of the electron and proton. Another important feature describing the heptazine chromophore in the water-splitting reaction was the existence of a low-lying dissociative 2πσ* state in the heptazinyl radical. A channel for nonstatistical photodissociation of the radical was unlocked, resulting from the predissociation of the 2ππ* states of the heptazinyl radical by this 2πσ* state. Thus, this photodissociation of the radical with the second photon promoted the closure of the catalytic cycle (first scenario). Moreover, the recombination of two heptazinyl radicals to produce H_2 and two $C_6N_7H_3$ molecules is an exothermic reaction, explained by the low H atom dissociation energy of the heptazinyl radical (≈2.0 eV), in particular. In this case (second scenario), a dark radical recombination reaction with an appropriate catalyst could close the catalytic cycle. The photochemical water oxidation mechanism has been investigated using first-principles DFT simulations.[90] The specific processes, electron- and proton-transfer involved in the OER with heptazine-based molecular gCNs, were reported. A simple model was developed to describe the photochemical OER mechanism. The results revealed that the solvent molecules have a critical role in the absorption properties of the heptazine chromophore and the overall photocatalytic cycle. Besides, the water oxidation reaction can occur since heptazine possesses suitable energy levels.

In a different work, the He ion irradiation method was implemented to tune the concentrations of both C- and N-vacancies (VC and VN) simultaneously in graphitic carbon nitride (g-C_3N_4) nanosheets.[91] The transient photocurrent response was used to probe the generation, separation, migration, and recombination of electrons and holes to assess the photocatalytic hydrogen production. The impact of vacancies on the PEC water-splitting performance was gauged using the *I–V* measurements. The He^+-ion-irradiated and annealed samples of different fluencies are named CN1, CN2, CN3, and CN4, respectively, while the untreated gC_3N_4 nanosheets are denoted as CN0. The results show that CN2 has the highest PEC response and, in general, it increases with increasing irradiation fluence. For instance, the photocurrent density of CN2 is superior to CN0 by 3-fold. However, for CN3 and CN4, a decrease in the PEC performance was noticed at excessively high irradiation fluence due to the serious lattice damage produced. Therefore, an enhanced photocatalytic activity can be achieved using the appropriate ion irradiation. The photocatalytic HER, under visible light ($\lambda > 420$ nm), was used to evaluate the photocatalytic performance of the CN0 and CN2 samples. As shown in Figure 4.11, the H_2 evolution rate over g-C_3N_4 nanosheets is 467 μmol g^{-1} h^{-1}, which is better than that of bulk g-C_3N_4 (66 μmol g^{-1} h^{-1}), while with optimized defect concentration, the CN2 sample showed a tremendous hydrogen evolution rate (1271 μmol g^{-1} h^{-1}).

First-principles DFT simulations, were used to realize the effect of VN and VC on the electronic structure of g-C_3N_4. The results show that the light absorption and the separation of charge carriers can be significantly enhanced by the defect states in the defective g-C_3N_4. It was observed that as the irradiation fluence increases, the visible light absorption and the

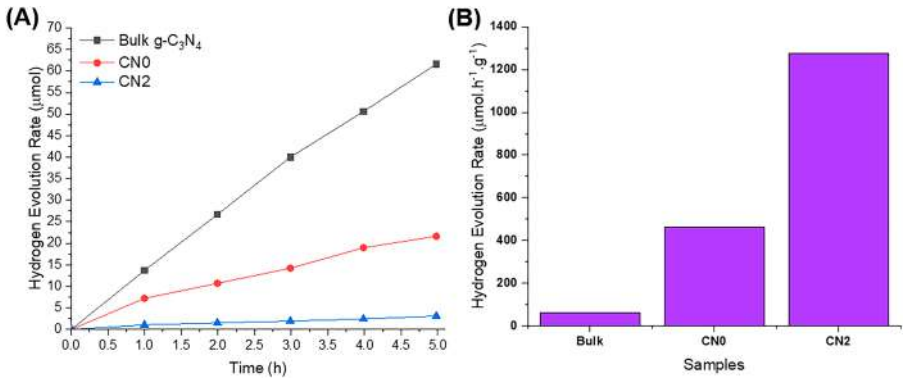

Figure 4.11 (A) Hydrogen evolution curves. (B) Photocatalytic hydrogen evolution rate over the bulk g-C_3N_4, CN0, and CN2 samples with 10 vol% triethanolamine aqueous solution, 3 wt% Pt co-catalyst, and 10 mg photocatalysts under visible light irradiation ($\lambda > 420$ nm).[91] Adapted from ref. 91 with permission from AIP Publishing, Copyright 2020.

redshifts of the absorption edges are significantly increased. Also, the presence of VC in g-C_3N_4 can redshift the light absorption edge effectively, while the VN can cause a defect state in the band gap. Thus, it can be concluded that C and N vacancies doping enhanced the photocatalytic performance of the g-C_3N_4 nanosheets. Moreover, the photocatalytic water-splitting performance of 2D materials can be improved by the ion irradiation technique. The advantages of this technique are that it could improve the photocatalytic efficiency of the other semiconductors with various functionalities.[91]

4.7 Transition Metal-free gCN Based Photocatalysts for Water Splitting

In the following section, we will be emphasizing the performance of transition metal-free g-C_3N_4 based photocatalysts in hydrogen evolution reactions from a theoretical point of view. It was found that carbon self-doping could induce the electronic and photocatalytic properties of g-C_3N_4 *via* a homogeneous substitution of lattice nitrogen with carbon.[92] The effect of carbon doped on the electronic and band structure of g-C_3N_4 was studied using DFT calculations. A facile method was then developed to synthesize carbon self-doped g-C_3N_4 (denoted C-g-C_3N_4) using melamine in ethanol. A solution to provide more carbon along with testing the photocatalytic HER was examined, as well as the irradiation reduction of Cr(VI) in an aqueous solution. The results show that the photoreduction rate (0.10126 h^{-1}) of Cr(VI) over C-g-C_3N_4 was 1.68 times that (0.06025 h^{-1}) over g-C_3N_4. In comparison, the HER rate on C-g-C_3N_4 was about 1.42-fold of that on g-C_3N_4 due to carbon doping. Also, these two evaluation methods revealed that the degradation

process follows first-order kinetics. To evaluate the band gap energy of the samples, UV-Vis diffusion reflectance spectrometry was employed and revealed that the band gap energy values of g-C_3N_4 and C-g-C_3N_4 were found to be 2.72 and 2.65 eV, respectively. Thus, C-g-C_3N_4 produces more photogenerated electron–hole pairs and therefore would absorb more visible light than g-C_3N_4. The electrical conductivity of g-C_3N_4 was enhanced by substituting the bridging N atoms with C atoms due to the formation of delocalized big π bonds, that favor electron transfer, among the substituted carbons and the hexatomic rings. Moreover, the visible light absorption was improved since the carbon self-doping narrowed the band gap of g-C_3N_4. These results indicate that carbon self-doping could enhance both photooxidation and photoreduction activities.

A group presented the fabrication of a transition metal-free catalyst consisting of g-C_3N_4 coupled with nitrogen-doped graphene (g-C_3N_4@NG).[61] Figure 4.12 illustrates the hybrid catalyst synthesis, where g-C_3N_4 was grown directly on the surface of graphene oxide (GO), resulting in a strongly bonded g-C_3N_4@NG. As depicted in Figure 4.12, the thermal reduction and intercalation of N heteroatom into the framework of GO occurred simultaneously, driven by the discharge of gaseous NH_3 during the polycondensation of dicyandiamide to the melem unit. The electrocatalytic properties of the hybrid were revealed by a combination of electrochemical and thermodynamic calculations. The results indicated that coupling these two materials together endowed the g-C_3N_4@NG with outstanding electrocatalytic properties, in which highly active hydrogen adsorption sites can be provided by g-C_3N_4, while NG promotes the electron-transfer process to accomplish proton reduction. According to the polarization curve (*I–V*), the hybrid catalyst achieved an overpotential of 240 mV corresponding to a 10 mA cm^{-2} HER current density and a Tafel slope of 51.5 mV dec^{-1}, while the calculated HER exchange current density (i_0) from the Tafel plot was 3.5×10^{-7} A.cm^{-2}, comparable to those of MoS_2-based metallic catalysts (at the same surface area

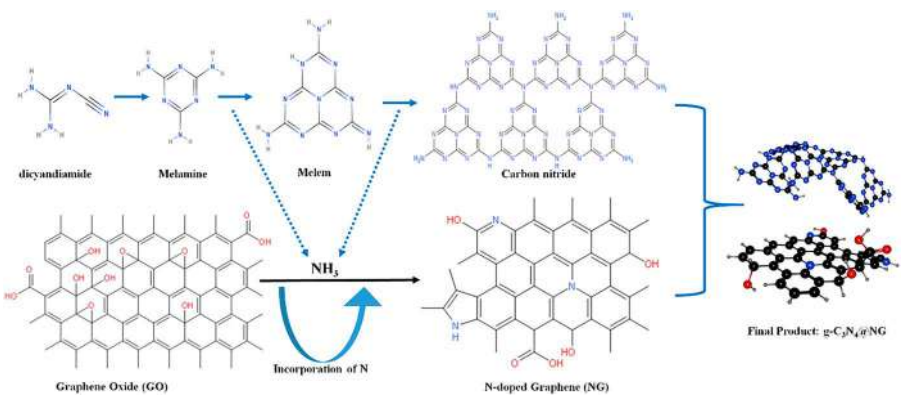

Figure 4.12 Schematic representation of the fabrication of g-C_3N_4@NG hybrid.

and catalyst loading).[51,93–95] Strikingly, the hybrid proved to be efficient for sustainable hydrogen production, originating from the robust stability of g-C_3N_4@NG in acidic and alkaline solutions. The electronic-coupling effect was evaluated by DFT calculations, showing that this metal-free catalyst has a decreased band gap compared to pristine ones. On the thermodynamics level, the $|\Delta G_{H^*}|$ value of g-C_3N_4@NG exhibited a value of 0.19 eV, which was the smallest compared to pristine C_3N_4 and NG; noting that the Pt catalyst has a value of $|\Delta G^{Pt}_{H^*}| \approx 0.09$ eV, the nearest to the optimum value ($|\Delta G_{H^*}| = 0$).[96] The HER mechanism revealed that the pathway selectivity on g-C_3N_4@NG is potential-dependent, where the Volmer–Heyrovsky mechanism with a rate-limiting step takes place at low overpotential and becomes the Volmer–Tafel mechanism at high overpotential. More importantly, assuming that g-C_3N_4@NG has equal energy barriers at all reaction steps, the Volmer–Tafel is greatly faster than Volmer–Heyrovsky at low potentials and could be equally fast at a potential around −1.0 V (*versus* a reversible hydrogen electrode). This study is important for replacing noble metals with metal-free counterparts and paved the way to investigate other types of metal-free catalysts.

Moreover, the interaction between g-C_3N_4 and trigonal/hexagonal-shaped C-dots was studied based on the DFT calculations to investigate their photocatalytic properties and performance.[97] Results concluded that the C-dots/g-C_3N_4 hybridization is joined *via* poor van der Waals bonds. Indeed, there was a clear reduction in the band gap value, causing a red-shift in the absorption spectrum. The C-dots play a role as spectral sensitizers in the hybrid system. Interestingly, the valence states and conduction states' shape of the g-C_3N_4 are changed after coupling with C-dots, demonstrating strong, stable interaction with bonding energy of 1.58 and 1.87 eV for the trigonal and hexagonal C-dots/g-C_3N_4, respectively. The highest occupied molecular orbital (HOMO) and the lowest unoccupied molecular orbital (LUMO) were segregated, which indicates the favorability of electron–hole pairs' separated states. Based on the HSE06 method, the CBM potential of g-C_3N_4 was evaluated as −0.88 eV (more negative than the H^+/H_2, 0 eV *vs.* NHE), while the VBM potential was 2.14 eV (more positive than the H_2O/O_2, 1.23 eV *vs.* NHE). Although the band-edge positions fit the water-splitting reaction on g-C_3N_4, the relatively large band gap inhibits the visible light absorption. Likewise, C-dots cannot split water independently. However, hybridizing both materials together, forming C-dots/g-C_3N_4, created a type II alignment, which enhanced the visible light absorption significantly. Moreover, the increment in the trigonal or hexagonal C-dots' size could narrow down the band gap and endow the hybrids with an enhanced response to the visible-light radiation. The narrow band gap with superior visible-light response and band alignment type of C-dots/g-C_3N_4 catalysts, makes them excellent for water splitting.

Then, the effect of different surface groups found in C-dots (–OH, –COOH, –CHO) on the redox potentials, charge transfer, and water-splitting efficiency of C-dots/g-C_3N_4 was further investigated using the high-level first principle methods.[98] Results revealed that the functional groups in C-dots could

determine the type of band alignment and solar-to-hydrogen efficiency of C-dots/g-C_3N_4 and the behavior of C-dots as electron donor/acceptors. Importantly, the C–H-dot and C–CHO-dot were found to be suitable for water splitting as they could decay into low energy charge-transfer states with carbon nitride, which indeed promotes the electron–hole separation. However, unlike the rest of the functional groups, the C–OH-dot does not form a type II heterojunction with g-C_3N_4, which inhibited the charge separation. Interestingly, the optical absorption spectra of each hybrid demonstrated that C-CHO/g-C_3N_4 has a higher absorption in the visible range compared with the rest (Figure 4.13A). Figure 4.13B illustrates the charge transfer process in C-CHO/g-C_3N_4 under light source by two routes. Route 1 suggested that charge transfer was excited by the light source, promoting the electron–hole separation. Route 2 indicates that the system could create a low energy charge-transfer state and facilitate the separation of the electron and the hole. Route 2 was explained by the light resonance with high-energy n.p* or p.p* transitions of the carbon nitride. Furthermore, the C-CHO-dot created H_2O_2 as an intermediate product, which could be catalytically decomposed during the process.

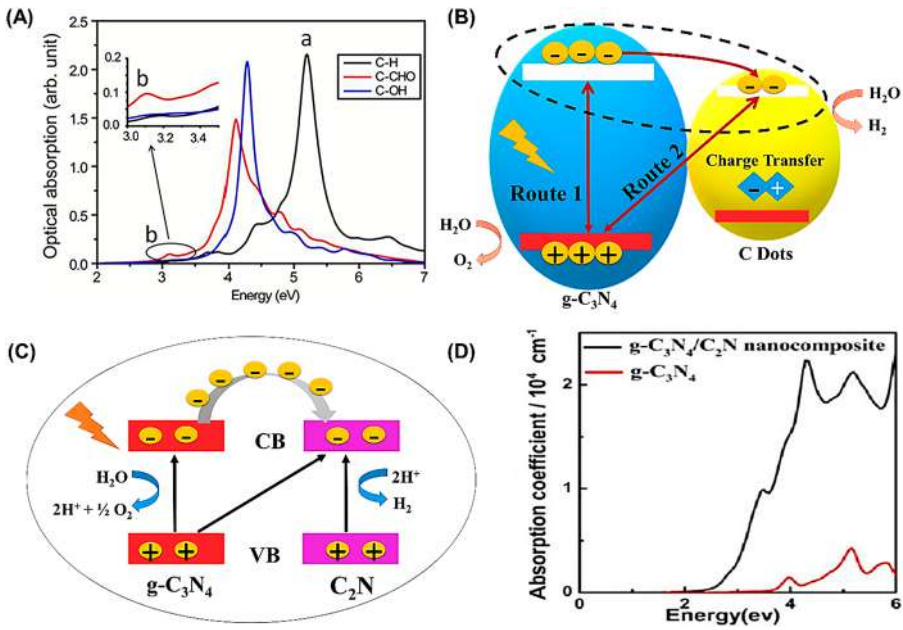

Figure 4.13 (A) Optical absorption spectra of C-dots (–OH, –COOH, –CHO)/g-C_3N_4. Reproduced and adapted with permission from ref. 98, Copyright 2017, Royal Society of Chemistry. (B) The mechanism of charge transfer and separation over the C-CHO/g-C_3N_4. (C) Proposed paths for separating electrons and holes in g-C_3N_4/C_2N. (D) Optical absorption coefficients for g-C_3N_4/C_2N and the bare counterpart. Reproduced from ref. 99 with permission from John Wiley & Sons, Copyright 2016 WILEY-VCH Verlag GmbH & Co. KGaA, Weinheim.

More efforts were dedicated to present a possible way to enhance the photo-absorption and electron–hole separation efficiencies of g-C_3N_4 by forming a metal-free g-C_3N_4/C_2N nanocomposite, based on first-principles DFT calculations.[99] It is noteworthy that such a nanocomposite coupled g-C_3N_4 with the C_2N, having a relatively wide, strong visible-light absorption with a band gap of about 1.96 eV. Electronic studies revealed that the interface of this nanocomposite is a type II band alignment, and the separation of photo-generated electron–hole pairs could be promoted by the chemical potential differences, and the three possible paths are further illustrated in Figure 4.4A. Furthermore, optical studies, shown in Figure 4.4B, demonstrated that the g-C_3N_4/C_2N nanocomposite possessed broad, strong visible-light absorption with an intensity of 10^4 cm^{-1}. However, the bare g-C_3N_4 monolayer shows clear absorption only above 3.6 eV,[73,100,101] while the absorption edge of g-C_3N_4/C_2N is notably shifted down by about 0.85 eV. This significant enhancement of g-C_3N_4/C_2N optical absorption is attributed to the properties of C_2N and coupling the interlayers of both components.[62]

Further theoretical predictions aimed to enhance solar water splitting over g-C_3N_4 by proposing two metal-free C_3N/g-C_3N_4 (monolayer/bilayer) heterojunctions.[102] Hybrid DFT calculations revealed that the transfer of photo-generated electrons and holes in the two photocatalysts caused a relatively strong built-in electric field, which subsequently created interfacial energy band bending. As a result, the transfer of photo-generated carriers in both C_3N/g-C_3N_4 heterojunctions followed the *Z*-scheme pathway, which promoted electron–hole separation within the photocatalyst. Moreover, the HSE06 calculated optical spectra revealed strong absorption peaks at 510 nm corresponding to the single-layer C_3N/g-C_3N_4 and monolayer C_3N/g-C_3N_4 heterojunctions, which means both heterojunctions could harvest the broad spectrum of solar light from the UV-visible light to the near infrared region. These findings show that the two proposed C_3N/g-C_3N_4 photocatalysts are promising for solar water splitting.

To summarize, the above studies highlighted the prospects of using transition metal-free g-C_3N_4 based photocatalysts in water-splitting reactions. These photocatalysts were proved to have effective charge separation and transfer, along with environmentally-friendly features and relatively low-cost. However, the efficiency and stability of these photocatalysts from a practical perspective is still unknown. Therefore, there is a need for further characterization of the designed materials.

4.8 Noble Metals/gCN Based Photocatalysts for Water Splitting

Improving the photocatalytic performance of carbon nitrides is a large area of interest. Many efforts have contributed to designing an effective co-catalyst to reduce the recombination rate, trap electrons, and endow more proton-reduction sites.[103,104] Noble metals, and platinum (Pt) in particular, were considered as the most effective co-catalysts in water-splitting reactions.[105,106] However, only surface active-site atoms contribute to most

noble-metal co-catalyst systems,[107] hindering industrial upscaling.[108,109] Hence, minimizing noble metals to clusters or single atoms is considered to be an efficient strategy to maximize the efficiency of atoms.[107] Although single atoms are highly efficient, optimization of single atoms' catalysts is required to reduce aggregation/coarsening and maintain their stability during catalytic reactions.[110] The unique tri-*s*-triazine structure of carbon nitrides promotes the intercalation of single atoms into their matrix,[20,111–116] which provides a potential way for trapping single-metal atoms, and then providing high-efficiency water-splitting systems. In the following section, the effect of single-metal atom modification on carbon nitride photocatalytic performance is highlighted and discussed from a theoretical perspective.

For example, in this work, the high valence, electrophilic Pt^{2+} single atom was confined on the g-C_3N_4 matrix to promote the reaction kinetics of water splitting through modifying band energy levels and increasing electron mobility around the Fermi level.[117] The photocatalytic performance of Pt^{2+}–C_3N_4 was investigated using a combination of experimental and theoretical measures. The Pt^{2+}–C_3N_4 demonstrated a superior H_2 production rate of ~140 μmol g^{-1} h^{-1}, ten times higher than Pt NP–C_3N_4 (15 μmol g^{-1} h^{-1}) (Figure 4.14A). It is noteworthy that Pt^{2+}–C_3N_4 maintained an H_2 production rate

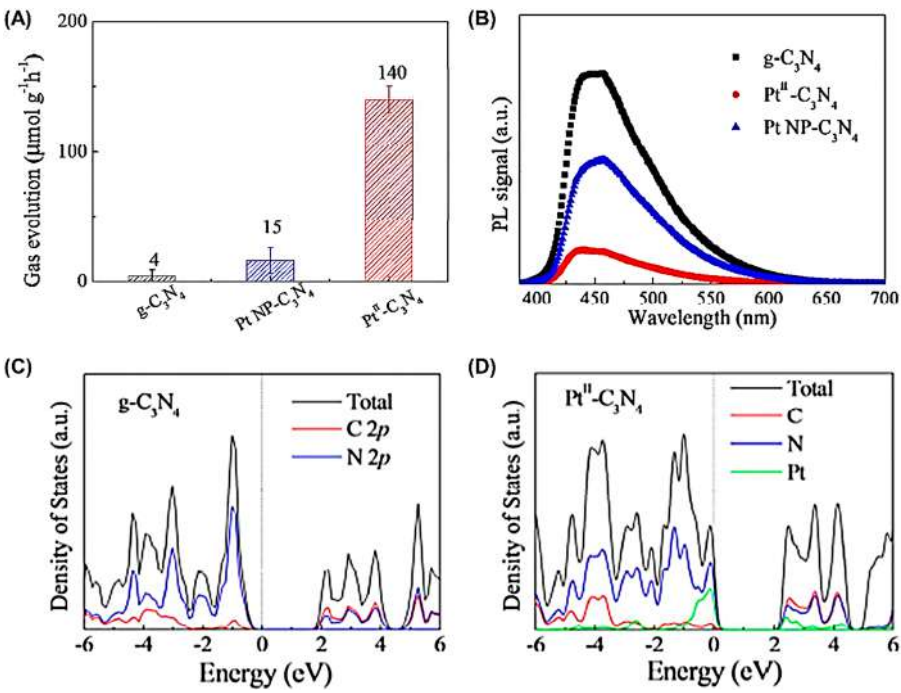

Figure 4.14 (A) H_2 evolution over time. (B) PL spectra of bare g-C_3N_4, Pt NP g-C_3N_4, and Pt^{2+}–C_3N_4. Density of states plots of (C), bare g-C_3N_4 (D), and Pt^{2+}–C_3N_4 (H). Reproduced from ref. 117 with permission from American Chemical Society, Copyright [2018].

of ~140 μmol g^{-1} h^{-1} even after 24 h, revealing its excellent robust chemical stability under various photocatalytic measures. Figure 4.14B demonstrates the PL spectra of g-C_3N_4, Pt^{2+}–C_3N_4, and Pt NP–C_3N_4. According to the results, Pt^{2+}–C_3N_4 revealed a significant reduction in the photocarrier transfer barrier compared to the rest, besides facilitating the separation and transfer of photocarriers. This was explained by the strong interaction between Pt^{2+} and N atom in carbon nitride. More interestingly, the band energy levels of Pt^{2+}–C_3N_4 (1.69 V) were significantly modified, in which the VBM was downshifted by 0.26 V, compared to that of the bare counterpart (1.43 V). The charge carrier behavior of Pt^{2+}–C_3N_4 was further illustrated by the first-principles band structure calculations. According to DOS (Figure 4.14C), the band gap of bare g-C_3N_4 was free of mobile electrons, showing typical semiconductor properties. In contrast, for the Pt^{2+}–C_3N_4, the VBM of Pt^{2+} 5d and N 2p is hybridized at the Fermi level, which promoted the transfer of electrons from the VBM to the CBM, leaving enough photo-generated holes at the VBM to carry out the water oxidation reaction (Figure 4.14D). This could be attributed to the highly electrophilic nature of the Pt^{2+} single atom.

Further explorations presented the fabrication of a single-site rhodium-phosphide modified carbon nitride photocatalyst (Rh-P/CN(H)), with significantly improved water-splitting performance.[118] In this study, porous g-C_3N_4 was prepared through a hydrothermal treatment approach, with a high specific surface area, compared to g-C_3N_4 prepared by the traditional thermal method. Then, Rh atoms were transformed into single-site Rh by extra phosphating to obtain the novel single-site Rh-P/CN(H) photocatalyst. The Rh-P dots were found to be dispersed all over the carbon nitride framework with a single-site state, revealed by structural analysis. The photocatalytic hydrogen evolution rate of the CN(H) (22.38 μmol) is four times higher than that of the former (5.06 μmol) in 4 h, which could be explained by the formation of the porous structure, endowing more active sites. Incredibly, the hydrogen production rate of the Rh-P/CN(H) surpasses the bare counterpart by almost 33 times (166.28 μmol) within 4 h. From the LSV curves of the fabricated photocatalyst, it can be seen that Rh-P/CN(H) exhibits more positive onset potential and higher current density compared to that of g-C_3N_4 (Figure 4.15A). This indicates that the presence of the Rh-P single site improved the photocatalytic performance of g-C_3N_4 by facilitating the transfer of photo-generated electrons from carbon nitride to the electrolyte for reducing water and decreasing the hydrogen evolution potential at the same time. DFT calculations were performed to investigate the electronic property of the prepared photocatalyst. According to the results, the atomically dispersed single-site Rh-P on g-C_3N_4 framework could accumulate photo-generated electrons by changing the electronic structure of g-C_3N_4.

Moreover, ΔG of g-C_3N_4 and Rh-P/CN(H) were found to be 2.3183 eV and 0.6499 eV, respectively, where the lower free energy of Rh-P/CN(H) is indeed more favorable for the HER (Figure 4.15B). The mechanism behind the performance of Rh-P/CN(H) was also investigated (Figure 4.15C). The accumulated photo-generated electrons by the single-site Rh-P made a whirl-like

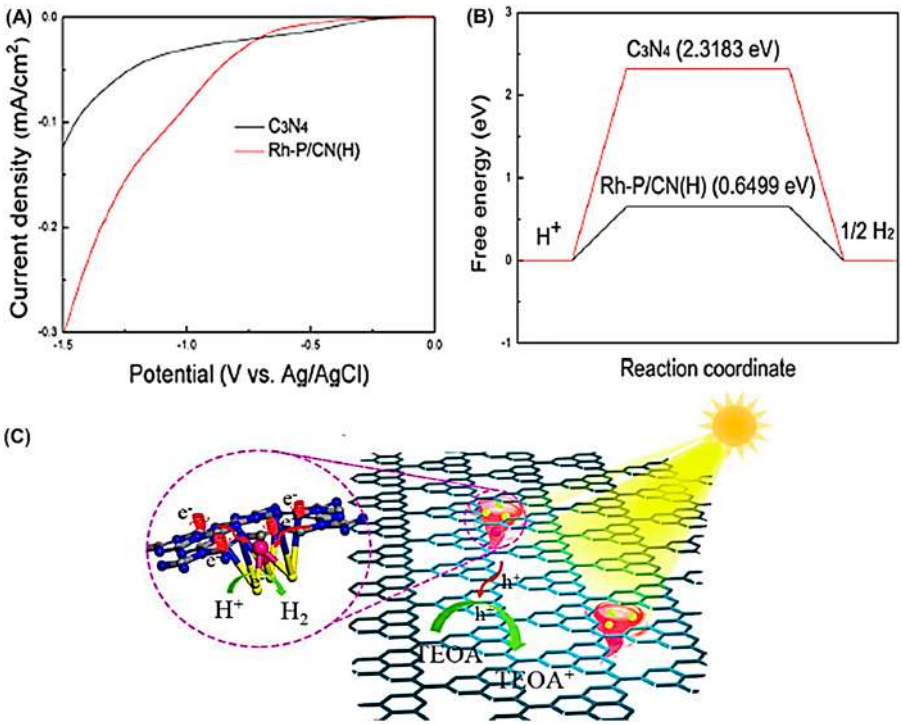

Figure 4.15 (A) LSV curves of the bare C_3N_4 and Rh-P/CN(H) under visible light. (B) Gibbs free energy for the hydrogen evolution of bare C_3N_4 and Rh-P/CN(H). (C) Schematic illustration of the HER mechanism on Rh-P/CN(H). Reproduced from ref. 118 with permission from Elsevier, Copyright 2020.

structure in water under visible light illumination, where the single-site Rh-P provides active sites for hydrogen evolution with the aid of the sacrificial agent (TEOA). Therefore, an enhanced water-splitting reaction was accomplished.

From the above results, we can conclude that the cooperation of a single-atom co-catalyst is an outstanding strategy to modify the electronic structures of carbon nitrides, providing long-term photo-generated electrons to enhance the overall water-splitting reaction. Besides, by using this strategy, the high cost of noble metals could be greatly minimized, and therefore, the development of other effective co-catalysts will be expanded.

4.9 Metal-based/Carbon Nitride Photocatalysts

This section presents the effect of transition metals (TMs) on enhancement of the water-splitting performance of graphitic carbon nitrides (gCNs). TMs, with their low-cost, natural abundance and their photocatalytic properties,

are highly promising for improving the water-splitting performance of gCNs. Also, TMs can modulate the physiochemical properties of gCNs such as electronic effect, and the band gap. This results in better reaction activity and more active sites with lower overpotential and better light adsorption. Various co-catalysts' evolution of hydrogen is compared in Figure 4.16, which will be further discussed in detail in this chapter.

Samples of 2D-C_3N_4 decorated with various co-catalysts including Ni, Ni_3N, $Ni(OH)_2$, NiO, Au, Ag, Pd, and Pt were prepared by the annealing and solvothermal process.[119] This includes annealing of melamine at 550 °C under nitrogen to obtain bulk g-C_3N_4, followed by two consequent annealing steps at 550 °C for exfoliation (Figure 4.17A).[119] The as-obtained 2D-C_3N_4 nanosheet was used as a support for the *in situ* growth of Ni_3N polyhedral, Ni(OH)2, NiO, Ni, Au, Ag, Pd, and Pt, respectively, by the solvothermal method.[119] Ni_3N/C_3N_4 and Ni/g-C_3N_4 were used as a typical model for the photocatalyst.[119] The preparation of Ni_3N involves annealing of $Ni(OH)_2$ under NH_3 for 180 min at 380 °C.[119] An *in situ* grown strategy was used to overcome the lack properties of Ni_3N as it possesses rough and grainy surface particles.[119] This causes material accumulation into blocks that have difficulty binding with the host semiconductor.[119] Intriguingly enough, the same method was used for the preparation of various catalysts supported on C_3N_4 including Ni, NiO, Au, Ag, Pd, and Pt, which could pave the way for the rational synthesis of the effect photocatalysis for water splitting.[119] Also, the water-splitting activity can be enhanced *via* using multi-metallic nanocrystals as co-catalysts with C_3N_4.[119]

The morphology of the as-prepared photocatalysts was investigated by TEM, which shows the formation of g-C_3N_4 in uniform and exfoliated ultrathin two-dimensional nanosheets.[119] The co-catalyst Ni_3N is anchored in an arranged dot-like shape on the surface of a 2D-C_3N_4 transparent sheet.[119] These 2D nanosheets – even after different thermal modification – withstood

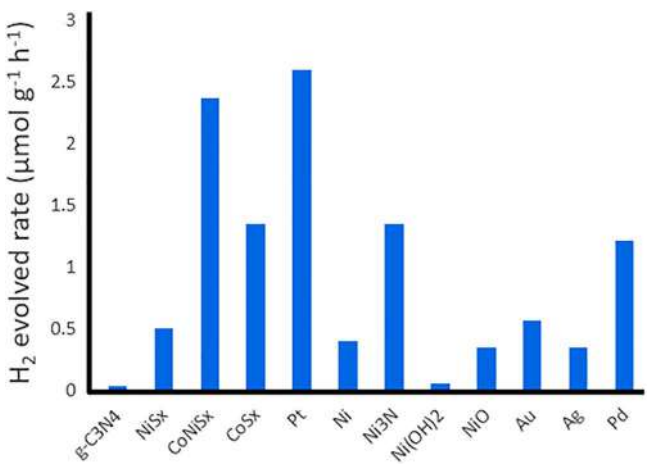

Figure 4.16 H_2 evolved using various co-catalysts supporting g-C_3N_4.

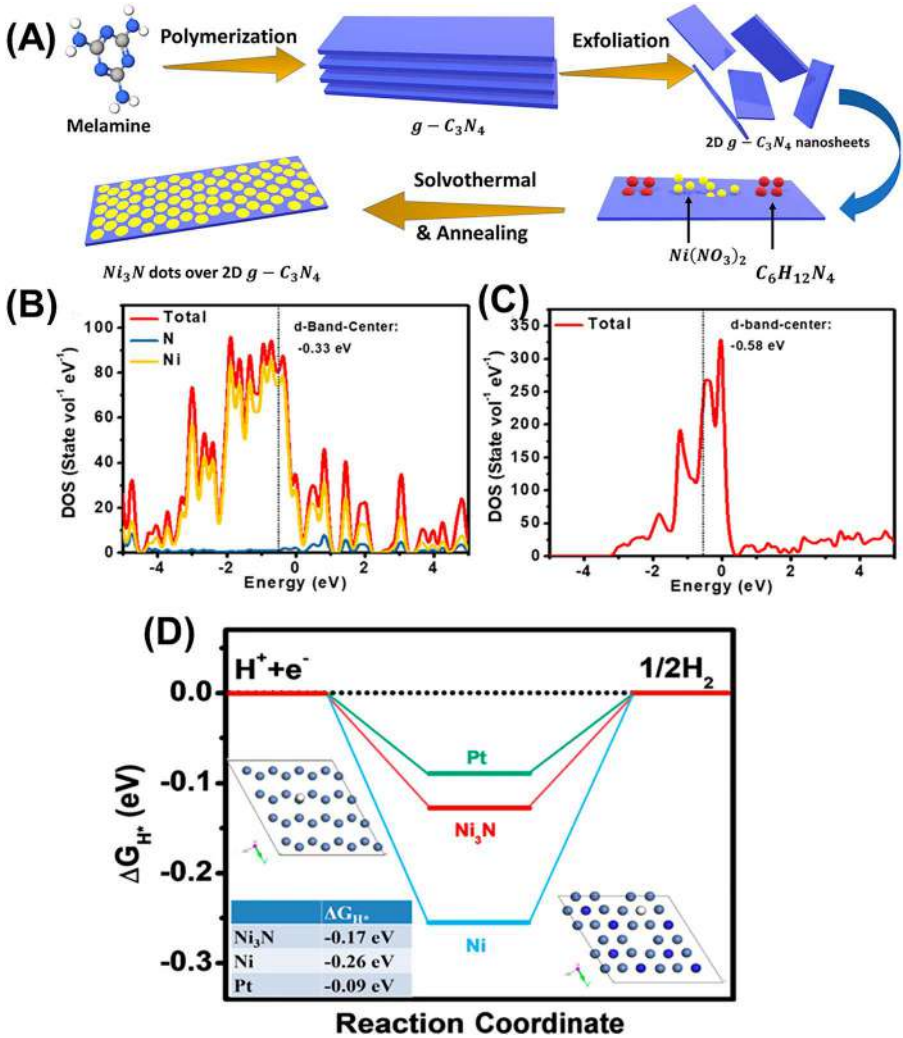

Figure 4.17 (A) Fabrication steps of Ni_3N/g-C_3N_4. (B) Calculated density of the states for Ni_3N, and (C) Ni. (D) Free energy diagram. Reproduced from ref. 119 with permission from American Chemical Society, Copyright 2019.

NH_3 treatment.[119] This indicates the vigorous stability of 2D-C_3N_4, which can enhance the water-splitting activity.[119] The anchored Ni_3N nano-size crystals were measured to be 2–3 nm, with lattice fringes of about 0.2 nm distance between lattices. This corresponds to the (111) facet of Ni_3N, which also exhibits the (002) facet, corresponding[119–121] to 2θ ~44.5° and ~42.1°, respectively.[119] These peaks possess weak intensity indicating the low loading content of the co-catalyst and successful loading on the 2D-C_3N_4 surface.[119] The bare 2D-C_3N_4 shows the same peaks before and after combining with the

co-catalyst, which is favorable to describe the vigorousness of its crystal structure against the different thermal modifications and NH_3 treatment.[119] These peaks of 002 and 100 correspond to 27.7° and 13.1° oriented from the contacted interface and graphitic carbon nitride, respectively.[119] The broadening of the (100) facet may be ascribed to the 2D structure of carbon nitride.[119] Furthermore, the Raman peaks of 704 and 1219 cm^{-1} refer to the *s*-triazine rings of C_3N_4.[119]

The significant water-splitting performance of Ni_3N/2D-C_3N_4, compared to 2D-C_3N_4 and other as-prepared co-catalysts/2D-C_3N_4, is plausibly attributed to its high surface area (172.1 $m^2\ g^{-1}$), which is two times higher than that of C_3N_4 (94.14 $m^2\ g^{-1}$), as calculated by the Brunauer–Emmett–Teller (BET) method from the nitrogen isotherm curves.[119] Along with providing more active sites, Ni_3N loading content also affects the efficiency of the reaction.[119] More loading of Ni_3N leads to more active sites but also affects the light absorption due to its dark color, which works as a light shield.[119] Various amounts of Ni_3N were tested to reach the best combination of the composite, which was detected to be 10%.[119] In terms of stability, the catalyst Ni_3N\2D-C_3N_4 performs for more than 30 h with high efficiency, which is greater than 80% of its initial one.[119] This reflects the stability and durability of the as-prepared composite, which is favorable over other tested ones.[119] This composite evolved 1347.8 μmol $g^{-1}\ h^{-1}$ H_2 over all the other as-prepared catalysts including noble metal-based catalysts Au, Ag, and Pd.[119] Although the Pt-based photocatalyst beat all the other as-prepared catalysts, Ni_3N may offer the benefits of low cost and stability of performance.[119]

A nickel-based co-catalyst was used as a water-splitting agent previously. In this work, CM–C_3N_4 decorated with Ni successfully produced H_2 at a rate of 313.2 μmol $g^{-1}\ h^{-1}$.[122] The selection of the cyanuric acid supported with carbon nitride increases the surface area, which leads to abundant active sites.[122] After loading 10% Ni@CM-C_3N_4, the recombination rate of the photo-generated charges occurs faster, which may ascribed to the successful loading.[122]

DFT was used to further illustrate the photocatalytic performance and explain the as-prepared catalysts Ni and Ni_3N in terms of conductivity and H* adsorption\desorption capacity ΔG.[119] The density of state was used to investigate the effect over the d-band of the catalyst that downshifted after nitriding, which might indicate the capacity of Ni_3N of decreasing the catalytic conversion barrier (Figure 4.17B and C).[119] Ni_3N exhibits outstanding H_2 adsorption/desorption efficiency that is comparable with noble metal Pt, with a zero-approach for both (Figure 4.17D).[119] The modeled structure of Ni_3N indicates a metallic composition with significant electronic state that crosses the fermi level, indicating its ability to transmit electrons during reaction.[119] Also, nitriding changes the Ni_3N electronic structure, so it no longer functions as a metallic conductor.[119] Thus, enhanced H* adsorption/desorption energy occurred and Ni_3N could be introduced as a useful water-splitting co-catalyst.[119]

Generating a *Z*-scheme heterostructure between titanium nanotubes and carbon nitride by the interfacial oxygen vacancy is of great significance promoting water splitting.[121] The limitation of TiO_2 owing to its wide band gap and high recombination rate of the photo-generated electron–hole could be overreached by combining with g-C_3N_4.[121] Credited to its narrow band gap and matched band structure, g-C_3N_4 is a suitable semiconductor to fabricate a catalyst that possesses higher visible light absorption for better HER activity.[121] Thus, 0D/1D g-C_3N_4/TiO_2 and 0D/1D g-C_3N_4/OV-TiO_2 catalysts were prepared to enhance water-splitting reactions.[121]

The fabrication process of the aforementioned catalysts starts with the construction of a TiO_2 nanotube following two independent phases of electrochemical anodization. In this process of anodic oxidization, titanium foil is used for oxidization under a 60 V DC source for two cycles in an electrolyte.[121] This electrolyte consists of ethylene glycol loaded with 0.25 wt% of NH_4F and two vol% of deionized water.[121] The applied voltage is constant while the oxidation time for the first and second cycles is 1 h and 2 h, respectively.[121] After each cycle, sonication is required to scrub the oxidized surface followed by drying under nitrogen flow.[121] The as-obtained substrate is denoted as a TiO_2 nanotube array.[121] The same method was used to prepare the second co-catalyst, OV-TiO_2. The resulting composition is reduced by 3M $NaBH_4$ *via* annealing for 2 h under air atmosphere then drenching in $NaBH_4$ for a further 2 h in 25 °C.[121] Air drying in the 60 °C process is required to ensure drying of the sample.[121] g-C_3N_4 was prepared from melamine using the traditional method of fabrication.[121] Chemical vapor deposition was used to load carbon nitride into different titanium co-catalysts.[121] Annealing under nitrogen flow for both catalysts is the last step in the fabrication of 0D/1D g-C_3N_4/TiO_2 and 0D/1D g-C_3N_4/OV-TiO_2 catalysts.[121] To conclude, three steps followed anodic deionization, $NaBH_4$ reduction, and chemical vapor deposition illustrated in Figure 4.18A.

FE-SEM analysis for the as-prepared catalysts 0D/1D g-C_3N_4/OV-TiO_2, and 0D/1D g-C_3N_4/TiO_2 reveals that g-C_3N_4 is successfully loaded on both sides of the pores of titanium nanotubes.[121] These nanotubes exhibit a diameter of about 100 nm and length of 11 μm.[121] This indicates that titanium nanotubes withstood against the vigorous reduction agent $NaBH_4$.[121] It was also found that g-C_3N_4 is well distributed inside and outside the pores of the TiO_2 nanotube along with EDS mapping.[121] EDS also shows the good distribution of C, N, O, and Ti. The crystal structure of the as-prepared TiO_2, OV-TiO_2, 0D/1D g-C_3N_4/TiO_2, and 0D/1D g-C_3N_4/OV-TiO_2 investigated by XRD obtained facets of (101), (004), (200), (105), and (211) corresponding to 2θ 25.3, 37.8, 47.9, 53.8, and 55.0°, respectively.[121] The existence of the 101 diffraction peak in all tested catalysts certifies that TiO_2 maintained the anatase phase before and after $NaBH_4$ reduction.[121] However, the intensity of the peak 101 decreased after reduction, which may correspond to the existence of an oxygen vacancy in the TiO_2 nanotube for OV-TiO_2.[121] The absence of diffraction peaks of 27.3 and 13.5 may ascribed to the low content of graphitic carbon nitride, which is below the detection level of XRD.[121] The chemical composition of the surface

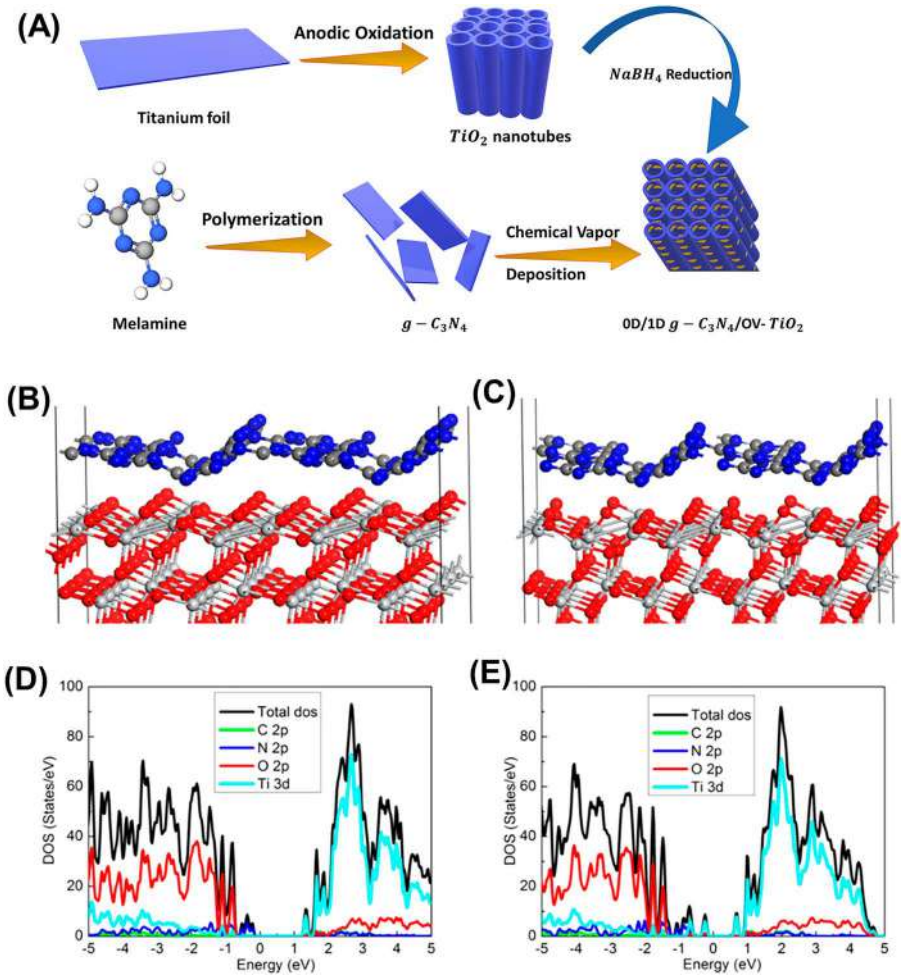

Figure 4.18 (A) Fabrication steps of 0D/1D g-C_3N_4/OV-TiO_2. (B) Structure of TiO_2, (C) containing oxygen vacancies. (D) DOS of the pure heterostructure, (E) containing oxygen vacancies. Reproduced from ref. 121 with permission from American Chemical Society, Copyright 2018.

of the catalyst 0D/1D g-C_3N_4/OV-TiO_2 is confirmed by XPS, which detects high resolution spectra of Ti 2p.[121] This spectra deconvoluted into two high intensity peaks located at 458.7 and 464.6 eV ascribed to Ti^{4+} species.[121] Two weak peaks detected at 458.0 and 463.8 eV correspond to Ti^{3+}.[121]

The significant hydrogen evolution is obvious from analyses curves that one can use to study the attribution of as-prepared catalysts.[121] *I–t*, *I–V*, EIS, and Mott–Schottky analyses were the methods to study all the prepared samples TiO_2, OV-TiO_2, 0D/1D g-C_3N_4/TiO_2, and 0D/1D g-C_3N_4/OV-TiO_2.[121] As is well-known, TiO_2 itself is a water-splitting catalyst, so it has been studied

even before being supported with the semiconductor g-C_3N_4.[121] The transient photocurrent response, *I–t* curve, of the mentioned catalysts exhibits a current range of 112 μA cm^{-2} (8, 60, 70, and 120, respectively).[121] The same was exhibited in the *I–V* curve in which the g-C_3N_4/OV-TiO_2 maximum current was measured to be (0.723 mA cm^{-2}), which was enhanced by more than 100 times that of TiO_2.[121] This wide range of results shows the enhancement of the catalyst efficiency after each preparation treatment. The formation of oxygen vacancies on OV-TiO_2 might be of great significance, enhancing the efficiency.[121] The oxygen vacancies' function is to capture migrant electrons and minimize the electron–hole recombination rate.[121] The formation of these vacancies occurs during $NaBH_4$ reduction in which the concentration is significant for the efficiency.[121] Concentration of 3M was found to be appropriate since more concentration results in bulk oxygen vacancies that reduce the photocurrent.[121] This decrease of current originates as the bulk vacancies function as a recombination center of carriers.[121] Combination with g-C_3N_4 is also of great significance, which promotes the current density.[121] The composite of g-C_3N_4/OV-TiO_2 possesses the highest photocurrent density which is 120 μA cm^{-2}, current 0.723 mA cm^{-2}, the lowest resistance among all of the as-prepared samples. This enhancement might reflect the faster charge transfer of the hybrid nanocomposite.[121]

Other work was done on this track to expand the investigation around the field. Monolayer InSe supported with g-C_3N_4 was theoretically discussed.[123] The improvement of the photocatalytic properties and enhancement of the band gap over the pristine carbon nitride were successfully observed.[123] The electronic properties exhibit higher efficiency than that of a single catalyst.[123] The photo-generated calculated current was supposed to be 290 μA cm^{-2}.[123] This is double the current of the titanium nanotube-based catalyst.

The oxygen vacancies function as electron donors, herein the donor density of the titania nanotube doubled after the $NaBH_4$ reduction.[121] This increase of donor density results in elevating the conductivity of the catalyst and enhancing the charge transfer.[121] Implementing the modeled structure of the pure composite after $NaBH_4$ reduction, which contains oxygen vacancies, provides additional confirmation of the experimental work (Figure 4.18B and C).[121] Furthermore, the Fermi level of TiO_2 is shifted more to the CB.[121] This might be interpreted as the effect of the heterostructure that was constructed after the reduction.[121] The vital role of the OV between graphitic carbon nitride and TiO_2 in this composite is to improve the separation efficiency of the carrier.[121] Moreover, the model structure and the density of the state model of the 0D/1D g-C_3N_4/TiO_2 and 0D/1D g-C_3N_4/OV-TiO_2 are shown in Figure 4.18D and E.[121] The formation of the oxygen vacancies leads to creation of the gap state that is close to the valence band maximum (VBM).[121] By the assumption of the DOS model, the electrons of the Ti 3d and N 2p are forming a *Z*-scheme by finding a path to recombine with each other.[121]

Coupling g-C_3N_4 with transition metal sulfides, monometallic and bimetallic, contributed to provide a large surface area and more active sites for HER.[124] Hence, CoS_x, NiS_x, and $CoNiS_x$ co-catalysts were fabricated to

investigate their abilities further to support graphitic carbon nitride and promote hydrogen evolution.[124]

Starting by preparing the precursors of the co-catalysts CoS_x, NiS_x, and $CoNiS_x$,[124] firstly, cobaltous and nickel nitrates with a ratio of 1:5 were added to 40 mL of methanol.[124] Comparing the yield of hydrogen in terms of different ratios of cobaltous and nickel nitrates, demonstrates the selection of 5:1 ratio.[124] The obtained mixture was then slowly dropped into the same amount of methanol in which 2-methylimidazole is presented by 9.65 mmol.[124] The precursor is ready to use after 12 h at room temperature. The same method was used to prepare other monometallic precursors CoS_x and NiS_x, obviously adding only one metal each.[124] The second step is to prepare the g-C_3N_4 using a traditional thermal polymerization method.[124] To obtain the catalyst, a hydrothermal approach is required. 0.1 g of prepared carbon nitride is dispersed in ethanol solution by sonication, to which 200 μL of the CoS_x, NiS_x, or $CoNiS_x$ precursors, followed by thioacetamide with 3× the amount of g-C_3N_4, is added. The selection of the MOF precursor volume occurs after different experiments in which 0.2 mL was found to have maximum H_2, compared to other volumes.[124] The reaction of the prepared composite occurs in an autoclave at 120 °C for 5 h.[124] The resulting composites of CoS_x-CN, NiS_x-CN, and $CoNiS_x$-CN are ready for HER and various testing methods to further investigate their contribution.[124]

XRD analysis was used to investigate the crystallinity (amorphosity) of the thus obtained g-C_3N_4, $CoNiS_x$, CoS_x–CN, NiS_x–CN, and $CoNiS_x$–CN. $CoNiS_x$ shows only a diffraction of broadening peak at 24.3, which represents its amorphous state.[124] Other tested catalysts all displayed the presence of peaks at 13.0 and 27.5° assigned to the 110 facet and 002 facets of carbon nitride.[124] There was no obvious difference between the diffraction of g-C_3N_4 and that of the as-prepared composites.[124] This might indicate the low content of metallic co-catalyst in the photocatalyst. This result was further proved by FT-IR spectra since the adsorption band of $CoNiS_x$ is missing in the catalyst $CoNiS_x$–CN. The composite also exhibits the presence of triazine units extracted from 810 cm^{-1} of FT-IR spectra.[124] SEM shows the polyhedral shape of $CoNiS_x$; however, $CoNiS_x$ disappeared at SEM of the $CoNiS_x$–gCN composite.[124] This is due to the low content of the co-catalyst in the composite, which supports XRD and FT-IR investigations.[124] Furthermore, the composite shows no lattice fringes when investigated by HRTEM.[124] This further certifies the previous results of the amorphous properties of the catalyst.[124] The presence of the elements was proved by EDS mapping, which confirms that C, N, S, Co, and Ni are offered on the composite even though Ni exhibits a weak signal.[124] The amount of $CoNiS_x$, CoS_x, and NiS_x in the catalyst $CoNiS_x$–gCN was measured by TG and ICP to be 0.93, 0.739, and 0.126%, respectively.[124] XPS results further confirm the surface composite of the catalyst and the presence of low amounts of the co-catalyst $CoNiS_x$.[124]

The as-prepared catalysts CoS_x–CN, NiS_x–CN, and $CoNiS_x$–gCN were tested to check which exhibits significant hydrogen evolution and catalytic performance.[124] A negligible amount of hydrogen was detected when using pristine

g-C_3N_4.[124] The evolution of hydrogen was remarkably enhanced when supported catalysts were introduced.[124] NiS_x and CoS_x gradually present growth of the reaction performance.[124] The significant hydrogen evolution of 2.366 μmol mg^{-1} h^{-1} occurs with the $CoNiS_x$–gCN catalyst, which is 76 times greater than that of g-C_3N_4.[124] This considerable result might be credited to the enlargement of the surface area and generation of abundant active sites.[124] The catalyst $CoNiS_x$–gCN was further investigated to check its stability and degradation resistance in terms of confirming its ability to function as a water-splitting catalyst.[124] After 8 h of catalytic activity the catalyst showed high performance compared to its initial one.[124] Moreover, the amount of Co and Ni content on the catalyst $CoNiS_x$–gCN after the reaction is more than 90%.[124] This illustrates the capacity of the photocatalyst to function as a water-splitting catalyst with high stability and durability.[124]

DFT was used to prove the experimental findings further and support the interpretation.[124] The work function of pristine g-C_3N_4 was calculated to be 4.76, which is lower than that of the co-catalyst $CoNiS_x$ (Figure 4.19A and B).[124] On the contrary, the fermi level of $CoNiS_x$ is lower than that of g-C_3N_4,

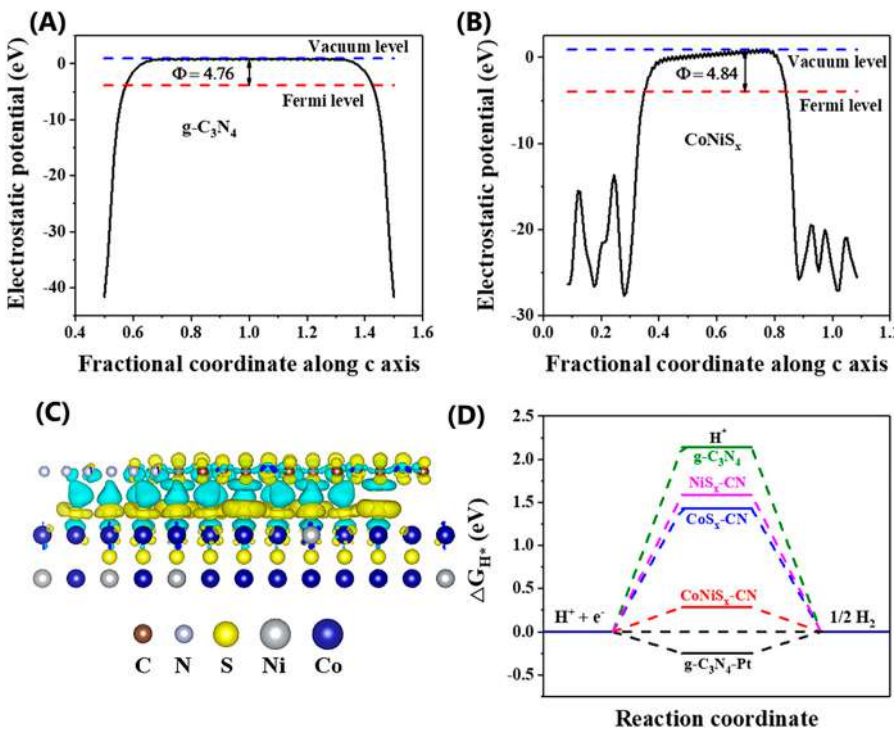

Figure 4.19 (A) Electronic potential of pristine carbon nitride, and (B) the co-catalyst $CoNiS_x$. (C) Charge density difference of the photocatalyst $CoNiS_x$–gCN model. (D) Calculated free-energy diagram of the photocatalytic HER for various photocatalysts. Reproduced from ref. 124 with permission from American Chemical Society, Copyright 2018.

which triggers the electron flow towards $CoNiS_x$ to satisfy equilibrium.[124] Figure 4.19C illustrates the charge density of the composite model in which charge accumulation and depletion appear in yellow and cyan colors.[124] This model further supports that the direction of the electrons is from g-C_3N_4 toward the co-catalyst $CoNiS_x$.[124] The ΔG indicator shows the outstanding performance of $CoNiS_x$–gCN that is close to the performance of noble metals (Figure 4.19D).[124]

4.10 Doped Carbon Nitride Materials

One of the first studies which served as a fundamental stage to deeply understand the photocatalytic activity of g-C_3N_4 material is the work done by Ma *et al.*[125] A novel structural doping approach has been used to alter the PEC properties of g-C_3N_4 using non-metal impurities such as sulfur or phosphorus for doping.[125] Here, different doped sites were used to construct the interstitial and substitutional doped models of the g-C_3N_4 systems. The stability and visible-light photoactivity were investigated through the dopant formation energies and electronic properties using first-principles DFT. The outcome of the study was that a P atom preferentially situates at the interstitial sites of in-planar g-C_3N_4; however, an S atom preferentially substitutes the edge N atom of g-C_3N_4. Furthermore, doping with non-metal impurities enhances the visible-light absorption of gC_3N_4 by reducing the energy gap. Also, the carrier mobility was enhanced by doping, which causes an increase in the dispersion of the contour distribution of the HOMO and LUMO; on the other hand, separation of photo-generated electron–hole pairs was noticed for the noncoplanar HOMO and LUMO. The presence of a new carrier channel migration shows the great potential of P interstitial doping. However, it is important to accurately control the proper doping form to achieve the desirable photoelectrochemical properties. Thus, the photocatalytic property limitation of g-C_3N_4 can be improved by doping with non-metal impurities. Doping accelerates the visible-light absorption of g-C_3N_4 since it alters the connectivity pattern and topology of the g-C_3N_4 sheets, which is essential for interstitial doped configurations.

In 2016, the activity of a carbon nitride (C_3N_4)-based electrocatalyst in the ORR and HER, under the effect of sulfur doping, was investigated experimentally and theoretically for the first time.[126] The study revealed that the presence of sulfur within the mesoporous carbon-supported C_3N_4 motif could significantly boost the ORR activity, coming closer to the commercial Pt/C even with enhanced durability and crossover tolerance. The composite catalyst HER performance was found to be superior to most other metal-free electrocatalysts and almost equivalent to the most active non-noble metal-based HER materials. DFT calculations showed that sulfur doping could change the charge, the electronic band structure, and spin densities within the C_3N_4 motif, which led to more adsorption sites for reaction intermediates in HER and ORR.

In another study, first-principles DFT calculations were used to study various hybrid g-C_3N_4@MG (M = B, N, O, F, P, and S) electrocatalysts.[127] The study demonstrated that as H atom coverage increases, the electron withdrawing influence for all the graphene substrates increases on the g-C_3N_4 active layer, resulting in modulating the overpotential, the binding of the H-atom intermediates, and the likely operational coverage. Moreover, B was found to be the most promising doping element for g-C_3N_4@MG electrocatalysts owing to its estimated overpotential of 0.06 eV at full coverage and large interfacial adhesion energy of −1.30 eV, which is significantly better than the n-dopant systems.

As an attempt to improve the surface area and charge separation, a non-metal doped with supramolecule-based g-C_3N_4 was designed.[128] The simulations done using DFT showed that carbon-doped g-C_3N_4 is thermodynamically stable, as it facilitates the charge separation, which in turn enhanced valence bands for photocatalytic oxidation and the energy levels of conduction compared to phosphorus-doped g-C_3N_4. By evaluating the performance of the carbon-doped, supramolecule based g-C_3N_4 under the irradiation of simulated visible sunlight, the results indicated that an enhancement of 2.3–10.5-fold in the reaction rate for the degradation of persistent organic micropollutants and phenol was noticed compared to that of conventional, melamine-based g-C_3N_4. This was also confirmed using DFT, where the reactivity for contaminant degradation was further improved compared with phosphorus-doping. Thus, it can be concluded that g-C_3N_4 can be a robust photocatalyst for contaminant degradation in partially treated water and wastewater.

In another study, component dopants' effect on the catalytic performance of graphitic C_3N_4 (g-C_3N_4)-based electrocatalysts were investigated using experimental and theoretical studies.[129] Three dopant elements (B, P, and S) embedded in either sites of the C–N skeleton were designed and synthesized. Theoretical and experimental methods were used to study the intrinsic activity, intermediate adsorption/desorption free energy, kinetics, and charge transfer process of the selected catalysts in ORR and HER. First, a controllable "bottom-up" synthetic method was used to prepare different heteroatom-doped g-C_3N_4 (X-CN) basal motifs to evaluate their electrocatalytic activities. For doping, ethylene diphosphonic acid and boric acid were adopted as P and B sources, respectively. To get a uniform element distribution, trithiocyanuric acid was used as the S-doped gCN monomer.

A thorough study on the dopant-induced impact was possible due to the incorporation of the X-CN/PC composites and successful heteroatom doping. The presence of nitrogen atoms in the g-C_3N_4 motif generates a high positive charge density on the adjacent carbon atoms due to their high electron affinity. Thus, the carbon atoms become potential active sites for oxygen adsorption and subsequent reduction reactions.

The HER catalytic activity of doped C_3N_4 composite catalysts was also evaluated using 0.5 M H_2SO_4 electrolyte.[129] The results showed that the N-PC provides the least HER activity, while the activity of CN/PC was much better.

The doped heteroatoms demonstrated a distinct influence, where S was found to be the best dopant, while the P and B elements have an adverse effect on the HER activity, as shown in Figure 4.20. The rotating ring-disk electrode (RRDE) technique was used to investigate the evolution of hydrogen gas. To remove the evolved H_2 bubbles radically, the parameters used were 1600 rpm for the electrode bearing the catalyst, and to oxidize the H_2, 0.7 V was set for the Pt ring potential. The results show that H_2 was generated by all four g-C_3N_4-based catalysts since the oxidation currents delivered follow the cathodic HER currents in the set potentials, as illustrated in Figure 4.20.[129]

The Tafel plots, shown in Figure 4.20, unveiled the primary H_2 evolution kinetics. A small Tafel slope (29 mV dec^{-1}) was observed for the benchmark Pt/C, corresponding to the Volmer–Tafel mechanism. In this system, hydrogen was generated most probably through the Volmer–Heyrovsky mechanism, where the electrochemical desorption process acts as a rate-determining

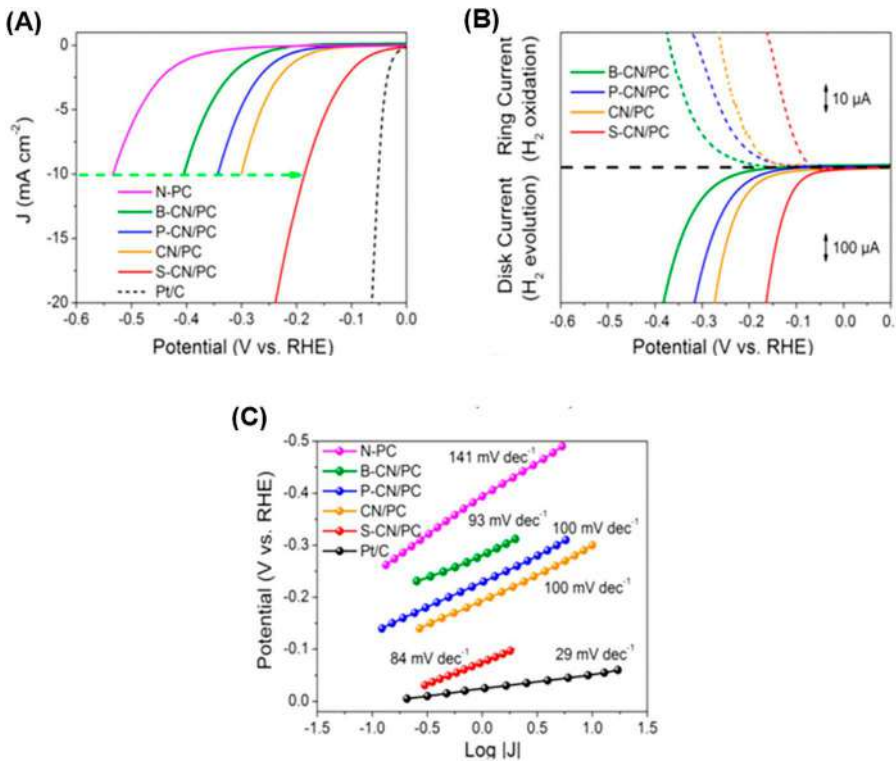

Figure 4.20 HER in 0.5 M H_2SO_4 solution electrochemical catalytic performance of different catalysts: (A) Polarization curves on an RDE with a scan rate and rpm of 5 mV s^{-1} and 3000, respectively. (B) RRDE measurements of hydrogen evolution; where the reduction and the oxidation currents during H_2 generation are recorded using the disk electrode and the ring electrode, respectively. (C) Tafel plots. Reproduced from ref. 129 with permission from American Chemical Society, Copyright 2017.

step. This was inferred from the calculated range of Tafel slopes (84–100 mV dec^{-1}) of g-C_3N_4-based samples. On the other hand, due to the low HER kinetics for the N-PC sample, a large Tafel slope of 141 mV dec^{-1} was observed, and the limiting step of its HER process was the elementary proton adsorption (*viz.*, the Volmer step). Thus, metal-free catalyst carbon nitride is superior to N-doped carbon as it could catalyze the HER with improved activity. gCN provides more proton adsorption sites, while despite being subjected to the same mechanism, its heteroatoms can significantly render different kinetics.

To sum up, the electrocatalytic HER and ORR performances of the macroporous carbon-supported g-C_3N_4 hybrid catalysts were investigated under the influence of dopants. Out of the three non-metal elements (B, P, and S) used, the S-doped hybrid exhibited the best intrinsic and reaction kinetics activities for enhancing both HER and ORR. The dopant elements could render different charge and spin densities within the g-C_3N_4 motifs, which was inferred from the theoretical calculations. In addition, they could lead to enhanced or deteriorated activities since they modify the sorption-free energies of different reaction intermediates. Elucidating clearly that doping can significantly affect the electrocatalytic performance of g-C_3N_4, and that a proper doping strategy is actually a valid technique to improve the composite hybrid, makes it one of the most stable and efficient metal-free electrocatalysts. In another study, the intermediate band gap states were introduced in the C_2N system by adsorbing halogen molecules for the first time.[130] Using hybrid density functional calculations, the influence of molecular adsorbates such as H_2, F_2, Cl_2, Br_2, and I_2 on the photocatalytic activity and electronic properties of the nitrogenated holey graphene (C_2N) was investigated. It was found that hydrogen and all the halogens, except F_2, prefer to physisorb on the holey site. The most promising halogen for hydrogen production was found to be the I_2 since it has appropriate band edge positions relative to the water redox potentials; also, both F_2 and Br_2 adsorbed C_2N have favorable band edge positions. The optoelectronic and photocatalytic properties can be significantly altered due to the new band states introduced when the halogens draw electrons from the C_2N monolayer owing to their high electronegativity. All these systems were found to be visible-light-active looking at their optical absorption spectra; hence, more light could be harvested.

Recently, DFT calculations were used to investigate the carrier separation efficiency, electronic structure, optical property, and band edge position of g-C_3N_4 catalyst altered by five-membered heterocyclic molecules (thiophene, furan, pyrrole, or pyrryl) as a ligand.[131] First, the structure stability was studied to determine the most stable configuration of the ligands-modified g-C_3N_4 surface. The results revealed that the binding energy between Pyrryl and g-C_3N_4 could reach −0.991 eV, forming a strong covalent bond. For furan, thiophene, or pyrrole on g-C_3N_4, no formation of chemical bonds was noticed, and their binding energies were −0.621 eV, −0.865 eV, and −0.637 eV, respectively, leading to relatively weak physical absorption. Regarding the electronic structure results, the band structures' energy splitting for the pyrryl-modified g-C_3N_4 system is significant compared with that of pure

g-C_3N_4. Besides, unlike the three modified systems, in the center of the forbidden band there is an empty impurity energy level, made up of the C and N 2p orbitals in g-C_3N_4. This empty impurity energy level is beneficial to the continuous transition of electrons and, in turn, improves the efficiency of utilizing visible light.[131] However, the influence of C 2p orbitals of ligands is more dominant than that of N 2p. To investigate the effect of four types of modifications on the separation efficiency of photo-generated carriers of g-C_3N_4, the relative ratio and the effective masses of photon-generated carriers were computed. The results indicated that they improved the separation efficiency of photo-induced electron–hole pairs and restrained the recombination of photo-generated electron–hole pairs effectively. Therefore, the modified g-C_3N_4 system improves its photon quantum effect, and at the same time, enhances its photocatalytic efficiency. Moreover, the band edge positions of each system were calculated to find out whether the band edge potential of pure and ligand-modified g-C_3N_4 satisfies the redox potential requirements of the PEC overall water splitting.[131]

In general, the requirements of the PEC overall water splitting to generate H_2 and O_2 are that the CBM should be above the reduction potential of H^+/H_2, while the VBM should be lower than the oxidation potential of O_2/H_2O. For the relative vacuum level of pure g-C_3N_4, the band edge potential of VB and CB is −6.18 eV and −3.50 eV, respectively (Figure 4.21). The calculated CB and VB edges of pure g-C3N4, furan, thiophene, and pyrrole-modified systems are −3.50 eV, −3.55 eV, −3.52 eV, and −3.64 eV above the water reduction potential and −6.18 eV, −6.51 eV, −6.48 eV, and −6.61 eV below the water oxidation potential, respectively. Thus, only the

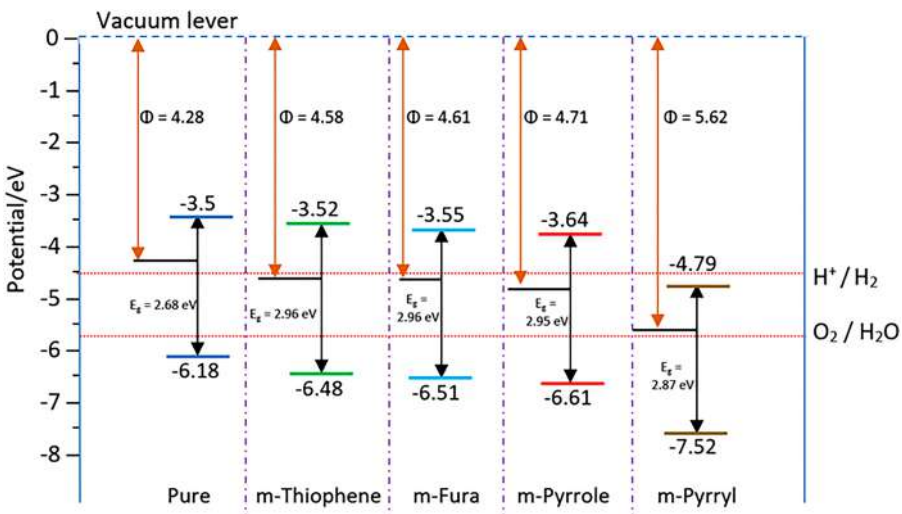

Figure 4.21 The redox potential of the relative vacuum level for the pure g-C_3N_4 and ligands-modified g-C_3N_4 systems.

pyrrole-modified g-C_3N_4 system met the overpotential requirements of the PEC overall splitting of water to generate O_2 and H_2. In addition, compared with the unmodified system, furan, thiophene, pyrrole, and pyrryl-modified g-C_3N_4 systems' valence band edge moved down 0.30 eV, 0.43 eV, 0.33 eV, and 1.34 eV, respectively. Thus, the oxidation capacity of g-C_3N_4 could be significantly improved by the ligands modified systems. For the pyrryl-modified g-C_3N_4 system, the band edge positions of VB and CB were −7.52 eV and −4.79 eV, respectively. Despite the fact that the pyrryl system did not meet the requirement of the PEC reduction-potential for the overall water splitting, it has exceptional properties in terms of photocatalytic oxidation owing to its strong oxidation potential. This in turn makes it more efficient in generating O_2 through water splitting, which is valuable in the degradation of organic pollutants.[131]

The photocatalytic performance was assessed using a semiconductor photocatalyst response to visible light, for that the absorption spectrum of pure and ligand-modified g-C_3N_4 was calculated. The results obtained showed that the pyrryl-modified g-C_3N_4 system absorption edge was noticeably red-shifted, and the light response range was increased towards the infrared region. Thus, the pyrrole-modified system is the only one that can rapidly transit the electrons, while for the other ligand-modified systems the impurity energy levels are favorable to the continuous transition of electrons. The distortion of the ligands-modified systems is the primary reason for the red-shift, and that improves the activity of n–π^* electrons' transition for these systems. Besides, the calculation of the effective carriers' mass showed that the ligand modifications have successfully improved the migration rate and separation efficiency of the carriers of g-C_3N_4. Thus, to improve the photocatalytic activity under visible light irradiation, pyrrole is an excellent candidate as a ligand for the modification of g-C_3N_4.

4.11 Conclusion and Future Perspectives

In brief, this chapter discussed the progress made in gCN for water-splitting reactions, including the HER and OER, from a theoretical perspective. This is including the utilization of gCN as metal-free catalysts for water splitting as well as gCN combined with transition metals and noble metals in the form of dopants or nanoparticles. The fundamentals and mechanisms of water oxidation and reduction on gCN materials is also discussed.

Despite the significant advances in the gCN for water splitting, there are several challenges that should be solved for further improvement to water-splitting performance.

This includes the gap between the obtained photocurrent density (0.1 mA cm^{-2}) of self-standing gCN at 1.23 V *vs.* RHE and theoretical value (4 mA cm^{-2}).[21] Thus, there is a crucial need for exhaustive research to enhance the photocurrent density of gCN experimentally as well as further theoretical studies that are needed to further understand the catalytic merits of gCN.

The photocatalytic activity of gCN for water oxidation is still very low and not studied enough compared to photocatalytic water reduction. For practical applications, gCN should possess an outstanding catalytic surface for both water reduction and water oxidation under different pH values (*i.e.*, acidic, neutral, and alkaline). To achieve this target, gCN could be integrated with novel kinds of multi-metallic Pt-based nanocrystals (*i.e.*, PtPdRu, PtCu, PtNi, PtRu, PtCo, PdPt, and AuPt), which have outstanding redox properties to enhance the water oxidation performance.[132–138] Additionally, the water oxidation performance of gCN could be plausibly enhanced by combining gCN with carbon-based catalysts (*i.e.*, carboxylated graphene oxide, carbon nanotubes, and carboxylated carbon, and 3D metal–organic framework), fullerene and upconversion nanomaterials.[4,6,139–143] Also, tailoring the morphology of gCN into porous 1D and 3D shapes can enhance the water-splitting performance due to their inimitable catalytic properties (*i.e.*, conductivity, accessible surface area, abundant active sites, and high surface area); however, fabrication of such shapes requires templates, multiple steps, and hazardous chemicals. Thereby, further studies are required to simplify the fabrication process of gCN into different shapes.

The long-term durability of gCN with various transition metals, noble metals, metal oxides, and carbon materials should be improved to be feasible for practical applications. This is besides enhancement of the current density under low potential. Further theoretical studies are also required to improve the physiochemical merits of gCN (*i.e.*, conductivity, surface area, and visible light absorption) to allow water redox under low applied potential.

References

1. K. Jlassi, K. Eid, M. H. Sliem, A. M. Abdullah and M. M. Chehimi, *Sep. Purif. Technol.*, 2020, **251**, 117383.
2. Y. Ibrahim, A. Mohamed, A. M. Abdelgawad, K. Eid, A. M. Abdullah and A. Elzatahry, *Nanomaterials*, 2020, **10**, 1916.
3. F. Wu, K. Eid, A. M. Abdullah, W. Niu, C. Wang, Y. Lan, A. A. Elzatahry and G. Xu, *ACS Appl. Mater. Interfaces*, 2020, **12**, 31309–31318.
4. X. Xu, T. Yang, Q. Zhang, W. Xia, Z. Ding, K. Eid, A. M. Abdullah, M. S. A. Hossain, S. Zhang and J. Tang, *Chem. Eng. J.*, 2020, **390**, 124493.
5. Y. Ibrahim, A. Kassab, K. Eid, A. M Abdullah, K. I. Ozoemena and A. Elzatahry, *Nanomaterials*, 2020, **10**, 885.
6. H. Idris Abdu, K. Eid, A. M. Abdullah, M. H. Sliem, A. Elzatahry and X. Lu, *Green Chem.*, 2020, **22**, 5437–5446.
7. H. I. Abdu, K. Eid, A. M. Abdullah, Z. Han, M. H. Ibrahim, D. Shan, J. Chen, A. A. Elzatahry and X. Lu, *Renewable Energy*, 2020, **153**, 998–1004.
8. Q. Wang and K. Domen, *Chem. Rev.*, 2020, **120**, 919–985.
9. K. Eid, K. A. Soliman, D. Abdulmalik, D. Mitoraj, M. H. Sleim, M. O. Liedke, H. A. El-Sayed, A. S. AlJaber, I. Y. Al-Qaradawi and O. M. Reyes, *Catal. Sci. Technol.*, 2020, **10**, 801–809.

10. Y. H. Ahmad, K. A. Eid, S. Y. AlQaradawi and N. K. Allam, *Sustainable Energy Fuels*, 2017, **1**, 1123–1129.
11. J. Lai, S. Li, F. Wu, M. Saqib, R. Luque and G. Xu, *Energy Environ. Sci.*, 2016, **9**, 1210–1214.
12. X. Zou and Y. Zhang, *Chem. Soc. Rev.*, 2015, **44**, 5148–5180.
13. L. Ma, W. Zhang, P. Zhao, J. Liang, Y. Hu, G. Zhu, R. Chen, Z. Tie, J. Liu and Z. Jin, *J. Mater. Chem. A*, 2018, **6**, 20076–20082.
14. S. K. Karuturi, H. Shen, A. Sharma, F. J. Beck, P. Varadhan, T. Duong, P. R. Narangari, D. Zhang, Y. Wan, J.-H. He, H. H. Tan, C. Jagadish and K. Catchpole, *Adv. Energy Mater.*, 2020, **10**, 2000772.
15. W. Wang, M. Xu, X. Xu, W. Zhou and Z. Shao, *Angew. Chem., Int. Ed.*, 2020, **59**, 136–152.
16. K. Eid, M. H. Sliem, K. Jlassi, A. S. Eldesoky, G. G. Abdo, S. Y. Al-Qaradawi, M. A. Sharaf, A. M. Abdullah and A. A. Elzatahry, *Inorg. Chem. Commun.*, 2019, **107**, 107460.
17. K. Eid, M. H. Sliem, H. Al-Kandari, M. A. Sharaf and A. M. Abdullah, *Langmuir*, 2019, **35**, 3421–3431.
18. K. Eid, M. H. Sliem, A. S. Eldesoky, H. Al-Kandari and A. M. Abdullah, *Int. J. Hydrogen Energy*, 2019, **44**, 17943–17953.
19. K. Eid, M. H. Sliem and A. M. Abdullah, *Nanoscale*, 2019, **11**, 11755–11764.
20. X. Wang, K. Maeda, A. Thomas, K. Takanabe, G. Xin, J. M. Carlsson, K. Domen and M. Antonietti, *Nat. Mater.*, 2009, **8**, 76–80.
21. J. Safaei, N. A. Mohamed, M. F. Mohamad Noh, M. F. Soh, N. A. Ludin, M. A. Ibrahim, W. N. Roslam Wan Isahak and M. A. Mat Teridi, *J. Mater. Chem. A*, 2018, **6**, 22346–22380.
22. J.-H. Zhang, M.-J. Wei, Z.-W. Wei, M. Pan and C.-Y. Su, *ACS Appl. Nano Mater.*, 2020, **3**, 1010–1018.
23. W. Niu and Y. Yang, *ACS Energy Lett.*, 2018, **3**, 2796–2815.
24. D. Wang, N. B. Saleh, W. Sun, C. M. Park, C. Shen, N. Aich, W. J. G. M. Peijnenburg, W. Zhang, Y. Jin and C. Su, *Environ. Sci. Technol.*, 2019, **53**, 7265–7287.
25. W.-J. Ong, L.-L. Tan, Y. H. Ng, S.-T. Yong and S.-P. Chai, *Chem. Rev.*, 2016, **116**, 7159–7329.
26. H. L. Lee, Z. Sofer, V. Mazánek, J. Luxa, C. K. Chua and M. Pumera, *Appl. Mater. Today*, 2017, **8**, 150–162.
27. J. Fu, J. Yu, C. Jiang and B. Cheng, *Adv. Energy Mater.*, 2018, **8**, 1701503.
28. M. Xiao, B. Luo, S. Wang and L. Wang, *J. Energy Chem.*, 2018, **27**, 1111–1123.
29. C. Jia, L. Yang, Y. Zhang, X. Zhang, K. Xiao, J. Xu and J. Liu, *ACS Appl. Mater. Interfaces*, 2020, **12**, 53571–53591.
30. Y. Wu, C. Li, W. Liu, H. Li, Y. Gong, L. Niu, X. Liu, C. Sun and S. Xu, *Nanoscale*, 2019, **11**, 5064–5071.
31. Y. Li, Y.-L. Li, B. Sa and R. Ahuja, *Catal. Sci. Technol.*, 2017, **7**, 545–559.
32. Y. Gurdal and M. Iannuzzi, *Titanium Dioxide*, 2017.
33. J. Yi, W. El-Alami, Y. Song, H. Li, P. M. Ajayan and H. Xu, *Chem. Eng. J.*, 2020, **382**, 122812.

34. A. Mishra, A. Mehta, S. Basu, N. P. Shetti, K. R. Reddy and T. M. Aminabhavi, *Carbon*, 2019, **149**, 693–721.
35. G. Zhang, Z.-A. Lan and X. Wang, *Chem. Sci.*, 2017, **8**, 5261–5274.
36. X. Lv, W. Wei, H. Wang, B. Huang and Y. Dai, *Appl. Catal., B*, 2020, **264**, 118521.
37. N. S. Lewis and D. G. Nocera, *Proc. Natl. Acad. Sci. U. S. A.*, 2006, **103**, 15729–15735.
38. J. A. Turner, *Science*, 2004, **305**, 972–974.
39. M. G. Walter, E. L. Warren, J. R. McKone, S. W. Boettcher, Q. Mi, E. A. Santori and N. S. Lewis, *Chem. Rev.*, 2010, **110**, 6446–6473.
40. B. E. Conway and B. V. Tilak, *Electrochim. Acta*, 2002, **47**, 3571–3594.
41. R. Subbaraman, D. Tripkovic, D. Strmcnik, K. C. Chang, M. Uchimura, A. P. Paulikas, V. Stamenkovic and N. M. Markovic, *Science*, 2011, **334**, 1256–1260.
42. A. Le Goff, V. Artero, B. Jousselme, P. D. Tran, N. Guillet, R. Métayé, A. Fihri, S. Palacin and M. Fontecave, *Science*, 2009, **326**, 1384–1387.
43. J. Zhuo, T. Wang, G. Zhang, L. Liu, L. Gan and M. Li, *Angew. Chem., Int. Ed.*, 2013, **52**, 10867–10870.
44. T. R. Cook, D. K. Dogutan, S. Y. Reece, Y. Surendranath, T. S. Teets and D. G. Nocera, *Chem. Rev.*, 2010, **110**, 6474–6502.
45. V. Artero, M. Chavarot-Kerlidou and M. Fontecave, *Angew. Chem., Int. Ed.*, 2011, **50**, 7238–7266.
46. M. Rakowski DuBois and D. L. DuBois, *Chem. Soc. Rev.*, 2009, **38**, 62–72.
47. S. Cobo, J. Heidkamp, P. A. Jacques, J. Fize, V. Fourmond, L. Guetaz, B. Jousselme, V. Ivanova, H. Dau, S. Palacin, M. Fontecave and V. Artero, *Nat. Mater.*, 2012, **11**, 802–807.
48. P. Du and R. Eisenberg, *Energy Environ. Sci.*, 2012, **5**, 6012–6021.
49. E. J. Popczun, J. R. McKone, C. G. Read, A. J. Biacchi, A. M. Wiltrout, N. S. Lewis and R. E. Schaak, *J. Am. Chem. Soc.*, 2013, **135**, 9267–9270.
50. T. F. Jaramillo, K. P. Jørgensen, J. Bonde, J. H. Nielsen, S. Horch and I. Chorkendorff, *Science*, 2007, **317**, 100–102.
51. J. Kibsgaard, Z. Chen, B. N. Reinecke and T. F. Jaramillo, *Nat. Mater.*, 2012, **11**, 963–969.
52. D. Voiry, H. Yamaguchi, J. Li, R. Silva, D. C. B. Alves, T. Fujita, M. Chen, T. Asefa, V. B. Shenoy, G. Eda and M. Chhowalla, *Nat. Mater.*, 2013, **12**, 850–855.
53. S. Najmaei, Z. Liu, W. Zhou, X. Zou, G. Shi, S. Lei, B. I. Yakobson, J.-C. Idrobo, P. M. Ajayan and J. Lou, *Nat. Mater.*, 2013, **12**, 754–759.
54. A. B. Laursen, S. Kegnæs, S. Dahl and I. Chorkendorff, *Energy Environ. Sci.*, 2012, **5**, 5577–5591.
55. D. Merki and X. Hu, *Energy Environ. Sci.*, 2011, **4**, 3878–3888.
56. J. Xu, G. Wang, J. Fan, B. Liu, S. Cao and J. Yu, *J. Power Sources*, 2015, **274**, 77–84.
57. G. Liu, P. Niu, L. Yin and H.-M. Cheng, *J. Am. Chem. Soc.*, 2012, **134**, 9070–9073.

58. F. Wang, W. K. H. Ng, J. C. Yu, H. Zhu, C. Li, L. Zhang, Z. Liu and Q. Li, *Appl. Catal., B*, 2012, **111–112**, 409–414.
59. G. Liu, L.-C. Yin, P. Niu, W. Jiao and H.-M. Cheng, *Angew. Chem., Int. Ed.*, 2013, **52**, 6242–6245.
60. X. Li, J. Zhao and J. Yang, *Sci. Rep.*, 2013, **3**, 1858.
61. Y. Zheng, Y. Jiao, Y. Zhu, L. H. Li, Y. Han, Y. Chen, A. Du, M. Jaroniec and S. Z. Qiao, *Nat. Commun.*, 2014, **5**, 3783.
62. F. Wu, Y. Liu, G. Yu, D. Shen, Y. Wang and E. Kan, *J. Phys. Chem. Lett.*, 2012, **3**, 3330–3334.
63. R. Li, *Chin. J. Catal.*, 2017, **38**, 5–12.
64. A. Naseri, M. Samadi, A. Pourjavadi, A. Z. Moshfegh and S. Ramakrishna, *J. Mater. Chem. A*, 2017, **5**, 23406–23433.
65. N. Dubouis and A. Grimaud, *Chem. Sci.*, 2019, **10**, 9165–9181.
66. A. K. Ipadeola and K. I. Ozoemena, *RSC Adv.*, 2020, **10**, 17359–17368.
67. T. Bhowmik, M. K. Kundu and S. Barman, *ACS Catal.*, 2016, **6**, 1929–1941.
68. R. C. P. Oliveira, M. Sevim, B. Šljukić, C. A. C. Sequeira, Ö. Metin and D. M. F. Santos, *Catal. Today*, 2020, **357**, 291–301.
69. T. Shinagawa, A. T. Garcia-Esparza and K. Takanabe, *Sci. Rep.*, 2015, **5**, 13801.
70. M. Tahir, L. Pan, F. Idrees, X. Zhang, L. Wang, J.-J. Zou and Z. L. Wang, *Nano Energy*, 2017, **37**, 136–157.
71. X. Wang, S. Blechert and M. Antonietti, *ACS Catal.*, 2012, **2**, 1596–1606.
72. K. Srinivasu and S. K. Ghosh, *J. Mater. Chem. A*, 2015, **3**, 23011–23016.
73. H.-Z. Wu, L.-M. Liu and S.-J. Zhao, *Phys. Chem. Chem. Phys.*, 2014, **16**, 3299–3304.
74. K. Srinivasu, B. Modak and S. K. Ghosh, *J. Phys. Chem. C*, 2014, **118**, 26479–26484.
75. C. Butchosa, P. Guiglion and M. A. Zwijnenburg, *J. Phys. Chem. C*, 2014, **118**, 24833–24842.
76. X. Wang, K. Maeda, A. Thomas, K. Takanabe, G. Xin, J. M. Carlsson, K. Domen and M. Antonietti, in *Materials for Sustainable Energy*, 2010, pp. 271–275.
77. A. B. Jorge, D. J. Martin, M. T. S. Dhanoa, A. S. Rahman, N. Makwana, J. Tang, A. Sella, F. Corà, S. Firth, J. A. Darr and P. F. McMillan, *J. Phys. Chem. C*, 2013, **117**, 7178–7185.
78. D. J. Martin, K. Qiu, S. A. Shevlin, A. D. Handoko, X. Chen, Z. Guo and J. Tang, *Angew. Chem., Int. Ed.*, 2014, **53**, 9240–9245.
79. J. Wirth, R. Neumann, M. Antonietti and P. Saalfrank, *Phys. Chem. Chem. Phys.*, 2014, **16**, 15917–15926.
80. S. Melissen, T. Le Bahers, S. N. Steinmann and P. Sautet, *J. Phys. Chem. C*, 2015, **119**, 25188–25196.
81. G. Algara-Siller, N. Severin, S. Y. Chong, T. Björkman, R. G. Palgrave, A. Laybourn, M. Antonietti, Y. Z. Khimyak, A. V. Krasheninnikov, J. P. Rabe, U. Kaiser, A. I. Cooper, A. Thomas and M. J. Bojdys, *Angew. Chem., Int. Ed.*, 2014, **53**, 7450–7455.

82. S. Zuluaga, L.-H. Liu, N. Shafiq, S. M. Rupich, J.-F. Veyan, Y. J. Chabal and T. Thonhauser, *Phys. Chem. Chem. Phys.*, 2015, **17**, 957–962.
83. P. Niu, L. C. Yin, Y. Q. Yang, G. Liu and H. M. Cheng, *Adv. Mater.*, 2014, **26**, 8046–8052.
84. L. Xu, W.-Q. Huang, L.-L. Wang, Z.-A. Tian, W. Hu, Y. Ma, X. Wang, A. Pan and G.-F. Huang, *Chem. Mater.*, 2015, **27**, 1612–1621.
85. G. A. Meek, A. D. Baczewski, D. J. Little and B. G. Levine, *J. Phys. Chem. C*, 2014, **118**, 4023–4032.
86. Y. Xu and S.-P. Gao, *Int. J. Hydrogen Energy*, 2012, **37**, 11072–11080.
87. W. Wei and T. Jacob, *Phys. Rev. B*, 2013, **87**, 085202.
88. H.-Z. Wu, L.-M. Liu and S.-J. Zhao, *Appl. Surf. Sci.*, 2015, **358**, 363–369.
89. J. Ehrmaier, T. N. V. Karsili, A. L. Sobolewski and W. Domcke, *J. Phys. Chem. A*, 2017, **121**, 4754–4764.
90. J. Ehrmaier, W. Domcke and D. Opalka, *J. Phys. Chem. Lett.*, 2018, **9**, 4695–4699.
91. X. Wang, L. Wu, Z. Wang, H. Wu, X. Zhou, H. Ma, H. Zhong, Z. Xing, G. Cai and C. Jiang, *Sol. RRL*, 2019, **3**, 1800298.
92. G. Dong, K. Zhao and L. Zhang, *Chem. Commun.*, 2012, **48**, 6178–6180.
93. Z. Chen, D. Cummins, B. N. Reinecke, E. Clark, M. K. Sunkara and T. F. Jaramillo, *Nano Lett.*, 2011, **11**, 4168–4175.
94. W.-F. Chen, K. Sasaki, C. Ma, A. I. Frenkel, N. Marinkovic, J. T. Muckerman, Y. Zhu and R. R. Adzic, *Angew. Chem., Int. Ed.*, 2012, **51**, 6131–6135.
95. D. Merki, H. Vrubel, L. Rovelli, S. Fierro and X. Hu, *Chem. Sci.*, 2012, **3**, 2515–2525.
96. J. K. Nørskov, T. Bligaard, A. Logadottir, J. R. Kitchin, J. G. Chen, S. Pandelov and U. Stimming, *J. Electrochem. Soc.*, 2005, **152**, J23.
97. G. Gao, Y. Jiao, F. Ma, Y. Jiao, E. Waclawik and A. Du, *Phys. Chem. Chem. Phys.*, 2015, **17**, 31140–31144.
98. J. Feng, G. Liu, S. Yuan and Y. Ma, *Phys. Chem. Chem. Phys.*, 2017, **19**, 4997–5003.
99. H. Wang, X. Li and J. Yang, *ChemPhysChem*, 2016, **17**, 2100–2104.
100. J. Wang, Z. Guan, J. Huang, Q. Li and J. Yang, *J. Mater. Chem. A*, 2014, **2**, 7960–7966.
101. J. Zhang, F. Ren, M. Deng and Y. Wang, *Phys. Chem. Chem. Phys.*, 2015, **17**, 10218–10226.
102. J. Wang, X. Li, Y. You, X. Yang, Y. Wang and Q. Li, *Nanotechnology*, 2018, **29**, 365401.
103. J. Yang, D. Wang, H. Han and C. Li, *Acc. Chem. Res.*, 2013, **46**, 1900–1909.
104. Q. Zhai, S. Xie, W. Fan, Q. Zhang, Y. Wang, W. Deng and Y. Wang, *Angew. Chem., Int. Ed.*, 2013, **52**, 5776–5779.
105. A. Kudo and Y. Miseki, *Chem. Soc. Rev.*, 2009, **38**, 253–278.
106. K. Maeda, K. Teramura, D. Lu, N. Saito, Y. Inoue and K. Domen, *Angew. Chem., Int. Ed.*, 2006, **45**, 7806–7809.
107. X. F. Yang, A. Wang, B. Qiao, J. Li, J. Liu and T. Zhang, *Acc. Chem. Res.*, 2013, **46**, 1740–1748.

108. J. Ran, J. Zhang, J. Yu, M. Jaroniec and S. Z. Qiao, *Chem. Soc. Rev.*, 2014, **43**, 7787–7812.
109. H. N. Kim, T. W. Kim, I. Y. Kim and S.-J. Hwang, *Adv. Funct. Mater.*, 2011, **21**, 3111–3118.
110. X. Li, W. Bi, L. Zhang, S. Tao, W. Chu, Q. Zhang, Y. Luo, C. Wu and Y. Xie, *Adv. Mater.*, 2016, **28**, 2427–2431.
111. J. Liu, Y. Liu, N. Liu, Y. Han, X. Zhang, H. Huang, Y. Lifshitz, S. T. Lee, J. Zhong and Z. Kang, *Science*, 2015, **347**, 970–974.
112. W. Wang, J. C. Yu, Z. Shen, D. K. L. Chan and T. Gu, *Chem. Commun.*, 2014, **50**, 10148–10150.
113. Y. Zhang, J. Liu, G. Wu and W. Chen, *Nanoscale*, 2012, **4**, 5300–5303.
114. J. Liu, T. Zhang, Z. Wang, G. Dawson and W. Chen, *J. Mater. Chem.*, 2011, **21**, 14398–14401.
115. J. Liu, Y. Zhang, L. Lu, G. Wu and W. Chen, *Chem. Commun.*, 2012, **48**, 8826–8828.
116. X. Wang, X. Chen, A. Thomas, X. Fu and M. Antonietti, *Adv. Mater.*, 2009, **21**, 1609–1612.
117. H. Su, W. Che, F. Tang, W. Cheng, X. Zhao, H. Zhang and Q. Liu, *J. Phys. Chem. C*, 2018, **122**, 21108–21114.
118. Z. Chen, Y. Bu, L. Wang, X. Wang and J.-P. Ao, *Appl. Catal., B*, 2020, **274**, 119117.
119. L. Li, J. Yi, X. Zhu, M. Zhou, S. Zhang, X. She, Z. Chen, H.-M. Li and H. Xu, *ACS Sustainable Chem. Eng.*, 2019, **8**, 884–892.
120. C. Chu, Q. Zhu, Z. Pan, S. Gupta, D. Huang, Y. Du, S. Weon, Y. Wu, C. Muhich and E. Stavitski, *Proc. Natl. Acad. Sci. U. S. A.*, 2020, **117**, 6376–6382.
121. L. Xiao, T. Liu, M. Zhang, Q. Li and J. Yang, *ACS Sustainable Chem. Eng.*, 2018, **7**, 2483–2491.
122. L. Bi, D. Meng, Q. Bu, Y. Lin, D. Wang and T. Xie, *Phys. Chem. Chem. Phys.*, 2016, **18**, 31534–31541.
123. Y. Liang, C. Long, J. Li, H. Jin, B. Huang and Y. Dai, *ACS Appl. Energy Mater.*, 2018, **1**, 5394–5401.
124. L. Jiang, K. Wang, X. Wu, G. Zhang and S. Yin, *ACS Appl. Mater. Interfaces*, 2019, **11**, 26898–26908.
125. X. Ma, Y. Lv, J. Xu, Y. Liu, R. Zhang and Y. Zhu, *J. Phys. Chem. C*, 2012, **116**, 23485–23493.
126. Z. Pei, J. Zhao, Y. Huang, Y. Huang, M. Zhu, Z. Wang, Z. Chen and C. Zhi, *J. Mater. Chem. A*, 2016, **4**, 12205–12211.
127. X. Tan, H. A. Tahini and S. C. Smith, *ACS Catal.*, 2016, **6**, 7071–7077.
128. Q. Zheng, D. P. Durkin, J. E. Elenewski, Y. Sun, N. A. Banek, L. Hua, H. Chen, M. J. Wagner, W. Zhang and D. Shuai, *Environ. Sci. Technol.*, 2016, **50**, 12938–12948.
129. Z. Pei, J. Gu, Y. Wang, Z. Tang, Z. Liu, Y. Huang, Y. Huang, J. Zhao, Z. Chen and C. Zhi, *ACS Nano*, 2017, **11**, 6004–6014.
130. M. A. Kishore, A. O. Sjåstad and P. Ravindran, *Carbon*, 2019, **141**, 50–58.

131. Y. Zhang, C. Ren, Y. Zhang, W. Lin and K. Ding, *Appl. Surf. Sci.*, 2019, **478**, 119–127.
132. H. Wang, Y. Li, C. Li, K. Deng, Z. Wang, Y. Xu, X. Li, H. Xue and L. Wang, *J. Mater. Chem. A*, 2019, **7**, 801–805.
133. S. Lu, K. Eid, D. Ge, J. Guo, L. Wang, H. Wang and H. Gu, *Nanoscale*, 2017, **9**, 1033–1039.
134. K. Eid, H. Wang, V. Malgras, S. M. Alshehri, T. Ahamad, Y. Yamauchi and L. Wang, *J. Electroanal. Chem.*, 2016, **779**, 250–255.
135. K. Eid, H. Wang, V. Malgras, Z. A. Alothman, Y. Yamauchi and L. Wang, *J. Phys. Chem. C*, 2015, **119**, 19947–19953.
136. K. Eid, H. Wang, P. He, K. Wang, T. Ahamad, S. M. Alshehri, Y. Yamauchi and L. Wang, *Nanoscale*, 2015, **7**, 16860–16866.
137. H. Wang, S. Yin, K. Eid, Y. Li, Y. Xu, X. Li, H. Xue and L. Wang, *ACS Sustainable Chem. Eng.*, 2018, **6**, 11768–11774.
138. H. Zhang, H. Wang, K. Eid and L. Wang, *Part. Part. Syst. Charact.*, 2015, **32**, 863–868.
139. C. Wei, H. Wang, K. Eid, J. Kim, J. H. Kim, Z. A. Alothman, Y. Yamauchi and L. Wang, *Chem. - Eur. J.*, 2017, **23**, 637–643.
140. H. I. Abdu, K. Eid, A. M. Abdullah and X. Lu, *Data Brief*, 2020, **30**, 105520.
141. K. Eid, M. H. Sliem, A. S. Eldesoky and A. M. Abdullah, *Data Brief*, 2019, **27**, 104734.
142. K. Eid and A. M. Abdullah, *Data Brief*, 2019, **26**, 104495.
143. M. A. Ahsan, T. He, K. Eid, A. M. Abdullah, M. L. Curry, A. Du, A. R. Puente Santiago, L. Echegoyen and J. C. Noveron, *J. Am. Chem. Soc.*, 2021, **143**, 1203–1215.

CHAPTER 5

Graphitic Carbon Nitride-polymer Hybrids: A Win–Win Combination with Advanced Properties for Different Applications

B. KUMRU[a], Q. CAO[a] AND B. V. K. J. SCHMIDT*[b]

[a]Max Planck Institute of Colloids and Interfaces, Am Mühlenberg 1, 14476 Potsdam, Germany; [b]University of Glasgow, Joseph Black Building, G128QQ Glasgow, UK
*E-mail: bernhard.schmidt@glasgow.ac.uk

5.1 Introduction

Hybrid materials most commonly feature a combination of organic and inorganic materials on the nanoscale.[1–5] These combinations introduce not only a sum of the properties but also completely new properties or opportunities that are not available with the individual materials.[1] As such, hybridization is a highly useful strategy in materials synthesis to develop materials with a broad range of properties and to tailor the properties precisely. In addition, composite materials also enable a broad range of properties.[6] Graphitic carbon-nitride (g-C_3N_4) consists of a regular arrangement of tri-*s*-triazine

Nanoscience & Nanotechnology Series No. 51
Carbon Nitride Nanostructures for Sustainable Energy Production and Environmental Remediation
Edited by Kamel Abdelmoniem Mohamed Eid and Aboubakr M. Abdullah

Published by the Royal Society of Chemistry, www.rsc.org

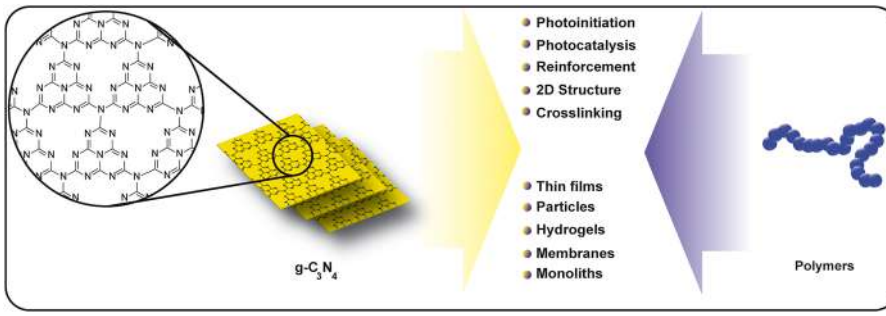

Scheme 5.1 Properties and materials derived from the combination of g-C_3N_4 with polymers highlighting the features that g-C_3N_4 introduces into polymers (top) and the achievable morphologies *via* combination of g-C_3N_4 and polymers (bottom). Reproduced from ref. 33 with permission from the Royal Society of Chemistry.

units forming a sheet-like material (Scheme 5.1),[7,8] which features visible and UV light photoactivity.[9–12] Therefore, g-C_3N_4 is employed often as a heterogeneous photocatalyst activated by visible light, *e.g.* for organic reactions,[13,14] hydrogen evolution,[15–17] pollution degradation or CO oxidation[18–21] or CO_2 reduction.[22,23] Additionally, g-C_3N_4 is used for membranes capable of ion transport,[24,25] photoelectrochemistry[26,27] or for emulsion stabilization[28,29] as well as in photovoltaics.[30–32]

As such, g-C_3N_4 as a material is of the highest interest as a semiconductor due to its metal-free structure and easy synthesis from benign precursors; however, g-C_3N_4 features a couple of serious drawbacks like structural disordering, and poor processability in bulk and dispersion, which hampers various research directions and applications. With regard to these issues, polymers and g-C_3N_4 can be favorably combined to obtain advanced materials (Scheme 5.1).[33–36] For example, polymers add improvements to processing, like film formation, to the materials and enhance dispersibility. In addition, a broad range of polymers with conductive properties enables a tailoring of electron transport processes. Thus, new properties can be implemented to g-C_3N_4 *via* polymers to improve common properties (*e.g.* conductivity or photocatalysis). Similarly, inclusion of g-C_3N_4 in polymers is a way to tune polymer mechanical properties, for example, in hydrogels or bulk. An additional useful feature of g-C_3N_4 is the property for radical formation under visible light irradiation that enables photoinitiation for the synthesis of polymers, *e.g.* particles or hydrogels (Section 5.2 and 5.3). As such, g-C_3N_4 and polymers feature a common ground, and combination facilitates enhanced novel properties.

Polymer materials belong to the most important industrial products and affect daily life considerably. Functional polymers especially are of significant interest today with properties like self-healing, stimuli response,[37–40] biodegradability,[41–43] self-assembly in aqueous environments[44–46] or electrical

conductivity.[47–49] Starting from this diversity, introduction of the metal-free semiconductor g-C_3N_4 can be a significant addition to the property portfolio (Scheme 5.1). Because of g-C_3N_4 introduction, photoluminescence, photocatalytic and enhanced physical/mechanical properties are achieved. At the same time, polymers add enhanced conductivity or processing.

Hybrid materials formed from g-C_3N_4 and polymers are used in various applications (refer to Section 5.5), *e.g.* biosensors, H_2 evolution, electrochemical energy storage or photocatalysis depending on the materials' properties of the hybrids. Film and membrane materials find frequent application in electrochemistry, while particles are commonly utilized in biosensors. Moreover, polymers enable inclusion of g-C_3N_4 into defined material morphologies (refer to Section 5.4), *e.g.* thin films or particles. In addition, g-C_3N_4 hybridization with polymers allows one to improve polymer properties, *e.g.* mechanical properties. Thus, g-C_3N_4 and polymers are a combination of mutual benefit. On one hand, polymers advance g-C_3N_4 processing amongst other properties. On the other hand, g-C_3N_4 enhances the properties of polymer materials, *e.g.* mechanical features.

In the following chapter, the hybridization of polymers and g-C_3N_4 is discussed. To begin with, the properties of g-C_3N_4 as a photoinitiator are discussed alongside their application in several polymerization examples. Subsequently, the area of g-C_3N_4-derived hydrogels is described focusing on photocatalysis abilities and mechanical features. Furthermore, g-C_3N_4 dispersibility and improvement *via* polymer- or functionalization-based avenues are presented. Most importantly, polymer/g-C_3N_4 composites and hybrids are highlighted. Finally, applications are discussed, *e.g.* photocatalysis, H_2 evolution, electrochemical energy storage, biosensors as well as polymer properties, films or nano particles. The chapter is closes with a summary and outlook.

5.2 g-C_3N_4 as a Polymerization Initiator for Polymer Synthesis

In recent years, photopolymerization has been a major topic in the field of polymer science.[50–52] Also, g-C_3N_4 holds several interesting features for photopolymerization. Most frequently, g-C_3N_4 was utilized as a highly active photocatalyst, which is due to a suitable band gap that enables absorption of visible light leading to electron and hole generation. Therefore, species like $O_2^{-\bullet}$, $^{\bullet}OH$, $HO_2^{\bullet}$, or CN-centered species are formed that are highly reactive and of interest for polymerization processes in addition to classical photocatalysis. This feature introduces two avenues for reactions (depicted in Scheme 5.2) where g-C_3N_4 initiates photopolymerization, which comes with considerable advantages. At first, g-C_3N_4 polymerizations are prone to be operated with visible light irradiation, as an abundant and benign trigger. As such, various monomers were polymerized *via* g-C_3N_4 photoinitiation, *e.g.* methyl methacrylate (MMA),[53] styrene,[54] methyl acrylate (MA)[55]

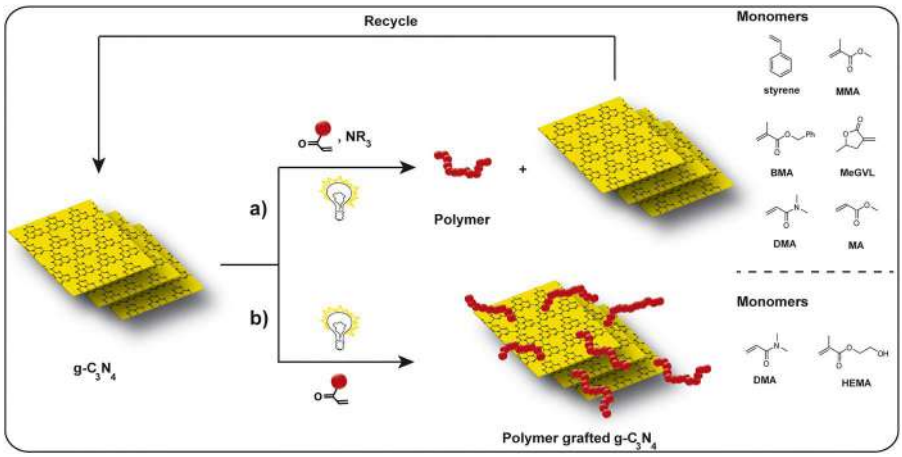

Scheme 5.2 Photopolymerization mediated by g-C_3N_4 and utilized monomers in the two approaches: Usage of g-C_3N_4 as a recyclable photoinitiator *via* radical transfer to an amine (top) and light initiated grafting of polymers onto g-C_3N_4 (bottom) (BMA: benzyl methacrylate; DMA: *N*,*N*-dimethylacrylamide; HEMA: 2-hydroxyethyl methacrylate; MA: methyl acrylate; MMA: methyl methacrylate; MeGVL: α-methylene-γ-valerolactone). Reproduced from ref. 33 with permission from the Royal Society of Chemistry.

or α-methylene-γ-valerolactone (MeGVL).[56] In addition, photoinitiated polymerizations feature spatial and temporal control. Due to the fact that g-C_3N_4 acts as catalyst in a heterogenous fashion, facile separation and reusage is achieved. Notably, the polymerization process can be tuned to graft polymers from g-C_3N_4. Nevertheless, polymer-grafting from g-C_3N_4 introduces several options for formation of hybrid materials that advance a usage in bio-related applications because of the photoluminescence features of g-C_3N_4.

One of the first examples was introduced by Yagci and coworkers, who described free radical polymerization initiated by g-C_3N_4 and a visible light trigger.[57] There, heterogeneous visible light photoinitiation was performed *via* mesoporous g-C_3N_4 (mpg-C_3N_4) and reactive co-initiators, *i.e.* tertiary amines. Vinyl monomers like MMA were polymerized that way. Due to the activity of mpg-C_3N_4 in photoredox chemistry, photoinitiated polymerization was performed *via* exposition of the reaction dispersion to visible light after removal of residual oxygen. Presumably, the initiation-step proceeds *via* the hole transfer from the g-C_3N_4 to the tertiary amine, *i.e.* the respective radical cations capable of abstracting hydrogen from another amine and initiating radical formation are derived from the photo-derived holes. Furthermore, mpg-C_3N_4 showed advanced activity in the polymerization reaction as it features an increased surface area in comparison to common g-C_3N_4.

Our team performed emulsion photopolymerization *via* g-C_3N_4 photoinitiation.[58] Therefore, monomers were emulsified (containing, *e.g.* MMA, benzyl methacrylate and styrene) in water and fabricated by Pickering stabilization

with g-C_3N_4 (*i.e.* g-C_3N_4 synthesized *via* cyanuric acid-melamine-complex (CM) or 1-decene grafted CM). Irradiation of the emulsion with visible light led to polymerization, where the surface of g-C_3N_4 generates radicals. Further investigations of kinetics and microscopy studies of synthesized particles showed that the surface of g-C_3N_4 functioned as a location of chain growth and particle formation. In order to investigate the polymerization mechanism hole or electron, scavengers were added to the reaction system, respectively, which indicated that the present emulsion photopolymerization was a hole-centered process. The process led to very well-defined latexes, which indicated latex particle formation by fast nucleation. In comparison to previously published works, the generation of initiating radicals occurred by the presence of holes on g-C_3N_4 without addition of co-initiators. Due to the formation of radicals in a direct way, crosslinked polymer particles were formed because of the multifunctional nature of g-C_3N_4 as a photoinitiator. The combination of surface-modified g-C_3N_4 with microfluidics was recently introduced, where g-C_3N_4, used as a Pickering stabilizer, allowed precise production of water/oil, oil/water and water/oil/water double emulsions.[59] For the double emulsion scenario, if the inner oil phase consists of styrene, polymerization under UV light (g-C_3N_4 as stabilizer and photoinitiator) grants an easy access for crosslinked hollow polymer spheres, without utilization of any commercial templates/surfactants/stabilizers. Another work reported by our team utilized heterogenous initiation *via* g-C_3N_4 in MeGVL free radical polymerization.[56] The monomer MeGVL was received over hierarchical basic zeolite in continuous flow from renewable γ-valerolactone. As MeGVL features a similar structure to methacrylic monomers, polymerization was straightforward. Valorization of this compound shows the ability to combine eco-friendly g-C_3N_4 materials with renewable biomass-derived monomers *via* efficient polymerization to synthesize novel biomass-derived polymers with considerable industrial interest. Yagci and coworkers showed an oxygen tolerant free radical polymerization process in connection with Fe(III) ions.[60] The introduction of Fe(III) allowed Fenton-type chemistry to form hydroxyl radicals after light irradiation and subsequent polymerization initiation. As initiation depends on *in situ* Fe(III) to Fe(II) reduction subsequently followed by oxidation to Fe(III) forming active species, photoexcited electrons were the driving factor to initiate Fenton-type polymerization.

The semiconductor g-C_3N_4 features a conduction band with a high negative position, which contributes to a considerable activity towards capturing oxygen and reduction. At the same time, g-C_3N_4 features a medium oxidation potential that inhibits the photogenerated hole-driven polymer decomposition efficiently. These two effects are crucial in the process of photopolymerization.[61,62] For these reasons, g-C_3N_4 was investigated as an electron transfer catalyst in reversible deactivation radical polymerization (RDRP). The team of Yagci used photoactivation by mpg-C_3N_4 for copper(II) species reduction. Formation of copper(I) species acted as an activator in atom transfer radical polymerization (ATRP), which could be conducted under sunlight or UV light. Furthermore, light-induced electron transfer

by g-C_3N_4 could be related to the large potential of reduction (E_{CB}) of −1.2 eV. During the reaction, polymers from styrene, MMA and MA were formed with significant control over molecular dispersity (*Đ*). In another work, the team of Qiao used amine cocatalysts and g-C_3N_4 for a photoinduced oxygen-tolerant electron/energy transfer (PET) reversible addition–fragmentation chain transfer (RAFT) polymerization (Figure 5.1).[63] Interestingly, direct utilization of g-C_3N_4 without prior deoxygenation of the polymerization mixture was possible in order to allow added tertiary amines, *i.e.* triethanolamine (TEOA), to transfer electrons to O_2 present in the solution. Chain transfer agents, *e.g.* trithiocarbonates (TTC), could be activated by reduction with oxygen, which led to polymers from *N*,*N*-dimethylacrylamide (DMA), MA and *n*-butyl acrylate (BA) (Figure 5.1a). Oxygen molecules play a significant part in

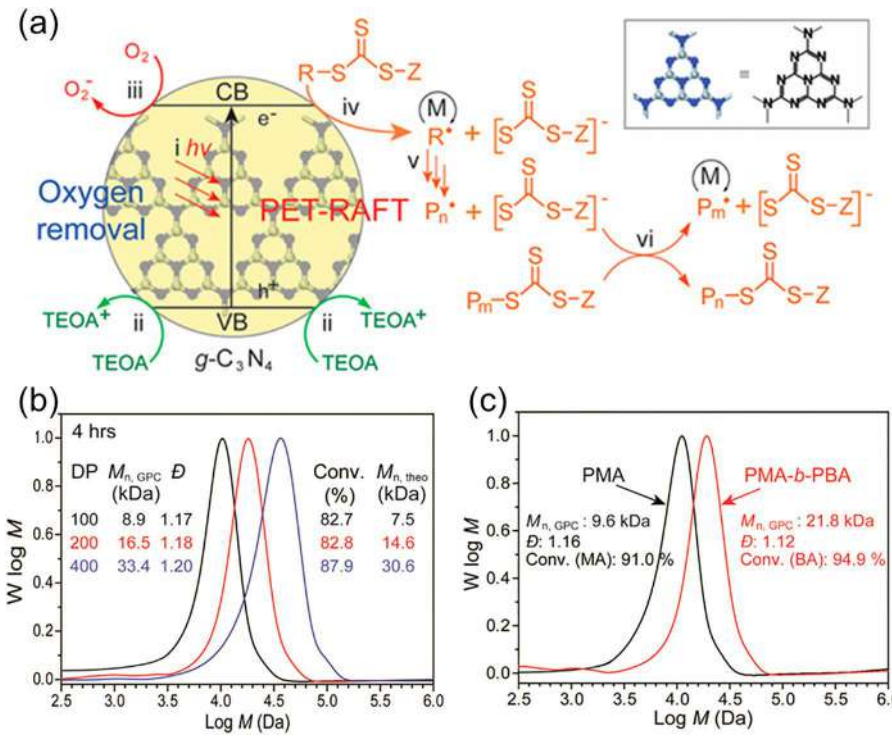

Figure 5.1 (a) Mechanism of deoxygenation and photoinduced electron/energy transfer-reversible addition–fragmentation chain transfer (PET-RAFT) polymerization *via* g-C_3N_4: (i) activation of g-C_3N_4 *via* light, (ii–iv) electron transfers from amine to g-C_3N_4, from g-C_3N_4 to O_2, and from g-C_3N_4 to the trithiocarbonate (TTC), respectively; (v) monomer initiation and chain propagation (M); and (vi) reversible degenerative chain transfer (RAFT process). (b) Traces from size exclusion chromatography (SEC) of the products, *i.e.* poly(methyl acrylate) (PMA) with different degrees of polymerization (DP) (DP = 100, 200, and 400). (c) SEC traces of diblock copolymers' product PMA-*b*-poly(*n*-butylacrylate) (PBA) and precursor PMA. Adapted from ref. 63 with permission from American Chemical Society, Copyright 2017.

the photoredox cycle of the mechanism. As such, reactions were performed *via* visible light without the requirement of deoxygenation of the polymerization mixture, which is a considerable advantage over common techniques. In the polymerization, polymers with a tailored degree of polymerization were achieved and analyzed by size exclusion chromatography (SEC) (Figure 5.1b). Block copolymers could be formed as expected from a RDRP process, for example PMA-*b*-PBA (Figure 5.1c). Moreover, the approach *via* PET-RAFT includes organic solvent tolerance, low toxicity and easy post-polymerization separation of the catalyst.[64] The group of Matyjaszewski investigated PET-RAFT as well.[64] A heteroatom-doped g-C_3N_4 was introduced to improve absorption of visible light. Vinyl monomers were polymerized using mild blue light irradiation. In a different work, the photocatalytic properties of g-C_3N_4 could be exploited to conduct dithiol–ene click conjugation of renewable lignocellulose-derived 4-pentenoic acid (4-PEA) and various dithiols.[65] Therefore, a visible light mediated click reaction was employed to couple 4-PEA with 2,2-(ethylenedioxy)-diethanethiol (EDDT), 1,2-ethanedithiol (EDT), or 1,4-benzenedimethanethiol (BDT) in order to form a dicarboxylic acid monomer that can be polymerized *via* polycondensation.

The g-C_3N_4-based photoinitiation process is further employed frequently for hydrogel synthesis. There, mechanisms of initiation of the same type are involved, *i.e.* radicals are generated on the g-C_3N_4 surface *via* light irradiation and hydrogelation is induced *via* g-C_3N_4 in the absence of a co-initiator or electron transfer agent. Hydrogel formation is described in Section 5.3 in detail. Interestingly, hydrogels were fabricated in the absence of an external crosslinker indicating g-C_3N_4 surface-driven initiation and inclusion of g-C_3N_4 in the hydrogel *via* covalent bonds.[66] These results underpin the g-C_3N_4 initiation mechanism for polymerization without radical transfer agent addition.

The photoinitiator properties of g-C_3N_4 have been employed to synthesize g-C_3N_4-derived polymer hybrids *via* visible light with a "grafting from" process. This method makes use of monomer propagation commencing from a surface for polymer formation, *i.e.* in the present case, g-C_3N_4 surface. The radical formation on g-C_3N_4 *via* irradiation of visible light for grafting is likely due to uncondensed $-NH_2$ or –NH groups being present. Such groups form active sites for initiation of chain growth starting at the g-C_3N_4 surface. Thus, g-C_3N_4-based polymer hybrid materials can be synthesized easily including a covalent attachment of polymer onto the g-C_3N_4 surface. Amin and coworkers utilized g-C_3N_4 as a photoinitiator to graft various monomers, *e.g.* MMA, *N*-isopropylacrylamide or *N*,*N*-dimethylaminoethylmethacrylate.[67] The materials showed enhanced dispersibility and were successively utilized for surface-enhanced Raman spectroscopy in connection with Ag nano particles.

In a similar way, the performance of polymerization on g-C_3N_4 enables to obtain g-C_3N_4/polymer nanocomposites to be obtained. Weber and teammates described the synthesis of g-C_3N_4-derived PBA composite materials by polymerization based on an aerosol (Figure 5.2a).[68] At first, spherical mpg-C_3N_4 (SMCN) was synthesized utilizing a template of mesoporous silica nanoparticles

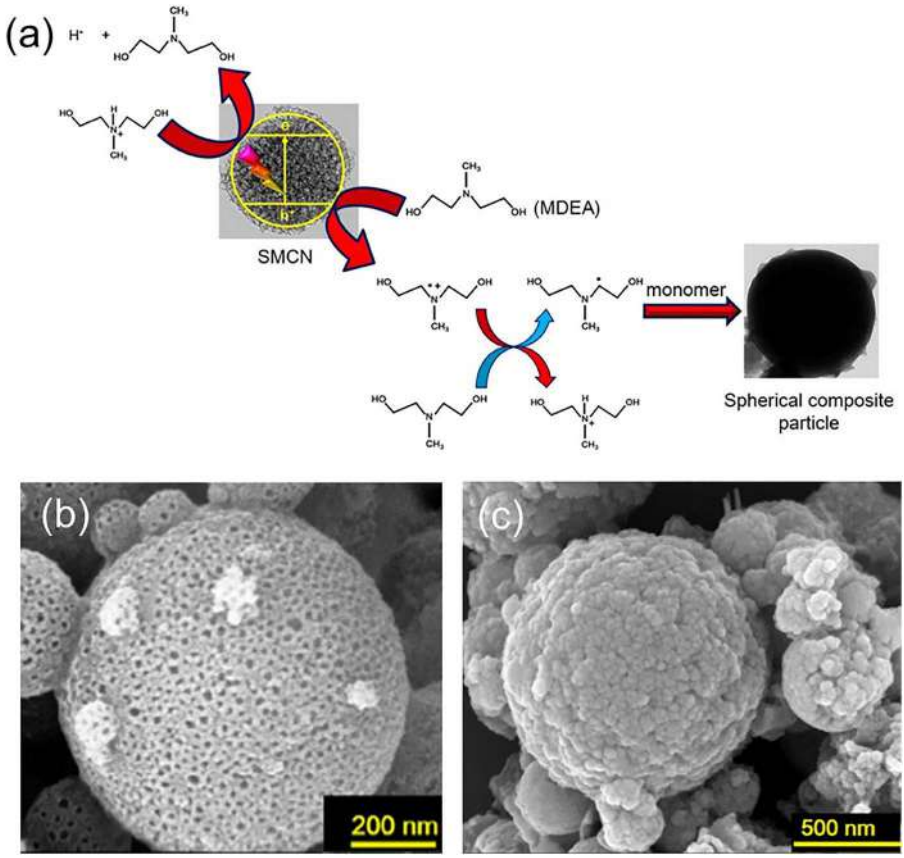

Figure 5.2 (a) Mechanism of initiation of the photopolymerization utilizing spherical mesoporous g-C_3N_4 (SMCN) together with methyl diethanolamine (MDEA) as co-initiator. (b) SEM image of SMCN replicas. (c) SEM image of PBA-SMCN composites from aerosol-photopolymerization. Adapted from ref. 68 with permission from American Chemical Society, Copyright 2016.

(Figure 5.2b). Continuous introduction of the monomer *via* the gas phase and photopolymerization in proximity of g-C_3N_4 under UV light was performed. The polymerization process yielded spherical g-C_3N_4/polymer composite particles (Figure 5.2c) in the absence of solvent or surfactant. As such, spherical nanocomposites with hydrophobic polymers are synthesized. In addition to being a photoinitiator, the mpg-C_3N_4 serves as a filler and template.

5.3 Carbon Nitride-based Hydrogels

Hydrogels present a highly relevant area in materials chemistry, which is mainly because of their special properties, *e.g.* ability to swell and shape persistence with elastic behavior.[69–72] As they consist of a crosslinked hydrophilic

network, hydrogels are porous networks that hold considerable amounts of water. As such, they are comparable with tissues in nature, which is an additional reason for their common occurrence in materials studies, especially in the case of biomedical applications, for example, drug-delivery or tissue-engineering.[73,74] But there are also other applications that are discussed, for example self-healing,[75] actuators,[76] contaminant absorption[77] or shape-memory materials.[78] In many cases, hydrogels feature mechanical properties that are quite weak, but considerable mechanical properties have been introduced with reinforced hydrogels in the past. Various avenues are performed for reinforcement, *e.g.* topological (slide-ring) gels,[79–81] double network hydrogels,[82,83] the introduction of charged supports[84–86] or nanofiber reinforced hydrogels.[87] The utilization of particles in hydrogels as reinforcing materials introduces enhanced dissipation of stress, for example, charge–charge repulsions from filler particles or sheets provides an additional compression stabilization.[17] A frequently used material is clay nanosheets, which feature ionic interactions as well as hydrogen bonding to polymer chains that act as supportive crosslinking points.[88–90]

As highlighted earlier, g-C_3N_4 acts as a photoinitiator in polymerizations. Hence, g-C_3N_4 is useable for hydrogel fabrication *via* visible light. A variety of mechanical features are available by incorporation of g-C_3N_4 into hydrogels.[91] Actually, g-C_3N_4-derived hydrogels have considerable mechanical properties including compressibility and significant storage moduli. The formation of hydrogels from g-C_3N_4 does not only rely on covalent bonds, but supramolecular and blended hydrogels are described as well, which is discussed in Section 5.4.6. Additionally, g-C_3N_4-derived hydrogels can be used for photocatalysis *via* included g-C_3N_4 allowing performance of contaminant degradation as well as hydrogen evolution (Section 5.5.5).

The photoactivity of g-C_3N_4 under visible light and corresponding active radical species formation in aqueous media was already discussed.[92] This behavior in aqueous media provides a platform for simple hydrogel synthesis if the monomer and crosslinker are present in the same environment (Scheme 5.3a). As many water-soluble monomer derivatives with diverse functional groups are available, g-C_3N_4 initiated hydrogels can present a variety of functionalities together with mechanical enhancement, where g-C_3N_4 plays the roles of photoinitiator and reinforcer. The synthesis of hydrogels based on sheet-like reinforcer dispersions is ideal when one desires tailored mechanical properties, as the interaction of reinforcer and hydrogel network can dissipate applied stress, such as in clay based hydrogels.[89] However, covalent incorporation of reinforcer to hydrogel networks promises additional mechanical stability.

For example, *N*,*N*′-methylene bisacrylamide (MBA) crosslinker and DMA monomer were included in a 0.6 wt% CM dispersion in water to facilitate hydrogel fabrication.[93] Some hours of irradiation with visible light led to hydrogel formation in closed vessels. Notably, the photocatalytic activity was retained by the porous hydrogels. In addition, properties like considerable stretchability or a combination of toughness and flexibility were noted

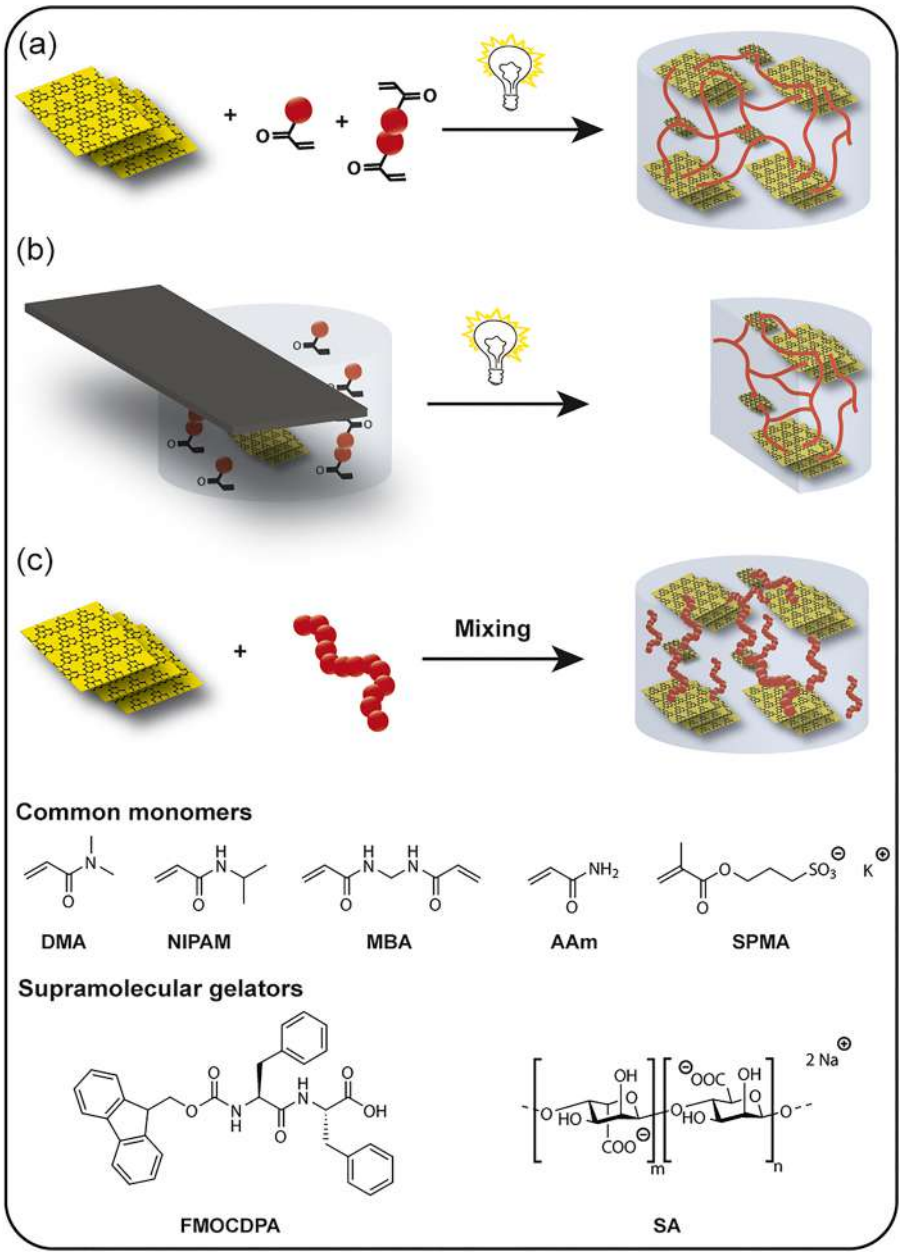

Scheme 5.3 Hydrogels derived from g-C_3N_4: (a) synthesis by visible light mediated polymerization of a crosslinker and water-soluble monomer, (b) hydrogel fabrication with spatial control by utilization of a photomask yielding polymerization in the irradiated part only and (c) physical interactions for hydrogel formation (AAm: acrylamide; DMA: *N*,*N*-dimethylacrylamide; FMOCDPA: Fmoc-diphenylalanine; MBA: *N*,*N*′-methylene bisacrylamide; NIPAM: *N*-isopropylacrylamide; SA: sodium alginate; SPMA: 3-sulfopropyl methacrylate potassium salt). Reproduced from ref. 33 with permission from the Royal Society of Chemistry.

due to a sheet-induced reinforcing effect of g-C_3N_4. Such behavior provides a new class of materials worthy of investigation. In the next step, the focus was oriented to address the mechanism of gel formation and, in parallel, mechanical reinforcement (Figure 5.3).[66] An investigation on the action of g-C_3N_4 during hydrogel synthesis was performed *via* reference reactions, *i.e.* formation of hydrogels *via* a commercial water-soluble photoinitiator or without g-C_3N_4 (Figure 5.3a), which provided hydrogels but weak mechanical properties. Hydrogel formation in the absence of a commercial crosslinker proves that g-C_3N_4 is indeed covalently attached to the network, as dispersed sheets possess 2D sheet-like structures; radical formation on both sides fits the description of a crosslinker (containing bifunctional or tetrafunctional vinyl groups). The employed monomer possesses a tertiary amino group that is prone to oxidation to give amine radical cation, which was the main initiating species for photopolymerization using g-C_3N_4 as depicted in previous reports.[55,57] However, a non-nitrogen containing monomer and crosslinker can form hydrogel as well, which broadens the spectrum of monomers. In addition, significant hydrogel properties could be measured (G' reaches 8.3 kPa with a solid content of 11 wt%) (Figure 5.3c). Two effects are responsible for such enhancement; the first one is g-C_3N_4 as a colloidal filler for the porous

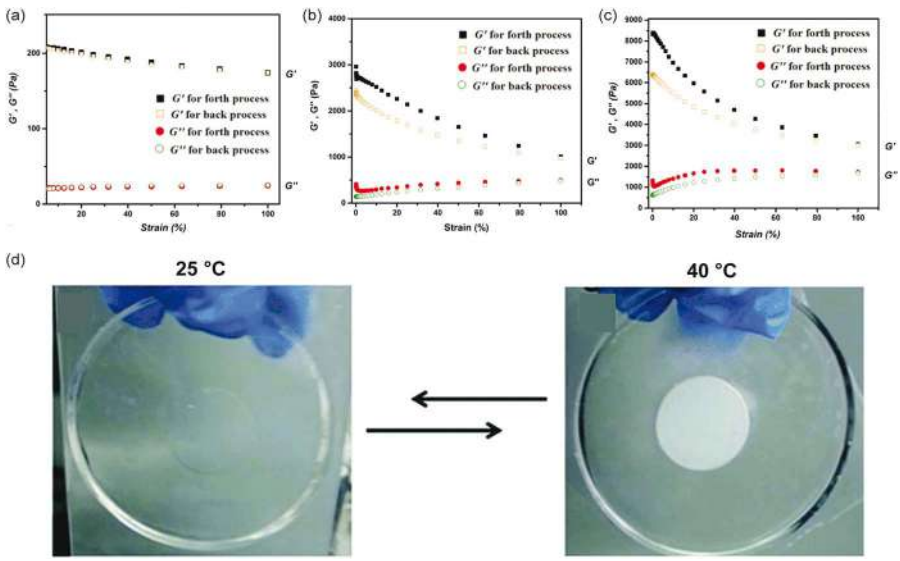

Figure 5.3 Storage (G′, black and orange) and loss modulus (G″, red and green) measurements of g-C_3N_4 free DMA hydrogel (a), g-C_3N_4 embedded DMA hydrogel without covalent bonding (b), and g-C_3N_4 derived DMA hydrogels with nanosheet integration (c). Adapted from ref. 66 with permission from American Chemical Society, Copyright 2017. (d) Images of a hydrogel in a monolithic shape fabricated from NIPAM/g-C_3N_4 at ambient temperature and elevated temperature, respectively. Reproduced from ref. 94 with permission from the Royal Society of Chemistry.

network that enhances mechanical properties regardless of bonding, and the second one is the covalent attachment and crosslinking effect of g-C_3N_4 leading to a more rigid network that is capable of dissipating stress more efficiently. This effect could be probed *via* embedding g-C_3N_4 in a hydrogel network by utilizing a redox initiator in the dark (Figure 5.3b). Introducing g-C_3N_4 enhances the mechanical properties of hydrogel in comparison with a reference sample free of g-C_3N_4; however, the mechanical properties are far from visible light g-C_3N_4 mediated hydrogels. In conclusion, both scenarios can help to improve the mechanical properties; however, a more pronounced effect is achievable by covalent attachment of g-C_3N_4. Such type of reinforcement results in shear thinning under stress, which is due to the weakened interaction of polymer chains and g-C_3N_4 interactions upon load.

Formation of the g-C_3N_4/N-isopropylacrylamide (NIPAM) hydrogel was shown by Liu and coworkers, who proposed a visible light induced hydrogel formation in the absence of an external crosslinker.[92] The thermoresponsive behavior of the NIPAM polymer was observed in hydrogels as well. In such a case, mechanical features such as storage and loss modulus of the synthesized hydrogels as well as viscosity can be tailored *via* the lower critical solution temperature (LCST). Moreover, the authors could fabricate hydrogels in designed patterns changing transparency *via* temperature in a reversible way due to a change in the hydrophilicity of PNIPAM (Figure 5.3d). g-C_3N_4 containing acrylamide based hydrogels was reported by Farzaneh and coworkers, who included physical incorporation of g-C_3N_4 with redox initiated polymerization of MBA and acrylamide (AAm).[94] As g-C_3N_4 is thermally conductive, electrophoresis in the hydrogels was improved by reduced Joule heating and lowered broadening of bands. Additionally, tetramethyl ethylenediamine as a polymerization catalyst could be replaced by g-C_3N_4 as well, which increases the compatibility with some analytes.

To gain a deeper understanding of which factor of g-C_3N_4 (zeta potential, surface area and light absorption)[95–97] dominantly affects the mechanical performance of hydrogels, a series of g-C_3N_4 species were employed for hydrogel formation. It was found that the zeta potential is the main factor governing mechanical properties, meaning more negative charges on g-C_3N_4 compounds yielded stronger hydrogels,[66] which is rationalized by repulsion of g-C_3N_4 sheets increasing with negative increment zeta potentials that is similarly described in the literature for other reinforcer particles.[86,90] To further discover such an effect and manipulate towards achieving more delicate hydrogels, we have employed AHPA (3-allyloxy-2-hydroxy-1-propanesulfonic acid sodium salt)-grafted g-C_3N_4 featuring considerably lower zeta potentials as well as higher dispersibility in water because of the sulfonic acid group.[98] Binary monomer mixtures of AAm and DMA together with a MBA crosslinker were used *via* initiation with CM-AHPA. Contrary to the expectation, rather soft hydrogels were synthesized with G' around 100–200 Pa containing solids even below 10 wt%. Still, the hydrogels had advanced properties regarding compression, *e.g.* withstanding loads over 12 MPa (Figure 5.4) and were stable against several hammer hits (shock resistance). The considerable

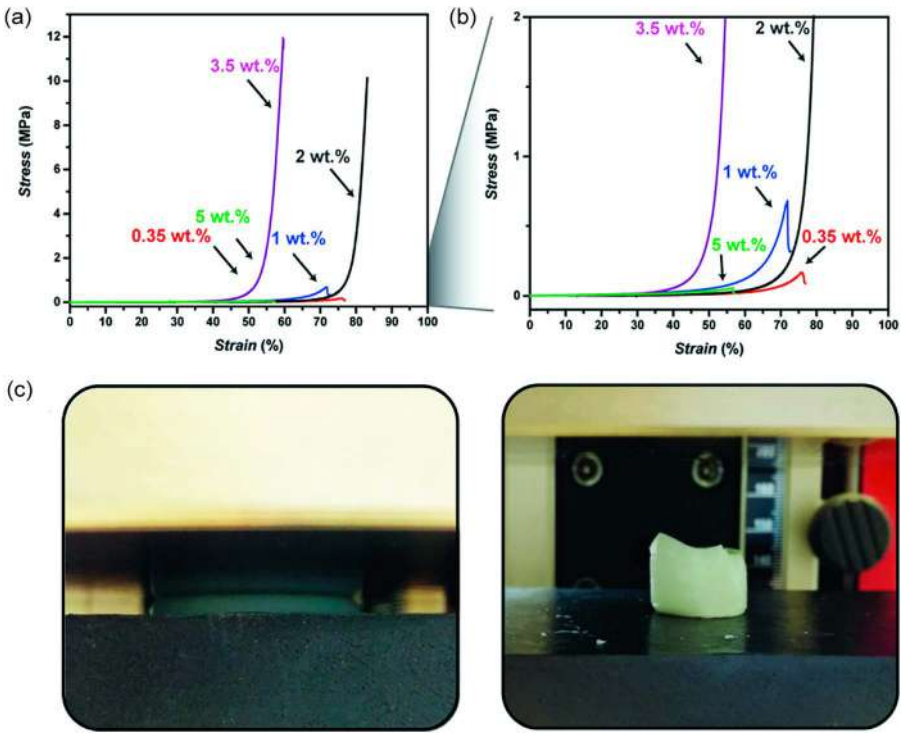

Figure 5.4 (a) Results from compression tests of g-C_3N_4-AHPA-based hydrogels (red: 0.35 wt%; blue: 1 wt%; black: 2 wt%; violet: 3.5 wt%; green: 5 wt%), (b) compression test results of g-C_3N_4-AHPA hydrogels in magnification, (c) pictures of 2 wt% g-C_3N_4-AHPA hydrogel during (left) and after (right) compression. Adapted from ref. 98 with permission from John Wiley and Sons, Copyright 2019 WILEY-VCH Verlag GmbH & Co. KGaA, Weinheim.

compressibility was attributed to significant repulsion arising from highly charged nanosheets, and the soft structure allows a dissipation of stress over a whole sample without any weakening point. Indeed, the cylindrical hydrogel undergoes complete flattening upon compression, yet the shape is recovered immediately once the stress is removed. To understand the role of each monomer, hydrogels were made from each monomer individually as well. While DMA seems to have an effect on toughening the hydrogel but less compression resistance, AAm has the effect of compression resistivity but weakness. Therefore, a combination of these monomers results in a soft and compressible hydrogel. Screening the charges by swelling the hydrogel in a solution of salts (NaCl or $CaCl_2$) revealed enhanced strength but inferior compression properties, which underlines the importance of surface chemistry in the hydrogel toughening mechanism. Therefore, the main reason for enhanced compressibility is the surface charge of g-C_3N_4. Furthermore, the

tailored monomer mixture enhances compressibility *via* improved elasticity that yields to advanced distribution of stress in the network.

In addition to the significant effect of the surface charge of the employed g-C_3N_4, the amount of employed g-C_3N_4 also plays a role for the final mechanical performance. In order to overcome the dispersibility issue of non-modified g-C_3N_4, ethylene glycol (EG)/water mixtures were used instead of pure water.[99] Enhancement in mechanical properties with increasing g-C_3N_4 content was reported, revealing G' of 88 kPa for 2 wt%, 430 kPa for 3 wt% and 729 kPa for 4 wt% of g-C_3N_4 at a strain of 0.1%, which constitutes considerable enhancement about two orders of magnitude in comparison to hydrogels including 0.6 wt% g-C_3N_4. It was also realized that hydrogelations were significantly faster by increasing the g-C_3N_4 amount, which agrees with the role of g-C_3N_4 as photoinitiator. Photoinduced hydrogel formation paves the possibility for patterning; for example, parts of the reaction mixture were covered with a simple homemade photomask obtaining an inversely shaped hydrogel (Scheme 5.3b/Figure 5.5).

These experiments also support a lack of radical transfer to a dark area (solution) as the polymerization proceeds only in the illuminated area *via* g-C_3N_4 initiation. An issue arises if one wants to employ charged monomers, as this disrupts the colloidal stability of g-C_3N_4 and causes sedimentation. To provide such a scenario, we have formed a g-C_3N_4-PDMA prepolymer, which is based on stirring g-C_3N_4 in water/EG mixture with DMA monomer under visible light irradiation. The resulted viscous prepolymer then can be mixed with a crosslinker and charged monomer such as 3-sulfopropyl methacrylate potassium salt (SPMA) and DMA as comonomer, to form hydrogel under visible light. The SPMA monomer produces negatively charged hydrogel structures, which are prime candidates for low friction surfaces in aqueous conditions.[100] Therefore, hydrogels inheriting both considerable compression properties due to the inclusion of g-C_3N_4 and friction coefficients with very low values around 0.03 were synthesized. In order to mimic artificial cartilage,[101] one must find the balance between mechanical stability and friction, which is highly demanding from a synthetic perspective.

Figure 5.5 Control of photopolymerization for gel synthesis in a spatial way: (a) self-standing half-circle, (b) self-standing club shape and (c) photopatterned stripes on glass. Reproduced from ref. 99 with permission from the Royal Society of Chemistry.

5.4 Functionalization-based Routes of g-C_3N_4/ Polymer Hybrid Materials and their Properties

Several avenues can be utilized to form hybrid materials from g-C_3N_4 and polymers (Scheme 5.4). (1) Physical adsorption or deposition, mainly formed in a liquid environment as well as mixing of the materials. (2) "Grafting from" where polymerization of monomers happens from the g-C_3N_4 surface. (3) "Grafting to" where pre-formed polymers with reactive end groups are conjugated to the g-C_3N_4 surface.

5.4.1 Dispersibility Enhancement of g-C_3N_4

One of the main challenges in the processing of g-C_3N_4 and bringing it into applications is poor dispersibility. Due to considerable interactions of g-C_3N_4 sheets, *e.g.* van der Waals interactions (π–π stacking), agglomeration proceeds in the liquid phase. Therefore, the formation of dispersions in an organic or aqueous environment is challenging,[102] which results in restricted applicability and activity.[102,103] Thin semiconductor films with a thickness of 2–3 nm and their formation is of considerable interest for applications in optoelectronics and photovoltaics. Nevertheless, the formation of g-C_3N_4 films has to be performed mainly with rather elaborate

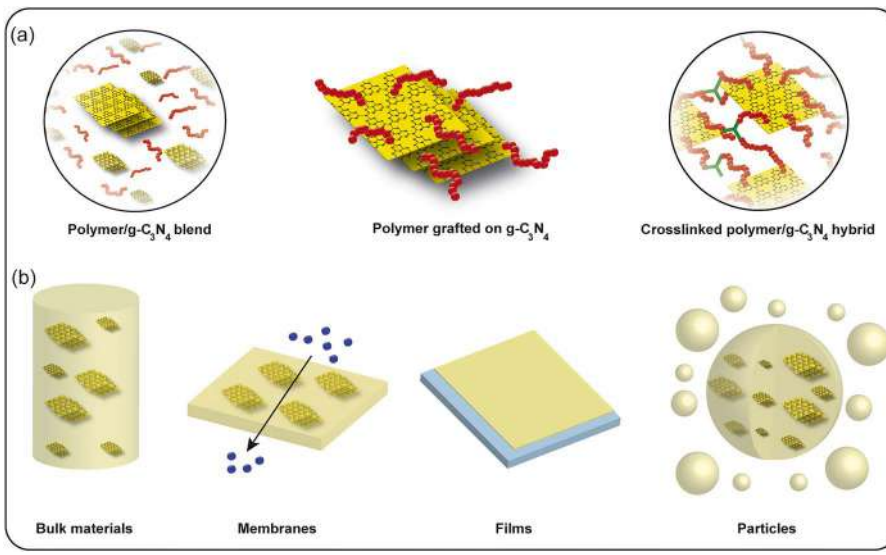

Scheme 5.4 Avenues to modification of polymers with g-C_3N_4: (a) Embedding g-C_3N_4 in polymers by grafting/crosslinking, blending and grafting, (b) types of morphologies of g-C_3N_4/polymer hybrids, *i.e.* bulk materials, membranes, films and particles. Reproduced from ref. 33 with permission from the Royal Society of Chemistry.

methods like chemical vapor deposition. In contrast, solution-based processing could introduce improved utilization in real life applications, and therefore, the enhancement of g-C_3N_4 powder dispersibility is a highly interesting task. Several research groups turned their attention to bulk g-C_3N_4 exfoliation in order to form sheets with low thickness that are stabilized by electrostatic repulsion between g-C_3N_4 sheets and feature colloids of g-C_3N_4 with good dispersibility. As such, stable dispersions of g-C_3N_4 can be formed but only low concentrations of dispersed g-C_3N_4 can be achieved. An avenue for g-C_3N_4 dispersion employs treatment *via* physical methods or additives, *e.g.* by solvent addition during the dispersion procedure,[104,105] chemical oxidation,[106] hydrothermal treatment,[107] ultrasonication[108] or thermal oxidation.[109] Another route employs modification in a chemical way, for example, *via* conjugation of molecular entities. Attachment of charged groups to the g-C_3N_4 surface leads to an enhanced dispersibility of g-C_3N_4 nanosheets in aqueous systems by electrostatic repulsion. Also, attachment of hydrophilic polymers leads to stabilization of g-C_3N_4 in an aqueous environment *via* repulsion in a steric way. In the case of organic solvents, g-C_3N_4 dispersion is enhanced by conjugation of small molecules that are soluble in organic solvents or polymers with increased stability of the dispersion due to repulsion. An avenue to enhance stability in an organic environment is *via* the formation of complexes with organic derivatized montmorillonite and was employed to form poly(styrene)/g-C_3N_4 composites.[110]

The exfoliation of g-C_3N_4 in the solvent 1,3-butanediol leads to g-C_3N_4 similar to graphene consisting of 2–6 layers of g-C_3N_4 featuring a 1–2 nm thickness. Nevertheless, 24 h of ultrasonication are needed and rather low amounts of exfoliated of g-C_3N_4 are drawbacks of the route.[31] Two avenues for functionalization of g-C_3N_4 to enhance dispersibility is pre-condensation or post-condensation. For pre-condensation, specific monomer mixtures are employed, *e.g.* phenyl groups are incorporated into the structure.[111] There, introduction of a phenyl-containing precursor for g-C_3N_4 formation hinders the formation of larger g-C_3N_4 structures that leads to a quantum dot structure, which possesses increased dispersion properties in comparison to pristine g-C_3N_4. Furthermore, functionalization after condensation allows incorporation of several functions by chemical means, *e.g.* oligo(ethylene glycol) (oligoEG) (Figure 5.6).[112] Colloids with considerable dispersibility and biocompatibility, and properties for bioimaging were formed like that. In order to achieve this, Kim and coworkers oxidized g-C_3N_4 *via* $KMnO_4$ at first and exfoliated the product *via* ultrasonication. A covalent modification step with monomesylated hexaethylene glycol was performed next. Therefore, oligoEG-grafted g-C_3N_4 sheets were created that featured increased dispersibility in water and could be used in bioimaging. Another method is utilization of oxygen plasma for the introduction of protonated hydroxylamine to the g-C_3N_4 structure that introduces significant hydrophilicity.[113] In addition, functions like hydroxyl,[114] sulfonic acid[115] or aromatic groups[103] are attachable to enhance dispersion

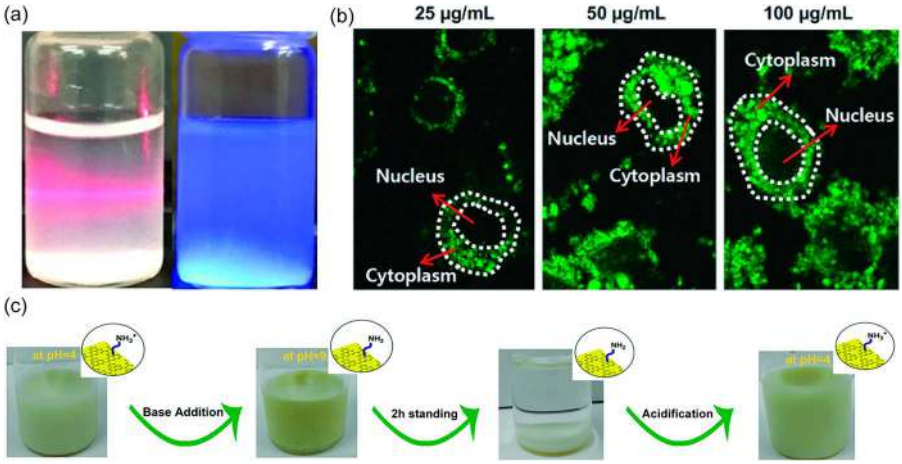

Figure 5.6 (a) An image of dispersions of oligo(ethylene glycol) (oligoEG)-grafted g-C_3N_4 in water showing the Tyndall effect (left) and fluorescence (right). (b) Confocal fluorescence microscopy image of RAW264.7 cells after incubation at different concentrations with the oligoEG-g-C_3N_4 nanodots (25, 50 and 100 μg mL^{-1}) for 24 h at 37 °C. Adapted from ref. 112 with permission from John Wiley and Sons, Copyright 2018 WILEY-VCH Verlag GmbH & Co. KGaA, Weinheim. (c) g-C_3N_4 with allylamine-modification in water (1 wt%) at acidic pH (pH = 4), formation of immediate precipitate after base addition (pH = 9), full sedimentation after standing for 2 h, and redispersion in acid (pH = 4). Adapted from ref. 118 with permission from American Chemical Society, Copyright 2017.

of g-C_3N_4 sheets. Nevertheless, other easy and less demanding avenues for dispersibility enhancement of g-C_3N_4 and improved yields of solid content could be a considerable advancement.

A way to improve dispersibility is the utilization of solvent mixtures (Scheme 5.5a). For example, water and EG mixed in equal volume allowed dispersibility of g-C_3N_4 up to 4 wt% – a significant improvement compared to 0.6 wt% in pure water. As mentioned before, g-C_3N_4 is a photoactive semiconductor capable of electron/hole pair formation *via* light irradiation, which was employed for photoinitiation of polymerizations (Scheme 5.5b). This could be used to enhance dispersion properties of g-C_3N_4 by a polymerization avenue. Therefore, DMA was combined with a dispersion of g-C_3N_4 in EG/water and initiated *via* visible light irradiation leading to a gel with weak association formed from g-C_3N_4 grafted with PDMA, which was dispersible in water. These dispersions showed considerable stability of up to two months because of sterically stabilized g-C_3N_4 colloids.[116]

A more defined approach to synthesize dispersible g-C_3N_4 that does not exploit polymerization was studied as well. Therefore, a dispersion of native g-C_3N_4 in aqueous or organic solution was prepared, a specific ene-molecule was introduced, and the dispersion irradiated with visible light (Scheme 5.5d).[117]

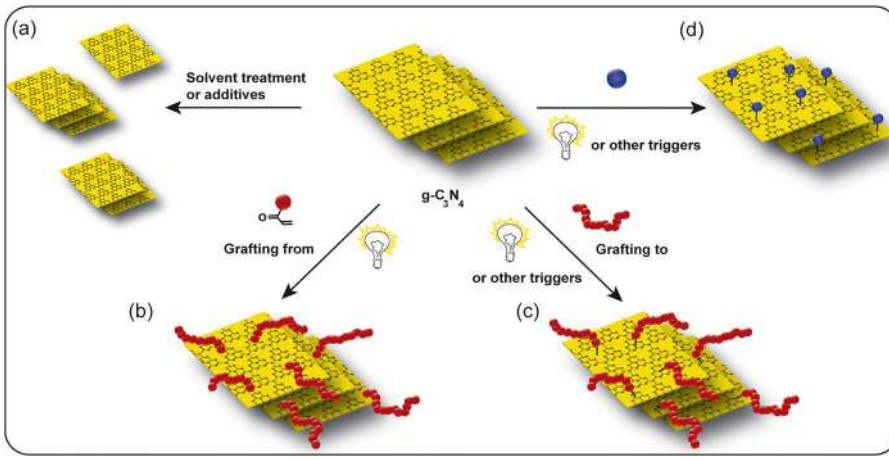

Scheme 5.5 Ways towards enhancement of g-C_3N_4 dispersion: (a) Usage of solvent mixtures (*e.g.* water/ethylene glycol (EG)), (b) polymer grafting from g-C_3N_4 *via* free radical polymerization, (c) polymer grafting to g-C_3N_4 by ene-functional polymers and (d) attachment of ene-containing small molecules. Reproduced from ref. 33 with permission from the Royal Society of Chemistry.

Because of radical formation on the g-C_3N_4 surface, a radical addition reaction takes place and a covalent bond is formed. In order to suppress polymerization of the small molecule, allylic compounds with no propagation activity were introduced. As such, the added small molecules were grafted onto g-C_3N_4 directly. In turn, surface modification considerably influences the dispersion properties of g-C_3N_4. The grafting of 3-allyloxy-2-hydrox y-1-propanesulfonic acid sodium salt (AHPA) onto g-C_3N_4 led to an improved dispersibility in water up to 10 wt% with high stability, *i.e.* for 48 h. Attachment of 1-decene introduced dispersibility in organic media of up to 2 wt% g-C_3N_4 in solvents like DCM, THF or toluene. Furthermore, allylamine grafting enabled pH-sensitive dispersibility with dispersion properties in acidic medium and precipitation in basic medium (Figure 5.6c). The conjugation with methyl vinyl thiazole on g-C_3N_4 formed a considerable enhancement of dispersibility in organic media due to an intrinsic stabilization *via* electrostatics. Both components formed a donor–acceptor type structure and enhanced separation of electron and holes.[118] In a similar way, attachment of tailored ene-end group containing polymers on g-C_3N_4 was performed (Scheme 5.5c, refer to Section 5.4.3).

One of the major issues of polymer hybrids and composites constitutes the compatibility of the polymer with the blended material, which is a less frequent problem with g-C_3N_4 as strong interactions take place frequently. As an example, g-C_3N_4 establishes π–π interactions with PS or PBMA. In addition, g-C_3N_4 features edges with polar groups that allow interactions, *e.g. via* hydrogen bonding, with polar polymers such as PDMA or poly(2-hydroxyethyl methacrylate) (PHEMA).

5.4.2 g-C_3N_4/Polymer Hybrid Materials for Biosensors

Even though hybrid g-C_3N_4 materials have been studied frequently, applications for sensing with g-C_3N_4 are still at an infant level. Nevertheless, since cathodic electrochemiluminescence (ECL) behavior of nanosheet g-C_3N_4 was reported,[119] increased attention has been paid to this useful luminophore for ECL biosensors. Due to the various advantages of g-C_3N_4, *e.g.* biocompatibility, non-toxicity, high thermal and chemical stability,[54,120] g-C_3N_4 functionalized with polymers has been studied to improve the sensitivity and selectivity of ECL sensors. Bovine serum albumin and phenoxy dextran (DexP) g-C_3N_4 were combined to fabricate a concanavalin A ECL sensor by Wei and colleagues.[121] There, g-C_3N_4/DexP nanocomposites were synthesized by overnight stirring to drive π–π stacking physical adsorption between g-C_3N_4 and DexP. Subsequently, the properties of the biosensor were studied, which showed an excellent ECL signal probe by the DexP–g-C_3N_4 composites. Moreover, formation of specific carbohydrate-Con A interactions was observed demonstrating a new sandwich-type interaction with a detection strategy *via* signal-on ECL. Poly(aniline) (PANI) was combined with g-C_3N_4 by Chen *via* an oxidative polymerization for *in situ* deposition utilizing ammonium persulfate as initiator. Next, nanoflower-shaped gold (AuNF) was synthesized *in situ* directly at the g-C_3N_4–PANI surface achieving hybrids of AuNF@g-C_3N_4–PANI.[122] Then, the hybrid was introduced into ECL biosensors for dopamine, which showed a low detection limit and considerable sensitivity. As such, the biosensors could have a prospective application in dopamine detection for the diagnosis of clinical diseases. Kim and team connected protonated g-C_3N_4 (g-$C_3N_4H^+$) with cylindrical-shaped spongy poly(pyrrole) (PPy) with an oxidative polymerization pathway.[123] In the next step, the prepared nanohybrids were decorated with cholesterol oxidase (ChOx) in order to fabricate cholesterol biosensors, showing several properties like significant selectivity for detection of cholesterol and long-term stability. An aptasensor based on CdS/PPy/g-C_3N_4 for detection of adenosine was introduced by Wei and coworkers.[124] Therefore, CdS/PPy/g-C_3N_4 covered electrodes were combined with a SH-aptamer to form a complex with adenosine *via* bioaffinity. According to the adenosine concentration the photocurrent readout varied linearly from 0.3 nmol L^{-1} to 200 nmol L^{-1}.

5.4.3 g-C_3N_4/Polymer Hybrid Film Materials

Because of the photocatalytic features of g-C_3N_4, formation of g-C_3N_4 containing films is highly interesting,[125] *e.g.* in ionic transport,[25,126] sensors or for solar cells.[127] However, usual ways of film formation and processes found only minor success in the past, *e.g.* inkjet printing or spin coating.[128] This is mostly because of poor colloidal dispersibility of g-C_3N_4 and the requirement of harsh processes to form films.[129] Therefore, various studies described the fabrication of g-C_3N_4 film materials.[130] An effective strategy constitutes an incorporation of g-C_3N_4 into polymers to improve dispersibility

and processability. Hence, thin films and coatings including g-C_3N_4 can be formed enabling easy g-C_3N_4 processing and avenues to new applications. For example, a combination with polymers is "grafting to" that makes use of g-C_3N_4 surface functionalities (*e.g.* –NH_2, –NH or –OH) in amide synthesis or hydrogen bonding. Another method is "grafting from" that is based on a polymerization started from g-C_3N_4 directly.

Hu and coworkers formed nanocomposite films from sodium alginate (SA) with various loadings of g-C_3N_4 by a casting process.[131] Physical adsorption was employed to form SA/g-C_3N_4 composite materials. Therefore, g-C_3N_4 and SA were treated with ultrasound at 40 °C to induce hydrogen bonding between –COOH on SA and –NH_2 groups on g-C_3N_4. Next, the composite was cast onto a flat dish and annealed for 36 h at 40 °C. Finally, the hydrogen bond formation, mechanical properties and thermal stability of the g-C_3N_4/SA films were investigated. Our group investigated a "grafting to" approach to graft g-C_3N_4 with ene-end functionalized polymers *via* visible light irradiation (Figure 5.7). At first, decene end-functionalized poly(isobornyl acrylate) (PIBA), PMMA and poly(glycidyl methacrylate) (PGMA) were formed *via* ATRP.[132] Then, g-C_3N_4 was mixed with the polymers in THF dispersion and subjected to visible light in order to induce covalent bond formation. Polymer grafted g-C_3N_4 with tailored density of grafting was utilized for synthesis

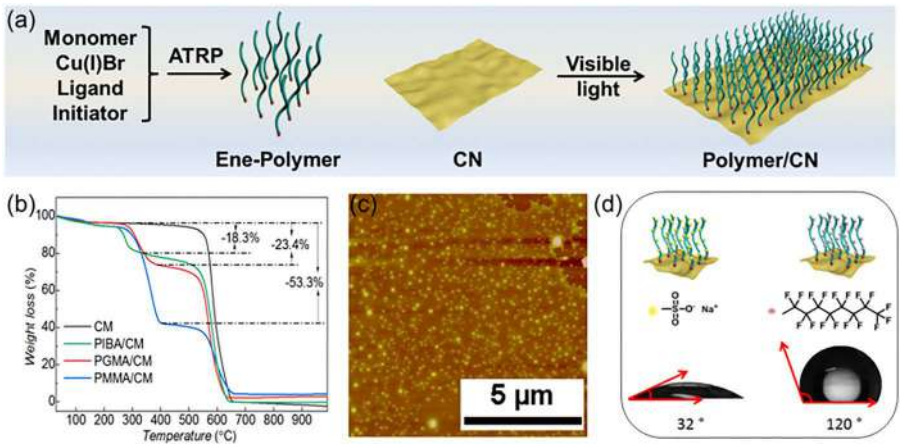

Figure 5.7 (a) Atom transfer radical polymerization and polymer brush grafting onto g-C_3N_4 *via* visible light irradiation, (b) thermogravimetric analysis of cyanuric acid-melamine-derived g-C_3N_4 (CM) precursor and ene-polymer grafted CM, (c) profile of atomic force microscopy of spin-coated poly(isobornyl acrylate)(PIBA)/CM film, (d) modulation of the surface of poly(glycidyl methacrylate)(PGMA)/CM by thiol-addition epoxy ring-opening with sodium 2-mercaptoethanesulfonate and 1H,1H,2H,2H-perfluorodecanethiol, respectively. Reproduced from ref. 132, https://doi.org/10.1021/acs.macromol.9b00894, under the terms of the ACS AuthorChoice/Editors' Choice *via* Creative Commons CC-BY agreement, https://pubs.acs.org/page/policy/authorchoice_ccby_termsofuse.html.

of polymer/g-C_3N_4 films by dispersion of the hybrids in THF followed by spin coating on glass slides, which led to thin polymer/g-C_3N_4 films featuring a thickness in the range of 60 nm. Moreover, the PGMA-based g-C_3N_4 hybrid materials were further functionalized *via* thiol-based nucleophilic epoxide ring-opening. Hence, 1H,1H,2H,2H-perfuorodecanethiol or sodium 2-mercaptoethanesulfonate could be attached onto the g-C_3N_4-grafts, which induced considerable variation in surface polarity.

A g-C_3N_4-based polymer thermoset coating was described by Kumru *et al.* that featured thicker films *via* a prepolymer route. The synthesis of the prepolymers was performed in the same way as the previously mentioned g-C_3N_4–PDMA prepolymers.[133] There, a PHEMA prepolymer was formed in EG/water mixture on g-C_3N_4 leading to a viscous material consisting of PHEMA grafted g-C_3N_4, EG and water. Moreover, the precursor viscosity could be tailored to obtain injectable material. Subsequently, the precursor was deposited on several surfaces, including wood, PS and copper, with control over the placement. The blending with citric acid, subsequent film formation on a glass slide and thermal annealing led to crosslinking. These thermosets constituted smooth hydrophobic coatings, which were utilized for subsequent modification. For example, PDMA and PS could be polymerized from the surface *via* photochemistry as the presence of g-C_3N_4 in the film retained photoactive properties. This "grafting from" methodology allowed one to vary the surface hydrophobicity, as observed by contact angle measurements. Additionally, the surfaces with photoactivity were employed in the degradation of dyes and photoelectrochemistry. As mentioned before, g-C_3N_4 thin films can be synthesized *via* chemical vapor deposition (CVD) with high precision and reproducibility. For example, melamine was utilized as precursor which showed uniform thin films with high refractive index.[134] Such films can be used as photoactive platforms to apply photoinduced grafting to form polymer/g-C_3N_4 hybrids. A variety of monomers (such as styrene and DMA) can be poured on the surface of the film and polymer brushes can be formed *via* a visible light induced reaction.[135] Covalently bonded polymers allow easy adjustment of surface wettability, and very thick polymer brushes (up to 600 nm) were obtained due to "clean" surface-initiated polymerization. Furthermore, light induced wettability independent of any photoswitchable groups was observed for g-C_3N_4-PS hybrids, indicating a possible hole transfer from g-C_3N_4 to PS upon illumination. The film can be placed at an aqueous-organic monomer interface and subsequent illumination from top and bottom results in centimeter-scale Janus film formation.

5.4.4 g-C_3N_4/Polymer Nanoparticle Composites

A frequently utilized class of polymer materials is latex based on polymer nanoparticles. Thus, a combination of g-C_3N_4 with particles of polymers has been a topic of increasing interest. Due to the property of g-C_3N_4 to perform as an emulsifier in emulsions of oil in water (o/w),[28,136] an easy avenue to

synthesize polymer nanoparticles/g-C_3N_4 is by utilization of Pickering stabilization *via* g-C_3N_4 in an emulsion polymerization.[137] For example, Pickering emulsion polymerization was employed by Li and team to fabricate latex based on g-C_3N_4.[54] The emulsion polymerization could be performed with g-C_3N_4 stabilization and potassium persulfate initiation. PS microspheres with monodisperse size distribution featuring tailorable sizes down to the 100 nm, tunable charge of the surface and tailored morphology was received. The g-C_3N_4 particles were dispersed in the aqueous phase and attached to the surface of monomer droplets installing a network structure to prevent coalescence of the emulsion. The formed latex particles of PS/g-C_3N_4 featured photoluminescent properties due to the g-C_3N_4 sheets. Moreover, the PS latex possessed considerable biocompatibility as investigated *via* standard MTT assays. Furthermore, PS/g-C_3N_4 particles were incubated with HeLa cells and analyzed *via* confocal laser scanning microscopy. Particle internalization by HeLa cells was observed, which pointed to a promising application of the fluorescent PS/g-C_3N_4 hybrid particles in bioimaging. Recently, the g-C_3N_4 stabilized Pickering polymerization system was expanded with sialic acid (SIA) that is a common marker for some cancer types. In-depth studies of g-C_3N_4 containing SIA-featured polymer nanoparticles revealed considerable biocompatibility and significant targeted imaging of DU 145 cells with an SIA-overexpressed surface.[137]

5.4.5 Improved Polymer Properties *via* Combination with g-C_3N_4

Hybridization of g-C_3N_4 and polymers enhances the photocatalytic and surface properties of g-C_3N_4 considerably, but also improves the thermal, surface and mechanical properties of polymers.[138–140] Si-doped CN (CN–Si) was immobilized on poly(propylene) (PP) discs with deposition based on a pulsed laser by Myllymaa and coworkers.[141] The PP surface was transformed from being hydrophobic to hydrophilic by coating with CN–Si, which led to increased Saos-cell adherence on PP. Hu and team described a blend of maleic anhydride-grafted PP (PP-*g*-MA) with g-C_3N_4 obtained *via* 4 h reflux in xylene.[142] The combination of PP-*g*-MA and g-C_3N_4 increased the storage modulus considerably, *i.e.* 2445 MPa for neat PP-*g*-MA and 2784 MPa for PP-*g*-MA/g-C_3N_4. In addition, optical measurements confirmed interesting UV absorption by the hybrid materials. An introduction of wood plastic compositions (WPCs) g-C_3N_4 filler reinforcement was shown by Cai and coworkers; PP-*g*-MA was introduced as an agent for coupling to enhance the connection of both components.[143] An increase of 143% in tensile modulus was indicated with g-C_3N_4 incorporation of 5 wt%, and higher values of the degradation temperature was observed as demonstrated by thermal analysis. Lin and coworkers synthesized nanocomposites of g-C_3N_4/poly(vinyl alcohol) (PVA) by casting a solution with the solvent water and demonstrated a good dispersion of g-C_3N_4 in a matrix of PVA.[144] The incorporation of g-C_3N_4 nanosheets led to an increase in crystallinity of the nanocomposites and glass transition temperature, which led to advanced mechanical performance with ~71%

increment in tensile strength.[144] The *in situ* formation of g-C_3N_4 on carbon fiber surfaces was described by Guo and coworkers to improve epoxy resin composite reinforced with carbon fibers and their interfacial properties.[145] The carbon fiber surface exhibited greatly increased roughness due to g-C_3N_4 addition as well as increased amount of polar functions and improved wetting behavior. Therefore, considerable advances in interfacial properties of the composites were introduced. High thermal stability of g-C_3N_4 has been an attractive potential to be implemented in rubbers instead of carbon black.[146] Thus, g-C_3N_4 was blended in rubber formulation and improved mechanical properties of the rubber with increasing g-C_3N_4 content were reported.

5.4.6 Blending and Supramolecular Hydrogels

Additionally, g-C_3N_4 based hydrogels are not accessible only *via* covalent bonding, but supramolecular interactions and blending strategy can be employed as well. For example, Park and coworkers utilized peptides and g-C_3N_4 in water.[147] There, Fmoc-diphenylalanine (FMOCDPA) underwent self-assembly with the presence of g-C_3N_4 leading to supramolecular hydrogels. The synthesized hydrogels were employed to convert NAD^+ to NADH, and in addition bifunctional catalysis, namely photo and enzymatic, was described. A combination of supramolecular hydrogel and 3D printing was presented by Fan and team, who connected g-C_3N_4 and the Ca^{2+}/alginate gelation with 3D printing (Figure 5.8a).[148] As such, 3D hydrogel scaffolds were fabricated for tasks in photocatalysis. Similarly, a carbon nitride nanosheet/sodium alginate (CNNS-SA)-derived ink was assembled and crosslinked with $CaCl_2$/glycerol solution (Figure 5.8b and c). To boost the photocatalysis properties of the scaffold, gold nanopyramids were integrated in a 3D printed network for solar-induced remediation of wastewater. Therefore, specific architectures of the gel were exploited to tune the efficiency of catalysis by improved transport of substrates. Ayajan and team described a gel formation by g-C_3N_4 and ionic liquids (IL) under solvothermal conditions (24 h at 200 °C). IL exfoliates g-C_3N_4 and fabrication under such conditions leads to an amphiphilic network, which could be used as a H_2S gas sensor at ambient temperature.[149]

A hydrogel based only on g-C_3N_4 was described by Zhang and team.[150] Therefore, hydrolysis of g-C_3N_4 was performed partially and exfoliated with NaOH solution. The dispersion led to hydrogels that were reversible depending on bubbling with CO_2 or N_2 based on supramolecular interactions, and this network was used for selective dye absorption. A traditional way to form hydrogels is *via* agar, which was also combined with g-C_3N_4 *via* heating–cooling cycles that led to hydrogels.[151] The agar-derived hydrogels could be employed for efficient photocatalysis in the dye degradation because of improved capacity of adsorption. Based on a similar principle, Zhu and team employed a g-C_3N_4/agar hydrogel for tasks in photocatalysis.[152] Thus, g-C_3N_4 and agar were mixed in an aqueous environment and subjected to heat. After cooling, a hydrogel was formed and employed for the degradation of methylene blue (MB) and phenol. A considerable photoactivity was observed because of the adsorption properties of the hydrogel.

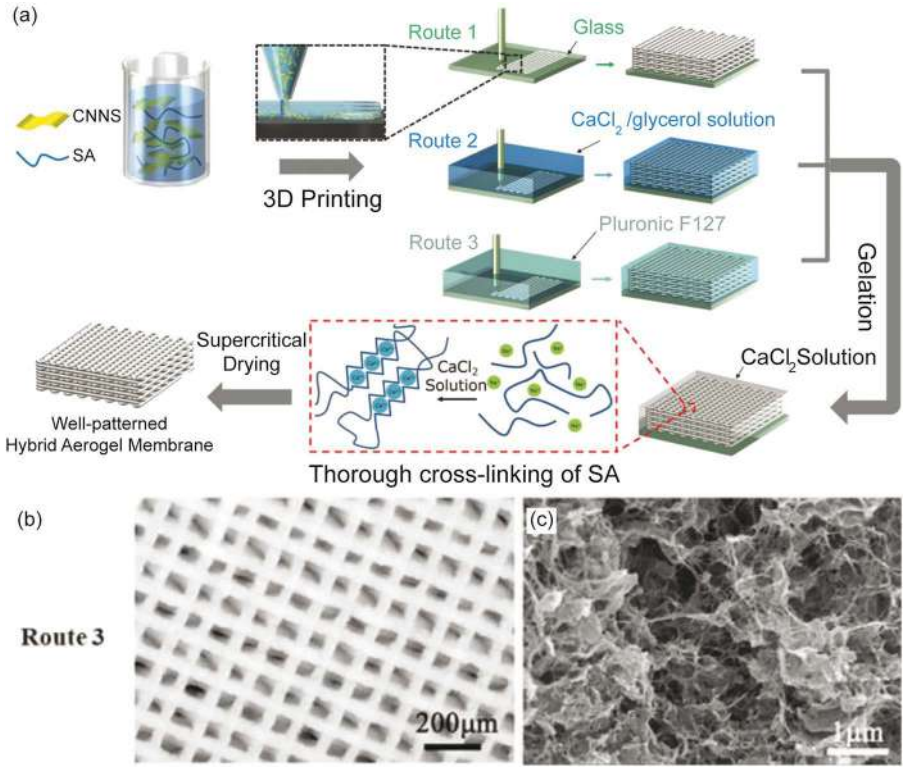

Figure 5.8 (a) 3D fabrication method: A significantly concentrated homogeneous CNNS–SA (g-C_3N_4 nanosheet–sodium alginate) ink is extruded and printed directly on a glass substrate covered with a layer of Vaseline (Route 1), into a $CaCl_2$/glycerol solution in a reservoir (Route 2) or Pluronic F127 (Route 3). Next, the lattices formed by printing are subjected to $CaCl_2$ aqueous solution overnight for crosslinking. (b) Picture of a woodpile structure (mass ratio CN : SA = 1 : 2) formed *via* Pluronic F127 (Route 3), and (c) a cross-sectional SEM image. Adapted from ref. 148 with permission from John Wiley and Sons, Copyright 2018 WILEY-VCH Verlag GmbH & Co. KGaA, Weinheim.

5.5 Applications of g-C_3N_4/Polymers for Photocatalytic Applications and Water Treatments

5.5.1 Photocatalysis for H_2 Evolution and CO_2 Reduction *via* g-C_3N_4/Polymer Hybrids

A traditional way to report the activity of photoredox catalysts is *via* light induced water splitting for H_2 evolution. Even though highly promising, g-C_3N_4 has major issues such as low surface area, high recombination rates

and low conductivity, which significantly hamper the realistic utilization of g-C_3N_4 towards H_2 production. The combination of g-C_3N_4 with polymers can provide a handle for enhanced properties. Typically, conductive polymers such as poly(pyrrole) (PPy),[153] poly(3-hexylthiophene) (P3HT)[154] or poly(aniline) (PANI),[155] are combined with g-C_3N_4 to form hybrids by self-assembly, physical interactions or thermal deposition. The rich surface chemistry of 2D sheet-like g-C_3N_4 (negative surface charge and non-condensed groups such as $-NH_2$, –NH or –OH) renders physisorption of polymers by van der Waals or electrostatic interactions. A physical composite based on P3HT and g-C_3N_4 was reported by Yan and coworkers, which relies on g-C_3N_4 suspension in P3HT chloroform solution with subsequent evaporation of solvent (Figure 5.9a).[156] Integration of P3HT results in a considerable enhancement of H_2 evolution by 300 times using electron donors Na_2S and Na_2SO_3. The enhanced photocatalytic activity arises from improved conductivity of electrons after incorporation of P3HT. Following this, the group introduced a g-C_3N_4/Au/P3HT/Pt layered architecture utilizing a self-assembly approach.[154] At first, a conjunction of g-C_3N_4/Au was engineered *via* photodeposition. Additionally, P3HT/Pt was formed and attached to a g-C_3N_4/Au composite because of the induction of Au–sulfur interaction between Au on g-C_3N_4 and sulfur in the P3HT polymer. Therefore, chemical bonds (Au–S) were employed to form a tight junction, which minimizes interfacial recombination. These layered structures showed high efficiency for H_2 evolution due to photoinduced separation of electron–hole pairs.

As g-C_3N_4 has restricted dispersibility in organic media, aqueous treatment would be beneficial, however P3HT has limited processability in aqueous media. A way to get around this issue is to change to PPy, which has considerable stability and conductivity in the doped form. Chen and team described the formation of a PPy–g-C_3N_4 hybrid by physical interactions induced by sonochemistry (Figure 5.9b).[153] There, a suspension of PPy–g-C_3N_4 was ultrasonicated for 12 h to grant exfoliation of g-C_3N_4 and provide better contact with the polymer network, and then the suspension was dried at 80 °C. The combination with nanoparticles from PPy had no impact on widening the edge of g-C_3N_4 absorption but enhanced g-C_3N_4 emission intensity, which indicated an improved separation of excited electron–hole pairs in PPy–g-C_3N_4 in comparison to common g-C_3N_4. Increasing PPy amount in the composite enhanced photocatalytic H_2 evolution capacity in parallel. Hao and coworkers demonstrated a thermal condensation in one step for the formation of a g-C_3N_4-graphitized-poly(acrylonitrile) (g-PAN) composite (Figure 5.9c).[155] As PAN is susceptible to undergo graphitization, the blending of PAN with g-C_3N_4 precursors and thermal treatment under 650 °C leads to PAN graphitization and therefore a g-PAN/g-C_3N_4 layer structure. In comparison to post-treatment derived structures, the g-PAN with a structure of aromatics features considerable amounts of reactive sites and short diffusion distances decreasing the rate of recombination for charge carriers generated by light. As such, g-PAN performs as an efficient channel for electron transfer in the composites of g-PAN/g-C_3N_4 and improves the performance of photocatalysis in hydrogen evolution.

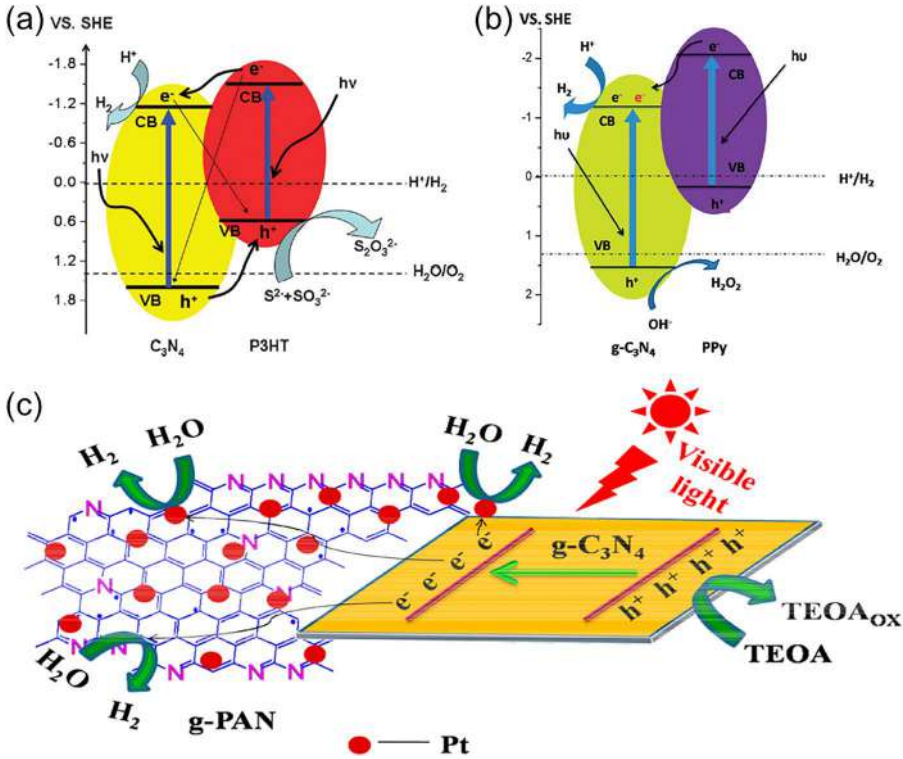

Figure 5.9 (a) Mechanism proposed for visible light-induced photocatalytic hydrogen evolution on g-C_3N_4–poly(3-hexylthiophene) (P3HT) polymer composites. Adapted from ref. 156 with permission from the Royal Society of Chemistry. (b) Mechanism to show the role of dispersed poly(pyrrole) (PPy) nanoparticles in enhancing photocatalytic efficiency of PPy–*g*-C_3N_4 for hydrogen evolution. Adapted from ref. 153 with permission from the Royal Society of Chemistry. (c) Enhancement of photogenerated charge carrier separation and transfer in the graphitized-poly(acrylonitrile) (g-PAN)/g-C_3N_4 composites under visible light irradiation ($\lambda > 400$ nm). Adapted from ref. 155 with permission from American Chemical Society, Copyright 2014.

Employing g-C_3N_4 in photocatalysis for reduction of CO_2 is a promising avenue as well, and improved performance can be achieved by polymer combination. For example, g-C_3N_4 with hydrophobic polymer grafts was utilized in a three-phase photocatalysis for improved activity and selectivity in the reduction of CO_2.[157] To access hydrophobicity, PGMA was grafted *via* photoinitiation onto g-C_3N_4, which was modified with 1H,1H,2H,2H-perfluorodecanethiol *via* a nucleophilic thiol-epoxy ring opening reaction. Next, photoloading was used *in situ* for depositing Pt on the pDFe-PGMA/g-C_3N_4 surface. The three-phase contact (CO_2 (gas), catalyst (solid) and H_2O (liquid)) photocatalyst provides a considerable CO_2 concentration on the catalyst due to the hydrophobic nature of the surface. As hydrogen evolution and CO_2 reduction are competing pathways, the CO_2 enriched surface simultaneously suppresses the hydrogen

evolution reaction so the equilibrium shifts towards CO_2 reduction. The measured performance reached around 34 times higher than common hydrophilic catalysts. Reisner and Roy presented a way to enable photoreduction of CO_2 also.[158] There, mpg-C_3N_4 and a phthalocyanine catalyst based on cobalt were combined. To ensure an excellent interfacial contact, Co^{2+} together with 1,2,4,5-tetracyanobenzene were polymerized in the surrounding of mpg-C_3N_4. A synergistic effect of the hybrid, including photosensitization, porosity and solar energy harvesting enabled considerable CO_2 reduction activity of the phthalocyanine catalyst with visible light.

5.5.2 Water Contamination Degradation by g-C_3N_4/Polymer Hybrid Photocatalysis

The promise of photoredox chemistry does not end at H_2 evolution, and indeed many other photocatalytic schemes are accessible. One of the great topics of interest has focused on water contaminant degradation, where g-C_3N_4/polymer hybrids are quite promising.[159] Considering dye-based pollution, some commercial dyes such as Methyl Red, Congo Red or MB[160] are unfortunately part of textile wastewater, which causes significant pollution as the dyes possess high water solubility. Several strategies, such as electrochemical treatment, ion exchange, catalytic reduction, adsorption and membrane separation[161–163] have been applied to prevent pollution. A photocatalytic approach under visible light based on g-C_3N_4/polymer hybrid composites is highly appealing as it includes low-cost processing and heterogeneous operation for reversibility and ease of separation.[164,165] As an example, Zhu and coworkers attempted the formation of PANI by oxidative polymerization *via* ammonium persulfate (APS) between g-C_3N_4 nanosheets.[166] The resulting g-C_3N_4 sheets with PANI nanofibers in between with a coral-like morphology, formed a hydrogel (Figure 5.10a)

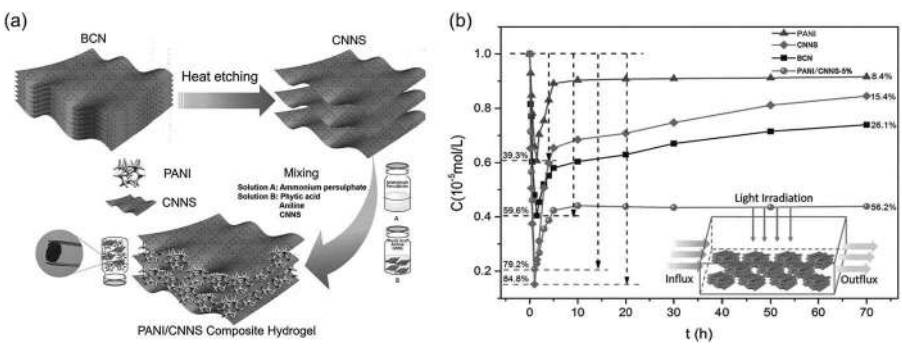

Figure 5.10 (a) Fabrication of a poly(aniline)/g-C_3N_4 nano sheet (PANI/CNNS) composite hydrogel from bulk g-C_3N_4 (BCN). (b) Photocatalysis based degradation of methylene blue (MB) in the flow (1.0 L s^{-1} flow rate, 200 mg catalyst, 1 10^{-5} mol L^{-1} MB). Adapted from ref. 166 with permission from John Wiley and Sons, Copyright 2016 WILEY-VCH Verlag GmbH & Co. KGaA, Weinheim.

with a hierarchical structure that featured enhanced contaminants' photodegradation properties, *i.e.* 5.1-fold improvement compared to pure g-C_3N_4 (Figure 5.10b). A similar strategy was adopted by Liu and team, who synthesized photocatalysts consisting of PANI–g-C_3N_4 composites *via* an *in situ* oxidative polymerization of aniline onto g-C_3N_4 by APS.[167] There, g-C_3N_4 served as a substrate and a platform for polymer growth, and the efficiency of the composite was reported *via* enhanced MB photodegradation, which is due to improved electron–hole separation. Phosphorous and sulfur co-doped g-C_3N_4 (SP-g-C_3N_4) was decorated with PANI *via* oxidative polymerization.[168] Incorporation of PANI helps to tailor the band gap structure and to extend the absorption of light. Thus, improvement of active sites for charge carrier generation *via* light at the interfaces were formed. Similarly, photoactivity of hybrid material was demonstrated *via* significantly improved MB photodegradation. PANI as an attractive partner for g-C_3N_4 was reported by polymerizing aniline *via* APS in g-C_3N_4 suspension in the presence of acid counterparts to dope PANI.[169] The resulting composite was employed as a photocatalyst for MB degradation (2.5 10^{-5} M) and Cr(VI) reduction, and detailed characterization by the means of work function and ionization potential revealed that high photoactivity arises from efficient charge separation on composite material. Similar *in situ* aniline oxidative polymerization *via* APS was attempted around g-C_3N_4 and TiO_2 to form a photoactive hybrid.[170] Photodegradation of Congo Red (20 mg L^{-1}) took place in 180 min at pH values of 5 and 7, and mechanistic insight into charge separation was reported. Consecutive photocatalytic cycles demonstrated the stability of the hybrid photocatalyst. Water contamination does not only include impurities arising from water-soluble molecules, oil and organic solvent spills are also part of the threat. Porous oleophilic foam based on g-C_3N_4 with acrylic resin was synthesized by Qian and coworkers, for efficient oil and organic solvent capture.[171] It is important to mention that this system is based on adsorption and does not utilize the photocatalytic activity of g-C_3N_4 for removal, but it deserves to be mentioned as it is a g-C_3N_4/polymer composite. In the end, the acrylic-based resin with g-C_3N_4 incorporation featured a fast capture rate, considerable adsorption capacity and excellent recycling properties for capturing oils and organic solvent in water.

Morphology of the composite can also be useful for water remediation applications. Forming fiber structures with inherent charge transport properties is a fruitful strategy. The Chen group has proposed the formation of visible light active fibers *via* electrospinning based on PAN and g-C_3N_4.[172] The hybrid g-C_3N_4/PAN revealed effective photocatalysis properties towards degradation of Rhodamine B (RhB) in a wide range of pH and could be recycled easily. Incorporation of g-C_3N_4 into PAN nanofibers by electrospinning was reported by Othman and coworkers.[173] Self-supporting nanofibers for photocatalysis with liquid permeability were synthesized that demonstrated a degradation capability of 85% for remediation of oil-contaminated water *via* visible light illumination. Moreover, g-C_3N_4 containing heterojunctions

(g-C_3N_4/BiOI) can also be implemented into PAN nanofibers by electrospinning, as shown by Liu and coworkers.[174] A self-supporting floating hybrid photocatalyst with enhanced charge separation and strong absorption in the visible range were applied for RhB and Cr(VI) removal.

Antibiotics pose a serious threat for water systems and are one of the major impurities that need to be removed. g-C_3N_4/polymer hybrids are promising as they provide heterogeneous photocatalysis conditions. As an example, nanofibers from g-C_3N_4@poly(ethylene terephthalate) were synthesized utilizing support *via* poly(ethylene terephthalate) and porogen *via* poly(ethylene glycol) (PEG) in electrospinning,[175] and the resulting material was able to degrade antibiotics like sulfadiazine and sulfaquinoxaline under sunlight. Furthermore, polyester fibers (*e.g.* poly(ethylene terephthalate)) can be combined with cellulose acetate (CA) and g-C_3N_4 nanosheets,[176] and the formed hybrid aerogel g-C_3N_4@CA/poly(ethylene terephthalate) showed improved photocatalysis activity for hexavalent chromium and antibiotics removal, at the same time. Utilization of support material poly(ethylene terephthalate) for g-C_3N_4 in electrospinning was proposed by Chen and coworkers. In addition they performed hydrothermal treatment to enable the exposure of g-C_3N_4 on the poly(ethylene terephthalate) interface, resulting in reduced aggregate formation and enhanced recycling properties.[177] In another work, composite polyester fibers with a low melting sheath-core were combined with g-C_3N_4 in order to install recycling properties and improve photocatalysis degradation properties.[178]

Acidified g-C_3N_4 was incorporated in a CA film *via* solution induced processing, and high porosity and enhanced mechanical properties after g-C_3N_4 addition was noted.[179] Furthermore, composite film was utilized as a photocatalytic center for RhB removal from water (10 mg L^{-1}), and complete removal was obtained after 150 min of visible light irradiation. The authors also demonstrated the photocatalysis activity of the films by degradation of MB, crystal violet and malachite green as well as photoinduced reduction of Cr(VI) to Cr(III). A graphene–g-C_3N_4–P3HT composite was prepared by incorporating graphene and g-C_3N_4 in a solution of P3HT in chloroform with subsequent solvent evaporation.[180] The composite was utilized for photocatalytic removal of MB (10^{-5} M), and the activity of the system was related to an effective inherent charge transfer scheme. An impregnation method was extended to prepare g-C_3N_4-poly(diphenylbutadiyne) composite from ethanol solution.[181] Photocatalysis activity of the composite was shown for catalytic degradation of RhB (10 mg L^{-1}) and phenol, and enhanced photocatalytic activity after composite formation was studied *via* electrochemical impedance spectroscopy and transient photocurrent responses. g-C_3N_4–polydopamine composites were formed *via in situ* polymerization of dopamine hydrochloride in g-C_3N_4 nanosheet dispersion.[182] Almost complete (99%) photocatalytic degradation of MB (20 mg L^{-1}) in 180 min was reported, and inherent charge transfer (excited electrons) from g-C_3N_4 to polydopamine units was attributed to be the major reason for efficient photocatalysis activity compared to bulk g-C_3N_4.

5.5.3 g-C_3N_4/Polymer Hybrids as Photocatalysts for Sterilization

Utilization of photoredox catalysts as sterilization agents has been an ongoing topic. As such, catalysts are able to form oxidative radical species *via* light illumination that can hinder bacterial activities. TiO_2 can perform under UV light, and g-C_3N_4 is highly promising as it has absorption maximum lying in the visible light range. Therefore, an improved antibacterial performance is obtained *via* the hybridization of g-C_3N_4 and polymers for sterilization. Additionally, to antibacterial properties of g-C_3N_4,[183] improved recyclability is obtained *via* polymer fibers that also provide aid for processing. Zhang and team assembled antibacterial and self-cleaning membranes by depositing g-C_3N_4 sheets on porous PAN substrates.[184] Bulk g-C_3N_4 was etched with HCl to obtain nanosheets, which were filtered onto PAN. Poly(vinyl alcohol) was filtered afterwards and the membrane was immersed into glutaraldehyde solution at 80 °C for crosslinking reactions to form a self-standing structure. Considerable water permeability (11.7 L m^{-2} h^{-1}) and excellent antibacterial properties by the membrane were observed. In addition, the original membrane permeability was preserved with g-C_3N_4/PAN, *e.g.* in dye rejection. Furthermore, the surface kept its initial color even after three cycles of visible light illumination post-treatment. A combination of g-C_3N_4, Ag_3PO_4 and a poly(ether sulfone) (PES) microfiltration membrane was described by Vatanpour and team.[185] An amino functionalized composite of g-C_3N_4-Ag_3PO_4 was prepared and a membrane was formed *via* a blending method. Considerable antifouling properties were described, which were related to synergistic effects of hydrophilicity, photocatalysis activity and porosity. The authors then presented a follow-up work utilizing the same nanoparticle composite embedded in non-woven fabrics *via* a filtration method, together with PES and PEG solutions.[186] Composite membrane bioreactors demonstrated high water flux capacity as well as antifouling and antibacterial activities. Natural macromolecular structures can be utilized as a matrix for blending g-C_3N_4 as well. Thermally etched g-C_3N_4 nanosheets were mixed with SA and filtered onto PAN substrate, followed by immersing in $CaCl_2$ solution for crosslinking.[187] The resulting hybrid membrane possessed high water permeability and separation efficiency due to inherent transport channels. Another example is the formation of reduced graphene oxide (rGO) and g-C_3N_4 composites on CA *via* a filtration method.[188] The resulting microfiltration composite membrane was utilized for visible light induced organic contaminant removal, and antibacterial activity and antifouling properties were also shown, which are highly promising for water treatment applications.

5.5.4 Electrochemical Energy Storage and Solar Cells *via* g-C_3N_4/Polymer Nanocomposites

Electrochemical energy generation and energy storage belong to the most impactful current research areas. Herein, g-C_3N_4 is endowed with the potential to take part in batteries, fuel cells and solar cells. Fuel cells are amongst

the most promising ways to receive electrical output from chemical energy. In particular, the intersection of polymer chemistry and electrochemistry highlights polymer electrolyte membrane fuel cells (PEMFCs). Some polymers were the milestones in this field, such as poly(vinyl pyrrolidone) (PVP),[189] poly(benzimidazole) (PBI),[190] PVP–PES[191] or PVP–PVA.[192] However, there are some major concerns that need to be solved, mainly lower durability, high cost and degradation of PEMFCs because of the low perseverance of membranes, which hinders the great potential for common usage of the technology considerably.[193,194] To answer these issues, g-C_3N_4 nanosheets were included into the polymer membrane.[195] g-C_3N_4 serves mainly two important functions; the first one is its significant temperature stability due to an energy of C–N and C=N of 305 KJ mol^{-1} and 615 KJ mol^{-1} of the chemical bonds, respectively.[196] Secondly, the presence of amino (–NH_2) and imino (–NH) groups in g-C_3N_4 due to uncondensed moieties that are prone for interaction with the acid functions in the polymer matrix leading to advancement of proton transfer *via* the Grotthuss mechanism. A solution casting method was introduced by Zhou and team to blend PVP-phosphonated-poly(2,6-dimethyl-1,4-phenylene oxide) (PVP/pPPO) with g-C_3N_4 sheets,[196] by mixing g-C_3N_4 with 70% PVP/pPPO solution, followed by casting onto a glass substrate and obtaining a nanocomposite membrane after solvent evaporation. The enhanced conductivity of protons and mechanical properties could be attributed to accepting sites for protons included *via* NH_2 and the interaction of polymer chains with g-C_3N_4, which led to improved proton conductivity (74.4 mS cm^{-1}) and power density (294 mW cm^{-2}) at 180 °C employing a content of g-C_3N_4 sheets of 5 wt%.

In another work, g-C_3N_4 nanosheets were employed to form a hybrid PES–PVP membrane material by a blending method to enhance the conductivity of protons in membranes, as shown by Lu and coworkers (Figure 5.11).[197] The as-prepared nanocomposite membrane showed a considerably enhanced conductivity of protons of 0.104 S cm^{-1} and power density of 512 mW cm^{-2} with 0.5% g-C_3N_4 content. In addition, the composite membranes showed enhanced mechanical properties in comparison to PES–PVP without g-C_3N_4, which is because of the reinforcing effect of g-C_3N_4 sheets similar to the mechanism observed in hydrogels (refer to Section 5.3). The bifunctional effect of g-C_3N_4 nanosheets' incorporation was demonstrated by Jiang and team, who employed nanosheets of g-C_3N_4 to mix with sulfonated poly(ether ketone) (SPEEK) composites.[198] Considering the mechanical features, an enhancement of 68% in tensile strength of nanocomposite membranes with g-C_3N_4 content of 0.5 wt% was reported because of the intrinsic mechanical stability of g-C_3N_4 nanosheets and supportive interfacial interactions of nanosheet g-C_3N_4 with the SPEEK matrix. Performance-wise, the composites of g-C_3N_4/SPEEK were employed to PEMFCs, which demonstrated a maximum power density increase of 39% with a g-C_3N_4 content of 0.5 wt%.

Other systems for energy storage such as lithium metal batteries, vanadium redox flow batteries (VRB) and supercapacitors feature enhanced efficiency for batteries and advanced stability *via* g-C_3N_4 incorporation.

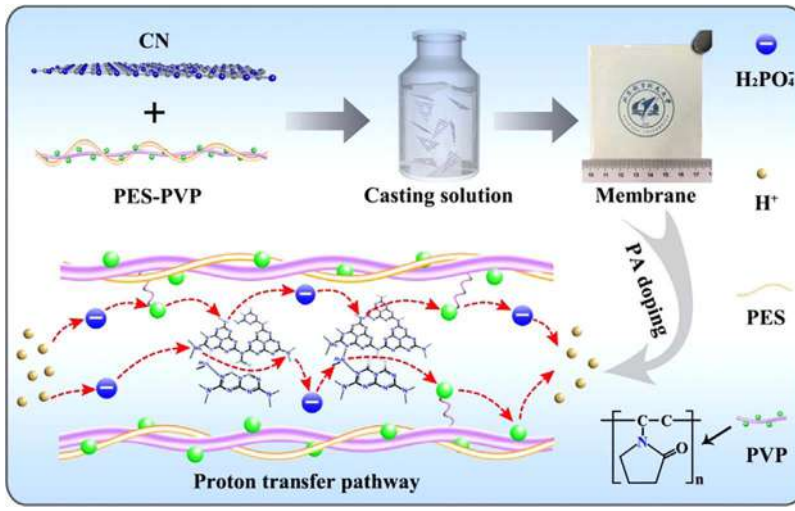

Figure 5.11 Synthesis and mechanism of proton conductivity of the g-C_3N_4 incorporated PES–PVP composite membranes. (PES: poly(ether sulfone); PVP: poly(vinyl pyrrolidone)). Adapted from ref. 197 with permission from Elsevier, Copyright 2019.

Considering VRB, negatively charged membranes such as sulfonated aromatic polymers (SPEEK,[199] sulfonated polyimide (SPI)[200] or sulfonated poly (sulfone) (SPSF)[201]) are prime candidates as they possess decent mechanical stability and proton conductivity. Yet, better performance by the means of proton conductivity and ion selectivity is still needed. The effect of g-C_3N_4 incorporation in such membranes can improve vanadium ion permeation, ion selectivity and structure stability due to interfacial interaction with the host matrix.[202–204] Highly acidic and negatively charged membranes with a Nafion matrix were decorated with g-C_3N_4 nanosheets as shown by Xiang and team, aiming to reduce vanadium ion crossover (Figure 5.12a).[205] The main issue arising from vanadium ion crossover could be partially solved by shrinking the membrane pores by the Nafion matrix and g-C_3N_4 nanosheet crosslinking (Figure 5.12b and c), which results in a lamellar structure. Therefore, an enhanced coulombic efficiency (CE) of 97% and energy efficiency (EE) of 85% was achieved at a current density of 80 mA cm^{-2} by preventing ion crossover *via* facile g-C_3N_4 nanosheets' incorporation (Figure 5.12d). A pore-filling effect of g-C_3N_4 was extended by Li and coworkers, who applied microspheres from mesoporous g-C_3N_4 as electrolyte fillers in lithium metal batteries,[206] to overcome lithium growth, which inhibits recyclability and overall performance. This tailored electrolyte with high mechanical stability and hierarchical structure could efficiently suppress the growth of lithium dendrites during cycling. Based on this electrolyte, the Li/Li symmetrical cell showed a long-term cycling of at least 120 cycles including a considerable capacity of 6 mA h cm^{-2}. Another possibility to include g-C_3N_4 in energy systems is based

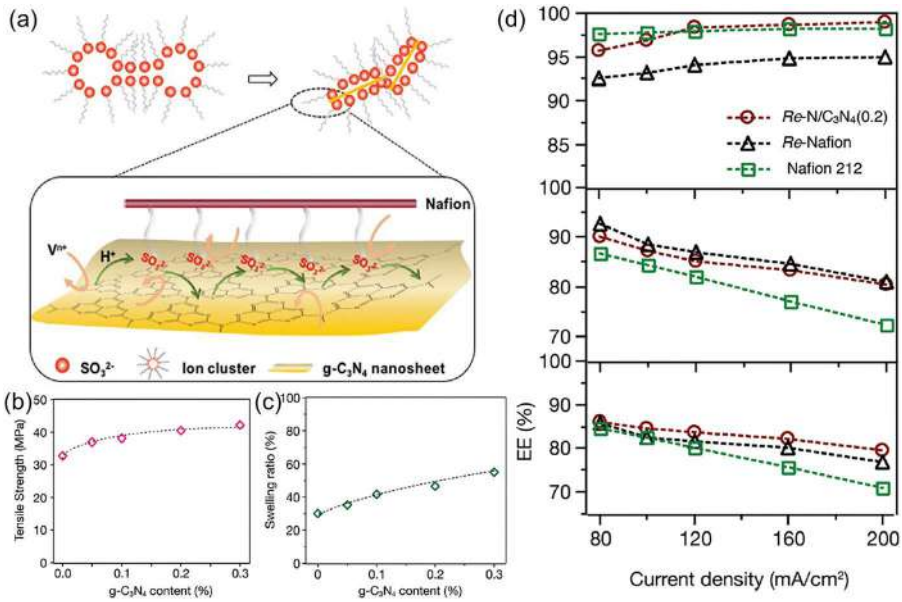

Figure 5.12 (a) Vanadium ion transport and proton transport features of the Re–N/CN(x) composite membrane. (b) Tensile strength and (c) swelling ratio of the composite Re–N/CN(x) membranes according to various amounts of g-C_3N_4 nanosheets in comparison to Re–Nafion membranes. (d) Single battery efficiency performance. Coulombic efficiency (CE), voltage efficiency (VE), and energy efficiency (EE) at current densities of 80–200 mA cm^{-2} of the vanadium redox flow battery (VRB) with the Re–N/g-C_3N_4 (0.2) membrane in comparison to those of the VRB with the Re–Nafion membrane and the commercial Nafion 212 membrane. Adapted from ref. 205 with permission from the Royal Society of Chemistry.

on embedding g-C_3N_4 onto conductive polymers to be utilized as supercapacitor electrodes to enhance mechanical and electrochemical stability.[207–209] Yang and team proposed a material for electrodes for supercapacitors relying on poly(3,4-ethylenedioxythiophene) (PEDOT):poly(styrenesulfonate) (PSS) and g-C_3N_4 *via* assembly layer-by-layer.[210] In comparison to pure PEDOT:PSS, the PEDOT:PSS/g-C_3N_4 composite exhibited considerable electrochemical stability in neutral electrolyte and improved electrochemical performance of capacitance of 137 F g^{-1} in H_2SO_4 and 200 F g^{-1} in Na_2SO_4, respectively.

Semiconductors are an important section of photovoltaic devices for energy generation from sunlight, and only a minor amount of studies have described the combination of g-C_3N_4 and polymers for utilization in solar cells.[211] The first report demonstrated a bottom-up approach to design organic photovoltaic devices.[212] g-C_3N_4 was formed *via* thermal condensation of precursors on a fluorine-doped tin oxide active surface. The resulting films were not transparent (meaning they were indeed thick);

however, combination with P3HT resulted in a device that showed V_{oc} over 1 V for the first time. The aromatic interaction of the polymeric network with the g-C_3N_4 layer provides better interfacial charge transport and therefore inhibits interfacial transfer recombination. A top-down approach is also possible to utilize dispersions of g-C_3N_4 to construct solar cell devices. Yang and team utilized g-C_3N_4 quantum dots (C_3N_4QDs) in the active layer of bulk-heterojunction (BHJ) polymer solar cells (PSCs).[213] C_3N_4QDs were synthesized by hydrolysis of bulk g-C_3N_4 sheets with acid, and subsequent solvothermal treatment resulted in dispersible C_3N_4QDs with distorted structure compared to the pristine one. Finally, they integrated C_3N_4QDs to the active layers of the PSC with a doping ratio of 0.2 mg mL^{-1}. The different active layers of the C_3N_4QDs-doped BHJ–PSC device showed an obvious enhancement of power conversion efficiencies (PCE) of 17.5%, 11.6% and 11.8%, respectively, in comparison to the reference device without C_3N_4QDs present. Optical absorption, surface morphology and PL properties as well as charge transfer properties were investigated in detail to shed light on the effect of incorporation of C_3N_4QDs. Additionally, g-C_3N_4 can be an attractive cathode layer for inverted polymer solar cells.[214] Solution-processed g-C_3N_4 as an electron transport layer modifies the bulk-heterojunction interface with a [6,6]-phenyl-C_{71}-butyric acid methyl ester ($PC_{71}BM$) unit. Some authors have demonstrated the effect of spin-coating and dip-coating g-C_3N_4 on the efficiency of energy devices as well. The best performing device with g-C_3N_4 incorporation shows a PCE of 6.40% compared to non-g-C_3N_4 containing analog PCE of 3.67%, as well as addition of g-C_3N_4 that provides increased V_{oc} (0.58 to 0.70 V) and fill factor (42 to 57%), which was attributed to full coverage of the active surface with g-C_3N_4 thin film without aggregation. Very recently, for photo-grafted 4-methyl-5-vinylthiazole (vTA) functionalized g-C_3N_4, unusual behavior based on spontaneous charge delocalization (negative charge migration to vTA rim) was reported, which can be advantageous for employment in energy conversion devices.[118] Hence, application of vTA-grafted g-C_3N_4 nanosheets (g-C_3N_4–vTA) as interfacial electron transport layers (ETLs) in inverted perovskite solar cells (PVSCs) was investigated.[32] Homogenous and transparent films of g-C_3N_4–vTA were produced by spin-coating from acetonitrile-DMSO dispersion and films were integrated into two different layers to investigate g-C_3N_4–vTA influence on the electronic properties of methylammonium lead iodide based PVSCs. The incorporation of g-C_3N_4–vTA decreased charge transport based interfacial recombination, yielding 1.09 V in V_{oc} and an increment to 20.17 mA cm^{-2} in the short circuit current. In addition, hydrophobic g-C_3N_4–vTA introduced this physical property on the perovskite layer in addition to its photophysical features, which hints toward enhanced stability of the system. Furthermore, the utilization of the g-C_3N_4–vTA interface layer as an alternative choice has highlighted the possibility of employing metal-free, cheap and processable material that is highly promising.

5.5.5 Photoactive Hydrogels Based on g-C_3N_4

The combination of hydrogels and g-C_3N_4 also adds photophysical properties to the network. As hydrogels feature high porosity, they could be prime candidates for photocatalysis under aqueous conditions. Hydrogels with g-C_3N_4 enable access to various properties, *e.g.* water contaminant degradation or photocatalytic reactivity.[215,216] Dong and team synthesized hydrogels based on acrylamide for "light filtering".[217] There, AAm was used in hydrogel formation *via* visible light induction. The interactions of g-C_3N_4 and PAAm *via* hydrogen bonding introduced self-healing in the material, with comparable mechanical properties (compression and tensile) after and before healing. Moreover, the hydrogels had considerable stability under light and were used for UV shielding because of the broad light absorption of g-C_3N_4 in the hydrogel, *e.g.* for UVA, UVB and UVC a transmittance of 0 to 28% was described. At the same time, a transmittance of 89% was observed at 550 nm leading to the assumption that these gels might be used as sunlight blockers.

Shalom and team synthesized g-C_3N_4-based hydrogels for photocatalysis (Figure 5.13a).[93] As such, dye degradation performance for several dyes was studied, which act as model compounds for impurities in wastewater. Absorption in the gel proceeded with different efficiency depending on the type of dye, which was due to ionic interactions. Furthermore, hydrogen evolution was done after incorporation of a platinum cocatalyst (Figure 5.13b) and facile recycling of the catalytic hydrogel was possible (Figure 5.13c). Yao and coworkers presented a hydrogel for wastewater treatment as well.[218] Therefore, bentonite, g-C_3N_4, AAm and MBA were introduced to synthesize monoliths of hydrogels in a thermal polymerization approach. Small cubes were cut out of the hydrogels, and absorption of tetracycline was tested. Due to the incorporation of bentonite, increased absorption of the organic contaminant was observed. At last, degradation of tetracycline by visible light irradiation was performed. Notably, absorption and degrading properties were investigated in a flow process showing a considerable removal efficiency and stability during cycling. Recently, Cao *et al.* showed the formation of g-C_3N_4-based hydrogel beads that were used for photocatalysis.[219] As such, efficient dye degradation and H_2 evolution were performed in aqueous medium. Moreover, the activity could be tailored by the bead structure, *e.g.* particle size or crosslinking density.

Lamkaho and Randorn described a photocatalytic process utilizing a g-C_3N_4-based hydrogel.[220] There, a hydrogel of PAAm was synthesized *via* light induced polymerization of AAm and MBA under UV irradiation. The hydrogel was employed for the photocatalytic reduction of Cr(VI) to Cr(III). A hydrogel fabricated from graphene, g-C_3N_4 and PPy was presented by Cui and coworkers.[221] An improved photocatalytic ability was yielded by graphene as an electron transporter and PPy as a hole transporter. Phenol photodegradation and reduction/adsorption of Cr(VI) was performed with these hydrogels. Tu and coworkers described an additional way to use g-C_3N_4 based hydrogels.

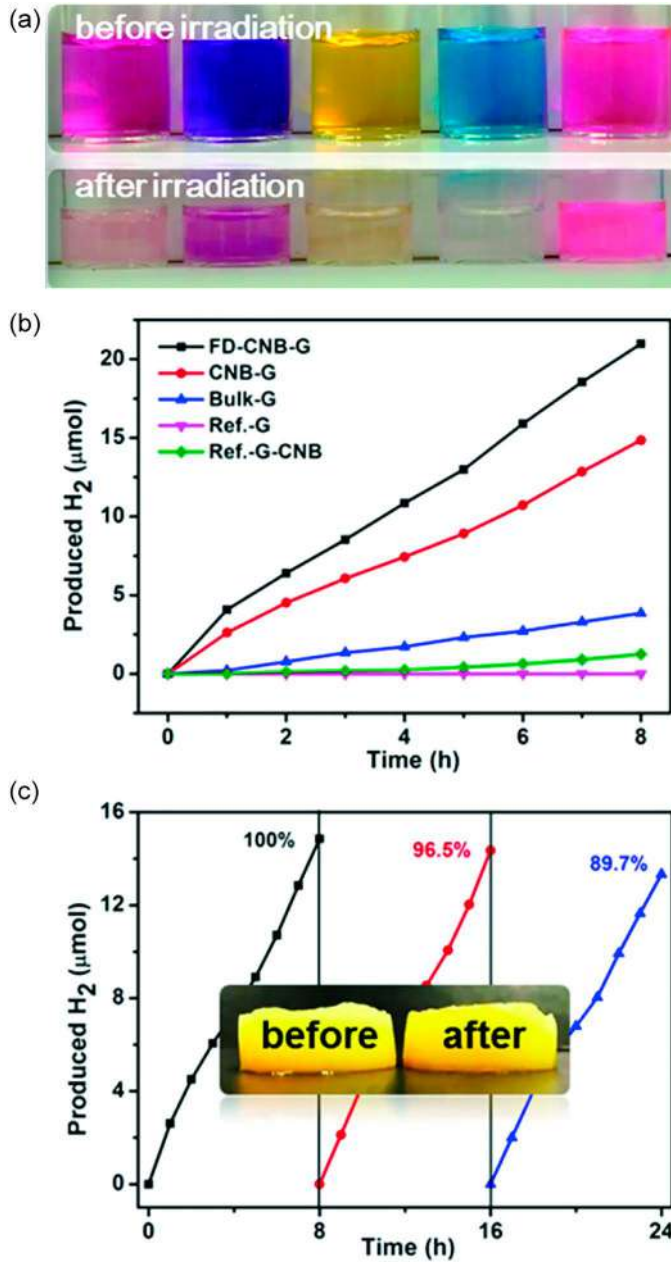

Figure 5.13 (a) Photodegradation of dyes catalyzed *via* a g-C_3N_4 hydrogel (congo red, crystal violet, methyl orange, MB, and RhB, from left to right). (b) Rate of hydrogen production from the aqueous environment with g-C_3N_4 hydrogels (FD-CNB-G: freeze-dried g-C_3N_4-based hydrogel and CNB-G: g-C_3N_4-based hydrogel) and references (Bulk-G: hydrogel from melamine-derived g-C_3N_4; ref.-G: hydrogel without g-C_3N_4 incorporation; ref.-G-CNB: reference gel after adsorption of g-C_3N_4 suspension) *via* white LED irradiation. (c) Cycling measurements of hydrogen evolution *via* wet g-C_3N_4 hydrogel (inset: g-C_3N_4 hydrogel before and after hydrogen generation). Adapted from ref. 93 with permission from American Chemical Society, Copyright 2017.

A hydrogel based on AAm/acrylic acid was synthesized with thermal initiation and used for Ag^+ ion sensing.[222] The incorporation of acrylic acid facilitated pH sensitivity of the hydrogels, *i.e.* the state of swelling changed with respect to pH. Additionally, fluorescent behavior was inherited in the hydrogels due to g-C_3N_4 inclusion, which was further exploited for sensing. Therefore, the variations in fluorescence were probed after metal ion addition. For Ag^+ a considerable effect of quenching was noted, down to concentrations of 6.31 μM. Moreover, Ag^+ could still be detected in the presence of other contaminant ions. Self-assembly oriented hydrogel formation was reported recently.[223] As such, self-assembly of g-C_3N_4-sulfur-protein results in a highly photoactive hydrogel for 86% reduced nicotinamide adenine dinucleotide (NADH) regeneration and 90% L-glutamate production under visible light that is highly promising for mimicking natural photosynthesis.

5.6 Conclusion and Outlook

The combination of polymers and exfoliated g-C_3N_4 sheets has become a hot topic in materials science recently that introduces many enhanced functions and hybrid materials featuring unprecedented properties pushing the field to a new level. In the beginning, the formation of these materials was put forward due to the common g-C_3N_4 properties, *e.g.* photocatalysis, photoinitiation or photoluminescence. Moreover, the hybrid formation introduced considerably improved or optimized properties, which can be related to improved delamination and to synergies of the two material classes. For example, the introduction of g-C_3N_4 with conducting polymers facilitates overcoming the low conductivity of electrons in g-C_3N_4, and photocatalysis or hydrogen evolution features of g-C_3N_4 were promoted that way. In systems of biosensors, g-C_3N_4 with polymer functionalization led to enhanced selectivity and sensitivity, which can be attributed to enhanced dispersibility and increased access to the sites of sensing. In addition, polymer modified g-C_3N_4 featured improved dispersion as well as processing that could be exploited in film formation.

Due to the multiple properties of g-C_3N_4, the advantages for polymer materials were also introduced. For instance, g-C_3N_4 doping of a polymer matrix increases the electrode materials' performance in energy storage and enhances stability and efficiency in comparison to the pure polymer. Polymerizations with g-C_3N_4 photoinitiation can be performed on g-C_3N_4 or in solution to obtain g-C_3N_4/polymer nanocomposites that feature photoluminescent properties for several applications. Moreover, the combination of g-C_3N_4 with polymers improves mechanical and thermal properties. In the area of bulk soft materials, g-C_3N_4 showed considerable reinforcing features in hydrogels and the ability to obtain hybrids of g-C_3N_4/hydrogel. All in all, the broad range of monomers and g-C_3N_4 types enables the synthesis of defined hydrogel materials with useful and unusual properties, *e.g.* thermoresponsivity, ultra-low friction or compressibility. The utilization of photopolymerization allows one to obtain reinforced hydrogels in a spatially

controlled way, where directions of additive manufacturing are a considerable approach for the future.[224,225]

Novel applications for g-C_3N_4 might be induced *via* the introduction of polymers. Nevertheless, there are some challenges that have to be addressed in the ongoing research. Although promising directions have been described so far, g-C_3N_4/polymer hybrid materials are still at the beginning. Thus, additional studies and developments are needed, for example, more research in methods that are beyond the blending of polymers and g-C_3N_4, more environmentally-friendly processing methods and more research into photocatalysis applications. Overall, g-C_3N_4 materials will have a bright future, for example, in energy conversion and storage, and increasing surface areas of g-C_3N_4 *via* polymers could turn into a key step for broad usage of g-C_3N_4 in supercapacitors, batteries and other high-efficiency energy conversion assemblies. Introducing polymers to g-C_3N_4 science adds a new perspective and has lot of benefits for advanced materials fabrication. To be of benefit and provide the best of both worlds will ultimately be a milestone for polymer chemistry and metal-free photocatalysis. The introduction of polymers to g-C_3N_4 introduced various new directions for the material that could not be expected some years past. In previous times, dispersion and processing constituted major challenges for a broad application of g-C_3N_4 materials. Nevertheless, with these actual directions, dispersion becomes less of a challenge. Overall, g-C_3N_4 constitutes a sustainable and non-expensive alternative for other types of semiconductors, and precision design of both g-C_3N_4 properties and tailoring of a polymer in the surroundings of different materials will enable a significant direction for the future both in academia and in the industry.

References

1. G. Kickelbick, *Hybrid Materials: Synthesis, Characterization, and Applications*, John Wiley & Sons, 2007.
2. B. V. K. J. Schmidt, *Macromol. Rapid Commun.*, 2020, **41**, 1900333.
3. A. Y. Sham and S. M. Notley, *Soft Matter*, 2013, **9**, 6645–6653.
4. T. Kuilla, S. Bhadra, D. Yao, N. H. Kim, S. Bose and J. H. Lee, *Prog. Polym. Sci.*, 2010, **35**, 1350–1375.
5. A. C. Balazs, T. Emrick and T. P. Russell, *Science*, 2006, **314**, 1107.
6. T. Clyne and D. Hull, *An Introduction to Composite Materials*, Cambridge university press, 2019.
7. X. Wang, K. Maeda, A. Thomas, K. Takanabe, G. Xin, J. M. Carlsson, K. Domen and M. Antonietti, *Nat. Mater.*, 2008, **8**, 76.
8. J. Liu, H. Wang and M. Antonietti, *Chem. Soc. Rev.*, 2016, **45**, 2308–2326.
9. G. Algara-Siller, N. Severin, S. Y. Chong, T. Björkman, R. G. Palgrave, A. Laybourn, M. Antonietti, Y. Z. Khimyak, A. V. Krasheninnikov, J. P. Rabe, U. Kaiser, A. I. Cooper, A. Thomas and M. J. Bojdys, *Angew. Chem., Int. Ed.*, 2014, **53**, 7450–7455.
10. W. J. Ong, L. L. Tan, Y. H. Ng, S. T. Yong and S. P. Chai, *Chem. Rev.*, 2016, **116**, 7159–7329.

11. J. Ran, T. Y. Ma, G. Gao, X.-W. Du and S. Z. Qiao, *Energy Environ. Sci.*, 2015, **8**, 3708–3717.
12. S. Hu, F. Li, Z. Fan, F. Wang, Y. Zhao and Z. Lv, *Dalton Trans.*, 2015, **44**, 1084–1092.
13. K. K. R. Datta, B. V. S. Reddy, K. Ariga and A. Vinu, *Angew. Chem., Int. Ed.*, 2010, **49**, 5961–5965.
14. B. Kurpil, B. Kumru, T. Heil, M. Antonietti and A. Savateev, *Green Chem.*, 2018, **20**, 838–842.
15. K. Schwinghammer, B. Tuffy, M. B. Mesch, E. Wirnhier, C. Martineau, F. Taulelle, W. Schnick, J. Senker and B. V. Lotsch, *Angew. Chem., Int. Ed.*, 2013, **52**, 2435–2439.
16. G. Zhang, G. Li, Z. A. Lan, L. Lin, A. Savateev, T. Heil, S. Zafeiratos, X. Wang and M. Antonietti, *Angew. Chem., Int. Ed.*, 2017, **56**, 13445–13449.
17. J. Yang, M. A. Cohen Stuart and M. Kamperman, *Chem. Soc. Rev.*, 2014, **43**, 8271–8298.
18. K. Eid, M. H. Sliem, H. Al-Kandari, M. A. Sharaf and A. M. Abdullah, *Langmuir*, 2019, **35**, 3421–3431.
19. K. Eid, M. H. Sliem and A. M. Abdullah, *Nanoscale*, 2019, **11**, 11755–11764.
20. K. Eid, M. H. Sliem, A. S. Eldesoky, H. Al-Kandari and A. M. Abdullah, *Int. J. Hydrogen Energy*, 2019, **44**, 17943–17953.
21. K. Eid, M. H. Sliem, K. Jlassi, A. S. Eldesoky, G. G. Abdo, S. Y. Al-Qaradawi, M. A. Sharaf, A. M. Abdullah and A. A. Elzatahry, *Inorg. Chem. Commun.*, 2019, **107**, 107460.
22. R. Kuriki, K. Sekizawa, O. Ishitani and K. Maeda, *Angew. Chem., Int. Ed.*, 2015, **54**, 2406–2409.
23. J. Lin, Z. Pan and X. Wang, *ACS Sustainable Chem. Eng.*, 2014, **2**, 353–358.
24. K. Xiao, L. Chen, R. Chen, T. Heil, S. D. C. Lemus, F. Fan, L. Wen, L. Jiang and M. Antonietti, *Nat. Commun.*, 2019, **10**, 74.
25. K. Xiao, B. Kumru, L. Chen, L. Jiang, B. V. K. J. Schmidt and M. Antonietti, *Beilstein J. Nanotechnol.*, 2019, **10**, 1316–1323.
26. G. Peng, M. Volokh, J. Tzadikov, J. Sun and M. Shalom, *Adv. Energy Mater.*, 2018, **8**, 1800566.
27. M. A. Ahsan, T. He, K. Eid, A. M. Abdullah, M. L. Curry, A. Du, A. R. Puente Santiago, L. Echegoyen and J. C. Noveron, *J. Am. Chem. Soc.*, 2021, **143**(2), 1203–1215.
28. J. Xu and M. Antonietti, *J. Am. Chem. Soc.*, 2017, **139**, 6026–6029.
29. J. Zhang, B. D. Frank, B. Kumru and B. V. K. J. Schmidt, *Macromol. Rapid Commun.*, 2020, 2000433.
30. X. Chen, Q. Liu, Q. Wu, P. Du, J. Zhu, S. Dai and S. Yang, *Adv. Funct. Mater.*, 2016, **26**, 1719–1728.
31. T. R. Chetia, M. S. Ansari and M. Qureshi, *J. Mater. Chem. A*, 2016, **4**, 5528–5541.
32. D. Cruz, J. Garcia Cerrillo, B. Kumru, N. Li, J. Dario Perea, B. V. K. J. Schmidt, I. Lauermann, C. J. Brabec and M. Antonietti, *J. Am. Chem. Soc.*, 2019, **140**, 17532–17537.
33. Q. Cao, B. Kumru, M. Antonietti and B. V. K. J. Schmidt, *Mater. Horiz.*, 2020, **7**, 762–786.

34. J. Zhang, M. Zhang, L. Lin and X. Wang, *Angew. Chem., Int. Ed.*, 2015, **54**, 6297–6301.
35. Z. Zhao, Y. Sun and F. Dong, *Nanoscale*, 2015, **7**, 15–37.
36. S. Patnaik, D. P. Sahoo and K. Parida, in *Nanocomposites for Visible Light-Induced Photocatalysis*, ed. M. M. Khan, D. Pradhan and Y. Sohn, Springer International Publishing, Cham, 2017, pp. 251–294, DOI: 10.1007/978-3-319-62446-4_9.
37. M. A. Stuart, W. T. Huck, J. Genzer, M. Muller, C. Ober, M. Stamm, G. B. Sukhorukov, I. Szleifer, V. V. Tsukruk, M. Urban, F. Winnik, S. Zauscher, I. Luzinov and S. Minko, *Nat. Mater.*, 2010, **9**, 101–113.
38. M. Wei, Y. Gao, X. Li and M. J. Serpe, *Polym. Chem.*, 2017, **8**, 127–143.
39. B. V. K. J. Schmidt, M. Hetzer, H. Ritter and C. Barner-Kowollik, *Macromolecules*, 2013, **46**, 1054–1065.
40. K. H. Ku, Y. J. Lee, G.-R. Yi, S. G. Jang, B. V. K. J. Schmidt, K. Liao, D. Klinger, C. J. Hawker and B. J. Kim, *Macromolecules*, 2017, **50**, 9276–9285.
41. L. S. Nair and C. T. Laurencin, *Prog. Polym. Sci.*, 2007, **32**, 762–798.
42. B. Laycock, M. Nikolić, J. M. Colwell, E. Gauthier, P. Halley, S. Bottle and G. George, *Prog. Polym. Sci.*, 2017, **71**, 144–189.
43. G. Becker and F. R. Wurm, *Chem. Soc. Rev.*, 2018, **47**, 7739–7782.
44. C. Huang, D. Quinn, Y. Sadovsky, S. Suresh and K. J. Hsia, *Proc. Natl. Acad. Sci. U. S. A.*, 2017, **114**, 2910–2915.
45. Y. Zhu, B. Yang, S. Chen and J. Du, *Prog. Polym. Sci.*, 2017, **64**, 1–22.
46. B. V. K. J. Schmidt, *Macromol. Chem. Phys.*, 2018, **219**, 1700494.
47. Y. Wang and X. Jing, *Polym. Adv. Technol.*, 2005, **16**, 344–351.
48. M. Bharti, A. Singh, S. Samanta and D. Aswal, *Prog. Mater. Sci.*, 2018, **93**, 270–310.
49. T. Nezakati, A. Seifalian, A. Tan and A. M. Seifalian, *Chem. Rev.*, 2018, **118**, 6766–6843.
50. J. Yeow, R. Chapman, J. Xu and C. Boyer, *Polym. Chem.*, 2017, **8**, 5012–5022.
51. J. Xu, K. Jung, N. A. Corrigan and C. Boyer, *Chem. Sci.*, 2014, **5**, 3568–3575.
52. H.-C. Lee, M. Fantin, M. Antonietti, K. Matyjaszewski and B. V. K. J. Schmidt, *Chem. Mater.*, 2017, **29**, 9445–9455.
53. B. Kiskan, J. Zhang, X. Wang, M. Antonietti and Y. Yagci, *ACS Macro Lett.*, 2012, **1**, 546–549.
54. Q. Cao, Q. Cui, Y. Yang, J. Xu, C. Han and L. Li, *Chem. - Eur. J.*, 2018, **24**, 2286–2291.
55. S. Dadashi-Silab, M. A. Tasdelen, B. Kiskan, X. Wang, M. Antonietti and Y. Yagci, *Macromol. Chem. Phys.*, 2014, **215**, 675–681.
56. M. Al-Naji, B. Puertolas, B. Kumru, D. Cruz, M. Baumel, B. V. K. J. Schmidt, N. V. Tarakina and J. Perez-Ramirez, *ChemSusChem*, 2019, **12**, 2628–2636.
57. B. Kiskan, J. Zhang, X. Wang, M. Antonietti and Y. Yagci, *ACS Macro Lett.*, 2012, **1**, 546–549.
58. Q. Cao, T. Heil, B. Kumru, M. Antonietti and B. V. K. J. Schmidt, *Polym. Chem.*, 2019, **10**, 5315–5323.

59. N. Yandrapalli, T. Robinson, M. Antonietti and B. Kumru, *Small*, 2020, **16**, 2001180.
60. K. Kaya, B. Kiskan, B. Kumru, B. V. K. J. Schmidt and Y. Yagci, *Eur. Polym. J.*, 2020, **122**, 109410.
61. D. J. Martin, K. Qiu, S. A. Shevlin, A. D. Handoko, X. Chen, Z. Guo and J. Tang, *Angew. Chem., Int. Ed.*, 2014, **53**, 9240–9245.
62. D. J. Martin, P. J. Reardon, S. J. Moniz and J. Tang, *J. Am. Chem. Soc.*, 2014, **136**, 12568–12571.
63. Q. Fu, Q. Ruan, T. G. McKenzie, A. Reyhani, J. Tang and G. G. Qiao, *Macromolecules*, 2017, **50**, 7509–7516.
64. L. Zhang, G. Ye, X. Huo, S. Xu, J. Chen and K. Matyjaszewski, *ACS Omega*, 2019, **4**, 16247–16255.
65. B. Kumru, J. Mendoza Mesa, M. Antonietti and M. Al-Naji, *ACS Sustainable Chem. Eng.*, 2019, **7**, 17574–17579.
66. B. Kumru, M. Shalom, M. Antonietti and B. V. K. J. Schmidt, *Macromolecules*, 2017, **50**, 1862–1869.
67. W. Sheng, W. Li, D. Tan, P. Zhang, E. Zhang, E. Sheremet, B. V. K. J. Schmidt, X. Feng, R. D. Rodriguez, R. Jordan and I. Amin, *ACS Appl. Mater. Interfaces*, 2020, **12**, 9797–9805.
68. J. Poostforooshan, A. Badiei, M. Kolahdouz and A. P. Weber, *ACS Appl. Mater. Interfaces*, 2016, **8**, 21731–21741.
69. J. L. Drury and D. J. Mooney, *Biomaterials*, 2003, **24**, 4337–4351.
70. A. M. Kloxin, A. M. Kasko, C. N. Salinas and K. S. Anseth, *Science*, 2009, **324**, 59–63.
71. T. Li, B. Kumru, N. Al Nakeeb, J. Willersinn and B. V. K. J. Schmidt, *Polymers*, 2018, **10**, 576.
72. J. Zhang, B. Kumru and B. V. K. J. Schmidt, *Langmuir*, 2019, **35**, 11141–11149.
73. J. Zhu and R. E. Marchant, *Expert Rev. Med. Devices*, 2011, **8**, 607–626.
74. T. R. Hoare and D. S. Kohane, *Polymer*, 2008, **49**, 1993–2007.
75. X. Dai, Y. Zhang, L. Gao, T. Bai, W. Wang, Y. Cui and W. Liu, *Adv. Mater.*, 2015, **27**, 3566–3571.
76. H. Yuk, S. Lin, C. Ma, M. Takaffoli, N. X. Fang and X. Zhao, *Nat. Commun.*, 2017, **8**, 14230.
77. P. Samaddar, S. Kumar and K.-H. Kim, *Polym. Rev.*, 2019, **59**, 418–464.
78. W. Guo, C. H. Lu, R. Orbach, F. Wang, X. J. Qi, A. Cecconello, D. Seliktar and I. Willner, *Adv. Mater.*, 2015, **27**, 73–78.
79. T. Murakami, B. V. K. J. Schmidt, H. R. Brown and C. J. Hawker, *Macromolecules*, 2015, **48**, 7774–7781.
80. A. Bin Imran, K. Esaki, H. Gotoh, T. Seki, K. Ito, Y. Sakai and Y. Takeoka, *Nat. Commun.*, 2014, **5**, 5124.
81. T. Murakami, B. V. K. J. Schmidt, H. R. Brown and C. J. Hawker, *J. Polym. Sci., Part A: Polym. Chem.*, 2017, **55**, 1156–1165.
82. A. Nakayama, A. Kakugo, J. P. Gong, Y. Osada, M. Takai, T. Erata and S. Kawano, *Adv. Funct. Mater.*, 2004, **14**, 1124–1128.

83. B. G. Cooper, R. C. Stewart, D. Burstein, B. D. Snyder and M. W. Grinstaff, *Angew. Chem., Int. Ed.*, 2016, **55**, 4226–4230.
84. M. Fukasawa, T. Sakai, U.-I. Chung and K. Haraguchi, *Macromolecules*, 2010, **43**, 4370–4378.
85. O. Okay and W. Oppermann, *Macromolecules*, 2007, **40**, 3378–3387.
86. S. Tamesue, M. Ohtani, K. Yamada, Y. Ishida, J. M. Spruell, N. A. Lynd, C. J. Hawker and T. Aida, *J. Am. Chem. Soc.*, 2013, **135**, 15650–15655.
87. A. Agrawal, N. Rahbar and P. D. Calvert, *Acta Biomater.*, 2013, **9**, 5313–5318.
88. J. Djonlagic, A. Lancuski, M. S. Nikolic, J. Rogan, S. Ostojic and Z. Petrovic, *J. Appl. Polym. Sci.*, 2017, **134**, 44535.
89. Q. Wang, J. L. Mynar, M. Yoshida, E. Lee, M. Lee, K. Okuro, K. Kinbara and T. Aida, *Nature*, 2010, **463**, 339.
90. M. Liu, Y. Ishida, Y. Ebina, T. Sasaki, T. Hikima, M. Takata and T. Aida, *Nature*, 2015, **517**, 68.
91. C. Hu, Y.-R. Lin and H.-C. Yang, *ChemSusChem*, 2018, **12**, 1794–1806.
92. J. Liu, T. An, Z. Chen, Z. Wang, H. Zhou, T. Fan, D. Zhang and M. Antonietti, *J. Mater. Chem. A*, 2017, **5**, 8933–8938.
93. J. Sun, B. V. K. J. Schmidt, X. Wang and M. Shalom, *ACS Appl. Mater. Interfaces*, 2017, **9**, 2029–2034.
94. M. Zarei, H. Ahmadzadeh, E. K. Goharshadi and A. Farzaneh, *Anal. Chim. Acta*, 2015, **887**, 245–252.
95. J. Barrio and M. Shalom, *ChemCatChem*, 2018, **10**, 5573–5586.
96. H. Li, L. Wang, Y. Liu, J. Lei and J. Zhang, *Res. Chem. Intermed.*, 2016, **42**, 3979–3998.
97. Y. Zheng, Y. Jiao, J. Chen, J. Liu, J. Liang, A. Du, W. Zhang, Z. Zhu, S. C. Smith, M. Jaroniec, G. Q. Lu and S. Z. Qiao, *J. Am. Chem. Soc.*, 2011, **133**, 20116–20119.
98. B. Kumru, V. Molinari, R. Dünnebacke, K. G. Blank and B. V. K. J. Schmidt, *Macromol. Rapid Commun.*, 2018, **40**, 1800712.
99. B. Kumru, V. Molinari, M. Shalom, M. Antonietti and B. V. K. J. Schmidt, *Soft Matter*, 2018, **14**, 2655–2664.
100. J. P. Gong, T. Kurokawa, T. Narita, G. Kagata, Y. Osada, G. Nishimura and M. Kinjo, *J. Am. Chem. Soc.*, 2001, **123**, 5582–5583.
101. M. M. Blum and T. C. Ovaert, *Mater. Sci. Eng., C*, 2013, **33**, 4377–4383.
102. E. G. Gillan, *Chem. Mater.*, 2000, **12**, 3906–3912.
103. J. Sun, R. Phatake, A. Azoulay, G. Peng, C. Han, J. Barrio, J. Xu, X. Wang and M. Shalom, *Chem. - Eur. J.*, 2018, **24**, 14921–14927.
104. G. Peng, L. Xing, J. Barrio, M. Volokh and M. Shalom, *Angew. Chem., Int. Ed.*, 2018, **57**, 1186–1192.
105. X. She, H. Xu, Y. Xu, J. Yan, J. Xia, L. Xu, Y. Song, Y. Jiang, Q. Zhang and H. Li, *J. Mater. Chem. A*, 2014, **2**, 2563–2570.
106. L. Chen, D. Huang, S. Ren, T. Dong, Y. Chi and G. Chen, *Nanoscale*, 2013, **5**, 225–230.
107. Q. Han, B. Wang, Y. Zhao, C. Hu and L. Qu, *Angew. Chem., Int. Ed.*, 2015, **54**, 11433–11437.

108. S. Yang, Y. Gong, J. Zhang, L. Zhan, L. Ma, Z. Fang, R. Vajtai, X. Wang and P. M. Ajayan, *Adv. Mater.*, 2013, **25**, 2452–2456.
109. P. Niu, L. Zhang, G. Liu and H.-M. Cheng, *Adv. Funct. Mater.*, 2012, **22**, 4763–4770.
110. Y. Shi, B. Wang, L. Duan, Y. Zhu, Z. Gui, R. K. K. Yuen and Y. Hu, *Ind. Eng. Chem. Res.*, 2016, **55**, 7646–7654.
111. Q. Cui, J. Xu, X. Wang, L. Li, M. Antonietti and M. Shalom, *Angew. Chem., Int. Ed.*, 2016, **55**, 3672–3676.
112. J. K. Kim, S. Park, R. J. Yoo, H. J. Jeong, J. Oh, Y. J. Lee, S. Park and D. W. Kim, *Chem. - Eur. J.*, 2018, **24**, 3506–3511.
113. X. Bu, J. Li, S. Yang, J. Sun, Y. Deng, Y. Yang, G. Wang, Z. Peng, P. He, X. Wang, G. Ding, J. Yang and X. Xie, *ACS Appl. Mater. Interfaces*, 2016, **8**, 31419–31425.
114. Y. Zheng, Z. Zhang, C. Li and S. Proulx, *Mater. Res. Bull.*, 2016, **84**, 46–56.
115. R. B. N. Baig, S. Verma, M. N. Nadagouda and R. S. Varma, *Sci. Rep.*, 2016, **6**, 39387.
116. B. Kumru, V. Molinari, M. Hilgart, F. Rummel, M. Schäffler and B. V. K. J. Schmidt, *Polym. Chem.*, 2019, **10**, 3647–3656.
117. B. Kumru, M. Antonietti and B. V. K. J. Schmidt, *Langmuir*, 2017, **33**, 9897–9906.
118. B. Kumru, D. Cruz, T. Heil, B. V. K. J. Schmidt and M. Antonietti, *J. Am. Chem. Soc.*, 2018, **140**, 17532–17537.
119. J. Tian, Q. Liu, C. Ge, Z. Xing, A. M. Asiri, A. O. Al-Youbi and X. Sun, *Nanoscale*, 2013, **5**, 8921–8924.
120. Q. Cui, J. Xu, X. Wang, L. Li, M. Antonietti and M. Shalom, *Angew. Chem., Int. Ed.*, 2016, **55**, 3672–3676.
121. X. Ou, X. Tan, X. Liu, Q. Lu, S. Chen and S. Wei, *Biosens. Bioelectron.*, 2015, **70**, 89–97.
122. Q. Lu, J. Zhang, X. Liu, Y. Wu, R. Yuan and S. Chen, *Analyst*, 2014, **139**, 6556–6562.
123. B. K. Shrestha, R. Ahmad, S. Shrestha, C. H. Park and C. S. Kim, *Biosens. Bioelectron.*, 2017, **94**, 686–693.
124. Y. Liu, H. Ma, Y. Zhang, X. Pang, D. Fan, D. Wu and Q. Wei, *Biosens. Bioelectron.*, 2016, **86**, 439–445.
125. H. Arazoe, D. Miyajima, K. Akaike, F. Araoka, E. Sato, T. Hikima, M. Kawamoto and T. Aida, *Nat. Mater.*, 2016, **15**, 1084.
126. K. Xiao, P. Giusto, L. Wen, L. Jiang and M. Antonietti, *Angew. Chem., Int. Ed.*, 2018, **57**, 10123–10126.
127. J. Xu, T. J. Brenner, L. Chabanne, D. Neher, M. Antonietti and M. Shalom, *J. Am. Chem. Soc.*, 2014, **136**, 13486–13489.
128. C. Tang, A. Tracz, M. Kruk, R. Zhang, D. M. Smilgies, K. Matyjaszewski and T. Kowalewski, *J. Am. Chem. Soc.*, 2005, **127**, 6918–6919.
129. X. Zhang, X. Xie, H. Wang, J. Zhang, B. Pan and Y. Xie, *J. Am. Chem. Soc.*, 2013, **135**, 18–21.
130. N. Karjule, R. Phatake, M. Volokh, I. Hod and M. Shalom, *Small Methods*, 2019, **3**, 1900401.

131. Y. Shi, S. Jiang, K. Zhou, C. Bao, B. Yu, X. Qian, B. Wang, N. Hong, P. Wen, Z. Gui, Y. Hu and R. K. Yuen, *ACS Appl. Mater. Interfaces*, 2014, **6**, 429–437.
132. Q. Cao, B. Kumru, M. Antonietti and B. V. K. J. Schmidt, *Macromolecules*, 2019, **52**, 4989–4996.
133. B. Kumru, J. Barrio, J. Zhang, M. Antonietti, M. Shalom and B. V. K. J. Schmidt, *ACS Appl. Mater. Interfaces*, 2019, **11**, 9462–9469.
134. P. Giusto, D. Cruz, T. Heil, H. Arazoe, P. Lova, T. Aida, D. Comoretto, M. Patrini and M. Antonietti, *Adv. Mater.*, 2020, **32**, 1908140.
135. P. Giusto, B. Kumru, J. Zhang, R. Rothe and M. Antonietti, *Chem. Mater.*, 2020, **32**(17), 7284–7291.
136. C. Han, Q. Cui, P. Meng, E. R. Waclawik, H. Yang and J. Xu, *Langmuir*, 2018, **34**, 10135–10143.
137. Y. Luo, Y. Yang, Q. Cui, R. Peng, R. Liu, Q. Cao and L. Li, *ACS Appl. Bio Mater.*, 2019, **2**(11), 5127–5135.
138. C. Duan, D. Yuan, Z. Yang, S. Li, L. Tao, Q. Wang and T. Wang, *Composites, Part A*, 2018, **113**, 200–208.
139. M. Khalifa, A. Mahendran and S. Anandhan, *J. Polym. Res.*, 2019, **26**, 73.
140. Y. Shi, B. Wang, L. Duan, Y. Zhu, Z. Gui, R. K. K. Yuen and Y. Hu, *Ind. Eng. Chem. Res.*, 2016, **55**, 7646–7654.
141. K. Myllymaa, S. Myllymaa, H. Korhonen, M. J. Lammi, H. Saarenpaa, M. Suvanto, T. A. Pakkanen, V. Tiitu and R. Lappalainen, *J. Mater. Sci.: Mater. Med.*, 2009, **20**, 2337–2347.
142. Y. Shi, Z. Gui, B. Yu, R. K. K. Yuen, B. Wang and Y. Hu, *Composites, Part B*, 2015, **79**, 277–284.
143. B. Lei, Y. Zhang, Y. He, Y. Xie, B. Xu, Z. Lin, L. Huang, S. Tan, M. Wang and X. Cai, *Mater. Des.*, 2015, **66**, 103–109.
144. S. He, J. Wang, M. Yu, Y. Xue, J. Hu and J. Lin, *Polymers*, 2019, **11**, .
145. B. Song, T. Wang, H. Sun, H. Liu, X. Mai, X. Wang, L. Wang, N. Wang, Y. Huang and Z. Guo, *Compos. Sci. Technol.*, 2018, **167**, 515–521.
146. N. D. Bansod, K. Roy, C. Das, D. Vidyasagar and P. Potiyaraj, *J. Appl. Polym. Sci.*, 2019, **136**, 48136.
147. J. W. Ko, W. S. Choi, J. Kim, S. K. Kuk, S. H. Lee and C. B. Park, *Biomacromolecules*, 2017, **18**, 3551–3556.
148. P. He, X. Tang, L. Chen, P. Xie, L. He, H. Zhou, D. Zhang and T. Fan, *Adv. Funct. Mater.*, 2018, **28**, 1801121.
149. J. Yan, M.-T. F. Rodrigues, Z. Song, H. Li, H. Xu, H. Liu, J. Wu, Y. Xu, Y. Song, Y. Liu, P. Yu, W. Yang, R. Vajtai, H. Li, S. Yuan and P. M. Ajayan, *Adv. Funct. Mater.*, 2017, **27**, 1700653.
150. Y. Zhang, Z. Zhou, Y. Shen, Q. Zhou, J. Wang, A. Liu, S. Liu and Y. Zhang, *ACS Nano*, 2016, **10**, 9036–9043.
151. L. Tan, C. Yu, M. Wang, S. Zhang, J. Sun, S. Dong and J. Sun, *Appl. Surf. Sci.*, 2019, **467–468**, 286–292.
152. M. Zhang, W. Jiang, D. Liu, J. Wang, Y. Liu, Y. Zhu and Y. Zhu, *Appl. Catal., B*, 2016, **183**, 263–268.
153. Y. Sui, J. Liu, Y. Zhang, X. Tian and W. Chen, *Nanoscale*, 2013, **5**, 9150–9155.

154. Y. Zhang, F. Mao, H. Yan, K. Liu, H. Cao, J. Wu and D. Xiao, *J. Mater. Chem. A*, 2015, **3**, 109–115.
155. F. He, G. Chen, Y. Yu, S. Hao, Y. Zhou and Y. Zheng, *ACS Appl. Mater. Interfaces*, 2014, **6**, 7171–7179.
156. H. Yan and Y. Huang, *Chem. Commun.*, 2011, **47**, 4168–4170.
157. A. Li, Q. Cao, G. Zhou, B. V. K. J. Schmidt, W. Zhu, X. Yuan, H. Huo, J. Gong and M. Antonietti, *Angew. Chem., Int. Ed.*, 2019, **58**, 14549–14555.
158. S. Roy and E. Reisner, *Angew. Chem., Int. Ed.*, 2019, **58**, 12180–12184.
159. K. Pandiselvi, H. Fang, X. Huang, J. Wang, X. Xu and T. Li, *J. Hazard. Mater.*, 2016, **314**, 67–77.
160. H. Lachheb, E. Puzenat, A. Houas, M. Ksibi, E. Elaloui, C. Guillard and J.-M. Herrmann, *Appl. Catal., B*, 2002, **39**, 75–90.
161. S. Xiao, Z. Wang, H. Ma, H. Yang and W. Xu, *Adv. Powder Technol.*, 2014, **25**, 574–581.
162. M. Panizza and G. Cerisola, *Chem. Rev.*, 2009, **109**, 6541–6569.
163. C. P. Athanasekou, N. G. Moustakas, S. Morales-Torres, L. M. Pastrana-Martínez, J. L. Figueiredo, J. L. Faria, A. M. T. Silva, J. M. Dona-Rodriguez, G. E. Romanos and P. Falaras, *Appl. Catal., B*, 2015, **178**, 12–19.
164. Y. Zhao, Y. Zhang, A. Liu, Z. Wei and S. Liu, *ACS Appl. Mater. Interfaces*, 2017, **9**, 4006–4014.
165. Y. Huang, H. Li, M. S. Balogun, W. Liu, Y. Tong, X. Lu and H. Ji, *ACS Appl. Mater. Interfaces*, 2014, **6**, 22920–22927.
166. W. Jiang, W. Luo, R. Zong, W. Yao, Z. Li and Y. Zhu, *Small*, 2016, **12**, 4370–4378.
167. L. Ge, C. Han and J. Liu, *J. Mater. Chem.*, 2012, **22**, 11843–11850.
168. B. Vellaichamy and P. Periakaruppan, *Ind. Eng. Chem. Res.*, 2018, **57**, 6684–6695.
169. H.-H. Wu, C.-W. Chang, D. Lu, K. Maeda and C. Hu, *ACS Appl. Mater. Interfaces*, 2019, **11**, 35702–35712.
170. M. A. Alenizi, R. Kumar, M. Aslam, F. A. Alseroury and M. A. Barakat, *Sci. Rep.*, 2019, **9**, 12091.
171. X. Bu, Y. Lu, S. Chen, D. Li, Z. Zhang and P. Qian, *Chem. Eng. Sci.*, 2019, **355**, 299–308.
172. T. Xu, F. Wu, Y. Gu, Y. Chen, J. Cai, W. Lu, H. Hu, Z. Zhu and W. Chen, *RSC Adv.*, 2015, **5**, 86505–86512.
173. N. H. Alias, J. Jaafar, S. Samitsu, N. Yusof, M. H. D. Othman, M. A. Rahman, A. F. Ismail, F. Aziz, W. N. W. Salleh and N. H. Othman, *Chemosphere*, 2018, **204**, 79–86.
174. X. Zhou, C. Shao, S. Yang, X. Li, X. Guo, X. Wang, X. Li and Y. Liu, *ACS Sustainable Chem. Eng.*, 2018, **6**, 2316–2323.
175. D. Qin, W. Lu, Z. Zhu, N. Li, T. Xu, G. Wang and W. Chen, *Ind. Eng. Chem. Res.*, 2017, **56**, 11151–11160.
176. S. Chen, W. Lu, J. Han, H. Zhong, T. Xu, G. Wang and W. Chen, *Chem. Eng. J.*, 2019, **359**, 119–129.
177. D. Qin, W. Lu, X. Wang, N. Li, X. Chen, Z. Zhu and W. Chen, *ACS Appl. Mater. Interfaces*, 2016, **8**, 25962–25970.

178. Y. Chen, W. Lu, X. Wang and W. Chen, *Appl. Surf. Sci.*, 2018, **453**, 110–119.
179. S. Wang, F. Li, X. Dai, C. Wang, X. Lv, G. I. N. Waterhouse, H. Fan and S. Ai, *J. Hazard. Mater.*, 2020, **384**, 121417.
180. S. Gawande and S. R. Thakare, *ChemCatChem*, 2012, **4**, 1759–1763.
181. J. Lei, F. Liu, L. Wang, Y. Liu and J. Zhang, *RSC Adv.*, 2017, **7**, 27377–27383.
182. Z. Yu, F. Li, Q. Yang, H. Shi, Q. Chen and M. Xu, *ACS Sustainable Chem. Eng.*, 2017, **5**, 7840–7850.
183. C. Zhang, Y. Li, D. Shuai, Y. Shen, W. Xiong and L. Wang, *Chemosphere*, 2019, **214**, 462–479.
184. R. Li, Y. Ren, P. Zhao, J. Wang, J. Liu and Y. Zhang, *J. Hazard. Mater.*, 2019, **365**, 606–614.
185. L. Ghalamchi, S. Aber, V. Vatanpour and M. Kian, *Chem. Eng. Res. Des.*, 2019, **147**, 443–457.
186. L. Ghalamchi, S. Aber, V. Vatanpour and M. Kian, *J. Ind. Eng. Chem.*, 2019, **70**, 412–426.
187. K. Cao, Z. Jiang, X. Zhang, Y. Zhang, J. Zhao, R. Xing, S. Yang, C. Gao and F. Pan, *J. Membr. Sci.*, 2015, **490**, 72–83.
188. H. Zhao, S. Chen, X. Quan, H. Yu and H. Zhao, *Appl. Catal., B*, 2016, **194**, 134–140.
189. A. Bozkurt and W. H. Meyer, *J. Polym. Sci., Part B: Polym. Phys.*, 2001, **39**, 1987–1994.
190. H. Pu, Q. Liu, L. Qiao and Z. Yang, *Polym. Eng. Sci.*, 2005, **45**, 1395–1400.
191. S. Lu, R. Xiu, X. Xu, D. Liang, H. Wang and Y. Xiang, *J. Membr. Sci.*, 2014, **464**, 1–7.
192. Y. Huang, L. Chuang, A. M. Kannan and C. Lin, *J. Power Sources*, 2009, **186**, 22–28.
193. N. G. Sahoo, Y. Pan, L. Li and S. H. Chan, *Adv. Mater.*, 2012, **24**, 4203–4210.
194. D. He, H. Tang, Z. Kou, M. Pan, X. Sun, J. Zhang and S. Mu, *Adv. Mater.*, 2017, **29**, .
195. P. Velayutham and A. K. Sahu, *J. Phys. Chem. C*, 2018, **122**, 21735–21744.
196. G. Zou, W. Wu, C. Cong, X. Meng, K. Zhao and Q. Zhou, *RSC Adv.*, 2016, **6**, 106237–106247.
197. H. Bai, H. Wang, J. Zhang, C. Wu, J. Zhang, Y. Xiang and S. Lu, *J. Membr. Sci.*, 2018, **558**, 26–33.
198. M. Gang, G. He, Z. Li, K. Cao, Z. Li, Y. Yin, H. Wu and Z. Jiang, *J. Membr. Sci.*, 2016, **507**, 1–11.
199. W. Dai, Y. Shen, Z. Li, L. Yu, J. Xi and X. Qiu, *J. Mater. Chem. A*, 2014, **2**, 12423–12432.
200. L. Cao, Q. Sun, Y. Gao, L. Liu and H. Shi, *Electrochim. Acta*, 2015, **158**, 24–34.
201. L. Semiz, N. Demirci Sankir and M. Sankir, *J. Membr. Sci.*, 2014, **468**, 209–215.
202. F. Wang, G. Wang, J. Zhang, B. Li, J. Zhang, J. Deng, J. Chen and R. Wang, *J. Electroanal. Chem.*, 2017, **797**, 107–112.
203. Z. Mai, H. Zhang, X. Li, S. Xiao and H. Zhang, *J. Power Sources*, 2011, **196**, 5737–5741.

204. R. Niu, L. Kong, L. Zheng, H. Wang and H. Shi, *J. Membr. Sci.*, 2017, **525**, 220–228.
205. C. Wu, S. Lu, J. Zhang and Y. Xiang, *Phys. Chem. Chem. Phys.*, 2018, **20**, 7694–7700.
206. J. Hu, J. Tian and C. Li, *ACS Appl. Mater. Interfaces*, 2017, **9**, 11615–11625.
207. P. Praveena, M. Sheril Ann, S. Dhanavel, D. Kalpana, T. Maiyalagan, V. Narayanan and A. Stephen, *J. Mater. Sci.: Mater. Electron.*, 2019, **30**, 8736–8750.
208. F. Li, Y. Dong, Q. Dai, T. T. Nguyen and M. Guo, *Vacuum*, 2019, **161**, 283–290.
209. J. Ma, X.-Y. Tao, S.-X. Zhou, X.-Z. Song, Y.-B. Zhu, L.-T. Guo, Z.-S. Liu, H.-L. Fan and X.-Y. Wei, *J. Electroanal. Chem.*, 2019, **835**, 346–353.
210. X. Chen, X. Zhu, Y. Xiao and X. Yang, *J. Electroanal. Chem.*, 2015, **743**, 99–104.
211. R. A. Senthil, J. Theerthagiri, J. Madhavan, K. Murugan, P. Arunachalam and A. K. Arof, *J. Solid State Chem.*, 2016, **242**, 199–206.
212. J. Xu, T. J. K. Brenner, L. Chabanne, D. Neher, M. Antonietti and M. Shalom, *J. Am. Chem. Soc.*, 2014, **136**, 13486–13489.
213. X. Chen, Q. Liu, Q. Wu, P. Du, J. Zhu, S. Dai and S. Yang, *Adv. Funct. Mater.*, 2016, **26**, 1719–1728.
214. L. Zhou, Y. Xu, W. Yu, X. Guo, S. Yu, J. Zhang and C. Li, *J. Mater. Chem. A*, 2016, **4**, 8000–8004.
215. G. Liu, T.-T. Li, X.-F. Song, J.-Y. Yang, J.-T. Qin, F.-F. Zhang, Z.-X. Wang, H.-G. Chen, M.-H. Wu and Y.-S. Li, *J. Thermoplast. Compos. Mater.*, 2020, 0892705720944214.
216. Y.-C. Chu, T.-J. Lin, Y.-R. Lin, W.-L. Chiu, B.-S. Nguyen and C. Hu, *Carbon*, 2020, **169**, 338–348.
217. B. Ye, C. Yao, M. Yan, H. Zhang, F. Xi, J. Liu, B. Li and X. Dong, *Macromol. Mater. Eng.*, 2018, 1800500.
218. Q. Hao, T. Chen, R. Wang, J. Feng, D. Chen and W. Yao, *J. Cleaner Prod.*, 2018, **197**, 1222–1230.
219. Q. Cao, J. Barrio, M. Antonietti, B. Kumru, M. Shalom and B. V. K. J. Schmidt, *ACS Appl. Polym. Mater.*, 2020, **2**, 3346–3354.
220. S. Lamkhao and C. Randorn, *J. Photopolym. Sci. Technol.*, 2017, **30**, 425–429.
221. Y. Liang, X. Wang, W. An, Y. Li, J. Hu and W. Cui, *Appl. Surf. Sci.*, 2019, **466**, 666–672.
222. M. Li, H. Liao, Q. Deng, Y. Wu, F. Xiao, X. Wei and D. Tu, *J. Macromol. Sci., Part A: Pure Appl.Chem.*, 2018, **55**, 408–413.
223. S. Chaubey, P. Singh, C. Singh, K. Sharma, R. K. Yadav, A. Kumar, K.-O. Baeg, D. K. Dwivedi and A. P. Singh, *Mater. Lett.*, 2020, **259**, 126752.
224. D. Gräfe, A. Wickberg, M. M. Zieger, M. Wegener, E. Blasco and C. Barner-Kowollik, *Nat. Commun.*, 2018, **9**, 2788.
225. S. C. Ligon, R. Liska, J. R. Stampfl, M. Gurr and R. Mülhaupt, *Chem. Rev.*, 2017, **117**, 10212–10290.

CHAPTER 6

Atomic and Molecular Functionalization of Graphitic Carbon Nitride for Solar Cell Applications

ALAA GHANEM*[a], MOHAMED A. MANDOR[b], RAGHDA EL-NAGAR[c] AND KAMEL EID*[d]

[a]PVT-lab, Production Department, Egyptian Petroleum Research Institute, Nasr City, 11727 Cairo, Egypt; [b]Chromatography Lab, Analysis & Evaluation Department, Egyptian Petroleum Research Institute, Nasr City, 11727 Cairo, Egypt; [c]Routine Lab, Analysis & Evaluation Department, Egyptian Petroleum Research Institute, Nasr City, 11727 Cairo, Egypt; [d]Gas Processing Center, College of Engineering, Qatar University, Doha 2713, Qatar
*E-mail: alaa_ghanem2001@yahoo.com, kamel.eid@qu.edu.qa

6.1 Introduction

The continued exaggerated consumption of non-renewable fossil fuels like oil, gas, and coal due to human civilization's growth will continue to grow in the future. Thereby, the global demand for renewable and green energy sources like water splitting, oxygen reaction, alcohol oxidation (*i.e.*, methanol, ethanol, and glycol), and glucose oxidation fuel

Nanoscience & Nanotechnology Series No. 51
Carbon Nitride Nanostructures for Sustainable Energy Production and Environmental Remediation
Edited by Kamel Abdelmoniem Mohamed Eid and Aboubakr M. Abdullah

Published by the Royal Society of Chemistry, www.rsc.org

cells alongside wind and solar sources has increased significantly in the last two decades and will keep rising.[1–13] Solar energy is a zero-emission, renewable, and low-cost source relative to fossil fuels and will be the main and largest electricity production source by 2050. Solar power converts sunlight to electricity either *via* photovoltaics using the photoelectric effect or indirectly by concentrated solar power with the assistance of mirrors or lenses.[14–17] Various materials such as quantum dots, transition metal oxides, carbon dots, polymers, and graphene have been developed for solar cells (SCs).[14,18–20]

Unlike these materials, graphitic carbon nitride (gCN) is a metal-free semiconductor with a band gap energy of 2.7 eV, various inherent physicochemical properties, stability (*i.e.*, chemical in various solvents, thermal, and mechanical), great accessible surface area, and rich electron density due to the presence of a C–N bond.[14,19,21–28] Also, gCNs, especially g-C_3N_4-based, have inbuilt surface characteristics (*i.e.*, basic surface sites, Lewis-base function, Brönsted basics, and H-bonding), which can enhance the photocurrent density and reduce the overpotential.[14,19,21–28] Additionally, gCNs can maximize the viable light absorption lower than 450 nm.[14,19,21–28] Meanwhile, gCNs could be prepared in a high yield from inexpensive and earth-abundant materials, could be easily mixed with various metals, metal oxides, metal sulfide or phosphide, and carbon materials to form heterojunction structures to maximize the utilization of visible light absorption and delay the electron–hole recombination.[14,19,21–30]

Despite great progress in the fabrication of gCN materials for SCs, their performance is still not sufficient to replace commercial metal-based semiconductors. This is attributed to the difficulties in the preparation of gCN thin films, poor visible light absorption > 460 nm, and prompt electron–hole recombination. Doping and functionalization are the main approaches for promoting enhancement of solar-driven energy production using gCNs. To this end, according to the Web of Science, 490 articles were published about gCNs for solar cell applications in the last decade compared to 21 651 articles for gCNs for various applications. Thereby, it is important to provide a periodic update on this field. There are various reviews for gCN for solar applications; however, most of the reported reviews were about photocatalytic properties without enough emphasis on SCs.[27,31–33]

This article emphasizes the atomic and molecular functionalization of gCNs for solar cell applications. This includes post-process (*i.e.*, nanosheets, coating, and self-assembly), direct growth methods (*i.e.*, solid/liquid mediated growth and CVD, TVC, and micro-contact printing assisted growth) for the tailored design of gCN films for solar cell applications. The utilization of gCN for solar cell applications, including dye-sensitized, organic, perovskite, and quantum dots, is also discussed along with the fundamentals and mechanisms. This is in addition to addressing the current challenges and future perspectives.

6.2 Synthesis Methods of g-C_3N_4 Film

There are two fundamental approaches for the synthesis of g-C_3N_4 films for solar applications.[27,34–37] The first one is the post-processing technique,[38–40] in which the g-C_3N_4 based photoanode is fabricated after multi-operations on the selected substrate. The second approach is the direct growth method,[35,41–43] in which the film is directly fabricated in one shot during the condensation of the g-C_3N_4 raw materials. The previous two approaches are also equivalent to the bottom-up and top-down strategies.[44,45]

6.2.1 Post-processing Techniques

These techniques include two main categories: the assembling method[46–49] and the coating method.[28,50,51] In the post-processing techniques, g-C_3N_4 is synthesized firstly as g-C_3N_4 nanosheets, then deposited on the appropriate substrate. The importance of g-C_3N_4 nanosheets is the simplicity of being converted into membranes.[52–54] Hence, it is of great importance to review how the g-C_3N_4 nanosheets are being synthesized.

6.2.1.1 Synthesis of g-C_3N_4 Nanosheets

Graphitic carbon nitride can be prepared as a powder material easily by heating the raw materials, which are rich in carbon and nitrogen in the solid-state condensation process.[55–58] According to the fact that the exfoliation of graphite into the monolayer is possible in easy ways, Ping *et al.* were the first team to obtain layered g-C_3N_4 in a simple and cost-effective method by the thermal oxidation of bulk g-C_3N_4 directly in the atmosphere. This technique is also based on the strong interactions between C–N in each layer due to the formation of the covalent bond and the feeble van der Waals interactions among the layers themselves in the bulk g-C_3N_4.[59,60] Later, a triazine based g-C_3N_4 was used to develop a 2D thin film with a narrow band gap between 1.6 eV and 2.0 eV.[61] The computational calculations using density functional theory (DFT) illustrated that the calculated band gap is proportional to the configuration of the g-C_3N_4.[62,63] There are many published techniques concerning the exfoliation of g-C_3N_4 nanosheets,[64–66] such as ionic liquid assisted technique,[67–69] in which the ionic liquid disrupts the attractive force of the stacked layers of the g-C_3N_4 to facilitate the formation of 2D nanosheets. This disruption may be due to the action of the π–π interaction and the hydrogen bonds in the ionic liquid.[67] Mechanical and chemical exfoliations are other techniques that are easily used to exfoliate graphite and graphene.[70–73] These two techniques allow the easy and efficient exfoliation of bulk g-C_3N_4 to well-defined isolated nanosheets in an easy manner without affecting the nanosheet size.[74] Recently, Jia *et al.* exfoliated g-C_3N_4 nanosheets on a large scale using the wet ball-milling technique. The produced film can be shifted easily to the multilateral substrate with good optical properties.[75] Another promising process that has been utilized

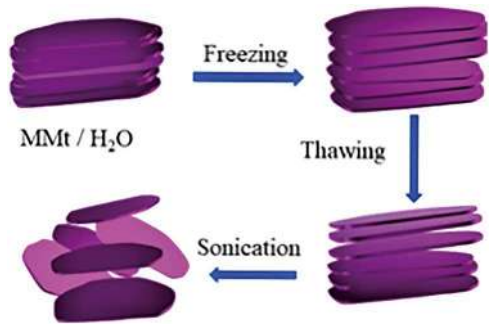

Figure 6.1 The mechanism of the freeze–thaw–sonication process for the exfoliation of g-C_3N_4 nanosheets.[76] Adapted from ref. 76 with permission from American Chemical Society, Copyright 2019.

before to peel the layered materials is the freeze-thaw-sonication process.[76,77] This method could be applied to exfoliate the g-C_3N_4 nanosheets with a high capability. The mechanism of this method could be summarized as: during the freezing process, the structure of water tends to be ordered and the volume rises slowly; while during the thawing process it tends to shrink. Multiple freezing and thawing in series will allow the substance to produce volume expansion and crack. According to this phenomenon, it is speculated to be a very successful process for exfoliation of g-C_3N_4 nanosheets[76] (Figure 6.1).

Graphitic carbon nitride has drawn attention as a potential photocatalyst because it shows fantastic optical, electronic, chemical, and thermal properties; moreover, it exhibits intrinsic UV-visible light absorption and profitable charge transfer. It has a reasonable band gap of 2.7 eV. The formation of the heterostructure of the g-C_3N_4 photocatalyst is one of the most effective methods to develop the band gap energy.[35,78,79] In addition, by using assembly methods or coating methods, g-C_3N_4 nanosheets can be fabricated on the desired substrate to form the photoanode or membrane. In contrast to other smaller semiconductors, the superior thermal–physical properties of g-C_3N_4 make it possible to produce new generations of SCs based on graphitic carbon nitride.[27]

6.2.1.2 Coating Methods

The photocatalytic performance of g-C_3N_4 could be improved by incorporating conductive carbon such as in multi-walled carbon nanotubes (MWCNTs).[80,81] The resulting paste material could be fabricated easily to the counter electrode in the DSCs by coating the paste onto fluorine-doped tin-oxide glass (FTO) employing the doctor-blade method. The morphology of g-C_3N_4 MWCNTs and g-C_3N_4/MWCNT composite was investigated. The SEM images revealed the nanosheets of the g-C_3N_4 (Figure 6.2b), while Figure 6.2c and d exhibited the microstructure of the g-C_3N_4/MWCNT composite with

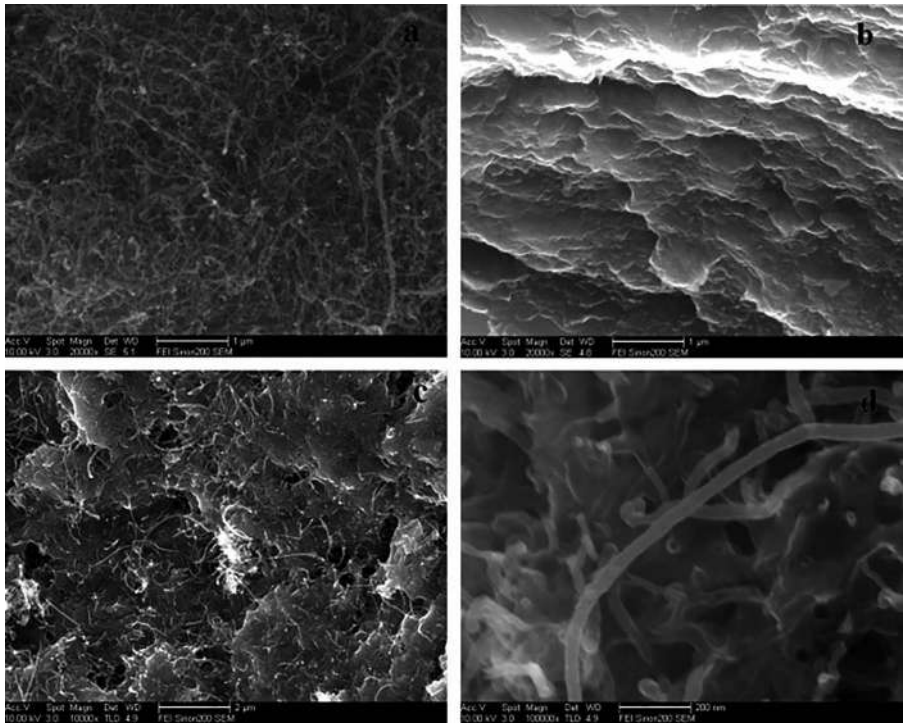

Figure 6.2 SEM images of (a) MWCNT, (b) pristine g-C_3N_4, and (c) and (d) g-C_3N_4/MWCNT composite. Reproduced from ref. 80 with permission from Elsevier, Copyright 2016.

Table 6.1 Parameters of photovoltaic counter electrodes in different DSCs. Reproduced from ref. 80 with permission from Elsevier, Copyright 2016.

Counter electrode	J_{sc} (mA cm^{-2})	V_{oc} (V)	FF	η[82]
g-C_3N_4	0.54 ± 0.01	8.8 ± 0.1	0.41 ± 0.01	1.95 ± 0.14
MWCNT	0.64 ± 0.01	12.6 ± 0.2	0.53 ± 0.01	4.27 ± 0.19
g-C_3N_4/MWCNT	0.72 ± 0.01	14.2 ± 0.2	0.62 ± 0.01	6.34 ± 0.21
Pt	0.71 ± 0.01	14.6 ± 0.2	0.66 ± 0.01	6.84 ± 0.21

a good incorporation of MWCNT in the g-C_3N_4 nanosheets, which was confirmed also using TEM.[80]

The authors fabricated four DSCs with different counter electrodes using a Pt, MWCNT, g-C_3N_4, and g-C_3N_4 based MWCNT composite to study and compare the photocatalytic efficiency of each counter electrode. Table 6.1 recapitulates the values of the photovoltaic parameters such as fill factor,[80] short-circuit current density (J_{sc}), open-circuit voltage (V_{oc}), and the conversion efficiency η %. The DSC shows that the values of V_{oc}, J_{sc}, FF, and η are equal to 0.72 V, 14.2 mA cm^{-2}, 0.62, and 6.34%, respectively, when the fabricated film of the g-C_3N_4 based MWCNT composite is utilized as the counter

electrode on FTO glass.[80] There are strong findings of increased photovoltaic efficiency in all photovoltaic parameters in relation to the g-C_3N_4/MWCNT counter electrode compared with each MWCNT and g-C_3N_4 electrode individually. This efficiency improvement is due to the excellent combination of the favorable characteristics of both g-C_3N_4 and MWCNTs.[80]

Coating slurry of g-C_3N_4 on the desired substrate to form an efficient homogenous photoelectrode is not a very simple process because of the attractive forces between the layers of g-C_3N_4.[83] This challenge could be overcome to a certain extent by reducing the particle size of the solid graphitic carbon nitride.[84] The doctor-blading technique was largely utilized in coating the g-C_3N_4 onto the ITO glass substrate by heating at 350 °C with a resulting film thickness equal to about 10 μm.[85] Zhang *et al.* were the first to investigate the electronic band gap of the g-C_3N_4 and the ability to generate photocurrent using a photoelectrochemical cell (PEC). Moreover, the authors reported the enhancement of the ionic conductivity, the light absorbance and tuned the electronic structure of the g-C_3N_4 after protonation using HCl and post-functionalization with Fe^{II}. In addition, this functionalization increased the surface area and tuned the band gap.[86]

The photocatalytic performance of the g-C_3N_4 was enhanced after the formation of a heterojunction with metal oxide.[87–90] ZnO–C_3N_4 hybrid material with two different ZnO concentrations (3% and 6%) was synthesized *via* an ultrasonic monolayer dispersion technique.[91] It was reported that g-C_3N_4 has the ability to extend the ZnO-based photoanode absorption spectrum into the visible light region and improve the emission of low energy photons. The image of the prepared ZnO nanoparticles under SEM has a prismatic shape, as shown in Figure 6.3a with a particle size around 20–50 nm. Figure 6.3b shows the TEM of pure ZnO with a very clear surface, while the surface of ZnO plated with 3% g-C_3N_4 is covered by several wrinkle-like patterns, as shown in Figure 6.3c. This is evidence suggesting the homogenous coating of the g-C_3N_4.[91]

Figure 6.4 displays the UV-visible spectra of the prepared photoanodes. The ZnO film intrinsic band edge absorption is clearly onset at 380 nm.

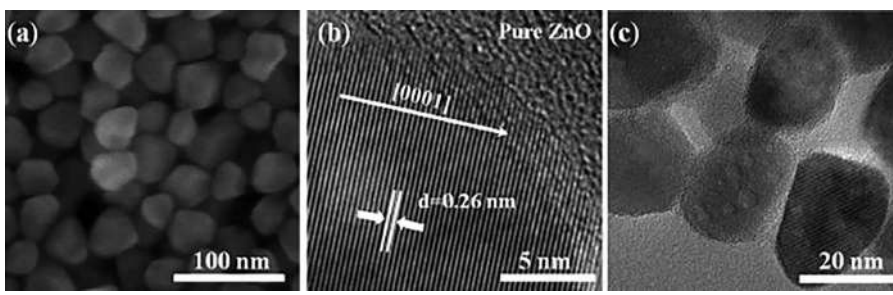

Figure 6.3 (a) SEM image of nanoparticles, (b) TEM image of ZnO nanoparticles, (c) TEM of ZnO coated with 3% g-C_3N_4. Reproduced from ref. 91 with permission from Elsevier, Copyright 2016.

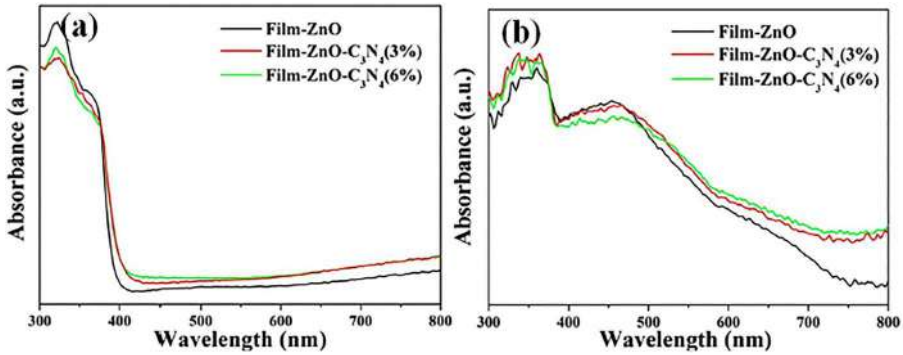

Figure 6.4 UV-visible absorbance spectra of the fabricated photoanode film (a) before, and (b) after the dye synthesis. Reproduced from ref. 91 with permission from Elsevier, Copyright 2016.

Table 6.2 The photo characteristics of the dye-sensitized solar cell based on ZnO and ZnO/g-C_3N_4 photoanodes. Adapted from ref. 91 with permission from Elsevier, Copyright 2016.

Photoanode	J_{sc} (mA cm^{-2})	V_{oc} (mV)	FF (%)	PCE (%)
ZnO	9.3	646	61.6	3.7
ZnO–C_3N_4	14.6	596	51.7	4.5

The incorporation of ZnO with g-C_3N_4 is the decisive reason for the reduction in the band gap energy, which showed a clear red-shift as well as a slight increase in absorption in the range of 400–800 nm.[92,93] Moreover, the charge transfer between g-C_3N_4 and ZnO/g-C_3N_4 was improved, and the photogenerated electrons and holes were effectively separated at the ZnO/g-C_3N_4 interface.[94,95] Using the doctor-blade technique, the prepared hybrid material and pure ZnO were deposited separately onto a fluorine-doped tin-oxide glass substrate for the application of a dye-sensitized cell (DSSC). The power conversion efficiency (PCE) of the ZnO/g-C_3N_4 photoanode was detected as 4.5% higher than the pure ZnO, as shown in Table 6.2, which demonstrates an increase in efficiency by 20% after using the hybrid material.[91]

6.2.1.3 Assembling Methods

The fabrication of g-C_3N_4 film using one of the assembling techniques becomes easier, especially after the progress in the exfoliation of bulk g-C_3N_4.[39,96] The vacuum filtration assembling method could be used to produce a large-area film after the fabrication of g-C_3N_4 nanosheets by the freeze–thaw–sonication process.[48,97] The size of the resultant ultra-thin g-C_3N_4 nanosheets was about 70–160 nm. Furthermore, the nanosheets were very stable under different conditions without any aggregation and could

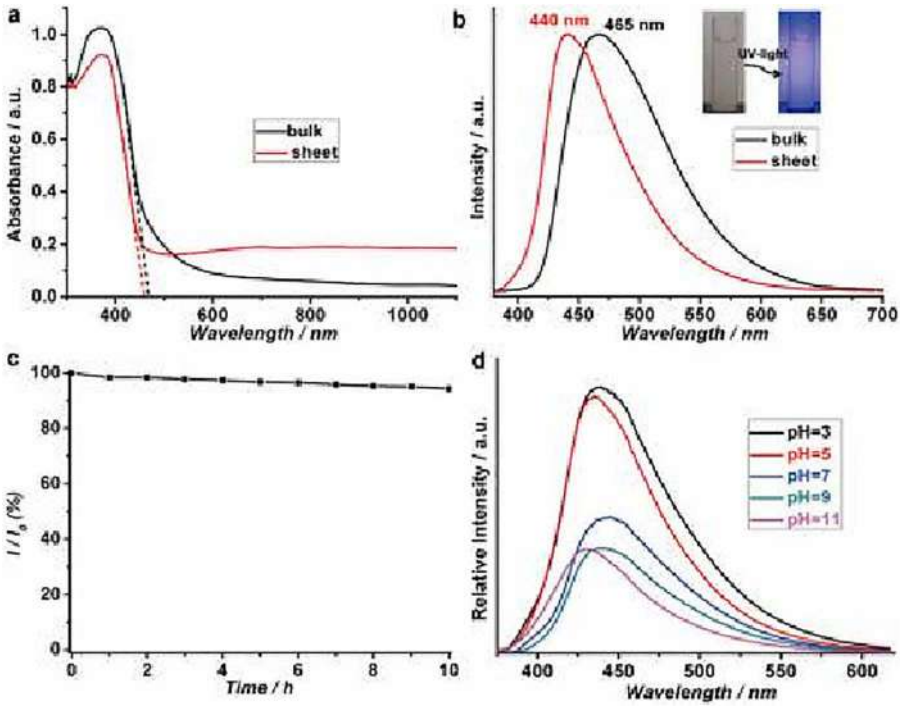

Figure 6.5 (a) UV-vis spectra of both bulk g-C_3N_4 and nanosheets, (b) PL spectra of both bulk g-C_3N_4 and nanosheets, (c) effect of time on PL intensity of g-C_3N_4 nanosheets, and (d) effect of pH on PL behavior of g-C_3N_4 nanosheets' solution. Reproduced from ref. 48 with permission from American Chemical Society, Copyright 2013.

be assembled easily into large films by the traditional filtration method.[48] The optical properties of the fabricated film were improved (Figure 6.5). The absorbance of UV-visible light by the prepared g-C_3N_4 nanosheets showed a small blue shift compared with the pristine g-C_3N_4. In addition, the band gap of the g-C_3N_4 nanosheets increased from 2.64 to 2.7 eV.[48] Consequently, the prepared ultra-thin g-C_3N_4 nanosheets showed higher photo activity than the pristine g-C_3N_4.

Later, Wu *et al.* were the first to prepare an effective thermally conductive material based on graphitic carbon nitride. The authors used the layer-by-layer assembly technique and vacuum filtration to fabricate a conductive membrane from nanofiber cellulose and g-C_3N_4 nanosheets on anodic aluminum oxide substrate (AAO).[98] g-C_3N_4 was prepared by the annealing of urea as a precursor at 550 °C then exfoliated to nanosheets by the sonication method. The nanofiber cellulose and the g-C_3N_4 nanosheets were rolled to form a cylindrical shape that acts as a phonon conductive pathway to enhance the thermal properties.[98,99] The XRD spectra for both the pristine g-C_3N_4 and the nanosheets exhibited a weak peak ascribed to the plane (100) in the bulk

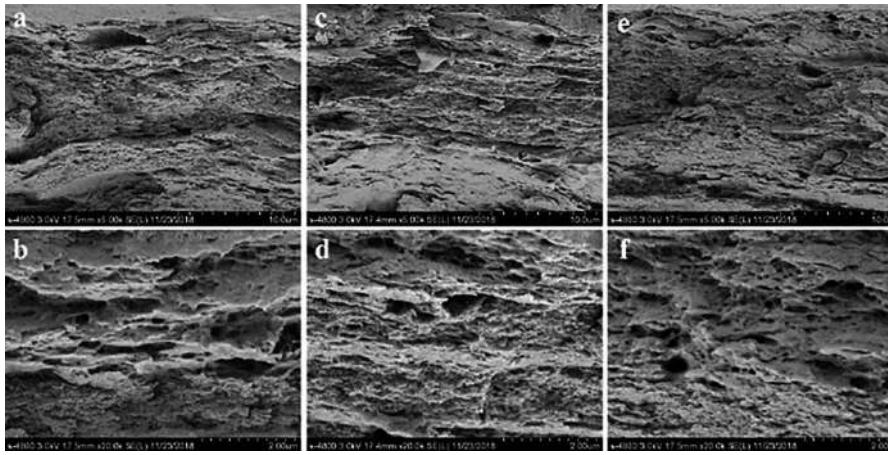

Figure 6.6 Cross-sectional SEM images of g-C_3N_4/NFCM (a) and (b) before measuring the thermal conductivity (c) and (d) after measuring the thermal conductivity, and (e) and (f) after measuring the thermal conductivity 10 times. Reproduced from ref. 98 with permission from John Wiley & Sons, Copyright 2018 WILEY-VCH Verlag GmbH & Co.

g-C_3N_4. This peak is diminished in the pattern of g-C_3N_4 nanosheets, which confirms the exfoliation of the bulk g-C_3N_4. Figure 6.6 shows that the morphology the g-C_3N_4 nano-film cellulose membrane (NFCM) almost did not change and demonstrated a stable structure even after measuring the thermal conductivity for 10 cycles, proposing stable thermal conduction power in the thermal conductivity process.[98]

A gas–liquid interface is another method that can be used to participate in the building of a thin film using 2D g-C_3N_4 nanosheets self-assembly.[100,101] The most important advantage of this method is to avoid nanosheets' aggregation.[101] In this method, pristine g-C_3N_4 was exfoliated to nanosheets using the wet ball-milling method.[75] The immersion of the substrate in the liquid could easily enable the fabrication of the g-C_3N_4 film *via* the assembly technique. Many substrate types may be assembled by this technique, such as titanium plates, FTO, and many other conductive substrates. Moreover, a hybrid graphene/g-C_3N_4 photoelectrode may easily be fabricated by the same technique.[75]

6.2.2 Direct Growth Methods

In these methods, the photoelectrode film or the delaminated membranes can be fabricated directly from the beginning of the thermal condensation of graphitic carbon nitride raw materials (triazine or tri-*s*-triazine).[102] The fabrication of the graphitic carbon nitride film is chiefly achieved by means of the CVD strategy, in which the precursors are exposed to three main processes

such as subliming or evaporation, thermal condensation, and film fabrication.[84,103,104] The direct growth of g-C_3N_4 on photoanodes requires variations of both the liquid phase and gas phase. Besides, the quality of the prepared film is affected by the two main factors; the amount of precursors and their interaction with the substrate.[37] The majority of the precursors in the solid phase at ambient temperature converted to the liquid phase at a higher temperature than the gas phase.[37,105]

6.2.2.1 *Solid/Liquid Mediated Growth*

These methods could be conducted by the immersion and heating of an appropriate substrate with nitrogen-rich precursors in the liquid phase. Then the solid g-C_3N_4 film can be formed after the condensation of the liquid phase on the substrate. The supramolecular assembly method of g-C_3N_4 could influence the fabrication of a photoanode using the solid/liquid mediated growth method because the precursors have the same chemical structures. From this standpoint, Shalom *et al.* used a cyanuric acid–melamine complex[21] as a salt to generate organized rods of g-C_3N_4 then deposited them on an appropriate glass substrate such as FTO, ZnO, or TiO_2 by annealing to fabricate a thin film of 40 nm in thickness on FTO.[106] Different morphologies could be obtained when different substrates are used because of the free –OH and –NH_2 groups. The presence of glass substrate contributed to the generation of orderly structures, and the absence of glass led to the formation of sheet-like structures.[21] Although this method was easy and very promising to fabricate photoanodes for photovoltaic or PEC cells, the light-harvesting capability was insufficient. Moreover, the enhanced mechanical properties of the synthesized films resulted from the robust adhesion force between the FTO substrate and g-C_3N_4 leading to challenges in exfoliation of the films to nanosheets using water sonication.[21,106] Xu *et al.* utilized the previous method with some modifications to synthesize continuous thicker thin films using the thermal condensation of the liquid mediated supramolecular precursor on many substrates like TiO_2 and FTO in crucibles (Figure 6.7).[107] TiO_2 thin film's size was about 500 nm, while it was 10 μm in the case of using FTO because both substrates are different in surface wettability.[107]

TEM imaging for a scratched powder from the photoelectrode was utilized to confirm the fabricated g-C_3N_4/TiO_2 film structure, while TEM, XRD, FTIR, and elemental analysis were used to confirm the composition and the structure of the photoelectrode itself.[107]

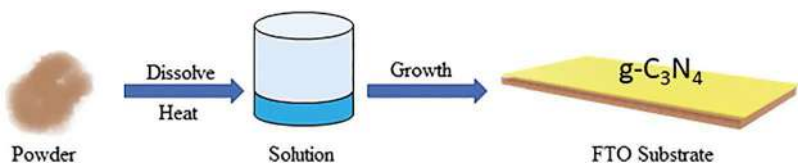

Figure 6.7 Synthesis of g-C_3N_4 on a FTO substrate using crucibles. Adapted from ref. 107 with permission from American Chemical Society, Copyright 2014.

A solar cell, consisting of g-C_3N_4/TiO_2 as the heterojunction, and photoanode deposited on ITO as the electron transfer layer, was fabricated. A solution of poly-(3-hexylthiophene), P3HT, was cast on g-C_3N_4 to act as the electron donor and hole acceptor. Xu reported that the use of 80 nm gold as the top electrode and the deposition of 10 nm molybdenum oxide on the P3HT layer would promote the hole extraction. The V_{oc} value was nearly 1 V of the g-C_3N_4/P3HT cell under sunlight. While in the case of using TiO_2/P3HT only as the photoelectrode, the highest V_{oc} value was 0.82 V.[106,107]

Photoanodes in SCs that are made of g-C_3N_4 demonstrate a higher photovoltaic value (V_{oc}) than metal-oxide polymer SCs. This may be due to the fact that g-C_3N_4 could influence and decrease some of the undesirable defects that may appear in the device, such as charge recombination, the formation of an interfacial dipole during the charge transport, or trapping in metal-oxide defect states.[19,28,107]

Peng *et al.* benefited from the supramolecular precursors and doctor-blade technique in synthesizing g-C_3N_4 films on a large scale. Solvation of a supramolecular precursor in a suitable solvent then calcination of the product on an appropriate substrate can easily produce g-C_3N_4 film with controlled chemical and optical properties.[108] The incorporation of transition metals such as nickel as an active site enhanced the photocurrent to around 69 μA cm^{-2} as reported by Zhang,[109] while the incorporation of non-metals such as sulfur using thiourea as a precursor yielded a photocurrent of only 30 μA cm^{-2}.[55] On another hand, the combination of sulfur-containing compounds with non-sulfur compounds could enhance the photocurrent to more than 100 μA cm^{-2} with very good mechanical properties. This is perhaps due to the fact that sulfur could favor the electrons' transportation in the solar cell system.[110]

Despite the relatively high efficiency of *in situ* thermal condensation *via* the use of a traditional furnace, it faces many challenges, the most important of which is the evaporation of precursors. Many other techniques were developed to curb the volatilization of the used precursors, such as pasting and confining. However, these techniques are still not satisfactory and are limited to only small precursors.[108,111–114] To mitigate this issue, Zhao *et al.* proposed very fast heating and growth to the precursors on FTO by utilizing a microwave instead of the traditional furnace that consumes many hours.[115] Consequently, the resulting photocurrent was increased to reach 110 μA cm^{-2} at photovoltaics equal to 1.2 V.[115] The cathodic ESL's efficiency in aqueous solution is duplicated by 7-fold of the benchmark $Ru(bpy)_3Cl_2$. This may be because fast heating using a microwave could decrease the precursor's evaporation and improve the transportation of charges.[115]

6.2.2.2 Gas-phase Noncontact Growth

The vapor deposition method (VDP)[116,117] was utilized to build up a strong adhesive (and free of crack) g-C_3N_4 thin film on a suitable substrate. In this technique, the precursors are subjected to sublimation before reaction on the appropriate substrate.[117,118] The precursor (guanidinium carbonate) was placed at the bottom of a test tube, while the proper substrate was reinforced

in the middle of it. The mixture was calcined at 550 °C until the color of the glass substrate became yellow. The produced film thickness was (0.1–1.8 μm) depending on the heating time and the reactant amount. Immersing the substrate in hot water could easily separate the film as one piece.[118] Later, the traditional VDP process was modified using powder precursors.[119] An ultra-thin layered and smooth g-C_3N_4 film (thickness is 10 nm) is obtained when powder precursors are placed at low temperature in the bottom of the test tube, while the glass substrate is placed at a higher one.[119] Another method based on the gas phase noncontact growth was developed based on a combination between the chemical vapor deposition (CVD)[103,120] and the micro-contact printing assisted method in generating g-C_3N_4 thin film.[113] In this technique, the pores of the anodic aluminum oxide (AAO) membrane substrate were used as traps for the precursors. The generated vapors due to the thermal condensation of the trapped precursors could be printed *in situ* on the two substrates. Thin film could be easily generated on many substrates like FTO or Gla (Figure 6.8).[113] The film's thickness and quality are related to the used precursor's volume.[118,121] The as-prepared thin film's photocurrent value was greater than the value belonging to pristine g-C_3N_4 (30.2 μA cm^{-2} at photovoltaic 1.23 V).[113]

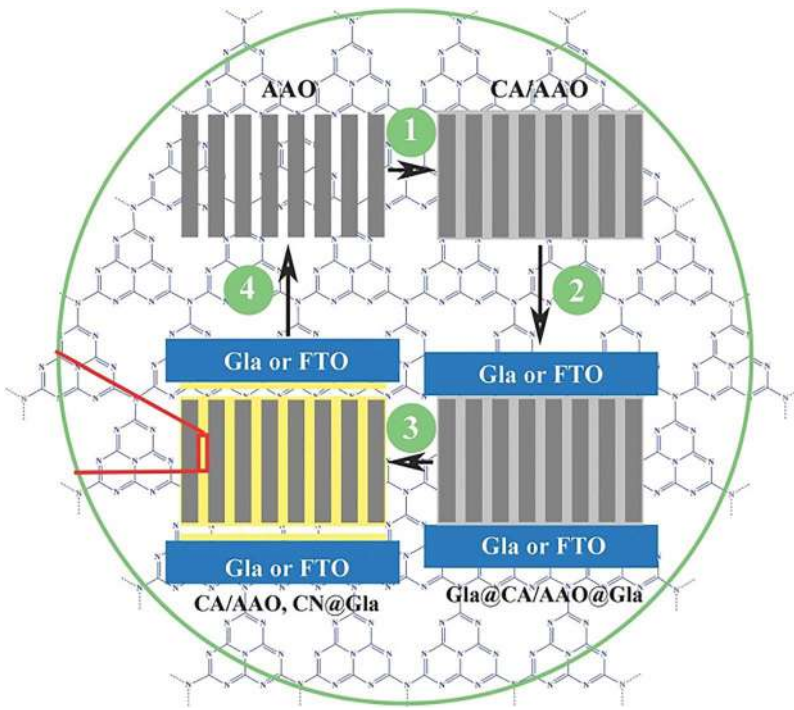

Figure 6.8 The process of printing g-C_3N_4 films on two altered substrates. Reproduced from ref. 113 with permission from John Wiley & Sons, Copyright 2014 WILEY-VCH Verlag GmbH & Co.

Transition metal doping is used to mend the electronic and optical characteristics of graphitic carbon nitride.[122–124] Cobalt doping with g-C_3N_4 can positively affect the morphology, diminish the band gap, and increase the illumination absorbed and, consequently, the prepared material's photocatalytic reactivity.[125,126] Actually, graphitic carbon nitride can quickly interact with transition metal cations because the cations interact strongly with the negatively charged nitrogen atoms.[127] Liu utilized the previous approach to the fabrication of ultra-thin molecular cobalt doped with g-C_3N_4 onto a FTO electrode (Figure 6.9).[128]

The optical properties and the photocatalytic activity of the fabricated electrode were redressed. The band gap belonging to the produced film was 2.81 eV, which is higher than the value of the pristine g-C_3N_4.[128] It was clear that the current density produced showed a prompt decline at every start of the cycle. A steady influx profile was then obtained, which may be due to the accumulation of the produced holes on the thin film's surface.[128] The photocurrent density decays after the recombination of the electrons and the assembled holes. The previous technique could be easily used in the synthesis of more functionalized g-C_3N_4 films.

The thermal vapor condensation (TVC) technique[27,129] was utilized to fabricate a smooth g-C_3N_4 film. In this method, the melamine precursors are placed inside a ceramic crucible covered with a suitable substrate.[129] The melamine vapors evolved after raising the temperature to more than 300 °C. Once the vapors' condensation temperature was reached, they condensed on the substrate forming a smooth film.[129] This method is easy to use and apply to get a g-C_3N_4 thin film using different solid substrates (Figures 6.10a, c and e).[129,130]

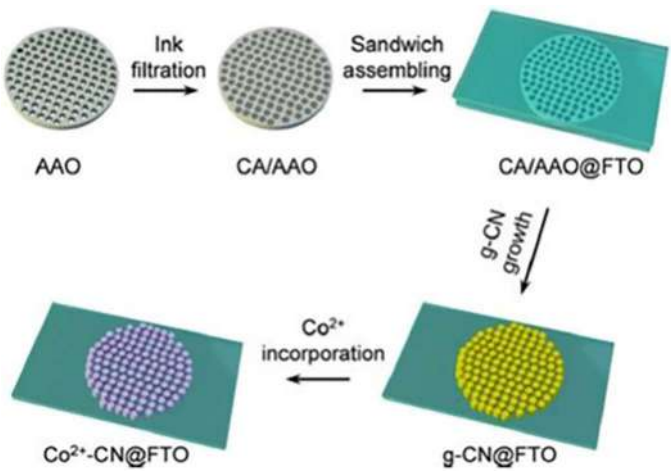

Figure 6.9 Explanation of incorporation of molecular cobalt into g-C_3N_4 films using the micro-printing method. Reproduced from ref. 128 with permission from John Wiley & Sons, Copyright 2018 WILEY-VCH Verlag GmbH & Co.

The thin film's morphologies on different substrates are quite different, (Figures 6.10b, d and f), while the film thickness is directly proportional to the amount of precursor.[129] The thin film was attached intimately with the substrate so that 2 h of sonication could not detach it from the substrate. This reduced the resistance for charge transfer and improved the photocurrent density to reach 0.12 mA cm^{-2} at 1.35 V_{RHE}. From the previous study, it is confirmed that metal and non-metal doping and a heterojunction of g-C_3N_4 with semiconductors have the ability to improve the performance, light absorbance, and decrease the band gap energy.[129,130]

By modifying the previous technique, Jia *et al.* wrapped the used crucible with aluminum foil to cover the substrate.[131] The resultant g-C_3N_4 thin film was deposited on both sides of the substrate and could be easily exfoliated in hot water. Cai *et al.* utilized another approach using the thermal vapor of melon to prepare freestanding g-C_3N_4 films. The film was deposited on the inner wall of a quartz furnace and exfoliated using hot water. The produced films showed excellent optical properties and mechanical flexibility; moreover, the absorption of natural sunlight was largely improved compared with pure g-C_3N_4.[132]

The TVC method is also utilized to produce g-C_3N_4 quantum dots (gCNQDs) with excellent photocatalytic properties and open-circuit voltages.[27,133] An *et al.* synthesized gCNQDs with the size of 5 ± 2 nm on TiO_2 nanowires using the TVC technique, and then the substrate was sonicated in water to peel off the gCNQDs.[134] The photocatalytic properties of the prepared photoanode was improved compared with the bare TiO_2 nanowires. The photocurrent was enhanced 2.5 times compared to the TiO_2 photoanode and reached 3.4 mA cm^{-2} at 0 V (Ag/AgCl). Besides this, the band gap energy was enhanced.[134] Another

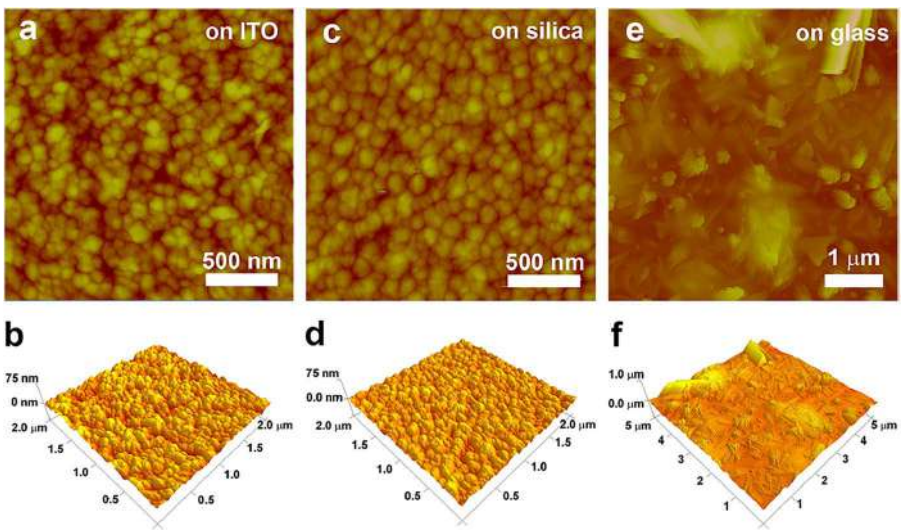

Figure 6.10 (a, c, e) AFM surface morphologies and (b, d, f) the 3D structures of g-C_3N_4 on (a, b) ITO, (c, d) silica, and (e, f) glass. Reproduced from ref. 129 with permission from Elsevier, Copyright 2015.

utilization of the TVC method was the build-up of a TiO_2 NT heterojunction with g-C_3N_4. The produced electrode exhibited a highly stable and enhanced photocurrent, which was increased 1.87 times, compared with the TiO_2 nanotubes themselves. The high photostability is evidence of the great contact between the substrate and prepared thin film with few defect sites on it.[129,135]

Li *et al.* used melamine as precursors to synthesize g-C_3N_4QDs and grafted it on the inner wall of TiO_2NT.[135] The heterojunction between g-C_3N_4QDs and TiO_2NT extremely enhanced the photocatalytic performance of the g-C_3N_4QD as it has the ability to improve electron transportation and inhibit the electron/hole recombination. In addition, the band gap energy was decreased, which allows the absorption of the largest possible amount of visible light.[135]

6.3 Solar Cells

Solar energy is of extensive interest nowadays, especially the conversion to electricity using SCs.[136–140] The basic technique of converting solar energy into electricity is *via* SCs.[141] A solar cell is an apparatus that transfers light into electricity in photovoltaic energy conversion frequently using silicon, semiconductor compounds, *etc.* This process is called the photovoltaic (PV) effect.[136] The aim these days is to discover a non-reducible and spotless energy source. The most useful and safe energy source is doubtless solar energy, which is so technically facile for use in several applications.[142] The cell materials absorb the photon energy that is converted to electrons in the atoms. Awareness of using solar energy started a long time ago *via* concentrating the sun's heat with mirrors to ignite a fire. The real studies on solar energy conversion began in 1839, when the French scientist Edmond Becquerel noticed the photovoltaic effect of an electrolytic cell.[143,144] He found that exposing the cell to light produced more electricity. Based on previous observations, an idea for solar-powered steam engines was proposed, and then the firstly used solar-powered engine for a diversity of purposes was constructed.[143] These engines became the prototypes of novel parabolic dish accumulators. Later, the first model of SCs was constructed using selenium wafers. The trials for superior solar cell fabrication continued until the first solar cell in its modern style was invented by Russel in 1946.[145] The first solar cell, which was able to exchange an adequate amount of the sun's energy into power to run daily electrical devices, was produced in Bell Telephone Laboratories. It was found that doping silicon with specific impurities gave it sensitivity to light absorption.[146]

6.4 Mechanism of PV Systems

PV solar cells are based on generating an electric current between two layers of n- and p-type semiconductors due to two opposing p–n semiconductor layers exposed to each other.[147] Electrons diffuse through the barrier to reach the p-type semiconductor forming static positive charges on the other side.[148,149] Simultaneously, in an opposite process, the holes diffuse across the barrier resulting in static negative charges behind it, giving a chance

for the free electrons in the system to recombine with the holes. At definite intensity, the depletion zone is created when there are no more probabilities of immigration of any charge carriers. Therefore, an electric field is generated through the system especially in the barrier zone *via* separated static charges (positive and negative), which provide the voltage required to flow the current through an outer circuit.[150] Once the sun emits photon energy, the semiconductor sheets absorb it through the electrons.[151,152] Then, the electrons depart from the holes in the outer cells (valence band) when they acquire enough required energy to be induced to the conduction band and come to be a part of the electric current. The produced voltage makes electrons and holes transfer to negative and positive ends, respectively (Figure 6.11).[141,151,153] A sufficient quantity of absorbed solar energy photons (more than the material band gap energy utilized in a PV cell) creates a current of electricity due to the collision of atoms and migration of free electrons.[141]

6.5 Classifications of Solar Cells

Crystalline silicon solar cells,[154] thin-film solar cells,[155] organic solar cells,[156] and tandem solar cells[157] are the main solar cell types.[158] Based on the categories of materials that are used in their fabrication, solar cells are commonly categorized into three generations.

6.5.1 Crystalline Silicon SCs

Crystalline silicon SCs are known as the first wafer-based or the first generation of SCs. According to their fabrication techniques, they can be divided into single-crystalline, polycrystalline, amorphous or thin-layer silicon solar

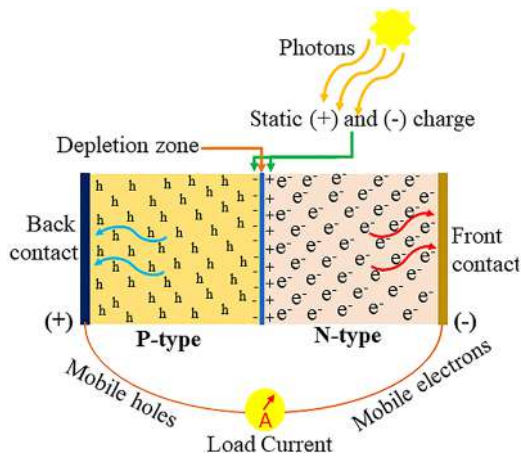

Figure 6.11 A simple design of a photovoltaic cell.[153] Adapted from ref. 153 with permission from Elsevier, Copyright 2018.

cell, and hybrid panel SCs.[154,159] Monocrystalline and polycrystalline silicon are highly popular SCs.

6.5.2 Monocrystalline Solar Cells

A monocrystalline SC is fabricated using a single crystal of silicon that is synthesized by the standard method of solar cell fabrication of high-quality silicon wafers called the Czochralski process.[160] In this process, a very high oven temperature of 1500 °C is used to fuse the precursors in a porcelain crucible, and then the silicon atom is doped by an impurity atom to be n-type or p-type.[160]

6.5.3 Polycrystalline

This method is cheaper than the monocrystalline method as it is made up of the recrystallized silicon, the cut saw of the very thin wafers. This method gives a solar cell with better performance and more space.[161]

6.5.4 Amorphous Silicon

Amorphous silicon is fabricated from a thin layer of a silicon atom. Its advantage is the ability to absorb light photons even lying down like a thin sheet, so it can be called a thin-film silicon solar cell.[162] For attaining high performance, it requires double the space facing the light. Generally, the disadvantage of wafer-based SCs is that they use materials with a highly expensive silicon cost.[162]

6.6 Thin-film Solar Cells

This kind of solar cell is known as the main emerging solar cell.[162] These cells were introduced to reduce using material with high film thickness of the crystalline silicon solar cell to a few nanometers to some micrometers.[162] This generation of SCs is prepared by the deposition of a heterojunction layer or more sandwiched between different substrates (Figure 6.12).[153] Many types of thin films are being utilized, such as copper–zinc–tin–sulfide/selenide

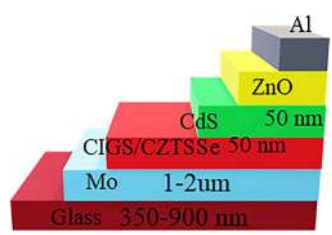

Figure 6.12 Simple structure of a thin film SC.[153] Adapted from ref. 153 with permission from Elsevier, Copyright 2018.

cell (CZTSSe), copper–indium–gallium–diselenide of chalcopyrite structure (CIGS), and CdTe thin films.[153,159] It was found that CZTSSe SC has a higher efficiency referring to the reduction in energy demise, and the ability to harvest more light photons from the sun due to the small thickness of the film (2.5 μm) compared with that in silicon SCs (170 to 250 μm).[163–165]

Thin-film SCs can be divided into four major categories:

I. Organic photovoltaics SCs (OPVs)[153,159]
II. Dye-sensitized SCs (DSSCs)[27,153,159]
III. Perovskite SCs and quantum dot photovoltaics (QDPVs)[27,153–156]
IV. Copper–zinc–tin–sulfide SCs (CZTSSCs).[27,153,]

These technologies are studied at high levels with improvement trials in material innovation and device manufacturing.[27,153,159]

6.6.1 Organic Solar Cells

6.6.1.1 Dye-sensitized SCs

DSSCs are considered beneficial commercially due to their band gap tunability, their solar light gathering ability over different ranges, molecule-to-molecule interactions, and flexible fabrication of modules from different materials.[27,153] DSSCs are an interesting and familiar alternative for conventional SCs for the reasons of high output, economically low cost, and simple fabrication.[153] Figure 6.13 displays a DSSC structure where the semiconductor's thin film is sandwiched between the photoanode and the electrolyte. Commonly, the photoanode in the solar cell is fabricated from TiO_2 nanoparticles,[27,75] while the sunlight absorption is initiated by ruthenium dye for electron generation and transportation

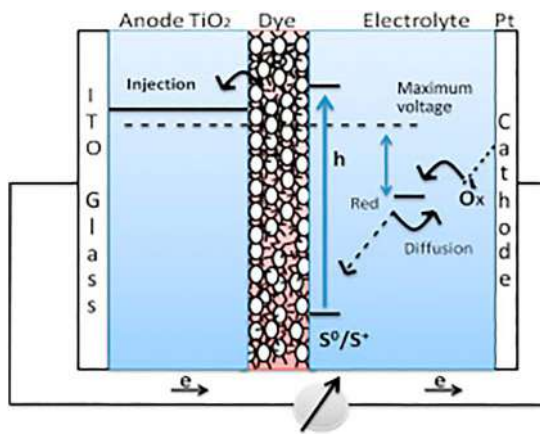

Figure 6.13 Illustrative image of DSSCs. Reproduced from ref. 153 with permission from Elsevier, Copyright 2018.

from the orbital lower level to this exciting level.[27,153,159] These electrons are inserted by the dye into TiO_2 while generating the outer circuit caused by the transmission of electrons generated from the TiO2 film into the ITO substrate.[153] After that, the emitted electrons come back obliging the used dye to regenerate to the "normal" state with the aid of the utilized electrolyte, which supports the transition of electrons through the cell. The cell's composition as two overlapped conducting glasses is identical to a "sandwich"; it has a platinum electrode that is the cathode electrode. At the same time, the electrolyte is composed of an iodide-triiodide redox mixture.[27,153,159]

6.6.1.2 Perovskite Solar Cells

Perovskites and quantum dot solar cells are announced as alternatives for DSSCs because of their chemical stability limitation as they are synthesized from organic dyes.[153–156] They can be divided into two main types: organic or inorganic halide perovskite solar cells. This kind of solar cell is promising, highly efficient as its power conversion efficiency PCE may achieve over 24%; moreover, it may be considered an economic nanostructured solar cell.[27,153] Figure 6.14 illustrates the composition of a perovskite solar cell that contains compacted TiO_2 or mesoporous TiO_2 as the photoanode on the ITO substrate.[153] The thickness of the compact TiO_2 film is about 40 nm on the transparent conducting oxide. Its mechanism for generating current is done by the illuminance absorption *via* the perovskite of the porous film, which promotes the hole/electron pairs' production.[27,75,153,159] The electrons are generated from the conduction band (CB), while the holes are formed from the valence band (VB). Fast recombination of the electrons/holes is one of the most disappointing issues.[75,156] In order to mitigate this challenge, platinum

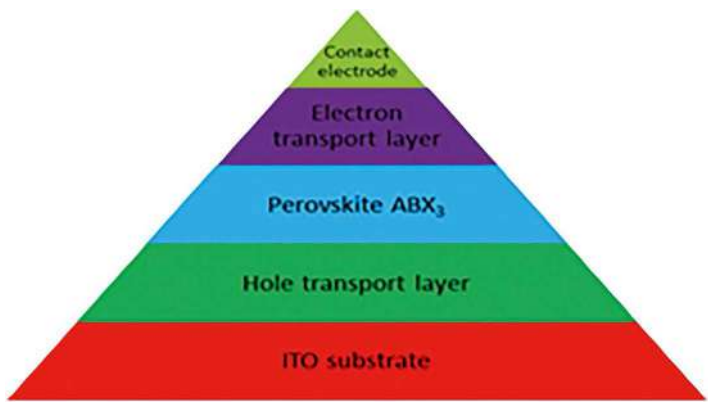

Figure 6.14 Different sheets of perovskite solar cells.[153] Adapted from ref. 153 with permission from Elsevier, Copyright 2018.

is incorporated to form a current in the cell device. This technique inserts more electrons into the TiO_2 film encouraging the formation of more positively charged holes.[153]

6.7 Graphitic Carbon Nitride (g-C_3N_4) in Solar Cells

Carbon nitride material is being acquired vastly because it reveals superior activity due to its effectual absorption of visible light.[21–28] Figure 6.15 demonstrates the composition and the structure of g-C_3N_4. In addition, it is also characterized by high levels of thermal and chemical stability, which is maybe owing to the strong covalent bonds that bind the nitrogen and the carbon atoms.[14,19] Moreover, g-C_3N_4 has a reasonable band gap (around 2.7 eV, 460 nm) that enables it to crop the visible light, besides convenient conduction and valence bands' edge location for the third generation of SCs. This is due to its attractive characteristics for semiconductor photocatalysts.[14,166–169]

Moreover, g-C_3N_4 can be fabricated from low-priced and obtainable precursors in a very easy method of synthesis for different applications of SCs.[27,75,153,159] In addition, g-C_3N_4 has a rare delocalized conjugated structure composed of stacked sheets connected with each other by tertiary amines, which enhances the electronic conductivity.[169] However, un-doped g-C_3N_4 has minor photo activity owing to its fast recombination of charge carriers, its low absorption coefficient, and low specific surface area. Therefore, many preparation methods have been operated to sweep away these weaknesses, such as doping with metal-oxide as TiO_2,[91,170,171] metal sulfate CuS,[172] and metal ion Ag.[173] In the upcoming sections, we will review some of these methods and develop g-C_3N_4 and its modifications in solar devices.

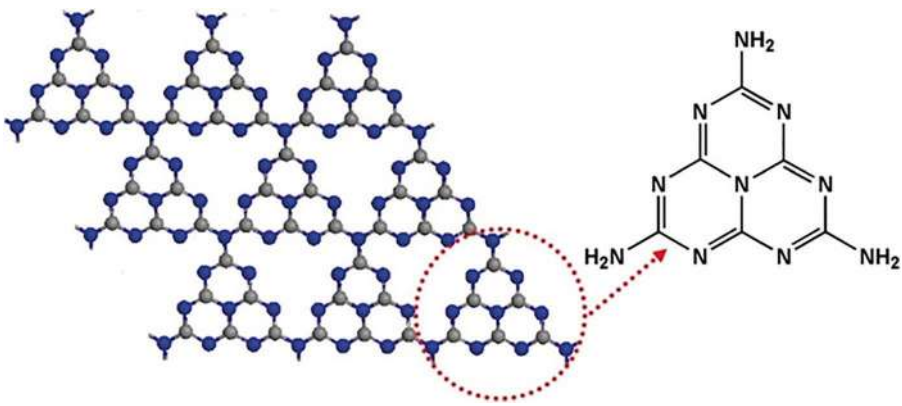

Figure 6.15 Tri-*s*-triazine-based two-dimensional structure of g-C_3N_4. Scheme: gray color for C, blue color for N. Reproduced from ref. 168 with permission from the Royal Society of Chemistry.

6.7.1 Application of g-C_3N_4 in Dye-Sensitized Solar Cells

Xu *et al.* used g-C_3N_4/TiO_2 nanosheets (CTS) to fabricate dye-sensitized solar cells (DSSCs).[174] They prepared heterostructure TiO_2/g-C_3N_4 nanosheets by the coating of g-C_3N_4 over the surface of TiO_2 nanosheets. This includes initial preparation of TiO_2 by the hydrothermal method to obtain TiO_2 nanosheets in the anatase phase with {001} facets, followed by a modification by g-C_3N_4 with various concentrations of urea as the g-C_3N_4 source to obtain CTS-4, CTS-6, CTS-8, CTS-10, and CTS-15.[174] The TEM images in Figure 6.16 display rectangular nanosheets' successful formation with a size of about 20–40 nm. In addition, it shows that the lattice spacing is 0.35 nm, that reveals the presence of the anatase phase with {001} planes.[174] In addition, HRTEM analysis shows that there is an amorphous layer with 2 nm thickness of polymeric g-C_3N_4 in all prepared samples covering TiO_2 nanosheets' surfaces.[174] The XRD technique analysis confirmed the TEM results in Figure 6.16 with no peaks observed for g-C_3N_4, but its existence is confirmed by FTIR spectra by its distinguishable peaks.[174]

The authors found an improvement in the DSSCs' photoelectric conversion efficiency PCE after modification *via* g-C_3N_4 (close to 28% at loading quantity of 5.5% g-C_3N_4 in the case of CTS-8),[174] in addition to the enhancement of the optical properties, the photocurrent density, and the photovoltage characteristics. The measurements of the photocurrent–voltage *I–V* characteristics using impedance spectroscopy[53] are shown in Figure 6.17.[174] This improvement is owing to the synthesis of g-C_3N_4 on the surface of TiO_2 nanosheets

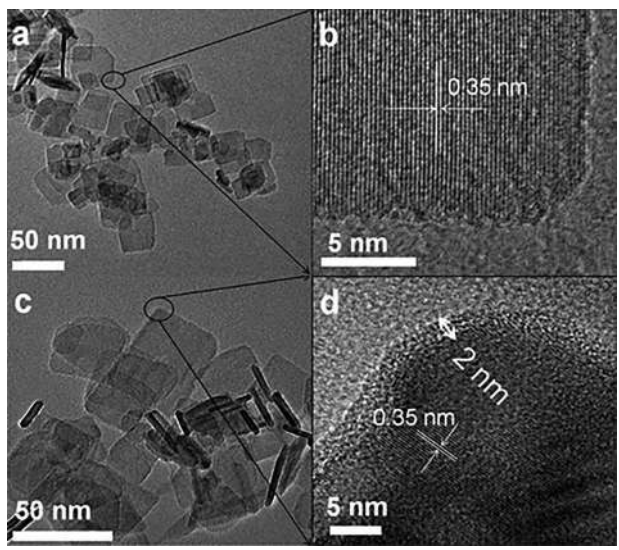

Figure 6.16 TEM images of (a) and (b) CTS-0 and (c) and (d) CTS-8 composites. Reproduced from ref. 174 with permission from Elsevier, Copyright 2014.

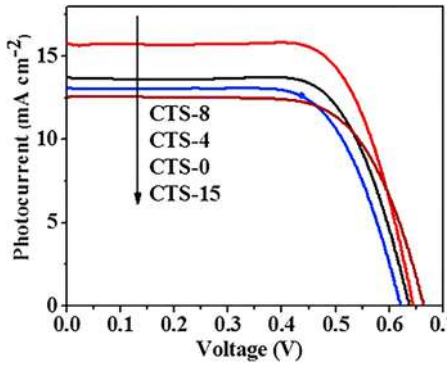

Figure 6.17 The photocurrent–voltage measurements of the different fabricated DSSCs. Reproduced from ref. 174 with permission from Elsevier, Copyright 2014.

Figure 6.18 Fabrication mechanism of a g-C_3N_4/ZnO photoanode in DSSCs. Reproduced from ref. 91 with permission from Elsevier, Copyright 2015.

as a thin layer, which holds up the recombination of the retrograde electrons and the holes between TiO_2 and the electrolyte.[27,75] This increases the electron's concentration in the media of the photoanode.[174]

Other metal-oxide nanoparticles like ZnO were coated with a multifunctional protecting layer of g-C_3N_4 nanosheets using ultrasonic irradiation-assisted methods for application as a photoanode in DSSC (Figure 6.18).[91] The incorporation of g-C_3N_4 enhanced the photoactivity of the ZnO photoanode in DSSC.[27,91] The absorption range of the fabricated photoanode was extended to include the visible region. Moreover, it improves the gathering of a wide range of energy photons according to the optical and electrochemical

analysis measurements.[27,91,174] Furthermore, a stepwise energy gradient was built up by the g-C_3N_4 with a compatible band gap at the interface of C_3N_4-ZnO/dye. This developed the added efficacy of the produced electrons by nearly 57% and improved the short circuit photocurrent (3%).[91] Moreover, a high PCE of 4.5% was proved, representing nearly a 20% improvement compared with a fabricated pure ZnO photoanode.[91]

Jing *et al.* reported a facile one-step mechanism for the counter electrode (CE) catalyst preparation for DSCs using a sacrificial template of ZIF-67.[104] DSCs are composed in general of an electrolyte, dye-sensitized photoanode, and a CE; the latter is essential for the DSCs' photovoltaic performance.[104] They synthesized porous CoO, Co, and N-doped graphitic carbon nanocomposites by controlling the temperature of carbonization for templates under N_2 atmosphere. They used thermo-gravimetric analysis to choose the calcination temperatures 550, 650, 750, 850, 950 °C to obtain ZIF-67-850, ZIF-67-550, ZIF-67-750, ZIF-67-650, and ZIF-67-950, respectively.[104] Besides, the effect of CoO and Co on ZIF-67-850 *via* its catalytic properties was studied. They found that the prepared DSCs using a ZIF-67-850 electrode obtained a high efficiency of photoelectric conversion PCE of about 7.92%, close to (8.18%) of a Pt CE in the solution I_3^-/I^- redox couple electrolyte. The porous nanostructures of Co/CoO besides Co@N-doped graphitic carbon with excellent stability were verified to be brilliant CE materials for DSCs and a favorable material to use instead of Pt-based materials in different applications like SCs.[27,104]

In the same year, Yan *et al.* fabricated a photoanode-based modified TiO_2 with g-C_3N_4/Ag to fabricate a heterojunction of a g-C_3N_4–Ag–TiO_2 photoanode.[173] The modification of a TiO_2 photoanode enhanced the power conversion efficiency (PCE) of spiro/OMeTAD as hole transport material in the DSSCs.[173] The surface plasmon resonance improved the optical properties and raised the visible light absorption by deposition of silver nanoparticles at the interface between g-C_3N_4 and TiO_2. The photoelectrons are transferred from g-C_3N_4 to Ag–TiO_2 by the stimulation of the interface between the two materials.[171,173] This leads to control of the electron/hole recombination (e^-:h^+). The PCE of the ss-DSSCs was enhanced close to more than about 65% at nearly 2 wt% and 5 wt% of Ag and g-C_3N_4, respectively. It was reported that the solar cell performance was attributed to the role of both g-C_3N_4 and Ag on the TiO_2 surface, which could not only promote extra electrons that enlarge the electron concentration in the photoanodes but also control the retrograde TiO_2 electrons' recombination and the transporting layer of the hole.[173]

A composite of graphitic carbon nitride/multi-walled carbon nanotubes was utilized as a Pt-free counter electrode for high-efficiency DSSCs.[80] The authors used a combination of refluxing process and heating polymerization as preparation methods.[80] The charge-transfer resistance of the g-C_3N_4/MWCNT composite electrode proved by the electrochemical impedance spectroscopy is 2.1 Ω cm^2, which is much lower than composites of the individual g-C_3N_4 and MWCNT electrodes.[75,80] They found that the dye-sensitized

solar cell based on the g-C_3N_4/MWCNT counter electrode achieves a conversion efficiency of 6.34% under the illumination of 100 mW cm^{-2}, which is equivalent to the illumination of cells based on the Pt counter electrode.[80]

Yuan *et al.* prepared TiO_2/g-C_3N_4 heterojunction photoanode materials and Co_9S_8 nanotube arrays (ANTAs) as counter electrodes (CEs) of DSSCs.[175] The Co_9S_8 hollow nano-needle array films, operated as CEs, have large surface areas and strong binding forces with the FTO substrates.[175] The results of Tafel polarization curves and cyclic voltammetry CV of Co_9S_8 ANTAs CE show higher electrocatalytic ability towards the I^-/I^{-3} reaction than Pt CE. Co_9S_8 ANTAs CE attains 6.19% power conversion efficiency of DSSCs, almost similar to Pt (6.79%).[175] Based on electrochemical impedance spectra[53] measurements, they confirmed that by introducing g-C_3N_4, it acts as a blocking layer in the photoanode as it reduces the retrograde electron recombination with electrolyte and thus improves the DSSCs' performance. Finally, they found that DSSCs contain an optimized TiO_2/g-C_3N_4 photoanode, and Co_9S_8 ANTAs CE attains the highest energy conversion efficiency of 8.07% (one sun illumination), nearly 1.3 times more than the bare TiO_2 nanosheets (6.19%).[175]

Wu *et al.*, on the other hand, prepared the carbon nitride itself as a transparent counter electrode for DSSC radio frequency magnetron sputtering.[176] The authors used fluorine-doped tin-oxide (FTO) glass as a substrate for carbon nitride (CNx) films with x = 0.15–0.25 and film thicknesses of 90–100 nm.[176] A heat treatment at 500 °C was conducted to obtain CNx-500 as a counter electrode in DSSC, which attains 4.45% energy conversion efficiency, much higher than the DSSC with CNx-RT without heat treatment.[176] Based on XPS analysis, they assumed that more sp^3 C–N bonds and sp^2 carbon are formed and C=N bonds reduced due to the rearrangement of C–N and C–C bonding of the obtained CNx by the heat treatment process, which is helpful for improving the electrochemical performance as a counter electrode in DSSCs. Besides, the magnetron sputtered CN_x electrodes permit incomplete transmittance of light.[176]

Zhang *et al.* enhanced the PCE of DSSCs using S-doped g-C_3N_4/TiO_2 nanoparticle composites.[177] They used these composites as promising photoanode materials for DSSCs and improved the efficiency of DSSCs in converting light into electricity 4.87%, 10.41 mA cm^{-2} for short-circuit photocurrent, and 0.65 V for open-circuit voltage, comparing with DSSCs based on undoped g-C_3N_4/TiO_2.[27,75,177] They assumed that this significant improvement in DSSC performance is owing to the inhibition of the electron–hole (e^-:h^+) pairs' recombination,[173] which consequently results in an enhancement in open-circuit photovoltage and the photocurrent density under short circuit. Furthermore, the noticeable reduction electron transfer resistance verified by electrochemical impedance spectroscopy analysis increases the PCE.[27,177]

Vijayanath *et al.* synthesized sensibly designed g-C_3N_4 modified by ZnO nanoparticles hybrid composites as photoanodes in high performance DSSCs by a one-step facile microwave irradiation route.[171] Spherical-shaped nanoparticles in the range of 15–25 nm size with a hexagonal crystalline structure with homogenous exfoliation of bare ZnO on the g-C_3N_4 sheets

were obtained.[171] The UV and PL analyses results showed an improvement in the light absorption properties towards the visible light region and reduced recombination of the electron–hole pairs.[171] The authors used the *J–V* characteristic to study various rational photoanodes on a sandwiched solar cell device.[171,178] They realized that the addition of g-C_3N_4 provides useful electrical connection among the bare ZnO and FTO substrates.[27,171] They found that the adjusted (15% ZnO/g-C_3N_4) ZG3 composite exhibited a higher PCE of 9.21%, comparable with bare ZnO (2.19%), along with long-lasting stability, than other electrodes. They ordered the devices according to the PV performance as g-C_3N_4 < ZnO < ZG1 < ZG2 < ZG3.[171] Furthermore, they suggested that the hybrid sensor could be widely used in commercial photovoltaic devices according to its suitable band structure, eco-friendly properties, low cost, and photostability.[171]

6.7.2 Application of g-C_3N_4 in Perovskite and QD Solar Cells

Few studies report the application of g-C_3N_4 in polymer solar cells.[18,27,75] Chen *et al.* enhanced the efficiency of bulk-heterojunction polymer solar cells (BHJ-PSCs) for the first time by incorporating graphitic carbon nitride (g-C_3N_4) quantum dots (QDs) in the active layer.[18] The acid treatment of bulk g-C_3N_4 and subsequently a solvothermal treatment was used to prepare solution-processable C_3N_4 QDs.[27,75] By doping C_3N_4 QDs in poly(3-hexylthiophene-2,5-diyl):[6,6]-phenyl-C61-butyric acid methyl ester (P3HT:PC 61 BM), poly(4,8-bis-alkyloxybenzo(l,2-*b*:4,5-*b*′) dithiophene-2,6-diylalt-(alkyl thieno (3,4-*b*) thiophene-2-carboxylate)-2,6-diyl):[6,6]-phenyl C71-butyric acid methyl ester (PBDTTT-C:PC71 BM), and poly[4,8-bis(5-(2-ethylhexyl)thiophen-2-yl)benzo[1,2-*b*:4,5-*b*′] dithiophene-*co*-3-fluorothieno [3,4-*b*] thiophene-2-carboxylate] (PTB7-Th):PC 71 BM active layer with a 0.2 mg mL^{-1} doping ratio, PCEs of the corresponding inverted BHJ–PSC devices reach 4.23%, 6.36%, and 9.18%, which are enhanced by ≈17.5%, 11.6%, and 11.8%, respectively, compared to the undoped devices.[18] The PCE improvement of the C_3N_4 QDs-doped BHJ–PSC device is found to be primarily attributed to the increase of short-circuit current (J_{sc}) as confirmed by external quantum efficiency (EQE) measurements.[18,27] Based on the C_3N_4 QDs' effects on the morphology of the surface, optical absorption and photoluminescence properties of the active layer film in addition to the charge transport properties of the device, the mechanism of the efficiency enhancement is suggested with the conjunct properties of the following:[178]

(i) the increase of the roughness of the active layer film that enhances the interfacial contact sandwiched between the active and the hole transport layers;[75] (ii) the simplified transfer of the photo-induced electron from donor to acceptor from conducting polymer to fullerene;(iii) the active layer conductivity improvement; (iv) the improved hole and electron charge transport.[18] They not only provide new insight into the common use of g-C_3N_4 as a photocatalyst but also bring a new way for incorporating semiconducting photocatalysts into BHJ–PSCs toward performance enhancement.[18,178]

Men *et al.* synthesized carbon nitride doped mesoporous TiO_2 as photoelectrodes in photocatalysis and QD–DSSCs. They compared g-C_3N_4 modified TiO_2 with TiO_2 mesoporous photoelectrodes and observed that g-C_3N_4 modified TiO_2 photoelectrodes displayed a noticeable enhancement in QDSSC device performance and photocatalytic activities.[170] They found that the performance is improved due to the suitable band structure of g-C_3N_4 that forms a type-II alignment between g-C_3N_4 and TiO_2 that induces effective separation of the photogenerated carriers. They used CdS QDs as a sensitizer and optimized an extra amount of g-C_3N_4 in the electrodes, which attained a PCE of 2.91%, and displayed enhancement of 29.3% compared with 2.25% for pure TiO_2 electrodes.[170]

Jiang *et al.* developed a convenient strategy to improve the crystallization of perovskite by combining a 2D polymeric material of g-C_3N_4 added to the perovskite layer.[27,179] By adding the 2D g-C_3N_4 polymeric material, the perovskite film crystallinity is improved, and the crystallization rate is delayed resulting in a large grain size of the crystal, and the charge recombination centers around the grain boundaries are passivated to reduce the intrinsic defect density.[179] Moreover, doping of g-C_3N_4 increases the film conductivity and charge transport in the light-absorption layer of perovskite, resulting in a maximum power conversion efficiency of 19.49%, a notable improvement from 0.65 to 0.74 in fill factor.[75,179] Wei *et al.* fabricated ultra-fine exfoliated g-C_3N_4 nanoparticles (*E*-g-C_3N_4) for improving the perovskite solar cells.[180] *E*-g-C_3N_4, which is synthesized by H_2SO_4 intercalation and NH_3 stripping, has a lot of N–H or O–H groups that could coil into the unforced nanoparticles of nanosheets by hydrogen bonds.[27] They assumed that *E*-g-C_3N_4 sandwiched between $MAPbI_3$ and HTMs in PSCs self-recognized and located on $CH_3NH_3PbI_3$ grain boundaries. They found that electron–hole (e^-:h^+) recombination is significantly reduced after combining *E*-g-C_3N_4 by decreasing the grain boundaries of electron trap centers.[173] So, the PCE of 15.8% is realized for the $MAPbI_3$ based PSCs, which is 35% higher than the reference cell.[180]

The perovskite solar module of large-scale is weakened from more significant durability problems than devices with small areas because of the mechanism of the highly complex degradation initiated by iodide diffusion.[27,153,159] So, control of the iodide diffusion process is highly desired in very efficient perovskite devices for earning long-standing stability. Therefore, Bi *et al.* increased the operational stability by approaching a low-temperature process for producing high-efficiency perovskite solar modules through the installation of barriers with a low-dimensional diffusion and the reduction of undesirable interfacial diffusion ions 10^3–10^7 times.[181] They firstly prepared ultra-thin g-C_3N_4 nanosheets from bulk-nanosheets.[27,153,159,181] Then a cationic photopolymerization process was utilized to improve the mechanical properties. This was conducted by functionalizing the diffusion barrier layer (DBL) with a trace amount of some epoxy resins.[181] Then, the coated substrate was photocured at ambient temperature by UV light.[179,181] Three different types of perovskite solar cells were fabricated using 0D-DBL, 1D-DBL, and 2D-DBL.[181] The 0D-DBL is utilized for the high thermal and chemically stable Al_2O_3 nanoparticles (Figure 6.19B), 1D-DBL is utilized for the chemically stable polydimethylsiloxane PDMS, which can readily fabricate a flat

layer (Figure 6.19C), and 2D-DBL is for tri-*s*-triazine-based g-C_3N_4 nanosheets (Figure 6.19D).[181]

The measurements of intensity *versus* sputter time revealed that the quantity of interfacial I_2 in addition to Ag diffusion of 2D-DBL (Figure 6.19G) is negligible compared with the Ag/1D-DBL/perovskite sheet (Figure 6.19F) that is reduced, while 0D-DBL (Figure 6.19E) does not have any effect on the diffusion process.[181] The SEM-EDX analysis shows the good diffusion of the iodide (I_2) across the whole 0D-DBL film (Figure 6.20a) and two-thirds of the 1D-DBL film (Figure 6.20b), and inferior diffusion in 2D-DBL (Figure 6.20c). The EDX scan line profile shows the distribution of I_2 from the perovskite to 0D-DBL and the 1 D-DBL film reveals a graded distribution in the perovskite/DBL film (Figure 6.20d–f).

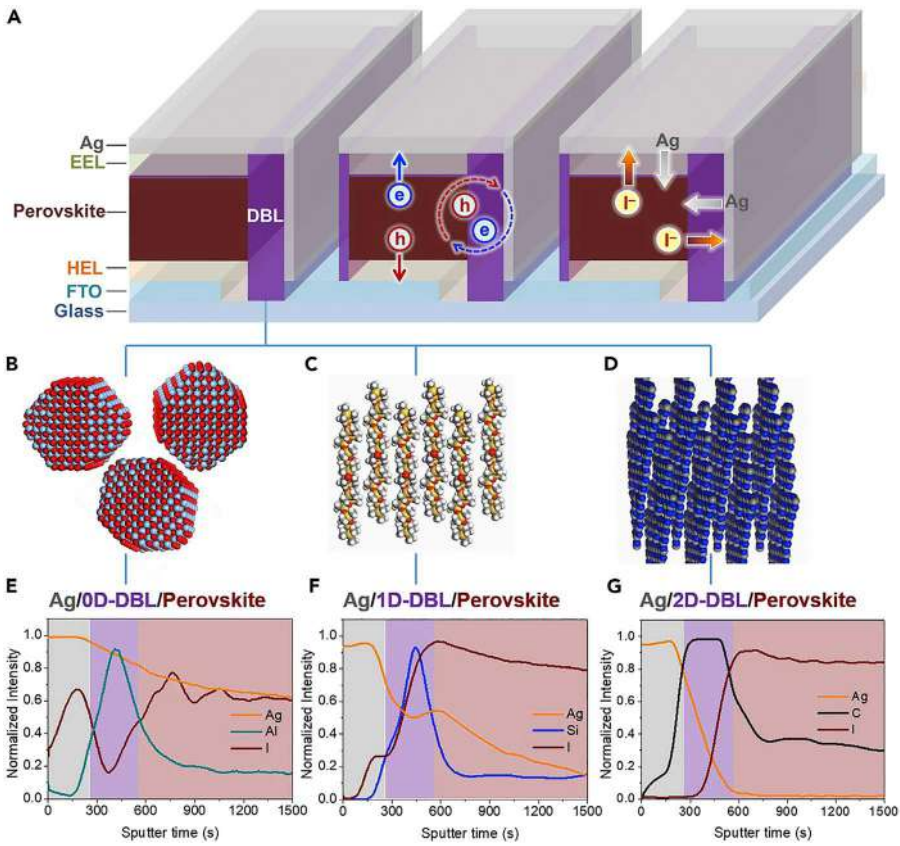

Figure 6.19 The proposed diffusion barriers within perovskite solar cell modules (Psc Modules) including (A) the diffusion process and interfacial charge transfer and recombination. EEL is the electron extraction layer and HEL is the hole extraction layer. (B) Al_2O_3 nanoparticles for 0D-DBL, and (C) PDMS for 1D-DBL. (D–G) g-C_3N_4 for 2D-DBL for (D) depth profile of diffused iodide and Ag in (E) Ag/0D-DBL/perovskite film with Al-signal, (F) Ag/1D-DBL/perovskite film with Si-signal, and (G) Ag/2D-DBL/perovskite film with C-signal. Reproduced from ref. 181 with permission from Elsevier, Copyright 2019.

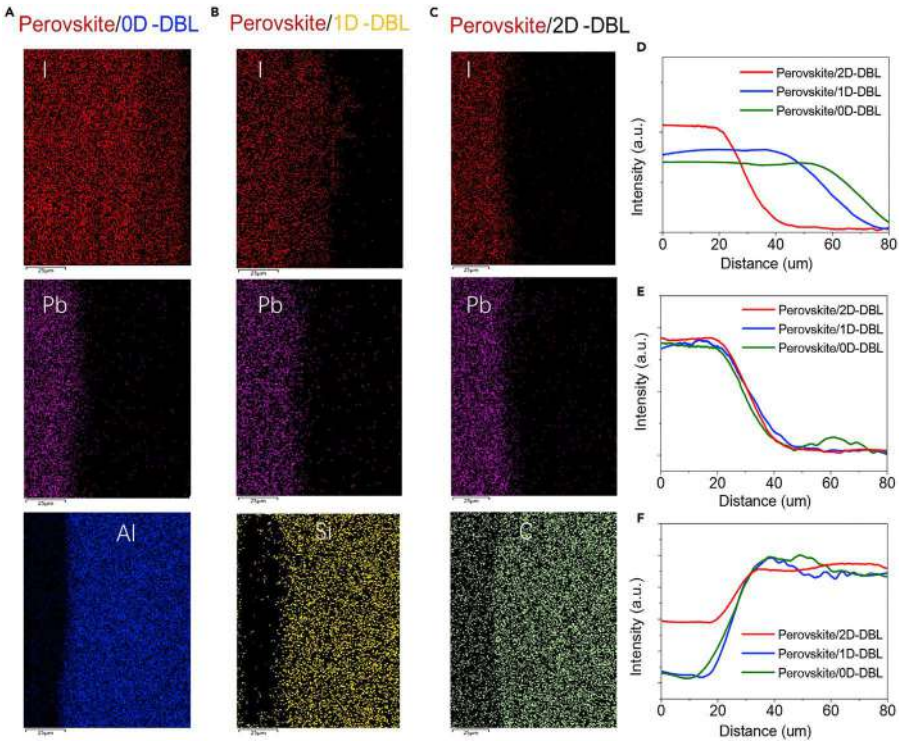

Figure 6.20 (A–C) SEM-EDX analysis of iodide (I_2) laterally diffused across 0D-DBL (A), 1D-DBL (B), and 2D-DBL (C). (D–F) The elemental intensity distribution of the EDX scan line profile of perovskite/DBL based on (D) 0D-DBL, (E) 1D-DBL, and (F) 2D-DBL. The scale bar in (A–C) is 25 μm. Reproduced from ref. 181 with permission from Elsevier, Copyright 2019.

These results indicate the ability of 2D-DBL to protect the Ag electrode from I_2 erosion upon precluding the interlayer diffusion process.[27,181]

Moreover, the measurements of both steady-state and photoluminescence (PL) confirmed the preference of the presence of 2D-DBL or 1D-DBL based perovskite film on the films without DBLs at all in the perovskite solar cell (Figure 6.21).[181]

The PL measurements indicate that 2D-DBL can passivate the surface of the used film in the solar cell. This inhibits the fast recombination of negatively charged electrons and positively charged holes in the perovskite solar cell device.[181]

An SEM image of the sub-cell cross-section of PSC modules is shown in Figure 6.22A, and the photo of the solar cell device that is composed of 10 sub cells in sequence construction is presented in Figure 6.22B.[181] The cell film is mainly composed of NiO, perovskite, N-doped graphene fullerene phenyl derivatives, C_{61}-butyric acid methyl ester, and BCP/Ag. The band gap energy of each film is presented in Figure 6.22C.[181] The devices with 2D-DBL have 15.6% PCE per area equal to 36.1 cm^2 for the perovskite solar cell. This is higher than perovskite solar cells without DBLs with a PCE of 14.01% (Figure 6.22D).[27,159,181] This efficiency is due to the enhanced voltage of the open circuit. The short-circuit current density (J_{sc}) was improved to 1.9 mA cm^{-2}

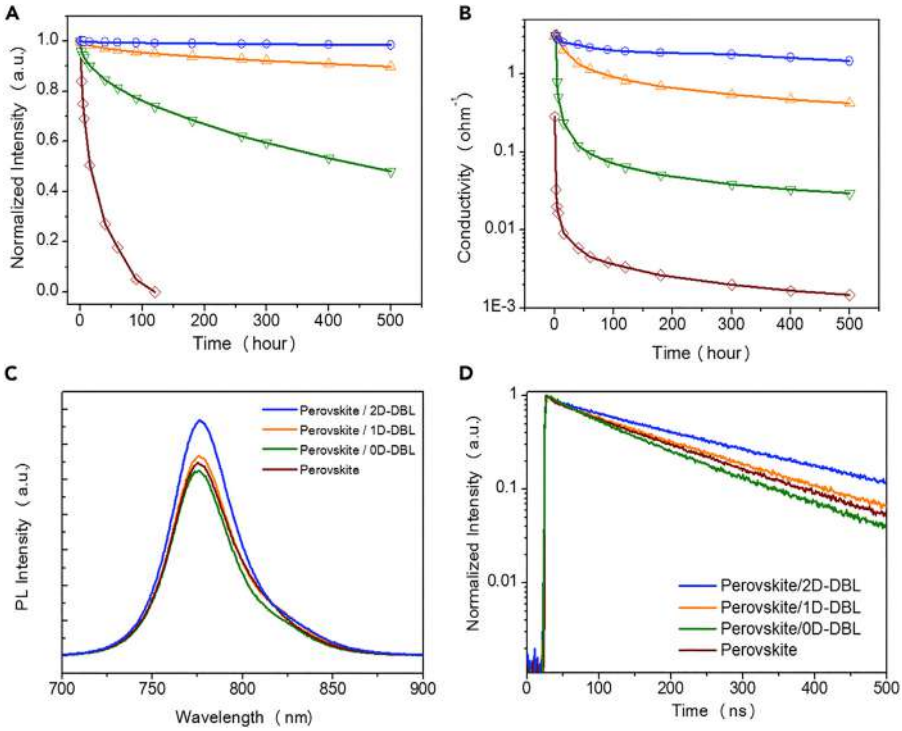

Figure 6.21 The role of different DBLs on the performance of the perovskite solar cell, especially on (A) light absorption, (B) electronic conductivity, (C) and (D) steady-state and time-resolved photoluminescence. All the measurements were conducted for the perovskite films with different DBLs and without any DBL. Reproduced from ref. 181 with permission from Elsevier, Copyright 2019.

(Figure 6.22E).[181] The constructed electronic barrier between the layers in the solar cell improved the charge transport between the sub-cells by virtue of the presence of 2D-DBL, as shown by the negligible change in J_{sc}.[181] Figure 6.22G demonstrates good reproducibility of the 2D-DBL-based devices. The data revealed that the fabricated perovskite solar cell with DBL was thermally stable with a high PCE over 1000 h at 85 °C (Figure 6.23).[181]

Pareek *et al.* explored the multi-functionality of g-C_3N_4 QDs as photovoltaic promoters for polymer solar cells.[182,183] They improved the photovoltaic performance of polymer solar cells using g-C_3N_4 QDs by merging Förster resonance energy transfer (FRET) with morphological effects.[182,183] They incorporated g-C_3N_4 QDs into a deep-rooted material blend of P3HT:$PC_{71}BM$ films, and observed the device performances by changing the concentration of QDs, which achieved a 40% performance improvement at an optimum concentration of 2% compared to the original devices.[183] They found that g-C_3N_4 QDs support FRET in between the QDs and host polymer, thus improving the whole energy gathering competence of the devices, and also enabling the QDs to transfer ultraviolet region photon energy to P3HT as

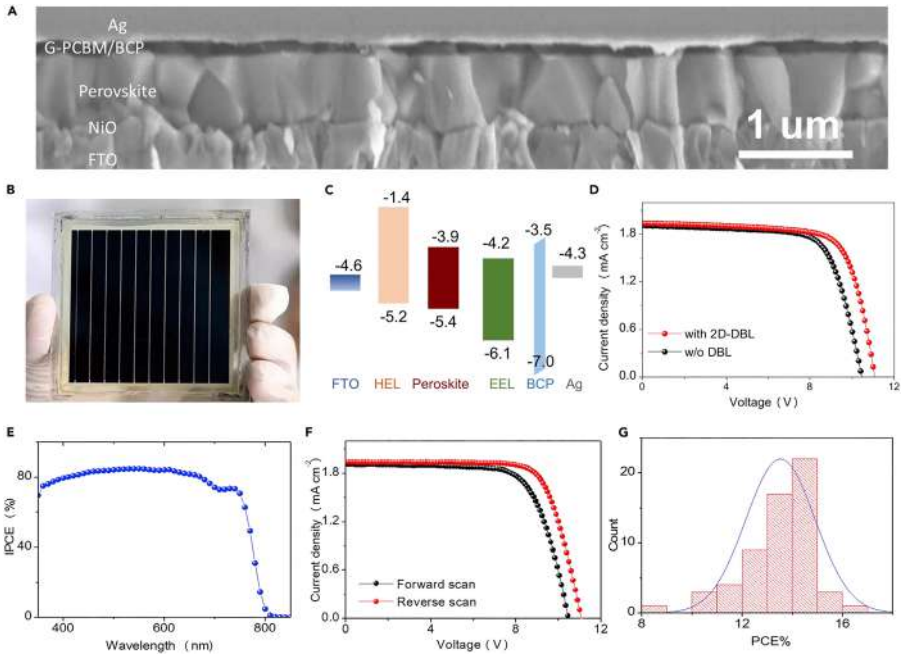

Figure 6.22 An illustration of the PSC film morphology and performance with and without DBL in the solar cell device using (A) an SEM image, (B) device photo, (C) the band gap energy, (D) the photocurrent voltage, (E) the IPC efficiency, (F) *J–V* curves and (G) the PCE for the solar cell. Reproduced from ref. 181 with permission from Elsevier, Copyright 2019.

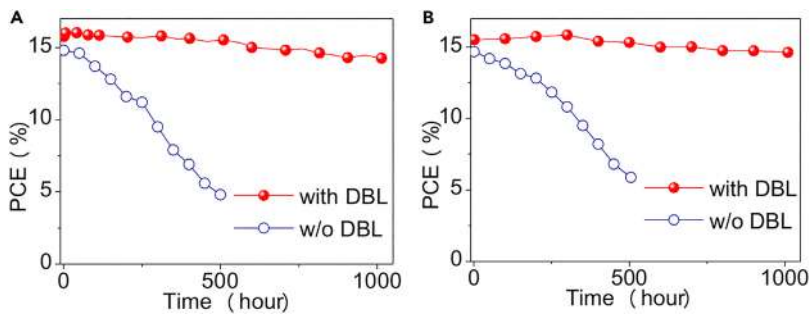

Figure 6.23 Monitoring the PCE of encapsulated PSC with and without DBL: (A) at 85 °C, humidity (85%) for 1000 h and (B) under a UV-filter at 60 °C in air and kept at a power of AM 1.5 solar light, 100 mW cm^{-1}. Reproduced from ref. 181 with permission from Elsevier, Copyright 2019.

emission spectra of g-C_3N_4 QDs (λ_{Ems} = 400–550) and absorption spectra of P3HT (λ_{Abs} = 400–600).[183] They also found that g-C_3N_4 QDs improve crystallinity through maintaining nanoscale phase exclusion of the active layer, which is vital for efficient excitation dissociation, and faster charge extraction.[179,184]

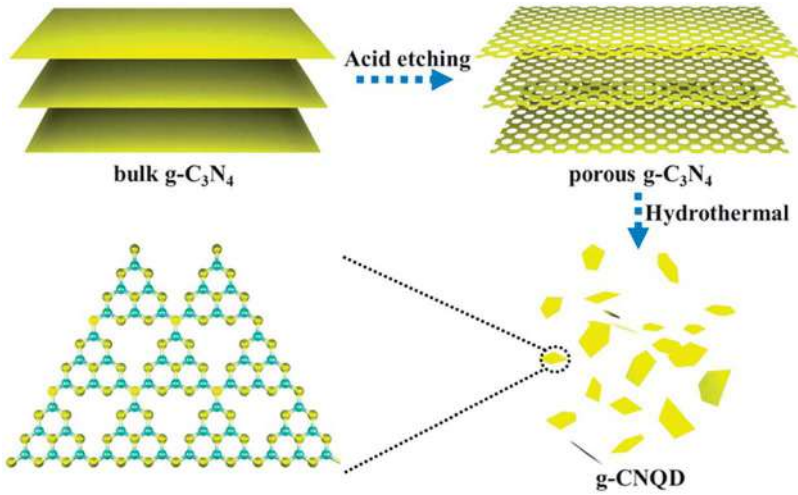

Figure 6.24 The mechanism utilized to prepare g-C_3N_4 quantum dots. Reproduced from ref. 82 with permission from the Royal Society of Chemistry.

They supposed that the enhanced PCE was due to the merged effects of improved morphology and FRET effect.[184] Chen *et al.* designed a functional electron transport layer (ETL) to adapt the interfacial charge dynamics for achieving high-performance PSCs using hybrid nanocomposite SnO_2/graphitic carbon nitride (g-C_3N_4) quantum dots. Acid etching of bulk g-C_3N_4 followed by the hydrothermal process are the fabrication steps for obtaining g-CNQDS (Figure 6.24).[82]

Then the authors used the ultra-sonication process to obtain SnO_2 and G-SnO_2 precursors.[82] The passivation of oxygen vacancies in the interfacial zone between SnO_2/g-C_3N_4 was encouraged by the charge redistribution generated by merging g-CNQDs into SnO_2.[82,185,186] In addition, the energy band position and performance of charge extraction at the interface of ETL/perovskite is controlled. The PCE of the device with GSnO_2 hybrid ETL was obtained as 22.13%, compared with 20.21% PCE for the control device. Additionally, the device with G-SnO_2 also offered durable stability, with PCE % equal to about 90% from the pristine PCE efficiency after 1500 h.[82]

Liu *et al.* achieved a PCE of 21.23% for PSC by the adaptation of SnO_2/perovskite using 2D g-CNQDs and the improvement of subsequent perovskite absorber crystallinity with low grain boundaries, high phase quality, fewer trap states, and charge recombination inhibition due to the inherent cross-linkable characteristics and quite a smooth surface of the g-CNQDs.[19]

Passivation is considered to be one of the most efficient methods for controlling the non-radiative recombination of organic-inorganic lead halide (PSCs), and many organic groups (amino, sulfonic, nitrate, and a hydroxyl group) are commonly used as passivation agents.[27,82,153,159] Passivation by 2D polymer g-C_3N_4 can not only rectify charged defects all over the grain boundaries by passivating the charge recombination center but also enhances the

crystalline quality resulting in an improvement in conductivity of perovskite light absorber films that is helpful for gentle charge extraction efficiency.[27,82] Li *et al.* recently improved the photovoltaic performance using a perovskite/surface-modified g-C_3N_4 heterojunction by various organic groups functionalized by g-C_3N_4.[185] They proved the fact that passivation with functionalized g-C_3N_4 maximizes the grain size and minimizes the energy disorder in the band edge and thus enhances nucleation and crystallinity of the perovskite.[27,75,82,185] They used prolonged PL lifetime analysis that indicates the inhibited free photogenerated carriers and trap-assisted recombination. This displays an improvement in charge mobility and enhancement of the retardation of charge recombination caused by functionalized g-C_3N_4 incorporation, which results in reduced charge recombination.[19,185] Furthermore, there was a significant improvement in open-circuit voltage (V_{oc}) and fill factor (FF), resulting in a PCE of 20.08%, comparable with 17.85% for the device without passivation.[185] By the same token, Liu *et al.* provide new guidance for dual-interfacial modification of 2D g-C_3N_4 to improve the PCE for high-efficiency and stability.[186] They used the dual interfacial modification method to modify an n-type 2D g-C_3N_4 semiconductor to adapt the electron-transport layer/perovskite and perovskite/hole-transport layer interfaces, respectively.[186] Likewise, coupling g-C_3N_4 with methylammonium lead iodide ($MAPbI_3$) enhanced the crystallization and grain sizes of $MAPbI_3$ as well as the conductivity of the perovskite layer. Also, g-C_3N_4 led to a decrease in the hysteresis and boosted the PCE from 16.22% to 19.34%.[27]

A CuS/g-C_3N_4 composite was first used as CEs in QDSCs by Zheng *et al.*, who coated a g-C_3N_4 micro sheet with nanocrystals of CuS on FTO substrate.[172] The authors deposited different amounts of CuS on g-C_3N_4 micro sheets (0, 1, 3, 5, and 7 cycle lifetimes), resulting in an increased amount of CuS nanocrystals by the CuS deposition cycle times. The photocatalytic activity and the charge transfer in the cell were greatly enhanced.[172] Fitting to results of the current density–voltage curve for all CuS/g-C_3N_4 CE based cells, the model that had 5-cycle times g-C_3N_4 quantum dot solar cell produced the best PCE and the lowest resistance to charge transfer.[172] This is essential for the high-performance of QDSCs.[27,75] On the other hand, the cell-based on CE of 7-cycle times offered poorer photocatalytic activity owing to the agglomerates of the extra particles of CuS.[172] Currently, the adaptation of g-C_3N_4 with different elements for use in QDSC has great potential and has attracted many researchers.[172,187–191]

6.8 Conclusions and Future Prospects

In summary, this chapter emphasized the recent progress and achievements in the atomic and molecular functionalization of gCN materials for solar cell applications. There are various methods that were developed for the successful fabrication of gCN thin films, including the fabrication methods of gCN thin films like post-processing (*i.e.*, nanosheets, coating,

and self-assembly), and direct growth methods (*i.e.*, solid/liquid mediated growth and gas-phase noncontact growth). These methods allowed the atomic doping and functionalization of gCNs with various metal oxides (*i.e.*, Fe, ZnO, and TiO_2) and carbon materials (*i.e.*, carbon nanotubes, carbon dots, and graphene oxide) on various substrates FTO, AAO, ZnO, and TiO_2. That not only led to increasing the surface area and modulating the band gap energy of gCNs but also enhancement of the visible light absorption ability and increase of the current density along with reducing overpotential. The direct growth methods (*i.e.*, solid/liquid mediated growth) and gas phase (*i.e.*, CVD, TVC, and micro-contact printing assisted) are preferred relative to post-treatment methods for tailoring thin-film thickness, shape, and composition as well as being feasible for various substrates. The mechanism of solar cell systems was also discussed in detail. However, various studies are needed to reduce the gap between the theoretical and experimental performance of SCs to meet the large-scale and practical applications. The utilization of hybrid gCNs in solar-cell devices, including dye-sensitized, organic, perovskite, and quantum dot solar cells, were emphasized and supported with various examples. Perovskites, carbon materials, and quantum dots reduce the band gap energy, delay the electron–hole recombination, and enhance the visible light absorption of gCNs along with boosting the photocurrent density under low applied potential and reducing the overpotential. This is in addition to incremental power conversion efficiency of gCNs. However, gCNs remain impractical and do not fare well in large-scale application due to the difficulties related to the fabrication of gCN thin film as photoanodes or photocathodes and poor visible light absorption over a wavelength of 460 nm. Also, the solar-driven current production is still insufficient for the practical usage. These barriers could be defeated by tailoring the shape and composition of gCNs into multi-dimensional nanostructures with unique surface features (*i.e.*, cavities, pores, and branches) due to their high surface area and abundant absorption sites. Also, the formation of gCN-based heterojunctions with porous metal nanocrystals can enhance the photocurrent density due to their great redox merits.[10,11,192–196] Likewise, gCN heterojunctions with novel metal carbide/nitride (MXenes), carbon dots, graphene, and metal–organic frameworks can delay the electron–hole recombination and enhance the visible light absorption due to the unique electron density, active sites, and visible light absorption power.[1,3,197–202]

Various theoretical-based methods like DFT and artificial intelligence should be carried out to predict the structural-compositional related photocatalytic properties of gCN materials as well as understand their mechanism. Meanwhile, there is a crucial need to develop facile, one-pot, template-free, and green methods for the rational design of novel gCN nanoarchitectonics feasible for supporting various metal, polymer, and hydride substrates.

References

1. Y. Ibrahim, A. Mohamed, A. M. Abdelgawad, K. Eid, A. M. Abdullah and A. Elzatahry, *J. Nanomater.*, 2020, **10**, 1916.
2. F. Wu, K. Eid, A. M. Abdullah, W. Niu, C. Wang, Y. Lan, A. A. Elzatahry and G. Xu, *ACS Appl. Mater. Interfaces*, 2020, **12**, 31309.
3. H. Idris Abdu, K. Eid, A. M. Abdullah, M. H. Sliem, A. Elzatahry and X. Lu, *Green Chem.*, 2020, **22**, 5437.
4. H. I. Abdu, K. Eid, A. M. Abdullah, Z. Han, M. H. Ibrahim, D. Shan, J. Chen, A. A. Elzatahry and X. Lu, *Renewable Energy*, 2020, **153**, 998.
5. Q. Wang and K. Domen, *Chem. Rev.*, 2020, **120**, 919.
6. K. Eid, K. A. Soliman, D. Abdulmalik, D. Mitoraj, M. H. Sleim, M. O. Liedke, H. A. El-Sayed, A. S. AlJaber, I. Y. Al-Qaradawi and O. M. Reyes, *Catal. Sci. Technol.*, 2020, **10**, 801.
7. Y. H. Ahmad, K. A. Eid, S. Y. AlQaradawi and N. K. Allam, *Sustainable Energy Fuels*, 2017, **1**, 1123.
8. S. K. Karuturi, H. Shen, A. Sharma, F. J. Beck, P. Varadhan, T. Duong, P. R. Narangari, D. Zhang, Y. Wan, J.-H. He, H. H. Tan, C. Jagadish and K. Catchpole, *Adv. Energy Mater.*, 2020, **10**, 2000772.
9. K. Eid, Y. H. Ahmad, S. Y. AlQaradawi and N. K. Allam, *Catal. Sci. Technol.*, 2017, **7**, 2819.
10. K. Eid, H. Wang, P. He, K. Wang, T. Ahamad, S. M. Alshehri, Y. Yamauchi and L. Wang, *Nanoscale*, 2015, **7**, 16860.
11. K. Eid, H. Wang, V. Malgras, Z. A. Alothman, Y. Yamauchi and L. Wang, *J. Phys. Chem. C*, 2015, **119**, 19947.
12. L. Sun, H. Wang, K. Eid, S. M. Alshehri, V. Malgras, Y. Yamauchi and L. Wang, *Electrochim. Acta*, 2016, **188**, 845.
13. Q. Lu, H. Wang, K. Eid, Z. A. Alothman, V. Malgras, Y. Yamauchi and L. Wang, *Chem. - Asian J.*, 2016, **11**, 1939.
14. D. Cruz, J. Garcia Cerrillo, B. Kumru, N. Li, J. Dario Perea, B. V. Schmidt, I. Lauermann, C. J. Brabec and M. Antonietti, *J. Am. Chem. Soc.*, 2019, **141**, 12322.
15. J. Y. Kim, J.-W. Lee, H. S. Jung, H. Shin and N.-G. Park, *Chem. Rev.*, 2020, **120**, 7867.
16. S. Gu, R. Lin, Q. Han, Y. Gao, H. Tan and J. Zhu, *Adv. Mater.*, 2020, **32**, 1907392.
17. Z. Hu, J. Wang, X. Ma, J. Gao, C. Xu, K. Yang, Z. Wang, J. Zhang and F. Zhang, *Nano Energy*, 2020, **72**, 105376.
18. X. Chen, Q. Liu, Q. Wu, P. Du, J. Zhu, S. Dai and S. Yang, *Adv. Funct. Mater.*, 2016, **26**, 1719.
19. P. Liu, Y. Sun, S. Wang, H. Zhang, Y. Gong, F. Li, Y. Shi, Y. Du, X. Li , S.-S. Guo, Q. Tai, C. Wang, and X.-Z. Zhao, *J. Power Sources*, 2020, **451**, 227825.
20. K. Fukuda, K. Yu and T. Someya, *Adv. Energy Mater.*, 2020, **10**, 2000765.
21. T. Miller, A. B. Jorge, T. Suter, A. Sella, F. Corà and P. McMillan, *Phys. Chem. Chem. Phys.*, 2017, **19**, 15613.

22. J. Zhu, P. Xiao, H. Li and S. A. Carabineiro, *ACS Appl. Mater. Interfaces*, 2014, **6**, 16449.
23. K. Eid, M. H. Sliem, K. Jlassi, A. S. Eldesoky, G. G. Abdo, S. Y. Al-Qaradawi, M. A. Sharaf, A. M. Abdullah and A. A. Elzatahry, *Inorg. Chem. Commun.*, 2019, **107**, 107460.
24. K. Eid, M. H. Sliem, H. Al-Kandari, M. A. Sharaf and A. M. Abdullah, *Langmuir*, 2019, **35**, 3421.
25. K. Eid, M. H. Sliem, A. S. Eldesoky, H. Al-Kandari and A. M. Abdullah, *Int. J. Hydrogen Energy*, 2019, **44**, 17943.
26. K. Eid, M. H. Sliem and A. M. Abdullah, *Nanoscale*, 2019, **11**, 11755.
27. J. Safaei, N. A. Mohamed, M. F. M. Noh, M. F. Soh, N. A. Ludin, M. A. Ibrahim, W. N. R. W. Isahak and M. A. M. Teridi, *J. Mater. Chem. A*, 2018, **6**, 22346.
28. L. Zhou, Y. Xu, W. Yu, X. Guo, S. Yu, J. Zhang and C. Li, *J. Mater. Chem. A*, 2016, **4**, 8000.
29. B. D. Boruah, A. Mathieson, B. Wen, C. Jo, F. Deschler and M. De Volder, *Nano Lett.*, 2020, **20**, 5967.
30. W. Xiong, M. Huang, F. Huang and R.-Q. Zhang, *Appl. Surf. Sci.*, 2020, **511**, 145535.
31. J. Xu, M. Antonietti and M. Shalom, *Chem. - Asian J.*, 2016, **11**, 2499.
32. Y. Zhang, T. Mori and J. Ye, *Sci. Adv. Mater.*, 2012, **4**, 282.
33. J. Bian, C. Huang and R. Q. Zhang, *ChemSusChem*, 2016, **9**, 2723.
34. B. Song, Z. Zeng, G. Zeng, J. Gong, R. Xiao, S. Ye, M. Chen, C. Lai, P. Xu and X. Tang, *Adv. Colloid Interface Sci.*, 2019, **272**, 101999.
35. J. Wen, J. Xie, X. Chen and X. Li, *Appl. Surf. Sci.*, 2017, **391**, 72.
36. C. Prasad, H. Tang, Q. Liu, I. Bahadur, S. Karlapudi and Y. Jiang, *Int. J. Hydrogen Energy*, 2020, **45**, 337.
37. C. Jia, L. Yang, Y. Zhang, X. Zhang, K. Xiao, J. Xu and J. Liu, *ACS Appl. Mater. Interfaces*, 2020, **12**, 53571.
38. N. A. Mohamed, J. Safaei, A. F. Ismail, M. F. A. M. Jailani, M. N. Khalid, M. F. M. Noh, A. Aadenan, S. N. S. Nasir, J. S. Sagu and M. A. M. Teridi, *Appl. Surf. Sci.*, 2019, **489**, 92.
39. N. A. Mohamed, J. Safaei, A. F. Ismail, M. F. M. Noh, N. A. Arzaee, N. N. Mansor, M. A. Ibrahim, N. A. Ludin, J. S. Sagu and M. A. M. Teridi, *J. Alloys Compd.*, 2020, **818**, 152916.
40. K. R. Reddy, C. V. Reddy, M. N. Nadagouda, N. P. Shetti, S. Jaesool and T. M. Aminabhavi, *J. Environ. Manage.*, 2019, **238**, 25.
41. W. Yu, J. Chen, T. Shang, L. Chen, L. Gu and T. Peng, *Appl. Catal., B*, 2017, **219**, 693.
42. R. Bhosale, S. Jain, C. P. Vinod, S. Kumar and S. Ogale, *ACS Appl. Mater. Interfaces*, 2019, **11**, 6174.
43. C. Zhang, Y. Li, D. Shuai, Y. Shen, W. Xiong and L. Wang, *Chemosphere*, 2019, **214**, 462.
44. A. Naseri, M. Samadi, A. Pourjavadi, A. Z. Moshfegh and S. Ramakrishna, *J. Mater. Chem. A*, 2017, **5**, 23406.
45. Y. Li, X. Li, H. Zhang and Q. Xiang, *Nanoscale Horiz.*, 2020, **5**, 765.

46. H. Miao, G. Zhang, X. Hu, J. Mu, T. Han, J. Fan, C. Zhu, L. Song, J. Bai and X. Hou, *J. Alloys Compd.*, 2017, **690**, 669.
47. J. Safaei, N. N. Rosli, M. F. Mohamad Noh, N. A. Mohamed, M. A. Ibrahim and M. A. M. Teridi, *Phys. Status Solidi RRL*, 2018, **12**, 1800441.
48. X. Zhang, X. Xie, H. Wang, J. Zhang, B. Pan and Y. Xie, *J. Am. Chem. Soc.*, 2013, **135**, 18.
49. Z. Zhou, J. Wang, J. Yu, Y. Shen, Y. Li, A. Liu, S. Liu and Y. Zhang, *J. Am. Chem. Soc.*, 2015, **137**, 2179.
50. B. Kumru, J. S. Barrio, J. Zhang, M. Antonietti, M. Shalom and B. V. Schmidt, *ACS Appl. Mater. Interfaces*, 2019, **11**, 9462.
51. Q. Gao, S. Sun, X. Li, X. Zhang, L. Duan and W. Lü, *Nanoscale Res. Lett.*, 2016, **11**, 1.
52. R. Li, Y. Ren, P. Zhao, J. Wang, J. Liu and Y. Zhang, *J. Hazard. Mater.*, 2019, **365**, 606.
53. L. F. Villalobos, M. T. Vahdat, M. Dakhchoune, Z. Nadizadeh, M. Mensi, E. Oveisi, D. Campi, N. Marzari and K. V. Agrawal, *Sci. Adv.*, 2020, **6**, eaay9851.
54. J. Ran, T. Pan, Y. Wu, C. Chu, P. Cui, P. Zhang, X. Ai, C. F. Fu, Z. Yang and T. Xu, *Angew. Chem., Int. Ed.*, 2019, **58**, 16463.
55. L. Ye and S. Chen, *Appl. Surf. Sci.*, 2016, **389**, 1076.
56. J. Liu, T. Zhang, Z. Wang, G. Dawson and W. Chen, *J. Mater. Chem. A*, 2011, **21**, 14398.
57. L. Jiang, X. Yuan, Y. Pan, J. Liang, G. Zeng, Z. Wu and H. Wang, *Appl. Catal., B*, 2017, **217**, 388.
58. H. Li, L. Wang, Y. Liu, J. Lei and J. Zhang, *Res. Chem. Intermed.*, 2016, **42**, 3979.
59. P. Niu, L. Zhang, G. Liu and H. M. Cheng, *Adv. Funct. Mater.*, 2012, **22**, 4763.
60. S. Ye, R. Wang, M.-Z. Wu and Y.-P. Yuan, *Appl. Surf. Sci.*, 2015, **358**, 15.
61. G. Algara-Siller, N. Severin, S. Y. Chong, T. Björkman, R. G. Palgrave, A. Laybourn, M. Antonietti, Y. Z. Khimyak, A. V. Krasheninnikov and J. P. Rabe, *Angew. Chem., Int. Ed.*, 2014, **53**, 7450.
62. Y. Chen, B. Wang, S. Lin, Y. Zhang and X. Wang, *J. Phys. Chem. C*, 2014, **118**, 29981.
63. F. Zhang, J. Zhang, J. Li, X. Jin, Y. Li, M. Wu, X. Kang, T. Hu, X. Wang and W. Ren, *J. Mater. Chem. A*, 2019, **7**, 6939.
64. J. Wang, Z. Yang, W. Yao, X. Gao and D. Tao, *Appl. Catal., B*, 2018, **238**, 629.
65. J. Xu, L. Zhang, R. Shi and Y. Zhu, *J. Mater. Chem. A*, 2013, **1**, 14766.
66. Y.-J. Yuan, Z. Shen, S. Wu, Y. Su, L. Pei, Z. Ji, M. Ding, W. Bai, Y. Chen and Z.-T. Yu, *Appl. Catal., B*, 2019, **246**, 120.
67. J. Yan, M. T. F. Rodrigues, Z. Song, H. Li, H. Xu, H. Liu, J. Wu, Y. Xu, Y. Song and Y. Liu, *Adv. Funct. Mater.*, 2017, **27**, 1700653.
68. D. Chen, Z. Wang, Y. Du, G. Yang, T. Ren and H. Ding, *Catal. Today*, 2015, **258**, 41.

69. D. Liu, B. Liu, C. Wang, W. Jin, Q. Zha, G. Shi, D. Wang, X. Sang and C. Ni, *ACS Sustainable Chem. Eng.*, 2020, **8**, 2167.
70. M. Yi and Z. Shen, *J. Mater. Chem. A*, 2015, **3**, 11700.
71. Z. Y. Xia, S. Pezzini, E. Treossi, G. Giambastiani, F. Corticelli, V. Morandi, A. Zanelli, V. Bellani and V. Palermo, *Adv. Funct. Mater.*, 2013, **23**, 4684.
72. K. Parvez, Z.-S. Wu, R. Li, X. Liu, R. Graf, X. Feng and K. Mullen, *J. Am. Chem. Soc.*, 2014, **136**, 6083.
73. J. Chen, M. Duan and G. Chen, *J. Mater. Chem.*, 2012, **22**, 19625.
74. M. J. Bojdys, N. Severin, J. P. Rabe, A. I. Cooper, A. Thomas and M. Antonietti, *Macromol. Rapid Commun.*, 2013, **34**, 850.
75. C. Jia, W. Hu, Y. Zhang, C. Teng, Z. Chen and J. Liu, *Inorg. Chem. Front.*, 2020, **7**, 2434.
76. T. Chen, Y. Yuan, Y. Zhao, F. Rao and S. Song, *Langmuir*, 2019, **35**, 2368.
77. G. R. Mahdavinia, R. Hosseini, F. Darvishi and M. Sabzi, *Iran. Polym. J.*, 2016, **25**, 933.
78. L.-X. Su, Z.-Y. Liu, Y.-L. Ye, C.-L. Shen, Q. Lou and C.-X. Shan, *Int. J. Hydrogen Energy*, 2019, **44**, 19805.
79. S. Cao and J. Yu, *J. Phys. Chem. Lett.*, 2014, **5**, 2101.
80. G. Wang, S. Kuang, J. Zhang, S. Hou and S. Nian, *Electrochim. Acta*, 2016, **187**, 243.
81. R. C. Pawar, S. Kang, S. H. Ahn and C. S. Lee, *RSC Adv.*, 2015, **5**, 24281.
82. J. Chen, H. Dong, L. Zhang, J. Li, F. Jia, B. Jiao, J. Xu, X. Hou, J. Liu and Z. Wu, *J. Mater. Chem. A*, 2020, **8**, 2644.
83. X. Zou, Z. Sun and Y. H. Hu, *J. Mater. Chem. A*, 2020, **8**, 21474.
84. C. Jia, L. Yang, Y. Zhang, X. Zhang, K. Xiao, J. Xu and J. Liu, *ACS Appl. Mater. Interfaces*, 2020, **12**, 53571.
85. Y. Zhang and M. Antonietti, *Chem. - Asian J.*, 2010, **5**, 1307.
86. Y. Zhang, A. Thomas, M. Antonietti and X. Wang, *J. Am. Chem. Soc.*, 2009, **131**, 50.
87. F. Zeng, W.-Q. Huang, J.-H. Xiao, Y.-Y. Li, W. Peng, W. Hu, K. Li and G.-F. Huang, *J. Phys. D: Appl. Phys.*, 2018, **52**, 025501.
88. P. Xia, B. Zhu, B. Cheng, J. Yu and J. Xu, *ACS Sustainable Chem. Eng.*, 2018, **6**, 965.
89. X. Li, J. Xiong, J. Huang, Z. Feng and J. Luo, *J. Alloys Compd.*, 2019, **774**, 768.
90. D. Jiang, T. Wang, Q. Xu, D. Li, S. Meng and M. Chen, *Appl. Catal., B*, 2017, **201**, 617.
91. D. Wu, K. Cao, F. Wang, H. Wang, Z. Gao, F. Xu, Y. Guo and K. Jiang, *Chem. Eng. J.*, 2015, **280**, 441.
92. S. Kumar, A. Baruah, S. Tonda, B. Kumar, V. Shanker and B. Sreedhar, *Nanoscale*, 2014, **6**, 4830.
93. A. M. Alhanash, K. S. Al-Namshah, S. K. Mohamed and M. S. Hamdy, *Optik*, 2019, **186**, 34.
94. N. Boonprakob, N. Wetchakun, S. Phanichphant, D. Waxler, P. Sherrell, A. Nattestad, J. Chen and B. Inceesungvorn, *J. Colloid Interface Sci.*, 2014, **417**, 402.

95. S. Raha and M. Ahmaruzzaman, *Chem. Eng. J.*, 2020, **387**, 123766.
96. L. Ma, H. Fan, K. Fu, S. Lei, Q. Hu, H. Huang and G. He, *ACS Sustainable Chem. Eng.*, 2017, **5**, 7093.
97. B.-S. Kong, J. Geng and H.-T. Jung, *Chem. Commun.*, 2009, **16**, 2174.
98. B. Wu, L. Ge, H. Wu, X. Wang, Q. Ge, J. Miao, M. Cao, P. Chen, R. Xia and J. Qian, *Adv. Mater. Interfaces*, 2019, **6**, 1801406.
99. Z. Gan, L. Liu, P. Pan, Y. Lin, J. Shen and B. Jia, *Nanoscale*, 2018, **10**, 22448.
100. Y. Wang, B. Gao, Q. Yue and Z. Wang, *J. Mater. Chem. A*, 2020, **8**, 19133.
101. X. Kan, Y. Ban, C. Wu, Q. Pan, H. Liu, J. Song, Z. Zuo, Z. Li and Y. Zhao, *ACS Appl. Mater. Interfaces*, 2018, **10**, 53.
102. J. Barrio, M. Volokh and M. Shalom, *J. Mater. Chem. A*, 2020, **8**, 11075.
103. J. Fu, J. Yu, C. Jiang and B. Cheng, *Adv. Energy Mater.*, 2018, **8**, 1701503.
104. L. Jing, R. Zhu, D. L. Phillips and J. C. Yu, *Adv. Funct. Mater.*, 2017, **27**, 1703484.
105. S. Cao, J. Low, J. Yu and M. Jaroniec, *Adv. Mater.*, 2015, **27**, 2150.
106. M. Shalom, S. Gimenez, F. Schipper, I. Herraiz-Cardona, J. Bisquert and M. Antonietti, *Angew. Chem.*, 2014, **126**, 3728.
107. J. Xu, T. J. Brenner, L. Chabanne, D. Neher, M. Antonietti and M. Shalom, *J. Am. Chem. Soc.*, 2014, **136**, 13486.
108. G. Peng, L. Xing, J. Barrio, M. Volokh and M. Shalom, *Angew. Chem., Int. Ed.*, 2018, **57**, 1186.
109. W. Zhang, J. Albero, L. Xi, K. M. Lange, H. Garcia, X. Wang and M. Shalom, *ACS Appl. Mater. Interfaces*, 2017, **9**, 32667.
110. Y. Fang, X. Li and X. Wang, *ACS Catal.*, 2018, **8**, 8774.
111. J. Xu and M. Shalom, *ACS Appl. Mater. Interfaces*, 2016, **8**, 13058.
112. J. Zhang, M. Zhang, L. Lin and X. Wang, *Angew. Chem.*, 2015, **127**, 6395.
113. J. Liu, H. Wang, Z. Chen, H. Moehwald and S. Fiechter, *Adv. Mater.*, 2015, **27**, 712.
114. B. Kumru, D. Cruz, T. Heil, B. V. Schmidt and M. Antonietti, *J. Am. Chem. Soc.*, 2018, **140**, 17532.
115. T. Zhao, Q. Zhou, Y. Lv, D. Han, K. Wu, L. Zhao, Y. Shen, S. Liu and Y. Zhang, *Angew. Chem.*, 2020, **132**, 1155.
116. A. Kubono, N. Kanae, S. Umemoto, T. Sakai and N. Okui, *Thin Solid Films*, 1992, **215**, 94.
117. K. Xiao, P. Giusto, L. Wen, L. Jiang and M. Antonietti, *Angew. Chem., Int. Ed.*, 2018, **57**, 10123.
118. H. Arazoe, D. Miyajima, K. Akaike, F. Araoka, E. Sato, T. Hikima, M. Kawamoto and T. Aida, *Nat. Mater.*, 2016, **15**, 1084.
119. L. Chen, R. Yan, M. Oschatz, L. Jiang, M. Antonietti and K. Xiao, *Angew. Chem., Int. Ed.*, 2020, **59**, 9067.
120. M. F. M. Noh, N. A. Arzaee, J. Safaei, N. A. Mohamed, H. P. Kim, J. Jang and M. A. M. Teridi, *J. Alloys Compd.*, 2019, **773**, 997.
121. J. Liu, H. Wang, Z. P. Chen, H. Moehwald, S. Fiechter, R. van de Krol, L. Wen, L. Jiang and M. Antonietti, *Adv. Mater.*, 2015, **27**, 712.

122. S. Hu, X. Chen, Q. Li, F. Li, Z. Fan, H. Wang, Y. Wang, B. Zheng and G. Wu, *Appl. Catal., B*, 2017, **201**, 58.
123. Z. Cui, K. Ren, Y. Zhao, X. Wang, H. Shu, J. Yu, W. Tang and M. Sun, *Appl. Surf. Sci.*, 2019, **492**, 513.
124. X. Guo, J. Duan, W. Wang and Z. Zhang, *Fuel*, 2020, **280**, 118544.
125. M. Xie, J. Tang, L. Kong, W. Lu, V. Natarajan, F. Zhu and J. Zhan, *Chem. Eng. J.*, 2019, **360**, 1213.
126. D. Zhou and C. Qiu, *Chem. Phys. Lett.*, 2019, **728**, 70.
127. Z. Zhu, X. Tang, T. Wang, W. Fan, Z. Liu, C. Li, P. Huo and Y. Yan, *Appl. Catal., B*, 2019, **241**, 319.
128. Z. Chen, H. Wang, J. Xu and J. Liu, *Chem. - Asian J.*, 2018, **13**, 1539–1543.
129. J. Bian, Q. Li, C. Huang, J. Li, Y. Guo, M. Zaw and R.-Q. Zhang, *Nano Energy*, 2015, **15**, 353.
130. J. Bian, J. Li, S. Kalytchuk, Y. Wang, Q. Li, T. C. Lau, T. A. Niehaus, A. L. Rogach and R. Q. Zhang, *ChemPhysChem*, 2015, **16**, 954.
131. F. Jia, Y. Zhang, W. Hu, M. Lv, C. Jia and J. Liu, *Front. Mater.*, 2019, **6**, 52.
132. Z. Cai, Z. Song and L. Guo, *ACS Appl. Mater. Interfaces*, 2019, **11**, 12770.
133. O. J. Achadu, K. Takemura, I. M. Khoris and E. Y. Park, *Sens. Actuators, B*, 2020, **321**, 128494.
134. T. An, J. Tang, Y. Zhang, Y. Quan, X. Gong, A. M. Al-Enizi, A. A. Elzatahry, L. Zhang and G. Zheng, *ACS Appl. Mater. Interfaces*, 2016, **8**, 12772.
135. G. Li, Z. Lian, W. Wang, D. Zhang and H. Li, *Nano Energy*, 2016, **19**, 446.
136. M. Grätzel, *Inorg. Chem.*, 2005, **44**, 6841.
137. G. W. Crabtree and N. S. Lewis, *Phys. Today*, 2007, **60**, 37.
138. D. Ginley, M. A. Green and R. Collins, *MRS Bull.*, 2008, **33**, 355.
139. D. J. Lipomi and Z. Bao, *Energy Environ. Sci.*, 2011, **4**, 3314.
140. J. Gong, J. Liang and K. Sumathy, *Renewable Sustainable Energy Rev.*, 2012, **16**, 5848.
141. T. Soga, *Nanostructured Materials for Solar Energy Conversion*, Elsevier, Amesterdam, Netherland, 2006.
142. L. Chaar, *Power Electronics Handbook*, Elsevier, Amesterdam, Netherland, 2007.
143. S. Tonzani, *Nat. Mater.*, 2010, **9**, S10.
144. B. Parkinson, *J. Chem. Educ.*, 1983, **60**, 338.
145. L. M. Fraas, in *Low-cost Solar Electric Power*, Springer International Publishing, Cham, 2014, pp. 1–12.
146. M. Taguchi, A. Suzuki, N. Ueoka and T. Oku, *AIP Conference Proceedings*, Tokyo, Japan, January, 2019, vol. 2067.
147. L. Etgar, *Materials*, 2013, **6**, 445.
148. H. Gerischer, *J. Electroanal. Chem. Interfacial Electrochem.*, 1975, **58**, 263.
149. D. Meneses-Rodríguez, P. P. Horley, J. Gonzalez-Hernandez, Y. V. Vorobiev and P. N. Gorley, *Sol. Energy*, 2005, **78**, 243.
150. S. G. Kumar and L. G. Devi, *J. Phys. Chem. A*, 2011, **115**, 13211.
151. G. Peng, M. Volokh, J. Tzadikov, J. Sun and M. Shalom, *Adv. Energy Mater.*, 2018, **8**, 1800566.
152. M. A. Green and S. P. Bremner, *Nat. Mater.*, 2017, **16**, 23.

153. O. Simya, P. Radhakrishnan, A. Ashok, K. Kavitha and R. Althaf, *Handbook of Nanomaterials for Industrial Applications*, Elsevier BV, Amsterdam, The Netherlands, 2018.
154. A. Richter, M. Hermle and S. W. Glunz, *IEEE J. Photovoltaics*, 2013, **3**, 1184.
155. K. Chopra, P. Paulson and V. Dutta, *Prog. Photovoltaics*, 2004, **12**, 69.
156. T. M. Clarke and J. R. Durrant, *Chem. Rev.*, 2010, **110**, 6736.
157. L. Meng, Y. Zhang, X. Wan, C. Li, X. Zhang, Y. Wang, X. Ke, Z. Xiao, L. Ding and R. Xia, *Science*, 2018, **361**, 1094.
158. K. L. Chopra and S. R. Das, *Thin Film Solar Cells, Springer*, Switzerland, 1983.
159. T. Ibn-Mohammed, S. Koh, I. Reaney, A. Acquaye, G. Schileo, K. Mustapha and R. Greenough, *Renewable Sustainable Energy Rev.*, 2017, **80**, 1321.
160. S. Fischer, E. Favilla, M. Tonelli and J. C. Goldschmidt, *Sol. Energy Mater. Sol. Cells*, 2015, **136**, 127.
161. M. Burgelman, P. Nollet and S. Degrave, *Thin Solid Films*, 2000, **361**, 527.
162. K. Yoon, Y. Kim, J. Park, C. H. Shin, S. Baek, J. Jang, S. Iftiquar and J. Yi, *J. Non-Cryst. Solids*, 2011, **357**, 2826.
163. G. Conibeer and A. Willoughby, *Solar Cell Materials: Developing Technologies*, John Wiley & Sons, United Kingdom, 2014.
164. G. Conibeer, *Mater. Today*, 2007, **10**, 42–50.
165. G. F. Brown and J. Wu, *Laser Photonics Rev.*, 2009, **3**, 394–405.
166. W. Iqbal, B. Yang, X. Zhao, M. Rauf, M. Waqas, Y. Gong, J. Zhang and Y. Mao, *Catal. Sci. Technol.*, 2018, **8**, 4576.
167. T. O. Ajiboye, A. T. Kuvarega and D. C. Onwudiwe, *Nano-Struct. Nano-Objects*, 2020, **24**, 100577.
168. J. Zhang, Y. Chen and X. Wang, *Energy Environ. Sci.*, 2015, **8**, 3092.
169. M. Ismael, *J. Alloys Compd.*, 2020, **846**, 156446.
170. J. Men, Q. Gao, S. Sun, X. Zhang, L. Duan and W. Lü, *Mater. Res. Bull.*, 2017, **85**, 209.
171. S. Vijayanath and K. Janaki, *Inorg. Chem. Commun.*, 2020, **120**, 108119.
172. W. Zheng, Q. Wang, D. Wang and H. Sun, *IEEE J. Photovoltaics*, 2020, **10**, 1340.
173. H. Yan, X. Tian, Y. Pang, B. Feng, K. Duan, Z. Zhou, J. Weng and J. Wang, *RSC Adv.*, 2016, **6**, 102444.
174. J. Xu, G. Wang, J. Fan, B. Liu, S. Cao and J. Yu, *J. Power Sources*, 2015, **274**, 77.
175. Z. Yuan, R. Tang, Y. Zhang and L. Yin, *J. Alloys Compd.*, 2017, **691**, 983.
176. C. Wu, G. Li, X. Cao, B. Lei and X. Gao, *Green Energy Environ.*, 2017, **2**, 302.
177. W. Zhang, H. Lei, S. Yao and H. Wang, *J. Mater. Sci.: Mater. Electron.*, 2019, **30**, 9861.
178. H. Mouridsen, J. Witten, P. Frederiksen and I. Hulsbaek, *Acta Pharmacol. Toxicol.*, 1978, **43**, 328.

179. L. L. Jiang, Z. K. Wang, M. Li, C. C. Zhang, Q. Q. Ye, K. H. Hu, D. Z. Lu, P. F. Fang and L. S. Liao, *Adv. Funct. Mater.*, 2018, **28**, 1705875.
180. X. Wei, X. Liu, H. Liu, S. Yang, H. Zeng, F. Meng, X. Lei and J. Liu, *Sol. Energy*, 2019, **181**, 161.
181. E. Bi, W. Tang, H. Chen, Y. Wang, J. Barbaud, T. Wu, W. Kong, P. Tu, H. Zhu and X. Zeng, *Joule*, 2019, **3**, 2748.
182. S. Pareek, S. Waheed, P. Sharma and S. Karak, *Mater. Charact.*, 2020, **169**, 110646.
183. S. Pareek, S. Waheed, A. Rana, P. Sharma and S. Karak, *Nano Express*, 2020, **1**, 010057.
184. Z. Li, S. Wu, J. Zhang, Y. Yuan, Z. Wang and Z. Zhu, *Sol. RRL*, 2020, **4**, 1900413.
185. Z. Liu, S. Wu, X. Yang, Y. Zhou, J. Jin, J. Sun, L. Zhao and S. Wang, *Nanoscale Adv.*, 2020, **2**, 5396.
186. W. Li, Q. Chen and Q. Zhong, *J. Mater. Sci.*, 2020, **55**, 10712.
187. Y. Wang, J. Sun, J. Li and X. Zhao, *Langmuir*, 2017, **33**, 4694.
188. Y. Zhang, J. Zhou, Q. Feng, X. Chen and Z. Hu, *Chemosphere*, 2018, **212**, 523.
189. H. Wang, X. Yuan, H. Wang, X. Chen, Z. Wu, L. Jiang, W. Xiong and G. Zeng, *Appl. Catal., B*, 2016, **193**, 36.
190. M. Shi, P. Xiao, J. Lang, C. Yan and X. Yan, *Adv. Sci.*, 2020, **7**, 1901975.
191. H. Wang, Y. Li, C. Li, K. Deng, Z. Wang, Y. Xu, X. Li, H. Xue and L. Wang, *J. Mater. Chem. A*, 2019, **7**, 801.
192. S. Lu, K. Eid, D. Ge, J. Guo, L. Wang, H. Wang and H. Gu, *Nanoscale*, 2017, **9**, 1033.
193. K. Eid, H. Wang, V. Malgras, S. M. Alshehri, T. Ahamad, Y. Yamauchi and L. Wang, *J. Electroanal. Chem.*, 2016, **779**, 250.
194. H. Wang, S. Yin, K. Eid, Y. Li, Y. Xu, X. Li, H. Xue and L. Wang, *ACS Sustainable Chem. Eng.*, 2018, **6**, 11768.
195. H. Zhang, H. Wang, K. Eid and L. Wang, *Part. Part. Syst. Charact.*, 2015, **32**, 863.
196. C. Wei, H. Wang, K. Eid, J. Kim, J. H. Kim, Z. A. Alothman, Y. Yamauchi and L. Wang, *Chem. - Eur. J.*, 2017, **23**, 637.
197. H. I. Abdu, K. Eid, A. M. Abdullah and X. Lu, *Data Brief*, 2020, **30**, 105520.
198. K. Eid, M. H. Sliem, A. S. Eldesoky and A. M. Abdullah, *Data Brief*, 2019, **27**, 104734.
199. K. Eid and A. M. Abdullah, *Data Brief*, 2019, **26**, 104495.
200. X. Xu, T. Yang, Q. Zhang, W. Xia, Z. Ding, K. Eid, A. M. Abdullah, M. S. A. Hossain, S. Zhang and J. Tang, *Chem. Eng. J.*, 2020, **390**, 124493.
201. K. Jlassi, K. Eid, M. H. Sliem, A. M. Abdullah, M. M. Chehimi and I. Krupa, *Environ. Sci. Eur.*, 2020, **32**, 1.
202. Y. Ibrahim, A. Kassab, K. Eid, A. M. Abdullah, K. I. Ozoemena and A. Elzatahry, *Nanomaterials*, 2020, **10**, 885.

CHAPTER 7

Hybrid Graphitic Carbon Nitride (gCN)-based Devices for Energy Storage and Production

MOUSTAFA M. ZAGHO[a], YASSEEN S. IBRAHIM[b] AND AHMED A. ELZATAHRY*[b]

[a]School of Polymer Science and Engineering, University of Southern Mississippi, Hattiesburg, MS 39406, USA; [b]Materials Science and Technology Program, College of Arts and Sciences, Qatar University, Doha 2713, Qatar
*E-mail: aelzatahry@qu.edu.qa

7.1 Introduction

To facilitate the accessibility of clean energy, the design of innovative materials to store and produce energy for continuous usage is crucial.[1–3] The increasing demands for, but reducing supply of, old-style batteries and fuel cells have motivated research to develop environmentally-friendly, abundant, and cheap energy storage and production devices.[1] Different catalysts or materials' electrodes have been used to enhance the storage and production efficiencies. Graphitic carbon nitride (gCN)-based devices have attracted attention due to their interesting characteristics, structures, and performance.[1,4,5] Graphitic carbon nitrides (gCNs) are one of the earliest used synthetic polymers in the scientific arena and have various chemical and structural properties. Some current reports in the literature have been described as reporting on g-C_3N_4 materials; however, this is not always the

Nanoscience & Nanotechnology Series No. 51
Carbon Nitride Nanostructures for Sustainable Energy Production and Environmental Remediation
Edited by Kamel Abdelmoniem Mohamed Eid and Aboubakr M. Abdullah

Published by the Royal Society of Chemistry, www.rsc.org

case. Most of the compounds discussed do not have a ratio 3:4 for C:N. They usually contain large contents of O and H atoms.[6] gCNs attract interest as robust metal-free compounds. An exciting class of gCNs involves graphene-like carbons, graphitic carbon, or carbon nanotubes. They possess metallic properties[7,8] and can be synthesized with different N content.[7,9] The largest CNs class includes various polymeric or graphitic systems with chemical compositions between C_3N_4 and C_2N_3H in the phase diagram of ternary C–N–H.[1] They can be synthesized by condensing melamine, urea, or dicyandiamide following thermal treatment at 500–700 °C.[10] Research into these compounds has become a fascinating hotspot in different fields, including water purification,[11,12] photocatalysis,[13–15] fuel cells,[16,17] and gas conversion reactions, on account of the facile preparation, earth-abundant nitrogen (N) and carbon (C), and environmentally–friendly properties.[18–27]

This chapter highlights the recent progress in the rational design of gCN-based devices for energy production and storage applications. This includes fabrication of gCN-hybrids with carbon materials, metal oxides, and metal sulfide for Li–S batteries (LSBs), Li-ion batteries (LIBs), and supercapacitors. The current challenges and future perspectives of gCN-based energy production devices are also discussed.

7.2 Synthesis of Graphitic Carbon Nitrides

For the chemical preparation of gCNs, most reactive oxygen-free and nitrogen-rich compounds containing a pre-bonded N–C core structure, such as heptazine and triazine derivatives, are highly explosive, unstable, and difficult to obtain. Because of the low thermodynamic stability of gCNs, the preparation of single-phase sp^3-hybridized CNs is a challenging approach.[29,30] Condensation or polymerization of cyanamide, dicyandiamide, or melamine represents a facile and efficient technique to design slightly defective gCN-based devices.[31] The reactivities, properties, and condensation degrees of gCNs can be controlled by reaction conditions. Highly ordered melon with pendant amino groups can be prepared.[31] Based on tri-*s*-triazine moieties as elementary building blocks, further reaction forms less defective and more condensed gCNs. Different nanoparticles and mesoporous structures can be synthesized due to the liquid precursor's polymerization. Additionally, those nanostructures represent a surface-rich candidate for heterogeneous reactions and they permit tuning of properties. gCNs display superior catalytic activity for different processes, including trimerization reactions and CO_2 and benzene activations. The cyanamide precursor is transformed to gCN at 550 °C with consequent NH_3 formation. The preparation process can be conducted in air or an inert atmosphere, with no remarkable structural alterations but may result in changes in surface properties, condensation degree, and product yield. The condensation process and temperature can be promoted by conducting the preparation process in a basic environment such as aqueous NaOH.[32] Pure gCNs can be prepared at 500 °C when the cyanamide precursor is pretreated with aqueous NaOH. The hydroxyl ions facilitate cyanamide transformation to gCN, presumably by reacting the hydroxyl ions with the hydrogen atoms on the intermediate edges.

Furthermore, the material surface area can be promoted by reducing the condensation temperature. gCNs are still far from commercial use because of their insolubility in most solvents, chemical inertness, and relatively low electrical conductivity. Hence, more studies are needed to design gCN-based hybrids for more potential applications. For improved performance and unique properties, hybrid gCNs are fabricated. Many strategies are used to design hybrid gCNs for advanced energy storage performance. Based on the aforementioned concepts, this chapter discusses the rational synthesis of hybrid gCN-based devices for storage of energy applications, involving supercapacitors, Li-ion and Li–S batteries.

7.3 Hybrid Graphitic Carbon Nitride-based Devices for Energy Storage

With dramatically varying climate changes and global concerns about environmental pollution, there are great demands for developing reliable and cleaner energy sources. To meet such demands, it is necessary to design promising energy storage devices. Supercapacitors and batteries have gained attention due to their unique characteristics, as discussed in the upcoming sections.

7.3.1 Supercapacitors

Supercapacitors exhibit exciting characteristics such as long cycle life, high current capability, and high efficiency,[44] whereas high discharge rate and gradual voltage loss represent significant disadvantages. gCNs have opened a new arena in supercapacitor applications due to their metal-free properties, N-rich structure, and environmental-friendliness. Compared to other materials, gCNs' usage in supercapacitor devices is limited due to their comparatively lower electronic conductivity and surface area.[45] Thus, great efforts are being devoted to overcome this limitation. The supercapacitance efficiency of gCNs can be improved by integrating carbon-based materials, metal oxides/hydroxides, or metal sulfides, which increase the active sites and facilitate the faradaic reaction.[46] Thus, the following sections address several hybrid gCN-based devices with improved supercapacitor efficiency.

7.3.1.1 Carbon-based Materials/gCN Hybrids

The hydrothermal treatment method can be used in the design of grafted-gCN hybrids with 3D morphology and promising electrochemical behavior as efficient electrodes for supercapacitors. For instance, Chen *et al.*[28] functionalized gCNs with graphene to design 3D gCN/graphene hybrids using one-step hydrothermal reduction. The preparation of this hybrid was demonstrated in Figure 7.1a. The SEM images in Figure 7.1c and d show the uniform dispersion of gCN in the hybrid and graphene basal planes without aggregates, which is also revealed in Figure 7.1e. Notably, the hybrid was fabricated by the hydrothermal reduction of graphene oxide (GO) and gCN sheets.

The resultant hybrid was then put in a closed autoclave at 180 °C, and the final 3D structure (see Figure 7.1b) was obtained through lyophilization. The composite's super-capacitive behavior was evaluated by designing a symmetrical supercapacitor (see Figure 7.2a). Two slices of gCN@G electrode that were cut from the cylindrical hybrid material were separated by wet filter paper of

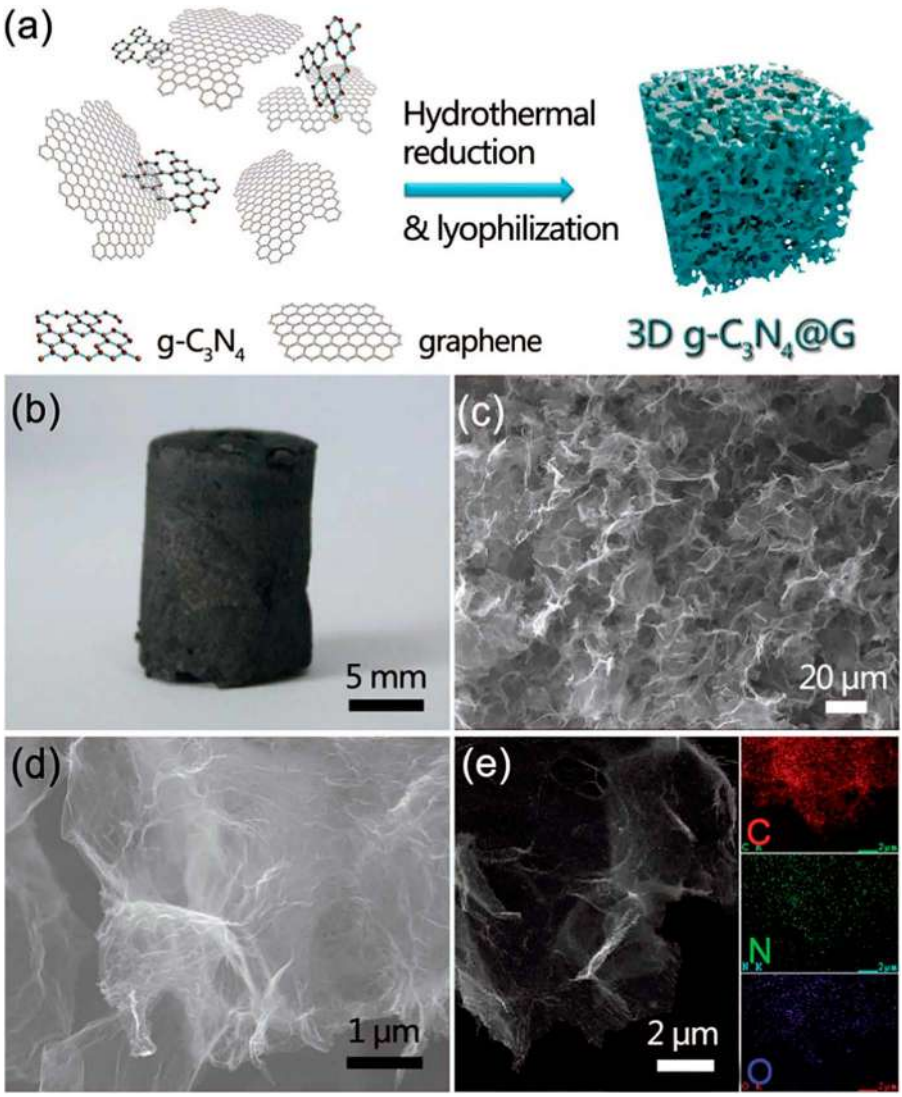

Figure 7.1 (a) Fabrication of a 3D gCN/graphene hybrid. (b) Photograph of a gCN/graphene hybrid. (c) SEM picture of a gCN/graphene hybrid. (d) The magnified SEM image of (c). (e) EDS elemental mapping of a 3D gCN/graphene hybrid. Reproduced from ref. 28 with permission from the Royal Society of Chemistry.

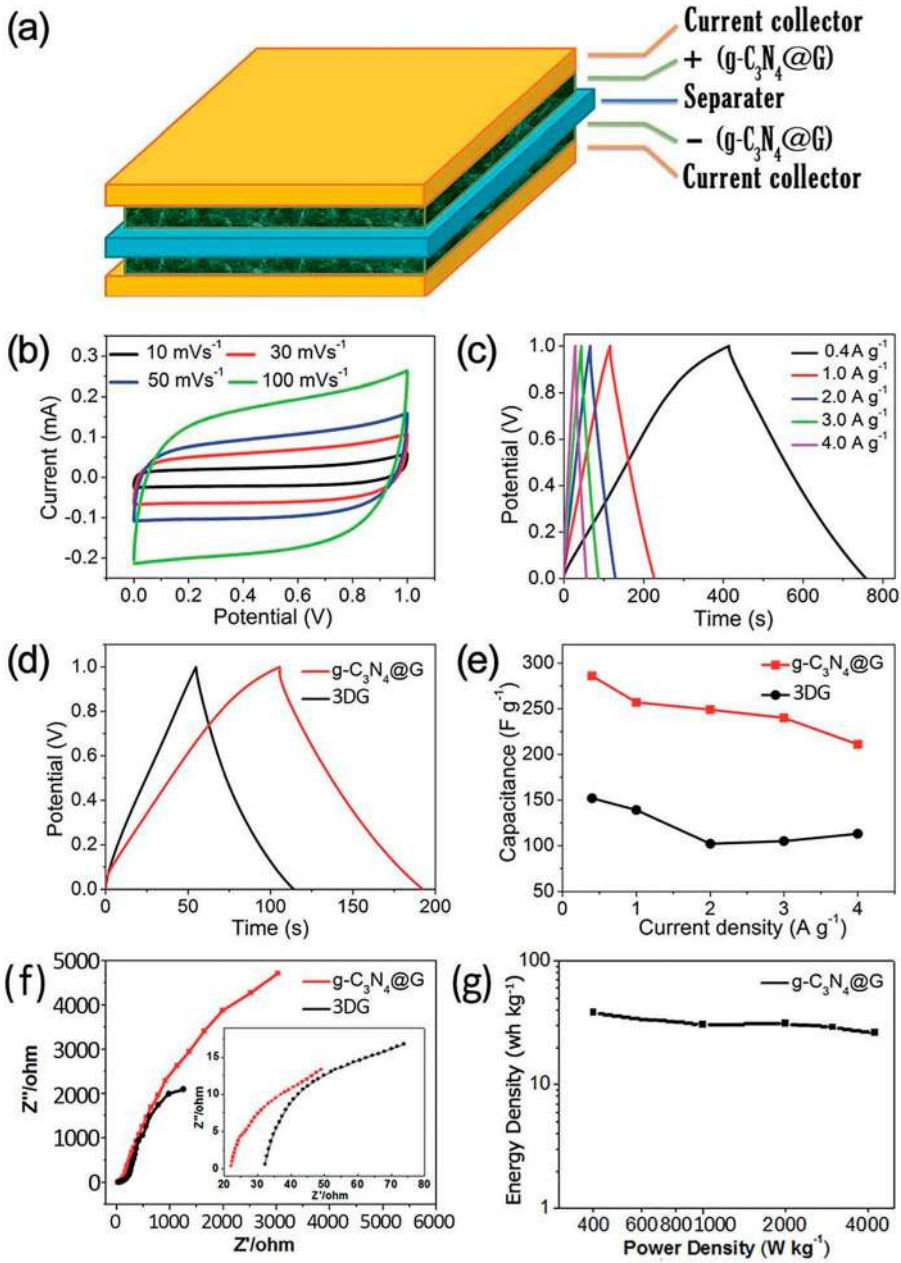

Figure 7.2 (a) Demonstration of a gCN/graphene supercapacitor device. (b) Curves for CV under different scanning rates. (c) Charge–discharge plot. (d) Charge–discharge plot of graphene and gCN/graphene hybrid at 1.0 A g^{-1}. (e) Capacitance. (f) Nyquist plots measured at open-circuit conditions. The inset image displays the high-frequency region. (g) Ragone plot of a gCN/graphene-based supercapacitor. Reproduced from ref. 28 with permission from the Royal Society of Chemistry.

(0.1 M) electrolyte and therefore gathered in a two-electrode system with gold flakes as the current collector. It was realized that the incorporation of gCN was beneficial in minimizing the creation of graphene aggregates, resulting in improved cycle performance and charge/discharge curves (see Figure 7.1c and d). The hybrid displayed great cyclic stability and an improved capacitance of 264 F g^{-1} with > 75% enhancement over the supercapacitor designed from neat 3D graphene electrodes (152 F g^{-1}) (see Figure 7.2e). Both gCN@G and 3D graphene showed almost an ideal capacitive behavior with a slightly lower equivalent series resistance for gCN@G in the electrochemical impedance spectroscopy plot (see Figure 7.2f). The Ragone plot indicates that a high power and energy density supercapacitor can function using gCN@G material (see Figure 7.2g). Table 7.1 summarizes the specific capacitance (C_m) of various 3D graphene-based materials' supercapacitors.[28] Furthermore, Wen *et al.*[4] designed reduced graphene oxide (rGO)/gCN hybrids for supercapacitors with improved power and energy densities. A facile hydrothermal method was applied to prepare the gCN/rGO hybrid. Typically, the GO/gCN nanosheets mixture was sonicated and then autoclaved at 180 °C. The hybrid displayed a great capacitance of 288 F g^{-1}. The electrodes were assembled by adding the slurry onto the nickel foam and dried at 60 °C. Afterwards, they were pressed at 10 MPa. The two electrodes were pressed together and separated by a cellulose. The supercapacitor offered a long cycling life along with a 5% decrease in its initial specific capacitance after 5000 cycles and an energy density about 36.6 W h kg^{-1} at 480 W kg^{-1}. This approach can be applied to the design of many promising electrodes for energy storage systems.

Table 7.1 Specific capacitance (C_m) of various 3D graphene-based materials' supercapacitors. Reproduced from ref. 28 with permission from the Royal Society of Chemistry.

No.	Category	Electrode materials	C_m (F g^{-1})	Reference
1		3D g-C_3N_4@G	264	28
2		Ag nanoparticles decorated 3D graphene	110	33
3		Graphene–polyoxometalate	123	34
4	Graphene–metal oxide	In_2O_3/reduced graphene oxide	178	35
5		Graphene/MnO2	216	36
6		G@$Ni(OH)_2$ and porous graphene	218.4	37
7		3D graphene/MnO_2 hydrogel	242	38
8	Graphene–organic/polymer	Functionalized graphene foam with pyrene carboxylic acid	133	39
9		Surfactant-modified reduced graphene oxide	168	40
10		3D graphene/polypyrrole nanotube hybrid aerogel	253	41
11		3D N-doped G-CNT networks	180	42
12		Fullerene (C60)/graphene composite	135	43

Moreover, Ding *et al.*[48] self-assembled gCN with GO using a solvothermal method at 180 °C to obtain a 3D porous structure, which offers rapid access for electrolytes and good mobility for electrons. The electrode was produced by blending the hybrid material, polytetrafluoroethylene, and acetylene in a mass ratio of 70 : 5:25 with ethanol. Each pair of electrodes was immersed in 6 M KOH for 24 h. The electrodes were assembled in a two-electrode system consisting of two electrodes, two stainless steel current collectors, and a porous separator. Beneath the optimum C-repairing loading of 5.99 atomic %, the hybrid provided 379.7 F g^{-1} specific capacity and 52.7 W h kg^{-1} at 0.25 A g^{-1} current density.

Recently, Lu *et al.*[47] reported a bottom-up preparation of ultra-thin 2D hybrids, which may favor the use of gCNs in energy storage applications (see Figures 7.3–7.5). They described an ultra-thin conductive gCN assembly using a graphene-templated van der Waals epitaxy approach toward advanced

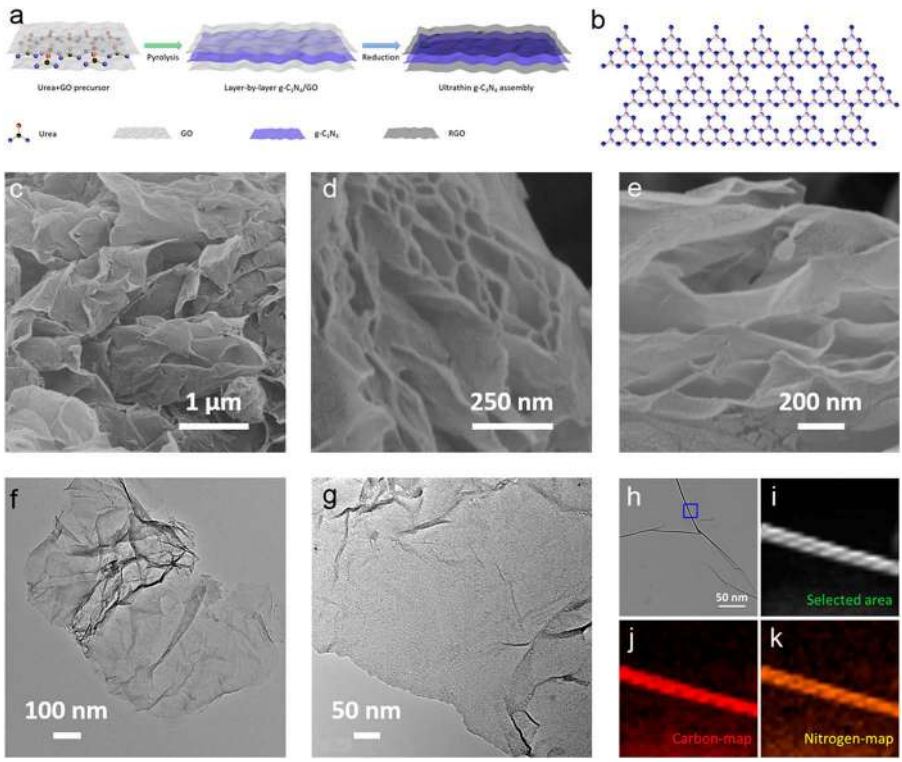

Figure 7.3 (a) Preparation of a thin layer of gCN assembly. (b) Model (ball–stick) of gCN. Pink and blue balls demonstrate nitrogen and carbon atoms, respectively. (c–e) SEM pictures of gCN assembly. (f–h) TEM pictures of gCN assembly. (i–k) TEM pictures of gCN assembly in the square region in image h and EDX mappings for C and N elements, respectively. Reproduced from ref. 47 with permission from American Chemical Society, Copyright 2019.

supercapacitors. The synthesis of the ultra-thin gCN assembly is demonstrated in Figure 7.3a. Lu *et al.* dispersed urea powder into GO through ultrasonication. The interactions of GO with urea go through H-bond formation. The uniform dispersion was beneficial for the following pyrolysis method. The precursor was transferred into a crucible under Ar flow and heated at 550 °C. Afterwards, the precursor was heated at 800 °C at 5 °C min^{-1} rate for 2 h. The hybrid was finally collected after HI acid reduction treatment. The chemical structure of gCN is shown in Figure 7.3b. SEM images (see Figure 7.3c–e) showed the layered morphology of the gCN assembly. TEM images in Figure 7.3f–h displayed the ultra-thin 2D planar morphology. Figure 7.3i–k reveals that the N and C atoms were evenly distributed. The hybrid displayed a pore size of 5.3 nm, is highly conductive at 12.2 S cm^{-1}, has a high surface area of 724.9 m^2 g^{-1}, and a N-doping content of ~18.3%. Notably, a 60 mg hybrid was dispersed in *N*,*N*-dimethylformamide, then filtered onto a polyvinylidene difluoride membrane. After that, the film was dried at 70 °C. The supercapacitor was produced by laminating two electrode films with polyelectrolyte film *via* a hot pressing method with 120 MPa and 180 °C. A sketch of the supercapacitor assembly procedure is shown in Figure 7.4a. In this design, the ultra-thin morphology with N-doping offered abundant active sites and

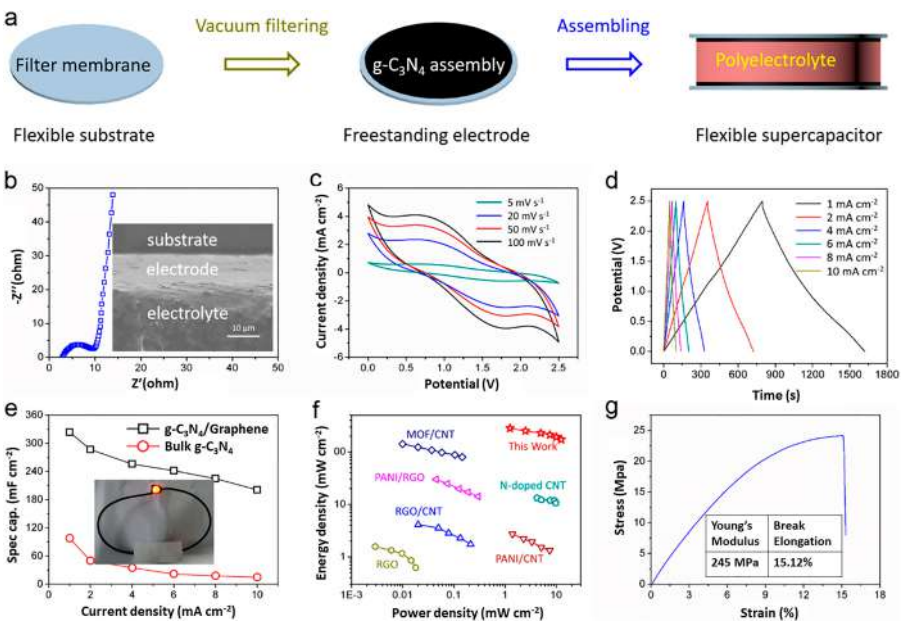

Figure 7.4 Electrochemical performance of a gCN-assembly-based supercapacitor. (a) Supercapacitor preparation steps. (b) EIS curve for the prepared gCN-based device. The inset shows the SEM cross-section. (c) CV of the supercapacitor at different rates. (d) Charge–discharge plot of the device at different density of current. (e) Capacitances per area of the supercapacitor at various current densities. Inset picture displays light (LED) turned on by the capacitor. (f) Ragone scheme for the device in comparison with previous reported devices. (g) Stress–strain plot. Reproduced from ref. 47 with permission from American Chemical Society, Copyright 2019.

paths for enhanced ion transportation and energy storage. At the same time, graphene layers played a role as micro-current collectors. The Nyquist plot confirms a good contact interface and excellent conductivity as the equivalent resistance is 9.7 ohm (see Figure 7.4b). Both the charge–discharge and CV plots were utilized to estimate the energy storage characteristics of the device. Figure 7.4c displays disordered cyclic voltammetry curves revealing a standard pseudocapacitive performance of the electrode. The charge–discharge plot affirms good coulombic efficiency (see Figure 7.4d). A superior specific capacitance is owing to the g-CN assembly-based device of 324 mF cm^{-1} at 1 mA cm^{-1}, which is more than triple the bulk g-CN (see Figure 7.4e). The designed g-CN assembly-based supercapacitor device exhibited energy densities of 171.9–281.3 μW h cm^{-2} at 12.5–1.25 mW cm^{-1} power densities (see Figure 7.4f), which is higher compared to previously reported devices using nanocarbon-based materials.[49–55] Moreover, the device's flexibility was tested and displayed 245 MPa Young's modulus with 15.12% elongation before breaking down (see Figure 7.4g), which is higher than previous reports.[56–58] Owing to the device's robustness and flexibility, it can be cut easily to form film or fibers (see Figure 7.5a). For example, a prototype was designed by integrating the device into a wearable soft fabric to power up a smartwatch (see Figure 7.5b). Such work introduces a scalable method for bottom-up fabrication of 2D nano-carbon material and wearable energy applications.

Zhu *et al.*[59] designed 3D N-doped carbon-based structures with a hierarchical and porous morphology by incorporating N-doped carbon spheres (NCSs) inside the interlayer of gCN spaces' nanosheets. The NCSs were prepared

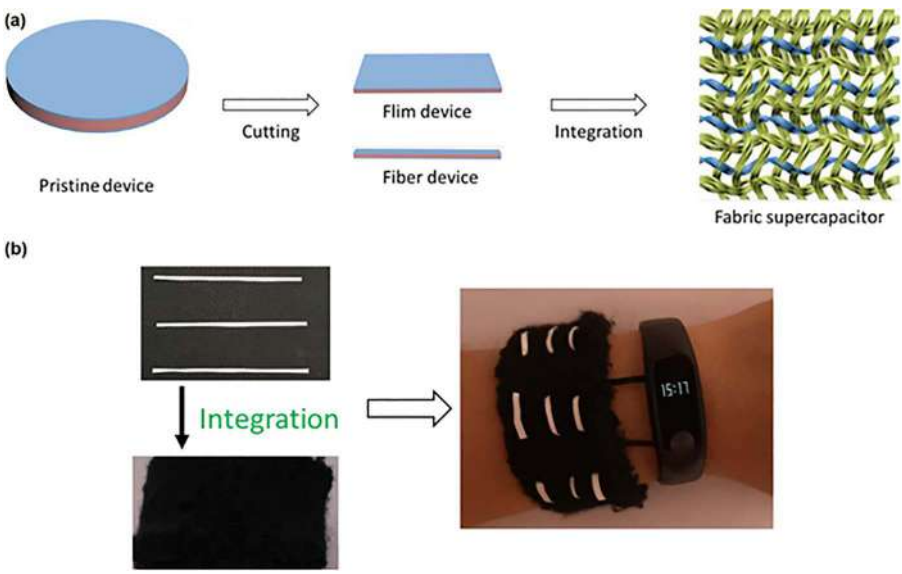

Figure 7.5 (a) Demonstration for the integration of supercapacitors. (b) Integration of flexible devices into fabrics with the capability of powering a smartwatch. Reproduced from ref. 47 with permission from American Chemical Society, Copyright 2019.

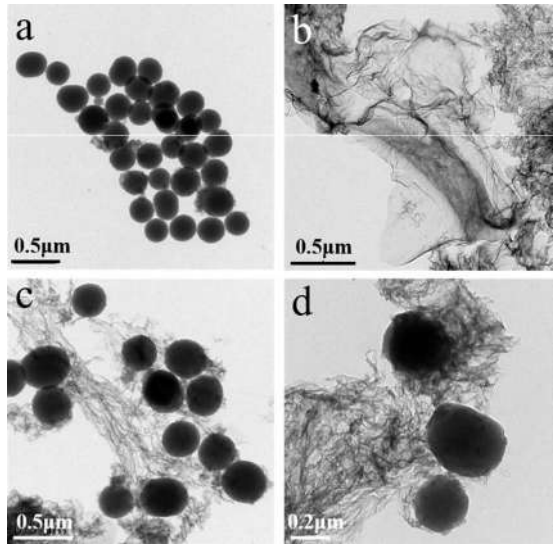

Figure 7.6 TEM pictures of (a) NCSs, (b) gCN, and (c,d) gCN/NCS hybrid using 0.125 g of NCSs. Reproduced from ref. 59 with permission from the Royal Society of Chemistry.

using dopamine hydrochloride and ammonia solution and carbonization at 750 °C, whereas the gCN was prepared from the thermal decomposition of urea and glucose. The spherical morphology of NCS and the thin sheet of gCN are displayed in TEM images in Figure 7.6a and b. The incorporation of NCS and gCN caused the latter's sheets to crumple (see Figure 7.6c and d). This unique morphology is probably due to the capture of heteroatoms from gCN,[60] consequently leading to defects, wrinkles, and pores on the gCN sheets. This characteristic feature of the hybrid plays its role in boosting the pseudocapacitance and electric double-layer capacitor. The hybrid demonstrated a high content of nitrogen and surface area of 448 $m^2\ g^{-1}$. Furthermore, the electrochemical behavior was tested in a 2032 coin-type system (see Figure 7.7a). The hybrid-based supercapacitor electrode delivered the highest capacitance of 221 $F\ g^{-1}$ at 0.1 $A\ g^{-1}$ compared to gCN (92 $F\ g^{-1}$) and NCS (154.1 $F\ g^{-1}$) (see Figure 7.7b–d). Furthermore, the composite-based electrode's capacitance maintained 85.53% of its original capacitance after 5000 cycles, indicating high stability. The hybrid's electrochemical capacitance's high performance is due to the unique morphology that increased the active sites and enhanced both the electrolyte ions' storage and diffusion rate.

7.3.1.2 Metal Oxide/gCN Hybrids

In addition to the hydrothermal method, pyrolysis can enable the design of novel gCN-based structures for energy storage applications. As a case in point, Liu *et al.*[61] prepared gCN/nanostructured α-Fe_2O_3 hybrids with improved

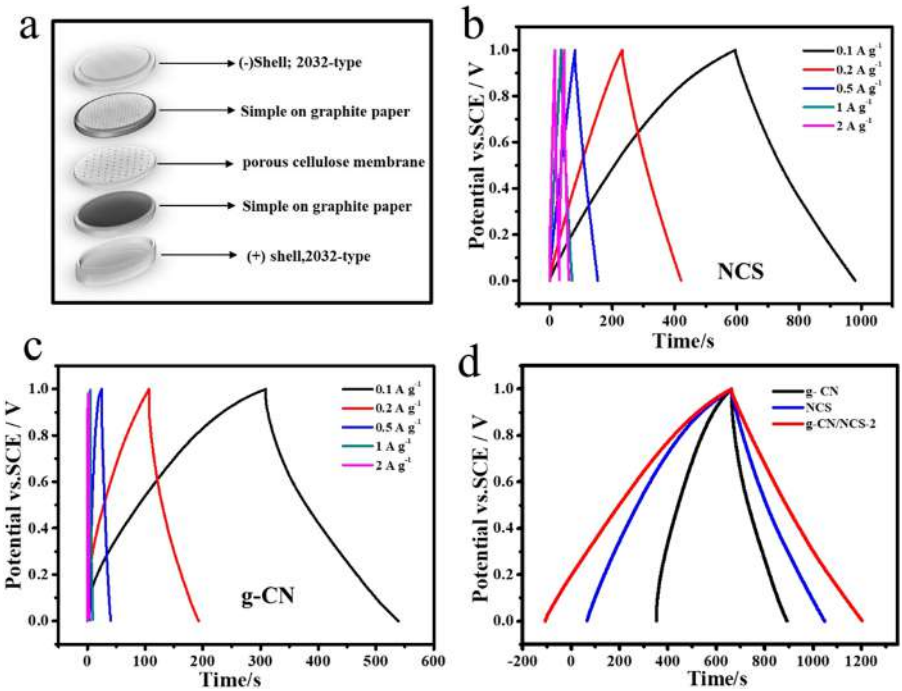

Figure 7.7 (a) A testing device of the 2032 coin-type. (b–c) Charge–discharge plots of NCSs and gCN. (d) Charge–discharge curves for NCSs, gCN, and gCN/NCS hybrid using 0.125 g of NCSs at 0.1 A g^{-1} current density. Reproduced from ref. 59 with permission from the Royal Society of Chemistry.

electrochemical behavior for advanced supercapacitors. The hybrid was synthesized by one-step pyrolysis of melamine and Prussian blue. The hybrids showed a large surface area, and the Fe_2O_3 nanoparticles effectively protected the thin gCN sheets from expanding and restacking. Figure 7.8a shows a thin sheet decorated with nanostructured α-Fe_2O_3; the inset figure (selected area electron diffraction) indicates the hybrid's polycrystalline nature. Figure 7.8b reveals two d-spacing of 0.27 and 0.25 nm, referring to 104 and 110 facets of α-Fe_2O_3. The microstructural morphology of the hybrid was studied using HAADF-STEM (see Figure 7.8c). Elemental mapping shows well-distributed elements in gCN/α-Fe_2O_3 (see Figure 7.8d). Ni-foam supported the gCN/nanostructured α-Fe_2O_3 hybrid. A slurry of hybrid material (85 wt%), polytetrafluoroethylene (5 wt%), and active carbon (10 wt%) mixed with ethanol were coated onto the nickel foam, then dried at 80 °C. The counter electrode consisted of activated carbon supported on the Ni foam surface, while the reference electrode was calomel. The composite demonstrated a synergetic effect on the improved electrochemical behavior for the supercapacitor. The cyclic voltammetry displays redox peaks referring to the anodic and cathodic sweeps of Fe(II) and Fe(III) (see Figure 7.9a), indicating the pseudocapacitive behavior of gCN/nanostructured α-Fe_2O_3. The galvanostatic charge/discharge plot is shown in Figure 7.9b at several current density values. The hybrid

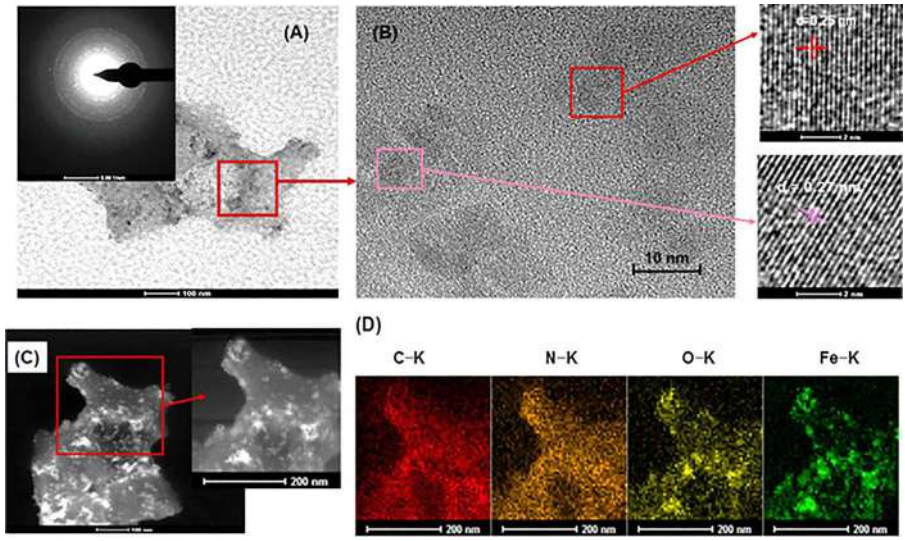

Figure 7.8 (A) HRTEM and the SAED image of the gCN/α-Fe_2O_3 hybrid. (B) FFT pattern for the gCN/α-Fe_2O_3 hybrid. (C) HAADF-STEM pictures of the gCN/α-Fe_2O_3 hybrid. (D) Elemental mappings for carbon, nitrogen, oxygen, and iron. Reproduced from ref. 61 with permission from Elsevier, Copyright 2016.

facilitated a faster faradaic reaction displaying a specific capacitance 580 F g^{-1} at 1.0 A g^{-1} (see Figure 7.9c) and good electrocatalytic activity (see Table 7.2). The hybrid also exhibited an outstanding long life cycle of about 1000 cycles at 2 A g^{-1} current density (see Figure 7.9d).

Furthermore, Vattikuti *et al.*[62] prepared C/CuO nanosphere-anchored gCN nanolayers as a ternary hybrid for supercapacitor applications. The ternary hybrid was self-assembled *via* co-pyrolysis *in situ* growth. Notably, a blend of thiourea, $CuSO_4$, and D-glucose was grounded and heated at 550 °C. The product was then rinsed with hydrazine and water. HRTEM images of C/CuO@g-CN are shown in Figure 7.10a–f. The images confirm the random distribution of spherical shapes corresponding to the carbon and CuO nanospheres (5–20 nm) anchored on the gCN sheets. The SAED pattern confirms the crystallinity of CuO (see Figure 7.10g). The hybrid was further characterized using FFt and elemental mapping to confirm its coexisting phase and the presence of its elements (see Figure 7.10h–o). The composite was first mixed with Nafion and ethanol and then dropped onto an indium-tin-oxide substrate to fabricate the working electrode. The CV curves show a higher current density and area for the hybrid than the pristine gCN (see Figure 7.11a); hence confirming the enhancement of the electrochemical results upon the incorporation of carbon and CuO with gCN. Redox peaks can be observed in Figure 7.11b, especially at high scan rates as the peak intensity increases and shifts towards more negative potential, suggesting that the capacitance is greatly dependent on the Faradaic reaction. The composite displayed a 247.2 F g^{-1} using 0.5 M sodium hydroxide with a scan rate of 1 A g^{-1},

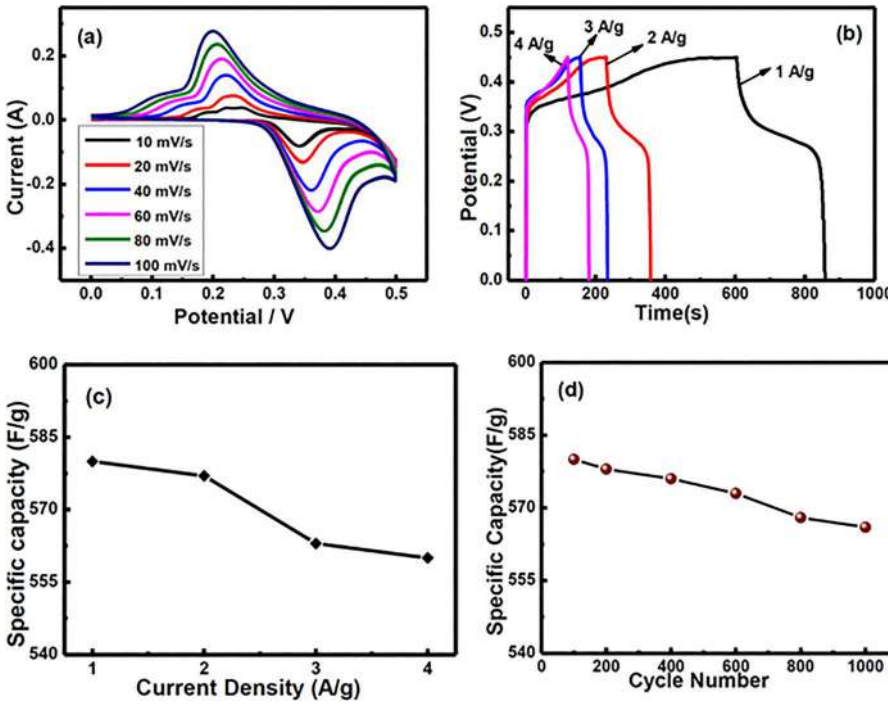

Figure 7.9 (a) Cycle voltammetry of the working electrodes at different scan rates. (b) The charge–discharge plot for the gCN/α-Fe_2O_3 hybrid electrode with current density from 1.0 to 4.0 A g^{-1}. (c) The charge/discharge of specific capacitance values of the hybrid electrode. (d) Specific capacitance *vs.* the cycle number of the hybrid electrode at 2.0 A g^{-1}. Reproduced from ref. 61 with permission from Elsevier, Copyright 2016.

Table 7.2 Electrochemical behavior of Fe_2O_3-based electrode materials in alkaline electrolyte.[61]

Fe_2O_3-based material electrodes	Electrolyte solution (1M)	Potential (V)	Capacitance per mass	Reference
$Ni(OH)_2$@α-Fe_2O_3 hybrid composites	NaOH	0–0.60	908 F g^{-1} at 21.8 A g^{-1}	63
α Fe_2O_3 nanorods	KOH	−0.05–0.45	534 F g^{-1} at 4 A g^{-1}	64
α Fe_2O_3 porous fibres	LiOH	0–0.50	348 F g^{-1} at 5 A g^{-1}	65
α Fe_2O_3 nanograins			159 F g^{-1} at 5 A g^{-1}	
α Fe_2O_3@NiO nanorod arrays	LiOH	−0.2–0.8	557 mF cm^{-2} at 1 mA cm^{-2}	66
V_2O_5-doped α-Fe_2O_3 nanotubes	KOH[a]	0–0.40	183 F g^{-1} at 1 A g^{-1}	67
α-Fe_2O_3/MnO_2 nano-heterostructures	KOH	−0.1–0.6	801 F g^{-1} at 1 A g^{-1}	68
g-C_3N_4/α-Fe_2O_3	KOH	0–0.45	580 F g^{-1} at 1 A g^{-1}	61

[a](3M)

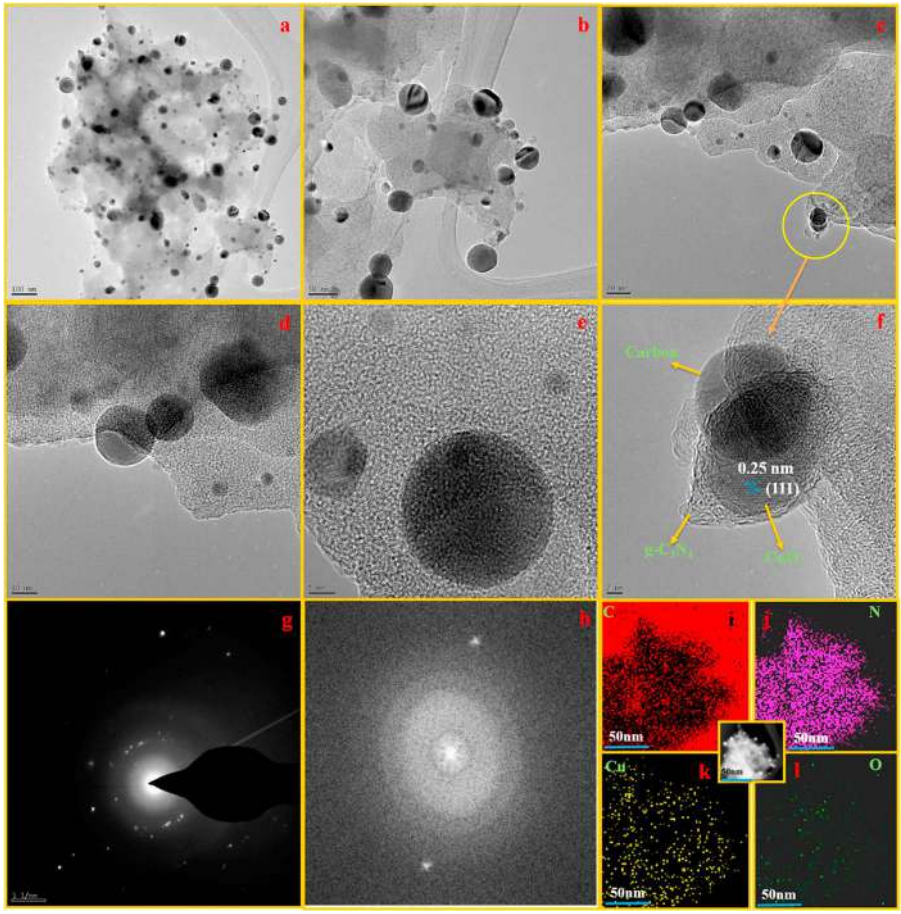

Figure 7.10 (a–f) HRTEM pictures, (g) SAED pattern, (h) FFT picture, and (i–o) elemental mapping analysis of a C/CuO@gCN composite. Reproduced from ref. 62 with permission from Elsevier, Copyright 2018.

and > 92.1% of the capacitance was reserved after 6000 cycles (see Figure 7.11d and e). Rapid transfer of charges was also observed by the C/CuO@gCN composite (see Figure 7.11f). This heterostructure's advanced performance was attributed to the presence of the inimitable heterojunctions, large surface area, as well as excellent conductivity.

Exploiting the synergistic effects of 2D/2D structures, C-doped gCN and birnessite MnO_2 were coupled by Shan *et al.*[69] to design C-doped gCN/MnO_2 hybrids with improved electrochemical efficiency for supercapacitors using the hydrothermal strategy without any surfactant. They introduced a one-pot approach to design hybrids using commercial melamine foam as a template. They used the simple hydrothermal method to decorate C-doped gCNs with

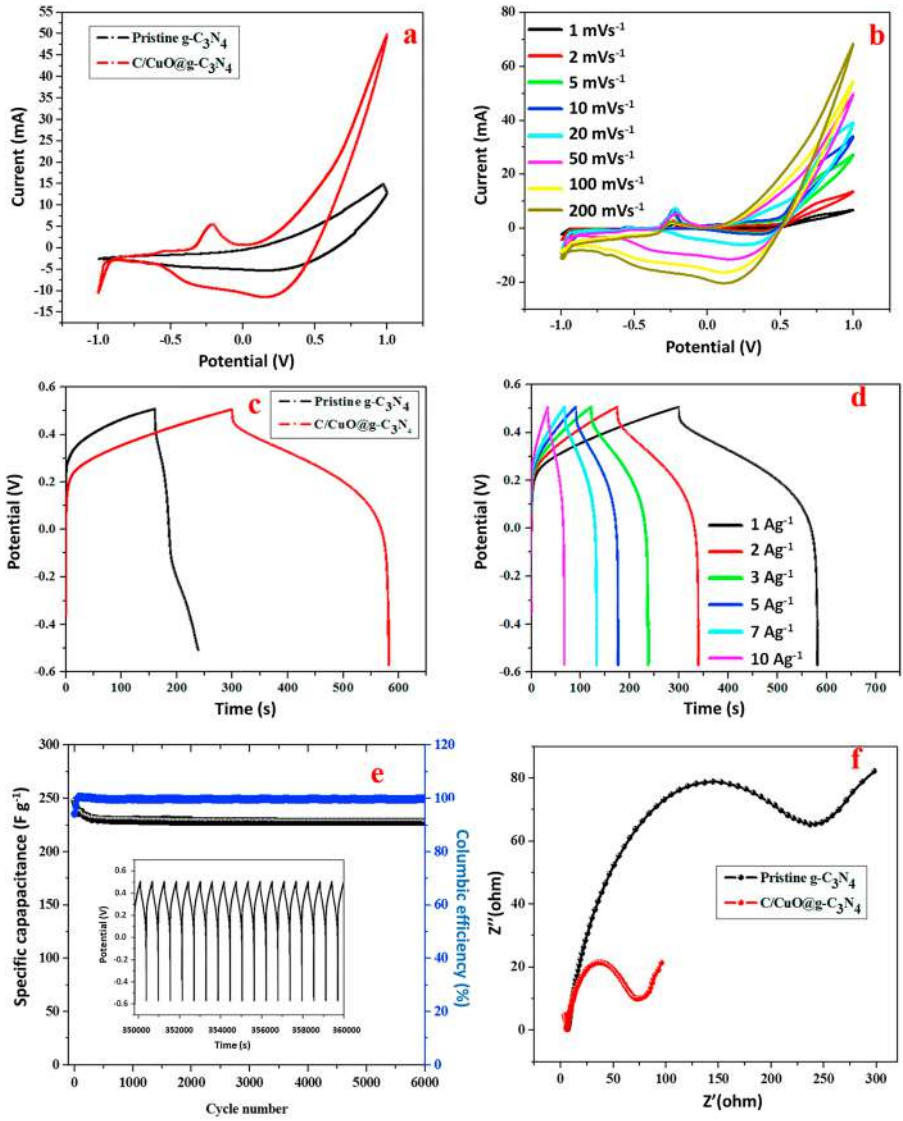

Figure 7.11 (a) CV curves of pure gCN and C/CuO@gCN composite. (b) CV curves of C/CuO@gCN composite at several scan rates. (c) Charge–discharge plot of pure gCN and C/CuO@gCN composite at 1 A g^{-1}. (d) Charge–discharge curves of the C/CuO@gCN composite at various current densities. (e) Specific capacitance retention and coulombic efficiency of a C/CuO@gCN composite. The inset shows a few immediate CD curves. (f) EIS plot of pure gCN and C/CuO@gCN composite. Reproduced from ref. 62 with permission from Elsevier, Copyright 2018.

flaky MnO_2. C-doped gCN was first dispersed in $KMnO_4$, then underwent heat treatment at 140 °C, and was then collected and dried at 60 °C. The working electrode comprised electro-active material and nickel foam as a current collector. The electro-active material consisted of hybrid, polyvinylidene

difluoride, and acetylene black with a weight ratio of 7 : 1 : 2. The C-doping was revealed to boost the rate performance of the hybrid electrode. This hybrid offered a high capacitance of 324 F g^{-1} at 0.2 A g^{-1} along with stability of 80.2% at 1000 cycles. This design could be a promising structure for cost-effective, large-scale, electrochemically stable, and environmentally-friendly supercapacitors.

Additionally, Guan *et al.*[70] directly synthesized nanoneedle and nanosheet-like porous $NiCo_2O_4$ on gCN using nickel nitrate, cobalt nitrate, ammonium fluoride, and urea. The nanoneedle-assembled $NiCo_2O_4$/gCN hybrid was obtained by transferring the nanosheet-assembled $NiCo_2O_4$/gCN hybrid into an autoclave and heated at 100 °C. The bulk morphology of the gCN (see Figure 7.12a) was decorated with nanosheets (see Figure 7.12b) and nanoneedles (see Figure 7.12c and d) of $NiCo_2O_4$. Electrochemical behavior testing demonstrated that both shapes had enhanced the capacitive behavior of gCN (see Figure 7.13a and b). Yet, the nanoneedle-assembled $NiCo_2O_4$/gCN hybrid illustrated a higher capacitance of 253 F g^{-1} using a current density of 2 A g^{-1} than the nanosheet hybrid (see Figure 7.13c and d). This advantage of the nanoneedle structure is due to (1) the flower-like and mesoporous structure that increases the active sites; (2) the spaces between the nanoneedles that enhance the diffusion rate; (3) the needle structure that offers a more efficient contact between the electrode and the electrolyte; and (4) the outstanding electric conductivity (see Figure 7.13e). In contrast, the nanosheet-assembled $NiCo_2O_4$/gCN hybrid displayed better cycling stability of 101.4% capacitance with 1000 cycles under 4 A g^{-1} (see Figure 7.13f).

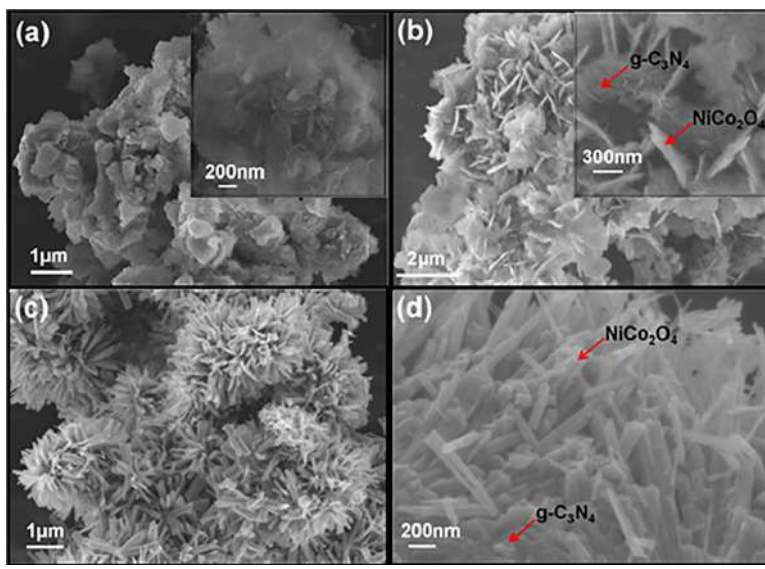

Figure 7.12 SEM images of (a) gCN, (b) nanosheet-assembled $NiCo_2O_4$/gCN hybrid, (c, d) nanoneedle-assembled $NiCo_2O_4$/gCN hybrid. Reproduced from ref. 70 with permission from Elsevier, Copyright 2016.

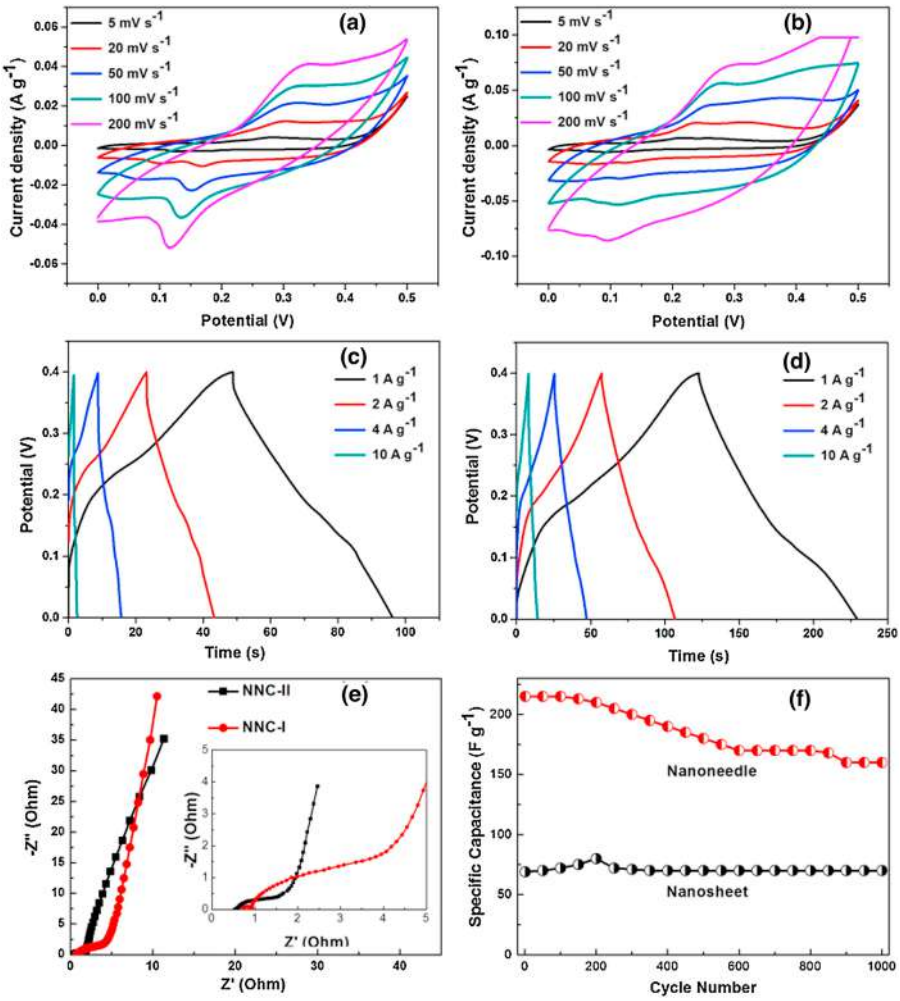

Figure 7.13 (a,b) Cyclic voltammetry plot, (c,d) charge–discharge plots, (e) EIS analysis, and (f) the change in capacitance with cycle number at 4 A g^{-1} of nanosheet-assembled $NiCo_2O_4$/gCN hybrid (a,c) and nanoneedle-assembled $NiCo_2O_4$/gCN hybrid (b,d). Reproduced from ref. 70 with permission from Elsevier, Copyright 2016.

7.3.1.3 Other gCN-based Hybrids

Using metal hydroxides, Shi *et al.*[71] designed flower-like β-$Ni(OH)_2$ hybridized gCNs for designing electrodes with excellent electrochemical efficiency. The composites were successfully prepared using the hydrothermal technique. Notably, gCN was incorporated into $Ni(CH_3COO)_2{\cdot}4H_2O$ dispersion in water. The resultant complex was then placed in an autoclave and heated at 180 °C. Pure nickel hydroxide was synthesized *via* the hydrolysis of $Ni(CH_3COO)_2{\cdot}4H_2O$ under the hydrothermal conditions of 180 °C for 8 h.

The structure of the $Ni(OH)_2$ in $Ni(OH)_2$/gCN hybrid is not the same as that of pure $Ni(OH)_2$. The hybrid showed a flower-like structure. After incorporating gCN, the $Ni(OH)_2$ nanoplates were converted to a flower-like structure. Such a 3D flower-like structure provides shorter path lengths of diffusion/transport for electrons and ions. The hybrid, carbon, and PTFE were mixed with ethanol in a 75 : 10 : 15 mass ratio to fabricate the electrode. The hybrid displayed 505.6 F g^{-1} capacitance at a current density of 0.5 A g^{-1}. The enhanced performance was ascribed to the hybrid's unique morphology and the improved adhesions between gCN and $Ni(OH)_2$. Jiang *et al.*[72] fabricated CoS/gCN hybrid nanosheets for high-performance supercapacitors by anchoring CoS on gCN sheets' surface using the solvothermal process. Typically, $CoCl_2{\cdot}6H_2O$ and CH_4N_2S were first dissolved in ethanol, and CN dispersion in ethanol was then added. The resultant complex was heat treated at 180 °C. The hybrid showed a specific capacitance up to 668 F g^{-1} at 2 A g^{-1} and 517 F g^{-1} at 10 A g^{-1} and cyclic stability with no significant decrease of capacitance after 5000 cycles. The developed behavior could be due to the facilitated ion-electron transport, high surface area, and strong interfacial adhesions.

7.3.2 Batteries

Batteries may be classified to three main classes: flow batteries, rechargeable batteries, and ultra-batteries. Rechargeable batteries can be charged and discharged several times. They are characterized by a long lifetime and low environmental impact properties. However, they suffer from large size and weight and high-cost issues. Second, flow batteries function by flowing a solution over a membrane where ions can transfer, and the Nernst equation is used to determine the voltage. They are flexible devices with lower energy densities compared to rechargeable ones. Ultra-batteries store energy with fast charging rates and high capacitance characteristics.

7.3.2.1 Lithium-ion Batteries

Although two-dimensional (2D) layered gCNs are promising candidates to be employed as anodes for lithium-ion batteries (LIBs), the pulverization and aggregation of electrodes and relatively low electrical conductivity represent major challenges for Li^+ storage. To overcome these limitations, metal oxides,[73] c-based materials,[74] and metal sulfides[75] have been incorporated, as discussed in the following sections. The enhanced Li storage efficiency is ascribed to both complementary and synergistic effects during preparation.

7.3.2.1.1 Carbon-based Materials/gCN Hybrids

Because of excellent energy density, high conductivity, nontoxicity, and low cost of carbon-based structures – including carbon nanofibers (CNFs),[76] carbon nanotubes (CNTs),[74] carbon nanosheets,[77] reduced graphene oxide

(rGO),[78] and porous carbon[79] – they are widely applied as anodes for lithium-ion batteries. Therefore, they are incorporated into gCNs for advanced Li storage performance. For instance, Tao *et al.*[76] designed P, N dual-doped CNFs/gCNs hybrids with a high reversible capacity of 1030 mA h g^{-1}, 1000 cycles at 1 A g^{-1} and a high rate capacity of 133 mA h g^{-1} at 30 A g^{-1}. For another carbon-based materials member, Subramaniyam *et al.*[80] hybridized rGO with layered gCN by the hydrothermal process. In this unique design, gCN was transformed from bulky format to sheets, then ultra-thin gCN nanosheets were sandwiched between rGO networks. The hybrid displayed a capacity of 970 mA h g^{-1} after 300 cycles, 15-fold more than that of bulk gCN. Additionally, Fu *et al.*[78] covalently coupled gCN with rGO using *in situ* polymerization of GO with the assistance of thermal reduction at high temperature. Besides, Wang *et al.*[81] designed gCN@rGO composites with rich N-active sites, large interlayer distances, and microporous structure for enhanced Li storage efficiency. A rGO hydrogel was first prepared and then mixed with urea and heated under N_2 flow. The electrical performance of gCN@rGO was tested using CV and charge/discharge curves (see Figure 7.14a and b). This hybrid offered a rate performance of 899.3 mA h g^{-1} at 350 cycles at 500 mA g^{-1} (see Figure 7.14c). In application, the hybrid was utilized in two coin-type batteries to power an electric watch and two light emitting diodes as shown in Figure 7.14d. Magnificently, the batteries ran the electronic watch continuously for over 20 days. Even after 1000 cycles, the hybrid still maintained a good cycle stability of 595.1 mA h g^{-1} under 1000 mA g^{-1} (see Figure 7.14e). A density functional theory (DFT) simulated study on using a 1D/2D CN/rGO heterostructure for lithium-ion batteries was reported by Adekoya *et al.*[82] This work showed the significance of material structure on the electrochemical performance. The DFT study revealed the occurrence of the common issue of C–N bond breakage in 2D/2D CN/graphene heterostructure. The 1D/2D CN/graphene system also displayed rapid charge transfer and high theoretical capacity, compared with the 2D/2D heterostructure.

Recently, Senthil *et al.*[83] functionalized GO nanosheets with N-rich gCN for high capacity LIBs. A single-step hydrothermal process was employed to self-assemble 2D layered gCN and GO for designing a 3D N-rich gCN/reduced GO composite. gCN and GO were mixed and heated at 180 °C. The fabricated hybrid displayed promising electrochemical behavior as an anode for LIBs with a reversible capacity of 302 mA h g^{-1} at a 5C rate and 901 mA h g^{-1} at a 0.1C rate and 99% of coulombic efficiency at a current rate of 0.5C. The GO to gCN ratio remarkably controlled the electrode performance. The vast interactions and interfaces between GO and gCN layers contributed to the enhanced Li^+ storage efficiency. The reduced GO promoted better electron mobility during electrode kinetics, and Li^+ storage and gCN layers served as spacer and substrate for ion movement. The excellent structural stability during Li^+ storage and improved charge transport can be attributed to the π–π stacking interactions.[83] For an improved performance LIB anode using ternary gCN-based hybrids, Tran *et al.*[84] designed a SnO_2 nanosheets/graphite oxide/gCN hybrid using thioglycolic acid (TGA) as a structure-directing agent for SnO_2

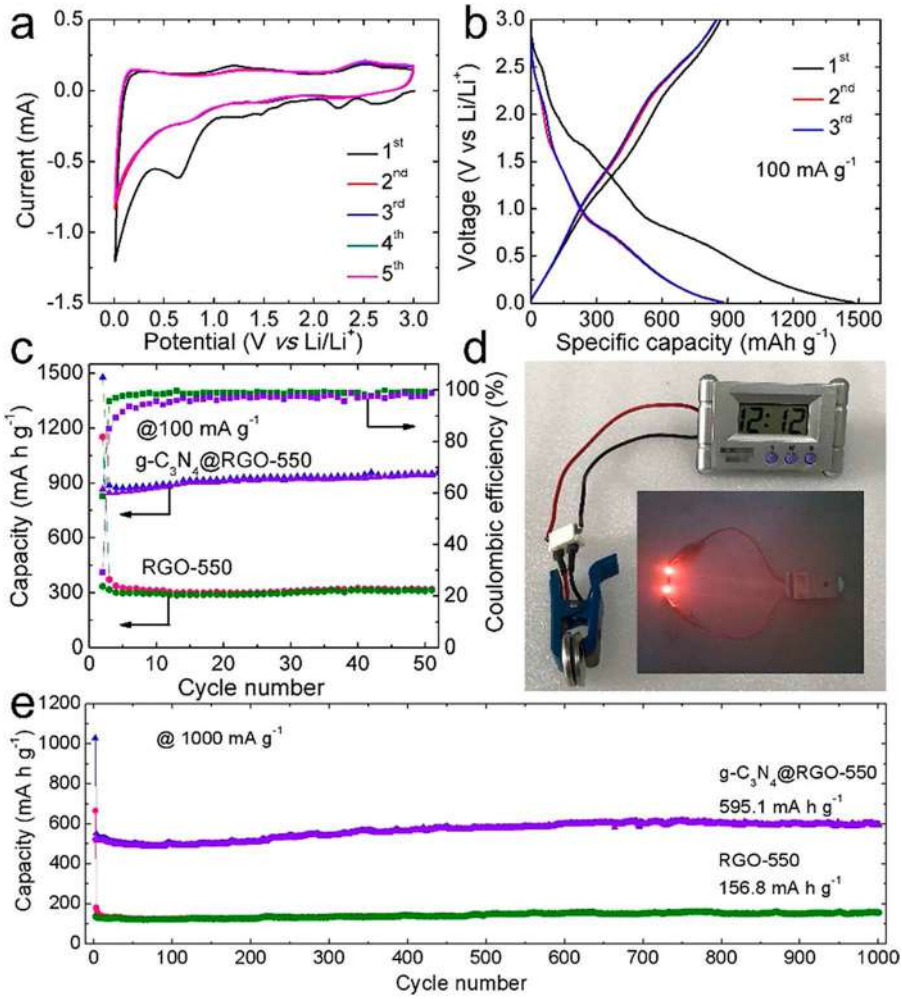

Figure 7.14 (a) CV curves of a gCN@rGO composite dried at 550 °C. (b) Discharge and charge curves of a gCN@rGO composite dried at 550 °C at 100 mA g^{-1}. (c) The cycling characteristics of a gCN@rGO composite dried at 550 °C with rGO dried at 550 °C. (d) Photograph demonstrating a coin-type half-battery (gCN@rGO composite dried at 550 °C) powering an electric watch and two red LEDs. (e) Long cycling performance of rGO dried at 550 °C and a gCN@rGO composite dried at 550 °C electrodes at 1000 mA g^{-1}. Reproduced from ref. 81 with permission from American Chemical Society, Copyright 2018.

and $SnCl_2{\cdot}2H_2O$ as a tin source. The hybrid of SnO_2 nanosheets aggregated to form a cauliflower-like structure on a graphite oxide/gCN support. The SnO_2 nanosheets/graphite oxide/gCN hybrid with the graphite oxide/gCN support improved cycling performance and rate performance (see Figure 7.15a–c). SnO_2 nanosheets/gCNs displayed the most promising results in discharge

capacities (1323.4 mA h g^{-1}) and initial coulombic efficiencies (53.6%). The cycle stability illustrates the rapid decrease for the pristine SO_2 until the 20th cycle (see Figure 7.15d), which indicates that the reduced graphene and g-CN help SO_2 maintain its sheet composition under the charge and discharge process.

7.3.2.1.2 Metal Oxide/gCN Hybrids. Enhancing the characteristics of metal oxides with gCNs is commonly done. For clarification, a Zn_2GeO_4/gCN hybrid exhibited a significant performance with a rate capability of 950 mA h g^{-1} at 2000 mA g^{-1} and a reversible capacity of 1370 mA h g^{-1} after 140 cycles.[85] This behavior is attributed to the synergy of the added ultra-thin gCN layers with Zn_2GeO_4. The hybrid was obtained by mixing gCN with $Zn(CH_3COO)_2{\cdot}2H_2O$ and Na_2GeO_3. Numerous Zn_2GeO_4 nanoparticles were homogenously coated with gCN layers.

Additionally, the same technique can be used to prepare similar hybrids, including $Li_4Ti_5O_{12}$/C,[86] SnO_2 nanosheet/gCN hybrids,[87] and anatase

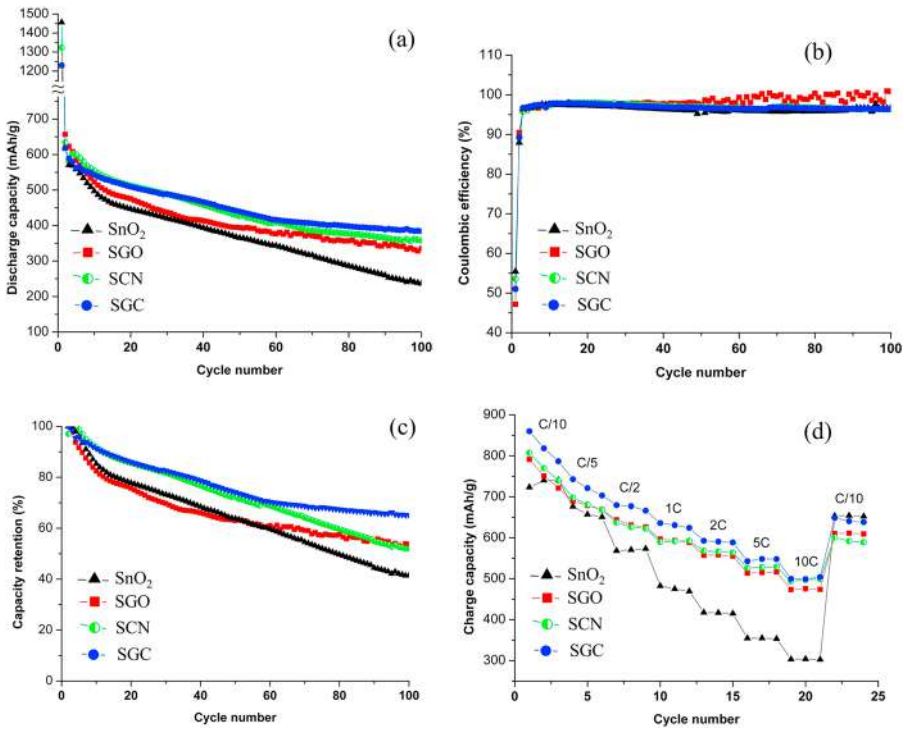

Figure 7.15 The performance of discharge capacity, Coulombic efficiency, and capacity retention per cycle (a–c) and rate performance (d) of the materials. Reproduced from ref. 84 with permission from Elsevier, Copyright 2019.

TiO_2/N-rich carbon nanosheets.[88] In particular, N-doped $Li_4Ti_5O_{12}$/C hybrids were designed by Zhou *et al.* with a reversible capacity of 122 mA h g^{-1} at 10C after 500 cycles with 102% capacity retention (see Figure 7.16a).[86] These hybrids were prepared using a large-scale solid-state reaction. Vo *et al.*[87] prepared SnO_2 nanosheet/gCN nanohybrids with improved cycling stability using a hydrothermal method. Figure 7.16b shows isolated SnO_2 nanosheets of the SnO_2 nanosheet/gCN hybrid with a 20–25 nm wall thickness. Moreover, Senthil *et al.*[88] designed TiO_2/carbon nanosheet hybrids with core–shell nanostructures using a robust self-assembly process, as demonstrated in Figure 7.16c.

Recently, Versaci *et al.*[89] described a simple strategy using gCN to enhance the rate performance of SnO_2 anodes for LIBs. Different methods, including dry and wet processes, can be used to prepare SnO_2 powders with different shapes. The complexity of the wet method represents a major challenge in scaling-up anode production using this technique. In contrast, simple solid–state processes can be accomplished at low temperatures with active carbon to avoid particles coarsening. They synthesized gCN by thermal condensation of urea and then homogenously distributed SnO_2 over the gCN phase through a scalable solid-state process to design low cost and high-power LIBs. The working electrode was fabricated by a solvent tape casting process. Notably, a slurry consisted of hybrid material with acetylene and PVD as a binder. This composite achieved good stability cycles at high rates

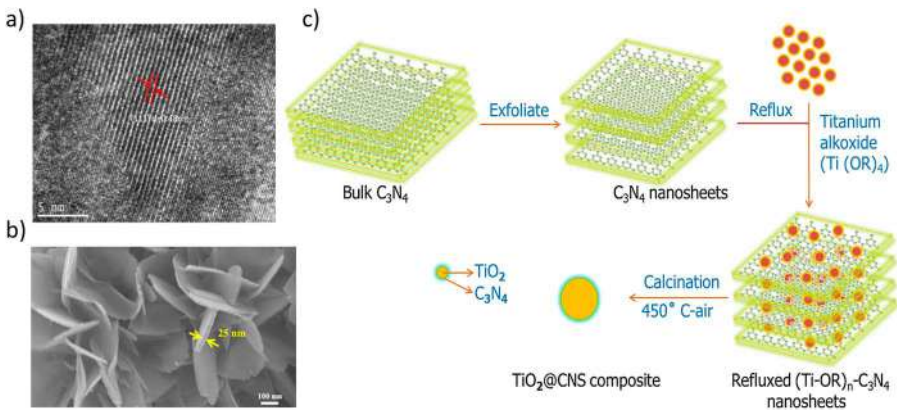

Figure 7.16 (a) TEM image of a $Li_4Ti_5O_{12}$/C hybrid calcined at 750 °C for 2 h. Reproduced from ref. 86 with permission from Elsevier, Copyright 2017. (b) SEM image of a SnO_2 nanosheet/gCN hybrid. Reproduced from ref. 87 with permission from Elsevier, Copyright 2017. (c) Synthetic scheme of anatase TiO_2/N-rich carbon nanosheet hybrids. Reproduced from ref. 88 with permission from Elsevier, Copyright 2017.

and excellent rate capability. The designed anodes (SnO_2@C_3N_4) offered high capacities of 490 mA h g^{-1} at 0.78 A g^{-1} after 100 cycles with 57% retention capacity, whereas pure SnO_2 exhibited only 130 mA h g^{-1} (see Figure 7.17a). The cycling performance was further studied at different current regimes up to 50 cycles for SnO_2@C_3N_4, as shown in Figure 7.17b. The differential capacity profile for SnO_2@C_3N_4 and pristine SnO_2 are shown in Figure 7.17c and d. For SnO_2@C_3N_4, the intensity of the cathodic peak experienced slow damping. On the other hand, several anodic peaks appeared at about the 40th cycle owing to lithiation (see Figure 7.17c). For SnO_2, all the peaks corresponding to alloying and conversion reactions experienced a significant hampering in its intensity, as shown in Figure 7.17d. The benefit of combined interaction between the g-C_3N_4 and SnO_2 for charge transfer is that it exhibited high capacity of 1075 mA h g^{-1} at 156 mA g^{-1} and retained almost 50% of the original capacity at a rate of 3.9 A g^{-1}. (see Figure 7.17e).

Iron oxide/C-based composites have been considered as potential candidates for application in LIBs. For instance, Shi *et al.*[90] designed a ternary gCN-based hybrid of porous sandwich-like hybrid nanosheets. This design

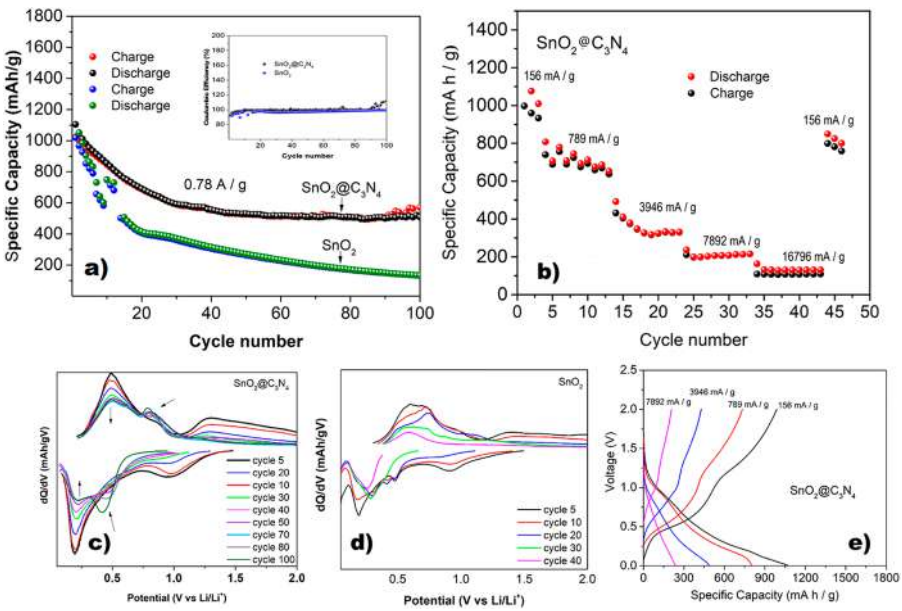

Figure 7.17 (a) Galvanostatic cycles at 0.78 A g^{-1} over the potential range against Li^+/Li of a SnO_2/gCN hybrid and pure SnO_2. (b) The rate performance of a SnO_2/gCN hybrid electrode. (c) Differential capacity profiles of a SnO_2/gCN hybrid. (d) Differential capacity plot of pure SnO_2. (e) Volt *versus* specific capacity of a SnO_2/gCN hybrid at different C rates. Reproduced from ref. 89 with permission from Elsevier, Copyright 2020.

consisted of Fe_2O_3 nanoparticles wrapped in porous gCN/graphene hybrid nanosheets. gCN was first added to a GO solution under a sonochemical process. Afterwards, $FeCl_3{\cdot}6H_2O$ and PVP were added to the suspension then heat treated at 160 °C. The highly conductive graphene provided conductive pathways and accessible channels for charge transport and ionic diffusion (see Figure 7.18a). Simultaneously, the sandwich-like design ensured the stability of Fe_2O_3 nanoparticles and inhibited the agglomeration and restacking of graphene. The LIB anode demonstrated an enhanced electrochemical behavior with a large reversible capacity of 1023 mA h g^{-1}, excellent coulombic efficiency of 97.6%, good rate performance, and good durability. This architecture striking electrochemical behavior in LIBs can be attributed to the graphene presence, active Fe_2O_3 nanoparticles, and gCN with abundant pores.

Furthermore, a simple self-assembly deposition of gCN nanosheets on a TiO_2/SnO_2 nanocomposite was prepared by Wang *et al.* to synthesize high capacity anodes for LIBs.[91] Using this strategy, gCN nanosheets uniformly coated TiO_2/SnO_2 nanoparticles. The SnO_2/TiO_2 composite was first synthesized by calcining $SnCl_2{\cdot}2H_2O$ and $TiCl_4$ as a precursor. Then, the composite was dispersed in the gCN suspension. This high-performance anode displayed a higher capacity (380.2 mA h g^{-1}) than both TiO_2/SnO_2 nanocomposite (114.1 mA h g^{-1}) and pure SnO_2 (51.6 mA h g^{-1}) at a 0.2C rate after 20 cycles. The coated nanohybrid rate test showed a slight fading of specific discharge capacities from 490 mA h g^{-1} to 330 mA h g^{-1} at a current rate range of 0.1–0.5C. Coating the TiO_2/SnO_2 nanoparticles with gCN nanosheets offered a buffer layer for the large volume change of TiO_2/SnO_2 nanocomposite during lithium intercalation. Additionally, the condensed packing of gCN nanosheets and SnO_2 and TiO_2 nanoparticles created mesopores, which offered more active sites for the Li^+ storage.

7.3.2.1.3 Molybdenum Disulfide (MoS_2)/gCN Hybrids. MoS_2/carbon-based materials are vastly applied in LIBs because of the high MoS_2 capacity of 670 mA h g^{-1}.[75,92] Therefore, MoS_2/gCN hybrids were prepared for enhanced Li storage performance. For example, a 2D hybrid with MoS_2 nanocrystals was anchored on nitrogen-rich graphene (MoS_2/NG_{gCN}) by mild temperature pyrolysis at 550 °C of a self-assembled precursor (MoS_2/gCN-H^+/GO).[93] This novel hybrid displayed a superior Li storage performance due to the coupled structure, the boosted electronic conductivity, and rich active sites. The hybrid offered rate capabilities of 1200 mA h g^{-1} at 1 A g^{-1} and 830 mA h g^{-1} at 10 A g^{-1} and good capacities with long term stability of 1450 mA h g^{-1} at 0.1 A g^{-1} for 200 cycles.

Moreover, 3D N-rich gCN/MoS_2 composites were synthesized by Senthil *et al.*[94] They designed N-rich CN/MoS_2 nanospheres from 2D materials that served as promising anodes for LIBs. Two steps synthesized the scaffold structure using ultrasonication followed by a hydrothermal process (see Figure 7.18b). The composite showed reversible capacity of 857 mA h g^{-1} at a

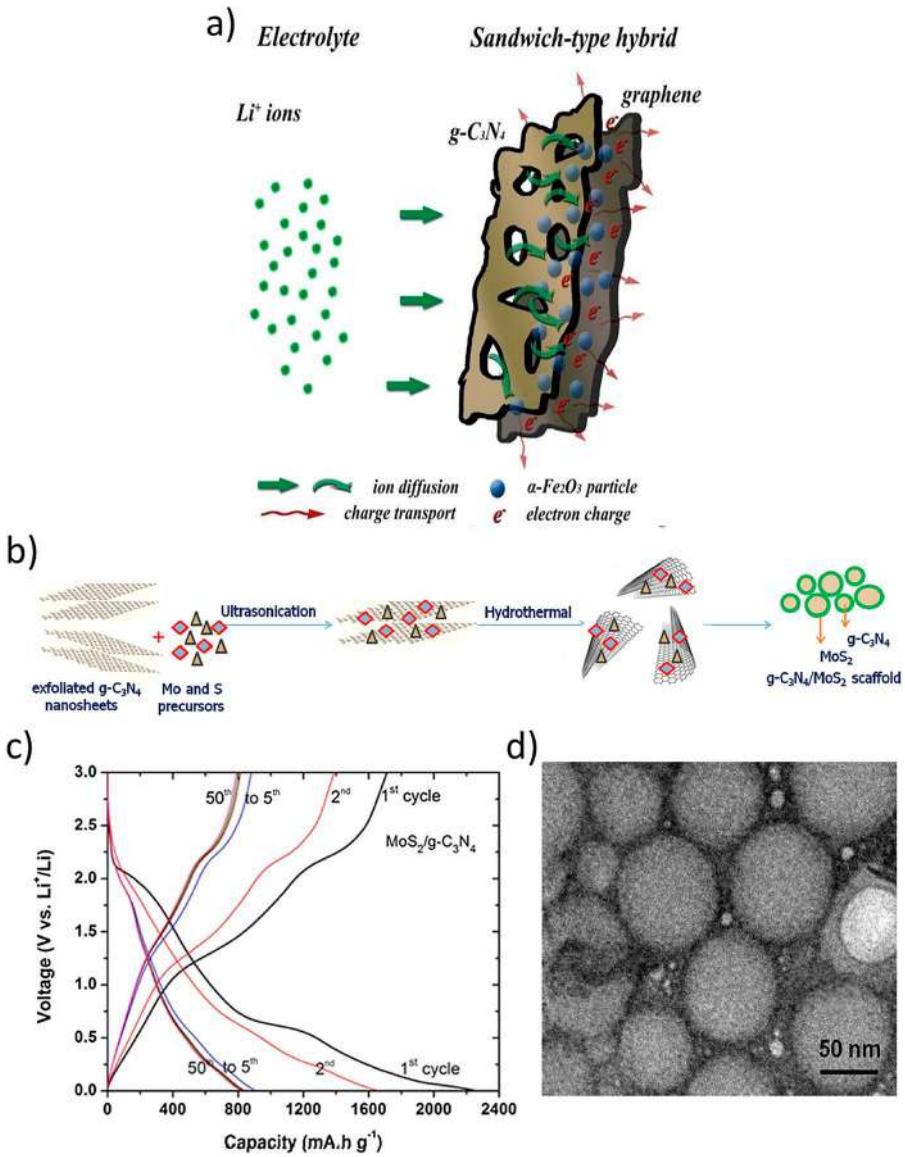

Figure 7.18 (a) Diffusivity of ions and charge transport in a porous Fe_2O_3/gCN/graphene hybrid with a 2D sandwich-like structure. Reproduced from ref. 90 with permission from the Royal Society of Chemistry, Copyright 2016. (b) Demonstrative scheme of the preparation of gCN/MoS_2 heterostructures. (c) Galvanostatic charge/discharge testing based on a gCN/MoS_2 electrode. (d) TEM image for spherical interconnected gCN encapsulated MoS_2 heterostructures. Reproduced from ref. 94 with permission from Elsevier, Copyright 2017.

0.1C rate after 50 cycles and a high performance with a reversible capacity of 383 mA h g^{-1} at a 10C rate (see Figure 7.18c), which is an enhancement compared to pure graphite. A TEM image revealed nitrogen-rich spheres covered by MoS_2 sheets creating a spherical structure (see Figure 7.18d). Recently, Tran Huu *et al.*[95] heated thiourea and sodium molybdate at 550 °C in an inert atmosphere to synthesize a MoS_2/gCN hybrid for enhanced Li storage efficiency. The composite consisted of MoS_2 nanosheets with a wall thickness of 10–15 nm and gCN in a heterojunction structure. The nanosheet design is promising for the large-scale production of innovative anodes for LIBs. The MoS_2/gCN hybrid exhibited high capacity and stable cycling behavior with a reversible capacity of 1204 mA h g^{-1} for 200 cycles, compared to 326 mA h g^{-1} for MoS_2. The gCN worked as a support to improve charge transfer and accommodate the volume change of MoS_2 nanosheets.

7.3.2.2 Lithium–sulfur Batteries

The integration of physical entrapment and chemical interactions with polysulfides could be a promising technique for advanced electrochemical behavior of lithium–sulfur batteries (LSBs). In this regard, ultra-thin sheets of a MoS_2/gCN hybrid were recently designed by Majumder *et al.*[96] The MoS_2/gCN/S hybrid was prepared *via* a melt-diffusion process. These ultra-thin sheets acted as an excellent host material with good cycling performance. The open-circuit voltage displays a rapid voltage drop of the MoS_2/gCN/S battery in the first 10 h, after that sustaining its stability at 2.4 V (see Figure 7.19a). The self-discharge curve shows 93.6% retention of the original capacity after 10 days rest (see Figure 7.19b). This novel composite exhibited a significantly reduced self-discharge compared to previous reports.[97,98] Additionally, it maintained cycling stability for 500 cycles at 1C with a 0.08% per cycle decay rate. Such results indicate the influential inhibition of self-discharge in the lithium-sulfur batteries (see Figure 7.19c). The strong interactions of lithium polysulfides provided a capacity of 430 mA h g^{-1} after 400 cycles at an 8C rate with a weak capacity rate of 0.028% per cycle. Stable cycling behavior was obtained at high sulfur content of 4.3 mg cm^{-2}. It provided excellent capacity stability with a decay rate of 0.070% per cycle after 500 cycles at 0.5C. The outstanding rate was ascribed to the high Li^+ diffusion coefficient.

Furthermore, Angamuthu *et al.*[99] designed MoS_2 anchored CN-based nanomaterials using the hydrothermal process, which traps sulfur onto the CN. Briefly, melamine was heated to 600 °C then washed with HNO_3 and distilled water to obtain CN. The as-prepared product was added to ammonium molybdate and thiourea solution, then subjected to hydrothermal treatment to form MoS_2/CN, as shown in Figure 7.19a. The interactions between MoS_2 and CN improved the surface area of the active sites. The composite has high sulfur content and excellent chemical absorption towards polysulfides. The cycling life and capacity of CN were improved by adding MoS_2. The initial charge–discharge capacity for CN was 1181 mA h g^{-1} and 1155 mA h g^{-1} at 0.5C rate at the 1st and 10th cycles (see Figure

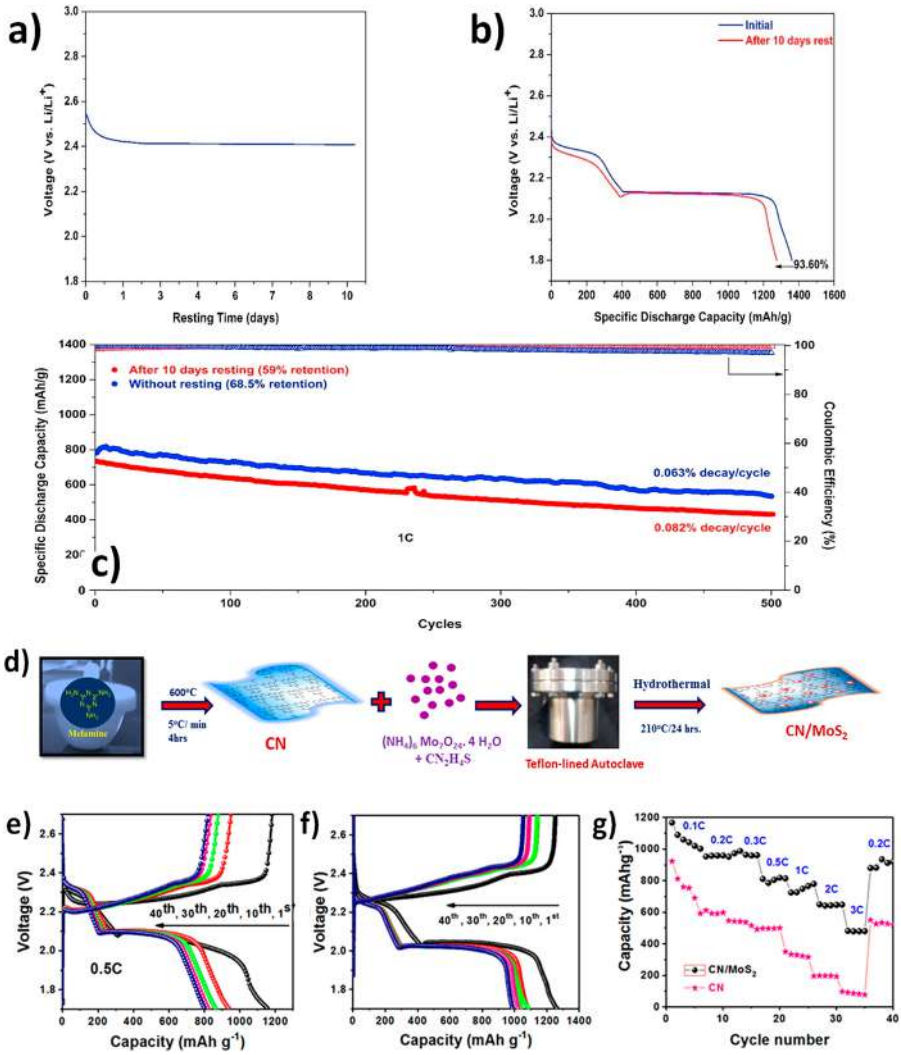

Figure 7.19 (a) Open-circuit voltage (OCV) plot demonstrating self-discharge behavior of a MoS_2/gCN/S hybrid cathode. (b) Self-discharge curves. (c) Cycling performance of a MoS_2/gCN/S cathode after 10 days rest. Reproduced from ref. 96 with permission from Elsevier, Copyright 2019. Synthesis of a MoS_2/CN hybrid, charge/discharge voltage profile of (d) CN, (e) MoS_2/CN. (f) Rate capability of CN and MoS_2/CN. Reproduced from ref. 99 with permission from Elsevier, Copyright 2019.

7.19b). In comparison, the MoS_2/CN composite displayed improvement in electrochemical behavior by exhibiting 1252 mA h g^{-1} and 1264 mA h g^{-1} at 0.5C rate at the 1st and 10th cycles and a reversible capacity of 680 mA h g^{-1} after 200 cycles (see Figure 7.19c and d). The improved cycling stability and capacity of the composite compared with the pure CN were ascribed

to the anchored MoS_2, which enhances the physicochemical and structural properties and electrochemically active surface area of the MoS_2/CN composite. After discussing the current concepts of using gCN-based hybrids for energy storage, the following sections will address their employment in energy production applications.

7.4 Conclusion and Future Perspectives

This chapter provides an updated overview of gCN-based hybrids used in supercapacitors, lithium-ion and Li–S batteries. The synthesis strategies and electrochemical performance are discussed in detail. With a unique structure analogous to graphite, gCNs have excited interest in electrochemical energy storage. The improved electrochemical behavior can be credited to the C–N–C species' high content and numerous surface defects induced by N atoms. gCN-based hybrids offer a larger surface area, enhanced catalytic activity, and better structural integrity.

To investigate more advanced electrochemical performance, future studies in the research of gCN-based hybrids could discuss the preparation of other gCN architectures with a higher surface area, such as nanorods and nanowires. Furthermore, future aims should be dedicated to the development of theoretical computational studies towards emphasizing various mechanisms of gCN-based hybrids to investigate the relationship between various electrochemical variables. The formation of gCN-based hybrid devices containing porous multi-metallic nanocrystals with their outstanding reduction and oxidation properties can enhance the performance of supercapacitors and batteries.[100–110] Likewise, carbon-based materials including fullerene, graphene oxide, carbon nanotubes, carbon dots, and metal–organic frameworks,[25–27,111–116] with their impressive electronic effect and physiochemical merits, can also improve the energy conversion and storage activity of gCN devices. Multi-dimensional core–shell rare-earth-based elements[117,118] and transition-metal oxides, transition metal carbides, or metal nitride MXenes are highly promising candidates for improving the energy production efficiency of gCN materials due to their great capacitance effect, high conductivity, and quick charge mobility.[119–121]

References

1. N. Mansor, T. S. Miller, I. Dedigama, A. B. Jorge, J. Jia, V. Brázdová, C. Mattevi, C. Gibbs, D. Hodgson, P. R. Shearing, C. A. Howard, F. Corà, M. Shaffer, D. J. L. Brett and P. F. McMillan, *Electrochim. Acta*, 2016, **222**, 44–57.
2. K. Liao, P. Mao, N. Li, M. Han, J. Yi, P. He, Y. Sun and H. Zhou, *J. Mater. Chem. A*, 2016, **4**, 5406–5409.
3. L. Zhang, S. Zheng, L. Wang, H. Tang, H. Xue, G. Wang and H. Pang, *Small*, 2017, **13**, 1700917.

4. P. Wen, P. Gong, J. Sun, J. Wang and S. Yang, *J. Mater. Chem. A*, 2015, **3**, 13874–13883.
5. Y. Huang, J. Huo, S. Dou, K. Hu and S. Wang, *RSC Adv.*, 2016, **6**, 66368–66372.
6. E. Kroke and M. Schwarz, *Coord. Chem. Rev.*, 2004, **248**, 493–532.
7. J. Shui, M. Wang, F. Du and L. Dai, *Sci. Adv.*, 2015, **1**, e1400129.
8. V. Di Noto, E. Negro, K. Vezzú, F. Bertasi and G. Nawn, *Electrochem. Soc. Interface*, 2015, **24**, 59–64.
9. H.-Y. Du, C.-H. Wang, H.-C. Hsu, S.-T. Chang, U.-S. Chen, S. C. Yen, L. C. Chen, H.-C. Shih and K. H. Chen, *Diamond Relat. Mater.*, 2008, **17**, 535–541.
10. A. Schwarzer, T. Saplinova and E. Kroke, *Coord. Chem. Rev.*, 2013, **257**, 2032–2062.
11. M. Tahir, N. Mahmood, L. Pan, Z.-F. Huang, Z. Lv, J. Zhang, F. K. Butt, G. Shen, X. Zhang, S. X. Dou and J.-J. Zou, *J. Mater. Chem. A*, 2016, **4**, 12940–12946.
12. L. Tang, C. Jia, Y. Xue, L. Li, A. Wang, G. Xu, N. Liu and M. Wu, *Appl. Catal., B*, 2017, **219**, 241–248.
13. J. Xu, S. Cao, T. Brenner, X. Yang, J. Yu, M. Antonietti and M. Shalom, *Adv. Funct. Mater.*, 2015, **25**, 6265–6271.
14. Y. Zheng, Z. Zhang and C. Li, *J. Mol. Catal. A: Chem.*, 2016, **423**, 463–471.
15. D. Lu, H. Wang, X. Zhao, K. K. Kondamareddy, J. Ding, C. Li and P. Fang, *ACS Sustainable Chem. Eng.*, 2017, **5**, 1436–1445.
16. N. Mansor, A. Belen Jorge, F. Cora, C. Gibbs, R. Jervis, P. F. McMillan, X. Wang and D. J. L. Brett, *ECS Trans.*, 2013, **58**, 1767–1778.
17. N. Mansor, A. B. Jorge, F. Corà, C. Gibbs, R. Jervis, P. F. McMillan, X. Wang and D. J. L. Brett, *J. Phys. Chem. C*, 2014, **118**, 6831–6838.
18. J. Xu, M. Antonietti and M. Shalom, *Chem. - Asian J.*, 2016, **11**, 2499–2512.
19. K. Eid, Y. H. Ahmad, A. T. Mohamed, A. G. Elsafy and S. Y. Al-Qaradawi, *Catalysts*, 2018, 11.
20. K. Eid, M. H. Sliem, H. Al-Kandari, M. A. Sharaf and A. M. Abdullah, *Langmuir*, 2019, **35**, 3421–3431.
21. K. Eid, M. H. Sliem, K. Jlassi, A. S. Eldesoky, G. G. Abdo, S. Y. Al-Qaradawi, M. A. Sharaf, A. M. Abdullah and A. A. Elzatahry, *Inorg. Chem. Commun.*, 2019, **107**, 107460.
22. K. Eid, M. H. Sliem, A. S. Eldesoky, H. Al-Kandari and A. M. Abdullah, *Int. J. Hydrogen Energy*, 2019, **44**, 17943–17953.
23. K. A. M. Eid and A. M. Abdullah, *US Pat.*, US20200239311A1, 2020.
24. K. Eid, M. H. Sliem and A. M. Abdullah, *Nanoscale*, 2019, **11**, 11755–11764.
25. M. A. Ahsan, T. He, K. Eid, A. M. Abdullah, M. L. Curry, A. Du, A. R. Puente Santiago, L. Echegoyen and J. C. Noveron, *J. Am. Chem. Soc.*, 2021, **143**, 1203–1215.
26. K. Eid and A. M. Abdullah, *Data Brief*, 2019, **26**, 104495.
27. K. Eid, M. H. Sliem, A. S. Eldesoky and A. M. Abdullah, *Data Brief*, 2019, **27**, 104734.
28. Q. Chen, Y. Zhao, X. Huang, N. Chen and L. Qu, *J. Mater. Chem. A*, 2015, **3**, 6761–6766.

29. L. Maya, D. R. Cole and E. W. Hagaman, *J. Am. Ceram. Soc.*, 1991, **74**, 1686–1688.
30. D. C. Nesting and J. V. Badding, *Chem. Mater.*, 1996, **8**, 1535–1539.
31. A. Thomas, A. Fischer, F. Goettmann, M. Antonietti, J.-O. Müller, R. Schlögl and J. M. Carlsson, *J. Mater. Chem.*, 2008, **18**, 4893–4908.
32. J. Zhu, P. Xiao, H. Li and S. A. C. Carabineiro, *ACS Appl. Mater. Interfaces*, 2014, **6**, 16449–16465.
33. A. Bello, M. Fabiane, D. Dodoo-Arhin, K. I. Ozoemena and N. Manyala, *J. Phys. Chem. Solids*, 2014, **75**, 109–114.
34. J. Suárez-Guevara, V. Ruiz and P. Gómez-Romero, *Phys. Chem. Chem. Phys.*, 2014, **16**, 20411–20414.
35. X. Xu, T. Wu, F. Xia, Y. Li, C. Zhang, L. Zhang, M. Chen, X. Li, L. Zhang, Y. Liu and J. Gao, *J. Power Sources*, 2014, **266**, 282–290.
36. G. Yu, L. Hu, N. Liu, H. Wang, M. Vosgueritchian, Y. Yang, Y. Cui and Z. Bao, *Nano Lett.*, 2011, **11**, 4438–4442.
37. J. Yan, Z. Fan, W. Sun, G. Ning, T. Wei, Q. Zhang, R. Zhang, L. Zhi and F. Wei, *Adv. Funct. Mater.*, 2012, **22**, 2632–2641.
38. S. Wu, W. Chen and L. Yan, *J. Mater. Chem. A*, 2014, **2**, 2765–2772.
39. A. Bello, M. Fabiane, D. Y. Momodu, S. Khamlich, J. K. Dangbegnon and N. Manyala, *J. Solid State Electrochem.*, 2014, **18**, 2359–2365.
40. Q. Ke, Y. Liu, H. Liu, Y. Zhang, Y. Hu and J. Wang, *RSC Adv.*, 2014, **4**, 26398–26406.
41. S. Ye and J. Feng, *ACS Appl. Mater. Interfaces*, 2014, **6**, 9671–9679.
42. B. You, L. Wang, L. Yao and J. Yang, *Chem. Commun.*, 2013, **49**, 5016–5018.
43. J. Ma, Q. Guo, H.-L. Gao and X. Qin, *Fullerenes, Nanotubes, Carbon Nanostruct.*, 2015, **23**, 477–482.
44. T. Wei, S. Wang and Z. Qi, A supercapacitor based ridethrough system for industrial drive applications, *International Conference on Mechatronics and Automation*, 2007, ICMA 2007, pp. 3833–3837.
45. Y. Luo, Y. Yan, S. Zheng, H. Xue and H. Pang, *J. Mater. Chem. A*, 2019, **7**, 901–924.
46. M. G. Ashritha and K. Hareesh, *J. Energy Storage*, 2020, **32**, 101840.
47. C. Lu, Y. Yang and X. Chen, *Nano Lett.*, 2019, **19**, 4103–4111.
48. Y. Ding, Y. Tang, L. Yang, Y. Zeng, J. Yuan, T. Liu, S. Zhang, C. Liu and S. Luo, *J. Mater. Chem. A*, 2016, **4**, 14307–14315.
49. H. M. Jeong, J. W. Lee, W. H. Shin, Y. J. Choi, H. J. Shin, J. K. Kang and J. W. Choi, *Nano Lett.*, 2011, **11**, 2472–2477.
50. Y. Wu, J. Zeng, Y. Si, M. Chen and L. Wu, *ACS Nano*, 2018, **12**, 10338–10346.
51. C. Lu, D. Wang, J. Zhao, S. Han and W. Chen, *Adv. Funct. Mater.*, 2017, **27**, 1606219.
52. X. Wu, G. Wu, P. Tan, H. Cheng, R. Hong, F. Wang and S. Chen, *J. Mater. Chem. A*, 2018, **6**, 8940–8946.
53. M. Beidaghi and C. Wang, *Adv. Funct. Mater.*, 2012, **22**, 4501–4510.
54. D. P. Dubal, N. R. Chodankar, Z. Caban-Huertas, F. Wolfart, M. Vidotti, R. Holze, C. D. Lokhande and P. Gomez-Romero, *J. Power Sources*, 2016, **308**, 158–165.

55. Y. Hu, H. Cheng, F. Zhao, N. Chen, L. Jiang, Z. Feng and L. Qu, *Nanoscale*, 2014, **6**, 6448–6451.
56. L. Kou, T. Huang, B. Zheng, Y. Han, X. Zhao, K. Gopalsamy, H. Sun and C. Gao, *Nat. Commun.*, 2014, **5**, 3754.
57. Z. Dong, C. Jiang, H. Cheng, Y. Zhao, G. Shi, L. Jiang and L. Qu, *Adv. Mater.*, 2012, **24**, 1856–1861.
58. Z. Xu and C. Gao, *Nat. Commun.*, 2011, **2**, 571.
59. J. Zhu, L. Kong, X. Shen, H. Zhou, G. Zhu, Z. Ji, K. Xu and S. A. Shah, *Dalton Trans.*, 2018, **47**, 9724–9732.
60. L. Kong, Q. Chen, X. Shen, Z. Xu, C. Xu, Z. Ji and J. Zhu, *Electrochim. Acta*, 2018, **265**, 651–661.
61. L. Liu, J. Wang, C. Wang and G. Wang, *Appl. Surf. Sci.*, 2016, **390**, 303–310.
62. S. V. P. Vattikuti, B. P. Reddy, C. Byon and J. Shim, *J. Solid State Chem.*, 2018, **262**, 106–111.
63. W. Tian, X. Wang, C. Zhi, T. Zhai, D. Liu, C. Zhang, D. Golberg and Y. Bando, *Nano Energy*, 2013, **2**, 754–763.
64. X. Xu, C. Cao and Y. Zhu, *Electrochim. Acta*, 2015, **155**, 257–262.
65. G. Binitha, M. S. Soumya, A. A. Madhavan, P. Praveen, A. Balakrishnan, K. R. V. Subramanian, M. V. Reddy, S. V. Nair, A. S. Nair and N. Sivakumar, *J. Mater. Chem. A*, 2013, **1**, 11698–11704.
66. Y. Jiao, Y. Liu, B. Yin, S. Zhang, F. Qu and X. Wu, *Nano Energy*, 2014, **10**, 90–98.
67. G. Nie, X. Lu, J. Lei, Z. Jiang and C. Wang, *J. Mater. Chem. A*, 2014, **2**, 15495–15501.
68. D. Sarkar, G. G. Khan, A. K. Singh and K. Mandal, *J. Phys. Chem. C*, 2013, **117**, 15523–15531.
69. Q. Y. Shan, B. Guan, S. J. Zhu, H. J. Zhang and Y. X. Zhang, *RSC Adv.*, 2016, **6**, 83209–83216.
70. B. Guan, Q. Y. Shan, H. Chen, D. Xue, K. Chen and Y. X. Zhang, *Electrochim. Acta*, 2016, **200**, 239–246.
71. L. Shi, J. Zhang, H. Liu, M. Que, X. Cai, S. Tan and L. Huang, *Mater. Lett.*, 2015, **145**, 150–153.
72. D. Jiang, Q. Xu, S. Meng, C. Xia and M. Chen, *J. Alloys Compd.*, 2017, **706**, 41–47.
73. Y. R. Lim, C. S. Jung, H. S. Im, K. Park, J. Park, W. Il Cho and E. H. Cha, *J. Mater. Chem. A*, 2016, **4**, 10691–10699.
74. S. Licht, A. Douglas, J. Ren, R. Carter, M. Lefler and C. L. Pint, *ACS Cent. Sci.*, 2016, **2**, 162–168.
75. X. Zhang, X. Li, J. Liang, Y. Zhu and Y. Qian, *Small*, 2016, **12**, 2484–2491.
76. H. Tao, L. Xiong, S. Du, Y. Zhang, X. Yang and L. Zhang, *Carbon*, 2017, **122**, 54–63.
77. Y. Wang, Y. Wang, J. Liu, L. Pan, W. Tian, M. Wu and J. Qiu, *Carbon*, 2017, **122**, 344–351.
78. Y. Fu, J. Zhu, C. Hu, X. Wu and X. Wang, *Nanoscale*, 2014, **6**, 12555–12564.
79. H. Liu, M. Jia, M. Wang, R. Chen, N. Sun, Q. Zhu, F. Wu and B. Xu, *RSC Adv.*, 2016, **6**, 78235–78240.

80. C. M. Subramaniyam, K. A. Deshmukh, Z. Tai, N. Mahmood, A. D. Deshmukh, J. B. Goodenough, S. X. Dou and H. K. Liu, *Electrochim. Acta*, 2017, **237**, 69–77.
81. S. Wang, Y. Shi, C. Fan, J. Liu, Y. Li, X.-L. Wu, H. Xie, J. Zhang and H. Sun, *ACS Appl. Mater. Interfaces*, 2018, **10**, 30330–30336.
82. D. Adekoya, S. Zhang and M. Hankel, *ACS Appl. Mater. Interfaces*, 2020, **12**, 25875–25883.
83. C. Senthil, T. Kesavan, A. Bhaumik and M. Sasidharan, *Mater. Res. Express*, 2018, **5**, 016307.
84. H. H. Tran, P. H. Nguyen, V. H. Cao, L. T. Nguyen, V. M. Tran, M. L. Phung Le, S.-J. Kim and V. Vo, *Chem. Phys. Lett.*, 2019, **715**, 284–292.
85. X. Li, Y. Feng, M. Li, W. Li, H. Wei and D. Song, *Adv. Funct. Mater.*, 2015, **25**, 6858–6866.
86. K. Zhou, X. Fan, W. Chen, F. Chen, X. Wei, A. Li and J. Liu, *Electrochim. Acta*, 2017, **247**, 132–138.
87. V. Vo, X. D. Nguyen Thi, Y.-S. Jin, G. Ly Thi, T. T. Nguyen, T. Q. Duong and S.-J. Kim, *Chem. Phys. Lett.*, 2017, **674**, 42–47.
88. C. Senthil, T. Kesavan, A. Bhaumik, M. Yoshio and M. Sasidharan, *Electrochim. Acta*, 2017, **255**, 417–427.
89. D. Versaci, J. Amici, C. Francia and S. Bodoardo, *Solid State Ionics*, 2020, **346**, 115210.
90. M. Shi, T. Wu, X. Song, J. Liu, L. Zhao, P. Zhang and L. Gao, *J. Mater. Chem. A*, 2016, **4**, 10666–10672.
91. Y. Wang, X. Ding, L. Huang, Y. Xu, Y. Zuo, S. Kang and L. Cui, *Int. J. Electrochem. Sci.*, 2016, **11**, 2461–2472.
92. Y. Liu, X. Wang, X. Song, Y. Dong, L. Yang, L. Wang, D. Jia, Z. Zhao and J. Qiu, *Carbon*, 2016, **109**, 461–471.
93. Y. Tang, D. Wu, Y. Mai, H. Pan, J. Cao, C. Yang, F. Zhang and X. Feng, *Nanoscale*, 2014, **6**, 14679–14685.
94. C. Senthil, K. S. Chandra and S. Manickam, *Appl. Surf. Sci.*, 2017, **410**, 215–224.
95. H. Tran Huu, X. D. Nguyen Thi, K. Nguyen Van, S. J. Kim and V. Vo, *Materials*, 2019, **12**, 1730.
96. S. Majumder, M. Shao, Y. Deng and G. Chen, *J. Power Sources*, 2019, **431**, 93–104.
97. L. Luo, X. Qin, J. Wu, G. Liang, Q. Li, M. Liu, F. Kang, G. Chen and B. Li, *J. Mater. Chem. A*, 2018, **6**, 8612–8619.
98. Z. A. Ghazi, X. He, A. M. Khattak, N. A. Khan, B. Liang, A. Iqbal, J. Wang, H. Sin, L. Li and Z. Tang, *Adv. Mater.*, 2017, **29**, 1606817.
99. G. Angamuthu, D. B. Babu, K. Ramesha and V. Rangarajan, *J. Electroanal. Chem.*, 2019, **843**, 37–46.
100. K. Eid, H. Wang, V. Malgras, Z. A. Alothman, Y. Yamauchi and L. Wang, *J. Phys. Chem. C*, 2015, **119**, 19947–19953.
101. K. Eid, H. Wang, V. Malgras, S. M. Alshehri, T. Ahamad, Y. Yamauchi and L. Wang, *J. Electroanal. Chem.*, 2016, **779**, 250–255.
102. Q. Lu, H. Wang, K. Eid, Z. A. Alothman, V. Malgras, Y. Yamauchi and L. Wang, *Chem. - Asian J.*, 2016, **11**, 1939–1944.

103. S. Lu, K. Eid, D. Ge, J. Guo, L. Wang, H. Wang and H. Gu, *Nanoscale*, 2017, **9**, 1033–1039.
104. K. Eid, H. Wang, P. He, K. Wang, T. Ahamad, S. M. Alshehri, Y. Yamauchi and L. Wang, *Nanoscale*, 2015, **7**, 16860–16866.
105. H. Wang, Y. Li, C. Li, K. Deng, Z. Wang, Y. Xu, X. Li, H. Xue and L. Wang, *J. Mater. Chem. A*, 2019, **7**, 801–805.
106. H. Zhang, H. Wang, K. Eid and L. Wang, *Part. Part. Syst. Charact.*, 2015, **32**, 863–868.
107. K. Eid, H. Wang, V. Malgras, Z. A. Alothman, Y. Yamauchi and L. Wang, *Chem. - Asian J.*, 2016, **11**, 1388–1393.
108. F. Wu, K. Eid, A. M. Abdullah, W. Niu, C. Wang, Y. Lan, A. A. Elzatahry and G. Xu, *ACS Appl. Mater. Interfaces*, 2020, **12**, 31309–31318.
109. S. Lu, K. Eid, Y. Deng, J. Guo, L. Wang, H. Wang and H. Gu, *J. Mater. Chem. A*, 2017, **5**, 9107–9112.
110. H. Wang, S. Yin, K. Eid, Y. Li, Y. Xu, X. Li, H. Xue and L. Wang, *ACS Sustainable Chem. Eng.*, 2018, **6**, 11768–11774.
111. K. Jlassi, K. Eid, M. H. Sliem, A. M. Abdullah, M. M. Chehimi and I. Krupa, *Environ. Sci. Eur.*, 2020, **32**, 12.
112. H. Idris Abdu, K. Eid, A. M. Abdullah, M. H. Sliem, A. Elzatahry and X. Lu, *Green Chem.*, 2020, **22**, 5437–5446.
113. C. Wei, H. Wang, K. Eid, J. Kim, J. H. Kim, Z. A. Alothman, Y. Yamauchi and L. Wang, *Chem. - Eur. J.*, 2017, **23**, 637–643.
114. H. I. Abdu, K. Eid, A. M. Abdullah, Z. Han, M. H. Ibrahim, D. Shan, J. Chen, A. A. Elzatahry and X. Lu, *Renewable Energy*, 2020, **153**, 998–1004.
115. X. Xu, T. Yang, Q. Zhang, W. Xia, Z. Ding, K. Eid, A. M. Abdullah, M. Shahriar, A. Hossain, S. Zhang, J. Tang, L. Pan and Y. Yamauchi, *Chem. Eng. J.*, 2020, **390**, 124493.
116. H. I. Abdu, K. Eid, A. M. Abdullah and X. Lu, *Data Brief*, 2020, **30**, 105520.
117. M. M. A. Abualrejal, K. Eid, R. Tian, L. Liu, H. Chen, A. M. Abdullah and Z. Wang, *Chem. Sci.*, 2019, **10**, 7591–7599.
118. M. M. A. Abualrejal, K. Eid, A. M. Abdullah, A. A. Numan, H. Chen, H. Zhang and Z. Wang, *Microchim. Acta*, 2020, **187**, 527.
119. Y. Ibrahim, A. Kassab, K. Eid, A. M. Abdullah, K. I. Ozoemena and A. Elzatahry, *Nanomaterials*, 2020, **10**(5), 885.
120. K. Eid, K. A. Soliman, D. Abdulmalik, D. Mitoraj, M. H. Sleim, M. O. Liedke, H. A. El-Sayed, A. S. AlJaber, I. Y. Al-Qaradawi, O. Mendoza Reyes and A. M. Abdullah, *Catal. Sci. Technol.*, 2020, **10**, 801–809.
121. Y. Ibrahim, A. Mohamed, A. M. Abdelgawad, K. Eid, A. M. Abdullah and A. Elzatahry, *Nanomaterials*, 2020, 1916.

CHAPTER 8

Emerging Applications for Graphitic Carbon Nitride-based Materials: CO_2 Reduction as a Case Study

HANY A. EL-SAYED*

Chair of Technical Electrochemistry, Department of Chemistry, Technical University of Munich, D-85748 Garching, Germany
*E-mail: hany.el-sayd@tum.de

8.1 Introduction

Carbon dioxide (CO_2) is one of the major greenhouse gases that significantly contributes to the greenhouse effect. The increasing levels of CO_2 emissions are causing a negative influence on the overall climate and life. It was reported that the annual global emissions of carbon dioxide have exceeded 30 billion tons, where only 1% of this amount is being removed annually.[1] These emissions are not considered to be completely waste as CO_2 is one of the very important micro-molecular resources for many industrial chemicals, such as methane, methyl alcohol, and dimethylformamide (DMF). In other words, capturing CO_2 from the atmosphere not only reduces its harmful effects on the environment, but also enables utilization of CO_2 through artificial synthesis to produce valuable chemical products for various industries.

Nanoscience & Nanotechnology Series No. 51
Carbon Nitride Nanostructures for Sustainable Energy Production and Environmental Remediation
Edited by Kamel Abdelmoniem Mohamed Eid and Aboubakr M. Abdullah

Published by the Royal Society of Chemistry, www.rsc.org

The electrochemical reduction of carbon dioxide is to convert CO_2 into organic feedstock using electrical energy. This includes formic acid,[2] carbon monoxide (for Syngas), ethylene, ethanol, and methane,[3–5] which can serve as energy storage to compensate for energy fluctuations from renewable energy sources by classical direct combustion or in combination with fuel cells through indirect combustion. Therefore, this method is also referred to as the artificial carbon dioxide cycle. The main advantages the electrochemical reduction method exhibits over classical heterogeneous gas catalysis are the direct use of electrical energy, its potential dependence (and therefore the product yield and specification are customizable), in addition to operation at ambient pressure and temperature.

Carbon dioxide reduction can be also achieved *via* photocatalytic processes. The photocatalytic CO_2 reduction is a process in which light energy is used to drive electrochemical reactions, and the reaction conditions and catalysts can be optimized to selectively obtain a certain product.[6,7]

There are three different types of CO_2 photoreduction systems that have been developed; a semiconductor-based photocatalytic system, a photocatalytic system that is based on metal complexes, and an enzyme-based photocatalytic system.[8] One of the earliest photocatalytic systems for CO_2 reduction was reported in 1979 by Fujishima *et al.*, where TiO_2 and CdS were used as photocatalysts.[9] A metal complex photocatalytic system for the reduction of CO_2 was reported for the first time by Lehn *et al.* in 1983. In this system, *fac*-$Re(bpy)(CO)_3Cl$ was used as a photocatalyst, and it exhibited high selectivity and high quantum yield.[10] Three years later, Willner *et al.* reported the first photocatalytic CO_2 reduction system using enzymes as catalysts.[11]

Although they have been significantly developed, the applicability and utilization of enzyme-based photocatalytic CO_2 reduction systems are very narrow due to the high substrate specificity, high cost, and their excessive sensitivity to reaction conditions.[12] Therefore, most of the interest has been focused on metal complex based or semiconductor photocatalytic systems for CO_2 reduction. The metal complex systems, that are based on homogeneous organic photocatalysts, have their own issues that lead to some limitation of their utilization. The catalytic efficiency and selectivity of these metal complex systems are sensitive to energy distribution as all the metal atoms can serve as active sites. Moreover, there are several side reactions accompanying metal complex photocatalysis due to the homogeneous nature of the catalytic material.[13] In addition, separation of reactants from products is technically difficult because of the homogeneous nature of the catalytic system, which limits the re-utilization of the catalytic material, and is therefore disadvantageous for sustainable development. On the other hand, photocatalysts based on semiconductors are mostly heterogeneous and it is easier to separate products from the catalytic material.[14] The photocatalytic performance of these systems can be improved through various chemical and structural modifications of the photocatalyst. This can be achieved by using porous semiconductor photocatalysts,[15,16] doping the photocatalyst with other materials, or even making a composite using the semiconductor.[17–20] These flexibilities in system development

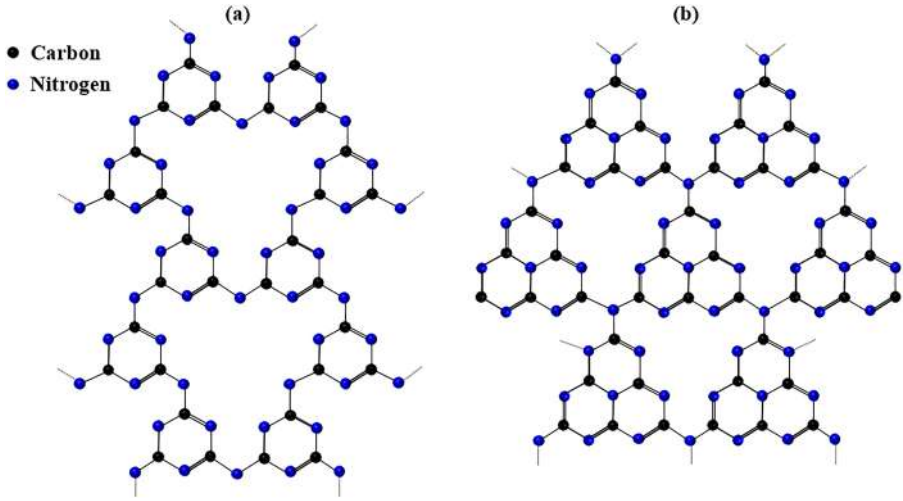

Figure 8.1 (a) *s*-triazine and (b) tri-*s*-triazine as tectons of gCN. Reproduced from ref. 21 with permission from the Royal Society of Chemistry.

have led to great interest and widespread usage of semiconductor-based photocatalysis over the last several years.

Polymeric semiconductor graphitic carbon nitride (gCN) has been extensively utilized in numerous forms in applications associated with energy and material science, primarily owing to its extraordinary thermal and chemical stability and its distinctive electronic structure. This polymeric gCN contains graphitic stacking of C_3N_4 layers, which are constructed from *s*-triazine and tri-*s*-triazine units connected by planar amino groups (see Figure 8.1).[21]

gCN is insoluble in most solvents, including water, ethanol, toluene, tetrahydrofuran (THF), ether, and dimethylformamide (DMF).[22] The band gap of gCN is about 2.7 eV and it can absorb visible light below 475 nm, therefore, it is considered a potential candidate for photocatalysis.[23,24] While the first photocatalytic application of gCN was reported in the year 2009 by Wang *et al.*, where it was demonstrated that gCN can be used as a semiconductor for hydrogen production,[25] the first attempt to use gCN for CO_2 photoreduction was reported in 2013 by Peng *et al.*[26] This chapter will shed some light on the recent development and applications of gCN in the area of CO_2 photoreduction, in addition to future prospects of this system as a photocatalyst for CO_2 reduction.

8.2 Graphitic Carbon Nitride for CO_2 Photocatalytic Reduction

The photocatalytic reduction of CO_2 is a process in which energy from visible light is absorbed by the semiconducting catalytic material, ultimately leading to the electrochemical reduction of CO_2 into various products. Controlling

which products are obtained from the reduction process can be achieved by tuning the reaction conditions, which will be explained in some detail in the next section. Below are the common reduction reaction pathways that result in different products.

$CO_2 + 2H^+ + 2e^- \rightarrow HCOOH$	$E^0 = -0.61\ V_{NHE}$	I
$CO_2 + 2H^+ + 2e^- \rightarrow CO + H_2O$	$E^0 = -0.53\ V_{NHE}$	II
$CO_2 + 4H^+ + 4e^- \rightarrow HCHO + H_2O$	$E^0 = -0.48\ V_{NHE}$	III
$CO_2 + 6H^+ + 6e^- \rightarrow CH_3OH + H_2O$	$E^0 = -0.38\ V_{NHE}$	IV
$CO_2 + 8H^+ + 8e^- \rightarrow CH_4 + 2H_2O$	$E^0 = -0.24\ V_{NHE}$	V

In general, light absorption is the first photochemical step in semiconductor photocatalysis, which is followed by charge separation, reactant adsorption on the catalyst surface, surface redox reaction, *i.e.*, charge transfer, and finally, product formation and release.[27] For a specific photocatalytic reaction to take place, the conduction band edge of the photocatalyst should be more negative than the reaction potential. In order to control the reduction products of the photocatalytic CO_2 reduction, the photocatalyst should be chosen in combination with the reactions provided above.[28] For full control of the reaction product, careful design of the semiconductor-based photocatalyst should be achieved in order to realize an efficient generation and transfer of the photo-excited charge carriers (electrons and holes). The following five key parameters should be considered when designing a semiconductor-based photocatalyst for CO_2 reduction.

(i) An ideal band gap of a semiconductor for CO_2 reduction should be in the 2.0–3.0 eV range in order to absorb visible light.[27]
(ii) The separation of the charge carriers is sufficiently large to limit their recombination.[29]
(iii) Enhancing the adsorption of CO_2 through increasing the specific surface area of the photocatalyst, or by introducing alkaline functional groups to the surface of the catalyst.[30]
(iv) Improving the efficiency of the redox reaction by introducing a co-catalyst or by making a composite that helps increase the charge transfer rate.
(v) Efficient removal of the products in order to free the active sites for further CO_2 adsorption and reaction, which ultimately increases the overall conversion rate.

While most oxide semiconductor photocatalysts have very large band gap energies to be utilized for light absorption and therefore are not very efficient at light harvesting, chalcogenide semiconductors have very narrow band gaps that allow recombination of charge carriers and thus are not efficient in charge separation (Figure 8.2).[31] On the other hand, the band gap of 2.7 eV of the gCN and the suitable valence and conduction band positions allow gCN to absorb visible light. Moreover, the synthesis of gCN is facile and its microstructure can be modified *via* several approaches to increase the surface area or to create porous structures in order to maximize light absorption.

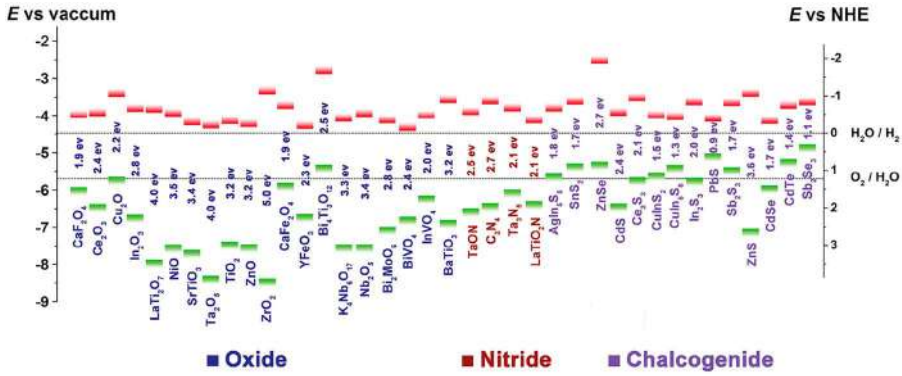

Figure 8.2 Band gap energies and conduction band (green) and valence band (red) edge positions of several semiconductors with respect to the vacuum level and NHE. The water redox reaction potentials are indicated by the two dashed lines. Reproduced from ref. 31 with permission from John Wiley & Sons, Copyright 2015 WILEY-VCH Verlag GmbH & Co. KGaA, Weinheim.

Although gCN is considered a superior photocatalyst for CO_2 reduction compared to common oxide semiconductors such as TiO_2, its band gap is not large enough and it allows recombination of charge carriers, thus limiting the charge separation efficiency and ultimately affecting the overall conversion rate. Although bulk gCN has several types of Lewis base sites that are preferred for the adsorption of CO_2, its specific surface area is relatively small as it is typically prepared *via* calcination methods. Therefore, several approaches have been applied to increase the adsorption of CO_2 on gCN and increase the overall conversion efficiency, these include structural tuning,[30,32–34] composite formation with other materials,[35–40] elemental doping or addition of co-catalyst.[41–50] In the next section, some of these approaches will be discussed alongside their impact on increasing the overall efficiency of gCN for the photocatalytic reduction of CO_2.

8.2.1 Nanostructured gCN and gCN with Defects

Although gCN has good potential as a CO_2 photo-electrocatalyst, most bulk gCN exhibits a small specific surface area, which reduces the overall efficiency of the conversion process. To increase the CO_2 adsorption efficiency and thus the catalytic activity, researchers have demonstrated several approaches.

Nanoporous gCN: Zhang *et al.* performed calcination of either melamine or melamine hydrochloride to result in a porous structured gCN, which was used for the photocatalytic reduction of CO_2 to CO under visible light irradiation.[30] Although the nanoporous gCN formed from melamine hydrochloride was found to have a surface area 39 times greater than that of bulk gCN due to its porous structure, its CO_2 photoreduction performance was not noticeably improved. This was attributed to the enlargement of the band gap that

was associated with the surface area increase due to the nanoporosity, and which resulted in poor excitation and thus lower CO_2 conversion yield.

Using similar approaches, several gCN nanostructures have been developed, such as porous structures, nanowires,1D nanorods, 2D nanosheets, and 3D nanostructures.[32–34,51–53] Zheng and Wang *et al.* utilized chiral silicon dioxide as templates to imprint helical gCN nanorods (Figure 8.3).[32] This helical structure resulted in multiple reflections of incident light, which led to a significant improvement in light-harvesting capability throughout the entire optical spectrum.

Although the nanostructuring of gCN resulted in increasing the band gap from 2.66 eV to 2.75 eV, the helical gCN still exhibited an overall improved light absorption compared to the bulk form of gCN, where a high selectivity (96.7%) of CO production was observed, in addition to a higher CO production rate during visible light CO_2 reduction, which reached 8.9 mmol g^{-1} h^{-1}. It was found that the recombination of photogenerated charge carriers was suppressed in the helical gCN nanorods, which was attributed to the lower photoluminescence (PL) intensity and the stronger PL quenching observed for the helical gCN nanorods in comparison to the bulk gCN.[54]

2D gCN: A great deal of effort has been given to the development of a large specific surface area 2D gCN for CO_2 photoreduction applications due to their expected advantages for both light harvesting and gas adsorption. Cao *et al.* reported the preparation of ultra-thin gCN nanosheets by a thermal exfoliation approach using NH_3 mediation.[33] The nanosheets were *ca.* 3 nm thick and characterized with a hierarchical structure as a result of the amine-induced assembly. This morphology resulted in a gCN of a very high specific surface area, and thus abundant active sites, increased adsorption of CO_2, and shorter diffusion distance of charge carriers. Upon photoreduction of

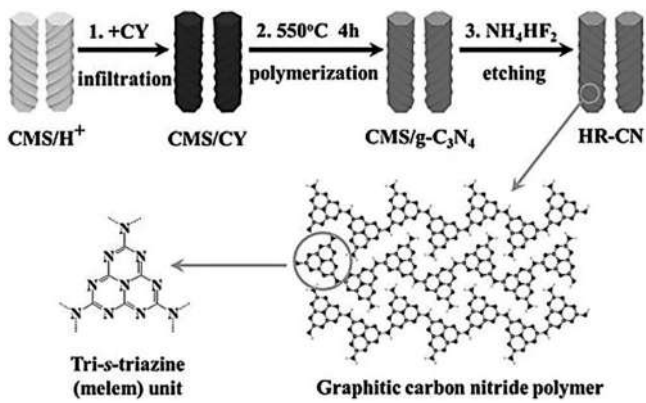

Figure 8.3 Fabrication of helical nanorod-like gCN based on a template of chiral mesoporous silica and cyanamide (CY) as the precursor. Reproduced from ref. 32 with permission from John Wiley & Sons, Copyright 2014 WILEY-VCH Verlag GmbH & Co. KGaA, Weinheim.

CO_2, these gCN nanosheets resulted in higher yields of CH_4 and CH_3OH production, 9.93 and 5.34 times higher than those obtained from bulk gCN as catalyst, respectively.

gCN with defects: Introducing carbon vacancies into gCN that was produced with urea and heat-treated under an NH_3 atmosphere was reported by Zhang *et al.* to result in an enhancement in CO photogeneration.[34] This C-rich gCN exhibited an evolution rate of CO production of 4.18 mmol g^{-1} h^{-1}, which is 2.3 times higher than that obtained from the bulk gCN. This improvement in CO_2 reduction was attributed to the greater adsorption of CO_2 in addition to the upshift of the conduction band, and the increase in the concentration of the charge carriers' concentration. The role of C vacancies was revealed via the electrochemical impedance spectroscopy (EIS) and reactive oxygen species (ROS) studies. It was found that these vacancies weaken the exciton effect and elevate the generation of charge carriers, and therefore enhance the overall performance of the CO_2 photoreduction.

Using a dynamic gas template, Chai *et al.* introduced N vacancies into gCN nanosheets where NH_4Cl was fed to the synthesis chamber and upon heating it decomposed to NH_3 and HCl gases, which resulted in the formation of a bubble film on the polymerized gCN surface.[51] The formation of bubbles reduced the π–π interlayer interactions between the nanosheets and resulted in forming an ultra-thin bubble/gCN film, afterwards, the N vacancies were formed by post treatment under a reducing gas. The introduction of N vacancies resulted in a mid-gap state, which facilitated multi-electron excitation and resulted in the extension of the gCN nanosheet optical absorption to the near infrared range, and therefore enhanced the utilization of solar energy (Figure 8.4). The decay lifetime of the N-enriched gCN nanosheets

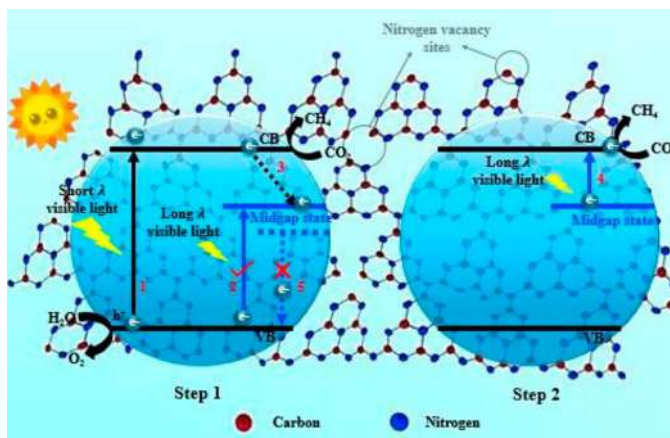

Figure 8.4 Schematic illustration of nitrogen defect-modified gCN atomic layers for photocatalytic formation of CH_4 from CO_2. Reproduced from ref. 51 with permission from the Royal Society of Chemistry.

was prolonged compared to bulk gCN due to the reduction of the radiative recombination rate caused by the mid-gap state. The N-enriched gCN nanosheets exhibited a higher efficiency in CH4 formation compared to that of the bulk gCN; specifically, an enhanced formation rate of 5.14-fold higher than gCN was measured. This work was one of the first to demonstrate the synergy of combining vacancy modulation and morphology control on the CO_2 photocatalytic reduction.

Controlling these two parameters (structural morphology and defects) modulates the energy band structure of the gCN and improves both the capability of light harvesting and charge transfer, and ultimately enhances the overall photocatalytic performance of the gCN.

8.2.2 Non-metal Doped gCN

The poor performance of gCN towards CO_2 photoreduction is due to the low adsorption of CO_2, the unoptimized band gap, and the poor utilization of charge carriers, which is mainly due to the deficiency of the catalytic sites that are responsible for electron donation.[53] The introduction of a heteroatom (doping) was proven to be a good approach to address the previous issues, especially the modulation of the electronic structure of the gCN. Some of the elements used for doping are B, O, C, S, and P.[41–43,55]

In undoped gCN, the photocatalytic reaction takes place mainly on the N atoms and the electrons are primarily localized around these atoms. Upon light irradiation, electron transfer, due to excitation from N to C is difficult as a result of the localization of the electron structure.[56–58] In addition, there is a high chance of charge carriers' recombination when the exited electrons transfer back for a redox reaction. These issues were addressed by doping gCN with boron through a one-step calcination in which urea and boric acid were used as precursors.[41] Density functional theory (DFT) studies showed that when B atoms are introduced between adjacent tri-*s*-triazine units through coordination with N atoms, a new pathway is formed for the electron transfer from N ($2p_x$, $2p_y$) to B ($2p_x$, $2p_y$), which enhanced the overall electron transfer and localization, and ultimately the reaction dynamics. The B atoms not only enhanced the electronic structure of the gCN, but they also enhanced the CO_2 gas adsorption by acting as active sites. An optimal B-doped gCN exhibited 32-fold higher CH_4 yield compared to undoped gCN.

Doping gCN with phosphorus was also performed by Tian *et al.* where P-doped gCN nanotubes were synthesized by the calcination of a melamine and sodium hypophosphite monohydrate mixture.[42] In addition to the large surface area provided by the gCN nanotubes, compared to nanosheets, the phosphorus doping resulted in downshifting both conduction and valence bands and narrowed down the band gap by 0.12 eV (Figure 8.5), which improved the photocatalytic performance towards CO_2 reduction. P-doping also resulted in creating extra amino groups on the surface of gCN, which increased CO_2 adsorption through the acid–base interaction. This was reflected on the increased formation rate of CO and CH_4 when P-doped gCN

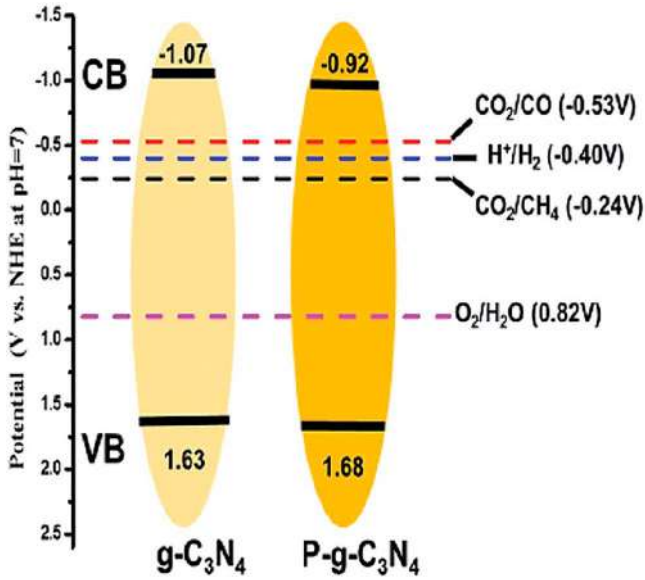

Figure 8.5 The electronic structure and reaction reduction potentials of H_2 evolution and CO_2 conversion into CO and CH_4. Reproduced from ref. 42 with permission from American Chemical Society, Copyright 2018.

nanotubes were used as catalyst, where yields that are 3.12 and 13.9 times higher than that of pristine gCN were reported, respectively.

Using thiourea as the precursor, Yu *et al.* synthesized S-doped gCN *via* calcination, which was shown to have a band gap of 2.63 eV, *i.e.*, slightly smaller (0.07 eV) than that of undoped gCN.[43] The smaller band gap resulted in more efficient light absorption and charge carrier formation, which improved the process of CO_2 photocatalytic reduction. Although the change in the band gap due to S-doping was experimentally proven, theoretical calculations estimated that S-doping should not alter the band gap and that the change in the band gap was rather due to an impurity level due to S-doping. The photoelectrons could jump from the impurity level to the conduction band or from the valence band to the impurity level. The yield of CH_3OH was 2.5 times higher than that of undoped gCN.

Recently, metal and non-metal co-doping of gCN for CO_2 photoreduction applications was reported, where metals such as Na, K and Co were found to improve the overall performance of CO_2 reduction.[59–62] Zheng *et al.* demonstrated a one-step synthesis in which a system of N vacancy-rich gCN co-doped with B and K was introduced.[59] In this photocatalytic material, an electron donor, K, was used to promote interlayer electron transfer, a high reduction potential was maintained with the help of B atoms, which also counteracted the drawbacks of K, and the conduction band minimum (CBM) was lowered by the N atoms, which resulted in enhanced CO_2 absorption. The relatively sophisticated system, in which multi-modifications were

simultaneously performed, resulted in synergetic effects that led to a significant improvement in the photocatalytic reduction of CO_2. The modified gCN demonstrated higher performance, where the yields of CH_4 and CO were 1.61 and 5.27 times higher than that of pristine gCN, respectively, when tested under identical conditions.

Overall, doping with non-metal elements was proven to increase the photocatalytic activity of gCN towards CO_2 reduction by modulating the energy band structure, which resulted in a smaller band gap that enabled the light absorption in a wider range of the visible light region. This doping with non-metals could also provide an impurity level or a new pathway for electron excitation of gCN, which facilitates the electron transfer. In addition, the doping process might introduce new surface groups where the doping element is the main atom of these groups, which ultimately enhances the adsorption of CO_2 due to the acid–base interaction.

8.2.3 gCN with co-catalyst

Co-catalysts are used in the field of photocatalysis as active sites for specific surface reactions and also to improve charge separation and utilization.[63] The list of co-catalysts that were used with gCN includes metal, carbon-based materials, reduction co-catalyst, and double co-catalyst.[64]

8.2.3.1 Metal co-catalyst

Most co-catalysts used in the field of photocatalysis are noble metals such as Pt, Ag, and Au. By the deposition of noble metal nanoparticles on a photocatalyst, the metal/semiconductor interface can form a Schottky barrier, which can make the metal nanoparticles function as electron traps for the enhancement of the photogenerated charges.[35]

Among the various noble metals, Pt is one of the most commonly used metals as a co-catalyst for the photocatalytic reduction of CO_2 due to its high selectivity for methane formation in a gas–solid system.[65] Yu *et al.* synthesized gCN by one-step calcination using thiourea as a precursor, and deposited Pt nanoparticles on the surface of gCN for the CO_2 photoreduction.[66] The Pt/gCN was found to absorb visible light much more efficiently compared to gCN; although the band gap was the same as that of gCN, the improvement was due to the Pt nanoparticles that absorbed most of the incident light.[67]

The Pt nanoparticles also promoted the transfer of the photogenerated electrons from gCN to Pt, which facilitated the reaction with CO_2. It was observed that Pt loadings up to 1% are efficient as the yield of CH_4 formation was found to increase with increasing the Pt loading from 0% to 1%, and then it started to decrease at loadings higher than 1%. A similar dependence of the Pt loading on the CO_2 photocatalytic reduction to CH_4 was also reported by Chai *et al.* (Figure 8.6).[44] The decrease in the CH_4 yield beyond 1% Pt loading was attributed to the excess Pt and that results in the increase of the negative charges on the gCN surface and therefore enhances the

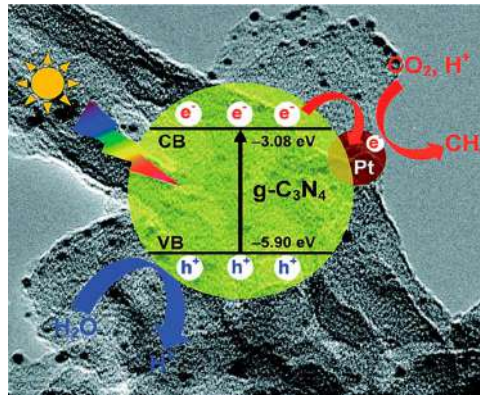

Figure 8.6 Photogenerated charge transfer process in the Pt/gCN catalyst for the formation of CH_4 from CO_2 reduction under visible light irradiation. Reproduced from ref. 44 with permission from the Royal Society of Chemistry.

recombination of the photo-excited charge carriers. Another explanation for this performance decay at high Pt loadings is the shielding effects, where excess Pt blocks the active sites on the gCN from the incident light. To avoid the latter concern, Du *et al.* deposited Pt single atoms on gCN and found that the Pt(single atom)/gCN enhanced the capability of gCN towards visible light absorption and exhibited a high selectivity towards CH_4 formation.[45] While other noble metals have been used as co-catalysts with gCN for CO_2 photoreduction,[46,68] non-noble metals were rarely utilized,[47,48] although DFT calculation predicted that Mo could be efficient in co-catalyzing CO_2 reduction to CO when combined with gCN.[49]

8.2.3.2 Carbon-based co-catalyst

Another type of co-catalyst that was used with gCN for CO_2 photoreduction utilized carbon-based materials, including graphene, graphene oxide, carbon nanotubes, and carbon nanodots. These C-materials were used as co-catalysts in order to promote the electron transfer within the gCN. Using one-step impregnation-thermal reduction, Chai *et al.* synthesized graphene–gCN–graphene nanocomposites.[69] The covalent bonds formed between the graphene sheets and gCN resulted in a redshift of the absorption band edge. The graphene-modified gCN exhibited a 2.3-fold higher CH_4 yield compared to the pristine gCN due to the increased charge transfer and the reduced electron–hole pair recombination.

In a different study, a composite of carbon nanosheets and 3D porous gCN was fabricated by a simple pyrolysis process followed by carbothermal activation.[70] Gas-phase photoreduction of CO_2 using simulated solar irradiation indicated that the photocatalytic activity of the graphene-modified gCN was at least twice that of the pristine gCN due to the incorporation of

carbon and also due to the 3D porous structure of the gCN. Specifically, the 3D porous gCN architecture may have contributed in increasing the overall conversion performance *via* (i) promoting the transportation of CO_2 to active sites and facilitating product diffusion, and (ii) increasing the ability of light harvesting. Another reason for this improved performance is that the photogenerated electrons could have shifted from the gCN to the hybrid carbon structure as a result of the inner electric field, which stems from the quantum confinement effect, and therefore decreased the rate of electron–hole pair recombination.

Another reason that may have caused this enhancement in the performance of the graphene-modified gCN is the inhibition of the electron–hole pair recombination through the formation of electron-withdrawing groups on the surface of the composite. X-ray photoelectron spectroscopy (XPS) analysis showed that electron-withdrawing C–O groups are formed on the composite surface, which could have led to an enhanced electron flow on the external surface.

Doping gCN with carbon quantum dots (CQDs) can also provide several advantages towards the photocatalytic reduction of CO_2 such as decreasing the band gap, the electron-withdrawing and the up-conversion effects.[71] CQDs-modified gCN was reported by Tang *et al.* to have a higher selectivity towards forming methanol from CO_2 reduction compared to bulk gCN, which was attributed to the hole-accepting effect of CQDs.[72]

The microwave-assisted synthesized CQDs are purely graphitic structures that facilitate the hole transfer to them and favor electron transfer and accumulation on the gCN surface. The hole-accepting CQDs were found to repel methanol from adsorption on the surface and therefore prevent it from further oxidation and increases its yield. Specifically, CQDs–gCN produced methanol from CO_2 and water with *ca.* 100% selectivity. This study demonstrated the great potential of CQDs–gCN in the selective CO_2 photochemical reduction.

8.2.3.3 Co-catalysts of Metal Oxide/sulfide/phosphide

In addition to metal, non-metal, and carbon-based co-catalysts, other co-catalysts have been also recently reported, these include metal oxides, sulfides, and phosphides. By loading chainmail Ni/NiO on gCN, Ye *et al.* showed that the photocatalytic reduction of CO_2 is higher than that on bulk gCN.[73] In this catalyst, the metallic nickel was protected from oxidation by the NiO shell, and therefore ensured high stability and photoactivity of the metallic Ni. XPS analysis of the Ni/NiO–gCN showed that there is an interaction between gCN and Ni/NiO through π–π interactions, which promote charge transfer at the gCN/co-catalyst interface of the photocatalyst. This interaction was also confirmed using other techniques such as electrochemical impedance spectroscopy, photocurrent responses, and PL spectra. Surface photovoltage (SPV) and transient photovoltage (TPV) measurements of the Ni/NiO–gCN indicated that the addition of Ni/NiO as a co-catalyst resulted in

stronger generation and enhanced separation of the photogenerated charge carriers. Using an optimum loading of Ni/NiO, the Ni/NiO–gCN resulted in a 9-fold increase in the CO yield compared to bulk gCN when exposed to identical conditions of CO_2 photoreduction. Specifically, a CO formation rate of 13.95 mmol g^{-1} h^{-1} was reported in this study.

Molybdenum phosphide (MoP) was also used as a co-catalyst by depositing it on gCN, and upon the photocatalytic reduction of CO_2, it was found that MoP promoted the separation of electron–hole pairs, facilitated electron transfer, and increased light absorption within the UV-vis region without changing the band gap of the gCN.[50] The MoP-modified gCN exhibited a 4.5-fold increase in CO yield compared to the bulk gCN.

Introducing a different co-catalyst, Pan *et al.* synthesized NiS_2 quantum dot-modified gCN using a hydrothermal method.[74] Upon CO_2 photoreduction, the new NiS_2 was found to be an ideal electro acceptor, which facilitated the photogenerated electron–hole separation and suppressed their recombination. The addition of NiS_2 QDs also increased the number of active sites available for CO_2 adsorption and contributed in closing interface contact. The NiS_2 quantum dot-modified gCN resulted in a CO yield of 10.68 mmol g^{-1} h^{-1}, which is *ca.* 3.9 times greater than that of pristine gCN.

The above examples are only a few to demonstrate that co-catalysts significantly enhance the photocatalytic activity of gCN towards CO_2 reduction *via* promoting the transfer of charge carriers and inhibiting the electron–hole pair recombination. In the next section, the heterojunctions that can form between gCN and some metal oxides, sulfides, or phosphides, will be discussed.

8.2.4 gCN-based Composites

Establishing heterojunctions between gCN and other semiconductors is a highly impactful strategy for the development of efficient CO_2 photocatalytic reduction systems as these junctions enhance light utilization, electron transfer, and even the adsorption of CO_2 on the surface of the photocatalyst.

8.2.4.1 gCN Absorbent Composites

The adsorption/activation of CO_2 on the surface of the photocatalyst is the first step in the photocatalytic conversion. It has been already demonstrated in previous sections that pristine gCN exhibits a small specific surface area due to the stacking nature of the gCN layers, which limits the number of active sites available for CO_2 adsorption and conversion and several strategies have been discussed through which this limitation is tackled. Another effective strategy that we discuss in this section is the combination of gCN with CO_2 adsorbents.

Layered double hydroxides (LDHs) are a category of compounds that are composed of positively charged brucite-like layers with charge-compensating anions and solvation molecules within the interlayered region (Figure 8.7).[75,76]

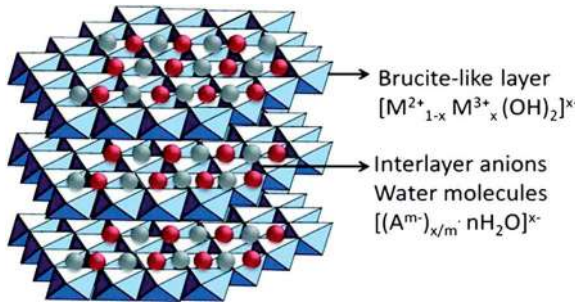

Figure 8.7 An illustration of the chemical composition and structure of layered double hydroxide. Reproduced from ref. 76 with permission from Elsevier, Copyright 2017.

By using a general formula $[MII_{1-x}MIII_x(OH)_2]^+_x\cdot(A^{n-})_{x/m}\cdot_m H_2O$ (M = metal, A = interlayer anion), LDHs were determined to favor CO_2 adsorption owing to their high surface areas, positive surface charges, and also their compositional flexibilities.[64] Mg–Al-LDH nanosheets were added to gCN in order to enhance the CO_2 adsorption on the surface of the photocatalyst by the exploitation of its anion exchange capacity.[35] By combining Pd co-catalyst with LDG/gCN that was assembled *via* electrostatic interaction, the photocatalytic reduction of CO_2 resulted in a remarkable enhancement in CH_4 formation yield compared to the same catalyst without LDH.

8.2.4.2 gCN-based Heterojunctions

gCN-based heterojunctions, which are composites of gCN with other semiconductors, are the most frequently used gCN-based photocatalysts for CO_2 reduction.[64]

(a) gCN-based type II heterojunction photocatalysts.

The heterojunction is simply a p–n junction that forms when two semiconductors come in contact. This can be realized through surface assembly or by internal crosslinking of the crystal interfaces, which speeds up the separation of the photogenerated charge carriers (electron–hole pairs) by the establishment of a built-in electric field.

Heterojunctions can be classified according to their band energy to three categories:

(i) Type I heterojunction, in which the forbidden gap of one of the semiconductors is fully covered by that of the other semiconductor.
(ii) Type II heterojunction, in which the forbidden bands of the two elements are staggered, and the semiconductor has a more −ve conduction band and a less +ve valence band

(iii) Type III heterojunction, is the type in which the forbidden bands of the two constituents are entirely separated.

The type II heterojunction is the most investigated system, and when a photocatalytic reaction takes place on the surface of such system, the photogenerated electrons transfer from the semiconductor of the more negative conduction band to the conduction band of the other semiconductor and initiate a reduction reaction. On the other hand, the holes move from the more positive valence band to the valence band of the other semiconductor and initiate an oxidation reaction.

To establish a type II heterojunction system using gCN, a semiconductor with a more negative conduction band or a more positive valence band is combined with gCN (Figure 8.8). There are some semiconductors whose conduction band is more negative than that of gCN, and therefore can be used to construct a type II heterojunction with gCN, as shown in Figure 8.8b. Several metal oxides, halides, sulfides and other semiconductors have been used to establish such a system,[77] and the choice of the semiconductor controls the properties of the heterojunction and can significantly affect the photocatalytic performance and the stability of the system.[78,79]

(b) gCN-based Z-scheme heterojunction.

This type of heterojunction, which mimics plant photosynthesis, was mainly proposed in order to provide a photocatalyst that is capable of simultaneously splitting water to hydrogen and oxygen. A typical Z-scheme photocatalyst is composed of two photoluminescence processes and corresponding redox reaction series, where the electron transfer takes place at two different photocatalytic systems (SI and SII).[80] In contrast to type II heterojunctions, the electrons formed on SI move to SII through an electronic mediator and the combination with the holes takes place on SII (Figure 8.9a). Therefore, separation of the electron–hole pairs generated in each semiconductor can be realized, while

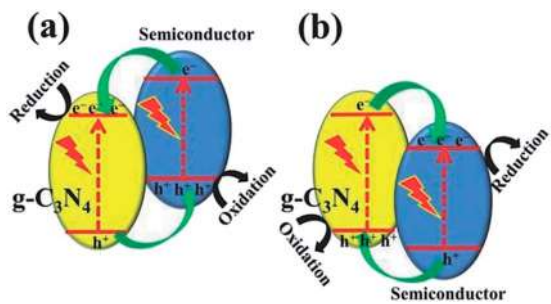

Figure 8.8 Charge transfer in the conventional type II gCN-based heterojunctions composed of gCN and a semiconductor (a) with more negative conduction band and (b) with more positive valence band. Reproduced from ref. 77 with permission from John Wiley & Sons, Copyright 2017 WILEY-VCH Verlag GmbH & Co. KGaA, Weinheim.

maintaining the high reduction and oxidation capabilities of the electrons and holes, respectively.[77,81] As stated earlier, in the Z-scheme photocatalytic system the electron transfer takes place through a mediator, but there is another mechanism of electron transfer that doesn't require a mediator, which is called the direct Z-scheme mechanism. In the latter mechanism, the electrons generated in SI jump to SII and therefore can combine with the holes formed in SII (Figure 8.9b).[82,83] This results in a faster charge transfer between the two components of the system due to the direct contact of the two semiconductors, and therefore increases the reaction the efficiency and reduces the cost.

Li *et al.* fabricated an indirect Z-scheme BiOI/gCN heterojunction system by a simple deposition of BiOI on gCN.[37] Using an optimum BiOI loading of 7.4 wt%, a significant enhancement in the CO yield (17.9 mmol g^{-1} h^{-1}) was achieved upon utilizing the photocatalyst for the CO_2 reduction. XPS, UPS, and DRS characterization confirmed the indirect Z-scheme mechanism of charge transfer, while the roles of the I_3^-/I^- pair as intermediates was confirmed using a contrast test.

Using $AlCl_3$ aqueous solution as a source of Al–O and *via* a wet chemical method, an Al–O-bridged gCN/α-Fe_2O_3 heterojunction was fabricated.[38] As expected, there was an enhancement in the charge transfer and separation due to the introduction of Al–O bridges, which in turn resulted in a higher overall CO_2 photoreduction (Figure 8.10). Upon CO_2 photoreduction, this catalyst exhibited *ca.* 4-fold increase in the CO formation yield (24 mmol g^{-1} h^{-1}). As a result of having a charge transfer mediator in the Z-scheme heterojunction system, this complex catalyst requires optimum design in order realize highly efficient charge separation and transfer. On the other hand, direct Z-scheme heterojunction systems are characterized by direct charge transfer that depends on the contact between the consisting components, and therefore, they exhibit high reaction efficiency and reasonable cost. These features resulted in an immense interest in this type of heterojunction photocatalytic system in recent years.

Without using any co-catalyst or sacrificial agent, Wong *et al.* synthesized a direct Z-scheme heterojunction photocatalytic system using gCN nanosheets

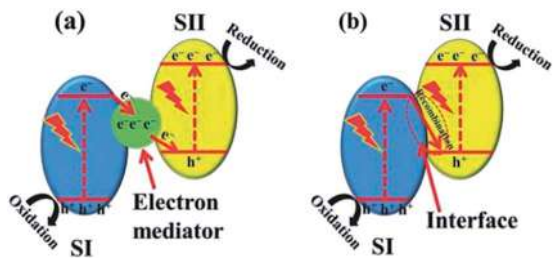

Figure 8.9 Schematic illustration of Z-scheme charge transfer between semiconductors (a) with or (b) without an electron mediator. Reproduced from ref. 77 with permission from John Wiley & Sons, Copyright 2017 WILEY-VCH Verlag GmbH & Co. KGaA, Weinheim.

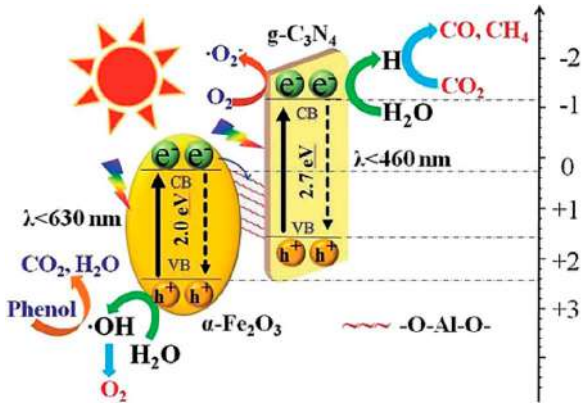

Figure 8.10 Transfer and separation of photogenerated charges in the Al–O-bridged gCN/α-Fe_2O_3 composites and the corresponding induced photochemical reactions. Reproduced from ref. 38 with permission from Elsevier, Copyright 2018.

and urchin-shaped α-Fe_2O_3,[39] and it exhibited a 2.2-fold increase in the CO production rate compared to bulk gCN. Specifically, a CO evolution rate of 27.2 mmol g^{-1} h^{-1} was obtained, which is higher than that of the Al–O-bridged gCN/α-Fe_2O_3 heterojunction system. The inclusion of 3D α-Fe_2O_3 in the catalyst resulted in a smaller band gap, more efficient light absorption, increasing the binding energy and the adsorption of CO_2. Overall, this led to increasing the number of CO_2 molecules that participate in the reaction and ultimately a more efficient photocatalyst for CO_2 reduction.

In addition to the enhancement in CO_2 adsorption, the direct Z-scheme system promoted the electron–hole separation in both components (gCN and α-Fe_2O_3), thus enhancing the reduction capability of the photoelectrons in the gCN conduction band. The enhancement in light harvesting, adsorption of CO_2, and charge carrier separation all led to a significant improvement in the performance of photocatalytic reduction of CO_2.

ZnO, Bi_2S_3, and NiAl-LDH are only a few examples of materials that can be combined with gCN to make a direct Z-scheme heterojunction system for the photocatalytic reduction of CO_2. In terms of structure, most of these materials are well designed in order to realize the highest CO_2 photoreduction yield.[40,84,85] For example, a direct Z-scheme heterojunction system, 2D gCN/NiAl-LDH, was established, in which the strong electrostatic interactions between negatively charged gCN and positively charged NiAl-LDH are essential to the construction of such system.[40] The strong interfacial 2D/2D contacts of this system significantly enhanced the photocatalytic activity towards CO_2 reduction. Precisely, the large interfacial contact area between gCN and NiAl-LDH inhibited the recombination of photogenerated charge carriers and enhanced their transfer and separation.

Guo *et al.* fabricated a composite photocatalyst of Bi_2S_3 quantum dots (QDs) and gCN by the uniform dispersion of Bi_2S_3 QDs on the gCN surface,

which enhanced the light absorption and the charge carriers' separation. The Z-scheme mechanism was confirmed using several characterization techniques and the CO yield was 4-fold higher than that obtained from the bulk gCN when exposed to identical conditions of CO_2 photocatalytic reductions.[84]

In general, the Z-scheme heterojunction photocatalytic mechanism can be confirmed by PL analysis and DFT calculations. Yu *et al.* synthesized a gCN/ZnO composite for the selective formation of CH_3OH from CO_2 photoreduction, where a 2.3-fold enhancement in the photocatalytic activity was obtained compared to the pristine gCN.[85] The verification of the photocatalytic mechanism was realized by performing PL analysis of the hydroxyl radicals ($^{\bullet}OH$) formed on the surface of pure gCN, pure ZnO, and their composite. Thermodynamically, both $^{\bullet}O_2^-$ and $^{\bullet}OH$ can only be produced from photogenerated electrons in the conduction band of the gCN and the holes from valence band of the ZnO, respectively. In line with the double-transfer mechanism, neither $^{\bullet}O_2^-$ nor $^{\bullet}OH$ could form on the composite system; it is acceptable to conclude that the charge transfer has taken place through the Z-scheme mechanism. This hypothesis was also confirmed using DFT calculations where the effective mass of charge carriers and separating tendency were calculated. It was found that the relative effective mass of electrons and holes ($D = m_h^* / m_e^*$) of ZnO are much higher than that of gCN, suggesting that the electrons that are photogenerated on the ZnO have higher tendency to transfer, and therefore, it is more likely that the charge transfer takes place from ZnO to gCN instead from gCN to ZnO.[86] The above findings support the Z-scheme mechanism hypothesis.

8.2.4.3 gCN/Metal Complex Photocatalysts

Although metal complexes have high efficiency and selectivity compared to traditional semiconductor catalysts, they are characterized with poor capability of oxidation and recycling, which significantly limits their applications.[87,88] Therefore, in recent studies, gCN and metal complexes were combined in order to integrate their advantages. In such a system, the active sites are mainly provided by the metal complex and the main function of the gCN is light harvesting.

A heterogeneous photocatalyst was reported by Maeda *et al.* in which a ruthenium (Ru) complex was used as the main catalytic unit and the gCN was merely used for light harvesting. It was reported that electron transfer in this system took place from gCN to the Ru complex as a result of the electronic interactions between the two photocatalyst constituents.[87] Specifically, in this study, was used as a catalyst, and DMA : TEOA mixture (4 : 1, v/v) as solvent. The photoreduction of CO_2 resulted in the formation of HCOOH and CO, where the selectivity of HCOOH formation was estimated to be *ca.* 80%, with a turnover number of 1061 after 20 h of the photocatalytic process. Overall, the apparent quantum yield was calculated to be 5.7% at 400 nm, which is higher than the yields reported in earlier studies.

In another study, Jain *et al.* synthesized various metal complex/gCN photocatalysts based on cobalt(II) phthalocyanine tetracarboxylate (CoPc-COOH), where different ratios of the two components were used.[89] The photocatalytic activities towards CO_2 reduction were estimated for CoPc-COOH, gCN, and gCN/CoPc-COOH in a water/DMF mixture using triethylamine as a sacrificial agent. After 24 h of CO_2 photoreduction, the gCN/CoPc-COOH resulted in the formation of CH_4 with a total yield of 12.9 mmol g^{-1}, which is 7.3 and 10.9 times higher than that obtained for CoPc-COOH and gCN, respectively. The enhancement in photocatalytic activity was attributed to the higher concentration of CO_2 and that resulted from the high binding ability of CO_2 on CoPc-COOH.

For the metal complex based gCN photocatalysts, the interaction between the metal complex and gCN is crucial for the enhancement in the migration of charge transfer and for the suppression of charge recombination. To reach a maximum interaction between the two components of the photocatalyst, either π–π interaction between the individual gCN units and organic ligands, or hydrogen/covalent bonds between the functional groups, should be introduced.

8.3 Conclusions

In this chapter, the recent progress in graphitic carbon nitride (gCN)-based materials for CO_2 photocatalytic reduction was reviewed. In addition, the basic properties of gCN and the various steps of CO_2 photoreduction have been explained in detail. Furthermore, various types of gCN-composites were covered, these included pristine gCN, non-metal doped gCN, gCN with a co-catalyst, gCN-based semiconductor, and gCN/metal complex. Among these categories of CO_2 photoreduction catalytic systems, gCN-based semiconductors are the most frequently studied systems due to their high performance. The mediator-based and direct Z-scheme structures were critically examined, and the direct Z-scheme heterojunctions realize charge transfer through well-defined interface contact, which accelerates the charge transfer and results in high CO_2 conversion performance and reduced cost. Furthermore, the photocatalytic activity of CO_2 reduction was also enhanced by exposing gCN to various treatments such as doping with different elements and structural modification. However, in contrast to gCN/metal complex photocatalysts, heterogeneous photocatalysts based on semiconductor photocatalysts are characterized by less efficient light absorption and lower photocatalytic activity. Through the optimization of the interaction between the active sites and light harvesting units, and using optimum reaction conditions, gCN/metal complex photocatalytic systems can enhance CO_2 conversion efficiency more than 10-fold, but this can make the separation and recycling more complicated.

These systems are not yet widely applicable to large-scale production due to financial limitations and industrial constraints. However, future recommended approaches will aid development of more efficient and sustainable technologies for the photocatalytic reduction of CO_2 based on gCN so that a cleaner environment will become evident for subsequent generations.

References

1. M. Aresta, A. Dibenedetto and A. Angelini, *Chem. Rev.*, 2014, **114**(3), 1709.
2. G. Valenti, M. Melchionna, T. Montini, A. Boni, L. Nasi, E. Fonda, A. Criado, A. Zitolo, S. Voci, G. Bertoni, M. Bonchio, P. Fornasiero, F. Paolucci and M. Prato, *ACS Appl. Energy Mater.*, 2020, **3**(9), 8509.
3. G. Centi and S. Perathoner, *Catal. Today*, 2009, **148**(3), 191.
4. J. Qiao, Y. Liu, F. Hong and J. Zhang, *Chem. Soc. Rev.*, 2014, **43**(2), 631.
5. A. M. Appel, J. E. Bercaw, A. B. Bocarsly, H. Dobbek, D. L. DuBois, M. Dupuis, J. G. Ferry, E. Fujita, R. Hille, P. J. A. Kenis, C. A. Kerfeld, R. H. Morris, C. H. F. Peden, A. R. Portis, S. W. Ragsdale, T. B. Rauchfuss, J. N. H. Reek, L. C. Seefeldt, R. K. Thauer and G. L. Waldrop, *Chem. Rev.*, 2013, **113**(8), 6621.
6. Y.-N. Li, R. Ma, L.-N. He and Z.-F. Diao, *Catal. Sci. Technol.*, 2014, **4**(6), 1498.
7. F. D. Meylan, V. Moreau and S. Erkman, *J. CO2 Util.*, 2015, **12**, 101.
8. X. Liu, S. Inagaki and J. Gong, *Angew. Chem., Int. Ed.*, 2016, **55**(48), 14924.
9. T. Inoue, A. Fujishima, S. Konishi and K. Honda, *Nature*, 1979, **277** (5698), 637.
10. J. Hawecker, J. M. Lehn and R. Ziessel, *J. Chem. Soc., Chem. Commun.*, 1983, (9), 536.
11. I. Willner, D. Mandler and A. Riklin, *J. Chem. Soc., Chem. Commun.*, 1986, (13), 1022.
12. W.-N. Wang, J. Soulis, Y. J. Yang and P. Biswas, *Aerosol Air Qual. Res.*, 2014, **14**(2), 533.
13. J. Qin, V. A. Larionov, K. Harms and E. Meggers, *ChemSusChem*, 2019, **12**(1), 320.
14. F. Chen, X. Jiang, L. Zhang, R. Lang and B. Qiao, *Chin. J. Catal.*, 2018, **39**(5), 893.
15. M. A. Ahsan, T. He, K. Eid, A. M. Abdullah, M. L. Curry, A. Du, A. R. Puente Santiago, L. Echegoyen and J. C. Noveron, *J. Am. Chem. Soc.*, 2021, **143**, 1203–1215.
16. K. Eid, M. H. Sliem and A. M. Abdullah, *Nanoscale*, 2019, **11**, 11755–11764.
17. C. Li, G. Chen, J. Sun, J. Rao, Z. Han, Y. Hu, W. Xing and C. Zhang, *Appl. Catal., B*, 2016, **188**, 39.
18. Q. Zhang, D. Q. Lima, I. Lee, F. Zaera, M. Chi and Y. Yin, *Angew. Chem., Int. Ed.*, 2011, **50**(31), 7088.
19. K. Eid, M. H. Sliem, K. Jlassi, A. S. Eldesoky, G. G. Abdo, S. Y. Al-Qaradawi, M. A. Sharaf, A. M. Abdullah and A. A. Elzatahry, *Inorg. Chem. Commun.*, 2019, **107**, 107460.
20. S. D. Perera, R. G. Mariano, K. Vu, N. Nour, O. Seitz, Y. Chabal and J. K. J. Balkus, *ACS Catal.*, 2012, **2**(6), 949.
21. A. Thomas, A. Fischer, F. Goettmann, M. Antonietti, J.-O. Müller, R. Schlögl and J. M. Carlsson, *J. Mater. Chem.*, 2008, **18**(41), 4893.
22. E. G. Gillan, *Chem. Mater.*, 2000, **12**(12), 3906.

23. L. Sun, X. Zhao, C.-J. Jia, Y. Zhou, X. Cheng, P. Li, L. Liu and W. Fan, *J. Mater. Chem.*, 2012, **22**(44), 23428.
24. Z. Jin-Shui, W. Bo and W. Xin-Chen, *Acta Phys.-Chim. Sin.*, 2013, **29**(9), 1865.
25. X. Wang, K. Maeda, A. Thomas, K. Takanabe, G. Xin, J. M. Carlsson, K. Domen and M. Antonietti, *Nat. Mater.*, 2009, **8**(1), 76.
26. J. Mao, T. Peng, X. Zhang, K. Li, L. Ye and L. Zan, *Catal. Sci. Technol.*, 2013, **3**(5), 1253.
27. J. Wu, Y. Huang, W. Ye and Y. Li, *Adv. Sci.*, 2017, **4**(11), 1700194.
28. J. Lee, D. C. Sorescu and X. Deng, *J. Am. Chem. Soc.*, 2011, **133**(26), 10066.
29. Y. S. Seo and S.-G. Oh, *Korean J. Chem. Eng.*, 2019, **36**(12), 2118.
30. G. Dong and L. Zhang, *J. Mater. Chem.*, 2012, **22**(3), 1160.
31. Q. Lu, Y. Yu, Q. Ma, B. Chen and H. Zhang, *Adv. Mater.*, 2016, **28**(10), 1917.
32. Y. Zheng, L. Lin, X. Ye, F. Guo and X. Wang, *Angew. Chem., Int. Ed.*, 2014, **53**(44), 11926.
33. P. Xia, B. Zhu, J. Yu, S. Cao and M. Jaroniec, *J. Mater. Chem. A*, 2017, **5**(7), 3230.
34. M. Shen, L. Zhang, M. Wang, J. Tian, X. Jin, L. Guo, L. Wang and J. Shi, *J. Mater. Chem. A*, 2019, **7**(4), 1556.
35. J. Hong, W. Zhang, Y. Wang, T. Zhou and R. Xu, *Chemcatchem*, 2014, **6**(8), 2315.
36. Y.-S. Bae and R. Q. Snurr, *Angew. Chem., Int. Ed.*, 2011, **50**(49), 11586.
37. J.-C. Wang, H.-C. Yao, Z.-Y. Fan, L. Zhang, J.-S. Wang, S.-Q. Zang and Z.-J. Li, *ACS Appl. Mater. Interfaces*, 2016, **8**(6), 3765.
38. J. Wang, C. Qin, H. Wang, M. Chu, A. Zada, X. Zhang, J. Li, F. Raziq, Y. Qu and L. Jing, *Appl. Catal., B*, 2018, **221**, 459.
39. Z. Jiang, W. Wan, H. Li, S. Yuan, H. Zhao and P. K. Wong, *Adv. Mater.*, 2018, **30**(10), 1706108.
40. S. Tonda, S. Kumar, M. Bhardwaj, P. Yadav and S. Ogale, *ACS Appl. Mater. Interfaces*, 2018, **10**(3), 2667.
41. J. Fu, K. Liu, K. Jiang, H. Li, P. An, W. Li, N. Zhang, H. Li, X. Xu, H. Zhou, D. Tang, X. Wang, X. Qiu and M. Liu, *Adv. Sci.*, 2019, **6**(18), 1900796.
42. B. Liu, L. Ye, R. Wang, J. Yang, Y. Zhang, R. Guan, L. Tian and X. Chen, *ACS Appl. Mater. Interfaces*, 2018, **10**(4), 4001.
43. K. Wang, Q. Li, B. Liu, B. Cheng, W. Ho and J. Yu, *Appl. Catal., B*, 2015, **176**, 44.
44. W.-J. Ong, L.-L. Tan, S.-P. Chai and S.-T. Yong, *Dalton Trans.*, 2015, **44**(3), 1249.
45. G. Gao, Y. Jiao, E. R. Waclawik and A. Du, *J. Am. Chem. Soc.*, 2016, **138**(19), 6292.
46. H. Li, Y. Gao, Z. Xiong, C. Liao and K. Shih, *Appl. Surf. Sci.*, 2018, **439**, 552.
47. F. Gonell, A. V. Puga, B. Julian-Lopez, H. Garcia and A. Corma, *Appl. Catal., B*, 2016, **180**, 263.
48. S. Neatu, J. Antonio Macia-Agullo, P. Concepcion and H. Garcia, *J. Am. Chem. Soc.*, 2014, **136**(45), 15969.

49. P. Li, F. Wang, S. Wei, X. Li and Y. Zhou, *Phys. Chem. Chem. Phys.*, 2017, **19**(6), 4405.
50. J.-Y. Tang, D. Yang, W.-G. Zhou, R.-T. Guo, W.-G. Pan and C.-Y. Huang, *J. Catal.*, 2019, **370**, 79.
51. J.-Y. Tang, X. Y. Kong, B.-J. Ng, Y.-H. Chew, A. R. Mohamed and S.-P. Chai, *Catal. Sci. Technol.*, 2019, **9**(9), 2335.
52. X. Wu, H. Ma, W. Zhong, J. Fan and H. Yu, *Appl. Catal., B*, 2020, **271**, 118899.
53. X. Wu, D. Gao, H. Yu and J. Yu, *Nanoscale*, 2019, **11**(19), 9608.
54. G. Zhang, M. Zhang, X. Ye, X. Qiu, S. Lin and X. Wang, *Adv. Mater.*, 2014, **26**(5), 805.
55. S. Samanta, R. Yadav, A. Kumar, A. K. Sinha and R. Srivastava, *Appl. Catal., B*, 2019, **259**, 118054.
56. G. Zhang, G. Li, T. Heil, S. Zafeiratos, F. Lai, A. Savateev, M. Antonietti and X. Wang, *Angew. Chem., Int. Ed.*, 2019, **58**(11), 3433.
57. D. Masih, Y. Ma and S. Rohani, *Appl. Catal., B*, 2017, **206**, 556.
58. S. Cao, H. Li, T. Tong, H.-C. Chen, A. Yu, J. Yu and H. M. Chen, *Adv. Funct. Mater.*, 2018, **28**(32), 1802169.
59. K. Wang, J. Fu and Y. Zheng, *Appl. Catal., B*, 2019, **254**, 270.
60. S. Wang, J. Zhan, K. Chen, A. Ali, L. Zeng, H. Zhao, W. Hu, L. Zhu and X. Xu, *ACS Sustainable Chem. Eng.*, 2020, **8**(22), 8214.
61. H. Zhang, Y. Tang, Z. Liu, Z. Zhu, X. Tang and Y. Wang, *Chem. Phys. Lett.*, 2020, **751**, 137467.
62. Z. Zhu, X. Tang, W. Fan, Z. Liu, P. Huo, T. Wang, Y. Yan and C. Li, *J. Alloys Compd.*, 2019, **775**, 248.
63. N. Sagara, S. Kamimura, T. Tsubota and T. Ohno, *Appl. Catal., B*, 2016, **192**, 193.
64. Z. Sun, H. Wang, Z. Wu and L. Wang, *Catal. Today*, 2018, **300**, 160.
65. Q. Zhai, S. Xie, W. Fan, Q. Zhang, Y. Wang, W. Deng and Y. Wang, *Angew. Chem., Int. Ed.*, 2013, **52**(22), 5776.
66. J. Yu, K. Wang, W. Xiao and B. Cheng, *Phys. Chem. Chem. Phys.*, 2014, **16**(23), 11492.
67. Q. Gu, J. Long, H. Zhuang, C. Zhang, Y. Zhou and X. Wang, *Phys. Chem. Chem. Phys.*, 2014, **16**(24), 12521.
68. X. Lan, Y. Li, C. Du, T. She, Q. Li and G. Bai, *Chem. - Eur. J.*, 2019, **25**(36), 8560.
69. W.-J. Ong, L.-L. Tan, S.-P. Chai and S.-T. Yong, *Chem. Commun.*, 2015, **51**(5), 858.
70. Y. Wang, Q. Xia, X. Bai, Z. Ge, Q. Yang, C. Yin, S. Kang, M. Dong and X. Li, *Appl. Catal., B*, 2018, **239**, 196.
71. H. Feng, Q. Guo, Y. Xu, T. Chen, Y. Zhou, Y. Wang, M. Wang and D. Shen, *ChemSusChem*, 2018, **11**(24), 4256.
72. Y. Wang, X. Liu, X. Han, R. Godin, J. Chen, W. Zhou, C. Jiang, J. F. Thompson, K. B. Mustafa, S. A. Shevlin, J. R. Durrant, Z. Guo and J. Tang, *Nat. Commun.*, 2020, **11**(1), 1–9.

73. C. Han, R. Zhang, Y. Ye, L. Wang, Z. Ma, F. Su, H. Xie, Y. Zhou, P. K. Wong and L. Ye, *J. Mater. Chem. A*, 2019, **7**(16), 9726.
74. H. Qin, R.-T. Guo, X.-Y. Liu, X. Shi, Z.-Y. Wang, J.-Y. Tang and W.-G. Pan, *Colloids Surf., A*, 2020, **600**, 124912.
75. Q. Wang and D. O'Hare, *Chem. Rev.*, 2012, **112**(7), 4124.
76. M. Zubair, M. Daud, G. McKay, F. Shehzad and M. A. Al-Harthi, *Appl. Clay Sci.*, 2017, **143**, 279.
77. J. Fu, J. Yu, C. Jiang and B. Cheng, *Adv. Energy Mater.*, 2018, **8**(3), 1701503.
78. H. Wang, L. Zhang, Z. Chen, J. Hu, S. Li, Z. Wang, J. Liu and X. Wang, *Chem. Soc. Rev.*, 2014, **43**(15), 5234.
79. H. Li, Y. Zhou, W. Tu, J. Ye and Z. Zou, *Adv. Funct. Mater.*, 2015, **25**(7), 998.
80. K. Maeda, *ACS Catal.*, 2013, **3**(7), 1486.
81. H. Tada, T. Mitsui, T. Kiyonaga, T. Akita and K. Tanaka, *Nat. Mater.*, 2006, **5**(10), 782.
82. J. Low, C. Jiang, B. Cheng, S. Wageh, A. A. Al-Ghamdi and J. Yu, *Small Methods*, 2017, **1**(5), 1700083.
83. P. Zhou, J. Yu and M. Jaroniec, *Adv. Mater.*, 2014, **26**(29), 4920.
84. R.-T. Guo, X.-Y. Liu, H. Qin, Z.-Y. Wang, X. Shi, W.-G. Pan, Z.-G. Fu, J.-Y. Tang, P.-Y. Jia, Y.-F. Miao and J.-W. Gu, *Appl. Surf. Sci.*, 2020, **500**, 144059.
85. W. Yu, D. Xu and T. Peng, *J. Mater. Chem. A*, 2015, **3**(39), 19936.
86. H. Zhang, L. Liu and Z. Zhou, *Phys. Chem. Chem. Phys.*, 2012, **14**(3), 1286.
87. T. Yui, Y. Tamaki, K. Sekizawa and O. Ishitani, *Photocatalysis*, 2011, **303**, 151.
88. B. Kumar, M. Llorente, J. Froehlich, T. Dang, A. Sathrum and C. P. Kubiak, *Annu. Rev. Phys. Chem.*, 2012, **63**, 541.
89. A. Kumar, P. K. Prajapati, M. S. Aathira, A. Bansiwal, R. Boukherroub and S. L. Jain, *J. Colloid Interface Sci.*, 2019, **543**, 201.

CHAPTER 9

Combination of Carbon Nitride and Semiconductors for the Enhancement of the Photocatalytic Degradation of Organic Pollutants and Hydrogen Production

MOHAMMED SHARAF*[a], ISMAIL BOZ*[b] AND KAMEL EID*[c]

[a]Department of Maritime Transportation Management Engineering, Istanbul University-Cerrahpasa, 34320 Avcılar, Istanbul, Turkey; [b]Department of Chemical Engineering, Istanbul University-Cerrahpasa, 34320 Avcılar, Istanbul, Turkey; [c]Gas Processing Center College Center for Advanced Materials, Qatar University, Doha 2713, Qatar
*E-mail: mohammed.sharaf@istanbul.edu.tr, ismailb@inc.edu.tr, kamel.eid@qu.edu.qa

9.1 Introduction

In the hot pursuit of a viable semiconductor photocatalyst that is responsive and active in harvesting visible light, graphitic carbon nitride (gCN), a polymeric semiconductor, was thought of as the next generation photocatalyst

Nanoscience & Nanotechnology Series No. 51
Carbon Nitride Nanostructures for Sustainable Energy Production and Environmental Remediation
Edited by Kamel Abdelmoniem Mohamed Eid and Aboubakr M. Abdullah

Published by the Royal Society of Chemistry, www.rsc.org

and it has stirred excitement in the scientific community due to its facile synthesis methods, natural abundance of precursors, lower electronic band gap structure, great catalytic activities, and high physicochemical stability.[1–7]

Practical applications are still impeded by several shortcomings of parent gCN; namely, lower electrical conductivity, low surface area, high recombination of charge carriers, a narrow absorption edge not exceeding 460 nm, and low electrical conductivity.[8–12] For example, modulation and modifications of bare gCN *via* improved synthesis procedures, electronic structure modulation, and heterojunction design, have been carried out to enhance photoactivity.[13,14] Also, copolymerization and doping are promising approaches in the modification of the electronic structure and energy band gaps,[15,16] as well as morphology control of pure gCN, heterojunction design metal doping,[17,18] noble metal deposition,[19,20] incorporation of carbonaceous nanomaterials,[21,22] and coupling with other semiconductors.[23,24]

Undoubtedly, there is a surge of interest in the development of photocatalytic activities for gCN-based nanohybrids and heterostructures, taking into consideration their unique electronic structure and intriguing visible-light response. The extraordinary growth of published papers since 2009 is mainly due to the publication on photocatalytic H_2 evolution by Wang *et al.*[25,26] A testament to this interest in gCN photocatalysis is confirmed by a proliferation in the number of comprehensive reviews documenting synthesis strategies, functionalization modulation, and the potential of favorable applications. A representative sample of such reviews is reported here.[27–30]

In this review, our emphasis will be primarily on the synthetic routes and applications as concerns H_2 generation, dye, and organic pollutants' remediation.

9.1.1 Preparation of gCN

The revived interest in the utilization of gCN as a heterogeneous catalyst began around 2006,[31] with the utilization of gCN as a conjugated metal-free semiconductor photocatalyst for H_2 evolution. This resulted in a shift in research to polymeric conjugated semiconductor photocatalysts rather than traditional inorganic ones.[25]

Seven phases exist for C_3N_4; namely, α-C_3N_4, β-C_3N_4, cubic C_3N_4, pseudocubic C_3N_4, g-h-triazine, g-o-triazine, and g-h-heptazine. Their band gaps vary between 0.93 and 5.49 eV.[32] Among all of the phases, tri-*s*-triazine based g-C_3N_4 is found to exhibit the largest stability in atmospheric surroundings.[33] Density functional theory (DFT) was applied by Kroke[34] and coworkers on the basic rings of triazene (C_3N_3) and tri-*s*-triazine/heptazine (C_6N_7) allotropes (Schemes 9.1 and 9.2). The results of the calculations were in satisfactory agreement with the experiment.[34] The basic building block units to create allotropes of gCN are triazine (C_3N_4) and tri-*s*-triazine/heptazine (C_6N_7) rings (Schemes 9.1 and 9.2).[35,36] Thus, the size of the carbon nitride pores and the other electronic natures of the N atom contribute to several energetic stabilities. Among all of the phases, tri-*s*-triazine based gCN

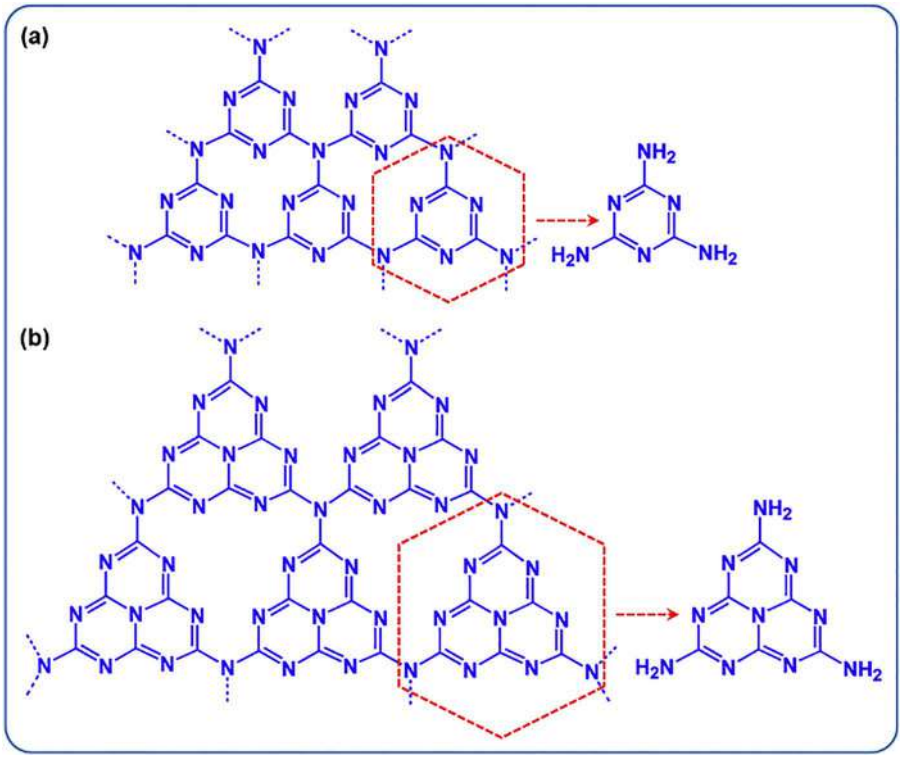

Scheme 9.1 Structure illustration of gCN in (a) triazine and (b) tri-*s*-triazine (heptazine). Reproduced from ref. 43 with permission from Elsevier, Copyright 2019.

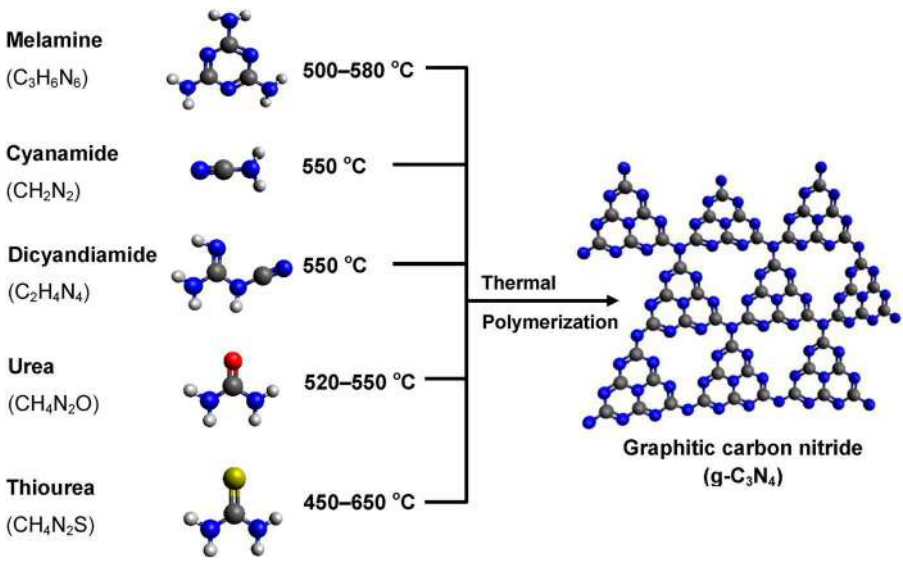

Scheme 9.2 Thermal polymerization of different precursors for gCN preparation. Reproduced form ref. 29 with permission from American Chemical Society, Copyright 2016.

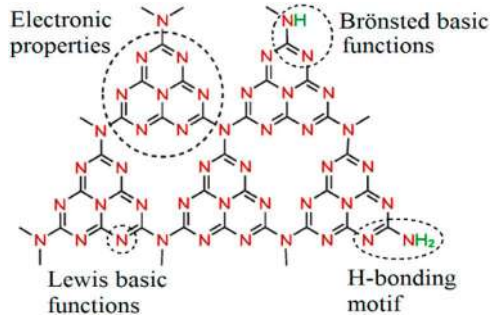

Scheme 9.3 Multiple surface functionalities were found on gCN. Reproduced from ref. 44 with permission from American Chemical Society, Copyright 2014.

was the most stable and vigorously favoured phase of C_3N_4 in atmospheric conditions.[33] This was in agreement with the previous DFT introduced by Kroke *et al.*[34] Much research has revealed that the polycondensation of melamine, cyanamide, dicyandiamide (DCDA), or urea (U) produced a melon polymer from the melem units.[37,38] This serves as a manifestation that these are the constructing blocks for the typical creation of gCN.

As polymeric gCN contains earth-rich elements such as C and N, it is adaptable for supplying reactions to modify its surface construction without substantially varying the hypothetical structure and configuration. Owing to the polymeric characteristic of gCN, the surface chemistry is easy to regulate through surface manufacturing at the molecular level (Scheme 9.3). Additionally, its band gap is considered as the lowest between the seven phases of C_3N_4, owing to the existence of sp^2-hybridized carbon and nitrogen, and so forming π-conjugated electronic constructions.[39] gCN has a band gap of 2.7–2.8 eV, leading to an onset of visible-light absorption in the range of 450–460 nm.[40] Since it is the most stable allotrope in all of the C_3N_4 configurations, gCN exhibits thermal stability at *ca.* 600 °C in air, which is due to the aromatic C–N heterocycles.[41] Also, gCN is chemically stable and does not dissolve in acids, alkaline or organic solvents.[42]

9.1.2 Preparation of Pristine gCN

N-rich precursors are used for the synthesis of amorphous gCN. Several synthesis alternatives have been reported.[45] They include chemical vapor deposition (CVD),[46] solvothermal,[47] plasma sputtering deposition,[48] and thermal polycondensation.[49] The small molecules could be polymerized into gCN during a facile heating method at 450–650 °C due to the abundant availability of nitrogen.[50] This process exhibits a strong effect on the electronic band structures and textual estates of the resulting bulky gCN. For illustration, the gCN prepared from thiourea (THU) tends to show a smaller band gap than gCN prepared from U.[51] The gCN prepared from U displays a larger specific surface area than that prepared using

melamine.[49] Thermal polycondensation of common organic monomers was utilized to synthesize graphitic carbon nitrides (gCNs) with various architectures.

9.2 Main Modification Strategies of Pristine gCN

The photocatalytic efficiency of bulk gCN can be enhanced through the alteration of the surface and textural properties, which can be modulated using various methods.[52] The methods applied are, for example, heterostructure formation,[29,53] nanostructure construction,[54,55] exfoliation into nanosheets,[56] surface property modification,[57,58] control of crystallinity,[59] and structural defect engineering.[51,60] Both graphene and gCN have a 2D layered structure. Nonetheless, bulk gCN possesses a 20 $m^2\ g^{-1}$ surface area, which is lower than that of graphene.

9.2.1 Exfoliation (Delamination)

Exfoliation of bulk gCN into thin or monolayers, as in the case of graphene, results in a marked improvement of the specific surface area. One should note that the theoretical specific surface area of a monolayer of gCN could reach 2500 $m^2\ g^{-1}$.[61] The exfoliation process is used to yield nanosheets (NSs) that are usually attained by thermal oxidation,[62] ultrasonic exfoliation,[63] chemical exfoliation,[64] and other methods.[61] The exfoliated nanosheets of gCN showed much higher surface area (306 $m^2\ g^{-1}$),[62] shorter transfer distance of electron–hole pairs, and improved distribution of reactants/products in comparison to bulk samples. In general, and along with synthetic methods of graphene, there are two other strategies that have been established for the manufacture of 2D gCN NSs (Scheme 9.4).[65] The top–down approach includes the delamination of laminar bulk gCN solids into freestanding NSs. Direct thermal oxidation etching of bulk gCN solids in air is a simple method to prepare NSs.[62] The second strategy depends on bottom–up fabrication, in which a simple method to prepare gCN NSs is possibly produced by anisotropic gathering of organic molecules in a 2D approach. The methods are both actively adopted for the construction of gCN NSs with necessary roles.

9.2.2 Structure Defect Engineering

Defect control is also an effective method to enhance the photocatalytic performance of gCN. A major route for defect engineering is elemental doping. It results in the modification of the electronic structure of gCN.[66,67] Nonmetal P-doped gCN NSs were prepared using P-doping and thermal exfoliation methods together. It led to the creation of blank mid-gap states in gCN. Therefore, the light-response range was substantially extended and an increase in the charge diffusion rate has been observed.[66]

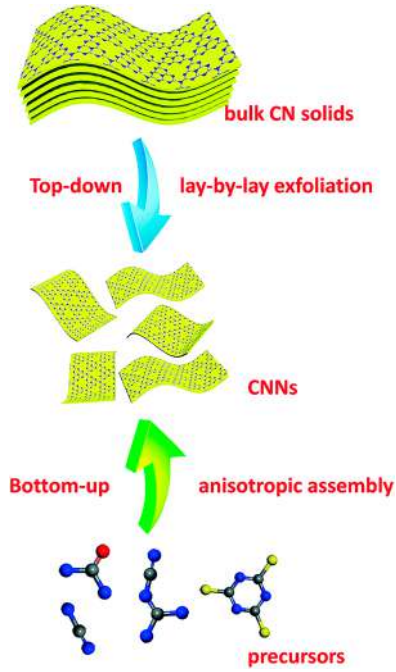

Scheme 9.4 Illustration of top–down and bottom–up synthetic strategies for gCN NSs. Reproduced from ref. 65 with permission from the Royal Society of Chemistry.

9.2.3 Surface Modification

Surface modification enhances the adsorption of reactants. Besides, it inhibits the surface recombination of photogenerated charge carriers, and thus facilitates the surface catalytic reactions. Amine-functionalized gCN was prepared by treating a bulk sample with a solution of monoethanolamine.[68] This surface modification process led to an enhancement of CO_2 adsorption capacity by gCN, owing to the presence of excess surface amine groups. The acid–base interaction among the surface amine groups and CO_2 molecules enhanced the adsorption capacity of CO_2; in consequence, improvement in the photocatalytic reduction of CO_2 has been observed.

Surface alkalinized gCN was synthesized through the introduction of KCl and NH_4Cl during the polycondensation process of melamine.[57] Thus, the recombination probability of photogenerated electrons and holes is reduced through trapping the holes by the ample grafted hydroxyl groups on the surface. The alkalinized surface, in consequence, resulted in enhanced photocatalytic H_2 production.

9.2.4 Crystal Structure Optimization

Band structure modulation could be achieved efficiently by controlling the crystal structure. The band structure relates to the optical properties and redox ability of the photogenerated charge carriers.[45] Amorphous gCN was formulated by disrupting the long-range atomic order with preserving the short-range atomic order.[59] This provided the amorphous gCN with a broader light absorption range because of its narrow band gap (1.9 eV).[59] Besides, an excellent photocatalytic H_2-generation activity has been observed.

9.2.5 The Morphological Features

The morphological features influence the photocatalytic activity. Constructing nanostructures has been a proven way for improving the photocatalytic efficiency of gCN. Such improvements owing to the presence of nanostructures endow more reactivity to the active sites, generate abundant pores, and provide a large surface area.

9.2.5.1 Templating

Whether a template is hard or soft, there is a need for it to be applied in the construction of nanostructures of the bulk gCN. Such structures include mesoporous gCN,[69] gCN nanotubes,[70] hollow gCN nanospheres,[71] and gCN nanorods.[72] These nanostructures exhibit multiple light effects and improved diffusion of reactants/products.

9.3 Newer Preparation Strategies for Pristine gCN

Traditionally, gCN has been generally synthesized by thermal condensation of N-rich precursors, such as U, DCDA, melamine, and so on.[73] However, the fast recombination of the electron–hole pairs hinders the photocatalytic activity of as-obtained gCN. Therefore, a new strategy ought to be designed to solve such a problem.

9.3.1 Supramolecular Pre-assembly for gCN Synthesis

It is obvious that in the design of gCN with improved photocatalytic activity, one should consider addressing the need for strong visible-light absorption, facilitated charge mobility, and exposure of sufficient active sites.

Traditionally, N-rich precursors such as DCDA, cyanamide, melamine, triazine derivatives, U, and THU, are utilized in the production of gCN by heating at 500–600 °C.[74] At this high temperature, thermal polymerization into gCN takes place, with the formation of various intermediates. Consequently, and due to the presence of such intermediates, it will lead to disorder in the gCN structure.[75]

Molecular self-assembly, in which the molecules adopt a specific arrangement under equilibrium and aggregates *via* non-covalent bonds, is a new strategy that helps solve these problems. The directionality and specificity of hydrogen bonding plays a paramount role in the reorganization of the structure of the supramolecular aggregate. Generally, this strategy includes producing supramolecular precursors followed by pyrolysis to obtain gCN.[76] Such supramolecular precursors are prepared by either the interactions between two reactants,[75,76] for illustration, melamine and cyanuric acid,[77] or the self-assembly of one monomer, such as DCDA,[78] melamine,[79] and other N-containing raw materials.[80] They have a similar crystalline structure to that of melamine-cyanurate.

Remarkably, the precursor melamine can link with triazine products, such as cyanuric acid, into supramolecular aggregates through hydrogen bonds. The supramolecular aggregate of MCA can result in the production of various morphologies depending on the solvent.[81] This MCA supramolecular prearrangement is structurally analogous to the local gCN arrangements. Thus, this organized precursor leads to the manufacture of an ordered network of gCN. Scheme 9.5 represents a depiction of fabrication of O-doped porous gCN from a hydrogen-bonded induced supramolecular precursor assembled under hydrothermal treatment.[82]

Recently, 1-amino-2-propanol MIPA was added during the hydrothermal treatment of DCDA. MIPA is a substance that has both NH_2 and OH groups.[83] The supramolecular DCDA precursors synthesized in the presence of MIPA showed obvious differences as regards the crystalline structures, morphologies of the precursors, the optical, photo electrochemical properties, and the photocatalytic hydrogen evolution rates when compared with those of the MC precursor and pure gCN.[83] The gCN samples prepared by implanting MIPA in the precursor helped extend the visible-light range absorption to 600 nm with an apparent obviation of charge recombination. Thus, a significant enhancement in the photocatalytic hydrogen evolution was

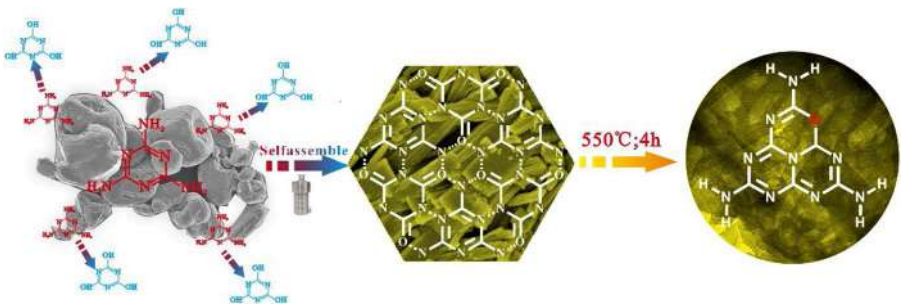

Scheme 9.5 Illustration of the fabrication of O-doped porous gCN from a hydrogen bond induced supramolecular precursor assembled under hydrothermal treatment. Reproduced from ref. 82 with permission from Elsevier, Copyright 2018.

achieved (13 840 μmol h^{-1} g^{-1} H_2 evolution rate that was 30.1 times higher than pure with a quantum efficiency of 18.25% at 420 nm, which was 30.1 times higher than gCN under visible-light irradiation $\lambda > 420$ nm).[83] Such remarkable performance is due to the significant improvement in specific surface area, more efficient light harvesting, stronger reduction capability, and better charge carrier separation and transfer. This research is a vivid example of the molecular engineering of supramolecular precursors used to prepare novel gCN.[83]

9.3.2 Rapid Microwave-assisted Production of gCN

It is noteworthy that the process of fabrication of gCN from N-rich precursors is performed by heating at elevated temperature for hours, which consumes much energy and time.[84] The process involves polycondensation time, heating rate, and the reaction atmosphere. These factors have a great influence on the physical properties and photocatalytic activity of gCN thus manufactured.[85]

The microwave (MW) represents an alternative as it can induce viable heating in the presence of an MW-absorber material like CuO.[86] Microwave-aided heating allows a brief preparation time within the order of a couple of minutes as well as the production of an inexpensive yield.[87] The generated temperature is high enough to polymerize N-rich precursors into gCN.

By employing this MW-assisted heating strategy, Yuan and colleagues[85] found that gCN is obtained in minutes by MW irradiation of carbamide and U. The as-produced gCN was crystalline as a result of localized and unvaried heating. High crystallinity ends up in improved H_2 production.[85] This process can be applied to different N-rich materials and may change the gram-scale production of gCN. In summary, the microwave is an attractive approach to prepare gCN.[87]

9.3.3 Molten and Ionic Liquid Salt Strategy for the Preparation of gCN

In general, molten salt serves as a solvent in the high-temperature synthesis of materials that include numerous natural and inorganic reactions. It also serves as a soft template tailoring the micro- and meso-porosity of the reaction products. In previous reports, it is suggested that crystalline gCN could result from polycondensation of DCDA ($NH_2C(NH)NHCN$) employing LiCl/KCl as a molten salt at 380–600 °C. The resulting product derived from the melted salt is presumably gCN with the *s*-heptazine units that are hexagonally organized.[88]

By using this strategy, Lotsch *et al.*[89] found that a new family of 2D triazine-based carbon nitrides could be used in photocatalytic H_2 production with enhanced photo activity. Enhanced crystallinity of the products obtained is the primary reason for the enhanced performance of the melted salt.[89]

Zou *et al.* effectively prepared a carbon nitride intercalation combination by heating up the melamine with low melting point eutectic mixed salts ($LiCl{\cdot}H_2O$–KCl–NaCl) under air and ambient pressure. Interestingly, gCN nanotubes were produced. The improved separation and transportation of the photogenerated carriers are due to the insertion of the alkali metal salts into the interlayer of gCN, which led to enhanced hydrogen generation. Owing to their characteristics, such as small vapor pressure, high chemical and thermal stability, and their fluid nature, ionic liquids are the preferred choice.

Recently, ionic liquids have been used to prepare gCN-based materials. Wang and co-workers[90] first reported the usage of 1-butyl-3-methylimidazolium tetrafluoroborate (BmimBF4), an ionic liquid. It was utilized as a soft template and the DCDA as a precursor for boron- and fluorine-containing mesoporous gCN. The largest surface area is as high as 440 $m^2\ g^{-1}$, with a pore volume of 0.32 $m^3\ g^{-1}$.

Here it is a necessity to adequately choose the ionic liquids for enhanced dispersion of the gCN owing to the ion–ion interaction. Ionic liquids act as templates for the preparation of inorganic semiconductors' precursors. The resulting composites and hybrids demonstrated improved photocatalytic activity as compared to the bare materials. This is primarily due to the intimate contact between gCN and the inorganic semiconductors.[91]

In Table 9.1, representative examples of the fabrication strategies and applications of bulk gCN are listed.

9.4 gCN-based Heterostructures

In gCN-based heterostructured photocatalysts, the recombination of photogenerated electrons and holes can be greatly restrained because of their efficient spatial split over the interface between the semiconductor components comprising the heterojunction. Moreover, better light absorption, optimized band positions, and higher surface-active sites are considered as supporting the second component. The design of gCN-based heterostructures has become a research hotspot due to its feasibility and effectiveness in improving photocatalytic performance.[27–30,107–110]

Wang *et al.*[25,26] carried out the first photocatalysis experiment with gCN in powder form in 2009. Steady production of H_2 was achieved over gCN from water that contained triethanolamine as a sacrificial electron donor, with illumination $\lambda > 420$ nm. This served as a clear indication that gCN is a stable 'metal-free' visible-light-driven photocatalyst for H_2 production. However, the H_2 evolution of bulk gCN fluctuated. The modification was based on the addition of a small amount of Pt to form a heterojunction composite that helped resolve the fluctuation problem. This modification facilitated the production of H_2 by a factor of 7 through the electron localization from the conduction band (CB) of gCN to the deposited Pt nanoparticles.[25,26]

Table 9.1 Pristine gCN photocatalysts: preparation and applications.

Photocatalyst	Preparation method	Wt% gCN	Application, efficiency, and enhancement factor	Reference
Hydrogen generation				
gCN porous NSs	Facile calcination with water included in the precursor	100	Photocatalytic H_2 evolution performance/Vis (3.214 mmol h^{-1} g^{-1}, enhanced 17.3 times/gCN. AQY 27% at λ = 420 nm)	92
gCN NSs	Facile hexamethylenetetramine (HETA) activation	100	One of the highest hydrogen production rates/Vis (rate > 27 mmol h^{-1} g^{-1}, 31.3-fold enhancement/gCN, AQE of 7.8% at λ = 420 nm)	93
gCN, NSs, with carbon vacancies and nanoholes	Two-step treatment (argon followed by air calcination)	100	Hydrogen production rate (5.261 mmol h^{-1} g^{-1}, 10 times higher efficiency/gCN, AQE of 29.2% at λ = 420 nm)	94
gCN NSs nitrogen-rich	Direct thermal polymerization	100	H_2 evolution/Vis (2.620 mmol h^{-1} g^{-1}, AQY is 8.5% at λ = 427 nm)	95
gCN HC ultra-thin donor–acceptor (D/A)	Thermal polycondensation. Calcination at 600 °C. Benzoyl isothiocyanate (BI) copolymer	—	Photocatalytic H_2 evolution/Vis (5.443 mmol h^{-1} g^{-1}, 11.96-fold enhancement/gCN, and AQE of 23.7% at 420 nm).	96
gCN NSs	Precursor-reforming and direct calcination of the melamine precursor	—	Hydrogen production/Vis (rate of 1.949 mmol h^{-1} g^{-1}, AQY of 10.8% at λ = 420 nm)	97
gCN NSs	Supramolecular assembly approach	70–95 mol%	Facile H_2 evolution/Vis (rate of 2.393 mmol h^{-1} g^{-1}, which was 68-fold/gCN, with the AQY at λ = 420, 450, and 520 nm of 10.6%, 6.4%, and 1.5%, respectively).	98
HC-gCN	KCl solid-salt-assisted growth technique	—	Hydrogen generation reaction/Vis (rate 1356 μmol h^{-1} g^{-1}, enhanced over 22 times higher/gCN, the AQY at λ = 420 nm is 11.4%)	99

gCN MTs	Liquid/liquid self-assembly under hydrothermal treatment	100	High H_2 production/UV-Vis (27.008 mmol h^{-1} g^{-1}. AQE of the MTs as high as 23.62% at λ = 420 nm)	100
mp-gCN, nitrogen defective	*In situ* silica gel templating strategy	84–95	H_2 evolution/Vis (highest rate 4.978 mmol g^{-1} h^{-1}, increased by 14.7-fold/gCN)	101
Organic pollutants' degradation				
gCN NSs	Thermal polymerization of U	100	Degradation of RhB (100% in 28 min, enhancement of 3.8-fold/gCN)	102
p-gCN NSs	Two-step thermal polymerization followed by thermal oxidation etching	100	Dehydrogenation of benzyl alcohols in water/Vis (conversion >99% and selectivity >99%)	103
p-gCN NSs	Hydrothermal and thermal etching	100	Disinfection of *Escherichia coli* (*E. coli*) cells/Vis (100% in 4 h, whereas only 77.1% are killed/gCN) Photodegradation of MB, Acid Red 27, and BPA (enhancements are 6.4, 4.0, and 1.9 times as fast, respectively,/gCN)	104
Supramolecular *p*-gCN NSs	Supramolecular self-assembly, 2, 4-diamino-6-phenoxy-[1,3,5]-triazine is the dopant	99–100	Decolorization of RhB/Vis (99% within 15 min). Degradation of tetracycline hydrochloride (TC-HCl) (92% in 30 min)	105
S-doped-*p*-gCN rods	One-pot hydrothermal method. Heating melamine-trithiocyanuric acid (MT) supramolecular complex	—	Photocatalytic activity degrading of RhB (90% in 120 min)	106
gCN NSs	Calcining DCDA. Exfoliating by Hummers treatment	100	Photodegradation of MB/Vis (96.6% within 120 min, enhancement of 2.5-fold/gCN)	64

9.4.1 Fabrication Strategies of gCN-based Heterojunctions

9.4.1.1 Isotype Heterojunctions

Wang *et al.*[111] prepared a S-gCN/gCN isotype metal-free heterojunction with enhanced visible-light activity by coating the precursor onto the surface of gCN followed by additional thermal treatment.

Isotype metal-free heterojunctions represent a novel alternative and pathway to address the intrinsic drawbacks of gCN, to enhance the photocatalytic performance without introducing any semiconductors. Coupling two components of gCN with a well-matched band structure to form a gCN/gCN isotype heterojunction could provide a viable alternative pathway. In general, the band gap of gCN can be adjusted between 2.4 and 2.8 eV through the proper choice of precursors. When irradiated with visible-light irradiation, the photogenerated electrons move from gCN (THU) to gCN (U) driven by the CB offset of 0.10 eV, whereas the reverse occurs for the holes that are driven by the valence band (VB) offset of 0.40 eV. In Scheme 9.6, the bias and the well-matched band structure in isotype heterojunctions is represented.[40]

A type II gCN/gCN metal-free isotype heterojunction has been also constructed with molecular composite precursors of U and THU in different weight ratios, which has proved to be an effective method to greatly enhance the charge separation and the transfer of charge carriers across the interface.[112] Consequently, this leads to a pronounced enhancement of the photocatalytic activity.

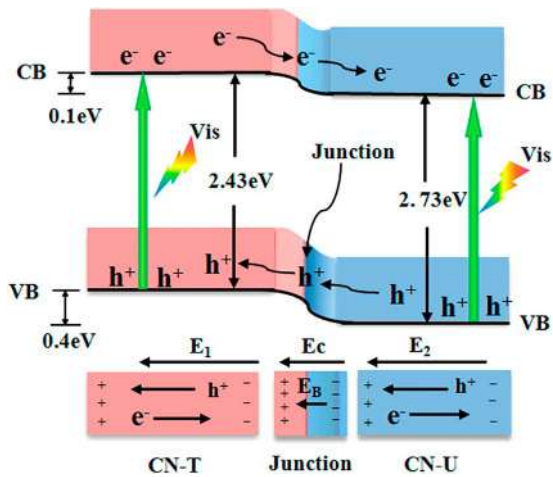

Scheme 9.6 Isotype gCN/gCN heterojunction prepared from U and THU separately. Reproduced from ref. 40, https://pubs.acs.org/doi/10.1021/am403653a, with permission from American Chemical Society, Copyright 2013. Further permissions requests related to the materials excerpted should be directed to the ACS.

9.4.1.2 Supramolecular Pre-assembly Method

In molecular self-assembly, molecules adopt a specific arrangement, under equilibrium, and aggregate *via* non-covalent bonds.[113] The directionality and specificity of hydrogen bonding plays a paramount role in the reorganization of the structure of the supramolecular aggregate.[113]

Electrostatic self-assembly strategy that included modification of the surface and metal deposition was applied in the synthesis of hybrid heterojunction-based photocatalysts.[114] The interfacial contact was achieved *via* mixing positively charged gCN with negatively charged TiO_2 nanoparticles. Charge transfer from gCN, excited by visible light was instrumental in the deposition of Pd nanoparticles on TiO_2 and consequently reducing Pd ions. To test the efficiency of this cascade of electron transfer, H_2 production from water was investigated. An increase in H_2 production rates was observed and attributed to enhanced charge separation. For H_2 production, the reaction rate showed an 8-fold enhancement upon irradiation with visible light when compared to that of Pd/gCN under identical conditions.[114] A high apparent quantum yield of 31% was obtained by a 0.1%Pd/20%TiO_2/gCN sample in a 420–443 nm range.

9.4.1.3 Hydrothermal Technique

This technique is the most common to synthesize gCN-based heterocomposites. Besides its ease, the hydrothermal route could lead to the formation of high purity nanocomposites.

Recently, CdZnS quantum dots have been fabricated on layered gCN nanocomposites for H_2 generation under visible illumination.[115] A hybrid mesoporous gCN/$CdLa_2S_2$ heterostructure has been fabricated for water splitting by visible light.[116] ZnS modified gCN by ZnS particles on gCN nanosheets has been synthesized from $Zn(Ac)_2{\cdot}2H_2O$, $Na_2S{\cdot}9H_2O$, and gCN, with melamine as the starting material.[117] Phosphate groups were combined in layered gCN nanosheets starting from melamine and phosphoric acid as a dopant.[118] In an additional investigation, CdZnS quantum dots anchored on two-dimensional sheets of gCN nanocomposites were prepared.[115] Scheme 9.7 illustrates the processes involved.

9.4.1.4 Solvothermal Method

The solvothermal process is also quite common and a successful synthetic technique for the production of structured nanomaterials. The method relies on the utilization of nonaqueous solvents as a reaction intermediate. This method speeds up the reaction kinetics, facilitates hydrolysis, and results in self-assembly of the nanocomposite of the gCN in the solution.

Nanocomposites of CdS/gCN nanowires have been fabricated for photocatalytic H_2 production.[119] Novel nanocomposites of a C,N-TiO_2 NP/gCN NS heterostructure were synthesized by the solvothermal method and showed

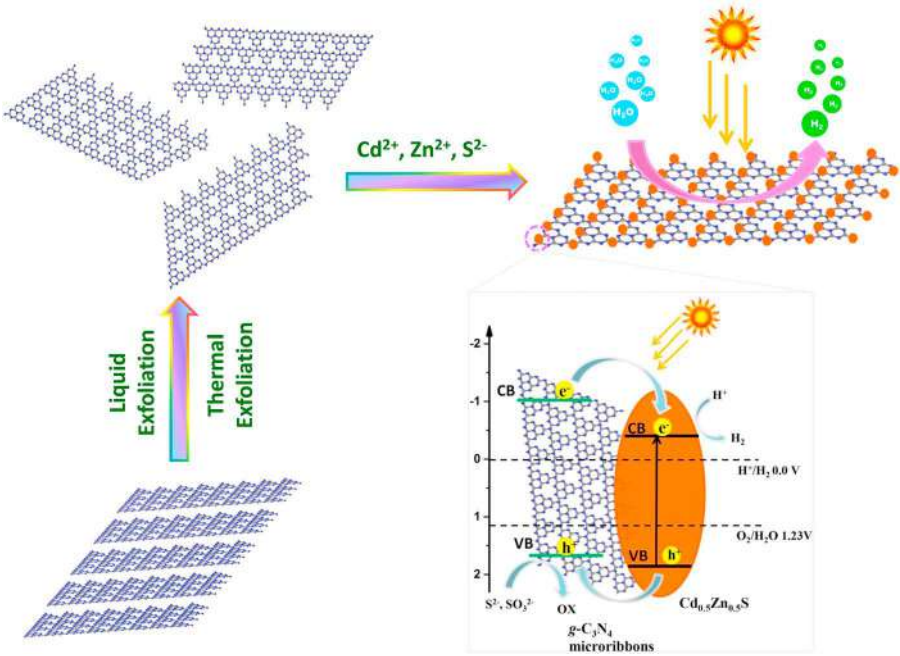

Scheme 9.7 Illustration of the hydrothermal treatment process of $Cd_{0.5}Zn_{0.5}S$@gCN and visible-light-driven H_2 generation. Reproduced from ref. 115 with permission from Elsevier, Copyright 2016.

excellent photocatalytic hydrogen production.[120] The fabrication strategy is facile where the anion group ($-C_4H_9O$) in tetra butyl titanate (TBT) serves as a carbon doping agent and concentrated HNO_3 is used as an N-doping agent.

9.4.1.5 Sol–Gel Technique

The sol–gel technique is a wet chemical method employed for the synthesis of nanomaterials. It is considered a proper technique because it is inexpensive, works at ambient temperature, and employs a simple preparation method. The precursors are usually metal alkoxides and metal chlorides that undergo hydrolysis and polycondensation reactions to form a colloidal substance. It represents a fruitful technique to load metal nanoparticles onto semiconductor surfaces and is commonly employed to make heterostructure gCN composites. For instance, a gCN/TiO_2 photocatalyst was fabricated employing a sol–gel process.[121] The resultant gCN/TiO_2 composite, after coupling, had a high surface area and homogeneous-sized mesopores of TiO_2.

9.4.1.6 Microwave Method

For the synthesis of gCN-based composites, thermal treatment is usually required during the preparation to decrease the interface energy of the constituent phases and to allow smooth passage of the photogenerated electrons through the interface.[122] Ultimately, this yields good contact between the semiconductor components and the gCN. The MW is an ideal technique for the fabrication of gCN-based heterojunctions for it provides a shorter processing time and high temperature.[122]

An impregnation method assisted with MWs in water as the dispersion medium was used to fabricate K-doped-gCN nanosheets/TiO_2 heterojunction composite material (KCNNT).[123] The novelty of the method lies in that KCNN and TiO_2 can be evenly dispersed during the preparation process to result in a large number of efficient heterojunctions and subsequently results in high photocatalytic efficiency. Above all, water as the dispersant renders this method cost-effective and environmentally friendly.[123]

9.4.1.7 Impregnation Method

In the impregnation fabrication route, an interaction exists between a solid precursor and a solution containing an active precursor that is to be deposited onto the surface of the solid.[124]

A facile one-step impregnation method had been used to prepare a series of efficacious and stable $LaCoO_3$/gCN heterojunctions.[124] The photocatalysts had different weight percentages of gCN. The results show that a well-characterized Z-scheme heterostructure formed on the interfaces between the oxide $LaCoO_3$ and the flake-like gCN. This resulted in an improved visible-light absorption, efficient separation of the photogenerated electron–hole pairs, and an apparent transformation of the photogenerated electrons.[124] The highest photocatalytic activity for the degradation of phenol (PH) under visible light was reported in the composite. These results reveal an enhancement in the pH degradation rate of 85% within 5 h when irradiated by visible light. Besides, the $LaCoO_3$/gCN composite also shows excellent stability. The higher photocatalytic activity has been mainly ascribed to an effective charge carrier separation as well as improvements in the dispersity *via* the Z-scheme $LaCoO_3$/gCN heterojunction. A possible mechanism has been proposed for the photodegradation process.[124]

9.4.1.8 Photodeposition Method

The photodeposition method involves metal nanoparticle (NP) deposition on the semiconductor surface under photo-irradiation of a solution containing both the metal ions and the semiconducting material. To utilize the photodeposition method, the CB band edge of the semiconductor photocatalyst ought to be more negative than the reduction potential, meanwhile, the

potential edge of the VB should be higher than the oxidation potential of the metal ion.[125,126]

Excellent photocatalytic H_2-generation activity occurs when gCN NSs are coupled with a cocatalyst platinum (Pt) and hole sacrificial agent triethanolamine (TEOA).[126] Researchers had found that the order of TEOA addition into the reaction system before or after the photodeposition of Pt has a marked effect on the photocatalytic hydrogen production. In particular, the amount of Pt was lower on the addition of TEOA beforehand. Upon reversal in the addition sequence of TEOA, a 4-fold increase in hydrogen production rate (4210.8 *vs.* 972.2 μmol h^{-1} g^{-1}) was observed.[126] Likewise, the apparent quantum efficiency (AQE) also quadrupled from 0.63% to 2.4% at 420 nm.[126] Consequently, a mechanism detailing this phenomenon was proposed.

9.4.1.9 Sonication Mixing Method

Solution mixing or sonication of gCN powders with the desired component in water or organic solvents offers the simplest method for the preparation of heterostructured composites. In this method, the composite formation between the two components could be prepared by distributing the desired semiconductor over the gCN surface during the stirring and mixing step. The nanocomposite could be obtained after the solvent or water solution evaporated.

Ong *et al.*[127] deposited a silver halide AgBr on the protonated-CN to form a photocatalyst by a sonication-assisted deposition–precipitation route at room temperature. The optimal 30% AgBr/proton-gCN presented the highest photocatalytic activity, amounting to a total evolution of CH_4 of 10.92 μmol g^{-1}, enhanced by 34.1, and 4.2 times greater than those of single-phase AgBr and protonated-CN, respectively.[127] The enhancement in photocatalytic activity was a result of the surface plasmon resonance (SPR) effect from Ag and also the formation of a heterojunction structure between AgBr/protonated-CN composite photocatalysts efficacious charge carrier transfer and separation to retard the recombination process.

9.4.2 Preparation of gCN-based Heterocomposites

9.4.2.1 Preparation of Noble Metal-doped (Decorated) gCN

The application of gCN as an excellent photocatalyst is inadequate and limited by the electron/hole recombination. To overcome this problem, various noble metal atoms, such as Ag, Au, Pd, and Pt were utilized as co-catalysts to promote the separation of photogenerated charge carriers from the bulk to the surface.

AuPd bi-metallic nanoparticle-loaded gCN was prepared by the mixing of $HAuCl_4$, H_2PdCl_4, and gCN nanosheets through photochemical deposition precipitation followed by hydrogen reduction.[128] A Pd/gCN NSs composite was constructed *via* using melamine, polyvinyl pyrrolidone, and a solution

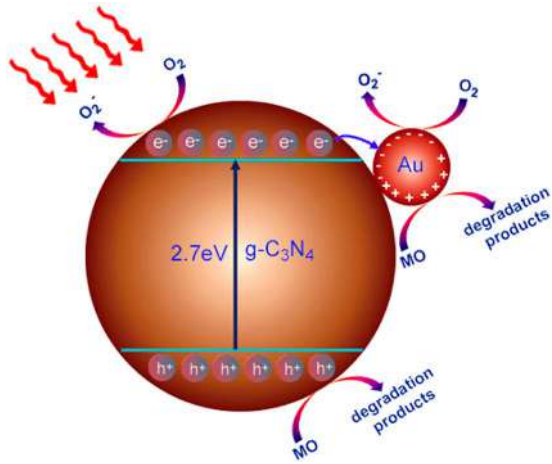

Scheme 9.8 Diagram illustrating the photocatalytic degradation of MO over a AuNP/gCN nanohybrid under visible-light irradiation. Reproduced from ref. 133 with permission from American Chemical Society, Copyright 2013.

Na_2PdCl_4 as the precursors.[129] The borohydrate reduction method has been utilized to prepare Au-sulfated gCN *via* using $HAuCl_4$ acid and gCN powder as the precursor.[130] A PtNi/gCN heterostructure was synthesized through a calcining technique that had been accompanied by the deposition of bi-metallic PtNi nanoparticles.[131] Also, an Ag-bridged gCN/WS_2 composite was fabricated *via* solvent evaporation followed by high-temperature calcination.[132]

NSs, prepared by ultrasonication-assisted liquid exfoliation *via* green photoreduction of gCN, were loaded with Au nanoparticles (AuNPs).[133] Photoreduction Au(III) was pursued under visible-light irradiation using gCN as an effective photocatalyst. The nanohybrids showed superior photocatalytic activities for the decomposition of methyl orange (MO). The photocatalytic process is schematically illustrated in Scheme 9.8.[133]

Isolated single Pt atoms represent a new type of co-catalyst.[134] They have been highly dispersed and anchored on gCN, and can achieve the maximum utilization of Pt atoms so enhancing the photocatalytic H_2 evolution activity.[134]

9.4.2.2 Preparation of Transitional Metals and Metal Oxide Doped gCN

The inhibiting cost of noble metals limits their large-scale utilization. Therefore, non-noble metal-based co-catalysts were doped on gCN taking advantage of their low cost and superior performance.[135] Core–shell Cu_2O/gCN demonstrated superior visible-light photocatalytic activity. Inexpensive $Ni(OH)_2$ as an alternate for noble metals was utilized as a photocatalyst over gCN.[136]

Liu *et al.* showed that the introduction of NiO acts as a co-catalyst with a gCN semiconductor.[137] In the process of synthesis of transition metal-based gCN samples, transitional metal salts are employed as precursors in a co-thermal condensation process.

9.4.2.3 Preparation of Metal-loaded gCN

Alkali metal ion (Li^+, Na^+, or K^+) doped gCN nanocomposites gCN were prepared *via* high-temperature treatment.[138] The prepared samples were characterized and analyzed using standard techniques. The photocatalysts displayed enhanced visible-light photocatalytic activities for hydrogen production due to increased specific surface areas, decreased band gaps for extended visible-light harnessing, and improved electronic structures for efficient charge carrier transfer. The Na-doped gCN displayed the most effective utilization of photogenerated electrons during the water reduction process. Therefore, high photocatalytic activity was observed over the Na-doped gCN photocatalyst (18.7 μmol h^{-1}), 3.7 times that of pristine gCN.

Scheme 9.9 is a representation of KOH-assisted band engineering of polymeric gCN for a photocatalytic visible light process of reduction of oxygen to hydrogen peroxide.[139]

Eco-friendly K-doped porous NSs gCN were prepared by a simple hydrothermal re-calcination method. The obtained gCN NSs were applied in the photodegradation of tetracycline (TC) under different reaction conditions. It was found that the pore size and specific surface area were enhanced and they led to an increase in the photoabsorption and the active sites. The results showed that the sample possessed a narrower band gap, lower recombination of photogenerated charges, and higher electron–hole transfer efficiency. As a result, K/gCN NSs photocatalysts demonstrated excellent

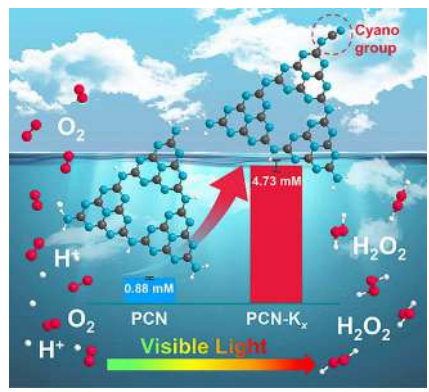

Scheme 9.9 KOH-assisted thermal polymerization of U incorporates cyano groups into the polymeric carbon nitride. This boosts the photocatalytic reduction of O_2 to H_2O_2 under visible light. Reproduced from ref. 139 with permission from American Chemical Society, Copyright 2019.

photocatalytic performance for TC degradation (85.13%), which was approximately a 2.88-fold and 1.40-fold increase compared to bare gCN (29.60%) and porous gCN NSs (60.84%). This is a reasonable way to construct highly efficacious photocatalysts.[140]

9.4.2.4 Preparation of Non-metal-loaded gCN

Substantial improvement in photocatalytic activity occurs through loading foreign non-metal (N, P, S, F, B, C, O, and I) atoms into gCN sheets. This incorporation plays a paramount role that results in a change in the electronic structure, enhanced visible-light absorption, improved carrier mobility, more active sites created, and most importantly helps the separation of photogenerated charge carriers to facilitate the evolution of hydrogen gas by water splitting.[141,142]

Peng *et al.*[143] prepared red phosphor (r-P) with gCN by annealing a mixture of red phosphor and gCN in an inert atmosphere. Treatment of bulk gCN in a gaseous H_2S atmosphere resulted in S-loaded gCN samples.[144]

In Table 9.2, some examples of the fabrication strategies and applications of metals and non-metals-doped bulk gCN are reported.

9.5 Heterojunctions: Coupling of gCN with Semiconductor Photocatalysts

Tailoring more efficient photocatalysts can be accomplished *via* coupling two or more semiconductors to form heterojunctions. Synergism between two semiconductors results in enhanced photocatalytic activity. Namely, it leads to improvements in stability, visible-light harvesting, charge separation and transfer, and efficacy in the formation of oxidizing species.[29,107]

9.5.1 Design Criteria of gCN-based Heterojunction Photocatalysts

The most important points to focus on in the design of heterostructures are extending visible-light absorption, increasing specific surface area, and active site density, introducing a co-catalyst to decrease the overpotential of catalytic reactions and improving the parting of photogenerated electron–hole pairs.[29] An appropriate semiconductor with a narrow band gap can not only act as a type II band configuration counterpart to couple with gCN for enhancing the charge separation, it also acts as a light sensitizer for better visible-light absorption. The construction of a suitable heterostructure amounts to the most feasible strategy for enhancing the separation efficiency of electron–hole pairs. Undoubtedly, this markedly enhances the photocatalytic performance.[166] According to the different charge transfer mechanisms between gCN and the second component, gCN-based heterostructures can be classified into the following types: gCN-based

Table 9.2 Noble metals, transition metals, metals, and non-metals' doping of gCN photocatalysts: preparation and photocatalytic activity.

Photocatalyst	Preparation method	Application, efficiency, and enhancement factor	Reference
Noble metals' decoration			
Au NPs	Alkali-assisted post-calcination route, efficient utilization of surface plasmon resonance.	Photocatalytic activity for hydrogen production (increased 8 times for Au/gCN).	145
	Constant temperature bath-reduction	Photodegradation of RhB (92.66% within 30 min. Enhanced by 3-fold/gCN NSs)	146
Pd NPs	Deposition-precipitation/mp-gCN	Degradation of BPA. Enhanced photocatalytic activity by 5 times/mp-gCN	147
	Calcination at 550 °C	The performance of photocatalytic hydrogen evolution/Vis (316.2 μmol g^{-1}, improved by 15.3 times/gCN)	148
Pt-SA	Incipient wetness impregnation method/gCN NSs	Photocatalytic H_2 production rate/Vis (1214 μmol g^{-1} h^{-1})	149
	Simple liquid-phase reaction, followed by annealing at a low temperature/gCN NSs	Photocatalytic H_2 generation (rate of 318 μmol h^{-1}, nearly 50 times higher/gCN)	134
Ag NPs	Photo-deposited Ag plasmonic photocatalysts	Enhanced degradation of MO and PNP under visible-light irradiation	150
	Calcination at 550 °C for 3 h	Photodegradation of 2-mercaptobenzothiazole (MBT) and RhB/Vis light irradiation	151
Transition metals' doping			
Ti-doped	Calcined at 550 °C	Photodegradation of RhB (99.4% in 100 min. Apparent rate const. k_{app} of 0.0461)	152
Zn-doped	Simple mixing and calcination	Transesterification of ethylene carbonate with CH_3OH to dimethyl carbonate (DMC) (superior catalytic activity and the highest DMC yield reached 83.3%)	153
Co-doped	Hydrothermal-calcination method	Degradation of monochlorophenols (MCPs) isomers (degradation of 4-CP in 15 min, at high catalyst loading. Peroxymonosulfate (PMS) was an oxidant. The order of MCPs degradation. 2-CP > 3-CP > 4-CP	154
Fe(III)-doped NSs	One-step pyrolysis	Hydrogen production rate (536 μmol h^{-1} g^{-1}, which was 1.8 higher/gCN NSs and 6 times higher/gCN). Photodegradation rate of MB (1.4 times higher/gCN NSs and 1.7/gCN)	155
	Calcination at 550 °C	Photo-Fenton-like degradation of RhB/Vis (98% in 100 min)	156

Zn(II)-doped	Calcination at 673 °C	Hydrogen evolution (more than 10 times higher for Zn/gCN, the AQY was 3.2 at λ = 420 nm)	157
Eu(III)-doped	Calcination at 500 °C	Photodegradation of RhB and TC/Vis (100% in 50 min RhB and 92% within 50 min TC. Enhanced by 6.03 times and 1.71 times higher for RhB and TC, respectively)	158
Metal ion doped			
K-doped	One-pot calcination	Hydrogen production rate (1.337 mmol g^{-1} h^{-1}, which is about 5.6 times higher/gCN)	159
KC-C-gCN	One-step thermo-polymerization, to introduce crystallinity, K and cyano-group co-doped with the precursor of THU	H_2 evolution rate (4.125 mmol g^{-1} h^{-1}, an increase of 16.8 times/gCN)	160
Non-metals			
O-doped	High voltage was supplied by a plasma generator for oxygen doping. After discharge, the reactor was cooled down to room temperature	Anoxic RhB degradation/Vis	161
	H_2O_2 hydrothermal approach	H_2 evolution/Vis (37.5 μmol h^{-1}). Enhanced 2.5-fold/gCN).	60
S-doped	gCN powder that was treated at 450 °C/gaseous H_2S atmosphere for 1 h	Hydrogen evolution rate is ≈8.0 times higher than pure gCN. The complete oxidation process of PH (λ > 400 nm)	144
	Direct thermal condensation	H_2 evolution under visible-light irradiation is 9.3 times higher than the reference gCN	162
P-doped	Two-step processing. Thermal condensation of P-doping, followed by phaco-fragmentation and smart post-thermal treatment	High H_2 production rate (15.921 mmol h^{-1} g^{-1}). Extended light absorption up to 800 nm	163
	Solid reaction method, P was doped into gCN and P nanostructures to form heterostructures	Efficient H_2 production rate of (941.80 μmol h^{-1} g^{-1}), rapid degradation of RhB	164
I-doped	*In situ* modification using DCDA and ammonium iodide	H_2 evolution/Vis (38 μmol h^{-1}, enhancement nearly 2 times/gCN, AQY 2.4 at λ = 420 nm)	165

conventional type II heterojunction, gCN-based Z-scheme heterojunction, gCN-based p–n heterojunction, gCN/metal heterostructure, and g-gCN/carbon heterostructure.

9.5.2 Type II Heterojunction Systems

Commonly, pristine gCN possesses a band gap of about 2.7 eV, and the CB and VB positions are located at about −1.1 and +1.6 eV *vs.* normal hydrogen electrode (NHE), respectively.[74]

Novel 2D/2D $SnNb_2O_6$/gCN NSs were manufactured by a facile two-step wet chemistry method.[167] As displayed in Scheme 9.10, the system represents a conventional gCN-based type II heterojunction system owing to the staggered band structures of the $SnNb_2O_6$ semiconductors. Having a proper band structure is a prerequisite in the choice of the semiconductor for the construction of a type II gCN-based heterojunction. Scheme 9.10 is an illustration of the heterojunction composed of gCN and a second semiconductor with a more negative CB position. The enhanced activity was mainly due to improved interfacial charge transfer. The hole and superoxide radicals are the two main photoactive species in the degradation of methylene blue (MB).[167]

Various semiconductors, for example: TiO_2,[168] ZnO,[169] MoO_3,[170] SnO_2,[171] Fe_2O_3,[172] *etc.* that have been used for constructing gCN-based conventional type II heterojunction systems have been reported in Table 9.3. Meanwhile, coupling gCN with mesoporous TiO_2 and other similar semiconductors results in enhanced surface area, the formation of active species, and efficient separation of the charge carriers. Usually, the holes accumulate on gCN while the electrons accumulate on TiO_2. Most often, the electrons react with oxygen to form the radical species that help decompose dyes and organic pollutants.[28] Under UV irradiation, both gCN and TiO_2 are activated. Electrons are promoted from their VBs to the CBs. Subsequently, TiO_2 CB electrons are transported to the VB of gCN, essentially a Z-scheme mechanism.[173]

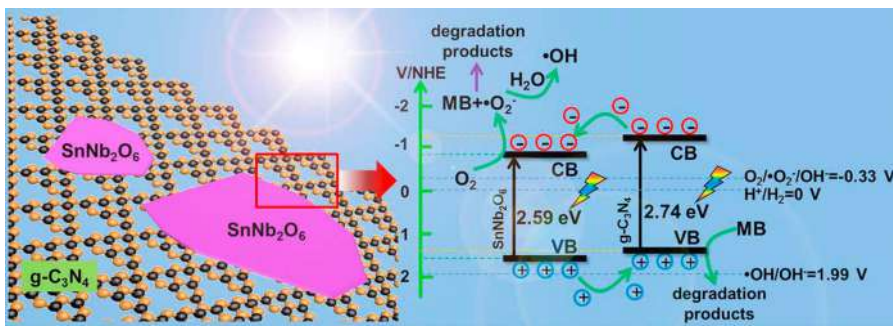

Scheme 9.10 Proposed mechanisms of charge transfer and dye degradation (visible light) in the type II based heterojunction system constructed by coupling $SnNb_2O_6$ to gCN. Reproduced from ref. 167 with permission from Elsevier, Copyright 2016.

Table 9.3 Type II heterojunction semiconductors: typical synthetic routes, photocatalytic H_2 generation, and photocatalytic organic pollutants' degradation.

Photocatalyst	Preparation method	Wt% gCN	Application, efficiency, and enhancement factor	Reference
Hydrogen generation				
gCN NTs/WS_2 NSs	Hydrothermal procedure	73	Photocatalytic H_2 production/UV-Vis (rate 1021 μmol h^{-1} g^{-1}. 17.6 times higher/gCN NTs, AQE of 11.23% at λ = 370 nm)	179
gCN NTs/MoS_2 NFs	Free drying and hydrothermal	85	Photocatalytic H_2 production rate/Vis (1124 μmol h^{-1} g^{-1}. Enhanced 18-fold/gCN and 6 times higher/gCN NTs)	180
gCN/Mo-doped	Hydrothermal	~97	Hydrogen evolution rate/Vis (~2008.9 μmol g^{-1} h^{-1}, which is 9.6-fold enhanced/gCN)	181
gCN/CN-co-doped Fe_2Ni_2P	Solvothermal, using the MOFs to derive hybrid hollow metal phosphide	7.47 (Ni_2P)	High H_2 evolution rate/Vis (13.81 mmol g^{-1} h^{-1} under 1.0 mmol L^{-1} Eosin Y (EY)-sensitization, enhanced 10-fold/gCN, AQE reached 48.5% at λ = 420 nm)	182
Montmorillonite/gCN/NiCoP	Calcination	85	Photocatalytic hydrogen evolution rate/Vis (10.930 mmol g^{-1} h^{-1} with Eosin Y (EY) sensitization, enhanced 10-fold/gCN, AQY reached at 40.3 at λ = 420 nm)	183
gCN/TiO_2	Vapor deposition method	—	Photocatalytic H_2 generation (513 μmol h^{-1} g^{-1}, enhanced 10.8 times/gCN, AQY of 31% at λ = 420 nm)	184
gCN/CdS	Solvothermal and chemisorption	—	Hydrogen evolution/Vis (4152 μmol h^{-1} g^{-1}, AQE of up to 4.3 at λ = 420 nm)	119
gCN NSs/Nb_2O_5 MSs	Solvothermal process with aid of P25 as a structure-directing agent	62	H_2 production rate/Vis (1710.04 μmol h^{-1} g^{-1}, enhanced 4.7 times/gCN)	185
gCN/$PtNi_x$	Polyol reduction method	—	Hydrogen production rate/Vis (8456 μmol h^{-1} g^{-1}, enhancement of 16.4 times/gCN)	186
gCN/NiS	Photochemical method	—	Photocatalytic H_2 evolution activity/Vis (16.400 mmol h^{-1} g^{-1}, enhanced 2500 times higher/gCN)	187
gCN/Ni_2P	Hydrothermal method	—	Photocatalytic H_2 production/Vis (3344 μmol h^{-1} g^{-1}, enhanced 8.2 times/gCN)	188

(*continued*)

Table 9.3 (*continued*)

Photocatalyst	Preparation method	Wt% gCN	Application, efficiency, and enhancement factor	Reference
Organic pollutants' degradation				
gCN/Fe_3O_4	Thermal polymerization. Subsequent *in situ* precipitation of Fe_3O_4	76	Degradation of phenanthrene (PHE) in soil/Vis (92.26 in 120 min)	189
gCN/TiO_2 SPHs	Solvothermal	66.7	Degradation/Vis of RhB (99.3% in 150 min, 8.2 times higher/gCN), MB (~95% in 180 min, 7 times higher/gCN), and ciprofloxacin (CIP) (97.3% in 150 min, 14.8 times higher/gCN)	190
gCN NSs/TiO_2 NRs	Calcination	30	Photodegradation of CIP/Vis (93.4% was achieved in 60 min)	191
gCN/TiO_2	Calcination	—	Degradation of Acid Orange 7 (100% in 5 h/Vis and 100% in 2 h/UV)	192
gCN/TiO_2	Sonication	—	Degradation of MB (95.3% in 120 min, 7 times higher/UV/gCN) and (9.27 times higher/Vis/gCN)	193
gCN/TiO_2	Solvothermal	88.8	Degradation of PH/simulated solar light (100% in 50 min, 2.8 times/gCN)	194
gCN NSs/mp-TiO_2	Seed-induced solvothermal	—	Degradation of MO and PH/Vis (degradation enhancement of 333 and 146 times higher for MO and PH, respectively/gCN; seeded titania) and (degradation enhancement of 6.9 and 5.8 times higher for MO and PHE, respectively,/gCN; directly grown titania)	195
gCN/TiO_2 (anatase)	Solvent evaporation	—	Degradation of MB/Vis (100% in 25 min/UV) and (60% in 5 h/Vis)	196
hc-gCN/CoP	Solvothermal	95	Degradation of TC/Vis (96.7% in 120 min, the enhancement rate was 10.2-fold/hc-gCN)	197
gCN NSs/In	Wet impregnation of In(III) ions	—	Degradation of RhB/Vis (100% in 60 min, enhanced 4.6-fold/gCN)	198
gCN NSs/S-doped	Calcination	96.5	Reduced biofouling by bacteria, *e.g.*, *Escherichia coli*/Vis (70% reduction by incubating the bacterial solution under light irradiation)	199

gCN/Al_2O_3	*In situ* thermal route	12	Nitrogen oxide NO removal/Vis (71.1% in 30 min)	200
gCN/WO_3	Mixing-calcination	20	Degradation of acetaldehyde/Vis (100% in 24 h)	201
$gCN/SnNb_2O_6$	Two-step wet chemistry	70	Degradation of MB/Vis (99% in 4 h, 3.9 times higher/gCN)	167
gCN/SnS_2	Ultrasonic dispersion	95	Degradation of RhB/Vis (99.8% in 20 min, enhanced 4 times/gCN), MO (95% within 40 min), and PH (31.3% in 120 min)	202
mp-gCN/Co_3O_4	Hard templating-impregnation	98.5	Degradation of BPA/Vis (93.6% in 180 min)	203
gCN/NiO	Calcination	93.7	Degradation of MB/Vis (100% in 40 min)	204
$gCN/Cd_{0.2}Zn_{0.8}S$	Hydrothermal	20	Degradation of RhB/Vis (95.8% in 80 min) and PH/Vis (76.1% in 180 min/gCN)	205
Isotype heterojunction				
gCN/gCN Isotype heterojunction	Thermal polymerization of DCDA and U	100	H_2 generation optimized to the ratio of DCAD/Vis (553 μmol h^{-1} g^{-1}, enhancement of 17 and 5 times/gCN prepared from (DCDA) and (U), respectively)	206
	Thermal polycondensation of melamine and U	100	Degradation of red orange RO-16/Vis (95% in 100 min) and for TCH (85.6% in 120 min)	207
	One-step thermal treatment using U and THU	—	Degradation of RhB and TC/Vis (99.8% and 95.1% in 1 h and 4 h, respectively)	208
	Molecular self-assembly and thermal polymerization methods		Photocatalytic degradation/Vis of RHB (96.2% within 60 min) and TCH (82.6% within 30 min)	209
	Thermal polymerization of single-source glucose-modified melamine		Photocatalytic H_2 production rate (1361.9 μmol h^{-1} g^{-1} 16.4 times high/gCN and 11.5 times high/gCN NSs)	210
gCN/gCN type I/type II junction	Calcination	—	Nitrogen oxide NO removal/Vis (41.3% within 30 min)	211

Due to its renowned photocatalytic properties, titania is a catalyst of choice to couple with gCN.[174] The composite photocatalyst (gCN/TiO_2) was obtained by a facile and environmentally-friendly biomimetic synthetic methodology. Improved photoactivity towards rhodamine B (RhB) degradation was observed compared to gCN, TiO_2, and their mixtures.[173] The composite photocatalyst reached 100% RhB degradation in 50 min, at a loading of gCN of 25.9%.[174]

An antibacterial effect was observed under visible-light illumination using a gCN/TiO_2 hetero-composite that was obtained by a hydrothermal-calcination route.[175] TiO_2 in micron-sized spheres was wrapped with lamellar gCN. Acute loss of the intracellular components of bacteria was observed upon exposure to gCN/TiO_2 under visible light for ~3 h, as displayed in Figure 9.1a and b. Photocatalytic inactivation of *Escherichia coli* was complete and the bacteria destructed, as can be seen in Figure 9.1a and b.[175] The photocatalytic activity of the catalyst was significantly higher under visible-light irradiation. The excellent photocatalytic activity is ascribed to efficient separation of the e^-–h^+ pairs and an enhancement in light absorption.[175]

Sonochemical impregnation has been used to link mesoporous ZnO nanotriangles (NTs) with gCN into hybrid nanostructures (ZnO-NTs/gCN). RhB degradation, under simulated solar light, was assessed. RhB degradation reached 100% in 60 min.[176] Silver carbonate nanoparticles were loaded on gCN nanosheets *via* a thermal exploitation method. The hybrid photocatalyst showed remarkable activity towards MO and RhB under visible-light irradiation.[177] This is attributed to a large specific surface area, efficient charge separation, and enhanced visible-light harvesting.[177] Degradation of RhB was reported to be 100% in 40 min under visible light over a gCN/Ag_2CO_3

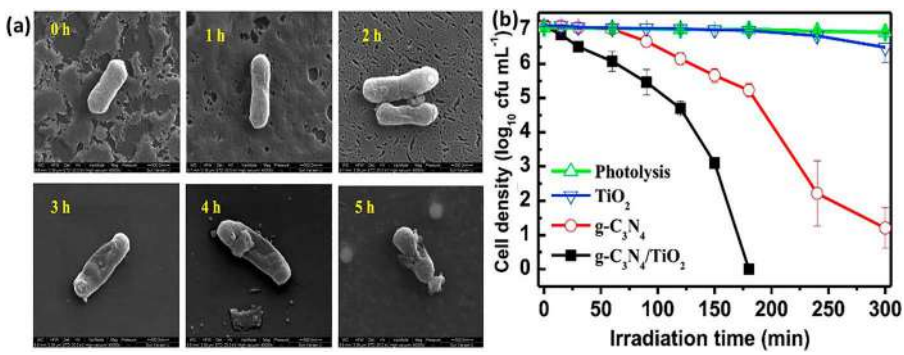

Figure 9.1 (a) SEM images of *E. coli* K-12 treated by gCN/TiO_2 hybrid photocatalysts under visible-light irradiation at different times, and (b) photocatalytic inactivation curves of *E. coli* K-12 under visible-light irradiation using TiO_2/gCN. Reproduced from ref. 175 with permission from Elsevier, Copyright 2015.

nanocomposite, and 8 times photocatalytic activity relative to pure gCN was reported.[177] Sun *et al.*[169] reported gCN/ZnO composites for photodegradation of MO and *p*-nitrophenol under visible light. The gCN/ZnO composites exhibited better photocatalytic activity than the pure gCN and ZnO. While gCNs in the gCN/ZnO compounds are favoured to absorb visible light and produce electrons and holes, it is not possible to excite ZnO by visible light due to the wide band gap. The spatial separation of the photogenerated charge carriers is realized. The photogenerated electrons in the CB of ZnO can reduce O_2 to produce superoxide radicals ($^{\bullet}O_2^-$), the main active species with high oxidation ability. The photogenerated holes in the VB of gCN can oxidize MO. The transfer of photogenerated electrons from gCN to ZnO was the key factor for hidden charge carrier recombination and the generation of more $^{\bullet}O_2$. $BiPO_4$@gCN core–shell composite photocatalysts were prepared by an electrostatic self-assembly method by Pan *et al.*[178] Better photocatalytic activity was demonstrated by the composite for the degradation of MB. This has been attributed to the high separation and transfer rates of the photogenerated electron–hole pairs at the interfaces between gCN and $BiPO_4$. The synthetic routes and the photocatalytic activity of some additional binary heterojunctions are summarized in Table 9.3.

9.6 gCN-based Z-scheme Heterojunction Composites

Composite-based gCN with type II heterojunctions could enhance the separation efficiency and could reduce the possibility of recombination of the photogenerated electron/hole pairs. However, there is a shortcoming, which is the poor redox ability of the system.[29] This is primarily due to the jumping of the photogenerated electrons from the CB of gCN to the less negative CB of the second semiconductor. There is a subsequent transfer of the holes from the VB of the second semiconductor to the less positive VB of gCN thus leading to a weakened oxidation/reduction ability. On the other hand, in the Z-scheme heterojunction system, the VB and CB of one semiconductor is lower relative to the other.[29] Then, during the photocatalytic process, the CB electrons of the lower CB semiconductor recombine with the VB hole with lower oxidation ability. Therefore, the CB electrons having a high reduction ability on one semiconductor, and the VB holes with high oxidation ability on the second semiconductor, will be retained.[29] Ultimately, this will lead to efficient charge separation in the Z-scheme heterojunction. An electron mediator (bridge) is required to connect the two semiconductors and thus enhances the efficiency of the charge transfer and its separation.[29] In comparison with type II heterojunctions, the gCN-based Z-scheme heterojunctions improve the charge separation and maintain the redox ability of the system. This is mainly ascribed to the fact that the photogenerated electrons and holes are still kept in the more negative CB and the more positive VB in this heterojunction, respectively.[212,213]

9.6.1 Z-scheme Heterojunction Photosystem Applications

NSs of Cu-doped gCN were prepared by a facile process of calcining dicyandiamide and copper chloride ($CuCl_2$) under a N_2 environment. The Cu species were coordinated in the pore among three tri-*s*-triazine units having oxidation states Cu(II)/Cu(I).[214] This manifested in an expanded visible-light absorption and a narrowed band gap of gCN. The degradation rate is about 2.3 times higher than that of pristine gCN. The authors performed DFT calculations that demonstrated that the doped Cu(II) ion was a strong reduction site, whereas the doped Cu(I) was a strong oxidation site. Thus, the Cu(II)/Cu(I) doping facilitates the photoinduced charge transfer through the formation of an S–S Z-scheme heterojunction photosystem.[214] Scheme 9.11 is a representative illustration of a Z-scheme photosystem.

The photoexcited electrons in the CB of V_o-ZnO quickly transfer to the VB of gCN, resulting in the recombination of the electrons in the CB of V_o-ZnO and photoexcited holes in the VB of gCN. Meanwhile, the photogenerated holes in the VB of V_o-ZnO oxidize OH^- to $^{\bullet}OH$, while the electrons on the CB of gCN are captured by O_2 to form $^{\bullet}O_2^-$, which transforms into $^{\bullet}OH$, therefore promoting the degradation of the pollutants. The Z-scheme assisted covalent bonded oxygen-doped carbon nitride/graphitic carbon nitride hybrid materials (O-CN/CN) have been synthesized.[215] They were prepared *via* solvothermal treatment utilizing cyanuric chloride, cyanuric acid, and U-derived graphitic carbon nitride as the sources. The very efficient O-CN/CN exhibited a high rate of H_2 generation at 6.97 mmol h^{-1} g^{-1} using visible-light irradiation.[215] The apparent quantum yield (AQY) of 21.4 was achieved at 425 nm. Certainly, the improvements are due to the extended visible-light absorption, the retarded charge carrier recombination, and the rapid charge carriers' transfer.[215]

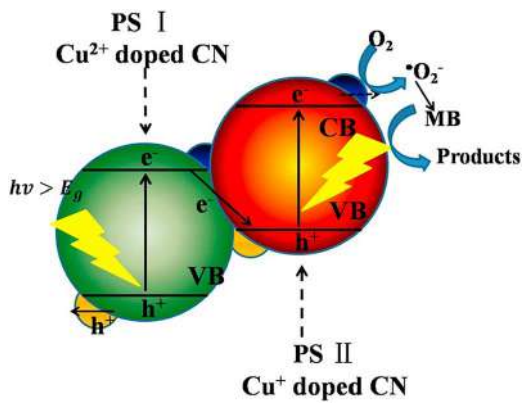

Scheme 9.11 Illustration of the charge transfer processes based on a direct Z-scheme heterojunction for a Cu(II) doped gCN photosystem (PSI) and Cu(I)-doped gCN (PSII) photocatalyst. Reproduced from ref. 214 with permission from Elsevier, Copyright 2018.

Mesoporous $AgIO_4$/gCN nanocomposite heterojunctions were synthesized by the sonochemical route.[216] They exhibited very high rates of photocatalytic degradation of fluorescein dye (FLU) and hydrogen production. $AgIO_4$ nanoparticles were deposited on the corners and edges of the wrinkled sheets of gCN. A perfect direct Z-scheme mechanism has been established owing to the small difference between the VB potential of gCN (E_{VB} = +1.4 eV) and the CB potential of $AgIO_4$ (E_{CB} = +1.08 eV).[216] It is noteworthy that one of the highest rates for hydrogen production of 23 mmol h^{-1} g^{-1} has been achieved.[216] The nanocomposites of gCN/Ag_3PO_4 were prepared *via* simple solvent evaporation with a mild band gap of 2.45 eV. They were evaluated for ethylene degradation under visible-light irradiation.[217] The samples were found to possess both photo activity and stability. The enhanced activity of the nanocomposites is due to a direct Z-scheme mechanism.[217] Zhang *et al.*[218] fabricated a novel Z-scheme porous *p*-gCN/Ag_3PO_4 composite by a facile and green method at room temperature. The photocatalytic activity of the catalysts was evaluated by the degradation of MB under visible-light illumination. The photocatalytic activity of *p*-gCN/Ag_3PO_4 was remarkably higher in comparison to *p*-gCN and Ag_3PO_4.[218] The kinetic constant k_{app} of MB degradation over *p*-gCN/Ag_3PO_4 was enhanced by 1.45 and 9.6 times that of Ag_3PO_4 and *p*-gCN, respectively. Finally, the Z-scheme photocatalytic mechanism is proposed.[218] A schematic of the synthetic route is shown in Scheme 9.12. Additional Z-scheme systems composed of gCN and other semiconductors are summarized in Table 9.4.

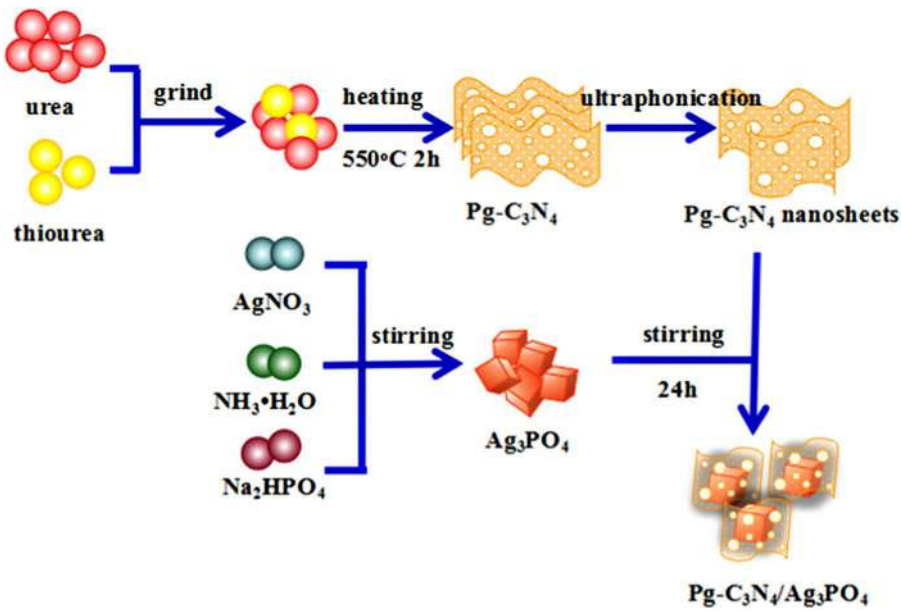

Scheme 9.12 The synthetic route of a PgCN/Ag_3PO_4 NP photocatalyst. Reproduced from ref. 218 with permission from Elsevier, Copyright 2017.

Table 9.4 Heterojunctions with Z-scheme assisted charge transfer: typical synthetic routes, photocatalytic H_2 generation, and photocatalytic organic pollutants' degradation.

Photocatalyst	Preparation method	Wt% gCN	Application, efficiency, and enhancement factor	Reference
Hydrogen generation				
gCN NSs/α- Fe_2O_3	Calcination	96.2	*Highest ever* photocatalytic H_2 evolution activity enhanced in hybrids containing α-Fe_2O_3 nanostructures, (reaching 31.4 mmol g^{-1} h^{-1}, loading of α-Fe_2O_3 was 3.8 wt%)	213
DC-gCN/$ZnIn_2S_4$	Regulation of the DC features of g-C_3N	—	H_2 evolution reaction (1650 μmol g^{-1} h^{-1}. AQE of 44.35% at λ = 420 nm). Charge kinetics switches from Type I to Z-scheme for gCN/$ZnIn_2S_4$	219
gCN/Sn-doped	High-valence metal salt oxidation method	~90	Photocatalytic H_2 evolution rate/Vis (1650 μmol g^{-1} h^{-1}, with an enhancement of ~2.6 times higher/gCN, AQE of about 18.2% at λ = 420 nm). N–Sn bond acted as a hole-trapping center. Switching charge kinetics from type-I to Z-scheme	220
gCN/α-Fe_2O_3	One-pot hydrothermal method	—	Photocatalytic H_2 evolution/Vis (77.6 μmol h^{-1} g^{-1}, enhanced 4.8 times/gCN)	221
Organic pollutants' degradation				
gCN NPs/WO_3 HMSPHs	Calcination	—	Degradation of TCH/Vis. (The kinetics was 2.42 times higher/gCN, and 6.88-fold/WO_3 HMSPHs)	222
gCN/TiO_2 nanotube array (TNTs)	Calcination at 500 °C with urea	—	Photocatalytic degradation of/Vis (96.3% degradation. Enhanced 3.7 times/gCN)	193
gCN NSs/$Bi(VaO_3)_2$ NSs	Hydrothermal	50	Photocatalytic oxidative coupling of benzylamine to *N*-benzylidene benzylamine/Vis (96% conversion in 6 h and 99% selectivity)	223
p-gCN/BiOI	Hydrothermal treatment, *in situ* growth of BiOI on the surface of *p*-gCN	—	Degradation of MO/Vis (rate is 0.01596 min^{-1}. Enhanced 5.7 times/gCN)	224
gCN/BiOBr MFs	Polycondensation and precipitation method	30	Degradation of reactive blue 198 (RB 198)/Vis (99% in 30 min). Degradation of reactive black 5 (RB 5)/Vis (91% in 30 min). Degradation of reactive yellow 145 (RY 145)/Vis (93% within 30 min)	225
P-S-gCN/Ag@AgI/WO_3	Simple one-pot precipitation method		Photodegradation of malachite green (MG) dye (90% removals of MG dye in 60 min. Enhancement of 7.0 times/P-S-gCN). Dual Z-scheme	226
$BiVO_4$/*p*-gCN	Hydrothermal process	60	Degradation of MB (rate constant was 0.05251 min^{-1}, 7.2 times higher/*p*-gCN, and 4.6-fold/$BiVO_4$)	227

gCN/SnO_{2-x} (x = 0 to 1)	Calcination	57.8	Degradation of RhB/Vis (100% degradation in 40 min, k_{app} 0.088 min^{-1}, enhanced 8.8 times/gCN), MO/Vis (100% degradation in 90 min), MB (100% degradation in 40 min), and PH/Vis (40% within 90 min)	228
gCN NSs/TiO_2 NSs vertical heterojunction	Facile hydrothermal assembly	—	Photocatalytic disinfection of *E. coli* (96.8 disinfected within 30 min)	229
gCN/gCN NTs/TiO_2	Self-assembly of gCN and TiO_2		Photodegradation of PH/Vis (removal reached up to 90% within 120 min)	230
0D/1D gCN@TiO_2 NTAs	Three-step method: Anodization, $NaBH_4$ reduction, and chemical vapor deposition (CVD)		Photodegradation of MO/Vis (100% within 60 min, Enhanced 14-fold/TiO_2)	231
P-S-doped-gCN NSs/Ag_3PO_4	Facile deposition–precipitation method	~50	DMP photodegradation (97% in 180 min, effectively degraded in 2 h, enhanced 2.2 times/P-S-gCN)	232
Cu/Zn/gCN NSs	Multistep ultrasound-assisted hydrothermal procedure	10	Dual Z-scheme Photocatalytic desulfurization (100% desulfurization of dibenzothiophene (DBT) in 60 min)	233
gCN/Bi_2MoO_6	Hydrothermal reaction	25	Photodegradation of MB/Vis (pseudo-first-order rate constant k_{app} of 0.0688 min^{-1}, which was 4.8 times and 8.2 times higher than that of gCN and Bi_2MoO_6, respectively)	234
gCN/ZnO (O-vacancy)	Calcination	1	Photodegrading MO and of humic acid (HA)/Vis (93% degradation after 60 min) and (80% photodegradation of HA in 60 min)	235
gCN NPs/WO_3 (1D NWs, 2D NSs, and 3D MFs)	Thermal polymerization of the composite	—	Degradation of PNP/simulated sunlight (100% in 60 min/NWs, 100% in 60 min/NSs, and 100% in 120 min/MFs) Methylparaben (MPB)/simulated sunlight (100% in 60 min/NWs and NSs)	236
p-gCN NSs/$BiVO_4$	Impregnated co-precipitation method	—	Photodegradation of TC/Vis (removal efficiency of 96.95% within 60 min, enhancement of 4-fold/gCN)	237
MoS_2/gCN dual defect	Ultrasonic dispersion and annealing method		Photodegradation of TC and BPA (rate normalized to the specific surface area of 3.22×10^{-4} g min^{-1} m^{-2}, enhancement of 10.0-fold/gCN)	238

9.7 Carbonaceous Carbon-quantum-dot Modified gCN

In photocatalysis, the generation of charge carriers (e^-/h^+ pairs) is quite essential. Again, the photocatalytic activity depends on the suppression of the recombination of the photogenerated charge carriers. Carbon dots (CDs) are used to suppress the recombination of the electron/hole pairs.[30,110] In subsequence, this leads to improved photocatalytic activity in gCN/CD-based nanostructures.[30,110,239] Hence, based on their exceptional multi-photon irradiation feature, CDs are utilized as spectral converters where the light with larger wavelengths could be converted to shorter wavelengths. Thus, an increase in charge carriers enhances the photocatalytic process.[30,110,239–241] Also, CDs can act as an electron mediator between the semiconductors in a type II heterojunction or Z-scheme photocatalytic system.[242,243] This is owing to the intrinsic property of the carbon dots' best electron acceptor/donor property and hence they perform as electron conduction mediators and so boost the photocatalytic process.[242,243] Therefore, gCN coupled with CDs plays an important role in environmental remediation and H_2 production applications. In this regard, gCN/CD-based nanohybrids are currently the subject of intensive research in photo catalysis and respective environmental remediation applications.

9.7.1 Applications of CQD Modified gCN-based Heterojunctions

gCN was coupled with different mole fractions of CDs by the facile thermal impregnation procedure to fabricate binary gCN/CD nanocomposites. It was found that the photocatalyst having 0.5 wt% of CDs was the most efficient in PH photodegradation.[244] The rate constant enhancement was 3.7-fold as compared with the gCN. This suggested a mechanism for the improved ability under visible light.[244] This behavior is ascribed to the upconversion photoluminescence (UCPL) features of CDs where they can convert longer wavelengths into light with shorter wavelengths. Moreover, they are reasonably stable with enhanced photocatalytic recoveries under visible light.

Carbon quantum dots (CQDs) combined with NSs of gCN show improved photo electrocatalytic properties in the elimination of MB upon visible-light illumination.[245] It had been apparent that the surface hybrid heterojunction structures among gCN nanosheets and CQDs have a pronounced effect on photo electrocatalytic activity.

Nitrogen-doped carbon dots (NCDs) decorated a direct Z-scheme gCN/Ag_3PO_4 photocatalyst. Liu *et al.*[246] prepared an all solid Z-scheme gCN/Ag_3PO_4/NCDs photocatalyst. Excellent photocatalytic activity has been exhibited by the photocatalyst gCN/Ag_3PO_4/NCDs in the degradation of MB, RhB, and PH under visible-light illumination. Solutions of MB and RhB were efficiently degraded within 20 min and 15 min, respectively. PH degraded to 36% within

80 min, which is much better than those of Ag_3PO_4 and gCN/Ag_3PO_4. NCDs improve oxygen activation, enhance light harvesting, and facilitate the separation of the photogenerated charge carriers.

Ternary composites were prepared by depositing both CQDs and Ag nanoparticles (NPs) onto the surface of gCN NSs.[247] For the evaluation of photocatalytic activities, MO and *p*-nitrophenol (PNP) were degraded under sunlight illumination. The UV-Vis, diffuse reflectance spectroscopy (DRS) of CQDs/gCN NSs showed that the nanocomposite exhibited a redshift to visible-light gCN NSs. This again confirms the existence of complete anchoring of the CQDs and the Ag NPs on gCN. Moreover, the synergism of the CQDs, Ag NPs, and the gCN NSs at the interface regions allows for simple production, separation, and transfer of electrons. The result is a boost in the photocatalytic H_2 generation activity. Scheme 9.13 illustrates the ensuing photocatalytic process in the presence of CQDs.

Li *et al.*[248] deposited CQDs on gCN NSs to construct CQDs/gCN heterocomposites. The composites exhibited higher photocatalytic activity under visible-light illumination. The optimized CQDs/gCN NSs sample showed higher photocatalytic activity, with an H_2 production rate of 116.1 μmol h^{-1} that is three-fold enhanced compared to that of gCN NSs. The improved photocatalytic ability is ascribed to the CQDs functioning as an electron trap and promotes the separation of the photogenerated electron–hole pairs.[248] A photocatalytic mechanism was proposed.

Due to their high efficiency, CDs are usually present in a minute amount of ~1.0 wt%. A nanohybrid CDs/TiO_2/gCN was used in the degradation of enrofloxacin (ENX).[249] This is mainly owing to the unique up-conversion features (UCPL), efficacious electron immigration, and enhanced charge separation of CDs. In essence, CDs can enhance the photocatalytic activity through the

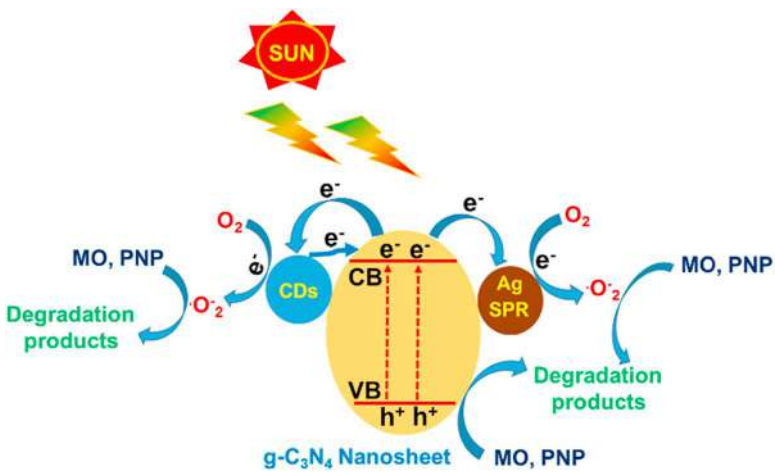

Scheme 9.13 The probable photocatalytic process over the Ag NPs/CQDs/gCN NSs under sunlight illumination. Reproduced from ref. 247 with permission from Elsevier, Copyright 2017.

conversion of light in the near-infrared (NIR) to light with visible wavelengths that improve the efficiency of the harnessing of light by the nanocomposites. Above all, the introduction of CDs in the TiO_2/gCN nanohybrid photocatalyst follows a direct Z-scheme type mechanism.[249] In the common heterostructured mechanism, ENX can be eliminated into inorganic compounds or be converted into H_2O and CO_2.

Additional CQDs/gCN based and other semiconductors are summarized in Table 9.5.

9.8 Applications of gCN-based Photocatalysts

9.8.1 Photocatalytic Hydrogen Generation

Since the discovery of titanium dioxide TiO_2 as a potential photocatalytic material, several alternatives have emerged as more efficient photocatalysts However, none has found as widespread usage as TiO_2. Now it is possible that we are reaching a corner of substitution of TiO_2 with carbon-based alternatives. Historically, owing to the pioneering study of Fujishima,[267] there is now a plethora of photocatalysts that have proved to be more effective in water splitting, especially in the visible region of the solar spectrum. gCN is one of the most promising non-metallic carbon-based candidates. There are rather rapid developments in this arena.[30,268]

The usage of gCN is intrinsically restricted due to the low conductivity and low surface area. Therefore, structural engineering to improve the conductivity and enhance the specific surface area is done by incorporation of abundant metal derivatives, size reduction, and sensitizing by organic dyes or inorganics.

The first thing one can do to eliminate such deficiencies is to incorporate heterogeneity by structural defects, oxygen substitution of nitrogen by oxygen or sulfur.[269] The structural defects have narrowed the band gap and charge separation efficiency. The band gap of modified gCNs has decreased from 2.67 to 2.40. The samples have shown stable photo activity as long as 40 h of time-on-stream. In another attempt,[270] carbon-rich gCNs have been synthesized and carbon-rich gCNs have shown 1.90 eV and much higher Brunauer–Emmett–Teller (BET) surface areas, 39.2 $m^2\ g^{-1}$, in comparison to bulk gCNs at 8.3 $m^2\ g^{-1}$. Carbon-rich gCN has shown a performance increase of over 20.5 times and has shown prolonged activity without a loss in activity.

The photocatalytic activity of gCN depends on the precursor chemicals. Dicyanamide (DCAD), U, THU or mixtures of U and THU have greatly affected polymerization products. A U-THU mixture was polymerized at 520 °C and this gCN has shown the highest activity reaching a record 720 μmol H_2 per gram. Changing the operating conditions, such as electrolyte and PH, has also had immense effects on the activity. Under the best operating conditions, PH = 13.3 and KOH electrolyte, hydrogen evolution rate (HER) activity (2.23 mmol $h^{-1}\ g^{-1}$, AQY 6.67% at 400 nm) under visible light was recorded.[270] Figure 9.2a shows the H_2 generation rate over the metal-free bulk gCN and

Table 9.5 CDs/CQDs/gCN-based heterojunctions: typical synthetic routes and photocatalytic activity.

Photocatalyst	Preparation method	Application, efficiency, and enhancement factor	Reference
Hydrogen generation			
CD@NH_2–UiO-66/gCN NSs	Immersion in a glucose solution and then calcining	Photocatalytic H_2 generation/Vis (2.930 mmol h^{-1} g^{-1}, which is 32.4-fold as high/gCN)	250
gCN NTs/CQDs	Thermal polymerization	Photocatalytic H_2 evolution rate/Vis (3.538 mmol h^{-1} g^{-1}, enhanced 13.6 times/gCN NTs, AQE of 10.94 at λ = 420 nm)	251
gCN/CDs	Hydrothermal	Photocatalytic H_2 evolution/Vis (183.0 μmol h^{-1})	252
gCN/CoP QDs	Thermal decomposition, followed by electroless plating	H_2 production rate (665 μmol g^{-1} h^{-1})	253
gCN/CdSe QDs 0D/2D	Simple *in situ* growth technique. Thiol functionalized gCN	Highest ever H_2 evolution at the rate of (31 mmol h^{-1} g^{-1}, which is enhanced over 103.3-fold/gCNNSs. AQY efficiency of 13.86% at an λ = 460 nm). [*Inserted for purposes of comparison*]	254
Organic pollutants' degradation			
gCN/CQDs/SnO_2	Thermal polymerization	Degradation of indomethacin/Vis (90.8% in 60 min)	255
gCN/CdS/CQDs Z-scheme	Simple calcination	Photodegradation of RhB/Vis (100% upon irradiation for 20 min); photodegradation of MB/Vis (98%) within 120 min); photodegradation of PH/Vis (58% in 120 min)	256
gCN NSs/CQD/BiOBr	Facile refluxing at low T	Photocatalytic degradations of RhB, MB, and MO/Vis (enhancement was 129, 29.8, and 20.5 times/gCN, respectively)	257
SA Ag-CQDs/gCN NSs	Thermo-polymerization	Degradation of naproxen (87.5% in 25 min)	258
gCN/CQDs	Hydrothermal	Degradation of MO/Vis (92.0% in 180 min)	259
gCN/Bi_2WO_6/CQDs	*In situ* calcination and hydrothermal	Degradation of RhB and TC/Vis (~95% in 45 min (RhB) and ~80% in 60 min TC)	260
gCN/CQDs	Polymerization	Degradation of diclofenac/Vis (100% in 60 min)	261
gCN NSs/CQDs/Ag NPs	Impregnation-hydrothermal method	Photodegradation of MO/Vis (98.6% in 100 min) Photodegradation of PNP/Vis (92% in 100 min)	247
gCN/AgCl/CQDs	Impregnation	Degradation of MB and RhB/Vis (100% in 75 min (MB) and ~90% in 75 min RhB)	262
gCN/CQDs	Precipitation	Degradation of RhB and TC/Vis (95.2% in 210 min RhB and 78.6% in 240 min TC)	263
gCN/CQDs	Deposition	Degradation of RhB (/Vis 100% in 210 min)	264
gCN NSs/Graphene/CQDs	Hydrothermal	Degradation of MO/Vis (91.1% in 240 min)	265
CQDs modified tubular gCN	Hydrothermal	Elimination of carbamazepine/Vis (100% in 60 min)	266

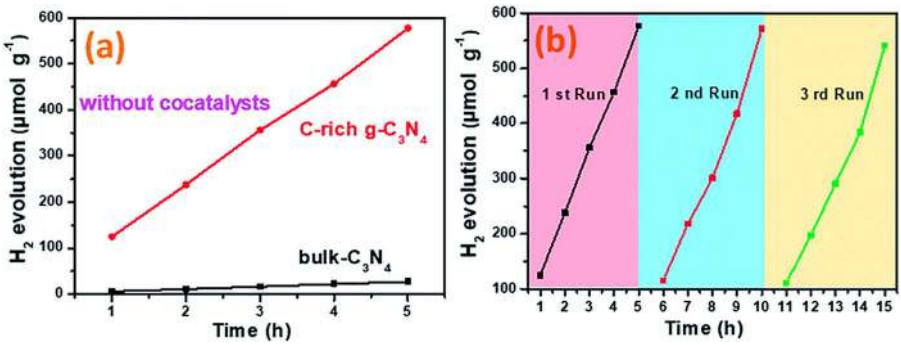

Figure 9.2 (a) H_2 generation rate over the metal-free bulk gCN and C-rich gCN photocatalysts (300 W Xe lamp), and (b) cycling of the H_2 evolution of the C-rich gCN metal-free photocatalyst. Reproduced from ref. 270 with permission from the Royal Society of Chemistry.

C-rich gCN photocatalysts and (b) displays the cycling of the H_2 evolution of the C-rich gCN.

In a recent study, Ni_2B has been used to modify gCNs catalysts. It is reported that incorporation of Ni_2B has helped to reduce the interlayer distance and specific conductivity. Ni_2B doped gCN showed superior electrocatalytic activity and has lowered the overpotentials from 707 mV of pristine gCNs to 300 mV of Ni_2B doped gCNs with correspondingly higher kinetics.

gCN is sensitized by naphthalimide-porphyrin of the so-called dye sensitizer. Photocatalytic activity of sensitized gCNs has tripled from 698 μmol h^{-1} g^{-1} of pristine gCN to 2297 μmol h^{-1} g^{-1} of 2% dye/gCNs.[271]

Metal sulfur doped gCN was also synthesized by co-thermal polymerization. The addition of small amounts of WS_2 increased the hydrogen production rates from 4.5 μmol h^{-1} g^{-1} to 154 μmol h^{-1} g^{-1}. WS_2 has improved the photocatalytic hydrogen production by facilitating photo carrier transport.

In a so-called double-doped gCN, two-dimensional reduced graphene oxide RGO and NiS_2 boosted the photocatalytic activity 67 times. NiS_2 acted as efficient electron transfer hubs and RGO helped to create high surface area and high conductivity. Apparently, RGO and NiS_2 both helped to improve the stability until 24 h of operation.[272]

9.9 Photocatalytic Degradation of Organic Pollutants Using gCN-heterojunctions

Novel photocatalysts, especially those that do not contain precious metals, have gained popularity among scientists. Several promising usages, such as solar energy cultivation and storage, water splitting, carbon dioxide capture and utilization, and remediation of environmental pollutants, are on the way to practical widespread exploitation. Due to the immense effects of the environmental pollution of air, earth and water on human beings, researchers

are looking for efficient and environmentally-friendly ways to remove such common pollutants. Besides the mature advanced oxidation processes, there are plenty of emerging technologies, one of them being photocatalytic oxidation using non-precious metal or non-metals containing photo and electro catalysts. gCN is one of the recent model catalysts among the plethora of emerging catalysts.

gCN photocatalysts have been widely used to photodegrade a variety of organic dye pollutants, VOCs and various others pollutants.[273] In various articles, exemplary chemicals, RhB, MB, MO, chlorophenol (CP), PH, and bisphenol A (BPA), have been used to represent real-life pollutants.

It is well known that photogenerated electrons (e−) and holes (h+) can generate radicals, such as hydroxyl radicals (•OH) and superoxide anion radicals ($•O_2^-$). Such radical species are produced to oxidize organic pollutants during photocatalytic reactions.[274] However, in polymeric semiconductors, electron–hole pairs exist in the form of couples (Frenkel excitons) due to the low dielectric constants where photogenerated electrons and holes are strongly bound by coulombic effects. In other words, the intramolecular coulombic interactions are so strong that the periodic structures of such organic molecules cause small-delocalized excited states – excitons – which give rise to excitation energy, and transfer from site to site. The exciton states are considered linear combinations of localized excited states.[275] To enhance the electron–hole separations from excitons, so-called disorders,[276] in this case, semiconductors are doped with other semiconductors in small quantities, which have excited states lower in energy than the host structure. Excitons migrating through the dopant semiconductors can be trapped at the junctions. Hence, semiconductor doping facilitates overcoming fast recombination leading to the low photocatalytic activity.[277,278]

In the degradation of MO, gCN synthesized from melamine resulted in a maximum of 54.67% whereas gCN from guanidine and DCAD resulted in 23.46% and 22.16%, respectively.[279]

Of course, morphological changes and increased surface area cannot account for the enhanced photocatalytic activity. The charge separation efficiency and light absorption capabilities can be additional responsible factors too. In CDs, promoted gCNs composites' increased photocatalytic reactivity is well correlated with the ultraviolet–visible diffuse reflectance spectra (UV–Vis DRS) results. It is believed that the π-conjugated CDs served as a photosensitizer and injected electrons to the CB of gCN, resulting in the extended absorption spectrum from the visible to the NIR region.[280] Wider absorption from Vis to NIR resulted in the generation of more electrons for the enhancement of BPA degradation. CDs' promoted degradation efficiency has shown a fourfold increase. More abundant surface species such as ($•O_2^-$), available due to electron transfer from the CB of gCNs to oxygen, facilitated BPA removal.

In another study,[281] photocatalytic removal of two model compounds were achieved in boron and phosphorus double promoted gCNs. Enhanced reactivity was correlated with appropriate band positioning. These co-dopants helped to shift the CBs and VBs of co-doped gCNs to more negative

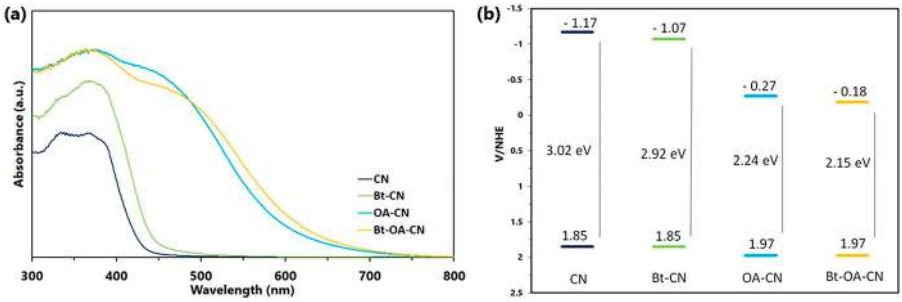

Figure 9.3 (a) UV-Vis DRS spectra, and (b) band structure alignments of CN, Bt-CN, OA-CN, and Bt-OA-CN. Reproduced from ref. 283 with permission from Springer Nature, Copyright 2019.

and positive directions.[281] From quenching experiments, it was concluded that both holes h^+ and ($^{\bullet}O_2^-$) radicals are the species in the photocatalytic oxidation.

A copper and chlorine doped gCN photocatalyst has shown a similar beneficial effect in the removal of tetracycline hydrochloride (TC-HCl), and other chlorinated pollutants.[282] Although co-doping of gCN has not increased the total BET surface area, it has substantially improved the degradation activity. The mechanism of the effect is thought to be due to the improved charge separation, extended light absorption and band positioning.

Without incorporation of dopants, the chemistry of gCN was studied in two ways. An oxygen enriching additive (KOH) and nitrogen defecting additive (oxalic acid) have helped to improve light absorption and band structure alignments too.[283]

From UV-Vis DRS and VB XPS experiments, modified gCNs possess lower CB energies. XPS analysis revealed that N/C ratios have lowered on the modified gCNs from a typical 1.30 to 1.23 in the double modified gCNs. Nitrogen defects and oxygen doping in gCNs are envisaged to have led to a reduction in recombination.[283] Figure 9.3 illustrates both (a) the DRS and (b) the band alignment of the oxygen rich with nitrogen deficient gCN.

A combination of several effects such as band repositioning and extensive light absorption, hence reduced charge recombination, seems to be the main causes of enhanced photocatalytic activity.

9.10 Concluding Remarks

The electronic structure and band gap engineering of gCN-based photocatalysts are the first steps taken in remediation of deficiencies of pristine gCN. Elemental doping, *i.e.*, S, N, or O, intercalation, and doping with various ions or oxides are found to be beneficial to increase charge separation, enhance visible-light absorption, and create the defect states to improve photocatalytic H_2 and O_2 production. In photocatalysis or catalysis in general, improvement

of the dispersion of dopants would also help to further photocatalytic activity and stability. Tailoring the surface characteristics of gCNs to enhance hydrophilicity or hydrophobicity would definitely help in facilitating adsorption, surface reaction, electron and hole transfer on the surface of gCNs. Coupling of gCNs with porous metal-based catalysts with unique surface merits (*i.e.*, high surface area, branches, and cavities) as well as outstanding redox and luminescence properties, can enhance the H_2 production and induce degradation of dyes or pollutants.[284–292] Additionally, novel MXenes, carbon dots, graphene, and metal–organic frameworks with their great viable light absorption, catalytic/photocatalytic and quick charge mobility properties, can induce the photocatalytic properties of gCN nanostructures.[293–299]

List of Abbreviations

AQE	Apparent quantum efficiency
AQY	Apparent quantum yield
BPA	Bisphenol A
CIP	Ciprofloxacin
CP	Chlorophenol
DC	Defective crystallinity
DCAD	Dicyanamide
DCDA	Dicyandiamide
DCP	Dicholoro phenol
DMP	Dimethyl phenol
DNP	Dinitrophenyl
HC	Highly crystalline
HMSPHs	Hollow microspheres
MB	Methylene blue
MFs	Microflowers
MO	Methyl orange
MTs	Microtubes
NDs	Nanodots
NFs	Nanofibers
NRs	Nanorods
NSs	Nanosheets
NTAs	Nanotube arrays
NWs	Nanowires
p	Porous
PH	Phenol
PHE	Phenanthrene
PNP	*p*-nitrophenol
QD	Quantum dot
RhB	Rhodamine B
SA	Single atom
SPHs	Spheres

TC Tetracycline
TCH Tetracycline hydrochloride
THU Thiourea
U Urea

References

1. H. Zhang, X. Zuo, H. Tang, G. Li and Z. Zhou, *Phys. Chem. Chem. Phys.*, 2015, **17**, 6280–6288.
2. S. Cao and J. Yu, *J. Phys. Chem. Lett.*, 2014, **5**, 2101–2107.
3. M. A. Ahsan, T. He, K. Eid, A. M. Abdullah, M. L. Curry, A. Du, A. R. Puente Santiago, L. Echegoyen and J. C. Noveron, *J. Am. Chem. Soc.*, 2021, **143**, 1203–1215.
4. K. Eid, M. H. Sliem, A. S. Eldesoky, H. Al-Kandari and A. M. Abdullah, *Int. J. Hydrogen Energy*, 2019, **44**, 17943–17953.
5. K. Eid, M. H. Sliem, K. Jlassi, A. S. Eldesoky, G. G. Abdo, S. Y. Al-Qaradawi, M. A. Sharaf, A. M. Abdullah and A. A. Elzatahry, *Inorg. Chem. Commun.*, 2019, **107**, 107460.
6. K. Eid and A. M. Abdullah, *Data Brief*, 2019, **26**, 104495.
7. K. Eid, M. H. Sliem, A. S. Eldesoky and A. M. Abdullah, *Data Brief*, 2019, **27**, 104734.
8. C. Ye, J.-X. Li, Z.-J. Li, X.-B. Li, X.-B. Fan, L.-P. Zhang, B. Chen, C.-H. Tung and L.-Z. Wu, *ACS Catal.*, 2015, **5**, 6973–6979.
9. S. Zhang, J. Li, X. Wang, Y. Huang, M. Zeng and J. Xu, *J. Mater. Chem. A*, 2015, **3**, 10119–10126.
10. K. A. M. Eid and A. M. Abdullah, *US Pat.*, US20200239311A1, 2020.
11. K. Eid, M. H. Sliem, H. Al-Kandari, M. A. Sharaf and A. M. Abdullah, *Langmuir*, 2019, **35**, 3421–3431.
12. K. Eid, M. H. Sliem and A. M. Abdullah, *Nanoscale*, 2019, **11**, 11755–11764.
13. S. Zhang, J. Li, M. Zeng, J. Li, J. Xu and X. Wang, *Chem. - Eur. J.*, 2014, **20**, 9805–9812.
14. J. Zhang, M. Zhang, C. Yang and X. Wang, *Adv. Mater.*, 2014, **26**, 4121–4126.
15. T. Y. Ma, J. Ran, S. Dai, M. Jaroniec and S. Z. Qiao, *Angew. Chem., Int. Ed.*, 2015, **54**, 4646–4650.
16. S. Chu, Y. Wang, Y. Guo, J. Feng, C. Wang, W. Luo, X. Fan and Z. Zou, *ACS Catal.*, 2013, **3**, 912–919.
17. Z. Li, C. Kong and G. Lu, *J. Mater. Chem. C*, 2016, **120**, 56–63.
18. X. Chen, J. Zhang, X. Fu, M. Antonietti and X. Wang, *J. Am. Chem. Soc.*, 2009, **131**, 11658–11659.
19. Y. Che, Q. Liu, B. Lu, J. Zhai, K. Wang and Z. Liu, *Sci. Rep.*, 2020, **10**, 721.
20. J. Zeng, T. Song, M. Lv, T. Wang, J. Qin and H. Zeng, *RSC Adv.*, 2016, **6**, 54964–54975.
21. L. Lu, K. Dai, Q. Liu, G. Zhu, X. Wei, J. Bai, L. Xuan and H. Wang, *Dalton Trans.*, 2014, **43**, 5.

22. B. Chai, X. Liao, F. Song and H. Zhou, *Dalton Trans.*, 2014, **43**, 982–989.
23. D. Jiang, J. Li, C. Xing, Z. Zhang, S. Meng and M. Chen, *ACS Appl. Mater. Interfaces*, 2015, **7**, 19234–19242.
24. L. Gu, J. Wang, Z. Zou and X. Han, *J. Hazard. Mater.*, 2014, **268**, 216–223.
25. X. Wang, K. Maeda, A. Thomas, K. Takanabe, G. Xin, J. M. Carlsson, K. Domen and M. Antonietti, *Nat. Mater.*, 2009, **8**, 76–80.
26. X. Wang, X. Chen, A. Thomas, X. Fu and M. Antonietti, *Adv. Mater.*, 2009, **21**, 1609–1612.
27. Q. Cao, B. Kumru, M. Antonietti and B. V. K. J. Schmidt, *Mater. Horiz.*, 2020, **7**, 762–786.
28. M. Ismael and Y. Wu, *Sustainable Energy Fuels*, 2019, **3**, 2907–2925.
29. W.-J. Ong, L.-L. Tan, Y. H. Ng, S.-T. Yong and S.-P. Chai, *Chem. Rev.*, 2016, **116**, 7159–7329.
30. Y. Chen and X. Bai, *Catalysts*, 2020, **10**, 142.
31. F. Goettmann, A. Fischer, M. Antonietti and A. Thomas, *Chem. Commun.*, 2006, 4530–4532.
32. D. M. Teter and R. J. Hemley, *Science*, 1996, **271**, 53–55.
33. Y. Zheng, L. Lin, B. Wang and X. Wang, *Angew. Chem., Int. Ed.*, 2015, **54**, 12868–12884.
34. E. Kroke, M. Schwarz, E. Horath-Bordon, P. Kroll, B. Noll and A. D. Norman, *New J. Chem.*, 2002, **26**, 508–512.
35. Y. Zhao, J. Zhang and L. Qu, *ChemNanoMat*, 2015, **1**, 298–318.
36. A. Zambon, J. M. Mouesca, C. Gheorghiu, P. A. Bayle, J. Pécaut, M. Claeys-Bruno, S. Gambarelli and L. Dubois, *Chem. Sci.*, 2016, **7**, 945–950.
37. Y. Wang, Y. Di, M. Antonietti, H. Li, X. Chen and X. Wang, *Chem. Mater.*, 2010, **22**, 5119–5121.
38. A. Sattler, S. Pagano, M. Zeuner, A. Zurawski, D. Gunzelmann, J. Senker, K. Müller-Buschbaum and W. Schnick, *Chem. - Eur. J.*, 2009, **15**, 13161–13170.
39. K. Maeda, X. Wang, Y. Nishihara, D. Lu, M. Antonietti and K. Domen, *J. Mater. Chem. C*, 2009, **113**, 4940–4947.
40. F. Dong, Z. Zhao, T. Xiong, Z. Ni, W. Zhang, Y. Sun and W.-K. Ho, *ACS Appl. Mater. Interfaces*, 2013, **5**, 11392–11401.
41. X. Wang, S. Blechert and M. Antonietti, *ACS Catal.*, 2012, **2**, 1596–1606.
42. D. J. Martin, P. J. T. Reardon, S. J. A. Moniz and J. Tang, *J. Am. Chem. Soc.*, 2014, **136**, 12568–12571.
43. L. Wang, Y. Tong, J. Feng, J. Hou, J. Li, X. Hou and J. Liang, *Sustainable Mater. Technol.*, 2019, **19**, e00089.
44. J. Zhu, P. Xiao, H. Li and S. A. Carabineiro, *ACS Appl. Mater. Interfaces*, 2014, **6**, 16449–16465.
45. Z. Wang, F. Liu, M. Sun, J. Xu, Z. Xu, R. Chen, Y. Kang and F. Hu, *FlatChem*, 2020, **20**, 100153.
46. J. Bian, Q. Li, C. Huang, J. Li, Y. Guo, M. Zaw and R.-Q. Zhang, *Nano Energy*, 2015, **15**, 353–361.
47. Y. Cui, Y. Tang and X. Wang, *Mater. Lett.*, 2015, **161**, 197–200.

48. L. Guan, N. Xu, X. Liu, Y. Zhao, H. Li, J. Sun, J. Wu and Z. Ying, *Carbon*, 2014, **79**, 578–589.
49. B. Zhu, P. Xia, W. Ho and J. Yu, *Appl. Surf. Sci.*, 2015, **344**, 188–195.
50. C. Yang, B. Wang, L. Zhang, L. Yin and X. Wang, *Angew. Chem., Int. Ed.*, 2017, **56**, 6627–6631.
51. K. Wang, Q. Li, B. Liu, B. Cheng, W. Ho and J. Yu, *Appl. Catal., B*, 2015, **176–177**, 44–52.
52. F. K. Kessler, Y. Zheng, D. Schwarz, C. Merschjann, W. Schnick, X. Wang and M. J. Bojdys, *Nat. Rev. Mater.*, 2017, **2**, 17030.
53. G. Mamba and A. K. Mishra, *Appl. Catal., B*, 2016, **198**, 347–377.
54. J. Zhang, F. Guo and X. Wang, *Adv. Funct. Mater.*, 2013, **23**, 3008–3014.
55. J. Xu, H. Zhou, K. Shi, R. Yan, Y. Tang, J. Liu, J. Ye, D. Zhang and T. Fan, *J. Mater. Chem. A*, 2017, **5**, 2195–2203.
56. P. Xia, B. Zhu, J. Yu, S. Cao and M. Jaroniec, *J. Mater. Chem. A*, 2017, **5**, 3230–3238.
57. Y. Li, H. Xu, S. Ouyang, D. Lu, X. Wang, D. Wang and J. Ye, *J. Mater. Chem. A*, 2016, **4**, 2943–2950.
58. M. Z. Rahman, J. Ran, Y. Tang, M. Jaroniec and S. Z. Qiao, *J. Mater. Chem. A*, 2016, **4**, 2445–2452.
59. Y. Kang, Y. Yang, L. C. Yin, X. Kang, G. Liu and H. M. Cheng, *Adv. Mater.*, 2015, **27**, 4572–4577.
60. J. Li, B. Shen, Z. Hong, B. Lin, B. Gao and Y. Chen, *Chem. Commun.*, 2012, **48**, 12017–12019.
61. X. Dong and F. Cheng, *J. Mater. Chem. A*, 2015, **3**, 23642–23652.
62. P. Niu, L. Zhang, G. Liu and H. M. Cheng, *Adv. Funct. Mater.*, 2012, **22**, 4763–4770.
63. S. Yang, Y. Gong, J. Zhang, L. Zhan, L. Ma, Z. Fang, R. Vajtai, X. Wang and P. M. Ajayan, *Adv. Mater.*, 2013, **25**, 2452–2456.
64. J. Feng, T. Chen, S. Liu, Q. Zhou, Y. Ren, Y. Lv and Z. Fan, *J. Colloid Interface Sci.*, 2016, **479**, 1–6.
65. J. Zhang, Y. Chen and X. Wang, *Energy Environ. Sci.*, 2015, **8**, 3092–3108.
66. J. Ran, T. Y. Ma, G. Gao, X.-W. Du and S. Z. Qiao, *Energy Environ. Sci.*, 2015, **8**, 3708–3717.
67. B. Zhu, J. Zhang, C. Jiang, B. Cheng and J. Yu, *Appl. Catal., B*, 2017, **207**, 27–34.
68. Q. Huang, J. Yu, S. Cao, C. Cui and B. Cheng, *Appl. Surf. Sci.*, 2015, **358**, 350–355.
69. D. Chen, J. Yang and H. Ding, *Appl. Surf. Sci.*, 2017, **391**, 384–391.
70. Q. Gao, S. Hu, Y. Du and Z. Hu, *J. Mater. Chem. A*, 2017, **5**, 4827–4834.
71. D. Zheng, C. Huang and X. Wang, *Nanoscale*, 2015, **7**, 465–470.
72. Y. Zheng, L. Lin, X. Ye, F. Guo and X. Wang, *Angew. Chem.*, 2014, **126**, 12120–12124.
73. F. Dong, L. Wu, Y. Sun, M. Fu, Z. Wu and S. Lee, *J. Mater. Chem.*, 2011, **21**, 15171–15174.
74. S. Cao, J. Low, J. Yu and M. Jaroniec, *Adv. Mater.*, 2015, **27**, 2150–2176.
75. Z. Lin and X. Wang, *Angew. Chem.*, 2013, **125**, 1779–1782.

76. Z. Zhou, Y. Zhang, Y. Shen, S. Liu and Y. Zhang, *Chem. Soc. Rev.*, 2018, **47**, 2298–2321.
77. Y.-S. Jun, E. Z. Lee, X. Wang, W. H. Hong, G. D. Stucky and A. Thomas, *Adv. Funct. Mater.*, 2013, **23**, 3661–3667.
78. Q. Liu, X. Wang, Q. Yang, Z. Zhang and X. Fang, *Appl. Surf. Sci.*, 2018, **450**, 46–56.
79. Z. Mo, H. Xu, Z. Chen, X. She, Y. Song, J. Wu, P. Yan, L. Xu, Y. Lei, S. Yuan and H. Li, *Appl. Catal., B*, 2018, **225**, 154–161.
80. P. Qiu, C. Xu, H. Chen, F. Jiang, X. Wang, R. Lu and X. Zhang, *Appl. Catal., B*, 2017, **206**, 319–327.
81. J. P. Mathias, E. E. Simanek, J. A. Zerkowski, C. T. Seto and G. M. Whitesides, *J. Am. Chem. Soc.*, 1994, **116**, 4316–4325.
82. J.-W. Zhang, S. Gong, N. Mahmood, L. Pan, X. Zhang and J.-J. Zou, *Appl. Catal., B*, 2018, **221**, 9–16.
83. Q. Yang, C. Chen, Q. Zhang, Z. Zhang and X. Fang, *Carbon*, 2020, **164**, 337–348.
84. Y. Zhang, K. Li, J. Liao, X. Wei and L. Zhang, *Appl. Surf. Sci.*, 2020, **499**, 143875.
85. Y.-P. Yuan, W.-T. Xu, L.-S. Yin, S.-W. Cao, Y.-S. Liao, Y.-Q. Tng and C. Xue, *Int. J. Hydrogen Energy*, 2013, **38**, 13159–13163.
86. Y.-P. Yuan, L.-S. Yin, S.-W. Cao, L.-N. Gu, G.-S. Xu, P. Du, H. Chai, Y.-S. Liao and C. Xue, *Green Chem.*, 2014, **16**, 4663–4668.
87. F. K. Butt, P. Hauenstein, M. Kosiahn, B. Garlyyev, M. Dao, A. Lang, D. Scieszka, Y. Liang and W. Kreuzpaintner, *Microporous Mesoporous Mater.*, 2020, **294**, 109853.
88. M. J. Bojdys, J. O. Müller, M. Antonietti and A. Thomas, *Chem. - Eur. J.*, 2008, **14**, 8177–8182.
89. K. Schwinghammer, B. Tuffy, M. B. Mesch, E. Wirnhier, C. Martineau, F. Taulelle, W. Schnick, J. Senker and B. V. Lotsch, *Angew. Chem., Int. Ed.*, 2013, **52**, 2435–2439.
90. Y. Wang, J. Zhang, X. Wang, M. Antonietti and H. Li, *Angew. Chem., Int. Ed.*, 2010, **49**, 3356–3359.
91. J. Di, J. Xia, S. Yin, H. Xu, L. Xu, Y. Xu, M. He and H. Li, *J. Mater. Chem. A*, 2014, **2**, 5340–5351.
92. Y. Li, Y. Lu, Y. Wang, L. Dong, M. Chao, J. Sun, Z. Zhao and J. Zhang, *Nanotechnology*, 2020, **31**, 464001.
93. H. Gao, R. Cao, S. Zhang, H. Yang and X. Xu, *ACS Appl. Mater. Interfaces*, 2018, **11**, 2050–2059.
94. M. R. Gholipour, F. Béland and T.-O. Do, *ACS Sustainable Chem. Eng.*, 2017, **5**, 213–220.
95. B. Antil, L. Kumar, K. Reddy, C. Gopinath and S. Deka, *ACS Sustainable Chem. Eng.*, 2019, **7**, 9428–9438.
96. H. Che, C. Li, C. Li, C. Liu, H. Dong and X. Song, *Chem. Eng. J.*, 2020, 127791.
97. Y. Hong, L. Wang, E. Liu, J. Chen, Z. Wang, S. Zhang, X. Lin, X. Duan and J. Shi, *Inorg. Chem. Front.*, 2020, **7**, 347–355.

98. C. Zhao, Z. Chen, J. Xu, Q. Liu, H. Xu, H. Tang, G. Li, Y. Jiang, F. Qu and Z. Lin, *Appl. Catal., B*, 2019, **256**, 117867.
99. Y. Xu, X. He, H. Zhong, D. J. Singh, L. Zhang and R. Wang, *Appl. Catal., B*, 2019, **246**, 349–355.
100. Q. Liu, C. Chen, K. Yuan, C. D. Sewell, Z. Zhang, X. Fang and Z. Lin, *Nano Energy*, 2020, **77**, 105104.
101. L. Liang, L. Shi, F. Wang, H. Wang and W. Qi, *Sustainable Energy Fuels*, 2020, **4**, 5179–5187.
102. B. Babu, B. Akkinepally, J. Shim and K. Yoo, *Ceram. Int.*, 2019, **45**, 15178–15187.
103. W. Zhang, J. Wang, Z. Liu, Y. Pi and R. Tan, *Green Energy Environ.*, DOI: 10.1016/j.gee.2020.11.019, in press.
104. J. Xu, Z. Wang and Y. Zhu, *ACS Appl. Mater. Interfaces*, 2017, **9**, 27727–27735.
105. D. Tang, Y. Chen, M. Yin, Q. Yang, Y. Zhou and L. Zhou, *Mater. Sci. Semicond. Process.*, 2020, **105**, 104735.
106. Q. Fan, J. Liu, Y. Yu, S. Zuo and B. Li, *Appl. Surf. Sci.*, 2017, **391**, 360–368.
107. C. Prasad, H. Tang, Q. Liu, I. Bahadur, S. Karlapudi and Y. Jiang, *Int. J. Hydrogen Energy*, 2020, **45**, 337–379.
108. L. Wang, K. Wang, T. He, Y. Zhao, H. Song and H. Wang, *ACS Sustainable Chem. Eng.*, 2020, **8**, 16048–16085.
109. J. Fu, J. Yu, C. Jiang and B. Cheng, *Adv. Energy Mater.*, 2018, **8**, 1701503.
110. S. Asadzadeh-Khaneghah and A. Habibi-Yangjeh, *J. Cleaner Prod.*, 2020, 124319.
111. J. Zhang, M. Zhang, R. Q. Sun and X. Wang, *Angew. Chem., Int. Ed.*, 2012, **51**, 10145–10149.
112. Z. Tong, D. Yang, Y. Sun, Y. Nan and Z. Jiang, *Small*, 2016, **12**, 4093–4101.
113. Y. Wang, N. Wu, Y. Wang, H. Ma, J. Zhang, L. Xu, M. K. Albolkany and B. Liu, *Nat. Commun.*, 2019, **10**, 1–8.
114. T. T. Isimjan, S. Rasul, M. Nasser Aloufi, M. A. Khan, I. K. Alhowaish and T. Ahmed, *Clean Energy*, 2019, **3**, 59–68.
115. L. Yao, D. Wei, Y. Ni, D. Yan and C. Hu, *Nano Energy*, 2016, **26**, 248–256.
116. H. Liu, Z. Xu, Z. Zhang and D. Ao, *Appl. Catal., B*, 2016, **192**, 234–241.
117. X. Hao, J. Zhou, Z. Cui, Y. Wang, Y. Wang and Z. Zou, *Appl. Catal., B*, 2018, **229**, 41–51.
118. L. Zhang, Q. Liu, Y. Chai and W.-L. Dai, *Int. J. Hydrogen Energy*, 2018, **43**, 5591–5602.
119. J. Zhang, Y. Wang, J. Jin, J. Zhang, Z. Lin, F. Huang and J. Yu, *ACS Appl. Mater. Interfaces*, 2013, **5**, 10317–10324.
120. W. Chen, T.-Y. Liu, T. Huang, X.-H. Liu, G.-R. Duan, X.-J. Yang and S.-M. Chen, *RSC Adv.*, 2015, **5**, 101214–101220.
121. F. Chang, J. Zhang, Y. Xie, J. Chen, C. Li, J. Wang, J. Luo, B. Deng and X. Hu, *Appl. Surf. Sci.*, 2014, **311**, 574–581.
122. H. Liu, D. Chen, Z. Wang, H. Jing and R. Zhang, *Appl. Catal., B*, 2017, **203**, 300–313.
123. Y. Liu, J. Tian, L. Wei, Q. Wang, C. Wang and C. Yang, *Opt. Mater.*, 2020, **107**, 110128.

124. Z. Jin, R. Hu, H. Wang, J. Hu and T. Ren, *Appl. Surf. Sci.*, 2019, **491**, 432–442.
125. U. Ghosh and A. Pal, *J. Ind. Eng. Chem.*, 2019, **79**, 383–408.
126. M. Liu, P. Xia, L. Zhang, B. Cheng and J. Yu, *ACS Sustainable Chem. Eng.*, 2018, **6**, 10472–10480.
127. W.-J. Ong, L. K. Putri, L.-L. Tan, S.-P. Chai and S.-T. Yong, *Appl. Catal., B*, 2016, **180**, 530–543.
128. C. Han, Y. Gao, S. Liu, L. Ge, N. Xiao, D. Dai, B. Xu and C. Chen, *Int. J. Hydrogen Energy*, 2017, **42**, 22765–22775.
129. Z. Mo, H. Xu, X. She, Y. Song, P. Yan, J. Yi, X. Zhu, Y. Lei, S. Yuan and H. Li, *Appl. Surf. Sci.*, 2019, **467**, 151–157.
130. S. Patnaik, S. Martha, G. Madras and K. Parida, *Phys. Chem. Chem. Phys.*, 2016, **18**, 28502–28514.
131. W. Peng, S.-S. Zhang, Y.-B. Shao and J.-H. Huang, *Int. J. Hydrogen Energy*, 2018, **43**, 22215–22225.
132. Y. Ma, J. Li, E. Liu, J. Wan, X. Hu and J. Fan, *Appl. Catal., B*, 2017, **219**, 467–478.
133. N. Cheng, J. Tian, Q. Liu, C. Ge, A. H. Qusti, A. M. Asiri, A. O. Al-Youbi and X. Sun, *ACS Appl. Mater. Interfaces*, 2013, **5**, 6815–6819.
134. X. Li, W. Bi, L. Zhang, S. Tao, W. Chu, Q. Zhang, Y. Luo, C. Wu and Y. Xie, *Adv. Mater.*, 2016, **28**, 2427–2431.
135. Y.-J. Yuan, Z. Shen, S. Wu, Y. Su, L. Pei, Z. Ji, M. Ding, W. Bai, Y. Chen and Z.-T. Yu, *Appl. Catal., B*, 2019, **246**, 120–128.
136. J. Yu, S. Wang, B. Cheng, Z. Lin and F. Huang, *Catal. Sci. Technol.*, 2013, **3**, 1782–1789.
137. J. Liu, Q. Jia, J. Long, X. Wang, Z. Gao and Q. Gu, *Appl. Catal., B*, 2018, **222**, 35–43.
138. J. Jiang, S. Cao, C. Hu and C. Chen, *Chin. J. Catal.*, 2017, **38**, 1981–1989.
139. J. Tian, D. Wang, S. Li, Y. Pei, M. Qiao, Z.-H. Li, J. Zhang and B. Zong, *ACS Sustainable Chem. Eng.*, 2019, **8**, 594–603.
140. W. Wang, P. Xu, M. Chen, G. Zeng, C. Zhang, C. Zhou, Y. Yang, D. Huang, C. Lai and M. Cheng, *ACS Sustainable Chem. Eng.*, 2018, **6**, 15503–15516.
141. X. Tian, Y.-J. Sun, J.-Y. He, X.-J. Wang, J. Zhao, S.-Z. Qiao and F.-T. Li, *J. Mater. Chem. A*, 2019, **7**, 7628–7635.
142. R. You, H. Dou, L. Chen, S. Zheng and Y. Zhang, *RSC Adv.*, 2017, **7**, 15842–15850.
143. Y.-P. Yuan, S.-W. Cao, Y.-S. Liao, L.-S. Yin and C. Xue, *Appl. Catal., B*, 2013, **140**, 164–168.
144. G. Liu, P. Niu, C. Sun, S. C. Smith, Z. Chen, G. Q. Lu and H.-M. Cheng, *J. Am. Chem. Soc.*, 2010, **132**, 11642–11648.
145. C.-C. Nguyen, M. Sakar, M.-H. Vu and T.-O. Do, *Ind. Eng. Chem. Res.*, 2019, **58**, 3698–3706.
146. X. Li, C. Liu, D. Wu, J. Li, P. Huo and H. Wang, *Chin. J. Catal.*, 2019, **40**, 928–939.
147. C. Chang, Y. Fu, M. Hu, C. Wang, G. Shan and L. Zhu, *Appl. Catal., B*, 2013, **142**, 553–560.

148. N. Wang, J. Wang, J. Hu, X. Lu, J. Sun, F. Shi, Z.-H. Liu, Z. Lei and R. Jiang, *ACS Appl. Energy Mater.*, 2018, **1**, 2866–2873.
149. M. Ou, S. Wan, Q. Zhong, S. Zhang and Y. Wang, *Int. J. Hydrogen Energy*, 2017, **42**, 27043–27054.
150. Y. Yang, Y. Guo, F. Liu, X. Yuan, Y. Guo, S. Zhang, W. Guo and M. Huo, *Appl. Catal., B*, 2013, **142**, 828–837.
151. T. Luo, X. Hu, Z. She, J. Wei, X. Feng and F. Chang, *J. Mol. Liq.*, 2020, 114772.
152. R. Zhang, S. Niu, X. Zhang, Z. Jiang, J. Zheng and C. Guo, *Appl. Surf. Sci.*, 2019, **489**, 427–434.
153. J. Xu, K.-Z. Long, Y. Wang, B. Xue and Y.-X. Li, *Appl. Catal., A*, 2015, **496**, 1–8.
154. M. Xie, J. Tang, L. Kong, W. Lu, V. Natarajan, F. Zhu and J. Zhan, *Chem. Eng. J.*, 2019, **360**, 1213–1222.
155. J. Gao, Y. Wang, S. Zhou, W. Lin and Y. Kong, *ChemCatChem*, 2017, **9**, 1708–1715.
156. W. Miao, Y. Liu, X. Chen, Y. Zhao and S. Mao, *Carbon*, 2020, **159**, 461–470.
157. B. Yue, Q. Li, H. Iwai, T. Kako and J. Ye, *Sci. Technol. Adv. Mater.*, 2011, **12**, 034401.
158. M. Wang, P. Guo, Y. Zhang, C. Lv, T. Liu, T. Chai, Y. Xie, Y. Wang and T. Zhu, *J. Hazard. Mater.*, 2018, **349**, 224–233.
159. Y. Wang, S. Zhao, Y. Zhang, J. Fang, Y. Zhou, S. Yuan, C. Zhang and W. Chen, *Appl. Surf. Sci.*, 2018, **440**, 258–265.
160. P. Deng, L. Shi, H. Wang and W. Qi, *Colloids Surf., A*, 2020, 125023.
161. X. Qu, S. Hu, J. Bai, P. Li, G. Lu and X. Kang, *New J. Chem.*, 2018, **42**, 4998–5004.
162. L.-L. Feng, Y. Zou, C. Li, S. Gao, L.-J. Zhou, Q. Sun, M. Fan, H. Wang, D. Wang and G.-D. Li, *Int. J. Hydrogen Energy*, 2014, **39**, 15373–15379.
163. H.-B. Fang, X.-H. Zhang, J. Wu, N. Li, Y.-Z. Zheng and X. Tao, *Appl. Catal., B*, 2018, **225**, 397–405.
164. J. Feng, D. Zhang, H. Zhou, M. Pi, X. Wang and S. Chen, *ACS Sustainable Chem. Eng.*, 2018, **6**, 6342–6349.
165. G. Zhang, M. Zhang, X. Ye, X. Qiu, S. Lin and X. Wang, *Adv. Mater.*, 2014, **26**, 805–809.
166. G. Dong, K. Zhao and L. Zhang, *Chem. Commun.*, 2012, **48**, 6178–6180.
167. Z. Zhang, D. Jiang, D. Li, M. He and M. Chen, *Appl. Catal., B*, 2016, **183**, 113–123.
168. R. Hao, G. Wang, C. Jiang, H. Tang and Q. Xu, *Appl. Surf. Sci.*, 2017, **411**, 400–410.
169. J.-X. Sun, Y.-P. Yuan, L.-G. Qiu, X. Jiang, A.-J. Xie, Y.-H. Shen and J.-F. Zhu, *Dalton Trans.*, 2012, **41**, 6756–6763.
170. L. Huang, H. Xu, R. Zhang, X. Cheng, J. Xia, Y. Xu and H. Li, *Appl. Surf. Sci.*, 2013, **283**, 25–32.
171. B. Tao and Z. Yan, *J. Colloid Interface Sci.*, 2016, **480**, 118–125.
172. K. C. Christoforidis, T. Montini, E. Bontempi, S. Zafeiratos, J. J. D. Jaén and P. Fornasiero, *Appl. Catal., B*, 2016, **187**, 171–180.

173. W.-K. Jo and T. S. Natarajan, *Chem. Eng. J.*, 2015, **281**, 549–565.
174. Z. Tong, D. Yang, T. Xiao, Y. Tian and Z. Jiang, *Chem. Eng. J.*, 2015, **260**, 117–125.
175. G. Li, X. Nie, J. Chen, Q. Jiang, T. An, P. K. Wong, H. Zhang, H. Zhao and H. Yamashita, *Water Res.*, 2015, **86**, 17–24.
176. K. Vignesh, S. Kang, B. S. Kwak and M. Kang, *Sep. Purif. Technol.*, 2015, **147**, 257–265.
177. Y. Li, L. Fang, R. Jin, Y. Yang, X. Fang, Y. Xing and S. Song, *Nanoscale*, 2015, **7**, 758–764.
178. C. Pan, J. Xu, Y. Wang, D. Li and Y. Zhu, *Adv. Funct. Mater.*, 2012, **22**, 1518–1524.
179. Z. Liang, S. Yang, X. Wang, H. Cui, X. Wang and J. Tian, *Appl. Catal., B*, 2020, 119114.
180. J. Sun, S. Yang, Z. Liang, X. Liu, P. Qiu, H. Cui and J. Tian, *J. Colloid Interface Sci.*, 2020, **567**, 300–307.
181. Y. Wang, Y. Zhang, S. Zhao, Z. Huang, W. Chen, Y. Zhou, X. Lv and S. Yuan, *Appl. Catal., B*, 2019, **248**, 44–53.
182. J. Xu, Y. Qi, C. Wang and L. Wang, *Appl. Catal., B*, 2019, **241**, 178–186.
183. J. Xu, Y. Qi, W. Wang and L. Wang, *Int. J. Hydrogen Energy*, 2019, **44**, 4114–4122.
184. Y. Tan, Z. Shu, J. Zhou, T. Li, W. Wang and Z. Zhao, *Appl. Catal., B*, 2018, **230**, 260–268.
185. Q.-Z. Huang, J.-C. Wang, P.-P. Wang, H.-C. Yao and Z.-J. Li, *Int. J. Hydrogen Energy*, 2017, **42**, 6683–6694.
186. L. Bi, X. Gao, Z. Ma, L. Zhang, D. Wang and T. Xie, *ChemCatChem*, 2017, **9**, 3779–3785.
187. H. Zhao, H. Zhang, G. Cui, Y. Dong, G. Wang, P. Jiang, X. Wu and N. Zhao, *Appl. Catal., B*, 2018, **225**, 284–290.
188. E. Liu, C. Jin, C. Xu, J. Fan and X. Hu, *Int. J. Hydrogen Energy*, 2018, **43**, 21355–21364.
189. J. Wang, Z. Luo, Y. Song, X. Zheng, L. Qu, J. Qian, Y. Wu, X. Wu and Z. Wu, *Chemosphere*, 2019, **221**, 554–562.
190. Z. Jiang, C. Zhu, W. Wan, K. Qian and J. Xie, *J. Mater. Chem. A*, 2016, **4**, 1806–1818.
191. K. Hu, R. Li, C. Ye, A. Wang, W. Wei, D. Hu, R. Qiu and K. Yan, *J. Cleaner Prod.*, 2020, **253**, 120055.
192. J. Lei, Y. Chen, F. Shen, L. Wang, Y. Liu and J. Zhang, *J. Alloys Compd.*, 2015, **631**, 328–334.
193. G. Song, Z. Chu, W. Jin and H. Sun, *Chin. J. Chem. Eng.*, 2015, **23**, 1326–1334.
194. H. Li, L. Zhou, L. Wang, Y. Liu, J. Lei and J. Zhang, *Phys. Chem. Chem. Phys.*, 2015, **17**, 17406–17412.
195. Y. Li, J. Wang, Y. Yang, Y. Zhang, D. He, Q. An and G. Cao, *J. Hazard. Mater.*, 2015, **292**, 79–89.
196. L. Gu, J. Wang, Z. Zou and X. Han, *J. Hazard. Mater.*, 2014, **268**, 216–223.

197. F. Guo, X. Huang, Z. Chen, H. Sun and L. Chen, *Chem. Eng. J.*, 2020, 125118.
198. H. Li, Y. Xia, Z. Liang, G. Ba and W. Hou, *ACS Appl. Energy Mater.*, 2019, **3**, 377–386.
199. Y.-R. Lin, G. V. C. Dizon, K. Yamada, C.-Y. Liu, A. Venault, H.-Y. Lin, M. Yoshida and C. Hu, *J. Colloid Interface Sci.*, 2020, **567**, 202–212.
200. F. Dong, Z. Wang, Y. Li, W.-K. Ho and S. Lee, *Environ. Sci. Technol.*, 2014, **48**, 10345–10353.
201. K.-I. Katsumata, R. Motoyoshi, N. Matsushita and K. Okada, *J. Hazard. Mater.*, 2013, **260**, 475–482.
202. Z. Zhang, J. Huang, M. Zhang, Q. Yuan and B. Dong, *Appl. Catal., B*, 2015, **163**, 298–305.
203. P. Qiu, H. Chen and F. Jiang, *RSC Adv.*, 2014, **4**, 39969–39977.
204. H.-Y. Chen, L.-G. Qiu, J.-D. Xiao, S. Ye, X. Jiang and Y.-P. Yuan, *RSC Adv.*, 2014, **4**, 22491–22496.
205. H. Liu, Z. Jin and Z. Xu, *Dalton Trans.*, 2015, **44**, 14368–14375.
206. J. Wang, Y. Chen, Y. Shen, S. Liu and Y. Zhang, *Chem. Commun.*, 2017, **53**, 2978–2981.
207. M. Solehudin, U. Sirimahachai, G. A. Ali, K. F. Chong and S. Wongnawa, *Adv. Powder Technol.*, 2020, 1891–1902.
208. Y. Wang, M. Qiao, J. Lv, G. Xu, Z. Zheng, X. Zhang and Y. Wu, *Fullerenes, Nanotubes, Carbon Nanostruct.*, 2018, **26**, 210–217.
209. Q. Liang, X. Liu, J. Wang, Y. Liu, Z. Liu, L. Tang, B. Shao, W. Zhang, S. Gong and M. Cheng, *J. Hazard. Mater.*, 2020, **401**, 123355.
210. S. Sun, J. Li, P. Song, J. Cui, Q. Yang, X. Zheng, Z. Yang and S. Liang, *Appl. Surf. Sci.*, 2020, **500**, 143985.
211. F. Dong, Z. Ni, P. Li and Z. Wu, *New J. Chem.*, 2015, **39**, 4737–4744.
212. T. Xiao, Z. Tang, Y. Yang, L. Tang, Y. Zhou and Z. Zou, *Appl. Catal., B*, 2018, **220**, 417–428.
213. X. She, J. Wu, H. Xu, J. Zhong, Y. Wang, Y. Song, K. Nie, Y. Liu, Y. Yang and M. T. F. Rodrigues, *Adv. Energy Mater.*, 2017, **7**, 1700025.
214. H. Dou, L. Chen, S. Zheng, Y. Zhang and G. Q. Xu, *Mater. Chem. Phys.*, 2018, **214**, 482–488.
215. Y. Chen, X. Liu, L. Hou, X. Guo, R. Fu and J. Sun, *Chem. Eng. J.*, 2020, **383**, 123132.
216. N. Al-Zaqri, A. Alsalme, M. Ahmed and A. Galal, *Diamond Relat. Mater.*, 2020, **109**, 108071.
217. X. Chen, X. Huang and Z. Yi, *Chem. - Eur. J.*, 2014, **20**, 17590–17596.
218. J. Zhang, J. Lv, K. Dai, Q. Liu, C. Liang and G. Zhu, *Ceram. Int.*, 2017, **43**, 1522–1529.
219. M. Wang, S. Huang, X. Pang, M. Song, C. Du and Y. Su, *Sustainable Energy Fuels*, 2019, **3**, 3422–3429.
220. Z. Liang, Y. Xia, G. Ba, H. Li, Q. Deng and W. Hou, *J. Mater. Chem. A*, 2019, **7**, 25824–25829.
221. Y.-P. Li, F.-T. Li, X.-J. Wang, J. Zhao, J.-N. Wei, Y.-J. Hao and Y. Liu, *Int. J. Hydrogen Energy*, 2017, **42**, 28327–28336.

222. H. Jing, R. Ou, H. Yu, Y. Zhao, Y. Lu, M. Huo, H. Huo and X. Wang, *Sep. Purif. Technol.*, 2021, **255**, 117646.
223. Y. Liu, A. Yuan, Y. Xiao, H. Yu and X. Dong, *Ceram. Int.*, 2020, **46**, 16157–16165.
224. J. Zhang, J. Fu, Z. Wang, B. Cheng, K. Dai and W. Ho, *J. Alloys Compd.*, 2018, **766**, 841–850.
225. T. Kanagaraj, S. Thiripuranthagan, S. M. K. Paskalis and H. Abe, *Appl. Surf. Sci.*, 2017, **426**, 1030–1045.
226. V. Hasija, P. Raizada, A. Sudhaik, P. Singh, V. K. Thakur and A. A. P. Khan, *Solid State Sci.*, 2020, **100**, 106095.
227. Z. Wang, J. Lv, J. Zhang, K. Dai and C. Liang, *Appl. Surf. Sci.*, 2018, **430**, 595–602.
228. Y. He, L. Zhang, M. Fan, X. Wang, M. L. Walbridge, Q. Nong, Y. Wu and L. Zhao, *Sol. Energy Mater. Sol. Cells*, 2015, **137**, 175–184.
229. Y. Liu, X. Zeng, X. Hu, J. Hu, Z. Wang, Y. Yin, C. Sun and X. Zhang, *Catal. Today*, 2019, **335**, 243–251.
230. Z. Fu, H. Wang, Y. Wang, S. Wang, Z. Li and Q. Sun, *Appl. Surf. Sci.*, 2020, **510**, 145494.
231. L. Xiao, T. Liu, M. Zhang, Q. Li and J. Yang, *ACS Sustainable Chem. Eng.*, 2018, **7**, 2483–2491.
232. P. Raizada, A. Sudhaik, P. Singh, P. Shandilya, V. K. Gupta, A. Hosseini-Bandegharaei and S. Agrawal, *J. Photochem. Photobiol., A*, 2019, **374**, 22–35.
233. A. Yaghoot-Nezhad, M. Moradi, M. Rostami, I. Danaee and M. R. Khosravi-Nikou, *Energy Fuels*, 2020, **34**, 13588–13605.
234. J. Lv, K. Dai, J. Zhang, L. Geng, C. Liang, Q. Liu, G. Zhu and C. Chen, *Appl. Surf. Sci.*, 2015, **358**, 377–384.
235. Y. Liu, R. Wang, Z. Yang, H. Du, Y. Jiang, C. Shen, K. Liang and A. Xu, *Chin. J. Catal.*, 2015, **36**, 2135–2144.
236. X. Zhang, X. Wang, J. Meng, Y. Liu, M. Ren, Y. Guo and Y. Yang, *Sep. Purif. Technol.*, 2020, **255**, 117693.
237. Y. Deng, L. Tang, G. Zeng, J. Wang, Y. Zhou, J. Wang, J. Tang, L. Wang and C. Feng, *J. Colloid Interface Sci.*, 2018, **509**, 219–234.
238. H. Liu, J. Liang, J. Du, Q. Gao, S. Fu, L. Li, M. Hu, F. Zhao and J. Zhou, *Colloids Surf., A*, 2020, 124668.
239. K. T. Wong, S. B. Jang, P. Saravanan, I. W. Nah, S. Park, J. Choi, C. Park, Y. Kim, Y. Yoon and M. Jang, *Appl. Surf. Sci.*, 2019, **471**, 703–713.
240. F. He, Y. Wang, J. Zhang, S. Wang, H. Zhao, P. Dong, F. Lin, Z. Tai, S. Qiao and L. Chen, *Appl. Surf. Sci.*, 2019, **495**, 143558.
241. S. Asadzadeh-Khaneghah, A. Habibi-Yangjeh and D. Seifzadeh, *J. Taiwan Inst. Chem. Eng.*, 2018, **87**, 98–111.
242. H. Zhang, W. Wu, Y. Li, Y. Wang, C. Zhang, W. Zhang, L. Wang and L. Niu, *Appl. Surf. Sci.*, 2019, **465**, 450–458.
243. J. Jia, C. Jiang, X. Zhang, P. Li, J. Xiong, Z. Zhang, T. Wu and Y. Wang, *Appl. Surf. Sci.*, 2019, **495**, 143524.
244. H. Zhang, L. Zhao, F. Geng, L.-H. Guo, B. Wan and Y. Yang, *Appl. Catal., B*, 2016, **180**, 656–662.

245. Z. Zhang, S. Lin, X. Li, H. Li and W. Cui, *RSC Adv.*, 2017, **7**, 56335–56343.
246. X. Miao, X. Yue, Z. Ji, X. Shen, H. Zhou, M. Liu, K. Xu, J. Zhu, G. Zhu and L. Kong, *Appl. Catal., B*, 2018, **227**, 459–469.
247. R. Dadigala, R. Bandi, B. R. Gangapuram and V. Guttena, *J. Photochem. Photobiol., A*, 2017, **342**, 42–52.
248. K. Li, F.-Y. Su and W.-D. Zhang, *Appl. Surf. Sci.*, 2016, **375**, 110–117.
249. Y. Su, P. Chen, F. Wang, Q. Zhang, T. Chen, Y. Wang, K. Yao, W. Lv and G. Liu, *RSC Adv.*, 2017, **7**, 34096–34103.
250. X. Zhang, H. Dong, X.-J. Sun, D.-D. Yang, J.-L. Sheng, H.-L. Tang, X.-B. Meng and F.-M. Zhang, *ACS Sustainable Chem. Eng.*, 2018, **6**, 11563–11569.
251. Y. Wang, X. Liu, J. Liu, B. Han, X. Hu, F. Yang, Z. Xu, Y. Li, S. Jia and Z. Li, *Angew. Chem.*, 2018, **130**, 5867–5873.
252. F. Wang, P. Chen, Y. Feng, Z. Xie, Y. Liu, Y. Su, Q. Zhang, Y. Wang, K. Yao and W. Lv, *Appl. Catal., B*, 2017, **207**, 103–113.
253. K. Qi, W. Lv, I. Khan and S.-Y. Liu, *Chin. J. Catal.*, 2020, **41**, 114–121.
254. S. R. Ar, H. M. Wilson, B. M. Momin, U. S. Annapure and N. Jha, *Renewable Energy*, 2020, 431–443.
255. D. Li, J. Huang, R. Li, P. Chen, D. Chen, M. Cai, H. Liu, Y. Feng, W. Lv and G. Liu, *J. Hazard. Mater.*, 2021, **401**, 123257.
256. S. Feng, T. Chen, Z. Liu, J. Shi, X. Yue and Y. Li, *Sci. Total Environ.*, 2020, **704**, 135404.
257. S. Asadzadeh-Khaneghah, A. Habibi-Yangjeh and K. Nakata, *J. Colloid Interface Sci.*, 2018, **530**, 642–657.
258. F. Wang, Y. Wang, Y. Feng, Y. Zeng, Z. Xie, Q. Zhang, Y. Su, P. Chen, Y. Liu and K. Yao, *Appl. Catal., B*, 2018, **221**, 510–520.
259. T. Qin, Z. You, H. Wang, Q. Shen, F. Zhang and H. Yang, *J. Electrochem. Soc.*, 2017, **164**, H211.
260. J. Jia, X. Zhang, C. Jiang, W. Huang and Y. Wang, *J. Alloys Compd.*, 2020, 155180.
261. W. Liu, Y. Li, F. Liu, W. Jiang, D. Zhang and J. Liang, *Water Res.*, 2019, **151**, 8–19.
262. X. Miao, Z. Ji, J. Wu, X. Shen, J. Wang, L. Kong, M. Liu and C. Song, *J. Colloid Interface Sci.*, 2017, **502**, 24–32.
263. Y. Hong, Y. Meng, G. Zhang, B. Yin, Y. Zhao, W. Shi and C. Li, *Sep. Purif. Technol.*, 2016, **171**, 229–237.
264. J. Shi, S. Feng, T. Chen and Y. Li, *J. Mater. Sci.: Mater. Electron.*, 2018, **29**, 17454–17462.
265. H. He, L. Huang, Z. Zhong and S. Tan, *Appl. Surf. Sci.*, 2018, **441**, 285–294.
266. C. Zhao, Z. Liao, W. Liu, F. Liu, J. Ye, J. Liang and Y. Li, *J. Hazard. Mater.*, 2020, **381**, 120957.
267. A. Fujishima and K. Honda, *Nature*, 1972, **238**, 37–38.
268. M. S. Nasir, G. Yang, I. Ayub, S. Wang, L. Wang, X. Wang, W. Yan, S. Peng and S. Ramakarishna, *Appl. Catal., B*, 2019, **257**, 117855.
269. C. Yang, Z. Xue, J. Qin, M. Sawangphruk, X. Zhang and R. Liu, *Appl. Catal., B*, 2019, **259**, 118094.

270. Z. Chen, T.-T. Fan, X. Yu, Q.-L. Wu, Q.-H. Zhu, L.-Z. Zhang, J.-H. Li, W.-P. Fang and X.-D. Yi, *J. Mater. Chem. A*, 2018, **6**, 15310–15319.
271. L. Li, G. B. Bodedla, Z. Liu and X. Zhu, *Appl. Surf. Sci.*, 2020, **499**, 143755.
272. J. Pan, B. Wang, Z. Dong, C. Zhao, Z. Jiang, C. Song, J. Wang, Y. Zheng and C. Li, *Int. J. Hydrogen Energy*, 2019, **44**, 19942–19952.
273. W. J. Ong, L. L. Tan, Y. H. Ng, S. T. Yong and S. P. Chai, *Chem. Rev.*, 2016, **116**, 7159–7329.
274. Z. Zhou, K. Li, W. Deng, J. Li, Y. Yan, Y. Li, X. Quan and T. Wang, *J. Hazard. Mater.*, 2020, **387**, 122023.
275. W. Wei and T. Jacob, *Phys. Rev. B*, 2013, **87**, 115431.
276. S. Pareek, S. Waheed, A. Rana, P. Sharma and S. Karak, *Nano Express*, 2020, **1**, 010057.
277. L. Shi, C. K. Lee and A. P. Willard, *ACS Cent. Sci.*, 2017, **3**, 1262–1270.
278. Y. Ren, D. Zeng and W.-J. Ong, *Chin. J. Catal.*, 2019, **40**, 289–319.
279. Z. Zhao, Y. Ma, J. Fan, Y. Xue, H. Chang, Y. Masubuchi and S. Yin, *J. Alloys Compd.*, 2018, **735**, 1297–1305.
280. L. C. Sim, J. L. Wong, C. H. Hak, J. Y. Tai, K. H. Leong and P. Saravanan, *Beilstein J. Nanotechnol.*, 2018, **9**, 353–363.
281. H. Zhang, X. Han, H. Yu, Y. Zou and X. Dong, *Sep. Purif. Technol.*, 2019, **226**, 128–137.
282. C. Li, S. Yu, X. Zhang, Y. Wang, C. Liu, G. Chen and H. Dong, *J. Colloid Interface Sci.*, 2019, **538**, 462–473.
283. H. Katsumata, F. Higashi, Y. Kobayashi, I. Tateishi, M. Furukawa and S. Kaneco, *Sci. Rep.*, 2019, **9**, 14873.
284. H. Wang, Y. Li, C. Li, K. Deng, Z. Wang, Y. Xu, X. Li, H. Xue and L. Wang, *J. Mater. Chem. A*, 2019, **7**, 801–805.
285. S. Lu, K. Eid, D. Ge, J. Guo, L. Wang, H. Wang and H. Gu, *Nanoscale*, 2017, **9**, 1033–1039.
286. K. Eid, H. Wang, V. Malgras, S. M. Alshehri, T. Ahamad, Y. Yamauchi and L. Wang, *J. Electroanal. Chem.*, 2016, **779**, 250–255.
287. K. Eid, H. Wang, V. Malgras, Z. A. Alothman, Y. Yamauchi and L. Wang, *J. Mater. Chem. C*, 2015, **119**, 19947–19953.
288. K. Eid, H. Wang, P. He, K. Wang, T. Ahamad, S. M. Alshehri, Y. Yamauchi and L. Wang, *Nanoscale*, 2015, **7**, 16860–16866.
289. H. Wang, S. Yin, K. Eid, Y. Li, Y. Xu, X. Li, H. Xue and L. Wang, *ACS Sustainable Chem. Eng.*, 2018, **6**, 11768–11774.
290. H. Zhang, H. Wang, K. Eid and L. Wang, *Part. Part. Syst. Charact.*, 2015, **32**, 863–868.
291. M. M. Abualrejal, K. Eid, R. Tian, L. Liu, H. Chen, A. M. Abdullah and Z. Wang, *Chem. Sci.*, 2019, **10**, 7591–7599.
292. M. M. Abualrejal, K. Eid, A. M. Abdullah, A. A. Numan, H. Chen, H. Zhang and Z. Wang, *Microchim. Acta*, 2020, **187**, 1–13.
293. C. Wei, H. Wang, K. Eid, J. Kim, J. H. Kim, Z. A. Alothman, Y. Yamauchi and L. Wang, *Chem. - Eur. J.*, 2017, **23**, 637–643.
294. H. I. Abdu, K. Eid, A. M. Abdullah and X. Lu, *Data Brief*, 2020, **30**, 105520.

295. H. Idris Abdu, K. Eid, A. M. Abdullah, M. H. Sliem, A. Elzatahry and X. Lu, *Green Chem.*, 2020, **22**, 5437–5446.
296. X. Xu, T. Yang, Q. Zhang, W. Xia, Z. Ding, K. Eid, A. M. Abdullah, M. S. A. Hossain, S. Zhang and J. Tang, *Chem. Eng. J.*, 2020, **390**, 124493.
297. Y. Ibrahim, A. Mohamed, A. M. Abdelgawad, K. Eid, A. M. Abdullah and A. Elzatahry, *Nanomaterials*, 2020, **10**, 1916.
298. K. Jlassi, K. Eid, M. H. Sliem, A. M. Abdullah, M. M. Chehimi and I. Krupa, *Environ. Sci. Eur.*, 2020, **32**, 1–13.
299. H. I. Abdu, K. Eid, A. M. Abdullah, Z. Han, M. H. Ibrahim, D. Shan, J. Chen, A. A. Elzatahry and X. Lu, *Renewable Energy*, 2020, **153**, 998–1004.

Subject Index